

Technische Universität Kaiserslautern  
Fachbereich Chemie

**Structure and Reactivity of Isolated  
Mononuclear and Oligonuclear Metal Complexes**

Am Fachbereich Chemie der Technischen Universität Kaiserslautern zur Erlangung des  
akademischen Grades “Doktor der Naturwissenschaften” genehmigte

Dissertation  
(D386)

vorgelegt von  
Dipl.-Chem. Fabian Menges

Betreuer: Prof. Dr. G. Niedner-Schatteburg

Tag der wissenschaftlichen Aussprache: 13.06.2013



Die vorliegende Arbeit wurde in der Zeit von September 2007 bis April 2013 im Fachbereich Chemie der Technischen Universität Kaiserslautern unter der Betreuung von Prof. Dr. G. Niedner-Schatteburg angefertigt.

Datum des Antrages auf Eröffnung des Promotionsverfahrens: 27.06.2012

Tag der wissenschaftlichen Aussprache: 13.06.2013

Promotionskommission:

Vorsitzender: Prof. Dr. W. Thiel

1. Berichterstatter: Prof. Dr. G. Niedner-Schatteburg

2. Berichterstatter: Prof. Dr. M. Gerhards





Jede Wissenschaft ist,  
unter anderem,  
ein Ordnen,  
ein Vereinfachen,  
ein Verdaulichmachen  
des Unverständlichen für den Geist.

*Hermann Hesse*



---

## Contents

<b>Chapter I: Introduction</b> .....	1
I-1: Electrospray ionization mass spectrometry and collision induced dissociation.....	3
I-2: H/D exchange of labile protons.....	4
I-3: Infrared multiple-photon dissociation (IR-MPD) spectroscopy.....	4
I-4: Estimation of activation barriers in CID processes.....	5
I-5: Reactivity of transition metal complexes .....	5
I-6: Density functional theory .....	6
I-7: Structure of the thesis.....	7
I-8: References.....	9
<b>Chapter II: Experimental and theoretical methods</b> .....	15
II-1: Experimental methods.....	15
II-2: Theoretical methods.....	29
II-3: References .....	38
<b>Chapter III: The interaction of the dipeptide carnosine with alkali metal ions studied by ion trap mass spectrometry</b> .....	41
III: Preamble.....	41
III-1: Abstract.....	41
III-2: Introduction.....	41
III-3: Experimental and theoretical methods.....	43
III-4: Results.....	46
III-5: Discussion.....	51
III-6: Conclusions.....	55
Acknowledgements .....	56
III-7: References .....	56
<b>Chapter IV: The dipeptides Carnosine, Anserine, GlyHis and HisGly and their Alkali metal complexes – influence of chain length, side groups, sequence and ion size studied with IRMPD spectroscopy, CID, DFT calculations and gas phase H/D exchange with ND<sub>3</sub></b> .....	59
IV: Preamble.....	59
IV-1: Abstract.....	59

---

IV-2: Introduction.....	60
IV-3: Methods.....	63
IV-4: Results.....	66
IV-5: Discussion.....	96
IV-6: Conclusions.....	103
IV-7: References.....	105
IV-8: Supplementary material.....	109
<b>Chapter V: Enhancement of vibrational bands derived by 2-color IR-MPD – a mechanistic study on [Carnosine-H,Zinc<sup>II</sup>]<sup>+</sup>.....</b>	<b>121</b>
V: Preamble.....	121
V-1: Abstract.....	121
V-2: Introduction.....	121
V-3: Methods.....	124
V-4: Results.....	126
V-5: Discussion.....	142
V-6: Conclusions.....	145
V-7: References.....	146
V-8: Supplementary material.....	149
<b>Chapter VI: ESI-MS studies on reaction intermediates of a ruthenium-catalyzed hydroamidation of terminal alkynes.....</b>	<b>151</b>
VI: Preamble.....	151
<b>Chapter VII: Dysprosium-based mono-, di- and tri-metallic complexes – assignment of vibrational bands utilizing IR-MPD and H/D exchange reactions.....</b>	<b>153</b>
VII: Preamble.....	153
VII-1: Abstract.....	154
VII-2: Introduction.....	155
VII-3: Methods.....	157
VII-4: Results and Discussion.....	158
VII-5: Conclusions.....	169
VII-6: References.....	171

---

<b>Chapter VIII: Ru-catalysts for transfer hydrogenation: a combined study of collision and light induced activation processes and experimental and DFT derived gas phase reactivities.....</b>	<b>173</b>
VIII: Preamble.....	173
VIII-1: Abstract.....	173
VIII-2: Introduction.....	174
VIII-3: Methods.....	184
VIII-4: Results and Discussion.....	189
VIII-5: DFT based modeling of the reaction of $[(\eta^6\text{-cymene})\text{RuCl}(\text{apypm})]^+$ catalysts with $\text{D}_2$ and $\text{D}_2\text{O}$ .....	200
VIII-6: Conclusions.....	207
VIII-7: References.....	209
VIII-8: Supplementary material.....	212
<b>Chapter IX: The <math>[(^4\text{CpCo})_2(\mu\text{-C}_2\text{Ph}_2)]</math> complex and its oxidation behavior studied with ESI-MS, IR-MPD and TD-DFT – vibrational excitation of electronic excited states.....</b>	<b>221</b>
IX: Preamble.....	221
IX-1: Abstract.....	221
IX-2: Introduction.....	222
IX-3: Methods.....	224
IX-4: Results of ESI-MS and IR-MPD on complex 2 and its reaction products.....	226
IX-5: Gauging the level of DFT theory by the help of model complex 1.....	238
IX-6: Comparison of IR-MPD spectra of $2^+$ and of its reaction products with DFT predictions	243
IX-7: Conclusions.....	249
IX-8: References.....	250
IX-8: References.....	250
IX-9: Supplementary material.....	253
<b>Chapter X: Appendix.....</b>	<b>257</b>
X-1: Documentation of data processing.....	257
<b>Chapter XI: Summary and outlook.....</b>	<b>267</b>
<b>List of publications.....</b>	<b>279</b>

<b>Danksagung</b> .....	281
<b>Curriculum Vitae</b> .....	283

## Abbreviations

<sup>4</sup> Cp	tetraisopropyl-cyclopentadiene
ADC	analog digital converter
Ans	Anserine
apypm	2-R-4-(2-pyridinyl)pyrimidine ligand
B3LYP	Becke three parameter hybrid Lee Yang Parr correlation functional
BLYP	Becke Lee Yang Parr correlation functional
bb	broadband
calc.	calculated
Carn	Carnosine
CID	collisional induced dissociation
cc	correlation consistent
COM	center of mass
CS	charge solvated
cymene	p-cymene ligand
dc bpy	2,2'-bipyridine-4,4'-dicarboxylic acid
DFM	difference frequency mixing
DZ	double zeta
ECCE	extensible computational chemistry environment
ECD	electron capture dissociation
ECP	effective core potential
eff.	Efficiency
ESI	electrospray ionization
FFT	fast Fourier transformation
Fig.	Figure
frag.	fragmentation
FT-ICR	Fourier-Transform Ion-Cyclotron-Resonance
FWHM	full width at half maximum
GGA	generalized gradient approximation
Gly	Glycine
HDX	hydrogen/deuterium exchange
HF	Hartree-Fock
His	Histidine
HSAB	hard/soft acids/bases
IR	infrared
IR-MPD	infrared multiple-photon dissociation
IVR	internal vibrational redistribution
KTA	Potassium titanil arsenate
KTP	Potassium titanil phosphate
LDA	local density approximation
MALDI	matrix assisted laser desorption ionization
MS	mass spectrometry <i>or</i> mass spectrum
MS <sup>n</sup>	mass spectra of fragments
nb	narrowband
n.o.	not observed
NR	non-relativistic
OPA	optical parametrical amplifier
OPO	optical parametrical oscillator

OS	oscillator strength
pVDZ	polarized valence double zeta
pVTZ	polarized valence triple zeta
RF	radio frequency
RRKM	Rice-Ramsperger-Kassel-Marcus
salen	2,2'-{[(2-aminoethyl)imino]bis[2,1-ethanediy]nitriloethylidyne}}bis-2-hydroxybenzoic acids
SB	salt bridge
SCF	self consistent field
sde	single and double H/D exchange per collision
se	single H/D exchange per collision
SMM	single molecule magnet
SQUID	superconducting quantum interference device
SRS	Stanford Research Systems
TD	time dependent
THF	tetrahydrofurane
TST	transition state theory
TZ	triple zeta
tren	tris(2-aminoethyl) amine
UV	ultraviolet
Vis	visible
Vol.	Volume
YAG	yttrium aluminum garnet
ZPE	zero point energy



## Chapter I: Introduction

Isolation of ionic molecular complexes and their mass determination allows for the application of a multitude of analytical methods [1-8]. Thereby one can obtain data related to geometrical and vibrational structure, reactivity, optical properties, proton affinity, binding strength and fragmentation behavior. The ions can be manipulated by collisional cooling, heating and by irradiation with photons across wide spectral ranges. They may undergo reactions, fragmentations or dissociations along sole or competing pathways, often in parallel to processes observed in solution. The main advantages of gas phase measurements are the possibilities to choose the active species e.g. by its mass to charge ratio, to exclude solvent molecules or to add a specific amount of them, to control the properties of the ensemble very precise and to compare the experimental results to high quality *ab initio* calculations.



**Scheme 1:** Liquid samples (orange ovals, top) provide for ionic complexes. Those are transferred to the gas phase (blue square) by electrospray ionization mass spectrometry. Mass selected, isolated ions can be object of different mass spectrometric techniques and density functional theory (green bubbles). Each technique and DFT calculations provide for specific data (wine red ovals). These data can be compared to each other (other arrows).

This thesis uses infrared multiple-photon dissociation (IR-MPD) spectroscopy in ion trap instruments beneath several other techniques like collision induced dissociation (CID), H/D exchange (HDX) and gas phase reactions [6, 7, 9, 10] (cf. Scheme 1). The thus obtained experimental data may lead to a structural and dynamic characterization of the investigated ionic complexes. It is imperative to compare the experimental data to quantum mechanical calculations, e.g. with density functional (DFT) theory methods [11]. This combination of experimental techniques and quantum mechanical calculations provides various informations about the molecules under study.

CID and IR-MPD can cause fragmentations of ionic complexes. Those two experimental techniques can be compared due to their relative abundances of fragment channels (cf. Scheme 1, upper ocher arrow). Differences may arise from a statistical or a non-statistical input of energy to the molecule. The efficiency of internal vibrational redistribution (IVR) processes after photon absorption determines wether IR-MPD is a statistical or a non-statistical process. DFT calculations can provide activation energies of dissociation processes (long central ocher arrow) and allow for the analysis and the assignment of vibrational modes within the IR-MPD spectra (two small ocher arrows). Furthermore, DFT calculations can derive data correlated to the basicity and the structure of ionic (metal) complexes which both affect their H/D exchange behavior (lower horizontal ocher arrow). Finally, local minima and transition states on the potential energy surface of gas phase ion – molecule reactions can be calculated by DFT (lower diagonal ocher arrow).

In the following, some mass spectrometric ion trap techniques are described alternately to the substance classes they were applied to. This approach shall clarify why a certain technique was applied to a substance class and which information can be transferred to other classes. For a deeper insight to mass spectrometric techniques, the reader is refered to established text books on mass spectrometry and to literature [12-14]. A description of experimental setups and basic equations can be found in the methods chapter of this thesis. Experimental details can be found in the individual chapters. A small overview of some substance classes is provided within this introduction, further details can be found in the corresponding chapters.

## **I-1: Electrospray ionization mass spectrometry and collision induced dissociation**

Mass spectrometry in combination with electrospray ionization is a useful technique to monitor a huge variety of charged or easy chargeable (metal containing) complexes and to study e.g. metal ion adducts of biological molecules [15, 16]. Single molecule reactions of ions with a collision gas enable to determine kinetic data. Those experiments can also provide data to elucidate single reaction steps within catalytic reactions [1]. Furthermore, liquid reaction mixtures can be monitored at different reaction states [7]. The appearance of new masses in a MS after the addition of a certain reactant to solution gives a hint to the formation of reaction intermediates. Comparison to simulated isotopic patterns allows for their assignment. Collision induced dissociation (CID) helps to elucidate the attachment behavior within the complexes. The use of isotopic labeled substances or modifications of the reactants like chain length or additional side groups is also a useful tool for the further assignment of reaction intermediates. Conclusions on the reaction mechanism can (partially) be drawn due to a systematic analysis of the observed masses [17, 18].

### **I-1.1: Mass spectrometry on peptides, proteins and enzymes**

One important field of the application of MS techniques is the characterization of (oligo)peptides, proteins and enzymes [19, 20]. The determination of the molecules mass to charge ration allows for the determination of its composition. Fragmentation techniques like CID and electron capture dissociation (ECD) offer the opportunity to assign peptide sequences [4, 6, 21, 22]. The conformation of peptide-metal complexes is important for their biological functions [23]. The position of the metal within the complex and the corresponding binding motive of the peptide-metal complex is dependent on many factors. The electronic configuration of the metal plays a crucial role regarding its charge state, its number of s, p and d electrons and its ionic radius. Those properties affect the number of metal-peptide interactions and the stability of the complex. Regarding the peptide, several characters have to be taken into account: the number and sequence of amino-acids, the acidity and basicity of the functional groups, the aliphatic or aromatic character of side-chains and the use of protective groups. Several groups are engaged in the investigation of those metal-peptide interactions and their systematization [24-40]. Two major binding motives have been identified - the salt bridge (SB) and the charge solvated (CS) type [24-26, 35, 39, 41-46]. The SB type originates from the zwitterionic form of the peptide. This form is normally not stable in the gas phase, but can be stabilized especially by doubly charged metal ions. Therefore, the metal ion is attached to a deprotonated functional group of the peptide. The CS type originates from the

canonical form of the peptide. Both binding motives can occur for singly charged metal ions complexed by (oligo)peptides.

## **I-2: H/D exchange of labile protons**

Gas phase reactions on isolated ions and especially on (oligo)peptides allow for the estimation of partial relative rate constants for H/D exchanges with e.g.  $\text{ND}_3$ ,  $\text{D}_2\text{O}$ ,  $\text{CD}_3\text{OD}$ ,  $\text{CD}_3\text{COOD}$  [3, 19, 47-50]. The exchange rate depends on the gas phase acidity of the proton/deuterium donor/acceptor groups as well as on steric constraints. Therefore, ion-molecule reactions can provide information on the ions' secondary structure [48]. Isotopic labeling techniques in solution are used for conformational studies of peptides and proteins [51, 52]. Furthermore, the combination of isotopic labeling with IR-MPD spectroscopy allows for the determination of proton binding sites due to vibrational shifts.

## **I-3: Infrared multiple-photon dissociation (IR-MPD) spectroscopy**

Furthermore, peptides provide for several well distinguishable IR active groups. This makes them also interesting objects for investigations on the IR-MPD mechanism. 1-color IR-MPD is counted among "action spectroscopy" techniques. The fragmentation of the trapped ion is the resulting action after an absorption of multiple-photons [53]. The IR-MPD absorption process is thought to be non-coherent [54, 55]. The excitation of a vibration by photon absorption with a subsequent intra-molecular vibrational redistribution [56, 57] of the absorbed energy to the bath of vibrational degrees of freedom allows for the repeated absorption of photons by one absorber [7]. This process, which is hindered in an anharmonic potential [10], circumvents the so called "ladder-climbing" from one excited vibrational state to the next. Nevertheless, the IR-MPD derived band intensities do not necessarily match the theoretical predicted IR absorption coefficients. Some bands can even disappear in the experimental spectrum [58, 59]. Furthermore, IR-MPD causes a heating of the molecules during the excitation process. The internal energy distributions of ions after laser irradiation was modeled by Oomens et al. [60]. The model is able to reproduce features of IR-MPD spectra like a broadening and red-shifting of bands.

### **I-3.1: Resonant 2-color IR-MPD**

The newly developed resonant 2-color IR-MPD technique allows partially for band specific enhancement of the overall fragmentation efficiency in metal-organic complexes [61]. This technique bases on the use of one laser with a fixed frequency (probe) at a resonant absorption of

the molecule, while the second laser is used for scanning (pump). This technique is similar to the use of a mid-IR OPO/A system combined with a CO<sub>2</sub> laser [62]. The use of a CO<sub>2</sub> laser allows for the (nonspecific) excitation of CO stretch motions and some other vibrational motions in the fingerprint region due its restriction in photon energy to CO<sub>2</sub> emission lines. Resonant 2-color IR-MPD enables to probe a mode specific excitation of bands in the CH, NH and OH stretch region (2500 – 4000 cm<sup>-1</sup>) while the second laser pumps the same/another band either in the same or the fingerprint region. Preliminary studies in our research group showed that the enhancement of bands is dependent on the probe laser frequency. No systematic study on the band specificity of the 2-color IR-MPD enhancement effect and its energy dependence has been carried out so far. The efficiency of the multiple-photon induced dissociation of ions and molecules is dependent on the photon flux of the laser pulse and also on the height of the activation barrier. One way to compare activation barriers of differently substituted molecules is the use of collision induced dissociation, another way is the use of *ab initio* calculations on the dissociation pathways.

#### **I-4: Estimation of activation barriers in CID processes**

Collision induced dissociation of catalyst precursor molecules can also provide information regarding the activation process of a catalyst [1, 63]. The control of the internal energy distribution of ions produced by electrospray ionization is crucial for several applications, like structural studies and the analysis of non-covalent complexes [2, 64, 65]. The amount of energy transferred by a collision of a neutral gas atom or molecule with an accelerated ion is dependent on several parameters: the velocity and mass of the ion and of the collision gas. The center-of-mass energy is the theoretical amount of energy that can be absorbed in such a reaction. A phenomenological  $E_{\text{COM}}^{50\%}$  value can be derived by the center of a sigmoid fit function applied to experimental data. Resulting  $E_{\text{COM}}^{50\%}$  values can be compared qualitatively or quantitatively within one group of molecules. Activation energies derived from *ab initio* calculations on the dissociation pathway of an ion can be correlated to experimental  $E_{\text{COM}}^{50\%}$  values. Substituted benzyropyridinium ions, so-called “thermometer ions”, can be used to calibrate the internal scales of the mass spectrometers fragmentation amplitudes towards appearance energies of the fragment ions [66-70].

#### **I-5: Reactivity of transition metal complexes**

The reactivity of transition metal complexes is an ongoing field of research in our group [17, 18]. Reaction intermediates and products can be formed in solution as well as in the gas phase. Gas phase reactions are in principle possible for all molecules with a sufficient vapor pressure. The use

of e.g. H<sub>2</sub>, D<sub>2</sub>, CH<sub>4</sub> and other hydrocarbons allows for the study of elementary steps in catalytic reactions [1, 71]. The study of gas phase reactions can also provide for a deeper insight into the single steps of a catalytic cycle. Relative partial rate constants for single collision reactions depend on several intrinsic coordinates of the molecules and the height of the activation barriers. The Arrhenius equation and Eyrings transition state theory (TST) allow to compare experimentally derived rate constants to activation energies or free enthalpies [72, 73]. A more generalized approach is RRKM theory named after Rice, Ramsperger, Kassel and Marcus [74-76] which enables the computation of unimolecular reaction rates from a few characteristics of the potential energy surface [77].

### **I-6: Density functional theory**

Density functional theory [78-80] is a widely used method for evaluation of several atomic and molecular properties. Approximate DFT derived expectation values are in most cases better in line with the experiment than results obtained from Hartree-Fock calculations [81]. DFT also has several advantages in the accuracy of calculations on metals, especially on transition metals [82]. Geometry optimization and calculation of harmonic vibrational frequencies can be applied to a huge range of molecules and can yield in satisfying accuracy with respect to experimental data, whereas the quality of DFT derived thermodynamic data is strongly dependent on the chosen level of theory and can show a large deviation from experimental data [11].

## I-7: Structure of the thesis

**Chapter I** provides for an introduction to the interdependency of results derived from liquid and gas phase by the use of various methods.

**Chapter II** describes the experimental and theoretical methods used in this thesis.

**Chapter III** reports on the interaction of the dipeptide carnosine with alkali metal ions. We used a combination of ion trap mass spectrometry, collision induced dissociation and density functional theory in order to derive energetic minimum isomer structures of dipeptide-metal complexes. The change of alkali ion size has a crucial effect on the binding energy of the alkali ion to the dipeptide and to the fragmentation behavior of complexes. (published in a similar version as a paper in *Zeitschrift für Physikalische Chemie* (2011), 225(5), 595-609 )

**Chapter IV** accomplishes the case study of chapter III by the use of 1- and 2-color IR-MPD spectroscopy and expands it to three other dipeptides consisting of similar mono-peptides. Furthermore, the alkali ion complexes of Carnosine, Anserine, GlyHis and HisGly are compared regarding their fragmentation behavior, their IR-MPD spectra, their structure types and their gas phase reactivity with  $\text{ND}_3$ . We figured out common binding motives of the metal-dipeptide complexes and a change of binding motives by the increase of the ion size. (publication in progress)

**Chapter V** utilizes again a metal complex of Carnosine. Its Zinc complex  $[\text{Carnosine-H,Zn}^{\text{II}}]^+$  was subject of several studies on the binding behavior in the liquid and gas phase. We provide 1- and 2-color IR-MPD spectra of this complex and compare them to preliminary studies. Furthermore, dipeptides provide for several IR active groups which allow for a systematic study of the band dependent 2-color IR-MPD enhancement effect on the fragmentation efficiency. (publication in progress)

**Chapter VI** provides for a comprehension of recent ESI-MS studies on a ruthenium-based protocol for the regio- and stereoselective catalytic hydroamidation of terminal alkynes and on mechanistic investigations of this ruthenium-catalyzed reaction. (published as separate articles in *Advanced Synthesis & Catalysis* (2008), 350(17), 2701 and in the *Journal of the American Chemical Society* (2011), 133(19), 7428-7449 )

**Chapter VII** expands the application of CID and IR-MPD experiments and DFT studies on the elucidation of gas phase structures, reaction mechanisms and rate constants of Ruthenium complexes for the catalysis of transfer hydrogenations. 2-color IR-MPD allows for the detection of dark bands, DFT allows for the qualitative comparison of experimentally derived rate constants with transition state theory.

**Chapter VIII** makes use of IR-MPD spectroscopy on protonated and H/D exchanged dysprosium-based one-, di- and trimetallic complexes in order to assign vibrational bands and to determine the most probable protonation sites of the molecules. This chapter provides important structural data to support further calculations on the magnetic properties of those molecules. (mass spectrometric characterizations of the dysprosium-based complexes are published as separate articles in *Inorganic Chemistry* (2012), 51(18), 9589-9597 and in *Dalton Transactions* (2013), 42(7), 2445-2450 )

**Chapter IX** displays the reaction behavior of a dimeric cobalt complex in solution and investigates the influence of the reactant on the fragmentation behavior and the optical properties of the molecules. IR-MPD spectra in the mid- and near-IR region exhibit low lying electronic vibrational excitations which are compared to TD-DFT derived absorption spectra.

**Chapter X** provides additional information on data processing and comprises several reprints of publications.

**Chapter XI** summarizes the obtained findings and provides for an outlook on future experiments.



## I-8: References

1. Eller, K. and H. Schwarz, *Organometallic Chemistry in the Gas-Phase*. Chemical Reviews, 1991. **91**(6): p. 1121-1177.
2. Vekey, K., *Internal energy effects in mass spectrometry*. Journal of Mass Spectrometry, 1996. **31**(5): p. 445-463.
3. Campbell, S., et al., *Deuterium exchange reactions as a probe of biomolecule structure. Fundamental studies of gas phase H/D exchange reactions of protonated glycine oligomers with D<sub>2</sub>O, CD<sub>3</sub>OD, CD<sub>3</sub>CO<sub>2</sub>D, and ND<sub>3</sub>*. Journal of the American Chemical Society, 1995. **117**(51): p. 12840-12854.
4. Zubarev, R.A., N.L. Kelleher, and F.W. McLafferty, *Electron Capture Dissociation of Multiply Charged Protein Cations. A Nonergodic Process*. Journal of the American Chemical Society, 1998. **120**(13): p. 3265-3266.
5. Drahos, L. and K. Vekey, *MassKinetics: a theoretical model of mass spectra incorporating physical processes, reaction kinetics and mathematical descriptions*. Journal of Mass Spectrometry, 2001. **36**(3): p. 237-263.
6. Sleno, L. and D.A. Volmer, *Ion activation methods for tandem mass spectrometry*. Journal of Mass Spectrometry, 2004. **39**(10): p. 1091-1112.
7. Roithova, J., *Characterization of reaction intermediates by ion spectroscopy*. Chemical Society Reviews, 2012. **41**(2): p. 547-559.
8. March, R.E., *Quadrupole ion trap mass spectrometry: a view at the turn of the century*. International Journal of Mass Spectrometry, 2000. **200**(1-3): p. 285-312.
9. Eyler, J.R., *Infrared Multiple Photon Dissociation Spectroscopy of Ions in Penning Traps*. Mass Spectrometry Reviews, 2009. **28**(3): p. 448-467.
10. Polfer, N.C., *Infrared multiple photon dissociation spectroscopy of trapped ions*. Chemical Society Reviews, 2011. **40**(5): p. 2211-2221.
11. Koch, W. and M.C. Holthausen, *A chemist's guide to density functional theory*. 2nd ed. 2001, Weinheim ; New York: Wiley-VCH. xiii, 300 p.
12. Steehler, J.K., *Introduction to Mass Spectrometry: Instrumentation, Applications, and Strategies for Data Interpretation, 4th Edition (by J. Throck Watson and O. David Sparkman)*. Journal of Chemical Education, 2009. **86**(7): p. 810.
13. Henderson, W. and J.S. McIndoe, *Mass spectrometry of inorganic, coordination, and organometallic compounds*. Inorganic Chemistry. 2005, Hoboken, NJ: J. Wiley. xx, 271 p.
14. Cole, R.B., *Electrospray ionization mass spectrometry : fundamentals, instrumentation, and applications*. 1997, New York: Wiley. xix, 577 p.
15. Fenn, J.B., et al., *Electrospray ionization for mass spectrometry of large biomolecules*. Science (New York, N.Y.), 1989. **246**(4926): p. 64-71.
16. Fenn, J.B., et al., *Electrospray ionization—principles and practice*. Mass Spectrometry Reviews, 1990. **9**(1): p. 37-70.

17. Goossen, L.J., et al., *A Practical and Effective Ruthenium Trichloride-Based Protocol for the Regio- and Stereoselective Catalytic Hydroamidation of Terminal Alkynes*. *Advanced Synthesis & Catalysis*, 2008. **350**(17): p. 2701-2707.
18. Arndt, M., et al., *Mechanistic Investigation of the Ru-Catalyzed Hydroamidation of Terminal Alkynes*. *Journal of the American Chemical Society*, 2011. **133**(19): p. 7428-7449.
19. Lifshitz, C., *A review of gas-phase H/D exchange experiments: The protonated arginine dimer and bradykinin nonapeptide systems*. *International Journal of Mass Spectrometry*, 2004. **234**(1-3): p. 63-70.
20. Kelleher, N.L. and L.M. Hicks, *Contemporary mass spectrometry for the direct detection of enzyme intermediates*. *Current Opinion in Chemical Biology*, 2005. **9**(5): p. 424-430.
21. Mitchell Wells, J. and S.A. McLuckey, *Collision-Induced Dissociation (CID) of Peptides and Proteins*, in *Methods in Enzymology*, A.L. Burlingame, Editor. 2005, Academic Press. p. 148-185.
22. Cooper, H.J., K. Håkansson, and A.G. Marshall, *The role of electron capture dissociation in biomolecular analysis*. *Mass Spectrometry Reviews*, 2005. **24**(2): p. 201-222.
23. Holm, R.H., P. Kennepohl, and E.I. Solomon, *Structural and functional aspects of metal sites in biology*. *Chemical Reviews*, 1996. **96**(7): p. 2239-2314.
24. Bouchonnet, S. and Y. Hoppilliard, *Proton and sodium ion affinities of glycine and its sodium salt in the gas phase. Ab initio calculations*. *Organic Mass Spectrometry*, 1992. **27**(2): p. 71-76.
25. Bouchonnet, S., J.P. Flament, and Y. Hoppilliard, *Desorption-ionization and in-flight fragmentation of monoalkali-glycine adducts: Plasma-desorption mass spectrometry and Ab initio calculations*. *Rapid Communications in Mass Spectrometry*, 1993. **7**(6): p. 470-476.
26. Jensen, F., *Structure and stability of complexes of glycine and glycine methyl analogs with H<sup>+</sup>, Li<sup>+</sup>, and Na<sup>+</sup>*. *Journal of the American Chemical Society*, 1992. **114**(24): p. 9533-9537.
27. Teesch, L.M. and J. Adams, *Fragmentations of Gas-Phase Complexes Between Alkali-Metal Ions and Peptides - Metal-Ion Binding to Carbonyl Oxygens and Other Neutral Functional-Groups*. *Journal of the American Chemical Society*, 1991. **113**(3): p. 812-820.
28. Baran, E.J., *Metal complexes of carnosine*. *Biochemistry-Moscow*, 2000. **65**(7): p. 789-797.
29. Solouki, T., et al., *Gas phase hydrogen deuterium exchange reactions of a model peptide: FT-ICR and computational analyses of metal induced conformational mutations*. *Journal of the American Society for Mass Spectrometry*, 2001. **12**(12): p. 1272-1285.
30. Jurchen, J.C., R.E. Cooper, and E.R. Williams, *The role of acidic residues and of sodium ion adduction on the gas-phase H/D exchange of peptides and peptide dimers*. *Journal of the American Society for Mass Spectrometry*, 2003. **14**(12): p. 1477-1487.
31. Kapota, C. and G. Ohanessian, *The low energy tautomers and conformers of the dipeptides HisGly and GlyHis and of their sodium ion complexes in the gas phase*. *Physical Chemistry Chemical Physics*, 2005. **7**(21): p. 3744-3755.
32. Pingitore, F. and C. Wesdemiotis, *Characterization of dipeptide isomers by tandem mass spectrometry of their mono- versus dilithiated complexes*. *Analytical Chemistry*, 2005. **77**(6): p. 1796-1806.

33. Polfer, N.C., et al., *Infrared fingerprint spectroscopy and theoretical studies of potassium ion tagged amino acids and peptides in the gas phase*. Journal of the American Chemical Society, 2005. **127**(23): p. 8571-8579.
34. Wang, P., et al., *The sodium ion affinities of simple di-, tri-, and tetrapeptides*. Journal of the American Society for Mass Spectrometry, 2007. **18**(3): p. 541-552.
35. Polfer, N.C., J. Oomens, and R.C. Dunbar, *Alkali metal complexes of the Dipeptides PheAla and AlaPhe : IRMPD spectroscopy*. ChemPhysChem, 2008. **9**(4): p. 579-589.
36. Balaj, O.P., et al., *Vibrational signatures of sodiated oligopeptides (GG-Na<sup>+</sup>, GGG-Na<sup>+</sup>, AA-Na<sup>+</sup> and AAA-Na<sup>+</sup>) in the gas phase*. International Journal of Mass Spectrometry, 2008. **269**(3): p. 196-209.
37. Prell, J.S., et al., *Structures of Protonated Dipeptides: The Role of Arginine in Stabilizing Salt Bridges*. Journal of the American Chemical Society, 2009. **131**(32): p. 11442-11449.
38. Prell, J.S., et al., *Role of Sequence in Salt-Bridge Formation for Alkali Metal Cationized GlyArg and ArgGly Investigated with IRMPD Spectroscopy and Theory*. Journal of the American Chemical Society, 2009. **131**(3): p. 1232-1242.
39. Dunbar, R.C., et al., *Peptide Length, Steric Effects, and Ion Solvation Govern Zwitterion Stabilization in Barium-Chelated Di- and Tripeptides*. The Journal of Physical Chemistry B, 2009. **113**(31): p. 10552-10554.
40. Menges, F., C. Riehn, and G. Niedner-Schatteburg, *The Interaction of the Dipeptide Carnosine with Alkali Metal Ions Studied by Ion Trap Mass Spectrometry*. Zeitschrift Fur Physikalische Chemie-International Journal of Research in Physical Chemistry & Chemical Physics, 2011. **225**(5): p. 595-609.
41. Bertrán, J., L. Rodríguez-Santiago, and M. Sodupe, *The Different Nature of Bonding in Cu<sup>+</sup>-Glycine and Cu<sup>2+</sup>-Glycine*. The Journal of Physical Chemistry B, 1999. **103**(12): p. 2310-2317.
42. Corral, I., et al., *An Experimental and Theoretical Investigation of Gas-Phase Reactions of Ca<sup>2+</sup> with Glycine*. Chemistry – A European Journal, 2006. **12**(26): p. 6787-6796.
43. Forbes, M.W., et al., *Infrared spectroscopy of arginine cation complexes: Direct observation of gas-phase zwitterions*. Journal of Physical Chemistry A, 2007. **111**(46): p. 11759-11770.
44. Dunbar, R.C., et al., *Conformation Switching in Gas-Phase Complexes of Histidine with Alkaline Earth Ions*. Journal of Physical Chemistry B, 2009. **113**(30): p. 10403-10408.
45. Dunbar, R.C., et al., *Dimeric Complexes of Tryptophan with M<sup>2+</sup> Metal Ions*. Journal of Physical Chemistry A, 2009. **113**(5): p. 845-851.
46. Dunbar, R.C., J.D. Steill, and J. Oomens, *Cationized phenylalanine conformations characterized by IRMPD and computation for singly and doubly charged ions*. Physical Chemistry Chemical Physics, 2010. **12**(41): p. 13383-13393.
47. Campbell, S., et al., *Structural And Energetic Constraints On Gas-Phase Hydrogen-Deuterium Exchange-Reactions Of Protonated Peptides With D<sub>2</sub>O, CD<sub>3</sub>OD, CD<sub>3</sub>CO<sub>2</sub>D, and ND<sub>3</sub>*. Journal of the American Chemical Society, 1994. **116**(21): p. 9765-9766.
48. Green, M.K. and C.B. Lebrilla, *Ion-molecule reactions as probes of gas-phase structures of peptides and proteins*. Mass Spectrometry Reviews, 1997. **16**(2): p. 53-71.

49. Evans, S.E., N. Lueck, and E.M. Marzluff, *Gas phase hydrogen/deuterium exchange of proteins in an ion trap mass spectrometer*. International Journal of Mass Spectrometry, 2003. **222**(1-3): p. 175-187.
50. Freitas, M.A. and A.G. Marshall, *Rate and extent of gas-phase hydrogen/deuterium exchange of bradykinins: evidence for peptide zwitterions in the gas phase*. International Journal of Mass Spectrometry, 1999. **182**: p. 221-231.
51. Katta, V. and B.T. Chait, *Conformational-Changes in Proteins Probed by Hydrogen-Exchange Electrospray-Ionization Mass-Spectrometry*. Rapid Communications in Mass Spectrometry, 1991. **5**(4): p. 214-217.
52. Katta, V. and B.T. Chait, *Hydrogen-Deuterium Exchange Electrospray-Ionization Mass-Spectrometry - a Method for Probing Protein Conformational-Changes in Solution*. Journal of the American Chemical Society, 1993. **115**(14): p. 6317-6321.
53. Chin, S.L., *Multiphoton Ionization of Molecules*. Physical Review A, 1971. **4**(3): p. 992.
54. Bagratashvili, V.N., et al., *Multiple Photon Infrared Laser Photophysics and Photochemistry*. 1985.
55. Lupo, D.W. and M. Quack, *IR-Laser Photochemistry*. Chemical Reviews, 1987. **87**(1): p. 181-216.
56. Fung, Y.M.E., et al., *Facile disulfide bond cleavage in gaseous peptide and protein cations by ultraviolet photodissociation at 157 nm*. Angewandte Chemie-International Edition, 2005. **44**(39): p. 6399-6403.
57. Grant, E.R., et al., *Is Multiphoton Dissociation of Molecules a Statistical Thermal Process*. Physical Review Letters, 1978. **40**(2): p. 115-118.
58. Schroeder, D., et al., *Dissociation routes of protonated toluene probed by infrared spectroscopy in the gas phase*. Journal of Physical Chemistry A, 2006. **110**(27): p. 8346-8353.
59. Simon, A., et al., *Infrared spectroscopy of  $XFeC_{24}H_{12}^+$  ( $X = C_5H_5, C_5(CH_3)_5$ ) complexes in the gas phase: Experimental and computational studies of astrophysical interest*. Journal of Physical Chemistry A, 2008. **112**(37): p. 8551-8560.
60. Oomens, J., et al., *Gas-phase infrared multiple photon dissociation spectroscopy of mass-selected molecular ions*. International Journal of Mass Spectrometry, 2006. **254**(1-2): p. 1-19.
61. Nosenko, Y., et al., *Identification by two-color IR dissociation spectroscopy of Hoogsteen-type binding in a metalated nucleobase pair mimic*. Phys. Chem. Chem. Phys., accepted.
62. Altinay, G. and R.B. Metz, *Comparison of IRMPD, Ar-tagging and IRLAPS for vibrational spectroscopy of  $Ag^+(CH_3OH)$* . International Journal of Mass Spectrometry, 2010. **297**(1-3): p. 41-45.
63. Schroder, D., S. Shaik, and H. Schwarz, *Two-state reactivity as a new concept in organometallic chemistry*. Accounts of Chemical Research, 2000. **33**(3): p. 139-145.
64. Gabelica, V. and E. De Pauw, *Internal energy and fragmentation of ions produced in electrospray sources*. Mass Spectrometry Reviews, 2005. **24**(4): p. 566-587.
65. Naban-Maillet, J., et al., *Internal energy distribution in electrospray ionization*. Journal of Mass Spectrometry, 2005. **40**(1): p. 1-8.

66. Zins, E.L., et al., *Theoretical and experimental study of tropylium formation from substituted benzylpyridinium species*. Journal of Mass Spectrometry, 2009. **44**(1): p. 12-17.
67. Zins, E.L., et al., *Investigations of the fragmentation pathways of benzylpyridinium ions under ESI/MS conditions*. Journal of Mass Spectrometry, 2009. **44**(12): p. 1668-1675.
68. Barylyuk, K.V., et al., *Fragmentation of Benzylpyridinium "Thermometer" Ions and Its Effect on the Accuracy of Internal Energy Calibration*. Journal of the American Society for Mass Spectrometry, 2010. **21**(1): p. 172-177.
69. Zins, E.L., C. Pepe, and D. Schroder, *Energy-dependent dissociation of benzylpyridinium ions in an ion-trap mass spectrometer*. Journal of Mass Spectrometry, 2010. **45**(11): p. 1253-1260.
70. Shen, J., R.C. Dunbar, and G.A. Olah, *Gas-Phase Benzyl Cations from Toluene Precursors*. Journal of the American Chemical Society, 1974. **96**(19): p. 6227-6229.
71. Böhme, D.K. and H. Schwarz, *Gas-Phase Catalysis by Atomic and Cluster Metal Ions: The Ultimate Single-Site Catalysts*. Angewandte Chemie International Edition, 2005. **44**(16): p. 2336-2354.
72. Arrhenius, S., *Zeitschrift für Physikalische Chemie*, 1889. **4**: p. 231-234.
73. Eyring, H. and M. Polanyi, *Concerning simple gas reactions*. *Zeitschrift für Physikalische Chemie B*, 1931. **12**(4): p. 279-311.
74. Rice, O.K. and H.C. Ramsperger, *Theories of Unimolecular Gas Reactions at Low Pressures*. Journal of the American Chemical Society, 1927. **49**(7): p. 1617-1629.
75. Kassel, L.S., *Studies in Homogeneous Gas Reactions. I*. The Journal of Physical Chemistry, 1927. **32**(2): p. 225-242.
76. Marcus, R.A., *Unimolecular Dissociations and Free Radical Recombination Reactions*. Journal of Chemical Physics, 1952. **20**(3): p. 359-364.
77. Baer, T. and W.L. Hase, *Unimolecular reaction dynamics : theory and experiments*. The international series of monographs on chemistry. 1996, New York: Oxford University Press. vi, 438 p.
78. Hohenberg, P. and W. Kohn, *Inhomogeneous Electron Gas*. Physical Review B, 1964. **136**(3B): p. B864-&.
79. Kohn, W. and L.J. Sham, *Self-Consistent Equations Including Exchange and Correlation Effects*. Physical Review, 1965. **140**(4A): p. 1133-&.
80. Becke, A.D., *Density-Functional Thermochemistry .3. The Role of Exact Exchange*. Journal of Chemical Physics, 1993. **98**(7): p. 5648-5652.
81. Ziegler, T., *Approximate density functional theory as a practical tool in molecular energetics and dynamics*. Chemical Reviews, 1991. **91**(5): p. 651-667.
82. Cramer, C.J. and D.G. Truhlar, *Density functional theory for transition metals and transition metal chemistry*. Physical Chemistry Chemical Physics, 2009. **11**(46): p. 10757-10816.



## Chapter II: Experimental and theoretical methods

### II-1: Experimental methods

#### II-1.1: Electrospray ionization

Electrospray ionization (ESI) and matrix assisted laser desorption and ionization (MALDI) allow for the transfer of peptides and biomolecules to the gas phase (almost) without fragmentation of the molecules [3-6]. The combination of these soft ionization methods with mass spectrometry has enabled substantial progress in the characterization of macromolecules and biopolymers like proteins and nucleic acids. ESI has also been proved to be applicable for the characterization of inorganic metal compounds and for the monitoring of reaction solutions.

The basic principle of the electrospray process is to inject a solution of the molecules in a (mostly) polar solvent through a small capillary while a constant flow of nitrogen (nebulizer gas) is applied around the opening of the capillary (cf. Fig. 1). The nitrogen gas flow leads to a disruption of the formed droplets leading to a spray of small aerosolic particles. Additionally an electric field between 2 and 6 kV is applied between the spray needle and the spray shield in front of the entrance capillary of the mass spectrometer. The electrostatic field preferentially attracts ions of one polarity to the droplet surface. Around the entrance of a glass capillary a constant flow of heated nitrogen (dry gas, between 100 and 350 °C, dependent on the application) is used to evaporate solvent molecules from the droplets. The droplet diameter shrinks continuously and the surface charges are forced closer together. As soon as the Coulomb repulsion equals that of the droplet tension, the Rayleigh limit is reached and the droplets start to undergo Coulomb explosions. This process repeats itself until all solvent molecules are removed from the ions and only the bare free molecules remain. There are also different desolvation mechanism discussed in literature, like the charged residue model. A deeper examination of the electrospray process reveals that most mass spectrometric features can be explained with both methods.

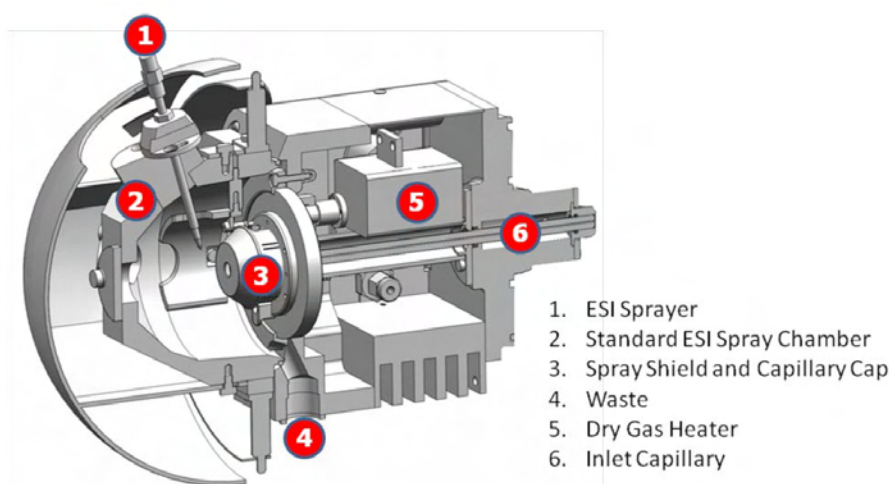


**Figure 1:** Scheme of an electrospray source, taken from [1].

The glass capillary serves as the inlet to the vacuum, reduces the flow of neutral gas molecules to the interior of the mass spectrometer and allows for a further desolvation of the ions. An electrostatic potential between the spray shield and the capillary focuses the ions to the capillary entrance. The charged micro-droplets enter the glass capillary which is metal-coated at both ends. An electrostatic potential is applied to the metal coatings of the glass capillary providing for an guidance of charged particles (dependent on ion mode of the instrument) through the glass capillary.

### II-1.2: Paul trap instruments

The 3D ion trap was developed by Paul et al. [7]. The motion of the ions in an electric field is described by the solution of the Mathieu equation [8]. Ions with a mass to charge ( $m/z$ ) ratio within a certain region of the stability diagram can be stored simultaneously (cf. Fig. 2). Ions with other  $m/z$  ratios do not have stable orbits and can be lost due to collision with the walls of the ion trap. Combinations of DC voltages with varying amplitudes and AC voltages with varying frequencies or amplitudes allow for the continuous ejection of the trapped ions (MS scan), the isolation of a certain  $m/z$  ratio and collisional induced dissociation ( $MS^n$  scan ( $n = 2, 3, 4...$ )).



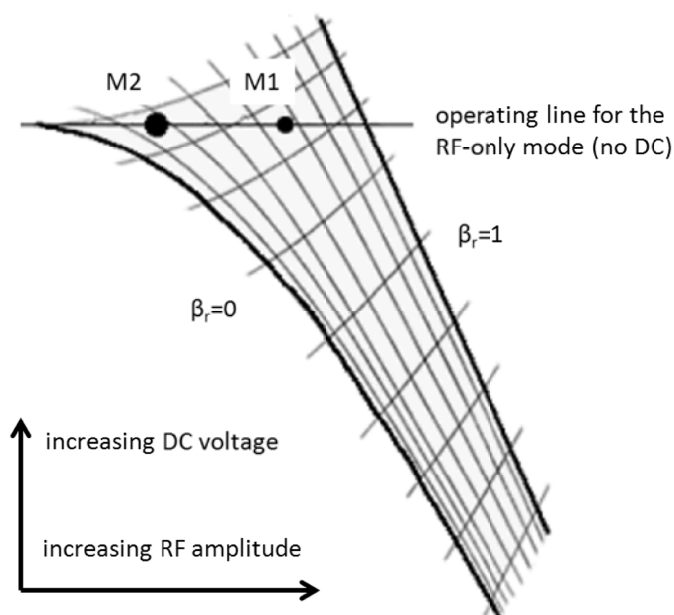


**Figure 2:** Stability diagram for ions in a Paul trap [1].

### II-1.2.1: Bruker Esquire6000 mass spectrometer

After the ions and the remaining droplets exit the capillary, they enter the CapExit region and are accelerated to skimmer (cf. Fig. 1 and 3). The pressure in this region is approximately 1 mbar and the ions undergo several collisions with neutral molecules. Dependent on the applied potential, the remaining solvent molecules are stripped of and also fragmentation of ions can occur.

Two linear octopole ion guides are installed on axis and guide the ions through two differentially pumped vacuum chambers to the ion trap. The ion beam is focused into the ion trap where the ions are accumulated and stored until detection. Inside the ion trap (cf. Fig. 3 and 5), Helium is provided with a constant pressure of ca.  $3 \times 10^{-3}$  mbar in order to slow down the ions and to allow for collision induced dissociation under the application of an accelerating potential.

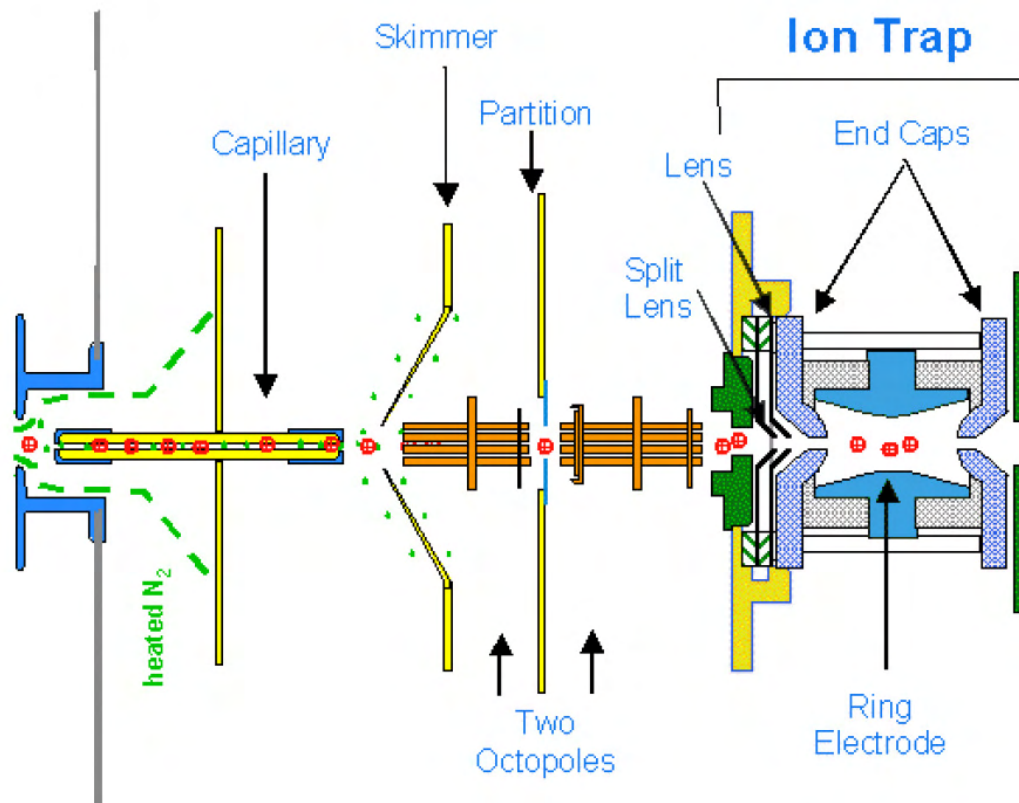


**Figure 3:** Scheme of the ion (red dots) transfer in a Bruker esquire mass spectrometer [2].

Standard measurement conditions:

Scan speed was 13000 m/z / s in normal resolution scan mode (0.3 FWHM / m/z), scan range was at least 50 to 500 m/z. Sample solutions at concentrations of appr.  $1 \times 10^{-4}$  M were continuously infused into the ESI chamber at a flow rate of 2  $\mu$ L/min using a syringe pump. Nitrogen is used as drying gas at a flow rate of 3.0 L/min at 300 °C and the solutions were sprayed at a nebulizer pressure of 4 psi with the electrospray needle held at 4.5 kV. Transfer parameters to the Paul trap of the mass spectrometer were tuned using the “target mass” option of the instrument software. The “target mass” was mostly chosen according to the m/z ratio of the selected molecule under study. Helium was used as a buffer gas with a partial pressure of about  $3 \times 10^{-3}$  mbar inside the ion trap. Bruker Esquire Control 5.3 software controlled the instrument and data analysis was performed using Bruker Data Analysis 4.0 software.

### II-1.2.2: Bruker amaZonSL mass spectrometer

After the ions and the remaining droplets exit the capillary, they enter the CapExit region and are accelerated to an ion funnel (cf. Fig. 1 and 4). The pressure in this region is approximately 1 mbar

and the ions undergo several collisions with neutral molecules. Dependent on the applied potential, the remaining solvent molecules are stripped of and also fragmentation of ions can occur. The ion funnel is installed off axis and has two functions. It focuses the ion beam and due to its off axis position, neutral molecules collide with the ring electrodes of the funnel and are pumped off. This allows for a good vacuum gradient and the use of a single turbomolecular pump which evacuates stage 3 and 4 of the mass spectrometer (cf. Fig. 4). The ion beam is focused into the ion trap where the ions are accumulated and stored until detection. Inside the ion trap (cf. Fig 4 and 5), Helium is provided with a constant pressure of ca.  $3 \times 10^{-3}$  mbar in order to slow down the ions and to allow for collision induced dissociation under the application of an accelerating potential.

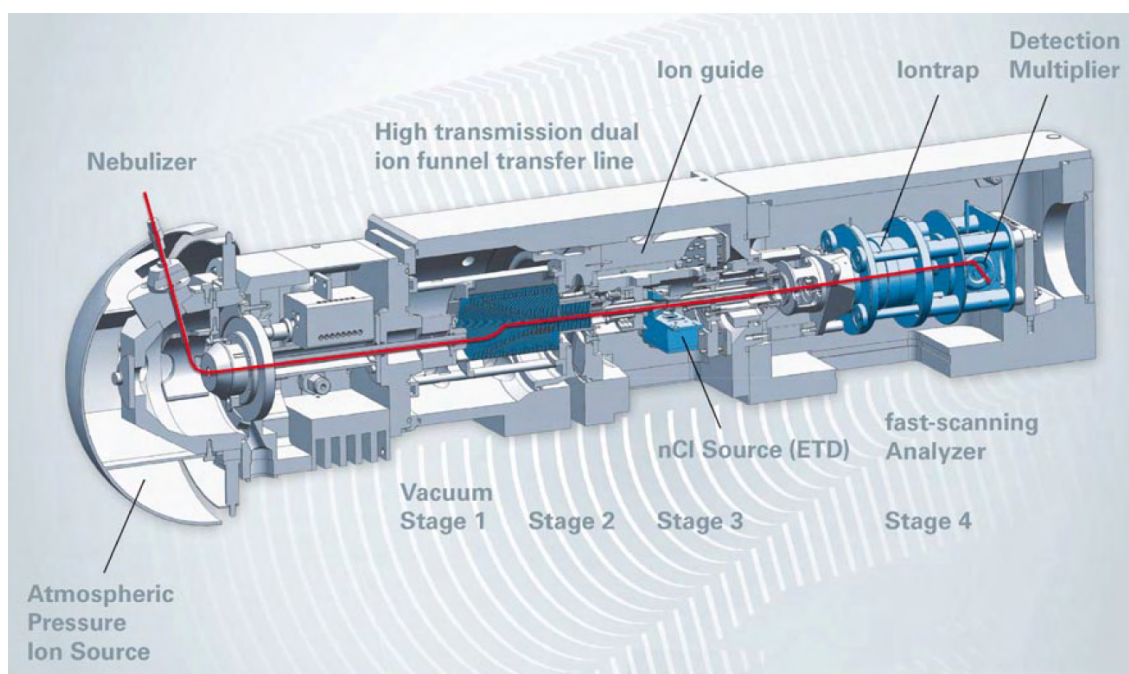


**Figure 4:** Scheme of the Bruker amaZon SL mass spectrometer [1]

Standard measurement conditions:

Scan speed was 32500 m/z / s in normal resolution scan mode (0.3 FWHM / m/z), scan range was at least 70 to 500 m/z. Sample solutions at concentrations of appr.  $1 \times 10^{-4}$  M were continuously infused into the ESI chamber at a flow rate of 2  $\mu$ L/min using a syringe pump. Nitrogen is used as drying gas at a flow rate of 3.0 L/min at 220 °C and the solutions were sprayed at a nebulizer pressure of 4 psi with the electrospray needle held at 4.5 kV. Transfer parameters to the Paul trap of the mass spectrometer were tuned using the “target mass” option of the instrument software. The “target mass” was mostly chosen according to the m/z ratio of the selected molecule under study. Helium was used as a buffer gas with a partial pressure of about  $3 \times 10^{-3}$  mbar inside the ion trap.

BrukerTrapControl 7.0 software controlled the instrument and we performed data analysis using Bruker Data Analysis 4.0 software.

### II-1.3: Modification of the Bruker amaZonSL mass spectrometer

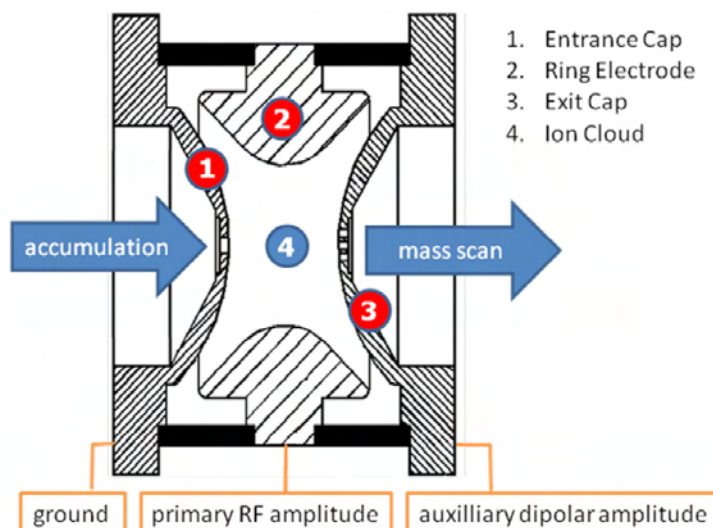


**Figure 5:** Scheme of an Paul type ion trap [1]

The ring electrode of the mass spectrometer was modified within a cooperation with the Bruker Daltonic GmbH under the supervision of C. Gebhardt. Two holes were drilled perpendicular to the surface of the ring electrode (cf. Fig. 5 and 6) in order to create an optical path through the center of the ion trap where stored ions have their highest probability of presence. The holes have a diameter of 6mm at the outer surfaces and are drilled with a constant diameter unless the last 3 mm of the material thickness is reached. Within those last 3 mm the drilling is reduced linearly to 2 mm on the inner surface of the ring electrode. The reduction of the diameter has two reasons. The inner holes serve as apertures for laser beam alignment on the one hand, on the other hand the loss of Helium atoms from inside the trap to the vacuum chamber is restricted. Furthermore a mount for two mirrors was constructed by Y. Nosenko and manufactured by Bruker Daltonic GmbH. The mount was installed at the support rods of the trap. One mirror is positioned under the ring electrode in line with the drilled holes, the second mirror adjacent to the trap in order to allow for a redirection of the laser beam after its transition through the trap back to the cover of the vacuum chamber (cf. Fig. 6).

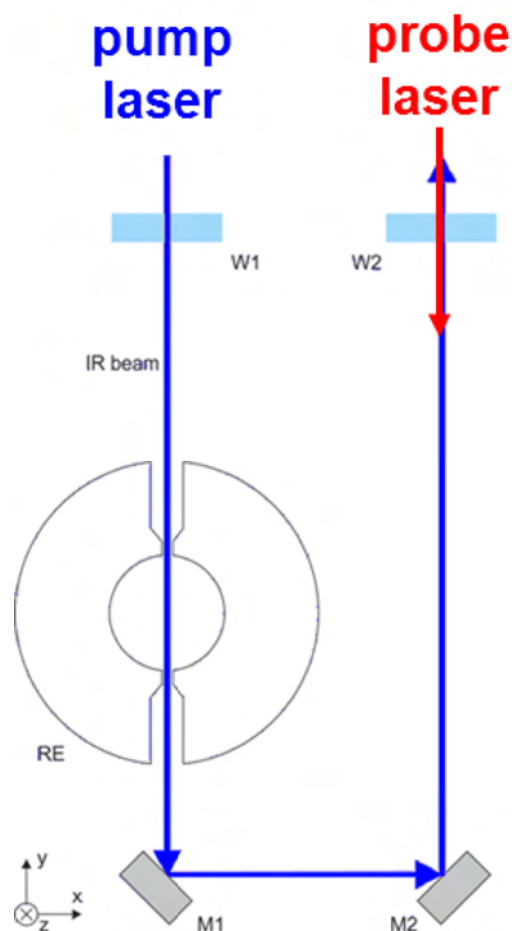


**Figure 6:** Scheme of the modified ring electrode (RE). IR laser beams of the pump and probe laser can pass the BaF<sub>2</sub> windows W1 and W2 and are reflected by the mirrors M1 and M2.

The cover of the vacuum chamber was provided with two openings for the laser beam and with a breadboard for the mount of optical elements on top of the vacuum chamber. The openings are closed with two BaF<sub>2</sub> windows on top of viton seals. Optical elements comprise two apertures for laser beam alignment, several mirrors for redirecting the beam and a plain mirror, a concave mirror respectively, on a magnet mount plate placed above the ion trap in order to allow for a quick change of the two types of mirrors. The plain mirror is needed for IR frequencies above 2200 cm<sup>-1</sup>. The laser beam in a frequency range from 2200 to 7400 cm<sup>-1</sup> is focussed by a plano-convex CaF<sub>2</sub> (f = 500 mm) lens positioned on top of the laser table breadboard. This lens has to be removed in order to access laser frequencies in the region between 800 and 2200 cm<sup>-1</sup> due to self absorption of the CaF<sub>2</sub> crystal. Laser beams in the latter region are focussed by a concave mirror (f = 150 mm) on top of the vacuum chamber.

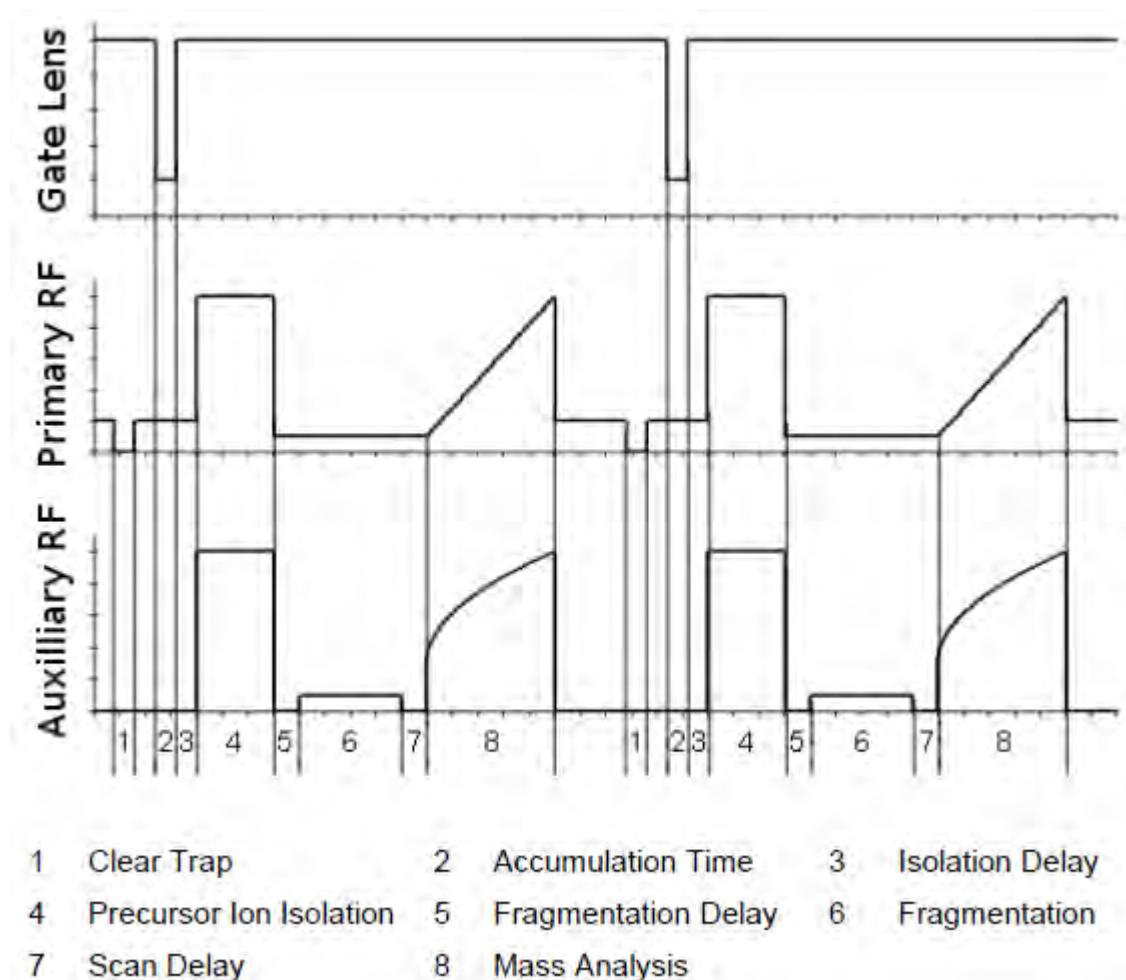


**Figure 7:** Delay scheme of the duty cycle of an amaZonSL mass spectrometer [1]

The original ion trap of the instrument was exchanged with the modified one and the capacity of the new trap was adapted to the oscillating circuit of the instrument. The instrument software was modified by Bruker Daltonics GmbH in order to allow for a synchronization of the duty cycle of the mass spectrometer to the 10 Hz trigger signal of the pump laser. A home-made connector to the auxiliary interface of the instrument allows for the transfer of the laser flashlamp sync. trigger output to the mass spectrometer trigger input. In this modification, the instrument waits for a trigger signal during the fragmentation time of an  $MS^n$  step (cf. Fig. 7, step 6) until it starts scanning the content (parent and fragment ions) of the trap. An exact number of laser pulses can be used to irradiate the ions within the cell by the change of the fragmentation time within the Bruker Trap Control software. If the instrument does not receive a trigger signal from an external source a scan is applied after 200 ms fragmentation time. The mass spectrometer software allows furthermore to send a trigger signal as soon as a certain step in the delay scheme of a measurement cycle is

reached, e.g. step 6 in Fig. 7. An electrical shutter was inserted in the beam path of the IR laser in order to allow for the exclusive irradiation of fragment ions in  $MS^{n>2}$  steps. Therefore the shutter remains closed during steps 1 to 5 and 7 to 8 unless the instrument receives a TTL pulse on the duration of the appendant  $MS^{n>2}$  step.

The remaining laser beam is directed to an energy or power meter head. The external connector to the auxiliary interface allows furthermore for the transmittance of the analog output of an power or energy meter to an analog digital converter of the mass spectrometer. The analog signal is digitized during each measurement and serves as a reference to laser frequency dependent photon flux within the measurements.

Mass spectra are processed with the help of several home-made scripts based on VisualBasic and an interface for data processing within the DataAnalysis software. An example script and a screenshot of the user interface for data processing are provided in Chapter X of this thesis. A LibreOffice Calc template file has been developed for the standardized calculation of spectra from exported raw data (cf. Chapter X).

#### **II-1.4: Penning-trap instruments**

Gas phase reactions with  $D_2$ ,  $D_2O$  and  $ND_3$  were performed with a modified Bruker Apex III FT-ICR-MS equipped with a 7.0-T magnet and an APOLLO I electrospray ion source. The standard setup and the standard operating conditions are described in the manual of the instrument [9]. The mass spectrometer was equipped with a cryogenic cooling unit, a two stage Sumitomo cold-head, which is connected to two copper tubings [10]. The copper tubings are connected to the first and the second stage of the cold head and enable a heat transport from the ICR cell to the cold-head. Three additional passive copper shields surround the actively cooled copper tubings in order to protect them from blackbody irradiation from the vacuum housing. The background pressure within the high vacuum region was approximately  $3 \times 10^{-10}$  mbar. Additionally, the instrument was equipped with a leak valve connected to the a copper tube which led the gas directly to the FT-ICR cell of the mass spectrometer. Solvents were degassed using the freeze-pump-thaw technique. The partial pressure of the reaction gas was monitored by an ion gauge. The pressure in the high vacuum region was set to a constant value between  $1 \times 10^{-9}$  and  $1 \times 10^{-8}$  mbar dependent on the reaction gas. Passivation of the surfaces of the vacuum chamber was facilitated for at least one hour.



Standard measurement conditions:

Sample solutions in water/acetonitrile 9:1 at concentrations of appr.  $1 \times 10^{-4}$  M were continuously infused into the ESI chamber at a flow rate of  $3 \mu\text{L}/\text{min}$  using a syringe pump. Nitrogen was used as drying gas with flow rate of  $10.0 \text{ L}/\text{min}$  at appr.  $300 \text{ }^\circ\text{C}$ . The solutions were sprayed at a nebulizer pressure of 25 psi and the electrospray needle was typically held at 4.0 kV.

### II-1.5: Collisional induced dissociation

During CID, the trapped ions were accelerated by an additional DC potential while they undergo collisions with Helium atoms. This leads to a transfer of kinetic energy to the internal degrees of freedoms of the ionic molecules. As soon as an ion has stored a sufficient amount of energy in its internal degrees of freedom a dissociation can occur. Those dissociations reactions mostly formed stable neutral molecules like  $\text{H}_2$ ,  $\text{H}_2\text{O}$ ,  $\text{CO}_2$  and  $\text{NH}_3$  and a ionic fragment of the precursor molecule. Besides those, also larger neutral fragments occurred, dependent on the ionic molecule and the height of dissociation barriers. A variation of the excitation magnitude allowed for the recording of CID appearance curves (cf. Fig. 8). Those were recorded with varying excitation magnitude from 0.0 to 1.0 corresponding to the internal energy scale of the mass spectrometer. Relative abundances of fragments were calculated according to:

$$I_{tot}^{fr}(E_{LAB}) = \frac{\sum_i I_i^{fr}(E_{LAB})}{\sum_i I_i^{fr}(E_{LAB}) + \sum_i I_i^p(E_{LAB})} \quad (1a)$$

and breakdown curves of parent intensities accordingly:

$$I_{tot}^p(E_{LAB}) = \frac{\sum_i I_i^p(E_{LAB})}{\sum_i I_i^{fr}(E_{LAB}) + \sum_i I_i^p(E_{LAB})} \quad (1b)$$

The amount of energy transferred by a single collision is dependent on the velocity and mass of the collision gas and the ion. The center-of-mass energy is the theoretical amount of energy that can be absorbed in such a reaction. Center of mass transferred fragmentation magnitudes  $E_{COM}$  were calculated from internal amplitudes  $E_{LAB}$  according to formular 2.  $m_{ion}$  was chosen according to the isotopically averaged mass of the molecule.

$$E_{COM} = \frac{m_{He}}{(m_{He} + m_{ion})} E_{LAB} \quad (2)$$



Thereby  $I_{tot}^{fr,p}(E_{LAB})$  converts to  $I_{tot}^{fr,p}(E_{COM})$ . Those entities may fit to analytical functions:

$$I_{fit}^{fr}(E_{COM}) = \frac{1}{(1 + e^{(E_{COM}^{50\%} - E_{COM})B})} \quad (3a)$$

$$I_{fit}^p(E_{COM}) = \frac{1}{(1 + e^{-(E_{COM}^{50\%} - E_{COM})B})} \quad (3b)$$

A phenomenological  $E_{COM}^{50\%}$  value can be derived by the center of these sigmoid fit functions

$I_{fit}^{fr,p}(E_{COM})$  (cf. Equation 3a and 3b) applied to experimental data  $I_{tot}^{fr,p}(E_{COM})$  using a least-squares criterion.  $E_{COM}^{50\%}$  is the amplitude at which the sigmoid function has reached half of its maximum,  $E_{COM}$  is the fragmentation amplitude and B describes the rise of the sigmoid curve. Alternatively,  $E_{COM}^{AE}$  values can be used to determine activation energies (AE) under consideration of the slope of the sigmoid function [11].  $E_{COM}^{AE}$  values were derived by linear extrapolation of the slope at the  $E_{COM}^{50\%}$  value to the baseline (cf. Fig. 8, lower green circle).

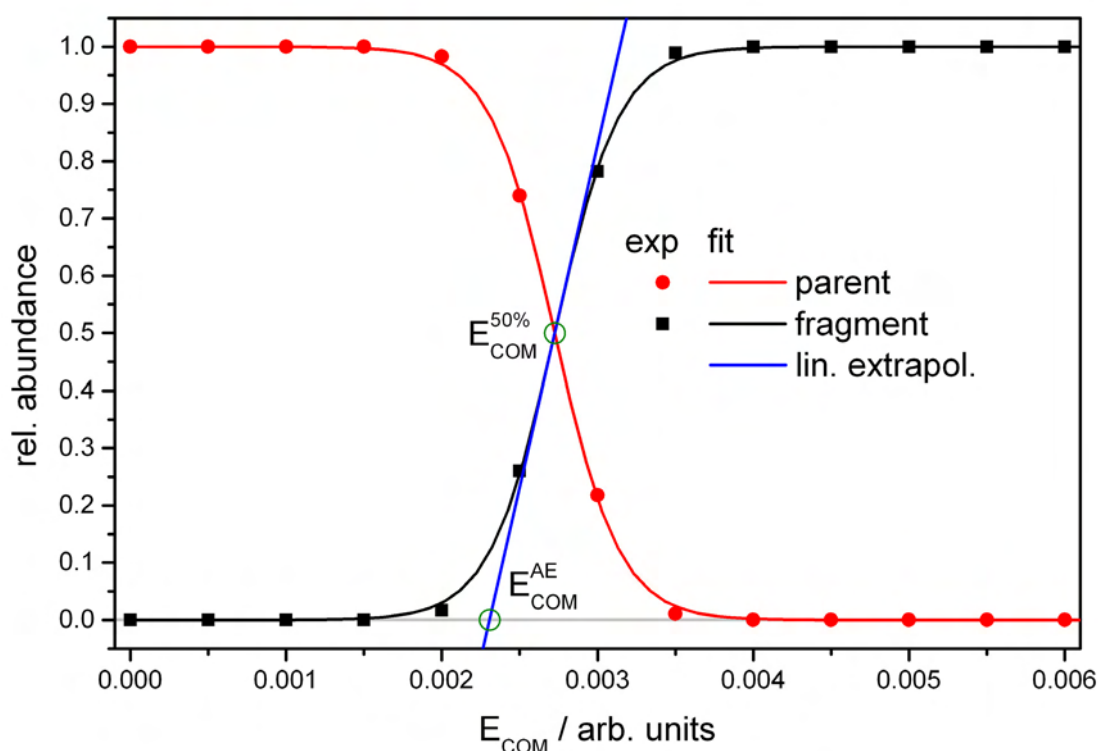


**Figure 8:** Relative abundances  $I_{tot}^p(E_{COM})$  (●) and  $I_{tot}^{fr}(E_{COM})$  (■) for the para-fluoro-benzylpyridinium parent cation and its ionic fragment. Sigmoid functions  $I_{fit}^p(E_{COM})$  (—) and  $I_{fit}^{fr}(E_{COM})$  (—) were derived from fits of the measured values. The blue line (—) was derived from the slope of the sigmoid fit function at  $E_{COM}^{50\%}$ . Positions of the  $E_{COM}^{50\%}$  and the  $E_{COM}^{AE}$  values are marked with green circles.

Resulting  $E_{\text{COM}}^{50\%}$  values can be compared qualitatively or quantitatively within one group of molecules. Activation energies derived from *ab initio* calculations on the dissociation pathway of an ion can be correlated to experimental  $E_{\text{COM}}^{50\%}$  values. Substituted benzylpyridinium ions, so-called “thermometer ions”, can be used to calibrate the internal scales of the mass spectrometers fragmentation amplitudes towards appearance energies of the fragment ions [11-15].

### II-1.6: Infrared multiple-photon dissociation

Nonlinear optical crystals like KTP provide for the generation of second-harmonic frequencies (or higher) [16], e.g. a frequency of  $\nu_{532\text{nm}} = 9394 \text{ cm}^{-1}$  from two photons with frequencies of  $\nu_{1064\text{nm}} = 18789 \text{ cm}^{-1}$  (cf. Equation 4). An optical parametrical oscillator (OPO) consists essentially of an optical resonator and a nonlinear optical crystal. The use of nonlinear optical crystals allows for the conversion of an intense laser wave of one frequency  $\nu_{532\text{nm}}$  to two output waves by means of second order nonlinear optical interaction [17] (cf. Fig. 9 and 10 and Equation 5). Those two output waves are named signal  $\nu_{1,s}$  and idler  $\nu_{1,i}$ . The wave with higher frequency is called signal. The bandwidth of the outcoming signal and idler waves can be reduced by the use of an optical grating inside the resonator of the OPO system [18]. Changing the angle of the crystals with respect to the incoming laser wave allows for a continuous tuning of the outcoming signal  $\nu_{1,s}$  and idler  $\nu_{1,i}$  waves [19]. An optical parametrical amplifier (OPA) allows for the amplification of the idler  $\nu_{1,i}$  wave from the OPO output. Therefore, the signal  $\nu_{1,s}$  wave is separated from the OPO outputs, the remaining idler  $\nu_{1,i}$  photons pass through four nonlinear optical crystals collinearly with the photons of the same wavelength  $\nu_{1064\text{nm}}$  as the pump. During the amplification process the pump wave  $\nu_{1064\text{nm}}$  is converted in a signal  $\nu_{2,s}$  and idler  $\nu_{2,i}$  wave (cf. Equation 7), where the idler  $\nu_{1,i}$  wave of the OPO serves as a seed beam (cf. Equation 6). After the pass through the crystals the remaining pump wave is separated from the signal  $\nu_{2,s}$  and idler  $\nu_{2,i}$  wave. The frequency of the resulting idler  $\nu_{2,i}$  wave is only dependent on the pump frequency and the frequency of photons of the signal  $\nu_{2,s}$  wave of the OPO process (cf. Equation 8). Both remaining beams can be used for differential frequency mixing (DFM) in an AgGaSe<sub>2</sub> crystal providing for frequencies  $\nu_{\text{DFM}}$  in the range from 2200 to 800  $\text{cm}^{-1}$  [20] (cf. Equation 9). Alternatively, the signal  $\nu_{2,s}$  wave (7400 – 4700  $\text{cm}^{-1}$ ) of the OPA process is separated by three silicium plates which are aligned in a Brewster angle for the idler  $\nu_{2,i}$  wave (4700 – 2200  $\text{cm}^{-1}$ ) of the OPA.

$$V_{532\text{nm}} = 2 V_{1064\text{nm}} \quad (4)$$

$$V_{532\text{nm}} = V_{1,s} + V_{1,i} \quad (5)$$

$$V_{1,i} = V_{2,s} \quad (6)$$

$$V_{1064\text{nm}} = V_{2,s} + V_{2,i} = V_{1,i} + V_{2,i} = V_{2,i} + V_{532\text{nm}} - V_{1,s} \quad (7)$$

$$V_{2,i} = V_{1064\text{nm}} - V_{532\text{nm}} + V_{1,s} = V_{1,s} - V_{1064\text{nm}} \quad (8)$$

$$V_{\text{DFM}} = V_{2,s} - V_{2,i} \quad (9)$$

**Table 1:** Optical elements (without mirrors) in the OPO/A laser system and their effect on polarization (v = vertical; h = horizontal) (cf. Fig. 9 for spatial arrangement).

optical element	in	out
OPO attenuator	$V_{1064\text{nm}}(\text{h})$	$V_{1064\text{nm}}(\text{v})$
SHG KTP	$V_{1064\text{nm}}(\text{v})$	$V_{532\text{nm}}(\text{v})$
OPO KTP	$V_{532\text{nm}}(\text{v})$	$V_{1,s}(\text{h})$ & $V_{1,i}(\text{v})$
dove prism and wave plate	$V_{1,s}(\text{h})$ & $V_{1,i}(\text{v})$	$V_{1,s}(\text{v})$ & $V_{1,i}(\text{h})$
Si filter 1	$V_{1,s}(\text{v})$ & $V_{1,i}(\text{h})$	$V_{1,i}(\text{h}) = V_{2,s}(\text{h})$
OPA attenuator	$V_{1064\text{nm}}(\text{h})$	$V_{1064\text{nm}}(\text{v})$
OPA KTA	$V_{2,s}(\text{h})$ & $V_{1064\text{nm}}(\text{v})$	$V_{2,s}(\text{h})$ & $V_{1064\text{nm}}(\text{v})$ & $V_{2,i}(\text{v})$
Si filter 2	$V_{2,s}(\text{h})$ & $V_{2,i}(\text{v})$	$V_{2,s}(\text{h})$ OR $V_{2,i}(\text{v})$
AgGaSe <sub>2</sub> + filter	$V_{2,s}(\text{h})$ & $V_{2,i}(\text{v})$	$V_{\text{DFM}}(\text{v})$

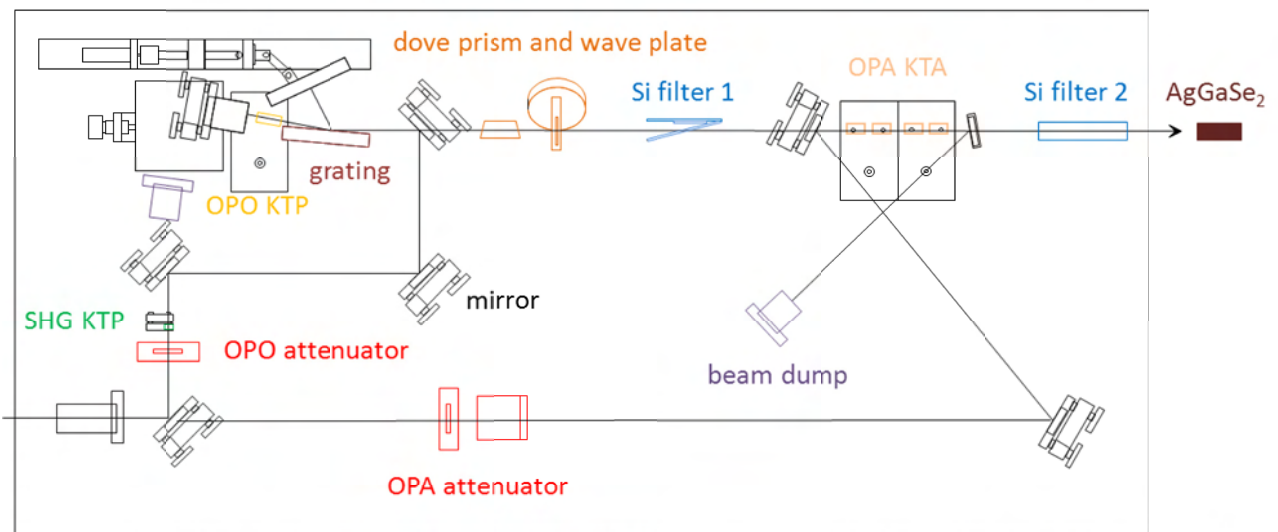


**Figure 9:** Optical setup of a LaserVision OPO/A narrowband laser system. Lines and arrows indicate the pathway of the incoming and outgoing laser beam (cf. Table 1 for assignment of beams).

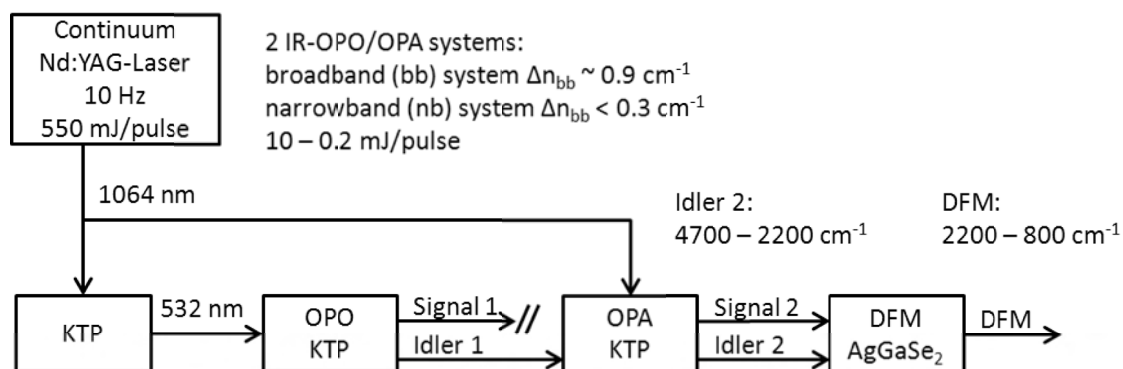


**Figure 10:** Schematic drawing of the laser setup and of the frequency conversion process in a LaserVision OPO/OPA laser system.

Standard measurement conditions:

IR-MPD measurements were performed with the Bruker amaZonSL ion trap mass spectrometer (cf. Chapter II-1.3) after its modification. Two KTP/KTA optical parametric oscillator/amplifier (OPO/A, LaserVision) systems pumped with two Q-switched 10 Hz injection seeded Nd<sup>3+</sup>:YAG lasers (PL8000, Continuum) provided for tunable IR radiation ( $\delta\nu = 0.9 \text{ cm}^{-1}$  resp.  $\delta\nu = 0.3 \text{ cm}^{-1}$ ,  $\delta t = 7 \text{ ns}$ ) in order to record vibrational spectra via the multi-photon dissociation scheme. We used the OPA idler wave ( $\leq 10 \text{ mJ/pulse}$ ) of the one system to scan spectra (pump laser) within 2800 - 3600  $\text{cm}^{-1}$ . On choice the second IR OPO/A served as probe laser, set to a selected and fixed vibrational resonance frequency. The probe laser beam was aligned counter-propagating with respect to the scanning pump laser beam. Probe pulses were delayed by 100 ns with respect to the scanning pump pulses (delay generator DG645, Stanford Research Systems). Each trapped and  $m/z$  isolated ion package was irradiated by 1-4 laser pulses (or pulse pairs in case of two-laser experiments) in order to produce sufficient fragment ions. IR spectra were recorded using Bruker chromatogram software for extracting the intensity of parent and fragment ions (three point averaging directly by BrukerTrapControl software). IR-MPD signal was evaluated corresponding to formula 1. Origin Plot Software served to apply a five point adjacent averaging for smoothing. IR frequency was calibrated by a wave meter (821B-NIR, Bristol instruments, resp. HighFinesse IRII WS7, Toptica Photonics). Laser power curve was recorded in parallel to the IR-MPD spectra through digitizing the analog output of the laser power meter by an ample ADC input of the amaZonSL mass spectrometer electronics.

## II-2: Theoretical methods

Besides the general introduction of the thesis, a short introduction to density functional theory (DFT) is given here in order to support the reader with the basic concepts of DFT calculations. Detailed introductions in the fundamentals of quantum chemistry and DFT can be found elsewhere [21-24]. In the following equations no fundamental physical constants will appear due to the introduction of atomic units. The explanation of the density functional formalism and most equations in this section accord to Ref. [25].

E. Schrödinger and W. Heisenberg [26, 27] formulated the fundamentals of quantum theory in 1926. A short time after that, L.H. Thomas [28] and E. Fermi [29] came up with the idea to express the energy  $E$  (and other properties) of a system as a functional of the electron density  $n(\mathbf{r})$ . The accuracy of those attempts were not satisfying due to a lack of appropriate molecular orbitals.

DFT is a (in principal exact theory) of the electronic structure of a system [30]. This electronic structure is based on the distribution of the electron density  $n(\mathbf{r})$ . DFT allows for the determination of the ground state energy of a system consisting of electrons and ionic nuclei using density matrices without a previous calculation of the many-electron wave function  $\Psi(r_1, r_2, \dots r_N)$ .

### II-2.1: Density functional theory

The fundamental theorems of the density functional theory formalism were formulated by P. Hohenberg and W. Kohn (1<sup>st</sup> Hohenberg-Kohn-Theorem) [31]. They showed that the properties of the ground state of a system consisting of electrons and ionic nuclei in an external field  $V_{\text{ext}}$  of the nuclei itself is exclusively determined by the electron density  $n(\mathbf{r})$ . W. Kohn received the Noble price for chemistry in 1998 due to his work on density functional theory together with J.A. Pople for the development of quantum mechanical computer programs for a broad group of users.

The electron density clearly determines the external potential and therefore the Hamiltonian operator. In turn, the Hamiltonian operator determines the wave function and therefore all properties of the molecule as expectation values of correspondent operators. The total energy is thus a functional of the density, e.g.  $E=E(n(\mathbf{r}))$ . Furthermore, P. Hohenberg and W. Kohn showed that the variational principle can be applied to density functionals (2<sup>nd</sup> Hohenberg-Kohn-Theorem). Equality for  $E(n(\mathbf{r})) \geq E_{\text{GS}}$  (GS = ground state) is achieved for  $n(\mathbf{r}) = n(\mathbf{r})_{\text{GS}}$ . This formalism became applicable to practice due to the observation of W. Kohn and L.J. Sham [32], that the minimization

of  $E(n(\mathbf{r}))$  is considerably simplified, if  $E(n(\mathbf{r}))$  is apportioned to:

$$E(n) = T_0(n) + \int d\mathbf{r} n(\mathbf{r}) (V_{eff}(\mathbf{r}) + \frac{1}{2}\varphi(\mathbf{r})) + E_{xc}(n) \quad (1)$$

$T_0$  is the kinetic energy of a system with an electron density  $n(\mathbf{r})$  without an electron-electron-interaction.  $\varphi(\mathbf{r})$  is the Coulomb potential and  $E_{xc}$  defines the exchange correlation energy. The variational principle yields 2 with the Lagrange-parameter  $\mu$ . The Lagrange parameter is associated with the condition of a constant number of particles.

$$\frac{\Delta E(n)}{\Delta n(\mathbf{r})} = \frac{\Delta T_0}{\Delta n(\mathbf{r})} + V_{ext}(\mathbf{r}) + \varphi(\mathbf{r}) + \frac{\Delta E_{xc}(n)}{\Delta n(\mathbf{r})} = \mu \quad (2)$$

Equation 2 is aimed at an interacting system of electrons and ionic nuclei. The solution of equation 3 for a system of non-interacting particles is derived by solving the Schrödinger equation 4. The density is yielded by equation 5 summarizing  $i$  orbitals with occupation numbers  $f_i$ .

$$\frac{\Delta E(n)}{\Delta n(\mathbf{r})} = \frac{\Delta T_0}{\Delta n(\mathbf{r})} + V(\mathbf{r}) = \mu \quad (3)$$

$$\left(-\frac{1}{2}\nabla^2 + V(\mathbf{r})\right)\psi_i(\mathbf{r}) = \varepsilon_i \psi_i(\mathbf{r}) \quad (4)$$

$$n(\mathbf{r}) = \sum_i f_i |\psi_i(\mathbf{r})|^2 \quad (5)$$

Equations 2 and 3 are mathematically identic, if  $V(\mathbf{r})$  is defined as in equation 6.

$$V(\mathbf{r}) = V_{ext} + \varphi(\mathbf{r}) + \frac{\Delta E_{xc}(n)}{\Delta n(\mathbf{r})} \quad (6)$$

This condition can be fulfilled within a self-consistent field (SCF) cycle. The method is analog to the self-consistent field method for solving the multi-particle Schrödinger equation. In both cases an iterative procedure is used. Additionally the value of  $E_{xc}$  is derived during density functional calculations, which can not be estimated analytically but has to be derived from numerical

integration.

A specific basis has to be chosen for solving the Schrödinger equation with the SCF method. The potential energy is derived from the distribution of electrons obtained by the basis. The Schrödinger equation of one molecule with  $m$  electrons is splitted into  $m$  one-electron equations and the Schrödinger equation for one-electron wave functions is solved numerically. This method is repeated for all electrons of the molecule in order to achieve an enhanced set of orbitals. The new set of orbitals differs normally with respect to the original basis. The method is continued as long as no significant change occurs during the iterations. The orbitals are self-consistent within this state and are accepted as the best solution for the system. This method was primarily used by D. Hartree and refined by W.A. Fock and is commonly known as Hartree-Fock-method [21].

The mathematical expression of the method for calculation of electron densities developed by W. Kohn and L.J. Sham arises from the approach of D. Hartree and W.A. Fock. The equations are quite similar and they can be solved with the same methods. The method for solving the density functional one-electron equation starts with a start density  $n$ , which reflects the initial distribution of the ionic nuclei. Most often this start density is derived from an extrapolation of atom densities. In the standard procedure the density functional equations are solved by expanding the one-electron wave functions (molecular orbitals) varying into basis sets. As soon as the Hamilton operator and the elements of the overlap matrix are calculated, the eigenvalues and the eigenvectors are determined. The orbitals are filled according to the aufbau principle (with the use of the Fermi-Dirac statistic) which leads to a new electron density distribution. This accomplishes one cycle of the SCF method.  $V(r)$  is derived by the start density distribution  $n$  and yields a new density distribution  $n'$ . This procedure is continued until  $n = n'$ .

The energy of the electron density of the ground state of a system and all derivable factors is yielded by the solution of the equation 6. In general the energetically lowest state of a given symmetry can be calculated with this method, if the variation of density is constricted to densities which are characterized by appropriate symmetry quantum numbers.

The problem within DFT is, that  $T_0$ , the one-electron interaction and the electron-electron interaction in 1 can be derived easily indeed, but  $E_{xc}$  is only defined as the difference between the sum of those terms and the exact energy.  $E_{xc}$  comprises all unknown factors.  $E_{xc}$  is relatively small for atoms and molecules, but it is not negligible. The approximation of  $E_{xc}$  plays therefore a crucial

role within DFT and is the main difference between the methods.

### II-2.2: Approximation methods

A preferably good approximation of  $E_{XC}$  is needed for DFT methods. Even the best solution of a density functional equation represents only the accuracy of the approximation of  $E_{XC}$ . There is no opportunity to enhance the accuracy of the calculations systematically. This is one of the most eminent differences with respect to Hartree-Fock methods, where in principle at least one systematic way exists for an enhancement of results.

Usually  $E_{XC}$  is splitted in an exchange and a correlation term:

$$E_{XC}(n) = E_X(n) + E_C(n) \quad (7)$$

Both functionals can belong to different types: local functionals, which are only dependent on the electron density or gradient corrected functionals which contain an additional gradient [33].

The most common approximation for  $E_{XC}$  is the local spin density approximation (LSD) (8).

$$E_{XC}(n) = \int dr n(\mathbf{r}) \varepsilon_{XC}(n\uparrow(\mathbf{r}), n\downarrow(\mathbf{r})) \quad (8)$$

$\varepsilon_{XC}(n\uparrow(\mathbf{r}), n\downarrow(\mathbf{r}))$  stands for the exchange and correlation energy per particle within a homogeneous, spin-polarized electron gas with densities  $n\uparrow$  and  $n\downarrow$  for spin  $\uparrow$  and spin  $\downarrow$ . Local density approximations are exact for systems with constant electron density, e.g. within an ideal metal. The more the electron density varies, the less exact is the method. Density distributions in atoms and molecules are highly inhomogeneous, therefore gradient corrected functionals are to be preferred at which the spin densities are expanded with a gradient.

### II-2.3: Geometry optimization

The electronic energy of molecules with an arbitrary arrangement of nuclei can be determined with the help of the Born-Oppenheimer approximation. The electronic energy of a molecule consisting of  $N$  atoms with three translational and rotational degrees of freedom each is a function of  $3N-6$  coordinates within the Born-Oppenheimer approximation. The electronic energy corresponds as potential energy to the Schrödinger equation for the nuclei and is therefore also named as potential surface. The so called stationary points of the potential surface are of special interest. All first



derivatives of the energy with respect to  $3N-6$  independent spatial degrees of freedom equal zero at those stationary points. Energetic minima are all those stationary points, at which all force constants (second derivatives of the energy with respect to the  $3N-6$  atomic coordinates) derive positive values. Transition structures are saddle points, i.e. exactly one of those second derivatives is negative. The strength of theoretical chemistry is due to the calculation of those stationary points with the help of iterative methods for gradient optimization. The method is finished as soon as the optimization has converged: possible convergence criteria are the change of energy or of the geometry between to cycles as well as the absolute value of the gradient.

#### **II-2.4: Calculation of frequencies**

Vibrational frequencies are normally derived subsequent to the geometry optimization in order to characterize the located stationary point at the potential energy surface as a minimum (number of imaginary vibrations  $i=0$ ), transition state ( $i=1$ ) or as a saddle point of higher order ( $i > 1$ ). A frequency analysis is only valid for minima or maxima at the potential energy surface, i.e. the first derivative of the energy with respect to the nuclei coordinates has to equal zero. One of the second derivatives of the energy with respect to the  $3N-6$  nuclear coordinates is negative for a transition state. The negative second derivative corresponds to a force constant for the motion along the reaction coordinate.

The second derivatives of the energy with respect to the cartesian coordinates are derived within a harmonic approach in order to calculate vibrational frequencies. The second derivatives are transformed to mass-weighted coordinates and  $3N$  eigenvectors and  $3N$  eigenvalues are determined. Rotational and translational motions of the molecule are sorted out and  $3N-6$  ( $3N-5$  for linear molecules) vibrational modes are yielded. Vibrational frequencies are calculated due to these vibrational modes. Also reduced masses, force constants and the displacement of the atom nuclei are yielded in cartesian coordinates.

#### **II-2.5: Analysis of transition states**

The analysis of transition states is mostly necessary in order to understand reaction mechanisms. A first order saddle point at the potential energy surface is searched within geometry optimization of a transition structure. This transition structure separates to adjacent energetic minima along the minimum energy reaction path. The concept of a transition structure is close to the concept of the transition state formulated by Eyring et al. [34], but not identical to it. Transition state theory defines a quasi-thermodynamic state which corresponds to a local maximum of free enthalpy along

the reaction coordinate, separating two free enthalpic minima.

Below the relation of energy  $E$  and the free enthalpy is described, whereat first the enthalpy  $H$  is defined.

$$\Delta H = \Delta U + p\Delta V = \Delta U + \Delta nRT \quad (9)$$

$\Delta U$  describes the change of the internal energy and  $\Delta n$  the change of the number of molecules during the reaction.  $\Delta U$  comprises:

$$\Delta U = \Sigma(\Delta E + \Delta ZPE + C_v\Delta T) \quad (10)$$

The zero-point energy and the thermal energy  $C_v\Delta T$  ( $C_v$  is the heat capacity at a constant volume) has to be added to the electronic energy in order to derive the internal energy  $\Delta U$  and therefore the enthalpy  $\Delta H$ . The calculation of the  $C_v\Delta T$  term succeeds due to the sum of states, whereas the calculation of the vibrational frequencies is necessary in order to derive the sum of vibrational states. The contribution of vibrations to the molecular sum of states composes of the real (non-imaginary) vibrational modes. Each of those  $3N-6$  ( $3N-5$  for linear molecules) vibrational modes has a characteristic vibrational temperature  $\theta_v$  ( $\theta_v = hv/k_B$ ;  $h$  = Planck constant;  $k_B$  = Boltzmann constant).

The Gibbs function connects the free enthalpy  $G$  to the enthalpy  $H$ :

$$\Delta G = \Delta H - T\Delta S \quad (11)$$

Free enthalpy differs from enthalpy by a term of  $-T\Delta S$ . The entropy of a molecule or of a transition state has to be comprised first due to sum of state calculations, like it was done for the heat capacity.

### II-2.6: Chosen functionals

Hartree-Fock theory comprises as well as DFT an exchange term. Becke et al. formulated functionals, at which the exchange term comprises a portion of Hartree-Fock and density functional theory while the correlation term origins from DFT.  $c$  terms stand for corresponding constants:

$$E_{XC\text{ hybrid}} = c^{HF} E_X^{HF} + c^{DFT} E_{XC}^{DFT} \quad (12)$$

The B3LYP functional consists of a three parameter hybrid method from Becke et al. and a correlation functional from C. Lee, W. Yang and R.G. Parr with local as well as non-local portions:

$$E_{XC}^{B3LYP} = E_X^{LDA} + c_0(E_X^{HF} - E_X^{LDA}) + C_X \Delta E_X^{B88} + E_C^{VWN3} + c_C(E_C^{LYP} - E_C^{VWN3}) \quad (13)$$

The parameter  $c_0$  allows for the contribution of each possible ratio of the Hartree-Fock and the local density assumption (LDA). Furthermore, the gradient correction for the LDA exchange term from Becke comprises a parameter  $c_X$ . Corrections can be drawn due to the VWN3 correlation correction term and parameter  $c_C$  allows for a LYP correlation correction.

Parameters within the B3LYP functional are:  $c_0 = 0.20$ ,  $c_X = 0.72$  and  $c_C = 0.81$ . Those were estimated by adaptation of the calculated values to experimental ionization potentials, proton affinities and the bond-dissociation energy of the elements of the first period within the G1 set of molecules.

It has to be noted, that Becke has used the correlation functional from Perdew-Wang 1991 instead of VWN3, LYP respectively, in his primary work. The fact, that the same coefficients yield good results with various functionals, reflects the appropriateness of the attempt to mix exchange terms from HF and DFT.

## II-2.7: Basis sets

The basis set is the mathematical description of the orbitals of a system. The larger a basis set is, the more exact can the description of the orbitals be as the electrons are less restricted to a given spatial distribution. This reflects that the electrons have a finite probability to exist everywhere in space within the quantum mechanical atom model.

Standard basis sets use linear combinations of gaussian like functions in order to describe the orbitals. Basis functions orient in the broadest sense at the eigenfunctions of the hydrogen atom. The exponential part consists commonly of a gaussian like function, the prefactor are the power of cartesian coordinates with respect to the particular atom. Minimal basis sets consist of the smallest possible set of basis functions for each atom. According to this the most simple way to enlarge a basis is to increase the number of basis functions for each atom. Split-valence basis sets consist of two or more basis functions for each valence orbital. Therefore, a double-zeta (DZ) basis set consists of a linear combination of two differently large functions for each molecular orbital.

Split valence basis sets allow for the change in size of the molecular orbitals but not for a change in their spatial form. For this purpose polarized basis sets are needed. Those basis sets incorporate basis functions with a higher angular momentum quantum number as needed for the determination of the ground state electron configuration within a minimal effort. Polarized basis sets add e.g. p-functions to hydrogen atoms, d-functions to second row atoms and f-functions to third row atoms. Another opportunity to enlarge orbitals is to use diffuse functions. Diffuse functions are expanded s- or d-functions. Diffuse functions are needed for calculations with electrons which are quite distant to the core, e.g. within molecules with free electron pairs, anions and other systems with a significant negative charge, systems within excited states or a low ionization energy etc.

### **II-2.8: Strategy of calculation procedure**

The Extensible Computational Chemistry Environment (ecce) was used for the setup, administration and monitoring of DFT calculations [35]. Calculations were mainly performed on a computing cluster of the department of Theoretical Chemistry (research group C. van Wüllen)

DFT [31, 32, 36, 37] calculations were performed at various levels of theory (BLYP, B3LYP, B3PB86, BPW91 [38-41], PBE1PBE [42, 43] and B97D [44]) with cc-pVDZ (C, H, N, O, Si, Cl), cc-pVTZ [45, 46] respectively, Stuttgart RSC 1997 ECP [47] and cc-pVTZ-NR (Co) [48] basis sets using the Gaussian 03 and 09 packages [49, 50]. Standard convergence criteria for energy optimization were applied. The optimized structures were checked for minima by 2<sup>nd</sup> derivative (frequency) calculations. Basis set superpositioning error (BSSE) corrections for the estimated Gibbs binding energies were determined as given in the Gaussian manual [46, 51]. Thermal energies, enthalpies and Gibbs energies were calculated at RT conditions.

## II-3: References

1. *amaZon Series User Manual*. 2009, Bruker Daltonics GmbH. p. 116.
2. *esquire series/HCT user manual, Version 1.1*. 2005, Bruker Daltonics GmbH. p. 60.
3. Fenn, J.B., et al., *Electrospray ionization for mass spectrometry of large biomolecules*. Science (New York, N.Y.), 1989. **246**(4926): p. 64-71.
4. Fenn, J.B., et al., *Electrospray ionization—principles and practice*. Mass Spectrometry Reviews, 1990. **9**(1): p. 37-70.
5. Karas, M., et al., *Matrix-assisted ultraviolet laser desorption of non-volatile compounds*. International Journal of Mass Spectrometry and Ion Processes, 1987. **78**(0): p. 53-68.
6. Cole, R.B., *Electrospray and MALDI mass spectrometry : fundamentals, instrumentation, practicalities, and biological applications*. 2nd ed. 2010, Hoboken, N.J.: Wiley. xxx, 847 p., 16 p. of plates.
7. Paul, W. and H. Steinwedel, *Ein Neues Massenspektrometer Ohne Magnetfeld*. Zeitschrift Fur Naturforschung Section a-a Journal of Physical Sciences, 1953. **8**(7): p. 448-450.
8. McLachlan, N.W., *Theory and application of Mathieu functions*. 1947, Oxford,: Clarendon Press. xii, 401 p.
9. *apex-Qe User Manual*. 2007, Bruker Daltonics, Inc. p. 104.
10. Kampschulte, H., *Entwicklung einer Tieftemperatur-FT-ICR Zelle und ihre Charakterisierung mittels Reaktionskinetiken und Synchrotron-Spektroskopie*. 2011.
11. Zins, E.L., C. Pepe, and D. Schroder, *Energy-dependent dissociation of benzylpyridinium ions in an ion-trap mass spectrometer*. Journal of Mass Spectrometry, 2010. **45**(11): p. 1253-1260.
12. Zins, E.L., et al., *Theoretical and experimental study of tropylium formation from substituted benzylpyridinium species*. Journal of Mass Spectrometry, 2009. **44**(1): p. 12-17.
13. Zins, E.L., et al., *Investigations of the fragmentation pathways of benzylpyridinium ions under ESI/MS conditions*. Journal of Mass Spectrometry, 2009. **44**(12): p. 1668-1675.
14. Barylyuk, K.V., et al., *Fragmentation of Benzylpyridinium "Thermometer" Ions and Its Effect on the Accuracy of Internal Energy Calibration*. Journal of the American Society for Mass Spectrometry, 2010. **21**(1): p. 172-177.
15. Shen, J., R.C. Dunbar, and G.A. Olah, *Gas-Phase Benzyl Cations from Toluene Precursors*. Journal of the American Chemical Society, 1974. **96**(19): p. 6227-6229.
16. Franken, P.A., et al., *Generation of Optical Harmonics*. Physical Review Letters, 1961. **7**(4): p. 118-119.
17. Giordmaine, J.A. and R.C. Miller, *Tunable Coherent Parametric Oscillation in LiNbO<sub>3</sub> at Optical Frequencies*. Physical Review Letters, 1965. **14**(24): p. 973-976.
18. Bosenberg, W.R. and D.R. Guyer, *Broadly Tunable, Single-Frequency Optical Parametric Frequency-Conversion System*. Journal of the Optical Society of America B-Optical Physics, 1993. **10**(9): p. 1716-1722.
19. Eckardt, R.C., et al., *Optical parametric oscillator frequency tuning and control*. J. Opt. Soc.

- Am. B, 1991. **8**(3): p. 646-667.
20. Gerhards, M., *High energy and narrow bandwidth mid IR nanosecond laser system*. Optics Communications, 2004. **241**(4-6): p. 493-497.
  21. Szabo, A. and N.S. Ostlund, *Modern quantum chemistry : introduction to advanced electronic structure theory*. 1996, Mineola, N.Y.: Dover Publications. xiv, 466 p.
  22. Simons, J. and J.A. Nichols, *Quantum mechanics in chemistry*. Topics in physical chemistry. 1997, New York: Oxford University Press. xxiii, 612 p.
  23. Levine, I.N., *Quantum chemistry*. 5th ed. 2000, Upper Saddle River, N.J.: Prentice Hall. x, 739 p.
  24. Koch, W. and M.C. Holthausen, eds. *A Chemist's Guide to Density Functional Theory*. 2. ed. 2001, Wiley-VCH: Weinheim. 300.
  25. Jones, R.O., *Molecular-Structures from Density Functional Calculations with Simulated Annealing*. Angewandte Chemie-International Edition, 1991. **30**(6): p. 630-640.
  26. Born, M., W. Heisenberg, and P. Jordan, *Quantum mechanics II*. Zeitschrift Fur Physik, 1926. **35**(8/9): p. 557-615.
  27. Heisenberg, W., *Quantum mechanics*. Naturwissenschaften, 1926. **14**: p. 989-994.
  28. Thomas, L.H., *The calculation of atomic fields*. Mathematical Proceedings of the Cambridge Philosophical Society, 1927. **23**(05): p. 542-548.
  29. Fermi, E., *A statistical Method for Determining some Properties of the Atoms and its Application to the Theory of the periodic Table of Elements*. Zeitschrift Fur Physik, 1928. **48**(1-2): p. 73-79.
  30. Kohn, W., A.D. Becke, and R.G. Parr, *Density functional theory of electronic structure*. Journal of Physical Chemistry, 1996. **100**(31): p. 12974-12980.
  31. Hohenberg, P. and W. Kohn, *Inhomogeneous Electron Gas*. Physical Review B, 1964. **136**(3B): p. B864-&.
  32. Kohn, W. and L.J. Sham, *Self-Consistent Equations Including Exchange and Correlation Effects*. Physical Review, 1965. **140**(4A): p. 1133-&.
  33. Foresman, J.B., A. Frisch, and Gaussian Inc., *Exploring chemistry with electronic structure methods*. 2nd ed. 1996, Pittsburgh, PA: Gaussian, Inc. li, 302 p.
  34. Eyring, H. and M. Polanyi, *Concerning simple gas reactions*. Zeitschrift Fur Physikalische Chemie-Abteilung B-Chemie Der Elementarprozesse Aufbau Der Materie, 1931. **12**(4): p. 279-311.
  35. Black, G., et al., *The extensible computational chemistry environment: A problem solving environment for high performance theoretical chemistry*. Computational Science - Iccs 2003, Pt Iv, Proceedings, 2003. **2660**: p. 122-131.
  36. Parr, R.G. and W. Yang, *Density-functional theory of atoms and molecules*. International series of monographs on chemistry. 1989, New York: Clarendon Press. x, 333 p.
  37. Salahub, D.R., et al., *The Challenge of d and f electrons : theory and computation*. ACS symposium series,. 1989, Washington, DC: American Chemical Society. x, 405 p.
  38. Becke, A.D., *Density-Functional Exchange-Energy Approximation with Correct Asymptotic-Behavior*. Physical Review A, 1988. **38**(6): p. 3098-3100.

39. Miehlich, B., et al., *Results Obtained with the Correlation-Energy Density Functionals of Becke and Lee, Yang and Parr*. Chemical Physics Letters, 1989. **157**(3): p. 200-206.
40. Becke, A.D., *Density-Functional Thermochemistry .3. The Role of Exact Exchange*. Journal of Chemical Physics, 1993. **98**(7): p. 5648-5652.
41. Perdew, J.P., *Density-Functional Approximation for the Correlation-Energy of the Inhomogeneous Electron-Gas*. Physical Review B, 1986. **33**(12): p. 8822-8824.
42. Perdew, J.P., K. Burke, and M. Ernzerhof, *Generalized gradient approximation made simple*. Physical Review Letters, 1996. **77**(18): p. 3865-3868.
43. Adamo, C. and V. Barone, *Toward reliable density functional methods without adjustable parameters: The PBE0 model*. Journal of Chemical Physics, 1999. **110**(13): p. 6158-6170.
44. Hamprecht, F.A., et al., *Development and assessment of new exchange-correlation functionals*. Journal of Chemical Physics, 1998. **109**(15): p. 6264-6271.
45. Dunning, T.H., *Gaussian-Basis Sets for Use in Correlated Molecular Calculations .1. The Atoms Boron through Neon and Hydrogen*. Journal of Chemical Physics, 1989. **90**(2): p. 1007-1023.
46. Simon, S., M. Duran, and J.J. Dannenberg, *How does basis set superposition error change the potential surfaces for hydrogen bonded dimers?* Journal of Chemical Physics, 1996. **105**(24): p. 11024-11031.
47. Dolg, M., et al., *Relativistic and correlation effects for element 105 (hahnium, Ha): a comparative study of M and MO (M = Nb, Ta, Ha) using energy-adjusted ab initio pseudopotentials*. The Journal of Physical Chemistry, 1993. **97**(22): p. 5852-5859.
48. Balabanov, N.B. and K.A. Peterson, *Systematically convergent basis sets for transition metals. I. All-electron correlation consistent basis sets for the 3d elements Sc-Zn*. Journal of Chemical Physics, 2005. **123**(6).
49. Frisch, M.J., et al., *Gaussian 03, Revision C.02*. 2003.
50. Frisch, M.J., et al., *Gaussian 09, Revision B.01*. 2009: Wallingford CT.
51. Boys, S.F. and F. Bernardi, *Calculation of Small Molecular Interactions by Differences of Separate Total Energies - Some Procedures with Reduced Errors*. Molecular Physics, 1970. **19**(4): p. 553-&.





## **Chapter III: The interaction of the dipeptide carnosine with alkali metal ions studied by ion trap mass spectrometry**

### **III: Preamble**

This chapter - in a slightly different version - has been accepted for publication by the *Zeitschrift für Physikalische Chemie - International Journal of Research in Physical Chemistry & Chemical Physics* with the title: "The Interaction of the Dipeptide Carnosine with Alkali Metal Ions Studied by Ion Trap Mass Spectrometry" within the special issue dedicated to Bernd Brutschy on the occasion of his 65<sup>th</sup> birthday. Measurements, data evaluations, structural and energetic calculations were done by myself. The basic manuscript was mainly written by myself and subsequently modified by Christoph Riehn and Gereon Niedner-Schatteburg.

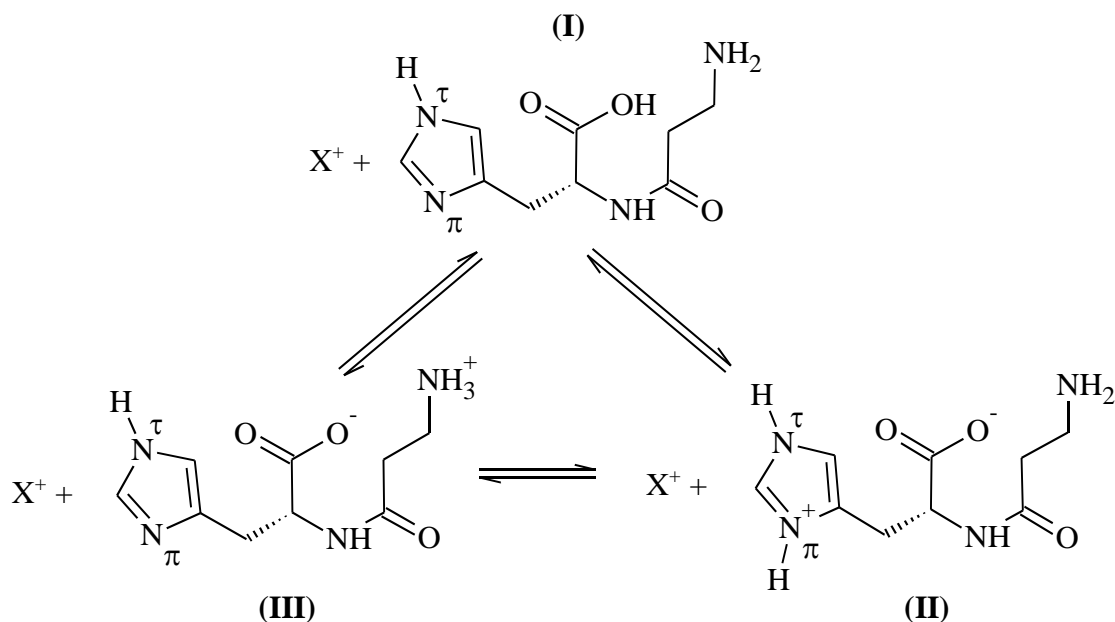
### **III-1: Abstract**

The complexation of alkali metal ions and the proton  $X^+$  ( $X = H, Li, Na, K, Rb, Cs$ ) by  $\beta$ -alanyl-L-histidine (carnosine, Car) was investigated by electrospray ionization mass spectrometry (ESI-MS) and MS/MS fragmentation studies. Collision-induced dissociation (CID) breakdown curves were recorded and the resulting apparent activation energies were compared to DFT calculations of binding energies at the B3LYP/cc-pVDZ level of theory. Additionally, the influence of metal complexation on hydrogen/deuterium exchange of  $CarX^+$  with  $D_2O$  was tested. Our investigations characterize the structures of Car-alkali complexes and elucidate the interaction with the differently sized solvated metal cations.

### **III-2: Introduction**

The interaction of amino acids and small peptides with alkali metal ions is of fundamental importance since  $Na^+$  and  $K^+$  cations are ubiquitous in biological systems and the resulting complexes might provide model structures for metal-peptide interaction relevant for specific biological functions [1]. The peptide chelation of the homologous series of alkali metal ions could be systematically explored by mass spectrometric selection and detection in the gas phase [2]. Under this condition, the identification of peptide binding sites and accompanying structures is possible. Usually the experimental results are interpreted by help of *ab initio* and DFT computations of the energies and spectroscopic properties of the possible isomeric structures. Thus, recently several model studies

have been published differentiating the main binding motifs of salt bridges (SB), charge solvation (CS) and cation- $\pi$  complexation. [3-11] We report here on the mass spectrometric investigation of cationized complexes comprised of the dipeptide L-carnosine ( $\beta$ -alanyl-L-histidine, Car, scheme 1 (I)) and alkali metal ions or a proton. L-carnosine is a naturally occurring dipeptide. Due to the presence of the imidazole group several tautomeric and zwitterionic forms are possible (see scheme 1). In addition, the imidazole side chain is a common coordinating ligand in metalloproteins and a part of catalytic sites in certain enzymes. From recent gas phase IRMPD (infrared multiphoton dissociation) studies [12] on  $\text{CarH}^+$  the protonation site was located on the side chain imidazole nitrogen  $\text{N}^\tau$ .



**Scheme 1:** Different binding motifs of carnosine. Note that the structures with the non-protonated imidazole ring ((I), (III)) could additionally exist in a tautomeric form ( $\text{N}^\tau\text{-H}$  instead of the depicted  $\text{N}^\tau\text{-H}$  tautomer).

Carnosine is present in the muscle and brain tissue of humans in high concentrations. [13] It is the major  $\beta$ -alanine source in the human body [14], and it is considered to play numerous additional biological roles in physiology [15,16]. For instance, it shows antioxidant activity and has been proven to scavenge reactive oxygen species. The antiulcer drug Polaprezinc consists of the  $\text{Zn(II)}$ -carnosine complex. Its biological function is still not fully understood. [17-22] Recently, the pH-dependent aggregation of Car with  $\text{Zn(II)}$  and  $\text{Cu(II)}$  was investigated by ESI-MS and dimeric carnosine to metal complexes (e.g.  $[\text{Cu(II)Car}_2]^+$ ) have been identified. [23]

We have performed preliminary IRMPD studies on Car-Zn(II) complexes [24,25]. The coordination of histidine to alkali [26] and alkaline earth metal ions [27] and the structure of protonated histidine [28] have been studied recently by calculations, IRMPD spectroscopy and H/D exchange (HDX) measurements, respectively. Also, *ab initio* calculations on the MP2 level have been performed for the tautomeric structures of HisGly, GlyHis and their Na<sup>+</sup> complexes [29]. In particular, GlyHis is closely related to carnosine, differing only by one CH<sub>2</sub> group. As far as we know, no systematic mass spectrometric work on the alkali metal ion adducts of Car was published so far.

This work is part of our ongoing research on the interaction of metals and metal ions with biomolecular systems. Here we use ESI-MS, CID and HDX to study the fragmentation behavior and structure of protonated carnosine and the alkali metal ion adducts of carnosine.

### **III-3: Experimental and theoretical methods**

#### ***III-3.1: Electrospray ionization mass spectrometry (ESI-MS)***

Electrospray ionization mass spectrometry (ESI-MS) was performed with a Bruker Esquire 3000plus ion trap instrument. The ion source was used in positive electrospray ionization mode. Scan speed was 13000 m/z / s in normal resolution scan mode (0.3 FWHM / m/z), scan range was 15 to 2800 m/z. All spectra were accumulated for at least one minute. Sample solutions in H<sub>2</sub>O:iPrOH (50:50) at concentrations of 1 x 10<sup>-4</sup> M were continuously infused into the ESI chamber at a flow rate of 2 μL/min using a syringe pump. Nitrogen was used as drying gas with flow rate of 3.0 L/min at 300 °C. The solutions were sprayed at a nebulizer pressure of 4 psi and the electrospray needle was typically held at 4.5 kV. Transfer parameters to the Paul trap of the mass spectrometer were held constant. Helium was used as a buffer gas with a partial pressure of about 5 x 10<sup>-6</sup> mbar. The instrument was controlled by Bruker Esquire Control 5.3 software and data analysis was performed using Bruker Data Analysis 3.4 software.

#### ***III-3.2: Collision-induced dissociation (CID) breakdown curves***

Recent investigations [30-32] on so called “thermometer ions” have demonstrated successfully that it is possible for different ion trap mass spectrometers to calibrate the internal voltage scales of the fragmentation amplitudes towards appearance energies (AE) of the fragment ions. From the good correlation of the loss of neutral pyridine (a direct bond-cleavage) from 15 para-substituted benzylpyridinium ions in comparison to the calculated reaction endothermicities a simple conversion

factor was obtained. However, the precision of such an approach is compromised if additional fragmentation channels are taken into account [31].

Nevertheless, we expect for the cationized carnosine complexes under study here at least qualitative correlation between the fragmentation amplitude and the internal energy of the ions so that appearance energies and binding energies could be compared within the  $\text{CarX}^+$  series.

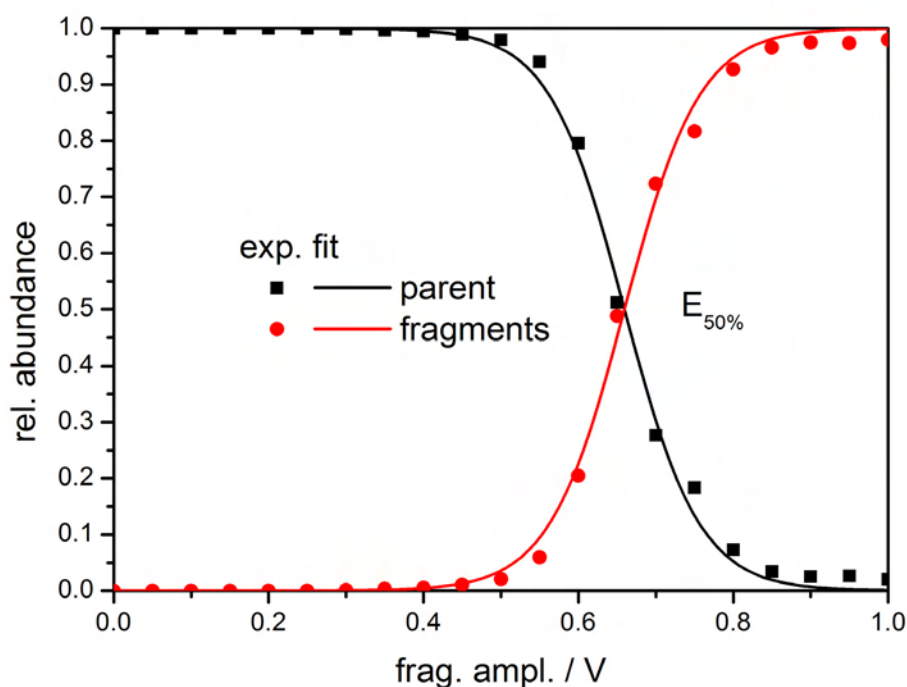


**Figure 1:** Breakdown diagram of mass-selected carnosine +  $\text{Li}^+$  as a function of the fragmentation amplitude. The dots are the experimental data; the solid lines are the sigmoid functions used for analysis.

Collision-induced dissociation (CID) breakdown curves, e.g., see Fig. 1 for  $\text{CarLi}^+$ , were recorded with varying excitation magnitude from 0.0 V to 1.0 V corresponding to the internal energy scale of the mass spectrometer. Relative abundances were calculated according to:

$$I(E) = \frac{\sum(\text{fragments})}{\sum(\text{fragments} + \text{parent})} \quad (1)$$

### III-3.3: Sigmoidal fitting of the breakdown curves

Fragmentation amplitude voltage dependent CID spectra were modeled and fitted by sigmoid functions of the type

$$I_i(E) = a_i / (1 + e^{(E_{50\%} - E)Bi}) \quad (2)$$

using a least-squares criterion.  $a_i$  denotes the branching ratio of a particular product ion ( $\sum a_i = 1$ ),  $E_{50\%}$  is the voltage at which the sigmoid function has reached half of its maximum,  $E$  is the fragmentation amplitude (in V) and  $B$  (in  $V^{-1}$ ) describes the rise of the sigmoid curve. Due to the correlation of fragmentation voltage and appearance energy it is assumed that the breakdown curves give hints on the binding energies of the different cationized complexes.

### ***III-3.4: Hydrogen/deuterium exchange (HDX)***

H/D exchange (HDX) reactions have been extensively used in order to determine the number of labile sites and to infer structural features of small peptides [33-35]. H/D exchange with  $D_2O$  was performed under single collision conditions at a background pressure of approx.  $1 \times 10^{-8}$  mbar (Bruker Apex III FT-ICR-MS equipped with a 7.0-T magnet and an APOLLO I electrospray ion source). Sample solutions in  $H_2O:iPrOH:MeCN$  (10:10:80) at concentrations of  $1 \times 10^{-4}$  M were continuously infused into the ESI chamber at a flow rate of 3  $\mu L/min$  using a syringe pump. Nitrogen was used as drying gas with flow rate of 10.0 L/min at approx. 300 °C. The solutions were sprayed at a nebulizer pressure of 25 psi and the electrospray needle was typically held at 4.0 kV. Transfer parameters to the Penning trap of the mass spectrometer were held constant.

### ***III-3.5: Computational methods***

The goal of the computations is to illustrate the possible structural motifs and give preliminary hints on their energetic order. We corrected the results for zero point energy (ZPE), but not for thermal energies. We assume that these additional corrections are constant for all complexes. The metal ion binding energies were calculated according to:

$$\Delta_{\text{bond}}E(\text{Car} + X^+) = E(\text{Car}X^+) - E(\text{Car}) - E(X^+) \quad (3)$$

We do not claim to have found all the minima and their precise energies. However, we consider these calculations sufficient for the available mass spectrometric data in order to give an overview about the probable metal ion binding sites and their possible variation with metal ion size.

The Gaussian 03 package [36] was used at the B3LYP/cc-pVDZ level of theory (Stuttgart RSC 1997 relativistic effective core potentials (ECP) used for K, Rb and Cs [37]) for energy optimization of selected starting conformations of the  $\text{Car}X^+$  complexes. Standard convergence criteria were applied. We did not perform a comprehensive search for starting conformations. The relevant structures were hand-chosen judiciously by allowing several H-bond contacts and coordination with the

imidazole ring. Our choice of starting conformations was guided by the results of a computational study on HisGly and GlyHis and its Na<sup>+</sup> complexes. [29] From the results of that work we can also exclude the N<sup>n</sup>-H tautomers of the imidazole ring since they were found to be energetically higher by ca. 40 kJ/mol with respect to the N<sup>H</sup> conformers. In addition, the metal ion adducts were constructed from the different protonated carnosine structures by replacing the proton by a metal ion followed by geometry optimization.

### III-4: Results

#### III-4.1: Comparison of CID derived fragmentation channels

The singly charged complexes of carnosine plus X<sup>+</sup> (X = H, Li, Na, K, Rb, Cs) were generated and analyzed by ESI-MS and fragmented by CID with He atoms in the ion trap. The fragmentation of the mass selected ions showed different neutral loss channels (table 1) depending on X<sup>+</sup>.

**Table 1.** Mass of carnosine + X<sup>+</sup> ions (X = H, Li, Na, K, Rb, Cs), and relative abundances<sup>a</sup>.

Sub-stance	Par-ent m/z	-17	-35	-47	-71	-89	-117	-137	-154	-226
CarH <sup>+</sup>	227	<b>0.77</b>	0.01	0.05	0.05	0.05	<b>0.07</b>			
CarLi <sup>+</sup>	233	<b>0.17</b>			<b>0.33</b>	0.01	0.01	<b>0.45</b>	0.02	
CarNa <sup>+</sup>	249	<b>0.12</b>			0.04	0.03		<b>0.80</b>		
CarK <sup>+</sup>	265	<b>0.14</b>			0.07	0.02		<b>0.77</b>		
CarRb <sup>+</sup>	311	0.02			0.01			0.06		<b>0.91</b>
CarCs <sup>+</sup>	359									<b>1.00</b>

<sup>a</sup> Only fragments with a rel. abund. > 1% were taken into account. Rel. abund. were normalized to the sum of parent and fragment intensities per single spectra, averaged due to const. fragmentation amplitudes and estimated by sigmoidal fits. Dominant channels in bold letters.

**Table 2.** Neutral mass losses and corresponding fragments.

	Mass loss / m/z	neutral frag-ment	ionic fragment	
1	17	NH <sub>3</sub>	[C <sub>9</sub> H <sub>11</sub> N <sub>3</sub> O <sub>3</sub> X] <sup>+</sup>	(X=H,Li,Na,K,Rb)
2	18 <sup>a</sup>	H <sub>2</sub> O	[C <sub>9</sub> H <sub>12</sub> N <sub>4</sub> O <sub>2</sub> X] <sup>+</sup>	(X=H)
3	35	NH <sub>3</sub> + H <sub>2</sub> O	[C <sub>9</sub> H <sub>9</sub> N <sub>3</sub> O <sub>2</sub> X] <sup>+</sup>	(X=H)
4	47	[CH <sub>5</sub> NO]	[C <sub>8</sub> H <sub>9</sub> N <sub>3</sub> O <sub>2</sub> X] <sup>+</sup>	(X=H)
5	71	[C <sub>3</sub> H <sub>5</sub> NO]	[C <sub>6</sub> H <sub>9</sub> N <sub>3</sub> O <sub>2</sub> X] <sup>+</sup>	(X=H,Li,Na,K,Rb)
6	89	[C <sub>3</sub> H <sub>7</sub> NO <sub>2</sub> ]	[C <sub>6</sub> H <sub>7</sub> N <sub>3</sub> O <sub>1</sub> X] <sup>+</sup>	(X=H,Li,Na,K)
7	117	[C <sub>4</sub> H <sub>7</sub> NO <sub>3</sub> ]	[C <sub>5</sub> H <sub>7</sub> N <sub>3</sub> X] <sup>+</sup>	(X=H,Li)
8	137	[C <sub>7</sub> H <sub>11</sub> N <sub>3</sub> ]	[(CO <sub>2</sub> )(CO)(NH <sub>3</sub> )X] <sup>+</sup>	(X=Li,Na,K,Rb)
9	154	[C <sub>7</sub> H <sub>14</sub> N <sub>4</sub> ]	[(CO <sub>2</sub> )(CO)X] <sup>+</sup>	(X=Li)
10	226	[C <sub>9</sub> H <sub>14</sub> N <sub>4</sub> O <sub>3</sub> ]	X <sup>+</sup>	(X=Rb,Cs)

<sup>a</sup> Only measured in case of CarH<sup>+</sup>, rel. abund. below 1%

### III-4.1.1: CarH<sup>+</sup>

Protonated Carnosine showed a large variety of fragmentation channels which could be assigned to the neutral losses as given in Table 2. The dominant channel is the loss of NH<sub>3</sub>. The loss of H<sub>2</sub>O is negligible (<1%). The CID breakdown/appearance curve for the fragment 210 m/z (-NH<sub>3</sub>) (Fig. 2) exhibits already an onset at 0.25 V fragmentation amplitude, which rises slowly to a value of ca. 20% of the maximum. Parallel to the appearance of the other fragments at 0.50-0.65 V a steep rise to the maximum follows. Nevertheless the sigmoid fit curve shows a reasonable agreement with slope and position of E<sub>50%</sub>. The loss of -137 m/z, which is the most abundant fragmentation channel for CarLi<sup>+</sup>, CarNa<sup>+</sup> and CarK<sup>+</sup>, was not observed for CarH<sup>+</sup>.

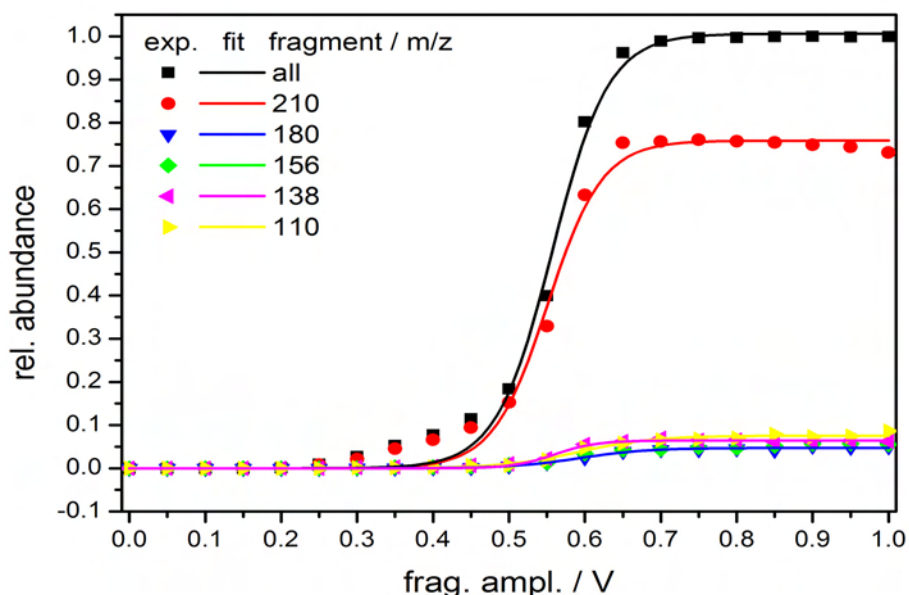


**Figure 2:** Breakdown diagrams per fragmentation channels of mass-selected carnosine + H<sup>+</sup> as a function of the relative collision energy. The dots are the experimental data; the solid lines are the sigmoid functions used for analysis.

### III-4.1.2: CarLi<sup>+</sup>, CarNa<sup>+</sup> and CarK<sup>+</sup>

These three complexes of the small alkali ions have similar fragmentation patterns. All of them show the loss of NH<sub>3</sub>, as well as the mass loss of 137 m/z with the largest abundance. Small fragment ions, e.g. K<sup>+</sup>, cannot be detected due to the cut off limit (ca. 1/3 of the parent ion mass) of the Paul trap. CarNa<sup>+</sup> and CarK<sup>+</sup> show almost the same fragments with similar relative abundances. The ion generated by the most abundant measurable loss of 137 m/z corresponds to an almost complete destruction of the dipeptide backbone. The remaining complex ion consists formally of CO<sub>2</sub>,

HCONH<sub>2</sub> (formamide) or alternatively CO<sub>2</sub>, CO and NH<sub>3</sub> and the metal ion: [(CO<sub>2</sub>)(HCONH<sub>2</sub>)X]<sup>+</sup>, or [(CO<sub>2</sub>)(CO)(NH<sub>3</sub>)X]<sup>+</sup>, X= Li, Na, K. However, CarLi<sup>+</sup> showed also a strong fragmentation channel with a mass loss of 71 m/z (residue mass of alanine) which represents a common peptide fragmentation with the remaining y<sub>1</sub> fragment ion (Biemann nomenclature [38]).

### III-4.1.3: CarRb<sup>+</sup> and CarCs<sup>+</sup>

Fragmentation of CarRb<sup>+</sup> and CarCs<sup>+</sup> mostly led to the loss of the solvated alkali ion. At a low abundance the loss of -137 m/z was detectable for CarRb<sup>+</sup>. CarCs<sup>+</sup> only gave Cs<sup>+</sup> as a detectable ion, all other channels being much smaller than 1% (relative abundance).

### III-4.2: Comparison of the CID breakdown curves

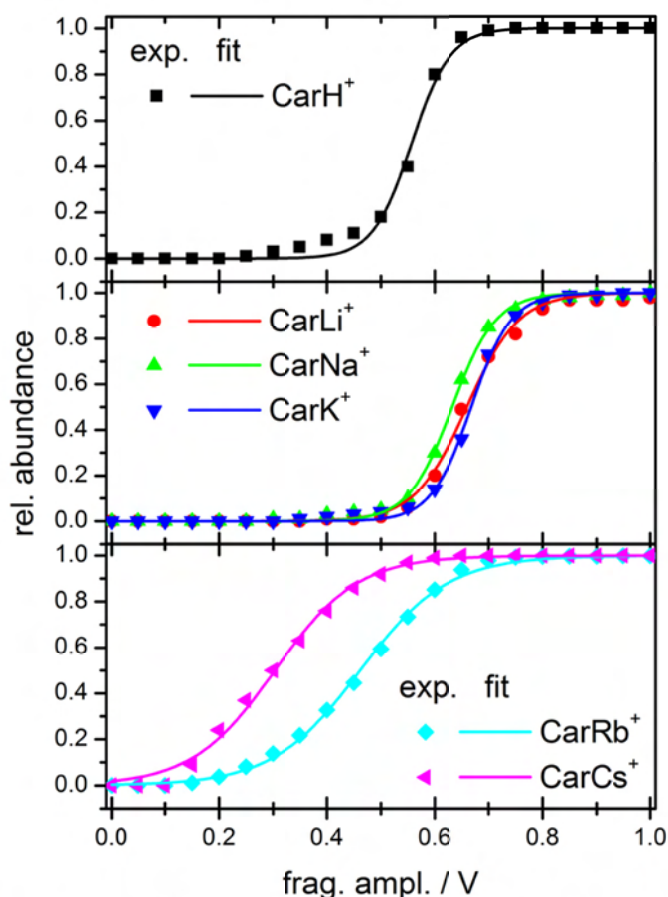


**Figure 3:** Breakdown diagram of mass-selected carnosine + X<sup>+</sup> ions (X = H, Li, Na, K, Rb, Cs) as a function of the relative collision energy. The dots are the experimental data; the solid lines are the sigmoid functions used for analysis. Fragmentation efficiencies (including dark channels) were normalized to a fixed parent intensity.



The experimental breakdown curves and their sigmoid fit functions for the different  $\text{CarX}^+$  ions are depicted in Fig. 3. The characteristic parameters of these functions, i.e., the 50% rise value  $E_{50\%}$  (in V) and the slope B (in  $\text{V}^{-1}$ ), are listed in Table 3. It is believed that the  $E_{50\%}$  values are proportional to the appearance potentials of the corresponding fragments and therefore also to the activation energies of these fragmentation channels.

For further discussion, the six investigated ion adducts of carnosine are divided into three groups related to their different fragmentation behavior as well as shape and onset of the breakdown graphs. We distinguish group 1:  $\text{CarH}^+$ , group 2:  $\text{CarLi}^+$ ,  $\text{CarNa}^+$ ,  $\text{CarK}^+$  and group 3:  $\text{CarRb}^+$ ,  $\text{CarCs}^+$ . The first two groups both show a steep rise (within 0.3 V) in the breakdown graphs at a large absolute value (0.6 V) of the fragmentation amplitude. However,  $\text{CarH}^+$  behaves differently from the complexed ions of group 2 due to its unique and widespread fragmentation pattern and the low-energy onset (see description above) of the  $\text{NH}_3$  elimination channel. The breakdown graphs of group 3 exhibit much broader rises (ca. 0.6 V) which are clearly centered at lower energy (ca. 0.4 V).  $\text{CarCs}^+$  shows the lowest fragmentation amplitude of all investigated complexes at only 0.3V.

**Table 3:** Parameters obtained in the modeling of the breakdown diagrams of mass-selected  $\text{CarX}^+$  ions ( $X = \text{H}, \text{Li}, \text{Na}, \text{K}, \text{Rb}, \text{Cs}$ ) as a function of the collision energy (in V) with sigmoid functions. Fragmentation efficiencies (including dark channels) were normalized to a fixed parent intensity.

Substance	$\mathbf{B} / \text{V}^{-1}$	$\mathbf{E}_{50\%} / \text{V}$
$\text{CarH}^+$	$28 \pm 2$	$0.557 \pm 0.003$
$\text{CarLi}^+$	$21 \pm 1$	$0.660 \pm 0.003$
$\text{CarNa}^+$	$25 \pm 1$	$0.632 \pm 0.002$
$\text{CarK}^+$	$27 \pm 1$	$0.668 \pm 0.002$
$\text{CarRb}^+$	$12 \pm 0.3$	$0.462 \pm 0.002$
$\text{CarCs}^+$	$13 \pm 0.5$	$0.304 \pm 0.004$

### III-4.3: Hydrogen/deuterium exchange (HDX)

H/D exchange with  $\text{D}_2\text{O}$  showed a consecutive exchange of up to six hydrogen atoms in case of  $\text{CarH}^+$ . After 30 s reaction delay the parent ion (227.13 m/z) completely disappeared from the mass spectra.  $\text{d}_5\text{-CarH}^+$  and  $\text{d}_6\text{-CarH}^+$  were the most abundant peaks. Additionally double exchange per

single collision reaction was tested by continuous ejection [33] of the mass 228.17  $m/z$  belonging to  $d_1\text{-CarH}^+$ . Under these reaction conditions no double exchange was found.

In case of  $\text{CarX}^+$  ( $X = \text{Li, Na, K, Rb, Cs}$ ) no H/D exchange could be observed after reaction times of up to 180 s. Also the dimeric structure  $\text{Car}_2\text{H}^+$  showed no exchange. In the reaction of  $\text{CarCs}^+$  with  $\text{D}_2\text{O}$  a loss of Car and a parallel increase of  $\text{Cs}^+$  were observed.

#### III-4.4: Results of the computations

The calculated binding energies (0 K, ZPE corrected) for the different  $\text{CarX}^+$  ( $X = \text{H, Li, Na, K, Rb, Cs}$ ) complexes are listed in Tab. 4. The three lowest minimum structures (numbered with increasing energy I, II, III) are considered and their relative energies are also given in Tab. 4. In the following figures we depict the obtained minimum energy structures.

##### III-4.4.1: $\text{CarH}^+$

Several low energy structures were found for protonated carnosine including a structure similar to the one proposed by Gregoire et al. [12] (Fig. 4).

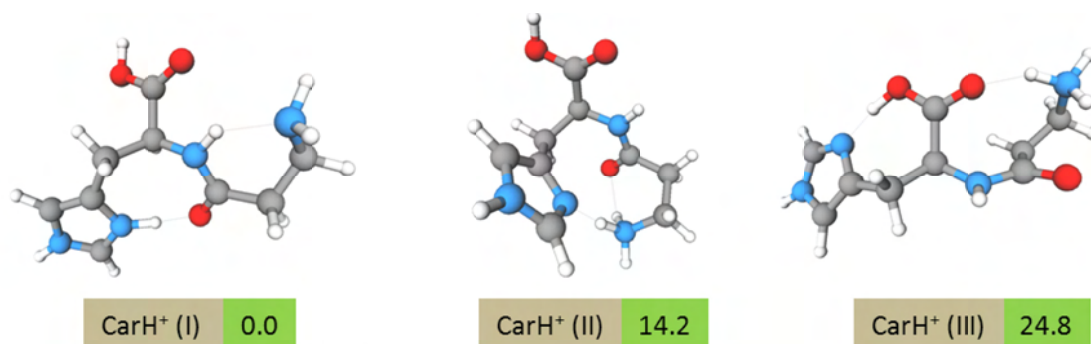


**Figure 4:** Selected low energy structures of protonated carnosine. Relative energies (in  $\text{kJ/mol}$ ) in respect to the low energy structure (I).

##### III-4.4.2: Alkalized $\text{CarX}^+$

Several minimum structures were found for all  $\text{CarX}^+$  ( $X = \text{Li, Na, K, Rb, Cs}$ ) ions. Three selected structures of  $\text{CarNa}^+$  (Fig. 5) show the two main binding sites for the metal ions.

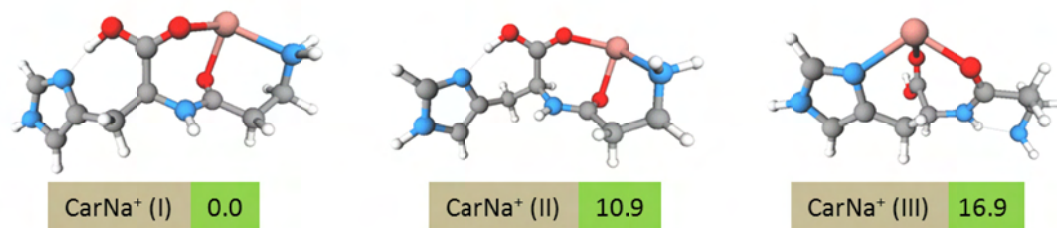


**Figure 5:** Selected low energy structures of  $\text{CarNa}^+$ . Relative energies (in kJ/mol) in respect to the low energy structure (I).

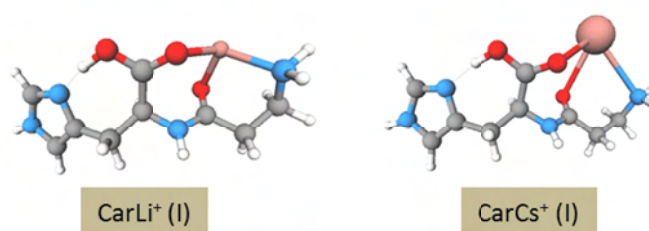


**Figure 6:** Selected low energy structures of  $\text{CarLi}^+$  and  $\text{CarCs}^+$  structure type (I).

These structure motifs were also found as almost size independent as can be seen from the comparison of  $\text{CarLi}^+(\text{I})$  and  $\text{CarCs}^+(\text{I})$  (Fig. 6).

**Table 4.** Calculated ZPE corrected binding energies of  $\text{X}^+$  ions ( $\text{X} = \text{H}, \text{Li}, \text{Na}, \text{K}, \text{Rb}, \text{Cs}$ ) to neutral carnosine. Relative binding energies of structure type (II) and (III) complexes as compared to type (I). In all cases type (I) structures provide for the strongest binding.

Substance	$\Delta_{\text{bond}}E(\text{I}) /$ kJ/mol	$\Delta\Delta E(\text{II}) /$ kJ/mol	$\Delta\Delta E(\text{III}) /$ kJ/mol
$\text{CarH}^+$	-1073.3	14.2	24.8
$\text{CarLi}^+$	-454.8	13.6	10.2
$\text{CarNa}^+$	-353.8	10.9	16.9
$\text{CarK}^+$	-242.8	9.1	16.5
$\text{CarRb}^+$	-216.5	8.7	17.5
$\text{CarCs}^+$	-186.4	7.7	17.5

### III-5: Discussion

The main goal of our research is to investigate the chelating behavior of small peptides towards different metal cations and thus we like to infer complexation structures from our mass spectrometric and theoretical investigations. However, a note of caution is mandatory. The deduction of binding energies and structures from CID breakdown curves alone could be misleading and is not unequivocal since activation energies not necessarily reflect the binding energies of the precursors or the energetics of the fragmentation products [10]. Therefore we compare our experimental findings to DFT calculations for the energies and structures of the  $\text{CarX}^+$  complexes. We are aware that ultimately IRMPD (infrared multiphoton dissociation) measurements are needed in order to foster our structural conclusions. However, such measurements are not routinely applied to any system. Moreover, our pilot study utilizing mass spectrometric and theoretical methods already provides for valuable hints on structural arrangements, poses new structural problems and helps in identifying candidates for more detailed spectroscopic investigations. In the following we like to discuss structural implications for the different  $\text{CarX}^+$  complexes.

As indicated by the data presented in the former chapter the protonated carnosine ( $\text{CarH}^+$ ) plays a special role in terms of the fragmentation channels among the chelated ions discussed here. For  $\text{CarH}^+$  the loss of  $\text{NH}_3$  is the dominant fragmentation (with a variety of other less important channels) which could be explained by a direct protonation of the terminal  $\text{NH}_2$  group. Another possibility is the protonation of the aromatic imidazole ring (the functional group with the highest proton affinity in carnosine) forming intramolecular H-bonds towards the  $\text{COOH}$  and further to the  $\text{NH}_2$  group enabling an efficient proton relay. The obtained calculated structures  $\text{CarH}^+(\text{II})$  and  $\text{CarH}^+(\text{III})$  (Fig. 4) come close to this situation, although in both cases the  $\text{NH}_2$  group is protonated and H-bonded directly (II) or via the  $\text{COOH}$  group (III) to the  $\text{N}^n$  of the imidazole ring. In any case a proton is easily transferred between the two acceptor sites.

A structure with a protonated imidazole ring was suggested by Gregoire et al. [12] based on IRMPD data in the  $\text{C}=\text{O}$  stretch and  $\text{N-H}$  bend region. However, it was noted in Ref. [12] that a single structure would not suffice to model the IR spectrum in the investigated frequency region. We have also geometry-optimized a similar structure ( $\text{CarH}^+(\text{I})$ , Fig. 4) and find it stabilized by ca. 14 kJ/mol and 25 kJ/mol with respect to the structures  $\text{CarH}^+(\text{II})$  and (III) mentioned above. Here the protonated imidazole is coordinated to the amid  $\text{C}=\text{O}$  and the amid  $\text{N-H}$  is nearby to the  $\text{NH}_2$  group which in total could also enable a proton transfer.

In addition, the low fragmentation amplitude onset of the CID breakdown curve of  $\text{CarH}^+$  gives a strong hint for at least two different conformers or a second low activation barrier in comparison to the other neutral losses. The HDX experiments show, despite the high binding energy, a fast and efficient hydrogen exchange which points towards a certain H-bonded network and structural flexibility.

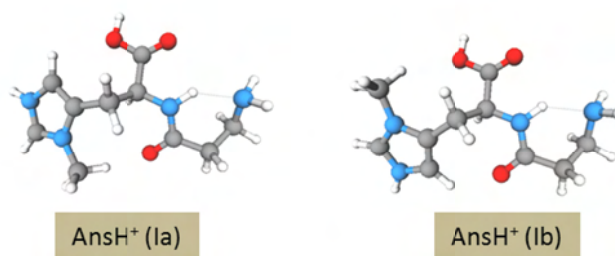


**Figure 7:** Calculated low energy structures of protonated anserine.

Moreover, we have performed additional fragmentation experiments with protonated anserine (Ans,  $\beta$ -alanyl-L-N-methyl-histidine) where the  $\text{N}^{\text{H}}$  atom close to the  $\text{C}_{\alpha}$  is methylated. The fragmentation of  $\text{AnsH}^+$  gave strongly different reaction channels compared to  $\text{CarH}^+$ . The loss of  $\text{NH}_3$  is not dominating any more, instead the loss of 71 m/z is the most abundant fragmentation. We consider this as an indication for the involvement of the H-bonded  $\text{N}^{\text{H}}$  in the  $\text{NH}_3$  loss reaction. The calculated minimum structures of  $\text{AnsH}^+$  also show that H-bonding towards  $\text{N}^{\text{H}}$  of imidazole is not possible ( $\text{AnsH}^+$  (Ia + b), Fig. 7).

Eventually, in accordance with our computational results we propose structure  $\text{CarH}^+(\text{I})$  for the protonated carnosine, close to the one of Gregoire et al. [12]. The lower energy part in the breakdown diagram is assigned to fragmentations of admixtures of structures  $\text{CarH}^+(\text{II})$  and  $\text{CarH}^+(\text{III})$ .

The comparison of the loss of  $\text{NH}_3$  between  $\text{CarH}^+$  and the  $\text{CarX}^+$  ( $\text{X}=\text{Li}, \text{Na}, \text{K}, \text{Rb}, \text{Cs}$ ) ions shows the decreasing role of this channel with increasing radius of the solvated ion. Instead the alkali metal complexes show the splitting of the peptide backbone (m/z -71, -137) and eventually the loss of the metal cations.

The slope of the CID breakdown curves of  $\text{CarLi}^+$ ,  $\text{CarNa}^+$  and  $\text{CarK}^+$  at  $E_{50\%}$  and the  $E_{50\%}$  values are very similar and higher than the ones of  $\text{CarRb}^+$  and  $\text{CarCs}^+$ . The remaining ions correspond to the formation of  $[(\text{CO}_2)(\text{CO})(\text{NH}_3)\text{X}]^+$  or  $[(\text{CO}_2)(\text{HCONH}_2)\text{X}]^+$  fragments ( $\text{X} = \text{Li}, \text{Na}, \text{K}$ ). This could be a hint on a strong binding of the small alkali ions to the carboxyl group and their further coordi-

nation to the free electron pairs from the CO and/or the NH or the NH<sub>2</sub> group of the peptide backbone. Binding to the histidine  $\pi$ -system seems to play no role, binding side-on to the free electron pairs on the nitrogen atoms seems to play a minor role for complexation. The results of our calculations support this idea. For illustration the structures CarNa<sup>+</sup>(I, II, III) are given in Fig. 5 and the size dependence is shown as an example with CarLi<sup>+</sup>(I), CarCs<sup>+</sup>(I) in Fig. 6. For all metal ion complexes a tridentate [COO,CO,H<sub>2</sub>N] binding pattern is found as an energy minimum. The calculated binding energy of the metal ion decreases considerably from Li<sup>+</sup> to Cs<sup>+</sup> (Tab. 4). The next higher energetic structures (increase by ca. 10-20 kJ/mol, Fig. 5 (II) and (III)) show also a tridentate complexation [His-N,COO,CO]. These structures are similar to the ones found for GlyHisNa<sup>+</sup> by MP2 calculations by Kapota and Ohanessian. [29] However, in the carnosine case the  $\beta$ -alanyl side chain allows for more flexibility so that the His-N binding is replaced by the H<sub>2</sub>N group and the structures CarX<sup>+</sup>(I) result as the minimum structures. In the common nomenclature these structures are considered as charge solvated (CS). We have not found computational hints on the stabilization of zwitterionic features.

CarX<sup>+</sup> (X = Rb, Cs) show very few detectable fragmentation channels of the peptide and the dominating loss of the alkali ion. In comparison to the breakdown curves of group 2 the slope of group 3 complexes is lower, thus the breakdown curves are significantly broader and the relative abundance of the NH<sub>3</sub> loss is nearly zero. Upon increase of the size of the solvated ion the calculated metal-carnosine binding energy decreases (Tab. 4), probably well below that of the NH<sub>3</sub> elimination and peptide backbone fragmentation. The tridentate minimum structures (see Fig. 6 CarCs<sup>+</sup>(I)) show more structural variability underlining their shallow binding potential.

Since it is known that the larger alkali ions can promote salt bridge (SB) structures [11] we have explicitly tested these as starting conformations in our calculations. However, no minima were found in this way. Thus, also for the complexes with the larger metal ions the energy minima related to charge solvated structures (Fig. 5 and 6) as discussed above were found.

H/D exchange reactions give hints on the number of basic sites and uncoordinated hydrogen atoms in peptide structures. The formation of hydrogen bonds between the peptide and the deuterating agents and also the proton mobility within the peptide seem to play a crucial role, especially in reactions with D<sub>2</sub>O [39]. Although the peptide backbone has less degrees of freedom by binding to an alkali metal ion there should be several sites for the formation of hydrogen bonds. However, we do

not observe hydrogen exchange in any of the alkali metal complexes. Thus, the mechanism for proton/deuteron migration in these complexes is presumably blocked and it is a goal for future studies to explore this mechanism in detail. In difference to alkali bonded carnosine complexes, protonation of carnosine allows for high proton mobility and accordingly the possibility for multiple H/D-exchange as observed in our experiments.

In summary, except for  $\text{CarH}^+$  the  $E_{50\%}$  values of the CID breakdown curves of all other complexes show the same trend as the calculated relative binding energies of the alkali metal ions to carnosine. Thus we assume that the proposed structures for the alkali metal complexes of carnosine are represented well by the computational minimum energy structures presented here.

### III-6: Conclusions

We come to the following conclusions. The measurement of CID breakdown curves (their positions and widths) in an ion trap mass spectrometer reflects the different binding energies of alkali atoms to dipeptides, here exemplified for carnosine (Car). Whereas the smaller metal ions  $X=\text{Li, Na, K}$  for  $\text{CarX}^+$  promote a dissociation of the peptide backbone the larger ones ( $X=\text{Rb, Cs}$ ) show exclusively complete ligand loss which is in agreement with the calculated binding energies.

For the protonated carnosine  $\text{CarH}^+$  we propose two low energetical structural motifs (protonation of the imidazole ring or the amino group). These conformations can easily be converted upon collisional excitation so that a loss of  $\text{NH}_3$  becomes favorable during CID. The comparison to the fragmentation behavior of anserine confirms the importance of the H-bonded  $\text{N}^{\text{H}}$  imidazole for this fragmentation channel. This agrees also with the results of H/D exchange reactions with  $\text{D}_2\text{O}$ . Protonated carnosine provides a hydrogen bond network for the reaction agent which leads easily to H/D exchanges. The binding of carnosine to alkali metals reduces the possible attachment sites and inhibits the proton migration.

For the complexes  $\text{CarX}^+$  ( $X = \text{Li, Na, K, Rb, Cs}$ ) we propose charge solvated tridentate structures obtained from DFT calculations. Likewise, the fragmentation product ions of the smaller metal ions ( $X= \text{Li, Na, K}$ ) point towards a strong  $[\text{COO,CO,H}_2\text{N}]$  coordination. No salt bridge binding motifs were found from the calculations for the larger metal ions. Regarding the low binding energy of large alkali metals to carnosine the loss of the metal ion becomes the more likely reaction path.

For confirmation of the proposed and calculated isomeric energy minimum structures IRMPD measurements on isolated CarX<sup>+</sup> complexes are necessary and planned in our laboratory.

## Acknowledgements

We thank Bernd Brutschy for being a mentor, colleague, friend and most of all an inspired and inspiring scientist. We hope that his competence and scientific foresight will continue to stimulate us and the whole research community. We thank the Stiftung Rheinland-Pfalz für Innovation, the DFG (Ni235-9/1), Landesforschungszentrum OPTIMAS and the SFB/TRR 88 (3MET) for financial support and the Hans-Böckler-Stiftung for a scholarship (F.M.).

## III-7: References

- [1] Holm, R. H.; Kennepohl, P.; Solomon: *Structural and Functional Aspects of Metal Sites in Biology*. E.I. Chem. Rev. **96**, 1996, p. 2239-2314.
- [2] Wyttenbach, T.; Bowers, M. T.: *Intermolecular Interactions in Biomolecular Systems Examined by Mass Spectrometry*. Annual Rev. Phys. Chem. **58**, 2007, p. 511-533.
- [3] Teesch, L..M.; Adams, J.: *Fragmentations of gas-phase complexes between alkali metal ions and peptides: metal ion binding to carbonyl oxygens and other neutral functional groups*. J Am Chem Soc, **113**, 1991, p. 812-820.
- [4] Pingitore, F.; Wesdemiotis, C.: *Isomeric  $\alpha$ -Dipeptide Radicals Derived from GlyPhe and PheGly*. Anal. Chem., **77**, 2005, p. 1796-1806.
- [5] Armentrout, P.B.; Gabriel, A; Moision, R.M.: *An experimental and theoretical study of alkali metal cation/methionine interactions*. Int. J. Mass Spect., **283**, 2009, p. 56-58.
- [6] Drayss, M.K.; Armentrout, P.B.; Oomens, J.; Schäfer, M.: *IR spectroscopy of cationized aliphatic amino acids: Stability of charge-solvated structure increases with metal cation size*. Int. J. Mass Spec., **297**, 2010, p. 18-27.
- [7] Dunbar, R.C.; Steill, J.D.; Oomens, J.: *Chirality-Induced Conformational Preferences in Peptide Metal-Ion Binding Revealed by IR Spectroscopy*. Phys. Chem. Chem. Phys. **12**, 2010, p. 13383-13393.
- [8] Polfer, N. C.; Oomens, J.: *Reaction products in mass spectrometry elucidated with infrared spectroscopy*. Phys. Chem. Chem. Phys., **9**, 2007, p. 3804-3817.
- [9] Polfer, N. C.; Oomens, J.; Dunbar, R. C.: *Alkali Metal Complexes of the Dipeptides PheAla and AlaPhe: IRMPD Spectroscopy*. Chem. Phys. Chem., **9**, 2008, p. 579-589.
- [10] Prell, J. S.; Demireva, M.; Oomens, J.; Williams, E. R.: *Role of Sequence in Salt-Bridge Formation for Alkali Metal Cationized GlyArg and ArgGly Investigated with IRMPD Spectroscopy and Theory*. J. Am. Chem. Soc., **131**, 2009, p. 1232-1242.
- [11] Contreras, C. S.; Polfer, N. C.; Chung, A. C.; Oomens, J.; Eyler, J. R.: *Hydrogen/deuterium exchange of phenylalanine analogs studied with infrared multiple photon dissociation*. Int. J. Mass Spectrom., **297**, 2010, p. 162-169.



- [12] Gregoire, G.; Gageot, M.P.; Marinica, D.C.; Lemaire, J.; Schermann, J.P.; Desfrancois, C.: *Resonant infrared multiphoton dissociation spectroscopy of gas-phase protonated peptides. Experiments and Car-Parrinello dynamics at 300 K*, Phys. Chem. Chem. Phys., **9**, 2007, p. 3082-3097.
- [13] Kohen, R.; Yamamoto, Y.; Cundy, K. C.; Ames, B. N.: *Antioxidant activity of carnosine, homocarnosine, and anserine present in muscle and brain*. Proc. Natl. Acad. Sci. U S A **85**(9), 1988, p. 3175.
- [14] Scriver, C.R.; Gibson, K.M.: *The Metabolic and Molecular Basis of Inherited Disease*. Mc. Graw Hill, New York, 7th ed., Vol. 1, p. 1349-1368.
- [15] Hipkiss, A. R.: *Carnosine, a protective, anti-ageing peptide?* Int. J. Biochem. Cell Biol, **30**, 1998, p. 863.
- [16] Baran, E. J.: *Metal complexes of carnosine*. Biochemistry-Moscow **65**, 2000, p. 789-797.
- [17] Yoshikawa, T.; Naito, Y.; Tanigawa, T.; Yoneta, T.; Kondo, M.: *The antioxidant properties of a novel zinc-carnosine chelate compound, N-(3-aminopropionyl)-L-histidinato zinc*. Biochim. Biophys. Acta, **1115**, 1991, p. 15-22.
- [18] Cho, C. H.: *Protective effects of zinc L-carnosine (2-1 03) on reserpine-induced gastric ulceration in rats*. Drug Developm. Res., **27**, 1992, p. 61-65.
- [19] Furuta, S.; Toyama, S.; Miwa, M.; Itabashi, T.; Sano, H.; Yoneta, T.: Jpn. J. Pharmacol., **67**, 1995, p. 271-278.;
- [20] Segawa, Y.; Tsuzuike, N.; Itokazu, Y.; Tagashira, E.; Yamaguchi, M.:  *$\beta$ -Alanyl-L-histidinato zinc prevents hydrocortisone-induced disorder of bone metabolism in rats*. Res. Exp. Med., **192**, 1992, p. 317-322.
- [21] Yamaguchi, M.; Kishi, S.: *Comparison of the Effect of  $\beta$ -Alanyl-L-histidinato Zinc and Its Zinc-Chelating Ligand on Bone Metabolism in Tissue Culture*. Biol. Pharm. Bull. **17**, 1994, p. 522-526.
- [22] O'Dowd, A.; O'Dowd, J. J.; Miller, D.J.: *The dipeptide carnosine constricts rabbit saphenous vein as a zinc complex apparently via a serotonergic receptor*. J. Physiol., **483**, 1995, 112P.
- [23] Mineo, P.; Vitalini, D.; La Mendola, D.; Rizzarelli, E.; Scamporrino, E.; Vecchio, G.: *Electrospray mass spectrometric studies of L-carnosine ( $\beta$ -alanyl-L-histidine) complexes with copper (II) or zinc ions in aqueous solution*. Rapid Commun. Mass Spectrom. **16**, 2002, p. 722-729.
- [24] Jaberg, S.: PhD thesis, TU Kaiserslautern, Germany, 2008.
- [25] Pfeffer, B.: PhD thesis, TU Kaiserslautern, Germany, 2008.
- [26] Remko, M.; Fitz, D.; Rode, B. M.: *Effect of metal ions ( $\text{Li}^+$ ,  $\text{Na}^+$ ,  $\text{K}^+$ ,  $\text{Mg}^{2+}$ ,  $\text{Ca}^{2+}$ ,  $\text{Ni}^{2+}$ ,  $\text{Cu}^{2+}$  and  $\text{Zn}^{2+}$ ) and water coordination on the structure and properties of L-histidine and zwitterionic L-histidine*. Amino Acids **39**, 2010, p. 1309-1319.
- [27] Dunbar, R. C.; Hopkinson, A. C.; Oomens, J.; Siu, C.-K.; Siu, K. W. S.; Steill, J. D.; Verkerk, U. H.; Zhao, J.: *Conformation Switching in Gas-Phase Complexes of Histidine with Alkaline Earth Ions*, J. Phys. Chem. B **113**, 2009, p. 10403-10408.
- [28] Kovačević, B.; Rožman, M.; Klasinc, L.; Srzić, D.; Maksić, Z. B.; Yáñez, M.: *Gas-Phase Structure of Protonated Histidine and Histidine Methyl Ester: Combined Experimental Mass Spectrometry and Theoretical ab Initio Study*, J. Phys. Chem. A **109**, 2005, p. 8329-8335.

- [29] Kapota, C.; Ohanessian, G.: *The low energy tautomers and conformers of the dipeptides His-Gly and GlyHis and of their sodium ion complexes in the gas phase*. Phys. Chem. Chem. Phys. **7**, 2005, p. 3744-3755.
- [30] Gabelica, V.; De Pauw, E.: *Internal energy and fragmentation of ions produced in electrospray sources*. Mass Spectrom. Rev. **24**, 2005, p. 566-587.
- [31] Barylyuk, K.V.; Chingin, K.; Balabin, R.M.; Zenobi, R.: *Fragmentation of Benzylpyridinium "Thermometer" Ions and Its Effect on the Accuracy of Internal Energy Calibration*. J. Am. Soc. Mass Spectrom. **21**, 2010, p. 172-177.
- [32] Zins, E.-L.; Pepe, C.; Schröder, D.: *Energy-dependent dissociation of benzylpyridinium ions in an ion-trap mass spectrometer*. J. Mass Spectrom. **45**, 2010, p. 1253-1260.
- [33] Campbell, S.; Rodgers, M.T.; Marzluff, E.M.; Beauchamp, J.L.: *Structural and Energetic Constraints on Gas Phase Hydrogen/Deuterium Exchange Reactions of Protonated Peptides with D<sub>2</sub>O, CD<sub>3</sub>OD, CD<sub>3</sub>CO<sub>2</sub>D and ND<sub>3</sub>*. J. Am. Chem. Soc. **116**, 1994, p. 9765-9766.
- [34] Campbell, S.; Rodgers, M.T.; Marzluff, E.M.; Beauchamp, J.L.: *Deuterium Exchange Reactions as a Probe of Biomolecule Structure. Fundamental Studies of Gas Phase H/D Exchange Reactions of Protonated Glycine Oligomers with D<sub>2</sub>O, CD<sub>3</sub>OD, CD<sub>3</sub>CO<sub>2</sub>D, and ND<sub>3</sub>*. J. Am. Chem. Soc. **117**, 1995, p. 12840-12854.
- [35] Gur, E.H.; de Koning, L.J.; Nibbering, N.M.M.: *The bimolecular hydrogen-deuterium exchange behavior of protonated alkyl dipeptides in the gas phase*. J. Am. Soc. Mass Spectrom. **6**, 1995, p. 466-477.
- [36] Gaussian 03, Revision C.02, Frisch, M. J.; Trucks, G. W.; Schlegel, H. B.; Scuseria, G. E.; Robb, M. A.; Cheeseman, J. R.; Montgomery, Jr., J. A.; Vreven, T.; Kudin, K. N.; Burant, J. C.; Millam, J. M.; Iyengar, S. S.; Tomasi, J.; Barone, V.; Mennucci, B.; Cossi, M.; Scalmani, G.; Rega, N.; Petersson, G. A.; Nakatsuji, H.; Hada, M.; Ehara, M.; Toyota, K.; Fukuda, R.; Hasegawa, J.; Ishida, M.; Nakajima, T.; Honda, Y.; Kitao, O.; Nakai, H.; Klene, M.; Li, X.; Knox, J. E.; Hratchian, H. P.; Cross, J. B.; Bakken, V.; Adamo, C.; Jaramillo, J.; Gomperts, R.; Stratmann, R. E.; Yazyev, O.; Austin, A. J.; Cammi, R.; Pomelli, C.; Ochterski, J. W.; Ayala, P. Y.; Morokuma, K.; Voth, G. A.; Salvador, P.; Dannenberg, J. J.; Zakrzewski, V. G.; Dapprich, S.; Daniels, A. D.; Strain, M. C.; Farkas, O.; Malick, D. K.; Rabuck, A. D.; Raghavachari, K.; Foresman, J. B.; Ortiz, J. V.; Cui, Q.; Baboul, A. G.; Clifford, S.; Cioslowski, J.; Stefanov, B. B.; Liu, G.; Liashenko, A.; Piskorz, P.; Komaromi, I.; Martin, R. L.; Fox, D. J.; Keith, T.; Al-Laham, M. A.; Peng, C. Y.; Nanayakkara, A.; Challacombe, M.; Gill, P. M. W.; Johnson, B.; Chen, W.; Wong, M. W.; Gonzalez, C.; Pople, J. A.: Gaussian, Inc., Wallingford CT, 2004.
- [37] Dolg, M.; Wedig, U.; Stoll, H.; Preuss, H.: *Energy-adjusted ab initio pseudopotentials for the first row transition elements*. J. Chem. Phys. **86**, 1987, p. 866.
- [38] Biemann, K.; Papayannopoulos, I.: *Amino acid sequencing of proteins*. A. Acc. Chem. Res. **27**, 1994, p. 370-378.
- [39] Wu, J.; Lebrilla, C.B.: *Gas-phase basicities and sites of protonation of glycine oligomers (Gly<sub>n</sub>; n = 1-5)*. J. Am. Chem. Soc. **115**, 1993, p. 3270.

## **Chapter IV: The dipeptides Carnosine, Anserine, GlyHis and HisGly and their Alkali metal complexes – influence of chain length, side groups, sequence and ion size studied with IRMPD spectroscopy, CID, DFT calculations and gas phase H/D exchange with ND<sub>3</sub>**

### **Keywords:**

Mass Spectrometry, Dipeptides, Carnosine, Anserine, HisGly, GlyHis, Alkali ions, IR-MPD, DFT, Gas Phase Reactions, H/D exchange, CID

### **IV: Preamble**

This chapter is formatted as to become a manuscript for publication. It is not submitted yet. All of the measurements, data evaluations, calculations and all of the text was done by myself. I received experimental support by Yevgeniy Nosenko, Maximilian Gaffga, Lars Barzen, Christine Merkert, Christine Mehlich and Manuel Zimmer. Christoph Riehn and Gereon Niedner-Schatteburg helped with discussions.

### **IV-1: Abstract**

The gas-phase structures of deprotonated, protonated and alkali metal (Li<sup>+</sup>, Na<sup>+</sup>, K<sup>+</sup>, Rb<sup>+</sup> and Cs<sup>+</sup>) cationized dipeptides Carnosine, Anserine, Glycyl-Histidine (GlyHis) and Histidyl-Glycine (HisGly) are investigated using infrared multiple photon dissociation (IR-MPD) spectroscopy utilizing light generated by a table-top OPO/OPA laser system. Measured IR-MPD spectra of the protonated, Li<sup>+</sup> and Cs<sup>+</sup> attached dipeptides in the region from 1300 to 2000 cm<sup>-1</sup> and 2600 to 3800 cm<sup>-1</sup> are compared to spectra calculated at the B3LYP/cc-pVDZ and Stuttgart RSC 1997 ECP level of theory. Additional conformers were calculated for Na<sup>+</sup>, K<sup>+</sup> and Rb<sup>+</sup> cationized dipeptides. The homologous series of alkali ions is showing both - continuous and interrupted - correspondence between the size of the ion and the binding motives of the dipeptides. The charge solvated binding motive is the most common within all isomers.

CID studies exhibit a change of fragmentation pathways from the dipeptide complexes of  $\text{Li}^+$ ,  $\text{Na}^+$  with multiple loss channels over  $\text{K}^+$  complexes with almost no detectable fragments to  $\text{Rb}^+$ ,  $\text{Cs}^+$  complexes which split the alkali ion. Gas phase H/D exchange reactions of protonated and alkali metal ( $\text{Li}^+$ ,  $\text{Na}^+$  and  $\text{K}^+$ ) cationized dipeptides with  $\text{ND}_3$  are used to elucidate the influence of the alkali cation to the gas phase acidity of exchangeable protons. In all cases the chelation of an alkali ion leads to a reduction of the partial relative rate constants and double H/D exchanges become less favorable than in the protonated structure.

## IV-2: Introduction

Structural conformation and the interaction with metal ions plays a crucial role for the behavior of peptides, proteins and amino acids under physiological conditions. Therefore, it is important to understand the effect of ion size and polarizability of the metal ion on the structure. Also the protonation site and proton-transfer pathways within amino acids and peptides are important to figure out basic binding motives and fragmentation mechanisms [1, 2]. The interaction of alkali and transition metal ions with amino acids and small peptides was studied extensively [3-10]. Mass spectrometric methods offer a broad variety of techniques to study the charge state, composition, conformation, H/D exchange reactivity and fragmentation behavior of protonated peptides and ionic peptide-metal complexes in the gas phase [11-19]. The absence of solvent molecules enables a direct comparison of experimental spectra to data derived from e.g. DFT calculations [19-34].

Four dipeptides were chosen, Carnosine, Anserine, Glycyl-Histidine and Histidyl-Glycine, consisting of similar basic modules (cf. Fig. 1). Carnosine and Anserine play also a crucial role in the human body [35]. The heteroaromatic amino acid Histidine is part of all four dipeptides while Anserine is methylated at the  $^1\text{N}$  position of the Histidine ring (cf. Fig. 2). Glycine or alternatively  $\beta$ -Alanyl serves as the second amino acid, since they vary only in one  $\text{CH}_2$  unit inside the N-terminus.

The energetic minimum structure of protonated Carnosine was identified by Gregoire et al. with a combination of IR-MPD and DFT calculations [36]. An intense search for energetic minimum isomers was carried out by MacDonald et al. in order to elucidate the proton transfer pathways of protonated HisGly [37]. The low energy tautomers and conformers of protonated and sodiated HisGly and GlyHis in the gas phase were identified by Kapota et al.[26]. In a former work we calculated several structures for the addition of alkali ions to neutral Carnosine in order to compare

them with data derived by CID [5]. Those calculations are now compared to IR-MPD measurements. We used structures from literature as a starting point for a search for minima of protonated and alkali ion attached species of Carnosine, Anserine, GlyHis and HisGly.

The alkali metal ions  $\text{Na}^+$  and  $\text{K}^+$  are essential for all animals and are some of the most abundant anorganic cations in the human body. The group of the alkali metal ions varies large in ion radius and hard/soft acids/bases (HSAB) behavior.  $\text{Li}^+$  is a small cation with a hardly polarizable electron valence shell whereas  $\text{Cs}^+$  has a large diameter and its valence electrons can be easily polarized. The addition of a proton or an alkali metal ions to amino acids and small peptides was subject of several studies [3, 4, 6-8, 10, 33].

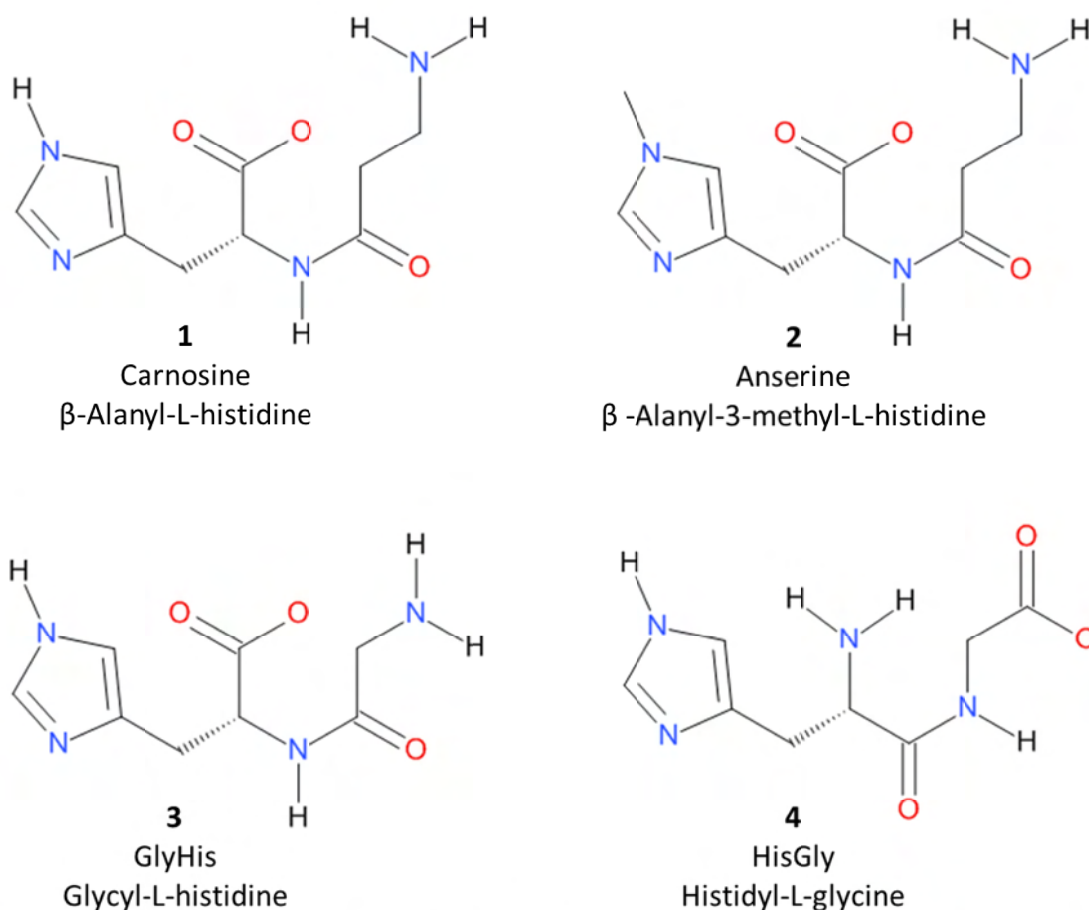


**Figure 1:** Structures and systematic names of the dipeptides Carnosine (1), Anserine (2), GlyHis (3) and HisGly (4).

We developed a generalized scheme of the four dipeptides in order to classify the different structure motives of the isomers derived by DFT calculations (cf. Fig. 2). We use a nomenclature concentrating on the rotation of the histidin ring and the amidic NH bond (for 1, 2 and 3), the

amidic CO bond (for **4**) respectively, in respect to the functional group at the central carbon atom to order the structures. Additionally, we list the electron donating oxygen and nitrogen atoms interacting with the additional proton or alkali ion (cf. Table 1) in an order starting at the histidin ring. In some cases it was necessary to add the approximate orientation (0, 90, 180 degrees) of the terminal COOH group of **4** in respect to the amidic CO.

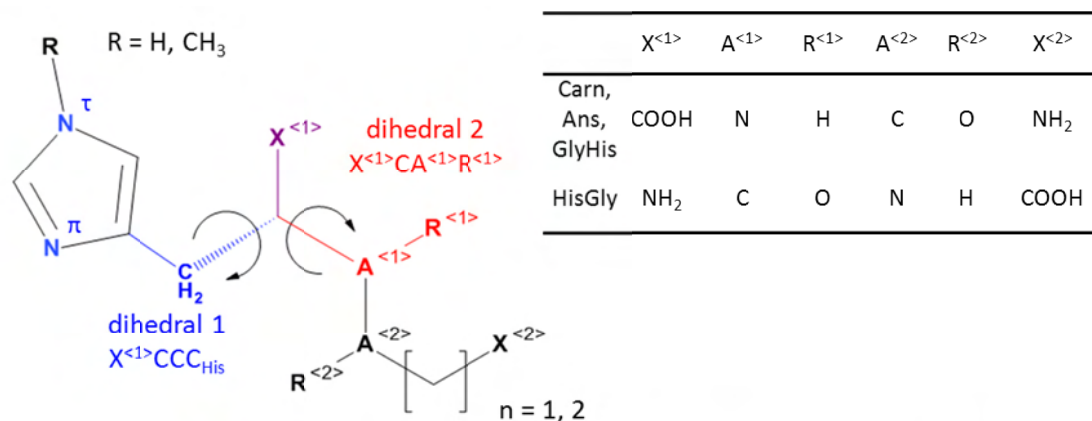


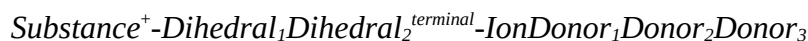
**Figure 2:** Generalized scheme for all four dipeptides under study. Dihedral angles 1 and 2 can be distinguished by clockwise ( $\alpha$ ) or counter-clockwise ( $\beta$ ) rotation.

In general we distinguish only between clockwise ( $\alpha$ ) or counter-clockwise ( $\beta$ ) rotation of the dihedral angles. In some special cases those angles are approximately 0 or 180 degrees and are therefore given with this values.

**Table 1:** Nomenclature of electron donor atoms (marked with underlines).

group	abbreviation
<u>COOH</u>	O <sub>c</sub>
<u>NH<sub>2</sub></u>	N <sub>a</sub>
amidic <u>CO</u>	O <sub>a</sub>
His- <u><math>\pi</math>N</u>	$\pi$ N <sub>h</sub>
His- <u><math>\tau</math>N</u>	$\tau$ N <sub>h</sub>

This leads to the following generalized nomenclature of isomers (e.g. Fig. 9-11). *Substance* stands for **1-4**, *Dihedral*<sub>1/2</sub><sup>terminal</sup> according to Figure 2, *Donor*<sub>1-3</sub> lists the electron donating oxygen and nitrogen atoms (cf. Table 1):



We use an additional nomenclature in order to distinguish between different isomers of the interaction of NH<sub>3</sub> with protonated Carnosine and its alkali ion complexes. Therefore we use the abbreviations listed in Table 1 with minor modifications. The different positions of the NH<sub>3</sub> at the terminal amine group are marked with N'<sub>a</sub>, N''<sub>a</sub> and N'''<sub>a</sub> and the amidic NH group is abbreviated with N<sub>am</sub>. This leads to the following nomenclature of Carnosine-NH<sub>3</sub> isomers (e.g. Fig. 22 and 23). *BindingSite* stands either for the hydrogen bearing group or the alkali ion interaction with the nitrogen atom of NH<sub>3</sub>, *AdjacentSite* lists the electron donating oxygen and nitrogen atoms (cf. Table 1) interacting with a hydrogen atom of NH<sub>3</sub>:



We assign bands in IR-MPD spectra in a first approach with an incremental appraisal of the position of bands (cf. Table 2) [38].

**Table 2:** Incremental appraisal of the excitation energy of vibrational bands (marked with underlines).

<b>group</b>	<b>mode</b>	<b>energy range / cm<sup>-1</sup></b>
free <u>COOH</u>	v <sub>s</sub>	3500 - 3650
free <u>NH</u>	v <sub>s</sub>	3400 - 3500
free <u>NH<sub>2</sub></u>	v <sub>as+ss</sub>	3300 - 3500
bridged <u>N-H-O</u>	v <sub>s</sub>	3100 - 3500
aromatic <u>CH</u>	v <sub>s</sub>	3000 - 3100
aliphatic <u>CH</u>	v <sub>s</sub>	2850 - 3000
<u>CO</u>	v <sub>s</sub>	1600 - 1800

## IV-3: Methods

### IV-3.1: ESI-MS and CID

Electrospray ionization mass spectrometry (ESI-MS) was performed with two ion trap instrument (Bruker Esquire 6000 for CID and amaZonSL for IR-MPD). The ion source yields anions/cations in negative/positive electrospray ionization mode. Scan speed was 13000 m/z / s in normal resolution scan mode (0.3 FWHM / m/z), scan range was at least 70 to 400 m/z. Sample solutions of 1-4 and alkali-halids in water/acetonitrile 9:1 at concentrations of appr. 1 x 10<sup>-4</sup> M were continuously

infused into the ESI chamber at a flow rate of 2  $\mu\text{L}/\text{min}$  using a syringe pump. We use nitrogen as drying gas at a flow rate of 3.0 to 4.0 L/min at 220 °C up to 300 °C and spray the solutions at a nebulizer pressure of 3 to 4 psi with the electrospray needle held at 4.5 kV. We held transfer parameters to the Paul trap of the mass spectrometer constant and used Helium as a buffer gas with a partial pressure of about  $3 \times 10^{-3}$  mbar inside the ion trap. BrukerEsquireControl 5.3 (Esquire) and BrukerTrapControl 7.0 (amaZonSL) software controlled the instrument and we performed data analysis using Bruker Data Analysis 4.0 software.

Collision induced dissociation (CID) appearance curves were recorded with varying excitation magnitude from 0.0 to 1.0 corresponding to the internal energy scale of the mass spectrometer. Relative abundances were calculated according to:

$$I_{tot}^{fr}(E_{LAB}) = \frac{\sum_i I_i^{fr}(E_{LAB})}{\sum_i I_i^{fr}(E_{LAB}) + \sum_i I_i^p(E_{LAB})} \quad (1)$$

Center of mass transferred fragmentation amplitudes were calculated from internal amplitudes by multiplication with

$$E_{COM} = \frac{m_{He}}{(m_{He} + m_{ion})} E_{LAB} \quad (2)$$

$m_{ion}$  was chosen according to the isotopically averaged mass of the molecule. Fragmentation amplitude dependent CID spectra were modeled and fitted by sigmoid functions of the type

$$I_{fit}^{fr,p}(E_{COM}) = \frac{1}{(1 + e^{(E_{COM}^{50\%} - E_{COM})B})} \quad (3)$$

using a least-squares criterion. A phenomenological  $E_{COM}^{50\%}$  value can be derived by the center of these sigmoid fit functions  $I_{fit}^{fr,p}(E_{COM})$  (cf. Equation 3) applied to experimental data  $I_{tot}^{fr,p}(E_{COM})$  using a least-squares criterion.  $E_{COM}^{50\%}$  is the amplitude at which the sigmoid function has reached half of its maximum,  $E_{COM}$  is the fragmentation amplitude and B describes the rise of the sigmoid curve.

### IV-3.2: IR-MPD

IR-MPD measurements were performed with the Bruker amaZonSL mass spectrometer (cf. ESI-MS part) after its modification. Two KTP/KTA optical parametric oscillator/amplifier (OPO/A,



LaserVision) systems pumped with two Q-switched 10 Hz injection seeded Nd<sup>3+</sup>:YAG lasers (PL8000, Continuum) provided for tunable IR radiation ( $\delta\nu = 0.9 \text{ cm}^{-1}$  resp.  $\delta\nu = 0.3 \text{ cm}^{-1}$ ,  $\delta t = 7 \text{ ns}$ ) in order to record vibrational spectra via the multi-photon dissociation scheme. We used the OPA idler wave ( $\leq 10 \text{ mJ/pulse}$ ) of the one system to scan spectra (pump laser) within  $2800 - 3600 \text{ cm}^{-1}$ . On choice the second IR OPO/A served as probe laser, set to a selected and fixed vibrational resonance frequency. The probe laser beam was aligned counter-propagating with respect to the scanning pump laser beam. Probe pulses were delayed by 100 ns with respect to the scanning pump pulses (delay generator DG645, SRS). Each trapped and m/z isolated ion package was irradiated by 2-4 laser pulses (or pulse pairs in case of two-laser experiments) in order to produce sufficient fragment ions. IR spectra were recorded using Bruker chromatogram software for extracting the intensity of parent and fragment ions (three point averaging directly by BrukerTrapControl software). IR-MPD signal was evaluated corresponding to formula 1. Origin Plot Software served to apply a five point adjacent averaging for smoothing. IR frequency was calibrated by a wave meter (821B-NIR, Bristol instruments). Laser power curve was recorded in parallel to the IR-MPD spectra through digitizing the analog output of the laser power meter by an ample ADC input of the amaZonSL mass spectrometer electronics.

### IV-3.3: Theoretical methods

DFT calculations were performed at the B3LYP [39-42] level of theory using cc-pVDZ (C, H, Li, N, O, Na) [43] and Stuttgart RSC 1997 ECP (K, Rb, Cs) basis sets and the Gaussian 03 and 09 packages [44, 45]. Standard convergence criteria were applied. Starting conformations were chosen according to literature as far as available [5, 36, 37, 46]. Full geometry optimization of all nuclear coordinates yields multiple locally stable minimum structures. The lowest structure is assumed to represent the most stable isomer. Thermal energies, enthalpies and free enthalpies were calculated at 298.15 K (RT conditions). DFT predicted vibrational spectra at the B3LYP/cc-pVDZ level of theory were scaled by 0.97 [47].

### IV-3.4: Gas Phase reactions

Gas phase reactions with ND<sub>3</sub> were performed under single collision conditions at a background pressure of  $2 \times 10^{-9}$  mbar in a Bruker Apex III FT-ICR-MS equipped with a 7.0-T magnet and an APOLLO I electrospray ion source. The partial pressure of the reaction gas was set to a constant value and we waited for passivation of the instruments surfaces (high vacuum part) for at least one hour. Sample solutions in water:acetonitrile 9:1 at concentrations of appr.  $1 \times 10^{-4}$  M were continuously infused into the ESI chamber at a flow rate of  $3 \mu\text{L}/\text{min}$  using a syringe pump.

Nitrogen was used as drying gas with flow rate of 10.0 L/min at appr. 300 °C. The solutions were sprayed at a nebulizer pressure of 25 psi and the electrospray needle was typically held at 4.0 kV. Transfer parameters to the Penning trap of the mass spectrometer were held constant.

## IV-4: Results

### IV-4.1: ESI-MS experiments

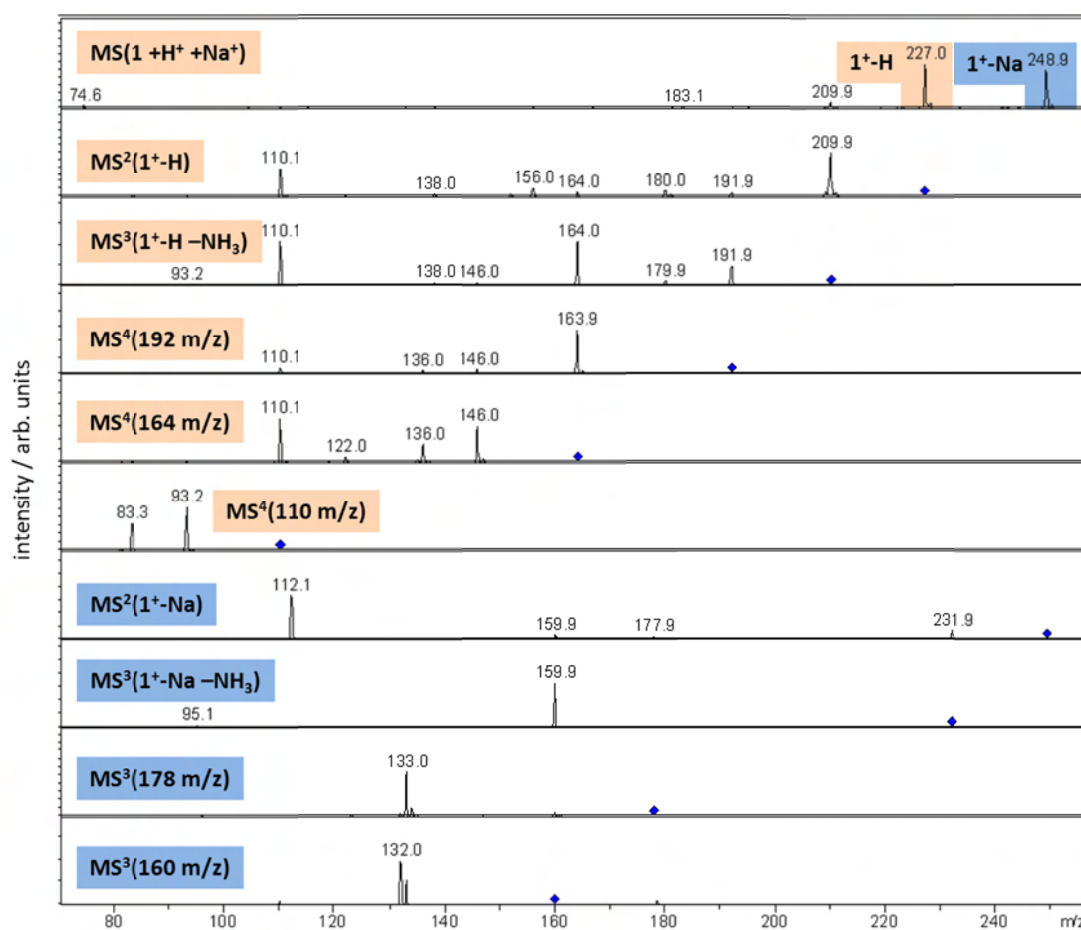


**Figure 3:** Mass spectrum of 1<sup>+</sup>-H and 1<sup>+</sup>-Na and resulting MS<sup>n</sup> spectra due to fragmentation of the labeled parent ions (♦).

We mixed separate solutions of **1-4** with solutions of the alkali-halids in water/acetonitrile 9:1 and transferred the ions derived from ESI inside a Paul trap. We characterized the formed ions and studied their fragmentation behavior under CID conditions. The resulting mass spectra show beneath a large variety of compounds (like e.g. dimers, trimers) the addition of H<sup>+</sup>, Li<sup>+</sup>, Na<sup>+</sup>, K<sup>+</sup>, Rb<sup>+</sup> or Cs<sup>+</sup> (corresponding to the added ion) to the dipeptides (cf. Fig. 3 for MS<sup>n</sup> spectra of 1<sup>+</sup>-H and 1<sup>+</sup>-Na). Fragmentation pathways differ with respect to the dipeptide X (X = 1, 2, 3, 4) and the cation

$M^+$  ( $M = H, Li, Na, K, Rb, Cs$ ). We averaged  $MS^2$  spectra of the  $X^+-M$  parent ions over varying fragmentation amplitudes in order to estimate relative abundances of the resulting ionic fragments (cf. Table 3).

**Table 3.** Relative abundances<sup>a,b</sup> of the fragment ions of protonated dipeptides **1-4** and their alkali ion complexes. Overlapping fragmentation patterns of  $\pm 1$  m/z with respect to the given loss mass are summarized.

Substance	Parent m/z	-17	-18	-35	-47	-71	-89	-117	-137	-226
1 <sup>+</sup> -H	227	53	8	2	7	5	5	15	-	-
1 <sup>+</sup> -Li	233	15	1	-	1	35	3	4	35	-
1 <sup>+</sup> -Na	249	14	-	-	-	4	6	-	76	-
1 <sup>+</sup> -K	265	17 <sup>b</sup>	-	-	-	-	-	-	83 <sup>b</sup>	-
1 <sup>+</sup> -Rb	311	10	-	-	-	-	-	-	52	38
1 <sup>+</sup> -Cs	358	1	-	-	-	-	-	-	-	99
		-17	-18	-44	-61	-71	-115	-117	-151	-240
2 <sup>+</sup> -H	241	49	2	5	4	19	2	2	-	-
2 <sup>+</sup> -Li	247	4	8	51	16	4	1	1	4	-
2 <sup>+</sup> -Na	263	33	2	3	2	32	-	5	3	-
2 <sup>+</sup> -K	279	100 <sup>b</sup>	-	-	-	-	-	-	-	-
2 <sup>+</sup> -Rb	325	1	-	-	-	-	-	-	-	98
2 <sup>+</sup> -Cs	373	-	-	-	-	-	-	-	-	100
		-18	-35	-46	-57	-75	-103	-137	-144	-212
3 <sup>+</sup> -H	213	69	5	2	7	4	12	-	-	-
3 <sup>+</sup> -Li	219	1	-	-	33	4	5	56	-	-
3 <sup>+</sup> -Na	235	-	-	-	-	20	-	80	-	-
3 <sup>+</sup> -K	251	-	-	-	-	-	-	100 <sup>b</sup>	-	-
3 <sup>+</sup> -Rb	297	-	-	-	-	-	-	2	-	98
3 <sup>+</sup> -Cs	345	-	-	-	-	-	-	-	2	98
		-18	-35	-46	-57	-75	-103	-137	-144	-212
4 <sup>+</sup> -H	213	37	2	1	1	13	44	-	-	-
4 <sup>+</sup> -Li	219	1	-	-	45	6	9	38	-	-
4 <sup>+</sup> -Na	235	-	-	-	1	20	2	76	-	-
4 <sup>+</sup> -K	251	6 <sup>b</sup>	-	-	-	8 <sup>b</sup>	-	85 <sup>b</sup>	-	-
4 <sup>+</sup> -Rb	297	-	-	-	-	-	-	-	-	100
4 <sup>+</sup> -Cs	345	-	-	-	-	-	-	-	-	100

<sup>a</sup> Only fragments with a rel. abund. > 1% were taken into account. Rel. abund. were normalized to the sum of parent and fragment intensities per single spectra. Dominant channels in bold letters.

<sup>b</sup> Due to the fact, that  $K^+$  ions can not be detected by the mass spectrometer, those values do not reflect the abundance of a loss channel resulting in a neutral dipeptide and  $K^+$

The loss of 17 m/z can be assigned to a neutral loss of  $NH_3$ . This is the dominant fragmentation channel for protonated **1<sup>+</sup>-H** and **2<sup>+</sup>-H** cations. Both ions show several neutral losses. The splitting of the molecule resulting in a loss of 18 m/z can be assigned to the loss of  $H_2O$ . This fragment

pathway rises in relative abundance for the protonated  $3^+ \text{-H}$  and  $4^+ \text{-H}$  cations. The complexation of  $\text{Li}^+$  or  $\text{Na}^+$  by the dipeptides leads to a crucial change in fragmentation behavior. No clear trend can be seen for  $X^+ \text{-K}$  ions due to the fact, that  $\text{K}^+$  ions can not be detected by the mass spectrometer under the given CID conditions. Therefore, the relative abundances of the listed species do not necessarily reflect the abundance of all loss channels (cf. Table 3). In case of  $\text{Rb}^+$  and  $\text{Cs}^+$  dipeptide complexes, the cleavage of the alkali ion becomes the most favorable fragmentation channel, except for  $1^+ \text{-Rb}$ .

#### IV-4.2: IR-MPD spectra

We measured 1-color IR-MPD spectra of the deprotonated, protonated and of all combinations of dipeptides and alkali metal ions. Partially, we measured 2-color IR-MPD spectra for some regions of interest.

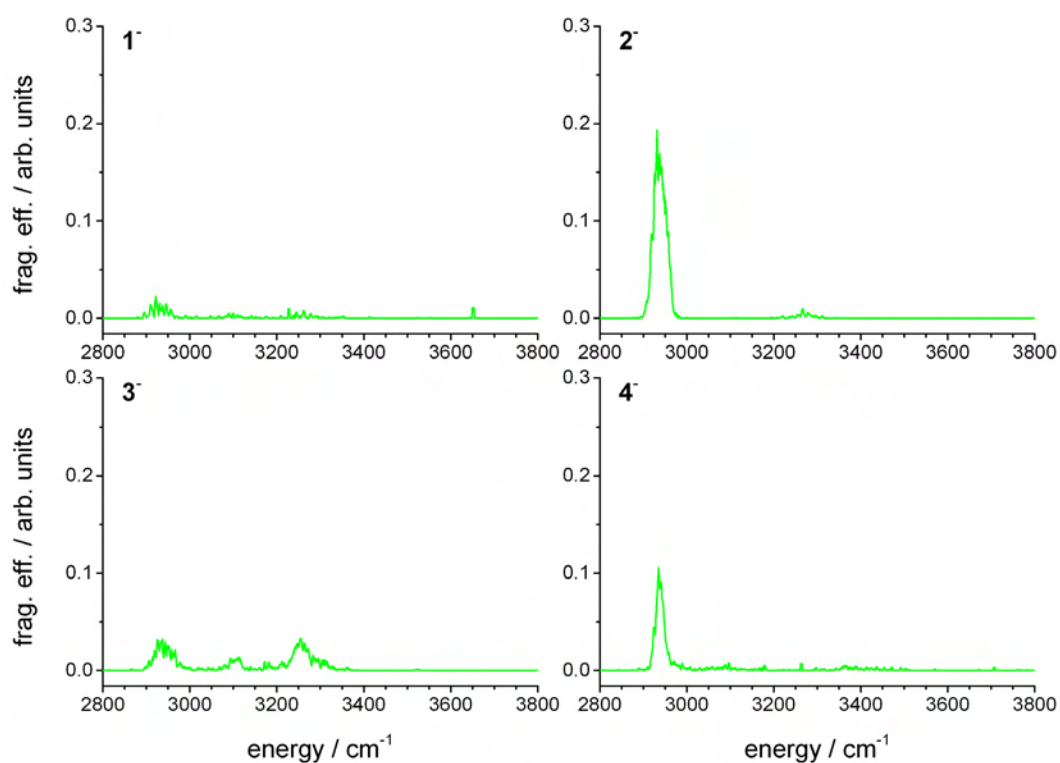


**Figure 4:** 1-color IR-MPD spectra of  $1^-$ ,  $2^-$ ,  $3^-$  and  $4^-$ .

The direct comparison of the spectra of all four deprotonated species shows always one more or less intense band in the CH stretch region about  $2940 \text{ cm}^{-1}$  (cf. Fig. 4). Relatively broad bands corresponding to NH stretch motions can be found in all spectra in the region between 3200 and

3350  $\text{cm}^{-1}$  with varying intensities. The stretch motion of the free  $^1\text{NH}$  bond above 3400  $\text{cm}^{-1}$  cannot be observed in the spectra, in contrast to the spectra of the cationic species (cf. Fig. 5-7, 8-26).

All of the protonated dipeptides show two intense bands above 3400  $\text{cm}^{-1}$  (cf. Fig. 5). The band around 3570 corresponds to stretch motions of the free OH and the band at 3480  $\text{cm}^{-1}$  corresponds free  $^1\text{NH}$  stretch motions.

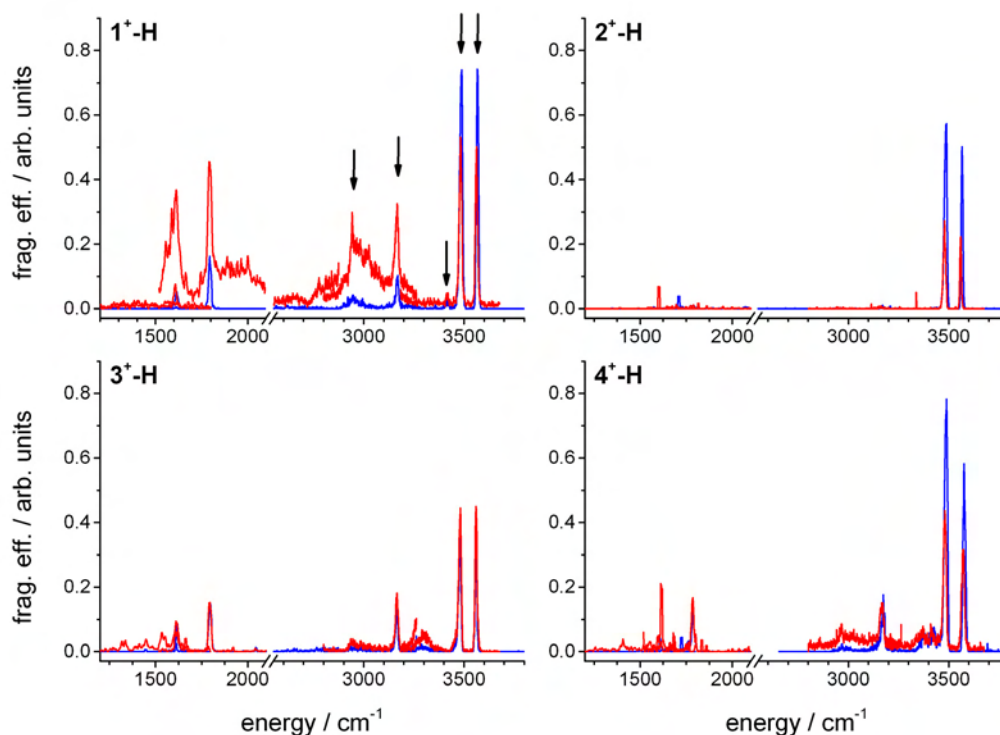


**Figure 5:** 1-color (blue) and 2-color (red) IR-MPD spectra of  $1^+\text{-H}$ ,  $2^+\text{-H}$ ,  $3^+\text{-H}$  and  $4^+\text{-H}$ . 2-color IR-MPD spectra of  $2^+\text{-H}$ ,  $3^+\text{-H}$  and  $4^+\text{-H}$  were measured with the probe laser fixed at 2950  $\text{cm}^{-1}$ . 2-color IR-MPD spectra of  $1^+\text{-H}$  were measured with the probe laser fixed at 2940  $\text{cm}^{-1}$ , 3000  $\text{cm}^{-1}$  respectively, below and above 2200  $\text{cm}^{-1}$ . Arrows indicate vibrational bands that were used in the mass spectra of band specific IR-MPD patterns (cf. Fig. 6). See Tables 4-7 for numerical values of band peak positions.

The spectrum of  $2^+\text{-H}$  shows less intense bands than all other three protonated substances under study. Only two bands can clearly be seen in the spectrum. Whereas, the spectrum of deprotonated anserine shows an intense band in the CH stretch region about 2940  $\text{cm}^{-1}$ . Besides the bands of OH and  $^1\text{NH}$  stretch motions, additional bands appear in the CH, NH and  $\text{NH}_2$  stretch region for  $\text{X}^+\text{-H}$  ( $\text{X}=1, 3, 4$ ). 2-color IR-MPD spectra of  $\text{X}^+\text{-H}$  ( $\text{X}=3, 4$ ) exhibit a slight increase of the fragmentation efficiency in the CH stretch and in the *finger*print region. This effect becomes more dominant by the use of various probe frequencies, which can be seen in the spectra of  $1^+\text{-H}$  (cf. Fig. 5). In all spectra the intensity of bands corresponding to free  $^1\text{NH}$  and OH stretch motions is reduced.

Averaging of the MS<sup>2</sup> mass spectra of **1<sup>+</sup>-H** depending to one vibrational band at a time shows an unequal contribution of the single channels to the overall fragmentation efficiency (cf. Fig. 6).

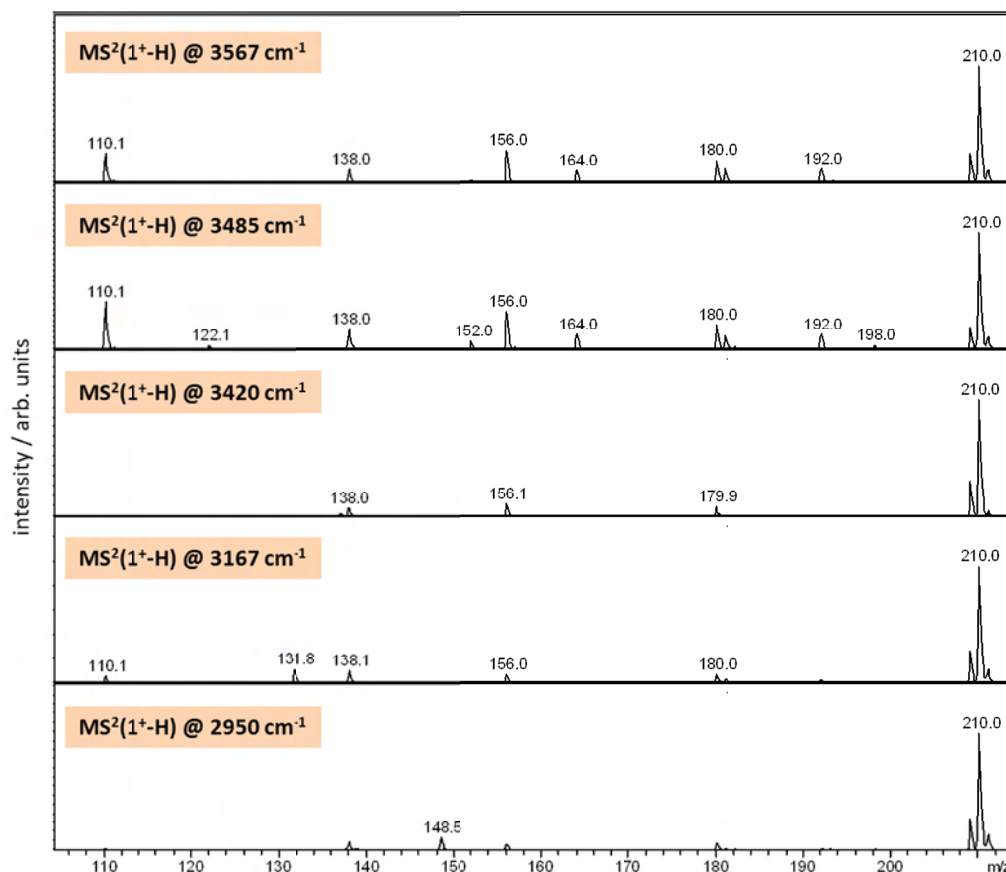


**Figure 6:** Band specific IR-MPD induced fragmentation pattern of **1<sup>+</sup>-H** (parent mass (227 m/z) is not shown). Vibrational band frequencies as indicated in Fig. 5.

The most intense bands at 3567 and 3485 cm<sup>-1</sup> (corresponding to OH and <sup>1</sup>NH stretch motions) show only slight differences in their fragmentation patterns. The weak band at 3420 cm<sup>-1</sup> correlates to the asymmetric stretch of the terminal NH<sub>2</sub> group and arises mostly from the loss of NH<sub>3</sub> (210 m/z). A new fragment at 131.8 m/z occurs inside the 3167 cm<sup>-1</sup> band, while the contribution of fragments at e.g. 164 m/z is reduced. The band at 3167 cm<sup>-1</sup> correlates to the amidic NH stretch motion while the band centered at 2950 cm<sup>-1</sup> results from the excitation of aliphatic CH stretch motions. A new fragment at 148.5 m/z can also be found in this band.

The complexation of Li<sup>+</sup> ions by the dipeptides leads to several changes in the IR-MPD spectra (cf. Fig. 7). The IR-MPD spectrum of **2<sup>+</sup>-Li** shows only two bands in the OH and NH stretch region, while all other molecules show three bands. The relative intensities of these bands are differing to the ones of the protonated species. 2-color IR-MPD with the probe laser fixed at 2950 cm<sup>-1</sup> does not

lead to an enhancement of fragmentation efficiency.

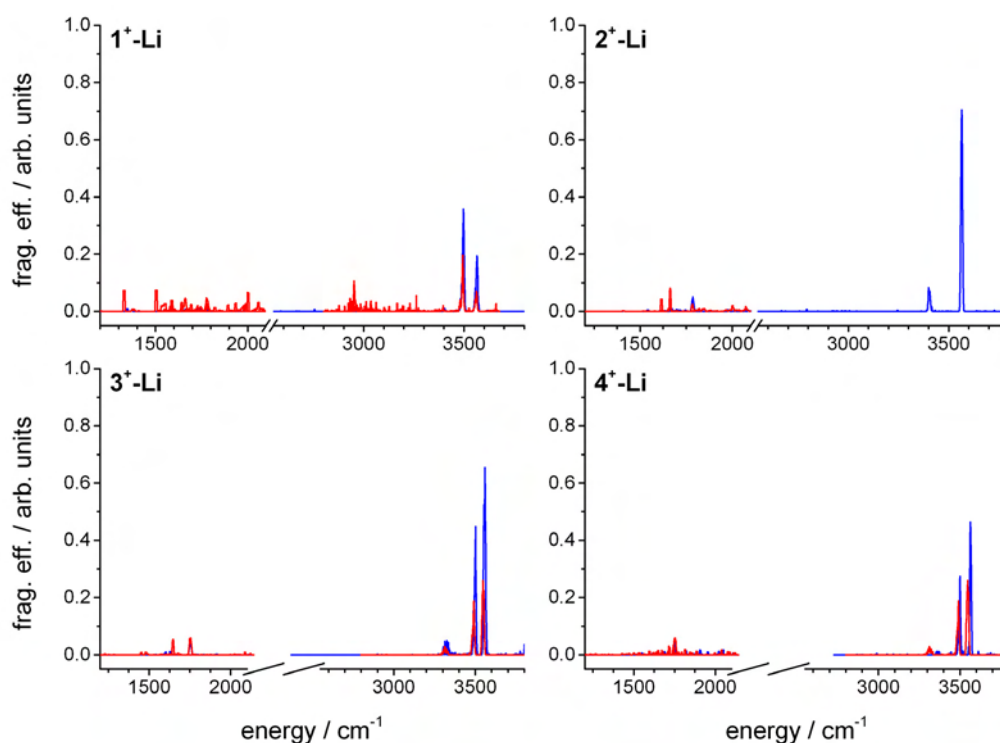


**Figure 7:** 1-color (blue) and 2-color (red) IR-MPD spectra of  $1^+\text{-Li}$ ,  $2^+\text{-Li}$ ,  $3^+\text{-Li}$  and  $4^+\text{-Li}$ . 2-color IR-MPD spectra were measured with the probe laser fixed at  $2950\text{ cm}^{-1}$ . See Tables 4-7 for numerical values of band peak positions

IR-MPD spectra of the  $\text{Na}^+$  complexes of the four dipeptides (cf. Fig. 24) show only small shifts of bands compared to the ones of the  $\text{Li}^+$  species. Spectra of  $\text{K}^+$  bearing complexes are hard to measure, show less intense bands and are more noisy than those of other species (cf. Fig. 25).  $\text{Rb}^+$  complexes of the dipeptides behave quite similar to the  $\text{Cs}^+$  dipeptide complexes and are therefore not described separately.

Spectra of  $\text{Cs}^+$  containing dipeptide complexes show several well structured bands in all regions described so far. In the region above  $3400\text{ cm}^{-1}$ ,  $2^+\text{-Cs}$  exhibits a band corresponding to a free OH stretch motion like in the  $2^+\text{-Li}$  spectrum. All other molecules exhibit the band corresponding to  $^1\text{NH}$  stretch motions as the most intense band. Besides this band, the free OH stretch motion contributes with 25% of the intensity of the  $^1\text{NH}$  band to the spectrum of  $4^+\text{-Cs}$ . This corresponding bands can only be observed at the threshold level in the spectra of  $1^+\text{-Cs}$  and  $3^+\text{-Cs}$ . 2-color IR-MPD with the probe laser fixed at  $2950\text{ cm}^{-1}$  does not lead to a significant enhancement of bands above  $2500\text{ cm}^{-1}$ . A slight enhancement can be observed in the *fingerprint* region, especially for  $2^+\text{-Cs}$ .

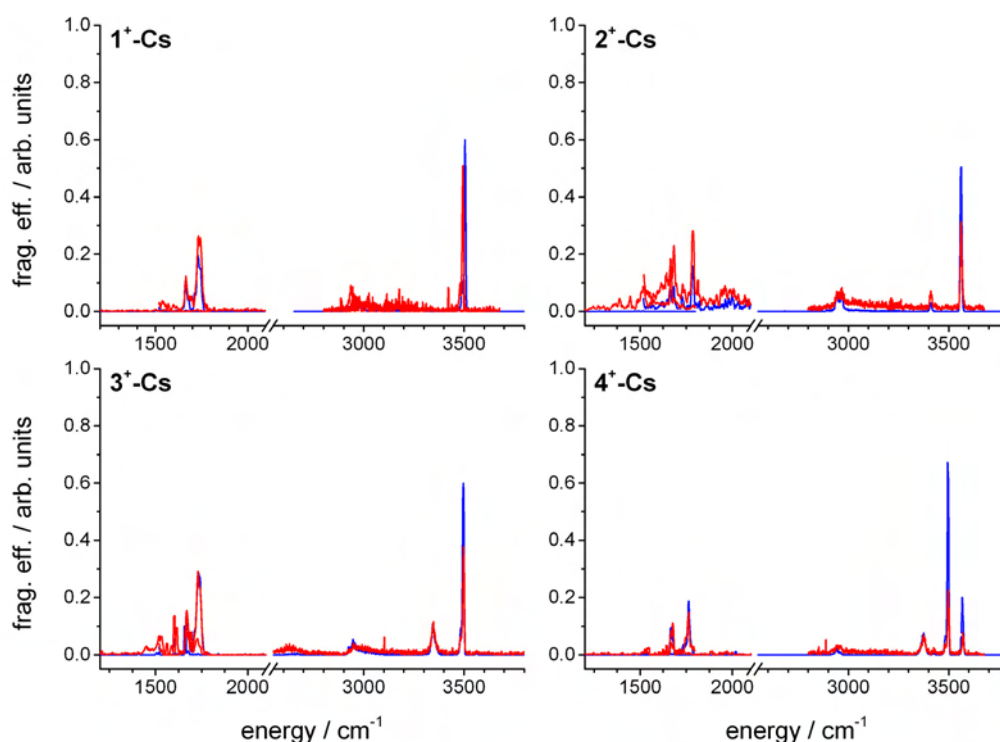


**Figure 8:** 1-color (blue) and 2-color (red) IR-MPD spectra of  $1^+$ -Cs,  $2^+$ -Cs,  $3^+$ -Cs and  $4^+$ -Cs. 2-color IR-MPD spectra were measured with the probe laser fixed at  $2950\text{ cm}^{-1}$ . See Tables 4-7 for numerical values of band peak positions.

We choose several bands which occur mostly in all spectra in order to trace the influence of the increasing size of the attached alkali metal ion to the conformation of the particular dipeptide. The spectra of cationic carnosine complexes show several variations in the positions of bands (cf. Table 4).  $\text{Rb}^+$  and  $\text{Cs}^+$  dipeptide complexes exhibit a slight shift in the positions of the OH stretch bands while those drop significantly in intensity (cf. Fig. 26 and 8). In the *fingerprint* region, the bands corresponding to OC=O stretch motions have the highest frequencies in the spectra of the  $1^+$ -H and  $1^+$ -Li complexes. This band is shifted about  $60\text{ cm}^{-1}$  to the red for all other alkali metal dipeptide complexes.

The positions of the  $^1\text{NH}$  bands for  $\text{X}^+$ -M ( $\text{X}=1,3,4$  M = H, Li, Na, K, Rb, Cs) and  $2^+$ -H can all be found in a range between  $3480$  and  $3505\text{ cm}^{-1}$ . The protonated form of anserine exhibits a band in the same region. We assume this band to correlate with a stretch motion of the  $^n\text{NH}$  group of the histidin ring.



**Table 4:** Experimental positions of assigned vibrational bands of protonated **1** (Carnosine) and of its alkali ion complexes.

ion	OH $\nu_s$	$^{15}\text{NH}$ $\nu_s$	OC=O $\nu_s$	C=O $\nu_s$
1-H <sup>+</sup>	3567	3485	1793	1613
1-Li <sup>+</sup>	3564	3495	1782	1661
1-Na <sup>+</sup>	3567	3500	1727	1662
1-K <sup>+</sup>	3567	3504	1729	1661
1-Rb <sup>+</sup>	3555	3499	1730	1664
1-Cs <sup>+</sup>	3554	3495	1733	1665

**Table 5:** Experimental positions of assigned vibrational bands of protonated **2** (Anserine) and of its alkali ion complexes.

ion	OH $\nu_s$	$^{15}\text{NH}$ $\nu_s$	amidic NH $\nu_s$	OC=O $\nu_s$
2-H <sup>+</sup>	3560	3480		
2-Li <sup>+</sup>	3559		3394	1787
2-Na <sup>+</sup>	3560		3400	
2-K <sup>+</sup>	3558		3403	
2-Rb <sup>+</sup>	3560		3403	
2-Cs <sup>+</sup>	3562		3403	1785

Protonated anserine and the anserine alkali metal complexes exhibit no strong shifts in the observed bands (cf. Table 5). The position of the band corresponding to  $^{15}\text{NH}$  stretch motions in **2<sup>+</sup>-H** is similar to the position of the  $^{15}\text{NH}$  stretch motion in **1<sup>+</sup>-H**. The band corresponding to amidic NH  $\nu_s$  stretch motions cannot be observed in the spectrum of **2<sup>+</sup>-H**, though it is clearly observable in the spectra of the alkali anserine complexes.

**Table 6:** Experimental positions of assigned vibrational bands of protonated **3** (GlyHis) and of its alkali ion complexes.

ion	OH $\nu_s$	$^{15}\text{NH}$ $\nu_s$	NH <sub>2</sub> $\nu_{as}$	OC=O $\nu_s$
3-H <sup>+</sup>	3572	3481	3372	1786
3-Li <sup>+</sup>	3547	3490	3310	1752
3-Na <sup>+</sup>	3563	3495	3362	
3-K <sup>+</sup>	3569	3496	3373	
3-Cs <sup>+</sup>	3570	3498	3377	1762

HisGly exhibits several parallel trends for the attached alkali metal ions (cf. Table 6, the Rb<sup>+</sup> adduct was not measured). With increasing size of the metal ion, the bands corresponding to OH, <sup>15</sup>NH, NH<sub>2</sub> and CO stretch motions shift continuously to the blue.

**Table 7:** Experimental positions of assigned vibrational bands of protonated **4** (HisGly) and of its alkali ion complexes.

ion	OH $\nu_s$	<sup>15</sup> NH $\nu_s$	NH <sub>2</sub> $\nu_{as}$	OC=O $\nu_s$
4-H <sup>+</sup>	3561	3480	3295	1794
4-Li <sup>+</sup>	3547	3490	3315	1753
4-Na <sup>+</sup>	3555	3492	3326	
4-K <sup>+</sup>		3491	3337	
4-Rb <sup>+</sup>	3562	3494	3343	
4-Cs <sup>+</sup>	3561	3497	3345	1735

GlyHis exhibits a quite similar absorption behavior like HisGly for the bands corresponding to OH and <sup>15</sup>NH stretch motions (cf. Table 7). Also the position of the band of the NH<sub>2</sub> asymmetric stretch motion rises continuously while the spectrum of **3<sup>+</sup>-H** exhibits the lowest frequency for this band. This is in contrast to the band in the spectrum **4<sup>+</sup>-H**, where the same band is shifted more to the blue.

#### IV-4.3: DFT derived minimum structures and relative energies

In the further description of the results from DFT calculations we focus on the protonated dipeptides and their Li<sup>+</sup> and Cs<sup>+</sup> complexes, although we calculated several structures also for Na<sup>+</sup>, K<sup>+</sup> and Rb<sup>+</sup> adducts and for anionic species. Anionic structures are hardly comparable to the other binding motives and are therefore not shown.

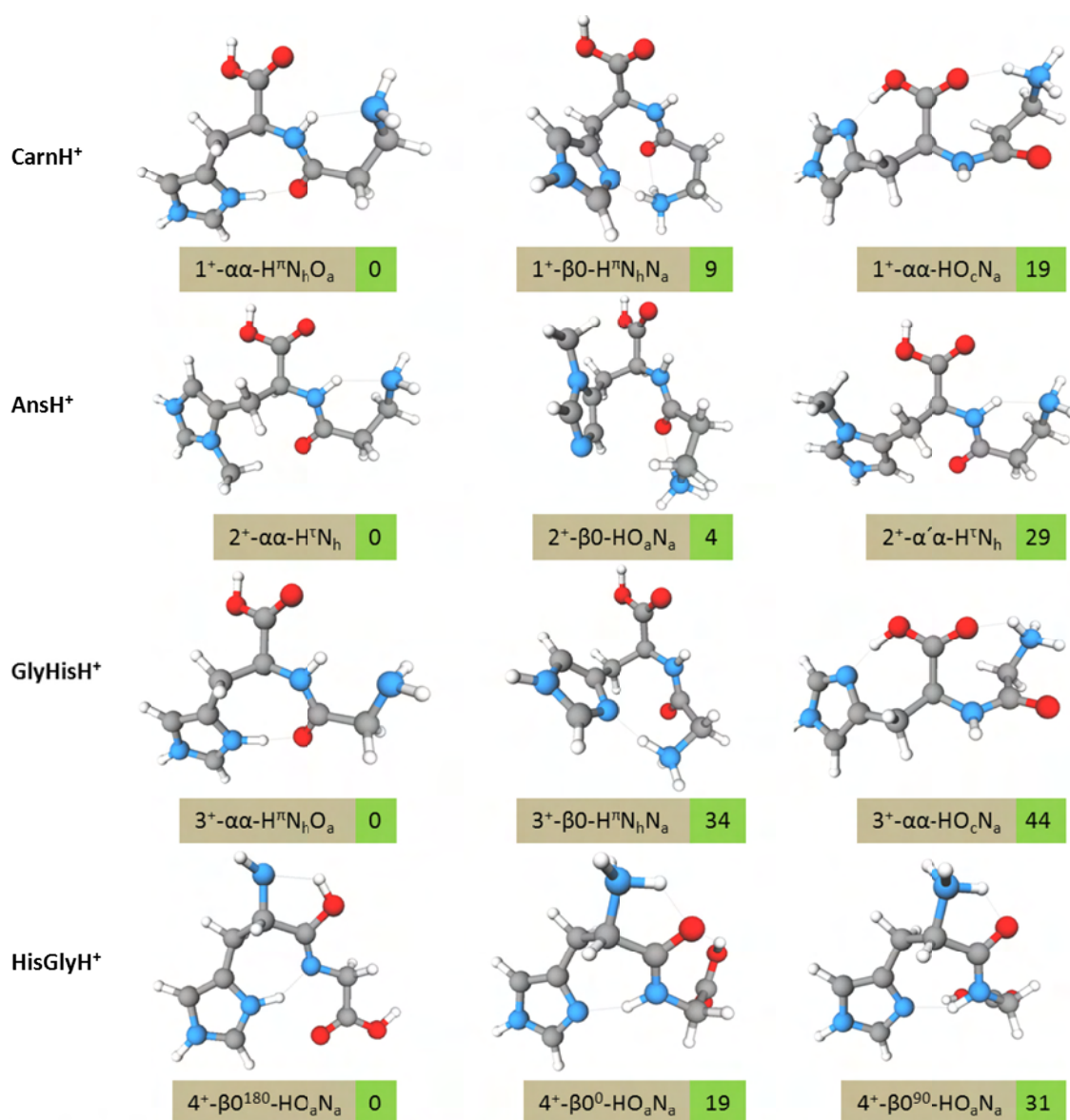


**Figure 9:** Calculated binding motives of protonated dipeptides 1-4 and relative energies in kJ/mol. (For definition of nomenclature, refer to page 62)

The found energetic minimum structures of the  $\text{X}^+-\text{H}$  ( $\text{X}=1-3$ ) complexes show related archetypes (cf. Fig. 9). In the minimum structure of carnosine ( $1^+-\alpha\text{-H}^{\text{H}}\text{N}_\text{h}\text{O}_\text{a}$ ) the additional proton is bound to the  $^{\text{H}}\text{N}$  atom of the histidin ring and the amidic oxygen, the same in  $3^+-\alpha\text{-H}^{\text{H}}\text{N}_\text{h}\text{O}_\text{a}$  (nomenclature of isomers according to Fig. 2 and Table 1). The formation of this hydrogen bridge is hindered by the methyl group of anserine and the additional proton is attached to the aromatic  $^{\text{H}}\text{N}$  atom. The second stable formation of  $3^+-\text{H}$  ( $3^+-\beta\text{O-H}^{\text{H}}\text{N}_\text{h}\text{N}_\text{a}$ ) shows the same binding motive as the corresponding structure of  $1^+-\text{H}$  but is less favorable due to the shortening of the alkyl chain.  $2^+-\beta\text{O-H}^{\text{H}}\text{N}_\text{h}\text{N}_\text{a}$  is therefore capable to form two hydrogen bonds from the protonated terminal amine to the amidic CO and to the  $^{\text{H}}\text{N}$  atom of the histidin ring. In the corresponding structure of  $2^+-\text{H}$  the proton is bound to

the terminal amine group, while the interaction with the amidic oxygen is stronger than in the other two molecules. The rotation of the histidin ring like in  $2^+-\alpha\text{-H}^{\text{N}}\text{N}_h$  leads to a rise in energy of 29 kJ/mol with respect to  $2^+-\alpha\text{-H}^{\text{N}}\text{N}_h$ . In the structure  $3^+-\alpha\text{-H}^{\text{N}}\text{O}_c\text{N}_a$ , the shorter alkyl chain (than in carnosine) hinders the formation of a hydrogen bond which makes the isomer 44 kJ/mol less stable than the  $3^+-\alpha\text{-H}^{\text{N}}\text{N}_h\text{O}_a$  isomer. Whereas, the structure  $1^+-\alpha\text{-H}^{\text{N}}\text{O}_c\text{N}_a$  is only 19 kJ/mol higher in energy than  $1^+-\alpha\text{-H}^{\text{N}}\text{N}_h\text{O}_a$ .

The energetic minimum structure of  $4^+-\text{H}$  ( $4^+-\beta\text{O}^{180}\text{-HO}_a\text{N}_a$ ) forms a seven-membered ring with the amidic proton located between the His  $^{\text{N}}$  and the amidic nitrogen. This is in difference to the minimum structures of  $1^+-\text{H}$  and  $3^+-\text{H}$  which form an eight-membered ring. Furthermore, the bridging hydrogen has an interaction with the carboxylic CO oxygen. The additional proton in  $4^+-\beta\text{O}^{180}\text{-HO}_a\text{N}_a$  is attached to the amidic oxygen resulting in a hydrogen bridge to the amine group. In contrast to  $\text{X}^+-\text{H}$  (X=1-3), the basic binding motive of the bridged hydrogen (forming a seven-membered ring) stays constant while the terminal  $\text{CH}_2\text{COOH}$  group rotates. The formation of a hydrogen bond between the carboxylic proton and the amidic oxygen in  $4^+-\beta\text{O}^0\text{-HO}_a\text{N}_a$  is 19 kJ/mol less stable than the energetic minimum structure.

All energetic minimum structures of  $1^+-\text{Li}$  to  $4^+-\text{Li}$  show a threefold chelated  $\text{Li}^+$  ion (cf. Fig. 10) where the carboxylic and amidic oxygens serve as electron donors. The third bond is either build between the amidic nitrogen or the His  $^{\text{N}}$  atom to the lithium cation. The two lowest energetic structures of  $1^+-\text{Li}$ ,  $2^+-\text{Li}$  respectively, show the same binding behavior to the attached  $\text{Li}^+$  ion. The rotation of the amidic group from an *alpha* ( $\alpha\text{-LiO}_c\text{O}_a\text{N}_a$ ) to a *beta* ( $\alpha\beta\text{-LiO}_c\text{O}_a\text{N}_a$ ) conformation leads to small differences in relative energies. The  $1^+-0\beta\text{-Li}^{\text{N}}\text{N}_h\text{O}_c\text{O}_a$  isomer corresponds to the minimum structure of  $3^+-\text{H}$  ( $3^+-0\beta\text{-Li}^{\text{N}}\text{N}_h\text{O}_c\text{O}_a$ ) and is similar to  $3^+-\beta\beta\text{-Li}^{\text{N}}\text{N}_h\text{O}_c\text{O}_a$ . The rotation of the histidin ring from a 0 degree to a *beta* conformation leads to a slight difference of 3 kJ/mol in energy between those two isomers. The  $\alpha\text{-LiO}_c\text{O}_a\text{N}_a$  binding motive, which is the most stable for  $1^+-\text{Li}$  and  $2^+-\text{Li}$ , can also be found for  $3^+-\text{Li}$ . The  $3^+-\alpha\text{-LiO}_c\text{O}_a\text{N}_a$  isomer is 22 kJ/mol less stable than  $3^+-0\beta\text{-Li}^{\text{N}}\text{N}_h\text{O}_c\text{O}_a$ . A new structural motive arises for  $2^+-\text{Li}$  ( $2^+-180\alpha\text{-Li}^{\text{N}}\text{N}_h\text{O}_a$ ) in which the metal ion is bound by only two electron donors. The methyl group forces the lithium cation to a different electron donating nitrogen of the histidine ring, hence the carboxylic oxygen is not able to chelate the ion like in  $1^+-0\beta\text{-Li}^{\text{N}}\text{N}_h\text{O}_c\text{O}_a$  any more.

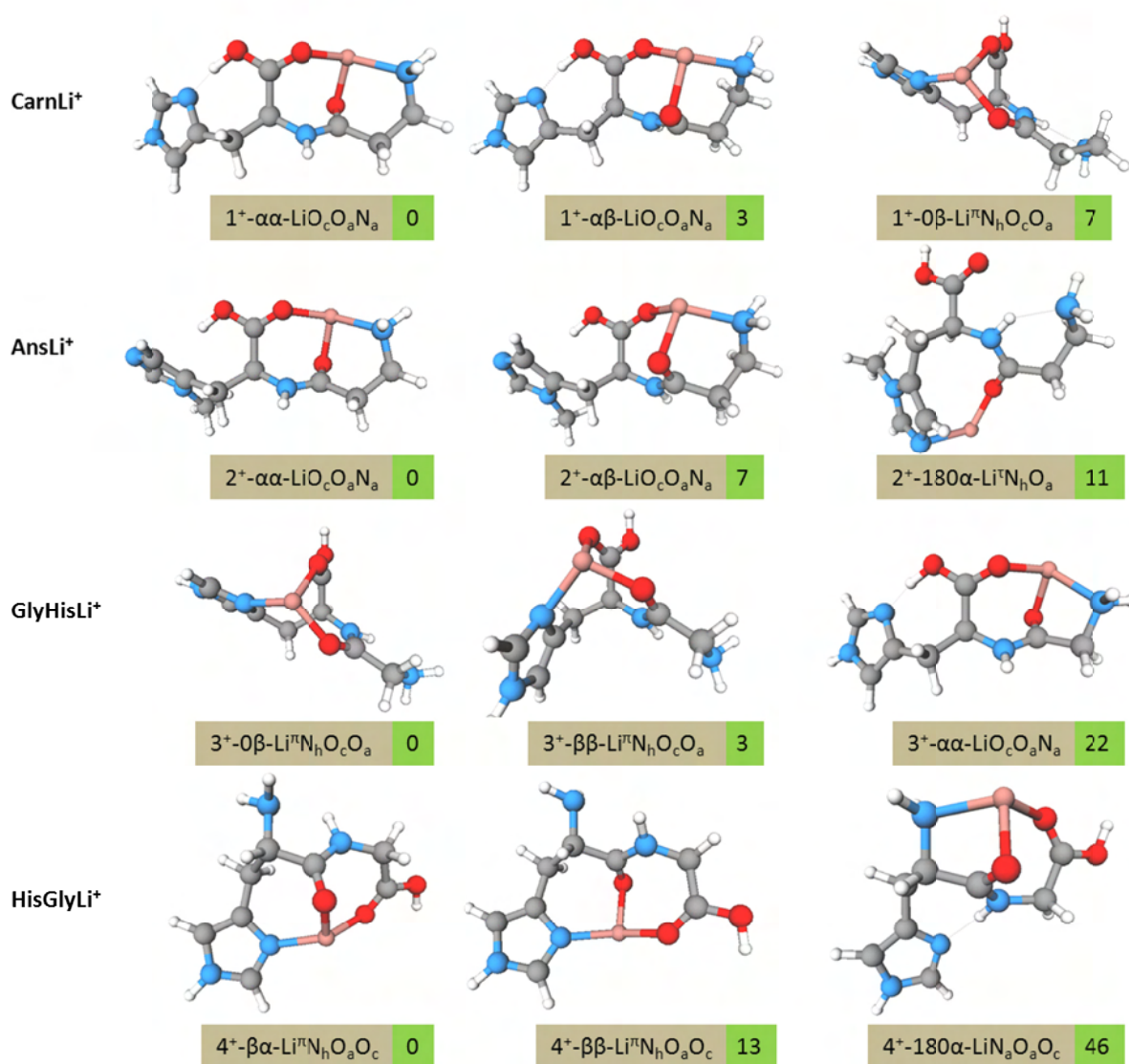


**Figure 10:** Calculated binding motives of dipeptides 1-4 with Li<sup>+</sup> and relative energies in kJ/mol. (For definition of nomenclature, refer to page 62)

In the two energetic minimum structures of 4<sup>+</sup>-Li (4<sup>+</sup>- $\beta\alpha$ -Li<sup>m</sup>N<sub>h</sub>O<sub>a</sub>O<sub>c</sub> and 4<sup>+</sup>- $\beta\beta$ -Li<sup>m</sup>N<sub>h</sub>O<sub>a</sub>O<sub>c</sub>), the lithium cation is part of two seven-membered rings like in the Li<sup>m</sup>N<sub>h</sub>O<sub>c</sub>O<sub>a</sub> conformations of 1<sup>+</sup>-Li and 3<sup>+</sup>-Li. The five- and seven-membered ring motive formed with lithium in 4<sup>+</sup>-180 $\alpha$ -LiN<sub>a</sub>O<sub>a</sub>O<sub>c</sub> is 46 kJ/mol higher in energy than the energetic minimum structure.

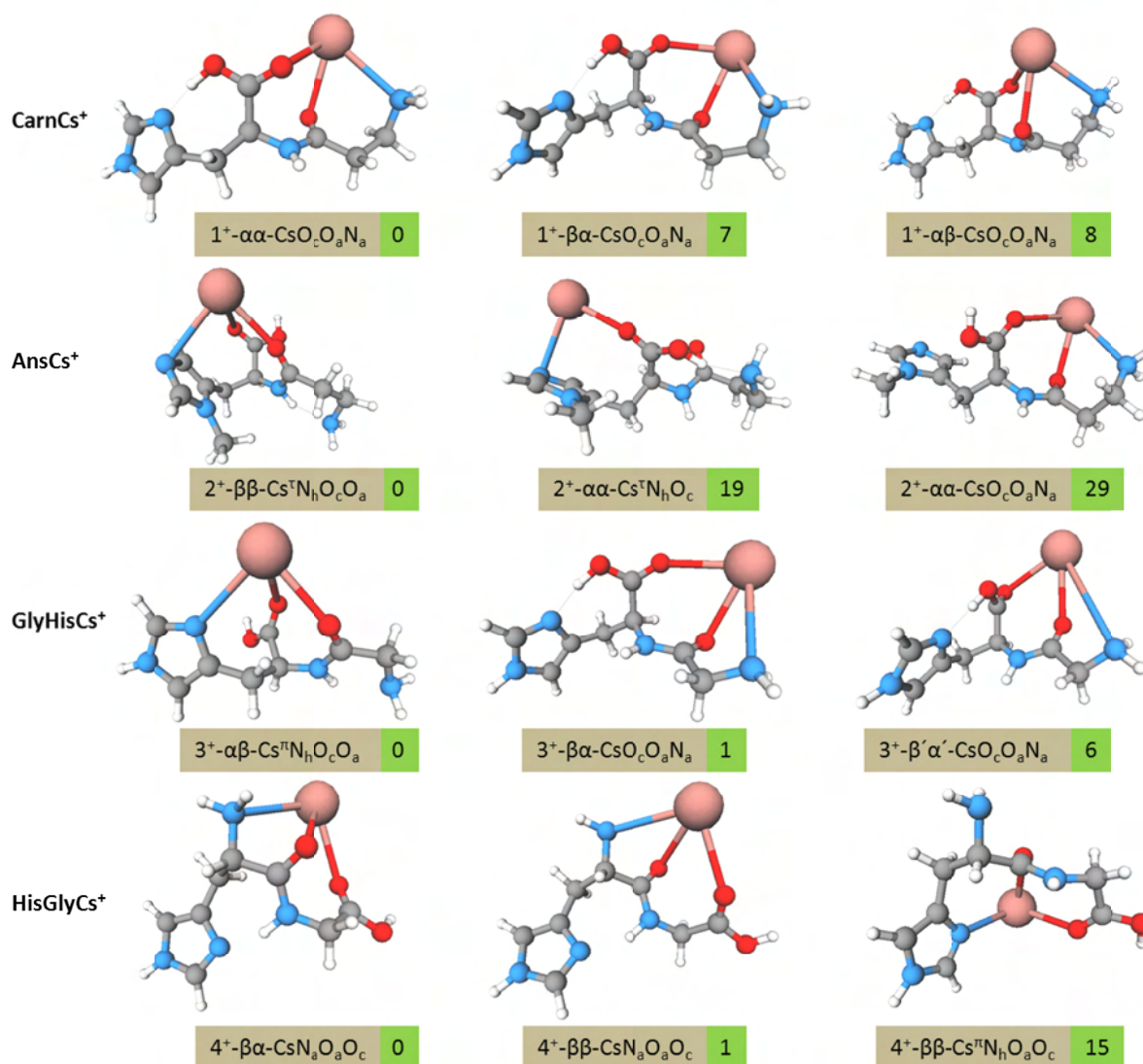


**Figure 11:** Calculated binding motives of dipeptides 1-4 with Cs<sup>+</sup> and relative energies in kJ/mol. (For definition of nomenclature, refer to page 62)

Complexation of the Cs<sup>+</sup> ion by **1** leads to similar binding motives like in the  $1^+-\alpha\alpha\text{-LiO}_c\text{O}_a\text{N}_a$  and  $1^+-\alpha\beta\text{-LiO}_c\text{O}_a\text{N}_a$  isomers. Additionally, a structure  $1^+-\beta\alpha\text{-CsO}_c\text{O}_a\text{N}_a$  arises showing a change of the dihedral angle 1 from *alpha* to *beta*.  $2^+\text{-Cs}$  and  $3^+\text{-Cs}$  show comparable minimum structures which mainly differ in the orientation of the histidin ring. In structure  $2^+-\beta\beta\text{-Cs}^{\text{N}}\text{N}_h\text{O}_c\text{O}_a$ , the metal ion binds to the His <sup>1</sup>N nitrogen atom, whereas it binds to the His <sup>2</sup>N nitrogen atom in  $3^+-\alpha\beta\text{-Cs}^{\text{N}}\text{N}_h\text{O}_c\text{O}_a$ . The  $2^+-\alpha\alpha\text{-Cs}^{\text{N}}\text{N}_h\text{O}_c$  structure is 19 kJ/mol higher in energy, 29 kJ/mol respectively for  $2^+-\alpha\alpha\text{-CsO}_c\text{O}_a\text{N}_a$ . The larger radius of the cesium cation with respect to the Li<sup>+</sup> cation leads to a rotation of the carboxyl group which hinders the formation of a hydrogen bond between the carboxylic proton and the aromatic histidin ring.



The  $\beta\alpha$ - $\text{CsO}_c\text{O}_a\text{N}_a$  binding type can be found in two slightly different conformations for the  $3^+$ -Cs complex. In the  $3^+-\beta'\alpha'$ - $\text{CsO}_c\text{O}_a\text{N}_a$  isomer, the carboxyl group and the N-terminus of the molecule is slightly rotated compared to the  $3^+-\beta\alpha$ - $\text{CsO}_c\text{O}_a\text{N}_a$  isomer. The energetical order of minimum structures of **4** strongly relates to the attached ion. The chelation of  $\text{Cs}^+$  by  $\text{N}_a\text{O}_a\text{O}_c$  becomes the favored binding motive for **4** while this binding motive is unfavorable for the complexation of a  $\text{Li}^+$  cation. For corresponding isomers of the  $\text{Na}^+$ ,  $\text{K}^+$  and  $\text{Rb}^+$  complexes of the dipeptides **1-4**, cf. Fig. 27-29.

#### IV-4.4: Comparison of experimental spectra and DFT predicted IR absorption spectra

##### IV-4.4.1: Results for Carnosine

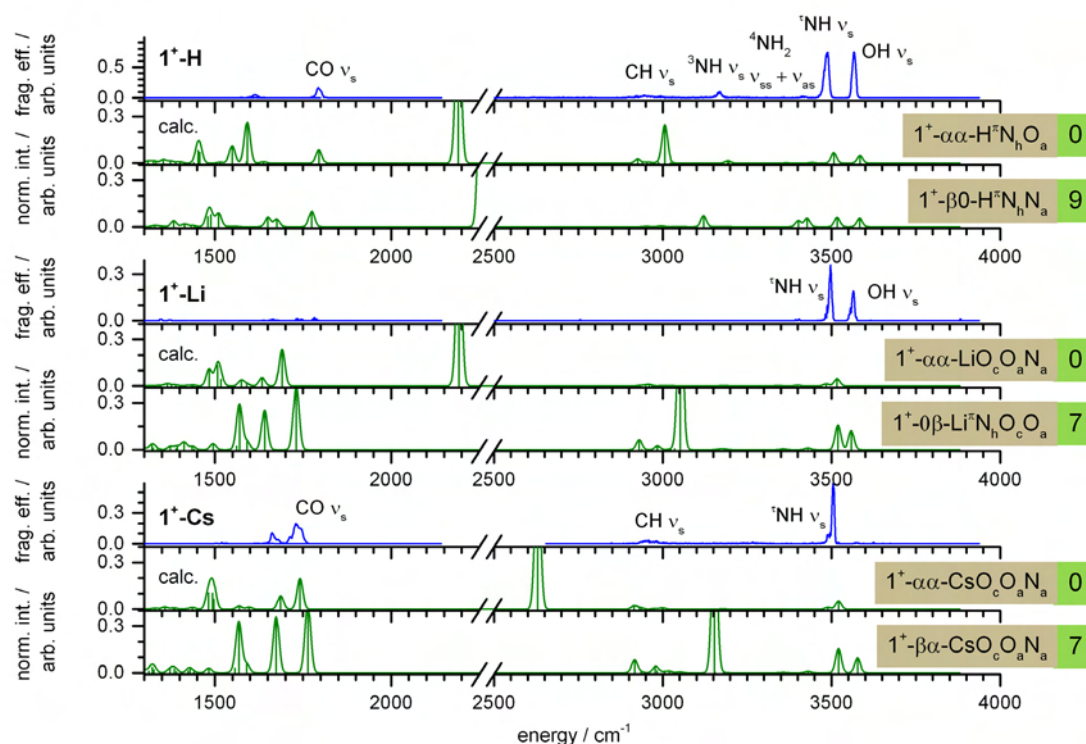


**Figure 12:** 1-color (blue) IR-MPD spectra of  $1^+-\text{H}$ ,  $1^+-\text{Li}$  and  $1^+-\text{Cs}$  and DFT predicted IR absorption spectra (dark green) scaled by 0.97.

The calculated spectrum of  $1^+-\alpha\alpha\text{-H}^+\text{N}_h\text{O}_a$  exhibits a quite good correlation with the IR-MPD spectrum of  $1^+-\text{H}$  (cf. Fig. 12). The scaling factor of 0.97 is appropriate for the fingerprint region below  $2000\text{ cm}^{-1}$  while a shift of approximately  $20\text{ cm}^{-1}$  to the blue remains for the CH, NH and OH stretch region above  $2500\text{ cm}^{-1}$ . The calculated absorption at  $2370\text{ cm}^{-1}$  corresponds to a stretch motion of the hydrogen bridge between the His  $^{\text{H}}\text{N}$  nitrogen atom and the amidic CO oxygen atom (cf. Fig. 9). The OPO/A system has an energy gap in this region and no experimental data could be

derived in this region. In the fingerprint region a broad band between 1500 and 1700  $\text{cm}^{-1}$  rises. This band corresponds to a combined stretch motion of CO and bending motion of the amidic NH group and aromatic CH groups.

The IR-MPD spectrum of  $1^+\text{-Li}$  exhibits only two intense bands for the  $^1\text{NH}$  and OH stretch motions. The calculated spectrum of  $1^+\text{-}\alpha\text{-LiO}_c\text{O}_a\text{N}_a$  shows only one small band corresponding to a  $^1\text{NH}$  stretch motion but no OH stretch motion can be expected according to the structure. Also isomer  $1^+\text{-}\alpha\beta\text{-LiO}_c\text{O}_a\text{N}_a$  does not involve a free OH group. We calculated the spectrum of  $1^+\text{-}\beta\beta\text{-Li}^n\text{N}_h\text{O}_c\text{O}_a$  which does partially agree with the experimental data. The band for the  $^1\text{NH}$  stretch motion shifts to the blue. The position of the free OH shifts approximately 10  $\text{cm}^{-1}$  to the red. The intensity distribution of the experimental spectrum gives hint that at least three isomers contribute to the spectrum.

The calculated spectrum of  $1^+\text{-}\alpha\alpha\text{-CsO}_c\text{O}_a\text{N}_a$  fits quite well to the 1-color IR-MPD spectrum of  $1^+\text{-Cs}$ . A weak band corresponding to a free OH stretch motion can be observed in the experimental data. This band cannot be explained by the three shown structures (cf. Fig. 11). Therefore we assume at least a fourth isomer of  $1^+\text{-Cs}$ . The search for isomers led to an additional structure with a free OH group which is 16 kJ/mol higher in energy than the minimum structure. The isomer corresponds to the structure of  $3^+\text{-}\alpha\beta\text{-Cs}^n\text{N}_h\text{O}_c\text{O}_a$  and has the following binding motive:  $1^+\text{-}\beta\beta\text{-Cs}^n\text{N}_h\text{O}_c\text{O}_a$



## IV-4.4.2: Results for Anserine

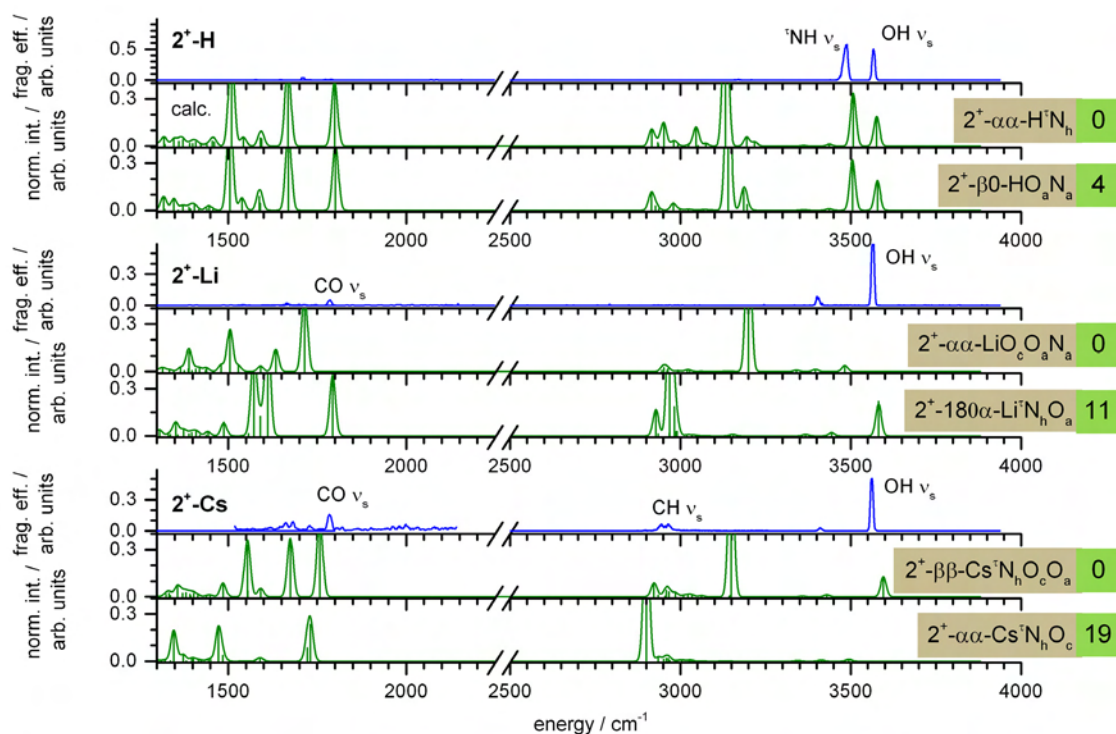


**Figure 13:** 1-color (blue) IR-MPD spectra of  $2^+\text{-H}$ ,  $2^+\text{-Li}$  and  $2^+\text{-Cs}$  and DFT predicted IR absorption spectra (dark green) scaled by 0.97.

The IR-MPD spectrum of  $2^+\text{-H}$  shows only two bands in the NH and OH stretch region (cf. Fig. 13). Both calculated minimum structures predict those bands and no further assumptions can be drawn. Experimental data for  $2^+\text{-Li}$  exhibits one intense band corresponding to a OH stretch motion and two small bands. The isomer  $2^+\text{-}\alpha\text{-LiO}_c\text{O}_a\text{N}_a$  has no free OH group and there is no clear evidence that this isomer contributes to the experimental spectrum. The isomer  $2^+\text{-180}\alpha\text{-Li}^+\text{N}_h\text{O}_a$  contains a free OH group and its calculated spectrum is therefore compared to the experiment instead of the one of  $2^+\text{-}\alpha\text{-LiO}_c\text{O}_a\text{N}_a$ . The calculated spectrum has a good accordance to all three experimentally derived bands.

The calculated bands for the  $2^+\text{-}\beta\text{-Cs}^+\text{N}_h\text{O}_c\text{O}_a$  isomer exhibit a moderate accordance to the experimental spectrum. Most bands shift either to the red or the blue. There is no clear evidence that isomer  $2^+\text{-}\alpha\text{-Cs}^+\text{N}_h\text{O}_c$  contributes to the measured spectrum.

## IV-4.4.3: Results for GlyHis

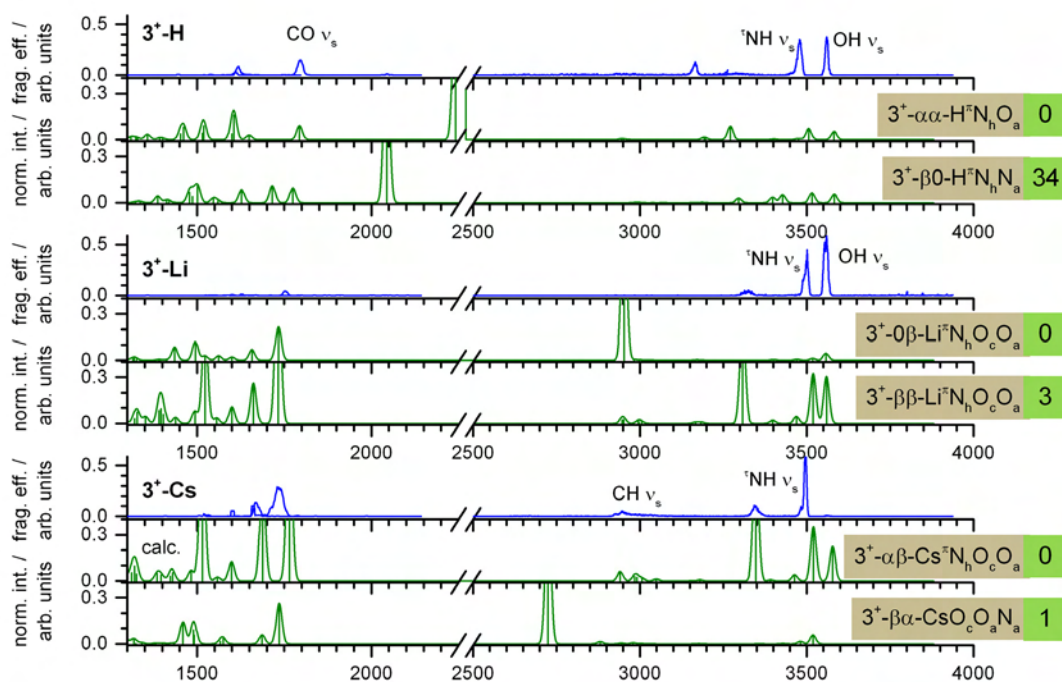


**Figure 14:** 1-color (blue) IR-MPD spectra of  $3^+$ -H,  $3^+$ -Li and  $3^+$ -Cs and DFT predicted IR absorption spectra (dark green) scaled by 0.97.

The calculated spectrum of the isomer  $3^+$ - $\alpha\alpha$ -H<sup>+</sup>N<sub>h</sub>O<sub>a</sub> is in a good accordance to all experimentally found bands (cf. Fig. 14). The band at 3270 cm<sup>-1</sup> corresponds to an amidic NH stretch motion which is broadened by the interaction with the terminal amine. The experimental band at 3165 cm<sup>-1</sup> may correlate to aromatic CH stretch motions of the histidine ring although the intensity is suddenly high. No evidence can be seen for the contribution of the  $3^+$ - $\beta 0$ -H<sup>+</sup>N<sub>h</sub>N<sub>a</sub> isomer to the experimental spectrum.

The experimental spectrum of  $3^+$ -Li can be explained by the superposition of the calculated spectra of the isomers  $3^+$ - $0\beta$ -Li<sup>+</sup>N<sub>h</sub>O<sub>c</sub>O<sub>a</sub> and  $3^+$ - $\beta\beta$ -Li<sup>+</sup>N<sub>h</sub>O<sub>c</sub>O<sub>a</sub>. In difference to the IR-MPD spectrum of  $3^+$ -Li, almost no contribution of bands corresponding to free OH stretch motions can be found in the spectrum of  $3^+$ -Cs. Neither the calculated spectrum of  $3^+$ - $\alpha\beta$ -Cs<sup>+</sup>N<sub>h</sub>O<sub>c</sub>O<sub>a</sub> nor the one of  $3^+$ - $\beta\alpha$ -CsO<sub>c</sub>O<sub>a</sub>N<sub>a</sub> can explain the experimental spectrum.

## IV-4.4.4: Results for HisGly

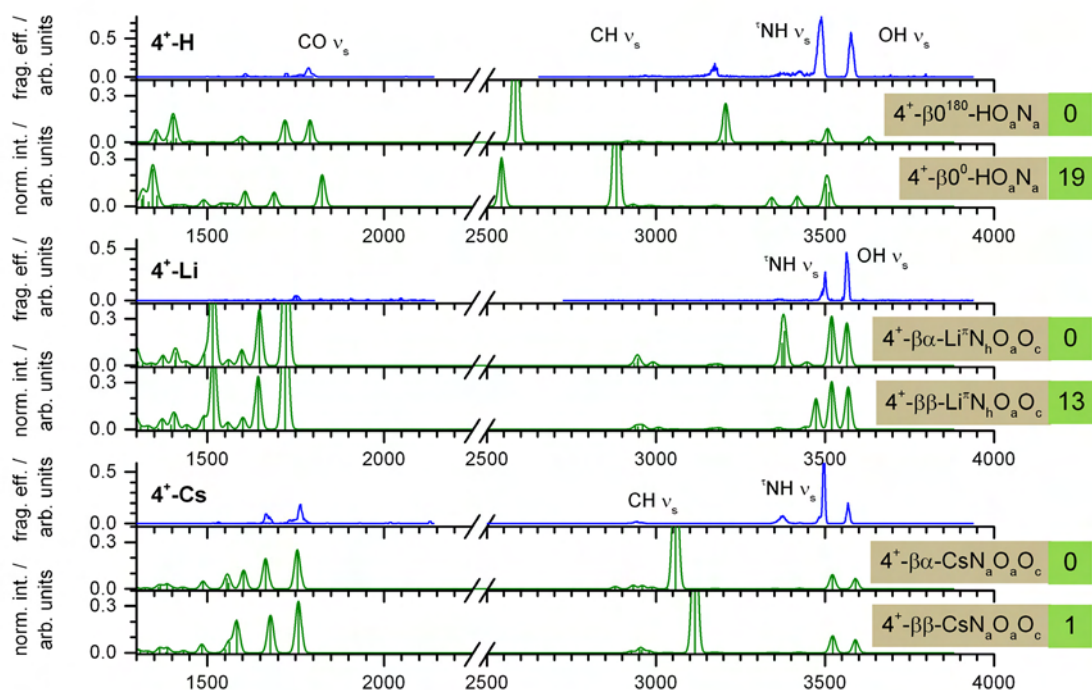


**Figure 15:** 1-color (blue) IR-MPD spectra of  $4^+$ -H,  $4^+$ -Li and  $4^+$ -Cs and DFT predicted IR absorption spectra (dark green) scaled by 0.97.

The calculated spectrum of  $4^+$ - $\beta 0^{180}$ -HO<sub>a</sub>N<sub>a</sub> exhibits a moderate accordance to the experimental spectrum of  $4^+$ -H (cf. Fig. 15). The position of the free OH stretch motion band is shifted approximately 50 cm<sup>-1</sup> to the blue which is 30 cm<sup>-1</sup> more than in the theoretical spectra discussed before. The occurrence of the small bands at 3367 and 3417 cm<sup>-1</sup> may correlate to a contribution of the  $4^+$ - $\beta 0^0$ -HO<sub>a</sub>N<sub>a</sub> isomer to the spectrum.

Both strong and both weak bands in the spectrum of the  $4^+$ -Li complex can be explained by the calculated spectrum of the  $4^+$ - $\beta\alpha$ -Li<sup>m</sup>N<sub>h</sub>O<sub>a</sub>O<sub>c</sub> isomer. Both minimum isomers  $4^+$ - $\beta\alpha$ -CsN<sub>a</sub>O<sub>a</sub>O<sub>c</sub> and  $4^+$ - $\beta\beta$ -CsN<sub>a</sub>O<sub>a</sub>O<sub>c</sub> of the  $4^+$ -Cs complex exhibit a similar theoretical spectrum. No clear distinction between or evidence for the contribution of both isomers can be drawn by comparison with the experimental data. Both isomers are capable to explain the measurements.

We used the structure types displayed in Figures 10 and 11 in order to determine the minimum structures of the Na<sup>+</sup>, K<sup>+</sup> and Rb<sup>+</sup> adducts to **1-4** (cf. Fig. 27-29). This procedure led directly to the energetic lowest isomers for each dipeptide alkali adduct combination with only a few exceptions. Those exceptions are mostly due to small variations in the orientation of side chains and are

therefore not further discussed. We plotted the relative energies of structure types against the chelated alkali ion in order to figure out trends in the binding behavior (cf. Fig. 16).

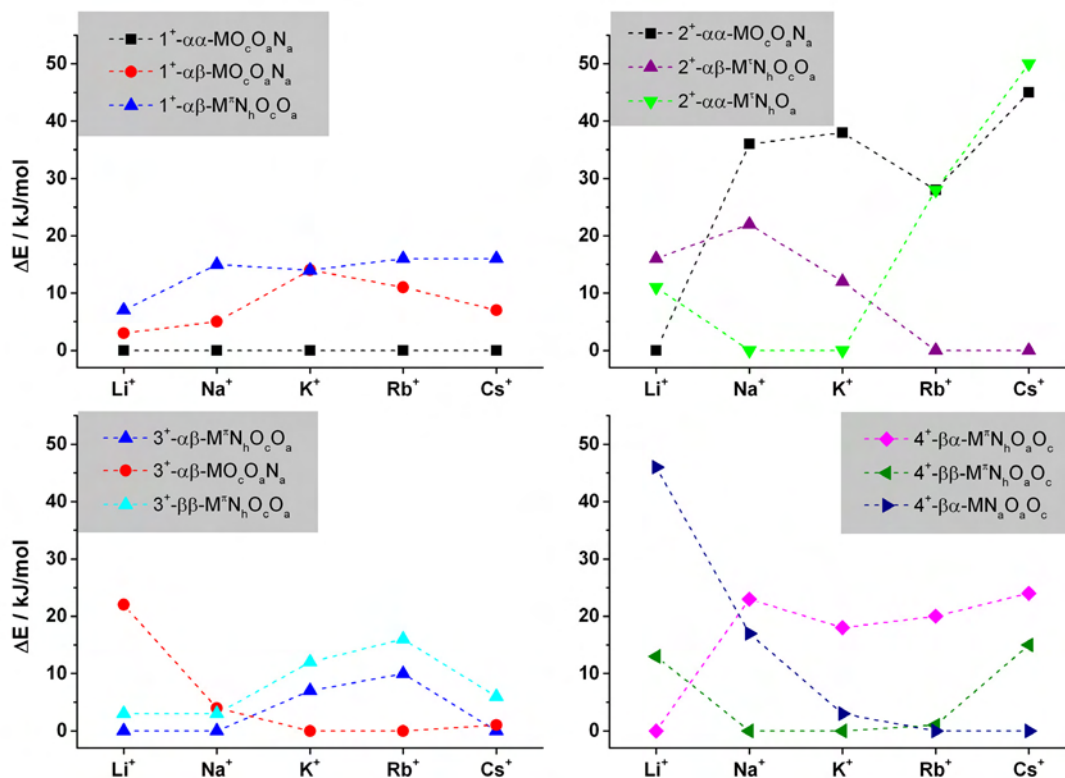


**Figure 16:** Relative energies (in kJ/mol) of calculated structure types of the alkali dipeptide complexes  $X^+-M$  (cf. Fig. 10, 11, 27-29) ( $X=1-4$ ;  $M=Li, Na, K, Rb, Cs$ ).

The  $1^+-\alpha\alpha\text{-MO}_c\text{O}_a\text{N}_a$  structure type is capable to chelate all alkali ions in the most stable way (cf. Fig. 16). The relative order in energy for  $1^+-\alpha\beta\text{-MO}_c\text{O}_a\text{N}_a$  and  $1^+-\alpha\beta\text{-M}^n\text{N}_h\text{O}_c\text{O}_a$  remains the same except for the  $K^+$  carnosine complex at which both isomers tend to be isoenergetic.

The  $\alpha\alpha\text{-MO}_c\text{O}_a\text{N}_a$  structure type represents the minimum energy structure for  $2^+\text{-Li}$  as shown before. This structure type becomes more than 30 kJ/mol energetically unfavorable for all alkali ions larger than  $\text{Li}^+$ .  $\text{Na}^+$  and  $\text{K}^+$  cations tend to form  $2^+-\alpha\alpha\text{-M}^n\text{N}_h\text{O}_a$  structures which become as unfavorable as the  $\alpha\alpha\text{-MO}_c\text{O}_a\text{N}_a$  structure types for  $\text{Rb}^+$  and  $\text{Cs}^+$ . The latter two ions form preferably the  $2^+-\alpha\beta\text{-M}^n\text{N}_h\text{O}_c\text{O}_a$  structure.

The relative energy distance of the  $3^+-\alpha\beta\text{-M}^n\text{N}_h\text{O}_c\text{O}_a$  and  $3^+-\beta\beta\text{-M}^n\text{N}_h\text{O}_c\text{O}_a$  isomers remains approximately the same for all alkali ions. The first structure type is the most favorable for  $\text{Li}^+$  and  $\text{Na}^+$  complexes of **3** as well as for  $3^+\text{-Cs}$  complexes. In the latter case, the  $3^+-\alpha\alpha\text{-MO}_c\text{O}_a\text{N}_a$  type is almost isoenergetic to  $3^+-\alpha\beta\text{-M}^n\text{N}_h\text{O}_c\text{O}_a$ .  $3^+-\alpha\alpha\text{-MO}_c\text{O}_a\text{N}_a$  isomers are the most stable structure types for  $\text{K}^+$  and  $\text{Rb}^+$  adducts.

The  $4^+$ - $\beta\alpha$ - $M^+N_hO_aO_c$  structure is the most stable isomer of the  $4^+$ -Li complex. This structure type becomes more than 20 kJ/mol energetically unfavorable for all other alkali ions. The  $4^+$ - $\beta\beta$ - $M^+N_hO_aO_c$  structure binds  $Na^+$  and  $K^+$  ions most favorable and is almost isoenergetic to the  $4^+$ - $\beta\alpha$ - $MN_aO_aO_c$  structure of the  $4^+$ -Rb complex. The latter structure type is the most stable of isomer of the  $4^+$ -Cs complex.

#### IV-4.5: Gibbs free dissociation energies of alkali cations to the most stable isomers of 1-4

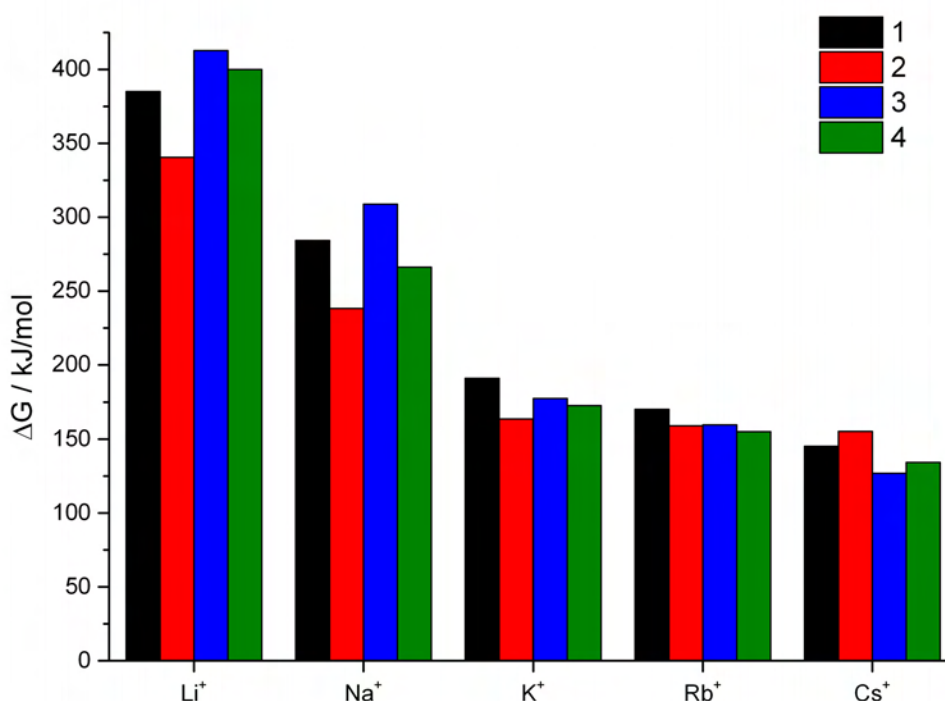


**Figure 17:** DFT derived Gibbs free energies (kJ/mol, 298.15 K, BSSE corrected) for the dissociation of alkali cations from the energetic minimum isomers of the dipeptide-alkali complexes. Structure of the neutral dipeptide obtained by a geometry optimization of the molecule after the dissociation of the alkali ion.

We calculated Gibbs free energies (cf. Fig. 17) for the separation of the alkali ions from the  $X^+-M$  complexes ( $X = 1-4$  and  $M = Li, Na, K, Rb, Cs$ ) in order to compare them to  $E_{CID}$  values derived from CID measurements (cf. Fig. 18 and Table 8). We used calculations of the minimum structures of the neutral dipeptides, the isolated metal ions and the energetic minimum isomers for  $Li^+$  and  $Cs^+$  corresponding to the IR-MPD measurements. For the  $Na^+$ ,  $K^+$  and  $Rb^+$  dipeptide complexes, we used the most stable isomers (cf. Fig. 16). We corrected the DFT energies by basis set superposition error (BSSE) calculations and by the Gibbs free energy correction for 298.15 K.

The binding energy decreases with the size of the alkali metal ion and the energy distribution within one adduct group (e.g. Fig. 17,  $\text{Li}^+$  vs.  $\text{Cs}^+$  groups) gets smaller.  $\text{Li}^+$  and  $\text{Na}^+$  ions are strongly bound to the dipeptides. Gibbs free dissociation energies of the  $\text{K}^+$ ,  $\text{Rb}^+$  and  $\text{Cs}^+$  dipeptide complexes have a comparable magnitude. In most cases, the dipeptide **2** exhibits the lowest energy needed for a splitting of the alkali ion.

#### **IV-4.6: Relation of CID fragmentation amplitudes to DFT derived Gibbs free dissociation energies**

We measured comparative CID appearance curves for each combination of dipeptide and alkali metal ion in order to estimate the relative energies of the dissociation channels. We isolated the most abundant isotope peak of the dipeptide alkali complexes and applied a stepwise rise of the fragmentation amplitude. For reasons of comparability we use center-of-mass transformed appearance curves in Fig. 18.

In case of the protonated dipeptides and the  $\text{Li}^+$ ,  $\text{Na}^+$ ,  $\text{Rb}^+$  and  $\text{Cs}^+$  dipeptide complexes, the slope and the position of the experimental CID appearance curves are quite uniform within a group, except for **2<sup>+</sup>-Na**. The mass spectrometer is only capable to store fragment ions resulting from CID processes which have a mass to charge ratio above 27% of the parents  $m/z$  value. Therefore, the deficient amount of ionic fragments within the measurements of dipeptide  $\text{K}^+$  complexes was compensated by the assumption of a constant total ion intensity during the measurement.

Table 8 summarizes the center of mass transformed fragmentation amplitude values ( $E_{\text{CID}}$ ) needed for a ratio of 50% ionic fragments in the total sum of ion intensities. A clear trend to lower amplitudes can be seen for  $\text{Rb}^+$  and  $\text{Cs}^+$ .  $\text{Li}^+$ ,  $\text{Na}^+$  and  $\text{K}^+$  dipeptide complexes exhibit comparable center of mass transformed amplitudes.

This values can be correlated to an amount of energy that has to be transferred to an ion during the CID process to give access to one or several fragmentation channels. Especially for complexes of the “small” ions like  $\text{H}^+$ ,  $\text{Li}^+$  and  $\text{Na}^+$  a huge variety of fragments occurs (cf. Table 1). The loss of  $\text{Rb}^+$  and  $\text{Cs}^+$  from their dipeptide complexes becomes the favorable fragmentation channel for the “large” ions.



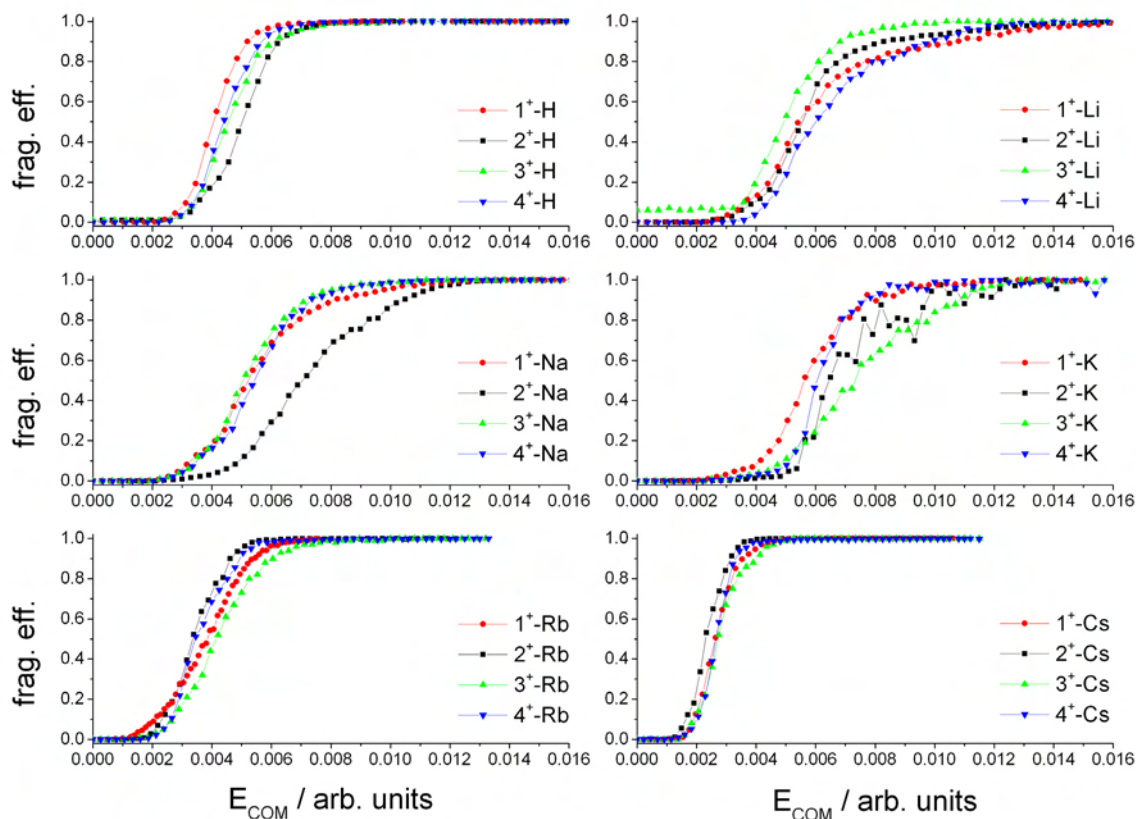


**Figure 18:** Center of mass transformed fragmentation amplitudes of CID appearance curves for the protonated dipeptides **1-4** and their complexes of the alkali cations  $Li^+$ ,  $Na^+$ ,  $K^+$ ,  $Rb^+$ ,  $Cs^+$ .

**Table 8.** Center of mass corrected fragmentation  $E_{CID}$  values ( $\times 10^{-3}$ ) of the alkali metal adducts of **1-4** derived from sigmoidal fit of the data depicted in Fig. 18. Calculated free enthalpy for the cleavage of  $M^+$  from the dipeptid complexes in kJ/mol.

M	1 (Carnosine)		2 (Anserine)		3 (GlyHis)		4 (HisGly)	
	$E_{CID}$	$\Delta G /$ kJ/mol	$E_{CID}$	$\Delta G /$ kJ/mol	$E_{CID}$	$\Delta G /$ kJ/mol	$E_{CID}$	$\Delta G /$ kJ/mol
$Li^+$	5.6	385	5.5	341	5.0	412	6.2	400
$Na^+$	5.3	284	7.2	238	5.1	309	5.4	266
$K^+$	5.7	191	6.6	164	7.4	178	6.1	173
$Rb^+$	3.8	170	3.4	159	4.2	160	3.6	155
$Cs^+$	2.7	145	2.4	155	2.8	127	2.7	134

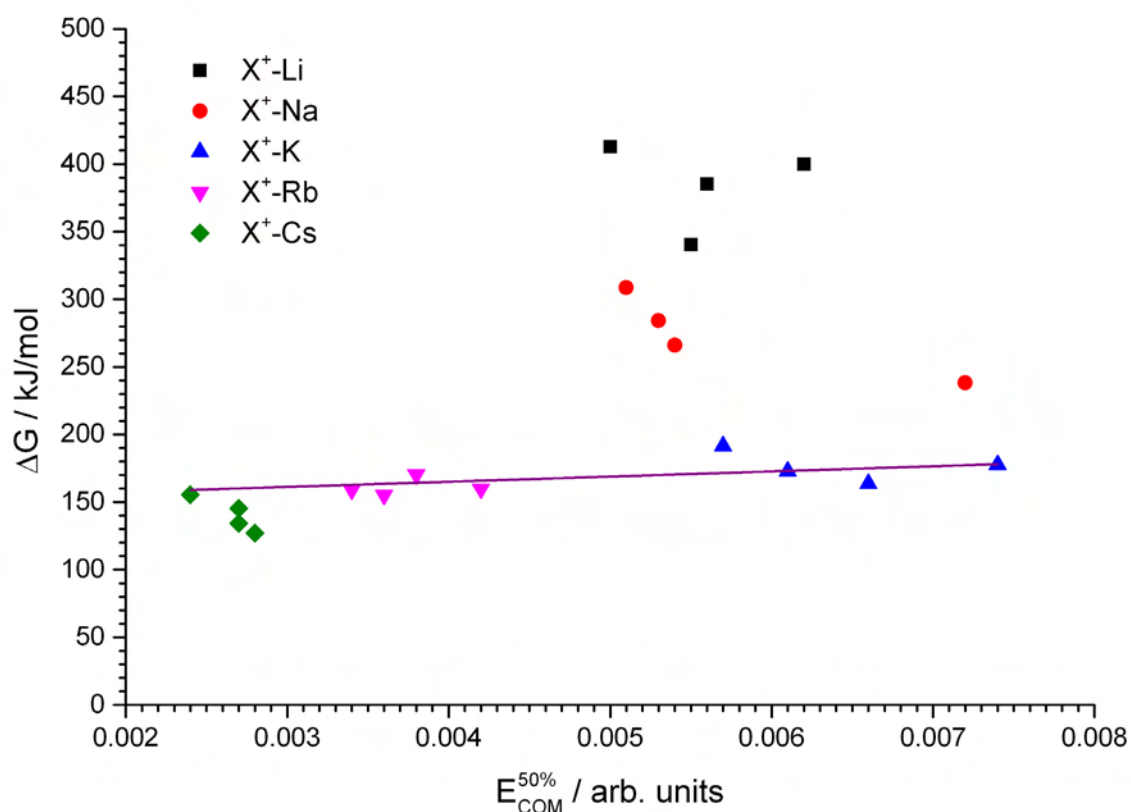


**Figure 19:** DFT derived Gibbs free energies (in kJ/mol) for the dissociation of  $M^+$  from the alkali dipeptide complexes of **1-4** in relation to the center-of-mass (COM) transformed  $E_{COM}^{50\%}$  values derived from CID experiments (cf. Fig. 18, for numerical values cf. Table 8). Data points of same color correspond to dipeptide complexes  $X^+-M$  of the same alkali ion ( $X = 1-4$ ,  $M = Li^+, Na^+, K^+, Rb^+, Cs^+$ ). Linear fit (–) of Gibbs free energy of  $Li^+$ ,  $Na^+$  and  $K^+$  dipeptide complexes versus  $E_{COM}^{50\%}$  values.

We plotted the Gibbs free energy for the dissociation of  $M^+$  from the neutral dipeptides against estimated  $E_{COM}^{50\%}$  values in order to correlate the internal energy scale of the mass spectrometer to Gibbs free energies for CID induced losses (cf. Table 2 and Figure 19). For reasons of clarity we did not mark the dipeptides separately and summarized them as groups belonging to one alkali ion. Data pairs can be classified into three categories.  $Rb^+$  and  $Cs^+$  dipeptide adducts form one category which exhibits low  $E_{COM}^{50\%}$  values and low free dissociation energies. The second one comprises the  $K^+$  adducts of **1-4** with high  $E_{COM}^{50\%}$  and low  $\Delta G$  values. The third category consists of the  $Li^+$  and  $Na^+$  complexes of the four dipeptides with  $E_{COM}^{50\%}$  values comparable to those of the  $K^+$  adducts but significantly higher free dissociation energies.

The Gibbs free dissociation energies for  $Li^+$  and  $Na^+$  dipeptide complexes do not correlate linearly to the  $E_{COM}^{50\%}$  values, since the calculated fragmentation pathway does not reflect the experimental findings. Therefore, those values are not taken into account for a linear fit. We correlate the  $E_{CID}$  values of the  $K^+$ ,  $Rb^+$  and  $Cs^+$  dipeptide complexes to the Gibbs free energy of the  $M^+$  dissociation



assuming a linear dependence. We applied a linear fitting function to the data pairs of twelve dipeptide alkali combinations resulting in a moderate correlation between  $\Delta G$  and  $E_{COM}^{50\%}$ .

$$\Delta G = (381 \pm 158 \text{ kJ/mol}) * E_{COM}^{50\%} + (150 \pm 7 \text{ kJ/mol}) \quad (4)$$

The standard deviation of the derived linear fitting function is quite large for the slope (ca. 41 %) while it is moderate for the intercept (ca. 5 %) (cf. Equation 4).

#### IV-4.7: H/D isotope exchange and relative rate constants

We studied the reactions of protonated and alkali ion complexed dipeptides **1-4** with  $\text{ND}_3$  under single collision conditions ( $2 \times 10^{-9}$  mbar) in order to determine the influence of alkali ion induced conformational changes to the acidity of the exchangeable protons of the dipeptides. Therefore, we stored the alkali-dipeptide ions for variable time in a FT-ICR ion trap. During this time the ions partially undergo H/D exchange reactions with  $\text{ND}_3$ .

We normalized intensities of the parent and H/D exchanged species and fitted the temporal evolution of the experimental data points to pseudo first order kinetics which provides for relative partial rate constants. We applied here two different models: one with a single H/D exchange (*se*) reaction per collision and one allowing for a single and double H/D exchange (*sde*) reaction per single collision (cf. Fig. 20-21 for **1<sup>+</sup>-H** and **1<sup>+</sup>-M**, cf. Fig. 30-35 for **X<sup>+</sup>-M** (X=2-4; M=H, Li, Na, K)). Under the chosen conditions, no H/D exchange reactions of the  $\text{Rb}^+$  and  $\text{Cs}^+$  dipeptide complexes with  $\text{ND}_3$  could be observed. The signal intensity of the parent ions was too poor.

The assumption of an additional double H/D exchange during one reaction step leads to a better accordance between the experimental data and the calculated fits (cf. Fig. 20). With increasing reaction delay, the fit of the normalized intensities of complexes **1<sup>+</sup>-h<sub>7</sub>d<sub>0</sub>**, **1<sup>+</sup>-h<sub>4</sub>d<sub>3</sub>**, **1<sup>+</sup>-h<sub>3</sub>d<sub>4</sub>**, **1<sup>+</sup>-h<sub>2</sub>d<sub>5</sub>** and **1<sup>+</sup>-h<sub>1</sub>d<sub>6</sub>** gets poor within both models. The correlation of the calculated fits with the experimental data increases for all other partially deuterated species using the *sde* model.

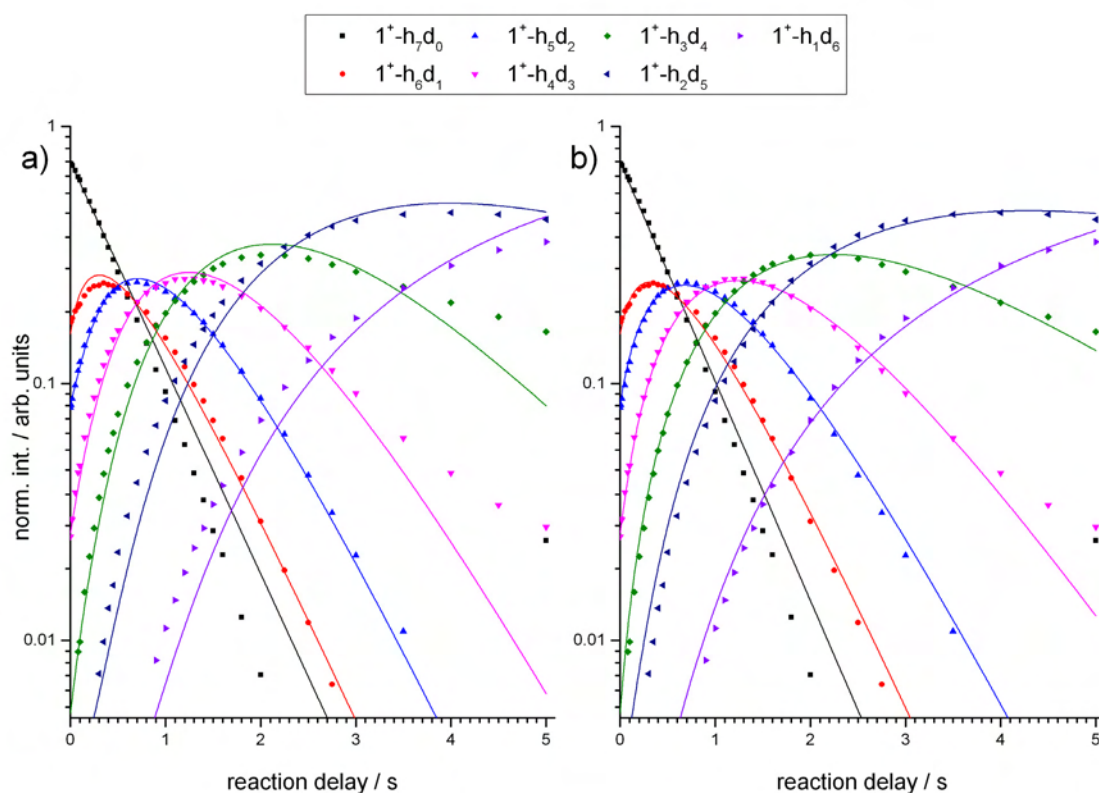


**Figure 20:** Normalized reactant and product intensities in the reactions of protonated  $1^+H$  with  $ND_3$ . The temporal evolution of the experimental data points (symbols) is fitted to pseudo first order kinetics (solid lines) which provides for relative partial rate constants. Fits correlate to single H/D exchange reactions (a) and to single and double H/D exchange (b) per single collision. Fits arise through application of generic algorithm code. Fits of (b) are superior to those of (a). (cf. Table 9 for numerical data)

All protonated dipeptides, except complex  $3^+h_5d_1$ , undergo the exchange of the second proton with the highest rate in the *se* model assumption. Furthermore, exchange rates of all protonated peptides have a similar progression until the exchange of the third proton. All rates decrease for the exchange of more than two protons. The complex  $3^+$  exchanges with the lowest rate constants within almost all reaction steps. The assumption of a consecutive exchange of a up to two protons in one reaction step (*sde*) leads to a crucial change in the derived rate constants. The *sde* rates of the complexes  $1^+H$  and  $4^+H$  predict the single exchange reaction as two up to four times faster (until  $k_{24}$ ) than the simultaneous exchange of two protons. Complex  $2^+H$  exhibits a nonuniform progression of the rates of single and double exchanges. The *sde* model does not lead to a better agreement between the fitting and the experimental data of complex  $3^+H$ .

**Table 9:** Relative partial rate constants  $k_{mn}$  by single H/D exchange (*se*) per collision only and by in parallel single and double H/D exchange (*sde*) per collision for reactions of protonated dipeptides with  $\text{ND}_3$  ( $p=2 \times 10^{-9}$  mbar) in the gas phase as obtained from fitting experimental data (cf. Fig. 20, 30-32). Indices of  $k_{mn}$  stand for the number of deuterium atoms in educt (*m*) and the exchanged product (*n*). (n.o. = not observed)

rel. par. rate constant	$1^+-\text{h}_{6-n}\text{d}_n$		$2^+-\text{h}_{5-n}\text{d}_n$		$3^+-\text{h}_{6-n}\text{d}_n$		$4^+-\text{h}_{6-n}\text{d}_n$	
	<i>se</i>	<i>sde</i>	<i>se</i>	<i>sde</i>	<i>se</i>	<i>sde</i>	<i>se</i>	<i>sde</i>
$k_{01}$	1.84	1.49	2.03	1.50	1.16	0.96	1.13	0.97
$k_{02}$	-	0.47	-	0.79	-	0.25	-	0.21
$k_{12}$	2.89	1.74	3.04	0.82	1.05	0.79	1.38	0.90
$k_{13}$	-	0.61	-	1.41	-	0.03	-	0.24
$k_{23}$	2.23	1.34	1.95	0.18	0.40	0.36	1.02	0.62
$k_{24}$	-	0.49	-	0.87	-	< 0.01	-	0.17
$k_{34}$	1.66	0.85	0.87	0.22	0.26	0.24	0.52	0.34
$k_{35}$	-	0.41	-	0.05	-	<< 0.01	-	0.02
$k_{45}$	0.88	0.50	0.08	0.01	0.10	0.07	0.10	0.05
$k_{46}$	-	<< 0.01	-	-	-	n.o.	-	n.o.
$k_{56}$	0.29	0.29	-	-	n.o.	n.o.	n.o.	n.o.

**Table 10:** Relative partial rate constants  $k_{mn}$  by single H/D exchange per collision only (*se*) and by in parallel single and double H/D exchange per collision (*sde*) for reactions of  $1^+-\text{M}$  ( $\text{M}=\text{Li}, \text{Na}, \text{K}$ ) with  $\text{ND}_3$  ( $p=2 \times 10^{-9}$  mbar) in the gas phase as obtained from fitting experimental data (cf. Fig. 21). Indices of  $k_{mn}$  stand for the number of deuterium atoms in educt (*m*) and the exchanged product (*n*). (n.o. = not observed)

rel. par. rate constant	$1^+-\text{Li}-\text{h}_{5-n}\text{d}_n$		$1^+-\text{Na}-\text{h}_{5-n}\text{d}_n$		$1^+-\text{K}-\text{h}_{5-n}\text{d}_n$	
	<i>se</i>	<i>sde</i>	<i>se</i>	<i>sde</i>	<i>se</i>	<i>sde</i>
$k_{01}$	0.76	0.76	0.37	0.37	0.07	0.05
$k_{02}$	-	<< 0.01	-	<< 0.01	-	0.03
$k_{12}$	0.43	0.42	0.05	0.05	0.10	<< 0.01
$k_{13}$	-	0.01	-	<< 0.01	-	n.o.
$k_{23}$	0.28	0.25	0.13	0.10	n.o.	n.o.
$k_{24}$	-	0.01	-	0.13	-	n.o.
$k_{34}$	0.06	0.02	n.o.	n.o.	n.o.	n.o.

The kinetic model combining single and double exchange does not lead to a significant increase of the accordance between experimental data and calculated fits for complexes  $1^+\text{-Li}$ ,  $1^+\text{-Na}$  and  $1^+\text{-K}$  (cf. Fig. 21).

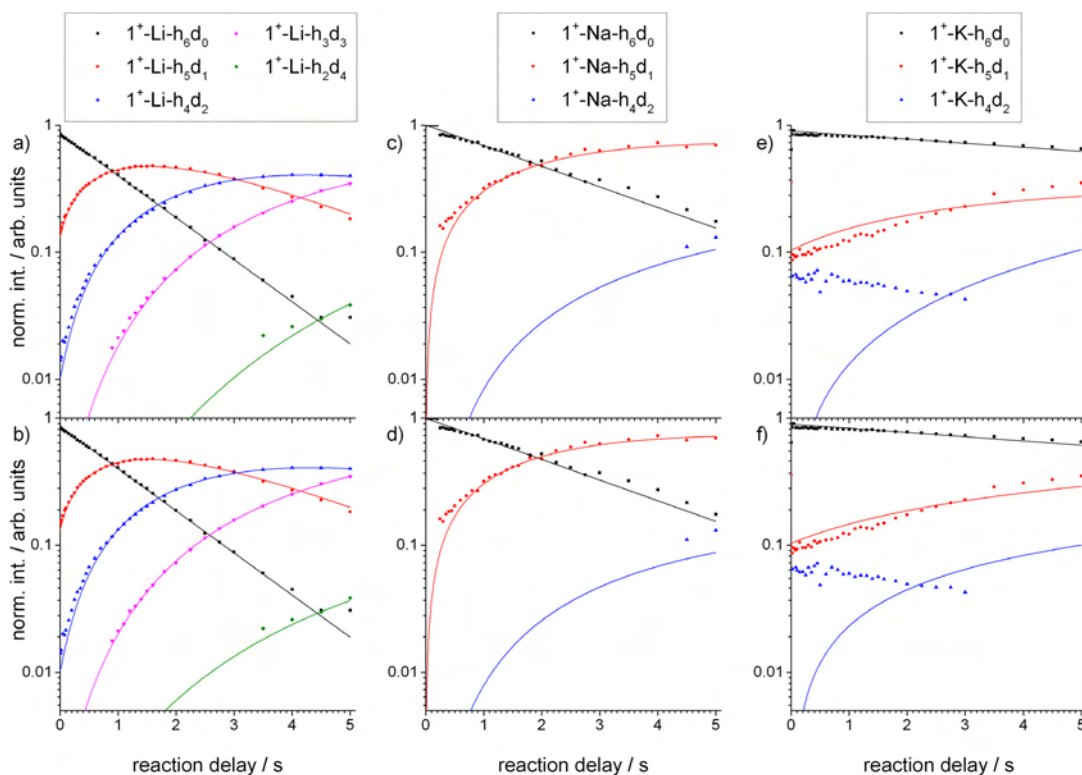


**Figure 21:** Normalized reactant and product intensities in the H/D exchange reactions of cationic  $1^+\text{-M}$  ( $M=\text{Li, Na, K}$ ) with  $\text{ND}_3$ . The temporal evolution of the experimental data points (symbols) is fitted to pseudo first order kinetics (solid lines) which provides for relative partial rate constants. Fits arise through application of generic algorithm code. Fits in (a, c, e) assume single H/D exchange reactions per single  $\text{ND}_3$  collisions. Fits in (b, d, f) assume single and possible double H/D exchange reactions per single  $\text{ND}_3$  collisions. Quality of fits is comparable, clear evidence of H/D double exchange is thus missing. (cf. Table 10 for numerical data)

Rate constants for the H/D exchange of  $\text{X}^+\text{-Li}$  complexes are lower than the rate constants of exchange reactions of the protonated dipeptides (cf. Tables 9-12). During the reaction time of up to 5 s, no exchanges above  $n = 2$  could be observed for 2-4. All rate constants decrease with the number of exchanged protons. 2 and 4 exhibit the largest drop of the rate constants in comparison to the protonated dipeptides.

**Table 11:** Relative partial rate constants  $k_{mn}$  by single H/D exchange per collision only (*se*) and by in parallel single and double H/D exchange per collision (*sde*) for reactions of of  $2^+M$  ( $M=Li, Na, K$ ) with  $ND_3$  ( $p= 2 \times 10^{-9}$  mbar) in the gas phase as obtained from fitting experimental data (cf. Fig. 33). Indices of  $k_{mn}$  stand for the number of deuterium atoms in educt (*m*) and the exchanged product (*n*). (n.o. = not observed)

rel. par. rate constant	$2^+Li-h_{4-n}d_n$		$2^+Na-h_{4-n}d_n$		$2^+K-h_{4-n}d_n$	
	<i>se</i>	<i>sde</i>	<i>se</i>	<i>sde</i>	<i>se</i>	<i>sde</i>
$k_{01}$	0.41	0.37	0.80	0.74	0.77	0.72
$k_{02}$	-	0.06	-	0.10	-	0.08
$k_{12}$	0.10	0.04	0.08	0.04	0.23	0.15
$k_{13}$	-	n.o.	-	n.o.	-	0.03
$k_{23}$	n.o.	n.o.	n.o.	n.o.	0.12	0.03

**Table12:** Relative partial rate constants  $k_{mn}$  by single H/D exchange per collision only (*se*) and by in parallel single and double H/D exchange per collision (*sde*) for reactions of of  $3^+M$  ( $M=Li, Na, K$ ) with  $ND_3$  ( $p= 2 \times 10^{-9}$  mbar) in the gas phase as obtained from fitting experimental data (cf. Fig. 34). Indices of  $k_{mn}$  stand for the number of deuterium atoms in educt (*m*) and the exchanged product (*n*). (n.o. = not observed)

rel. par. rate constant	$3^+Li-h_{5-n}d_n$		$3^+Na-h_{5-n}d_n$		$3^+K-h_{5-n}d_n$	
	<i>se</i>	<i>sde</i>	<i>se</i>	<i>sde</i>	<i>se</i>	<i>sde</i>
$k_{01}$	0.86	0.84	0.35	0.32	0.05	0.06
$k_{02}$	-	0.06	-	0.03	-	< 0.01
$k_{12}$	0.02	0.01	0.02	<< 0.01	<< 0.01	<< 0.01

**Table 13:** Relative partial rate constants  $k_{mn}$  by single H/D exchange per collision only (*se*) and by in parallel single and double H/D exchange per collision (*sde*) for reactions of of  $4^+M$  ( $M=Li, Na, K$ ) with  $ND_3$  ( $p= 2 \times 10^{-9}$  mbar) in the gas phase as obtained from fitting experimental data (cf. Fig. 35). Indices of  $k_{mn}$  stand for the number of deuterium atoms in educt (*m*) and the exchanged product (*n*). (n.o. = not observed)

rel. par. rate constant	$4^+Li-h_{5-n}d_n$		$4^+Na-h_{5-n}d_n$		$4^+K-h_{5-n}d_n$	
	<i>se</i>	<i>sde</i>	<i>se</i>	<i>sde</i>	<i>se</i>	<i>sde</i>
$k_{01}$	0.26	0.24	0.15	0.14	0.05	0.05
$k_{02}$	-	0.02	-	< 0.01	-	<< 0.01
$k_{12}$	0.03	<< 0.01	<< 0.01	<< 0.01	<< 0.01	<< 0.01

For the  $\text{Na}^+$  adducts of the four dipeptides, only two H/D exchanges could be observed in a reaction delay of up to 5s. All rate constants decrease with the number of exchanged protons, while there is no direct correlation to the relative trends of rate constants for the  $\text{X}^+\text{-Li}$  complexes. The  $\text{X}^+\text{-K}$  complexes undergo mostly less exchange reactions under the given reaction conditions, except for complex  $2^+\text{-K}$ . Complex  $1^+\text{-K}$  exchanges up to two protons, complex  $2^+\text{-K}$  up to three, the  $3^+\text{-K}$  and  $4^+\text{-K}$  complexes only one. Complex  $2^+\text{-K}$  exhibits the highest rate constants of all  $\text{X}^+\text{-K}$  ions. The *sde* model does not lead to significantly better quality of the fits.

#### IV-4.8: Conceivable relation of binding motives in protonated Carnosine and its $\text{Li}^+$ complex and H/D exchange rates with $\text{ND}_3$

We calculated relative energies of the interaction between  $\text{NH}_3$  (which is energetically almost equivalent to  $\text{ND}_3$ ) and the exchangeable protons of the energetic minimum isomers of complexes  $1^+\text{-H}$  and  $1^+\text{-Li}$  (cf. Fig. 22 & 23). We assume that a strong interaction of  $\text{NH}_3$  with a protonated group leads to a high probability for a H/D exchange.

$\text{NH}_3$  has the strongest interaction with the proton at the  ${}^1\text{N}_\text{h}$  nitrogen atom and with the hydrogen atom of the carboxyl group of complex  $1^+\text{-}\alpha\text{-H}{}^m\text{N}_\text{h}\text{O}_\text{a}$  (cf. Fig. 22). The His  ${}^m\text{N}_\text{h}$  proton is sterically less reachable due to its interaction with the amidic oxygen. The interaction with the terminal amine, at which double exchanges could occur, is energetically less favorable than the interactions described before.

The most favorable interaction site of  $\text{NH}_3$  with  $1^+\text{-}\alpha\text{-LiO}_\text{c}\text{O}_\text{a}\text{N}_\text{a}$  is due to theory at the  $\text{Li}^+$  ion. This leads to a fourfold coordination of the alkali metal (cf. Fig. 23). The interaction of  $\text{NH}_3$  with the His  ${}^m\text{N}_\text{h}$  proton is less favorable and the interaction with the terminal amine is more favorable than within the protonated carnosine ion. The carboxylic proton in isomer  $1^+\text{-}\alpha\text{-LiO}_\text{c}\text{O}_\text{a}\text{N}_\text{a}$  binds via a hydrogen bridge to the His  ${}^m\text{N}_\text{h}$  nitrogen atom. One possible energetic minimum structure for the interaction of  $\text{NH}_3$  with this proton is the insertion of the ammonia molecule between the protonated  ${}^m\text{N}_\text{h}$  nitrogen atom and the deprotonated carboxylic group in structure  ${}^m\text{N}_\text{h}\text{-H-NH}_3\text{-O}_\text{c}$ .

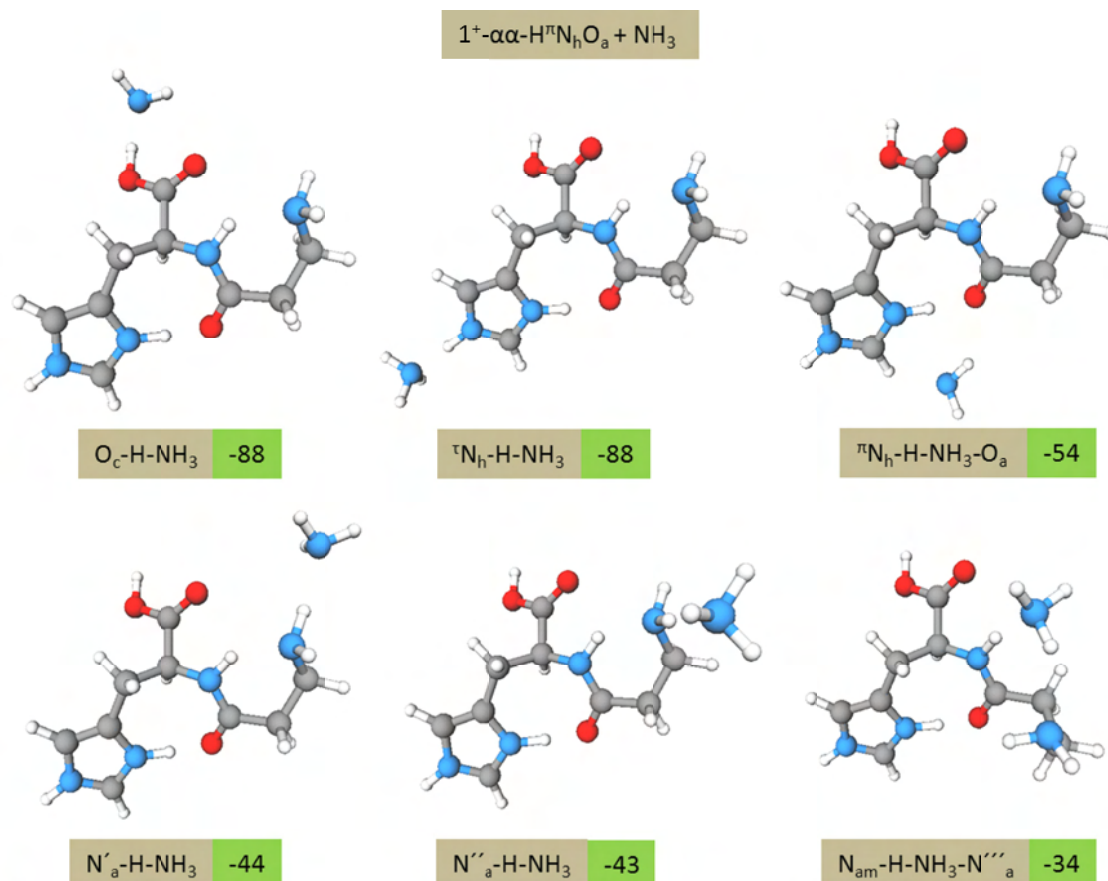


**Figure 22:** Structures and binding energies  $\Delta_B H^{0K}$  (in kJ/mol) in various isomers of the  $1^+-\alpha\text{-H}^{\pi}\text{N}_h\text{O}_a\text{-NH}_3$  complex (for definition of nomenclature, refer to page 62).

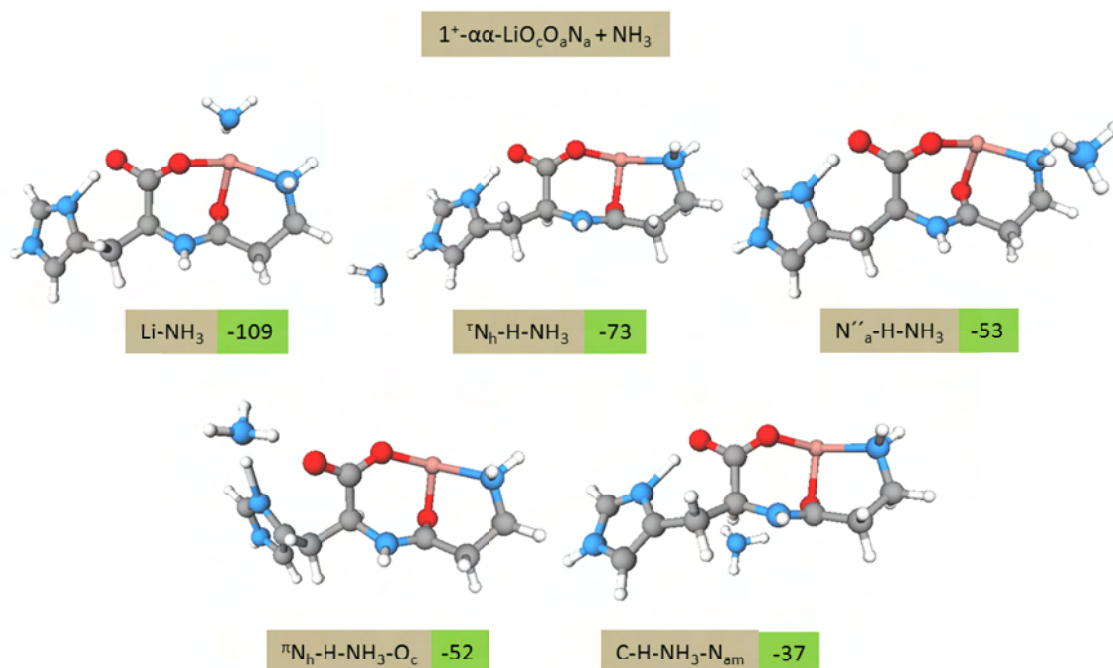


**Figure 23:** Structures and binding energies  $\Delta_B H^{0K}$  (in kJ/mol) within various isomers of the  $1^+-\alpha\text{-LiO}_c\text{O}_a\text{N}_a\text{-NH}_3$  complex (for definition of nomenclature, refer to page 62).

## IV-5: Discussion

### IV-5.1: ESI-MS

All four dipeptides **1-4** form alkali ion complexes under ESI-MS conditions. In mixtures of equimolar concentrations of alkali ions with one of the dipeptides the complexes arise in different ratios beneath the protonated form of the particular dipeptide which is always present. This demonstrates the high binding affinity of protons to the dipeptides. Our experimental data from CID measurements demonstrate that the complexation of an alkali metal ion by a dipeptide changes the fragmentation behavior crucially, except for the  $\text{Rb}^+$  and  $\text{Cs}^+$  complexes which mostly exhibit the cleavage of the metal ion as the dominant pathway (cf. Table 3).  $\text{K}^+$  can not be detected by the mass spectrometer which implies that CID spectra and relative abundancies of fragments of dipeptides- $\text{K}^+$  complexes include a high uncertainty regarding the preferred fragmentation channels.

In a former study we provided an insight into the fragmentation behavior of protonated Carnosine and its alkali ion complexes [5], wherefore we will not discuss all dipeptides separately. Relative abundancies of fragmentation channels of  $\mathbf{1}^+\text{-M}$  ( $\text{M}=\text{H}, \text{Li}, \text{Na}, \text{K}, \text{Rb}, \text{Cs}$ ) were estimated in different ways in the former and the current work which leads to deviations within the derived values.

Some parallel loss channels with strong varying relative abundancies could be figured out for the protonated dipeptides and their alkali metal complexes. The loss of  $-17 \text{ m/z}$  (according to  $\text{NH}_3$ ) is dominant for  $\mathbf{1}^+\text{-H}$  and  $\mathbf{2}^+\text{-H}$  while this fragmentation pathway was not observed for  $\mathbf{3}^+\text{-H}$  and  $\mathbf{4}^+\text{-H}$ . It was shown that the preferred protonation site of  $\mathbf{1}^+\text{-H}$  is at a nitrogen atom of the Histidine ring [36]. Therefore the formation of  $\text{NH}_3$  as neutral loss has a need for a proton transfer from an adjacent  $\text{CH}_2$  group. In case of  $\mathbf{1}^+\text{-H}$  and  $\mathbf{2}^+\text{-H}$  an olefinic terminal  $-\text{CH}=\text{CH}_2$  group can be formed while  $\mathbf{3}^+\text{-H}$  seems not to be capable to form a stable ionic fragment after a potential loss of  $\text{NH}_3$ . In the case of  $\mathbf{4}^+\text{-H}$  the loss of  $\text{NH}_3$  would lead to a  $\text{C}=\text{C}$  double bond in the backbone of the molecule resulting in strong conformational changes. The loss of e.g.  $-71, -117$  and  $-137 \text{ m/z}$  from several  $\mathbf{1}^+\text{-M}$  complexes can be correlated to the loss of  $-57, -103$  and  $-117 \text{ m/z}$  from several  $\mathbf{3}^+\text{-M}$  and  $\mathbf{4}^+\text{-M}$  complexes due to the mass difference of  $-14 \text{ m/z}$  (according to a shorter amine side chain) of **3** and **4** with respect to **1**. The loss channel of  $-151 \text{ m/z}$  from  $\mathbf{2}^+\text{-Li}$  and  $\mathbf{2}^+\text{-Na}$  can also be correlated to the loss of  $-137 \text{ m/z}$  from several  $\mathbf{1}^+\text{-M}$  complexes due to the mass shift of  $+14 \text{ m/z}$  (methyl group at the His  $^1\text{N}$  atom) from **1** to **2**. These fragmentation pathways are mostly not in a direct correlation to



performed loss groups in the minimum energy structures (cf. Fig. 9-11). Most pathways can only be described taking proton shifts and reorganization processes into account. Additionally the superposition of different fragment species appears which can lead to broad and hardly assignable isotopic patterns. Nevertheless, the difference in the mass shifts of neutral losses between the dipeptide-alkali complexes can be used to assign the origin of neutral losses.

#### IV-5.2: IR-MPD

IR-MPD spectra of the deprotonated dipeptides **1<sup>-</sup>**-**4<sup>-</sup>** exhibit well discernible bands of varying intensities (cf. Fig. 4). There are no bands that would correspond to free OH or NH stretch. Deprotonation should take place at the group with the highest acidity, which is the COOH group in all four molecules. The absence of stretch motions of the free NH bond can be explained by a hydrogen bonding with the negatively charged carboxy group. This would lead to red-shifted and broadened bands. Therefore, we assume that the weak absorptions above 3000 cm<sup>-1</sup> in the spectra of **1<sup>-</sup>**-**4<sup>-</sup>** may correspond to vibrational modes of N-H-O hydrogen bridges. Spectra of **2<sup>-</sup>** and **4<sup>-</sup>** exhibit stronger bands in the CH stretch region with respect to **1<sup>-</sup>** and **3<sup>-</sup>** which may correspond to conformational changes allowing for low lying transition states during fragmentation.

Spectra of the protonated dipeptides **1-3** exhibit two intense and at least three minor intense bands each, spectra of **2<sup>+</sup>-H** only two intense and a very small band (cf. Fig. 5). Comparison of CID and IR-MPD induced fragmentation pathways of **1<sup>+</sup>-H** reveals partially different relative abundancies of fragmentation channels (cf. Fig. 3 And 6). Seemingly effective internal vibrational redistribution (IVR) of initially localized excitation leads in the cases of all bands to a dominant loss of NH<sub>3</sub>. This is regardless where the excitation takes place in the molecule. On the other hand not all excitations lead to the same fragmentation patterns. During CID the molecule heats up with a statistical energy distribution according to the frequency of the manifold vibrational and rotational modes. Furthermore a CID spectrum consists of the contribution of fragments of the parent ion as well as from different fragment ions formed during collisions with He in a ms time range. Relative abundancies of fragments within the two bands at 3567 and 3485 cm<sup>-1</sup> are comparable to those derived from CID measurements although the absorption of IR photons takes place within a ~7 ns laser pulse. It can be assumed that IVR processes are fast enough to enable multiple photon absorptions from vibrational ground states of the free OH and NH stretch motions and energy dissipates statistically to several other modes. In the three other bands the energy seems not to be statistically transported to other modes and an unequal distribution of fragmentation channels occurs. This may lead to the new fragments in the 3167 and 2950 cm<sup>-1</sup> bands (cf. Fig. 6).

IR-MPD spectra of dipeptide-Li<sup>+</sup> complexes exhibit three bands above 3000 cm<sup>-1</sup> except for **2<sup>+</sup>-Li** (cf. Fig. 7). The additional proton in the protonated dipeptides is attached to one of the nitrogen atoms of the Histidine ring or to the nitrogen atom of the amine group [26, 36] giving rise to up to three bands (without the contribution of NH<sub>2</sub> stretch motions) corresponding to OH and NH stretch motions. Those spatial positions do not necessarily reflect the preferred binding sites of the alkali ions. The Li<sup>+</sup> ion has to be complexed in binding motives which lead to remaining free OH and NH groups. The spatial position of electron donating oxygen and nitrogen atoms allows for several binding sites of the Li<sup>+</sup> ion. Nevertheless each binding motive should lead to at most two vibrational bands corresponding to OH and NH bands due to the absence of the additional proton.

The occurrence of up to three OH and NH bands for **X<sup>+</sup>-Li** (X=**1-3**) with varying intensities in the spectra (without the contribution of NH<sub>2</sub> stretch motions) can be interpreted to arise from a mixture of the two most stable isomers. The overlay of the calculated IR absorption spectra of those isomers is capable to explain most experimental bands. The lower fragmentation efficiency of all bands with respect to the spectra of the protonated dipeptides may arise from a reduction of oscillator strength of the vibrational modes and/or a rise in the transition energy for neutral loss channels.

The fragmentation efficiency in the spectra of **X<sup>+</sup>-M** (X=**1-4**, M=Na, K) drops down (cf. Fig. 24 and 25) and less bands can be observed compared to the spectra of the dipeptide-Li<sup>+</sup> complexes. Spectra of Rb<sup>+</sup> and Cs<sup>+</sup> bearing dipeptide complexes exhibit a rise of the fragmentation efficiency within several bands. The comparison of spectra shows that the relative intensity of the bands corresponding to OH and NH stretch motions changes with the size of the attached ion (cf. Fig. 7, 8, 24-26). This is in good accordance to the results of the DFT calculations, which also show that the relative distribution of isomers is dependent on the size of the alkali ion (cf. Fig. 10, 11, 27-29).

The weakly bound alkali ions Rb<sup>+</sup> and Cs<sup>+</sup> can be interpreted as messenger atoms which can be more or less easily split off from the molecule. Particularly, the Cs<sup>+</sup> ion is the most weakly bound alkali metal, which can also be seen in CID experiments. The use of a 2-color IR-MPD pump/probe scheme leads to various effects. Bands in the *fingerprint* region are mostly enhanced for the protonated dipeptides **1-4** and the dipeptide Cs<sup>+</sup> complexes (cf. Fig. 5 and 8). In the CH, NH and OH stretch region a slight enhancement of bands corresponding to CH stretch motions can be observed. The intensity of the bands corresponding to His-NH and OH stretch motions is mostly reduced, maybe due to a change in the distribution of isomers after photon absorption.

#### IV-5.3: DFT derived minimum structures and relative energies

Several conformational archetypes were found for the energetic minimum structures of the protonated dipeptides (cf. Fig. 9). Preferred protonation sites for are the nitrogen atoms of the Histidine ring and the nitrogen atom of the amine group. In case of  $4^+ \text{-}\beta\text{O}^{180}\text{-HO}_a\text{N}_a$  the amidic oxygen atom is protonated and the amidic NH forms a hydrogen bridge to the His  $^n\text{N}$  atom. These rearrangements can be interpreted in terms of a tautomeric change from the amidic form of **4** to an imidic acid tautomer of  $4^+\text{-H}$  due to protonation.

Hydrogen bonds stabilize the conformations of  $X^+\text{-H}$  ( $X=1\text{-}4$ ) leading mostly to five-, six- and seven-fold intramolecular rings. The methyl group at the Histidine ring of  $2^+\text{-H}$  partially hinders the formation of a binding motive according to  $1^+\text{-}\alpha\text{-H}^n\text{O}_c\text{N}_a$ . Also the shortening of the terminal alkylamine side chain in  $3^+\text{-H}$  with respect to  $1^+\text{-H}$  leads to a rise in energy for the  $3^+\text{-}\alpha\text{-H}^n\text{O}_c\text{N}_a$  isomer. The  $\beta$ -alanyl side chain and the unsubstituted His  $^n\text{N}$  atom of  $1^+\text{-H}$  allows for several energetically favorable isomers.

In case of the  $\text{Li}^+$  complexes of **1**, **2** and **3** the shorter alkyl side of chain leads to a less favorable binding pocket for the  $\text{Li}^+$  ion in the  $3^+\text{-}\alpha\text{-LiO}_c\text{O}_a\text{N}_a$  conformation (cf. Fig. 10). Therefore the binding motive  $3^+\text{-}\beta\text{-Li}^n\text{N}_h\text{O}_c\text{O}_a$  becomes more favorable, even for the large  $\text{Cs}^+$  ion, while the energetic difference between the latter two mentioned isomers of  $3^+\text{-M}$  ( $M=\text{Li}, \text{Cs}$ ) gets small. In general the energetic differences between the binding motives for the  $\text{Cs}^+$  complexes of the dipeptides gets smaller except for  $2^+\text{-Cs}$ . A lower rigidity of the metal – electron donor interaction in  $\text{Cs}^+$  complexes with respect to  $\text{Li}^+$  complexes allows the molecules for a larger degree of conformational freedom.

#### IV-5.4: Comparison of experimental spectra and DFT predicted IR absorption spectra

DFT predicted IR absorption spectra of protonated dipeptides exhibit a relatively good agreement with experimental band positions in the *fingerprint* region when applying a linear scaling factor of 0.97 [47]. Bands above  $2500\text{ cm}^{-1}$  corresponding to CH, NH and OH stretch motions are shifted approximately  $20\text{ cm}^{-1}$  to the blue (cf. Fig. 12-15). The systematic shift of  $+20\text{ cm}^{-1}$  implies that the scaling factor of 0.97 is not appropriate for the region above  $2500\text{ cm}^{-1}$ . We abstained from determination of a second scaling factor for the upper region for two reasons. First, the contribution of different isomers can be sufficiently estimated from the number and relative intensities of bands in the NH and OH stretch region and second, due to the fact that hydrogen bridges are not described

correctly within the harmonic approach. No better correlation of the DFT predicted positions of hydrogen bonded vibrations to experimental IR bands can be derived by a change of the scaling factor.

DFT predicted and rescaled (by 0.97) spectra of dipeptide-Li<sup>+</sup> complexes shift the bands corresponding to <sup>1</sup>NH stretch motions ~20 cm<sup>-1</sup> to the blue. Those of free OH stretch motions are approximately at the same position as the measured bands (cf. Fig. 12-15). In dipeptide-Cs<sup>+</sup> complexes all bands above 2500 cm<sup>-1</sup> are shifted to the blue. In all isomers of dipeptide-Li<sup>+</sup> complexes depicted in Fig. 10 the Li<sup>+</sup> ion interacts with one carboxylic oxygen atom, except for **2<sup>+</sup>-180α-Li<sup>+</sup>N<sub>h</sub>O<sub>a</sub>**. In the latter case the DFT predicted band corresponding to the OH stretch motion is shifted to the blue as described for the protonated dipeptides and their Cs<sup>+</sup> complexes. It can be assumed that the not existing shift of bands corresponding to free OH stretch motions in dipeptide-Li<sup>+</sup> complexes results from an inadequate description of the Li-O<sub>a</sub> interaction. The electronegativity of the Li<sup>+</sup> ions seems to be overestimated at the B3LYP/cc-pVDZ level of theory. The shift of electron density from the carboxy group to the Li atom results in a weakening of the OH bond strength and therefore to a shift of the corresponding band to the red.

We used structures from literature [26] and an intuitive search for isomers of **X<sup>+</sup>-M** (X=**1-4**, M=Na<sup>+</sup>, K<sup>+</sup>, Rb<sup>+</sup>). Additionally we used the replacement of the Li<sup>+</sup> ion in the three depicted energetic minimum isomers of the dipeptide complexes (cf. Fig. 10), Cs<sup>+</sup> respectively (cf. Fig. 11), with Na<sup>+</sup>, K<sup>+</sup> or Rb<sup>+</sup> ions. The latter method led either to the structures known from literature or mostly to even more stable structures than those derived from a random search.

We use a plot of relative energies of isomers in order to compare the conformational changes due to increasing alkali ion size (cf. Fig. 16). The transition from Li<sup>+</sup> to Na<sup>+</sup> leads to strong conformational changes for **2** and **4**, for **3** the first change takes place from Na<sup>+</sup> to K<sup>+</sup>. The size of the alkali ion does hardly affect the conformations of **1**, except for K<sup>+</sup> which leads to a distinct rise in relative energy for the **1<sup>+</sup>-αβ-MO<sub>c</sub>O<sub>a</sub>N<sub>a</sub>** isomer. Former unfavorable structure types displace the Li<sup>+</sup> bearing minimum structures for the K<sup>+</sup> adducts of **2-4**. In most cases the addition of Rb<sup>+</sup> and Cs<sup>+</sup> leads to the same stable structures. The exception for **3** can be neglected due to the small energy difference between both energetic favorable isomers.

Carnosine is capable to bind all alkali metal ions in the same motive. This can be seen in the correspondence of the structure types for the Li<sup>+</sup> and Cs<sup>+</sup> adducts to **1** (cf. Fig. 10 & 11). Increasing

ion size leads to a hinderance of the OH - histidine interaction in the structures of **2**. The OH -  $^1\text{N}$  interaction stabilizes the  $1^+-\alpha\text{-CsO}_c\text{O}_a\text{N}_a$  isomer at about 29 kJ/mol in respect to the corresponding  $2^+-\alpha\text{-CsO}_c\text{O}_a\text{N}_a$  isomer. The shorter terminal amine side chain of **3** in respect to **1** is less capable to provide space for small alkali ions. Larger ions are less affected, the energy difference between the structures types  $\alpha\text{-O}_c\text{O}_a\text{N}_a$  for  $1^+\text{-Li}$  and  $3^+\text{-Li}$  decreases from 22 kJ/mol to 6 kJ/mol for  $1^+\text{-Cs}$  and  $3^+\text{-Cs}$ . Also the  $^1\text{N}_h\text{O}_c\text{O}_a$  binding motive in **3** is capable to complex alkali ions of all sizes. The change of the peptide sequence from **3** to **4** enables a higher binding affinity to larger alkali ions. The  $^1\text{N}_h\text{O}_a\text{O}_c$  binding motive of **4** changes completely from  $\text{Li}^+$  to  $\text{Cs}^+$  adducts, while the latter shows a  $\text{N}_a\text{O}_a\text{O}_c$  motive.  $4^+-180\alpha\text{-LiN}_a\text{O}_a\text{O}_c$ , which corresponds to the  $4^+-\beta\alpha\text{-CsO}_c\text{O}_a\text{N}_a$  isomer, is 46 kJ/mol higher in energy than  $4^+-\beta\alpha\text{-Li}^1\text{N}_h\text{O}_a\text{O}_c$ .

The influence of the methyl group at the  $^1\text{N}$  of the histidine ring in **2** is therefore stronger than the shorting of the terminal amine side chain. The ethylamine side in chain in **1** allows for a more variable binding pocket for the alkali ions and is therefore capable to bind small as well as large ions.

#### IV-5.5: Dissociation energies of alkali cation dipeptide complexes

The most favorable fragmentation pathway is predicted to be the splitting of the alkali ions in the case of  $\text{Rb}^+$  and  $\text{Cs}^+$  complexes (cf. Table 3). Fragmentation of  $\text{K}^+$  dipeptide complexes leads to a drop in the intensity of the ionic fragments due to the fact that  $\text{K}^+$  ions cannot be detected by the mass spectrometer. Nevertheless, we assume the splitting of  $\text{K}^+$  as the most favorable fragmentation pathway. Calculations predict free dissociation enthalpies of  $\text{K}^+$ ,  $\text{Rb}^+$  and  $\text{Cs}^+$  dipeptide complexes in the order of 120 – 190 kJ/mol (cf. Table 8 and Fig. 17). Furthermore, free dissociation enthalpies of  $\text{Li}^+$  and  $\text{Na}^+$  dipeptide complexes are calculated regardless to the experimentally found fragmentation pathways.

#### IV-5.6: Relation of CID fragmentation amplitudes to DFT derived dissociation enthalpies

While there is a large distribution within the data for the loss of the same alkali ion, the free dissociation enthalpies of  $\text{K}^+$ ,  $\text{Rb}^+$  and  $\text{Cs}^+$  derived from DFT correlate linearly in a positive slope of their  $\Delta G(E_{\text{CID}})$  function with their  $E_{\text{CID}}$  values (cf. Table 8, Fig. 18 and 19). In contrast, the  $E_{\text{CID}}$  values of the  $\text{Li}^+$  and  $\text{Na}^+$  dipeptide complexes do not correlate to the DFT derived dissociation enthalpies. Therefore, the splitting of  $\text{Li}^+$  and  $\text{Na}^+$  from the dipeptide complexes can be ruled out as a dominant fragmentation channel.

#### IV-5.7: H/D isotope exchange and relative rate constants

It is known, that the complexation of alkali ions has an influence to the gas phase acidity of (di)peptide complexes [48]. We used gas phase H/D exchange reactions with ND<sub>3</sub> under single collision conditions in order to study the influence of the spatial structure of protonated dipeptides and their alkali metal ions to their reaction behavior.

Pseudo first order kinetic fits proof the in parallel occurrence of single and double H/D exchange reactions per single collision of the protonated dipeptides with ND<sub>3</sub> (cf. Fig. 20 and Table 9). Rate constants for multiple H/D exchanged protonated dipeptides decrease on the one hand due to competing D/D exchanges which do not change the mass of the ions (and can therefore not be accounted for the determination of rate constants). They decrease on the other hand due to lower concentrations of ions with n-1 exchanged protons (n > 2; n = number of H/D exchanges). Higher rate constants for the second exchange in respect to the first one can be interpreted under the assumption that more than one proton is exchanged during the first reaction. This gives rise to doubly exchanged products X<sup>+</sup>-d<sub>2</sub> (X = 1, 2, 4) in one reaction step while a single exchange at X<sup>+</sup>-d<sub>1</sub> can also take place in a second step.

Relative rate constants drop for the H/D exchange reactions of the X<sup>+</sup>-M (M=Li, Na, K) complexes with ND<sub>3</sub>. Pseudo first order kinetic fits do not derive a clear evidence for an occurrence of parallel single and double H/D exchange reactions per single collision of the X<sup>+</sup>-M ions. We estimated the binding energy of NH<sub>3</sub> (according to ND<sub>3</sub>) to different exchangeable protons and to the alkali ion, respectively.

#### IV-5.8: Correlation of binding motives and H/D exchange rates with ND<sub>3</sub> in protonated Carnosine and its Li<sup>+</sup> complex

The interaction of NH<sub>3</sub> (according to ND<sub>3</sub>) with 1<sup>+</sup>-α-H<sup>n</sup>N<sub>b</sub>O<sub>a</sub> leads to a preference of single H/D exchange reactions assuming a correlation between calculated relative energies and the exchange probability. This assumption is in good accordance to the *sde* values for 1<sup>+</sup>-H (cf. Table 8) which exhibit three single H/D exchange reactions with high relative partial rate constants and a lower, almost constant rate of double exchanges up to the fifth incorporated deuterium atom. In order to refine this model assumptions further isomers may have to be regarded.

$2^+ \text{-H}$  has at least two almost isoenergetic isomers (cf. Fig. 9). This could explain the quite different rate constants for single and double H/D exchange reactions in respect to  $1^+ \text{-H}$ . It could be expected that  $3^+ \text{-}\alpha\text{-H}^{\text{r}}\text{O}_c\text{N}_a$  undergoes H/D exchange reactions with similar relative partial rate constants like  $1^+ \text{-}\alpha\text{-H}^{\text{r}}\text{O}_c\text{N}_a$  as both have the same binding motive.  $3^+ \text{-H}$  shows double exchange reactions only for the first step and reacts significantly slower than  $1^+ \text{-H}$ . This can be interpreted by means of considering the contribution of the  $1^+ \text{-}\beta\text{O-H}^{\text{r}}\text{N}_h\text{N}_a$  isomer to the overall rate constants whereas the corresponding isomer of  $3^+ \text{-H}$  is relatively high in energy and therefore less abundant.

The strong interaction of  $\text{ND}_3$  (according to  $\text{NH}_3$ ) with the  $\text{Li}^+$  cation in  $1^+ \text{-}\alpha\text{-LiO}_c\text{O}_a\text{N}_a$  may correspond to the significant drop of the relative partial rate constants for the H/D exchange at  $1^+ \text{-Li}$ . Furthermore double exchanges at the amine group may be hindered due to the interaction with the adjacent  $\text{Li}^+$  cation. The number of observed exchange reactions and the decreasing rates are in relative good accordance to the preferred binding sites of  $\text{NH}_3$  at  $1^+ \text{-}\alpha\text{-LiO}_c\text{O}_a\text{N}_a$ .  $\text{Na}^+$  and  $\text{K}^+$  adducts of **1** show decreasing rate constants in respect to  $1^+ \text{-Li}$  (cf. Table 9) although the alkali ion  $\text{NH}_3$  interaction gets weaker with increasing ion size and the characteristic bond lengths increase (cf. Fig. 24 and Table 13). (Interpretation?)

The rise of the relative partial rate constants for the H/D exchange of  $2^+ \text{-Na}$  and  $2^+ \text{-K}$  in respect to the ones of  $2^+ \text{-Li}$  may be explained by the change of the binding motive (cf. Fig. 16). The isomers  $2^+ \text{-}\alpha\text{-Na}^{\text{r}}\text{N}_h\text{O}_a$  and  $2^+ \text{-}\alpha\text{-K}^{\text{r}}\text{N}_h\text{O}_a$  exhibit no direct interaction between the alkali ion and atoms with exchangeable protons. Rate constants for  $3^+ \text{-M}$  ( $\text{M} = \text{Li}, \text{Na}, \text{K}$ ) are in the same order than those of  $1^+ \text{-M}$  while they have different energetic minimum isomer structures. In contrast to  $1^+ \text{-M}$  almost no H/D exchanges after the first single exchange could be observed.

## IV-6: Conclusions

We investigated a combination of the four dipeptides Carnosine, Anserine, GlyHis and HisGly with alkali metal ions with the help of CID, IR-MPD spectroscopy and H/D exchange reactions with  $\text{ND}_3$ . The aim of the survey is to elucidate the influence of the methyl-group at the histidine ring, of the peptide sequence and chain length on the binding motives of the alkali ions. We identified the energetic minimum structures of the protonated dipeptides and their  $\text{Li}^+$  and  $\text{Cs}^+$  ion complexes by a combination of IR-MPD and DFT calculations. A moderate accordance was found for DFT predicted IR absorptions to IR-MPD spectra. By means of this assignment of isomers, we figured out the size dependent relative energy for at least three isomer types per dipeptide alkali ion

complex. We developed a systematic nomenclature reflecting all binding motives of the four dipeptides to alkali ions. Carnosine is able to complex all alkali metal ions in an uniform binding motive. DFT derived energetical minimum isomers of the three other dipeptides show strong conformational changes with increasing size of the alkali ion. The most favored binding motive of all peptides is the tridentate complexation of the alkali ion by a carboxylic and an amidic oxygen atom, while the electron donating nitrogen atom either belongs to the Histidine ring or the amine group. The ability to form hydrogen bonds in a certain binding motive is essential for the preference of the Histidine or amine nitrogen atom as an electron donor. The charge solvated binding motive is the most common within all found isomers. Several structures exhibit hydrogen bonded protons. Those can be interpreted as intermediates between the charge solvated and the salt bridge binding motive. CID breakdown curves of the cationic complexes of the dipeptides with  $K^+$ ,  $Rb^+$  and  $Cs^+$  result in a fair agreement of  $E_{com}^{50\%}$  values with DFT derived Gibbs free binding energies. CID leads to multiple fragments of the  $Li^+$  and  $Na^+$  dipeptide complexes and to an insufficient correlation between the  $E_{com}^{50\%}$  values and metal-dipeptide free binding enthalpies. Gas phase H/D exchange reactions of the protonated dipeptides with  $ND_3$  resulted in the exchange of all labile protons with comparable relative partial rate constants. The assumption of coexisting single and double exchange reactions per single collision leads to an enhancement in the quality of the pseudo first order kinetic fits of the experimental derived data. The  $Li^+$ ,  $Na^+$  and  $K^+$  complexes of the dipeptides exhibit a reduction in the number of exchanged protons, significantly lower rate constants for H/D exchange and only single exchange reactions.



## IV-7: References

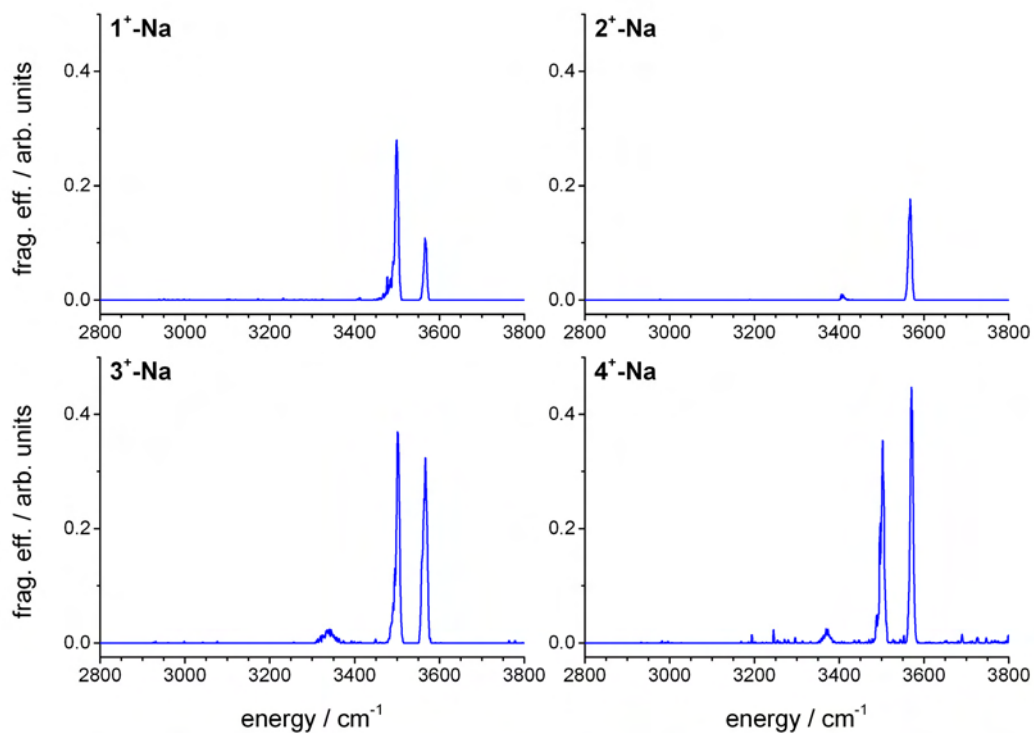
1. Gabelica, V. and E. De Pauw, *Internal energy and fragmentation of ions produced in electrospray sources*. Mass Spectrometry Reviews, 2005. **24**(4): p. 566-587.
2. Pingitore, F. and C. Wesdemiotis, *Characterization of dipeptide isomers by tandem mass spectrometry of their mono- versus dilithiated complexes*. Analytical Chemistry, 2005. **77**(6): p. 1796-1806.
3. Remko, M., D. Fitz, and B.M. Rode, *Effect of metal ions ( $Li^+$ ,  $Na^+$ ,  $K^+$ ,  $Mg^{2+}$ ,  $Ca^{2+}$ ,  $Ni^{2+}$ ,  $Cu^{2+}$ , and  $Zn^{2+}$ ) and water coordination on the structure and properties of L-histidine and zwitterionic L-histidine*. Amino Acids, 2010. **39**(5): p. 1309-1319.
4. Remko, M., D. Fitz, and B.M. Rode, *Effect of metal ions ( $Li^+$ ,  $Na^+$ ,  $K^+$ ,  $Mg^{2+}$ ,  $Ca^{2+}$ ,  $Ni^{2+}$ ,  $Cu^{2+}$ , and  $Zn^{2+}$ ) and water coordination on the structure and properties of L-arginine and zwitterionic L-arginine*. Journal of Physical Chemistry A, 2008. **112**(33): p. 7652-7661.
5. Menges, F., C. Riehn, and G. Niedner-Schatteburg, *The Interaction of the Dipeptide Carnosine with Alkali Metal Ions Studied by Ion Trap Mass Spectrometry*. Zeitschrift Fur Physikalische Chemie-International Journal of Research in Physical Chemistry & Chemical Physics, 2011. **225**(5): p. 595-609.
6. Armentrout, P.B., A. Gabriel, and R.M. Moision, *An experimental and theoretical study of alkali metal cation/methionine interactions*. International Journal of Mass Spectrometry, 2009. **283**(1-3): p. 56-68.
7. Armentrout, P.B., et al., *Infrared multiphoton dissociation spectroscopy of cationized serine: Effects of alkali-metal cation size on gas-phase conformation*. Journal of Physical Chemistry A, 2008. **112**(11): p. 2248-2257.
8. Drayss, M.K., et al., *IR spectroscopy of cationized aliphatic amino acids: Stability of charge-solvated structure increases with metal cation size*. International Journal of Mass Spectrometry, 2010. **297**(1-3): p. 18-27.
9. Bush, M.F., et al., *Infrared spectroscopy of cationized lysine and epsilon-N-methyllysine in the gas phase: Effects of alkali-metal ion size and proton affinity on zwitterion stability*. Journal of Physical Chemistry A, 2007. **111**(32): p. 7753-7760.
10. Jockusch, R.A., W.D. Price, and E.R. Williams, *Structure of cationized arginine ( $Arg\ center\ dot\ M^+$ ,  $M = H, Li, Na, K, Rb,$  and  $Cs$ ) in the gas phase: Further evidence for zwitterionic arginine*. Journal of Physical Chemistry A, 1999. **103**(46): p. 9266-9274.
11. Gard, E., et al., *Gas-Phase Hydrogen-Deuterium Exchange as a Molecular Probe for the Interaction of Methanol and Protonated Peptides*. Journal of the American Society for Mass Spectrometry, 1994. **5**(7): p. 623-631.
12. Campbell, S., et al., *Deuterium exchange reactions as a probe of biomolecule structure. Fundamental studies of gas phase H/D exchange reactions of protonated glycine oligomers with  $D_2O$ ,  $CD_3OD$ ,  $CD_3CO_2D$ , and  $ND_3$* . Journal of the American Chemical Society, 1995. **117**(51): p. 12840-12854.
13. Freitas, M.A. and A.G. Marshall, *Rate and extent of gas-phase hydrogen/deuterium exchange of bradykinins: evidence for peptide zwitterions in the gas phase*. International Journal of Mass Spectrometry, 1999. **182**: p. 221-231.
14. Evans, S.E., N. Lueck, and E.M. Marzluff, *Gas phase hydrogen/deuterium exchange of*

- proteins in an ion trap mass spectrometer*. International Journal of Mass Spectrometry, 2003. **222**(1-3): p. 175-187.
15. Wyttenbach, T., et al., *The effect of the initial water of hydration on the energetics, structures, and H/D exchange mechanism of a family of pentapeptides: An experimental and theoretical study*. Journal of the American Chemical Society, 2003. **125**(45): p. 13768-13775.
  16. Cox, H.A., et al., *Gas-phase H/D exchange of sodiated glycine oligomers with ND<sub>3</sub>: Exchange kinetics do not reflect parent ion structures*. Journal of the American Chemical Society, 2004. **126**(20): p. 6485-6490.
  17. Lifshitz, C., *A review of gas-phase H/D exchange experiments: The protonated arginine dimer and bradykinin nonapeptide systems*. International Journal of Mass Spectrometry, 2004. **234**(1-3): p. 63-70.
  18. Rozman, M., et al., *Gas phase H/D exchange of sodiated amino acids: Why do we see zwitterions?* Journal of the American Society for Mass Spectrometry, 2006. **17**(1): p. 29-36.
  19. Huang, Y., et al., *A Mechanistic Study of the H/D Exchange Reactions of Protonated Arginine and Arginine-Containing Di- and Tripeptides*. Journal of the American Society for Mass Spectrometry, 2009. **20**(11): p. 2049-2057.
  20. Balaj, O.P., et al., *Vibrational signatures of sodiated oligopeptides (GG-Na<sup>+</sup>, GGG-Na<sup>+</sup>, AA-Na<sup>+</sup> and AAA-Na<sup>+</sup>) in the gas phase*. International Journal of Mass Spectrometry, 2008. **269**(3): p. 196-209.
  21. Branham, M.L., et al., *Preparation, Spectrochemical, and Computational Analysis of L-Carnosine (2- (3-Aminopropanoyl)amino -3-(1H-imidazol-5-yl)propanoic Acid) and Its Ruthenium (II) Coordination Complexes in Aqueous Solution*. Molecules, 2011. **16**(12): p. 10269-10291.
  22. Dookeran, N.N. and A.G. Harrison, *Gas-Phase H-D Exchange-Reactions of Protonated Amino-Acids and Peptides with ND<sub>3</sub>*. Journal of Mass Spectrometry, 1995. **30**(5): p. 666-674.
  23. Green, M.K. and C.B. Lebrilla, *The role of proton-bridged intermediates in promoting hydrogen-deuterium exchange in gas-phase protonated diamines, peptides and proteins*. International Journal of Mass Spectrometry, 1998. **175**(1-2): p. 15-26.
  24. Green, M.K. and C.B. Lebrilla, *Ion-molecule reactions as probes of gas-phase structures of peptides and proteins*. Mass Spectrometry Reviews, 1997. **16**(2): p. 53-71.
  25. Jurchen, J.C., R.E. Cooper, and E.R. Williams, *The role of acidic residues and of sodium ion adduction on the gas-phase H/D exchange of peptides and peptide dimers*. Journal of the American Society for Mass Spectrometry, 2003. **14**(12): p. 1477-1487.
  26. Kapota, C. and G. Ohanessian, *The low energy tautomers and conformers of the dipeptides HisGly and GlyHis and of their sodium ion complexes in the gas phase*. Physical Chemistry Chemical Physics, 2005. **7**(21): p. 3744-3755.
  27. Lucas, B., et al., *Infrared multiphoton dissociation spectroscopy of protonated N-acetyl-alanine and alanyl-histidine*. International Journal of Mass Spectrometry, 2005. **243**(2): p. 105-113.
  28. Lucas, B., et al., *Investigation of the protonation site in the dialanine peptide by infrared multiphoton dissociation spectroscopy*. Physical Chemistry Chemical Physics, 2004. **6**(10):

- p. 2659-2663.
29. Polfer, N.C., J. Oomens, and R.C. Dunbar, *Alkali metal complexes of the Dipeptides PheAla and AlaPhe : IRMPD spectroscopy*. ChemPhysChem, 2008. **9**(4): p. 579-589.
  30. Prell, J.S., et al., *Role of Sequence in Salt-Bridge Formation for Alkali Metal Cationized GlyArg and ArgGly Investigated with IRMPD Spectroscopy and Theory*. Journal of the American Chemical Society, 2009. **131**(3): p. 1232-1242.
  31. Prell, J.S., et al., *Structures of Protonated Dipeptides: The Role of Arginine in Stabilizing Salt Bridges*. Journal of the American Chemical Society, 2009. **131**(32): p. 11442-11449.
  32. Solouki, T., et al., *Gas phase hydrogen deuterium exchange reactions of a model peptide: FT-ICR and computational analyses of metal induced conformational mutations*. Journal of the American Society for Mass Spectrometry, 2001. **12**(12): p. 1272-1285.
  33. Teesch, L.M. and J. Adams, *Fragmentations of Gas-Phase Complexes Between Alkali-Metal Ions and Peptides - Metal-Ion Binding to Carbonyl Oxygens and Other Neutral Functional-Groups*. Journal of the American Chemical Society, 1991. **113**(3): p. 812-820.
  34. Green, M.K., et al., *H-D Exchange Kinetics of Alcohols and Protonated Peptides - Effects of Structure and Proton Affinity*. Journal of Mass Spectrometry, 1995. **30**(8): p. 1103-1110.
  35. Kohen, R., et al., *Antioxidant Activity Of Carnosine, Homocarnosine, And Anserine Present In Muscle And Brain*. Proceedings of the National Academy of Sciences of the United States of America, 1988. **85**(9): p. 3175-3179.
  36. Gregoire, G., et al., *Resonant infrared multiphoton dissociation spectroscopy of gas-phase protonated peptides. Experiments and Car-Parrinello dynamics at 300 K*. Physical Chemistry Chemical Physics, 2007. **9**(24): p. 3082-3097.
  37. MacDonald, B.I. and M. Thachuk, *Gas-phase proton-transfer pathways in protonated histidylglycine*. Rapid Communications in Mass Spectrometry, 2008. **22**(18): p. 2946-2954.
  38. Pretsch, E., P. Bühlmann, and M. Badertscher, *Structure determination of organic compounds : tables of spectral data*. 4th, rev. and enl. ed. 2009, Berlin: Springer. xv, 433 p.
  39. Becke, A.D., *Density-Functional Exchange-Energy Approximation with Correct Asymptotic-Behavior*. Physical Review A, 1988. **38**(6): p. 3098-3100.
  40. Lee, C.T., W.T. Yang, and R.G. Parr, *Development of the Colle-Salvetti Correlation-Energy Formula into a Functional of the Electron-Density*. Physical Review B, 1988. **37**(2): p. 785-789.
  41. Miehlich, B., et al., *Results Obtained with the Correlation-Energy Density Functionals of Becke and Lee, Yang and Parr*. Chemical Physics Letters, 1989. **157**(3): p. 200-206.
  42. Becke, A.D., *Density-Functional Thermochemistry .3. The Role of Exact Exchange*. Journal of Chemical Physics, 1993. **98**(7): p. 5648-5652.
  43. Dunning, T.H., *Gaussian-Basis Sets for Use in Correlated Molecular Calculations .1. The Atoms Boron through Neon and Hydrogen*. Journal of Chemical Physics, 1989. **90**(2): p. 1007-1023.
  44. Frisch, M.J., et al., *Gaussian 03, Revision C.02*. 2003.
  45. Frisch, M.J., et al., *Gaussian 09, Revision B.01*. 2009: Wallingford CT.
  46. Kapota, C., et al., *Vibrational signature of charge solvation vs salt bridge isomers of sodiated amino acids in the gas phase*. Journal of the American Chemical Society, 2004.

**126(6)**: p. 1836-1842.

47. Byrd, E.F.C., C.D. Sherrill, and M. Head-Gordon, *The theoretical prediction of molecular radical species: a systematic study of equilibrium geometries and harmonic vibrational frequencies*. Journal of Physical Chemistry A, 2001. **105(42)**: p. 9736-9747.
48. Mertens, L.A. and E.M. Marzluff, *Gas Phase Hydrogen/Deuterium Exchange of Arginine and Arginine Dipeptides Complexed with Alkali Metals*. The Journal of Physical Chemistry A, 2011. **115(33)**: p. 9180-9187.

**IV-8: Supplementary material**

**Figure 24:** 1-color IR-MPD spectra of 1<sup>+</sup>-Na, 2<sup>+</sup>-Na, 3<sup>+</sup>-Na, and 4<sup>+</sup>-Na. See Tables 4-7 for numerical values of band peak positions.

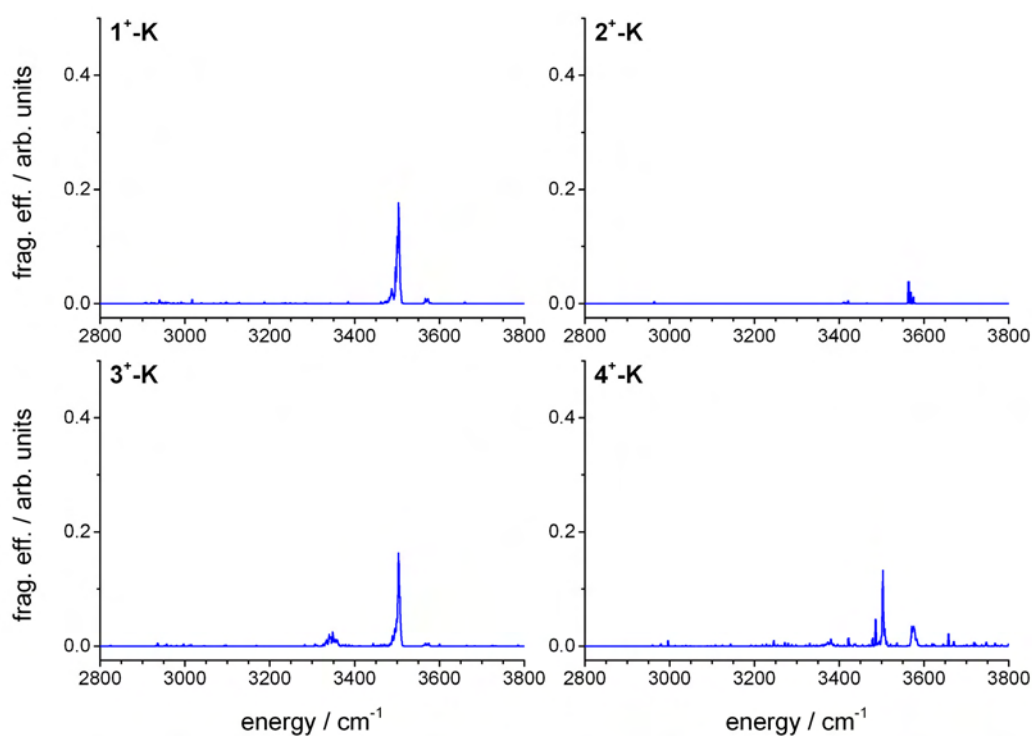


**Figure 25:** 1-color IR-MPD spectra of  $1^+K$ ,  $2^+K$ ,  $3^+K$ , and  $4^+K$ . See Tables 4-7 for numerical values of band peak positions.

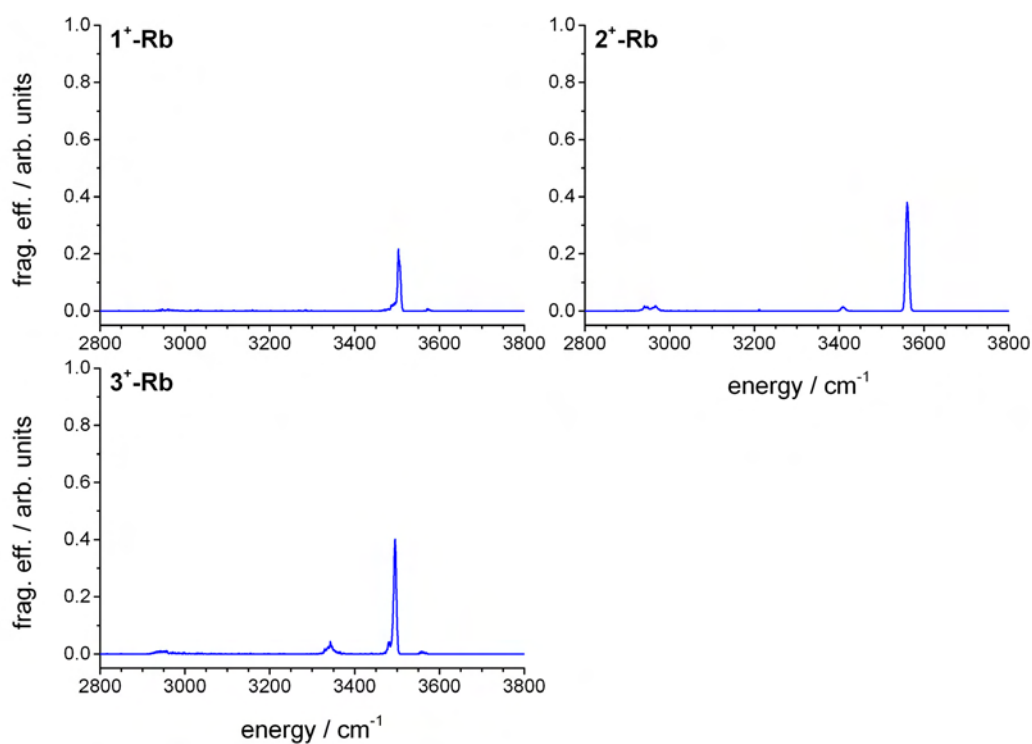


**Figure 26:** 1-color IR-MPD spectra of  $1^+Rb$ ,  $2^+Rb$ ,  $3^+Rb$ , and  $4^+Rb$ . See Tables 4-7 for numerical values of band peak positions.

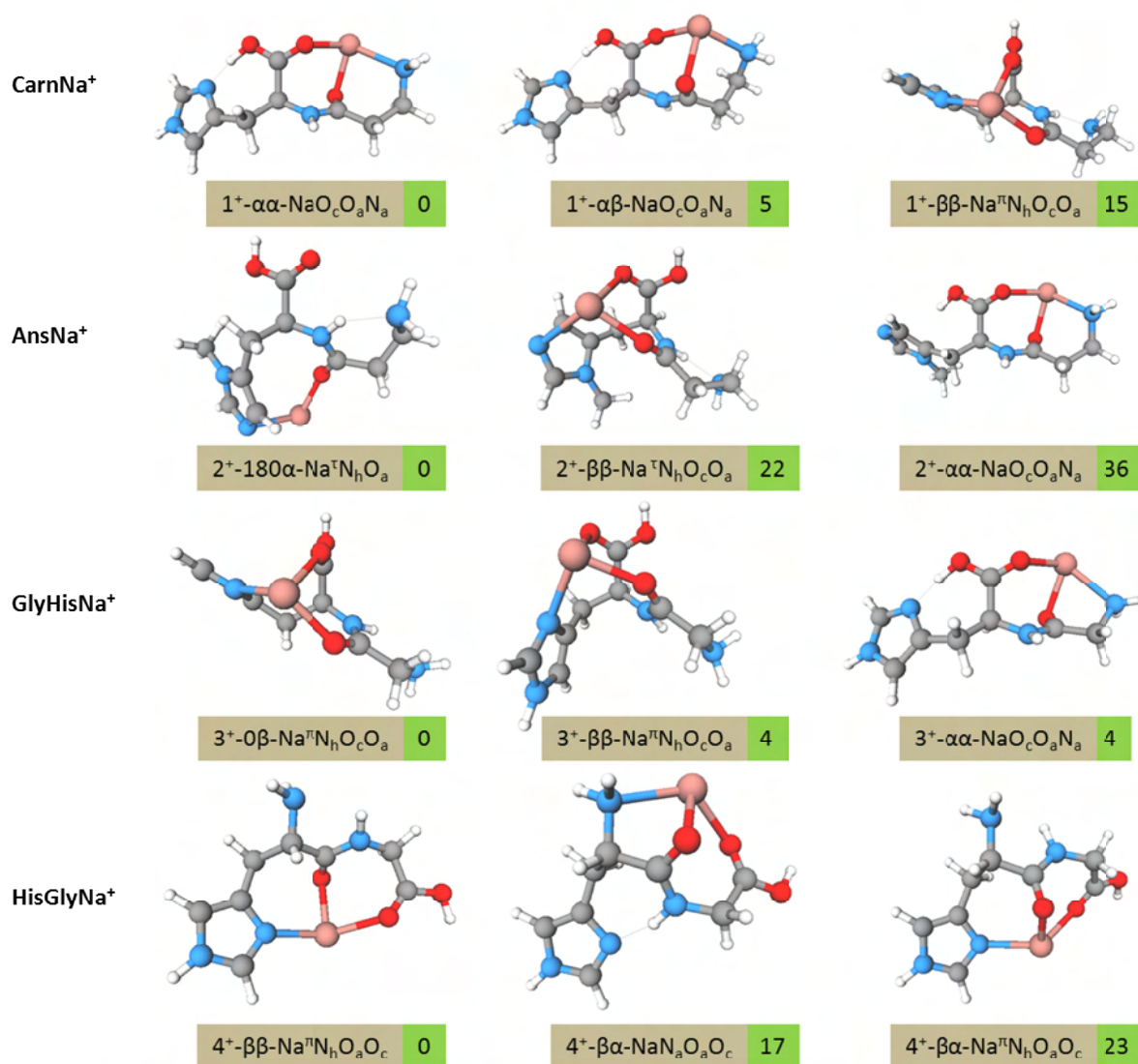


**Figure 27:** Calculated binding motives of dipeptides 1-4 with Na<sup>+</sup> and relative energies in kJ/mol. (For definition of nomenclature, refer to page 62)

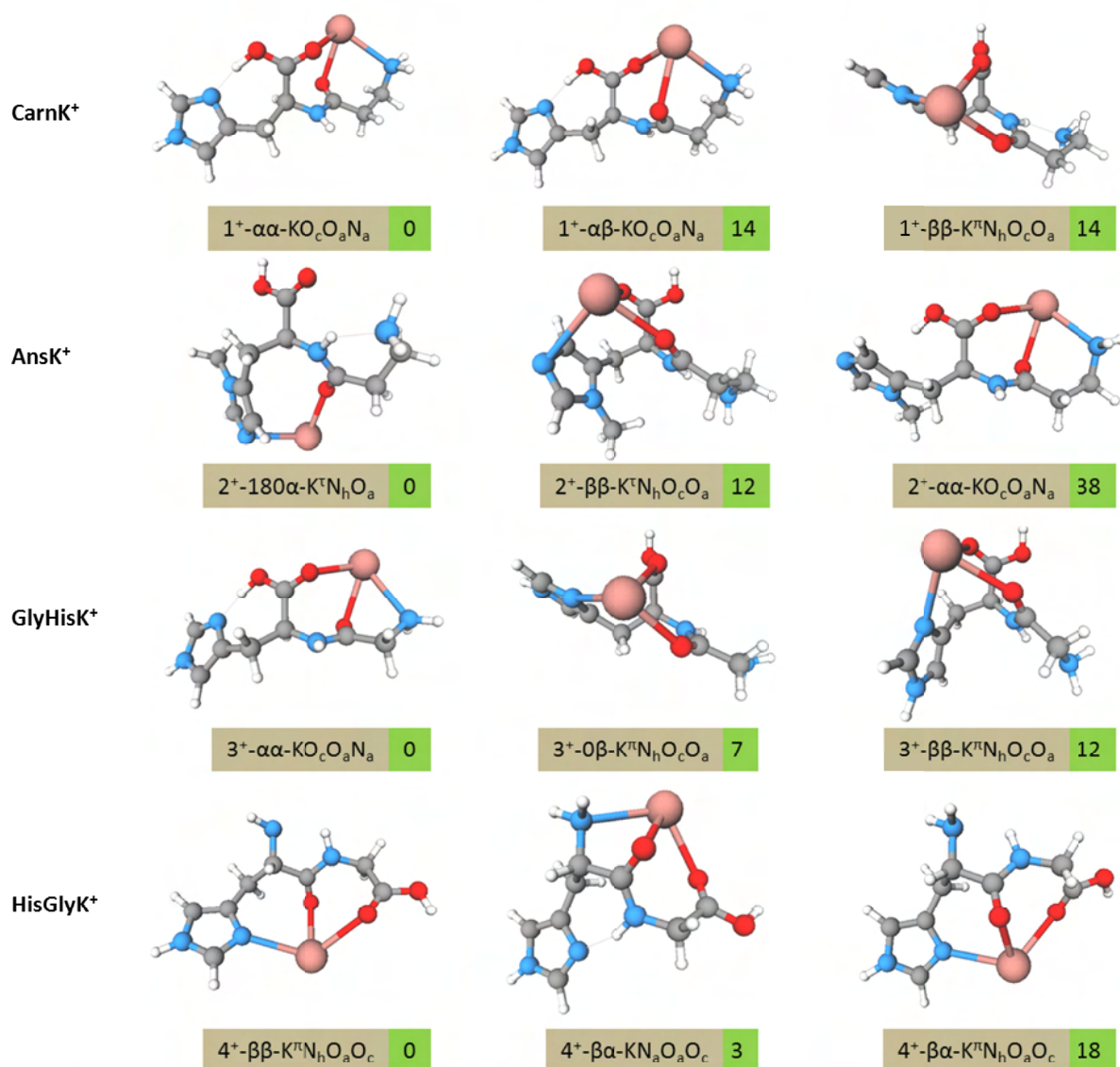


**Figure 28:** Calculated binding motives of dipeptides 1-4 with K<sup>+</sup> and relative energies in kJ/mol. (For definition of nomenclature, refer to page 62)



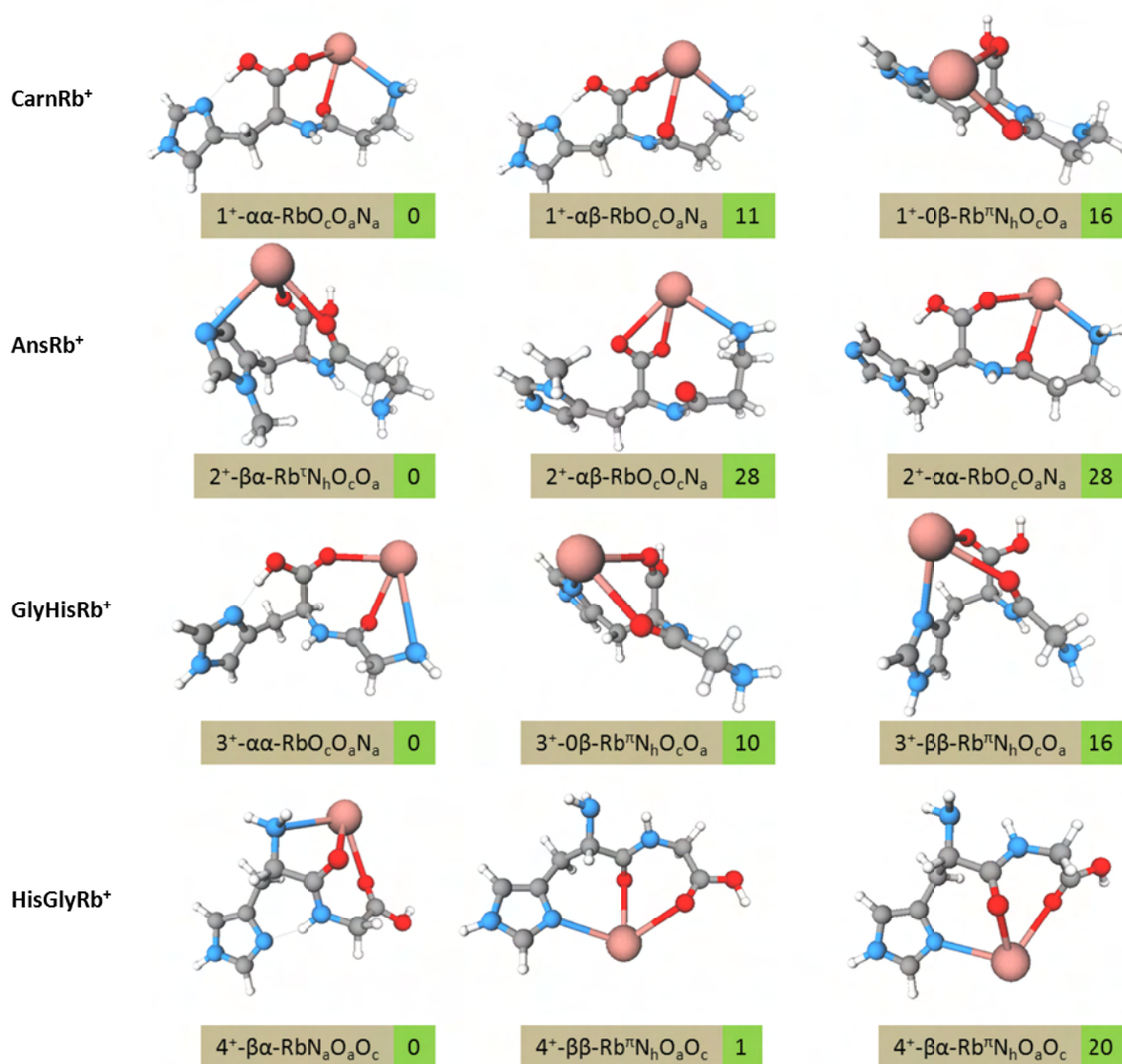


**Figure 29:** Calculated binding motives of dipeptides 1-4 with Rb<sup>+</sup> and relative energies in kJ/mol. (For definition of nomenclature, refer to page 62)

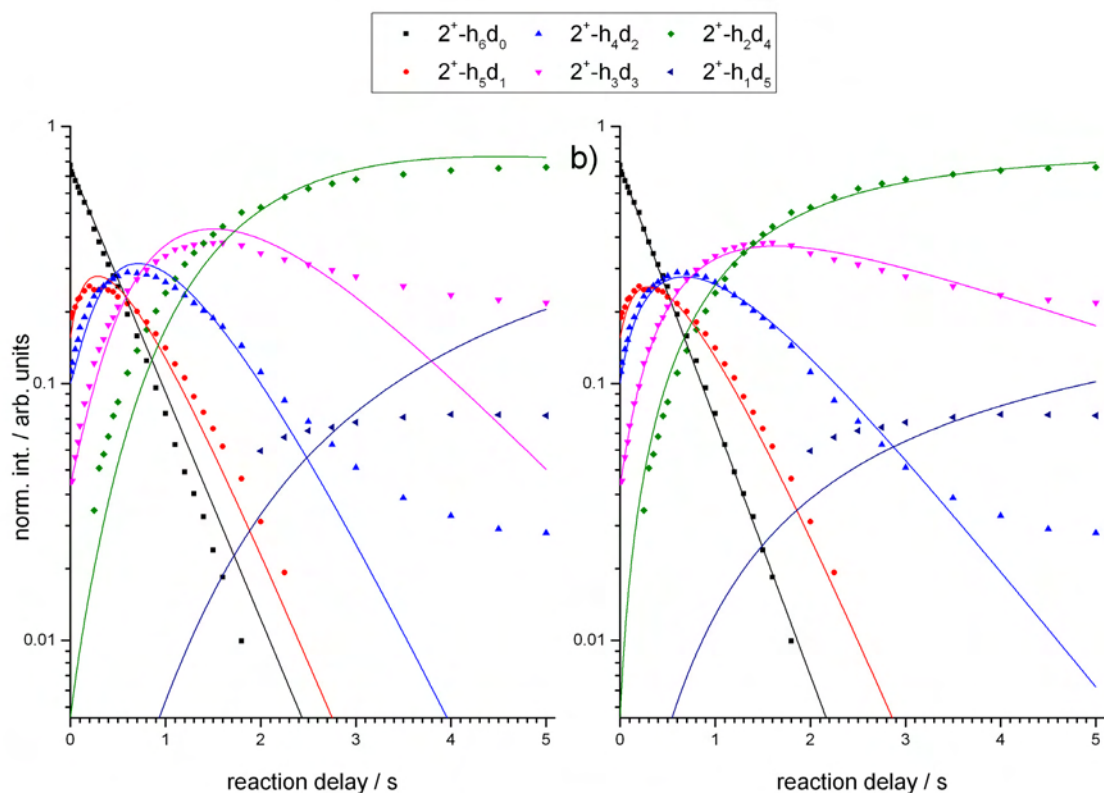


**Figure 30:** Normalized reactant and product intensities in the reactions of protonated  $2^+-H$  with  $ND_3$ . The temporal evolution of the experimental data points (symbols) is fitted to pseudo first order kinetics (solid lines) which provides for relative partial rate constants. Fits correlate to single H/D exchange reactions (a) and to single and double H/D exchange (b) per single collision. Fits arise through application of generic algorithm code. Fits of (b) are superior to those of (a). (cf. Table 9 for numerical data)

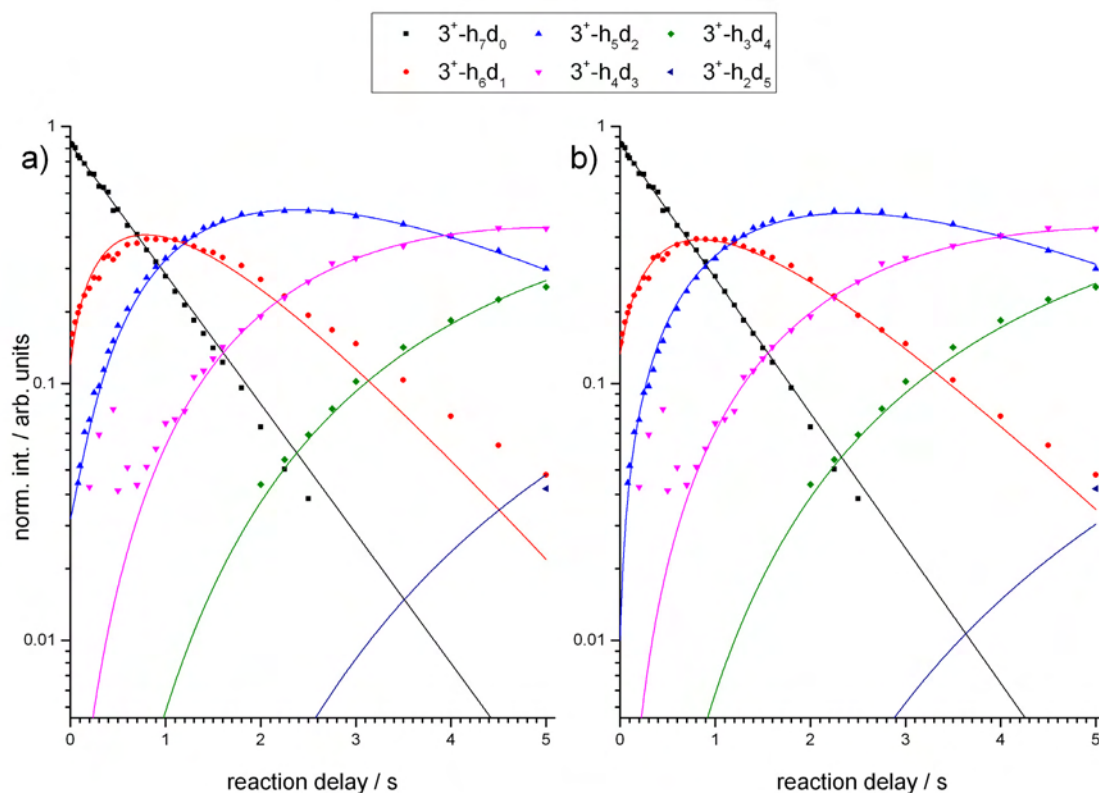


**Figure 31:** Normalized reactant and product intensities in the reactions of protonated  $3^+-H$  with  $ND_3$ . The temporal evolution of the experimental data points (symbols) is fitted to pseudo first order kinetics (solid lines) which provides for relative partial rate constants. Fits correlate to single H/D exchange reactions (a) and to single and double H/D exchange (b) per single collision. Fits arise through application of generic algorithm code. Fits of (b) are superior to those of (a). (cf. Table 9 for numerical data)

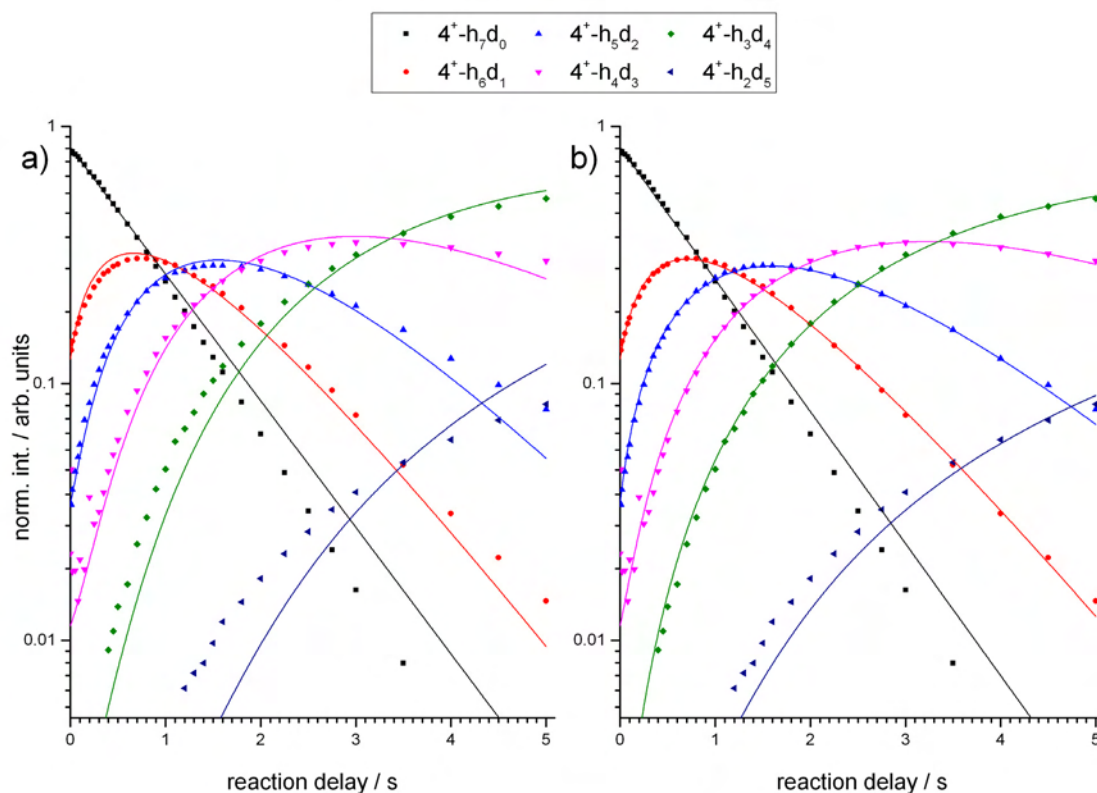


**Figure 32:** Normalized reactant and product intensities in the reactions of protonated  $4^+H$  with  $ND_3$ . The temporal evolution of the experimental data points (symbols) is fitted to pseudo first order kinetics (solid lines) which provides for relative partial rate constants. Fits correlate to single H/D exchange reactions (a) and to single and double H/D exchange (b) per single collision. Fits arise through application of generic algorithm code. Fits of (b) are superior to those of (a). (cf. Table 9 for numerical data)

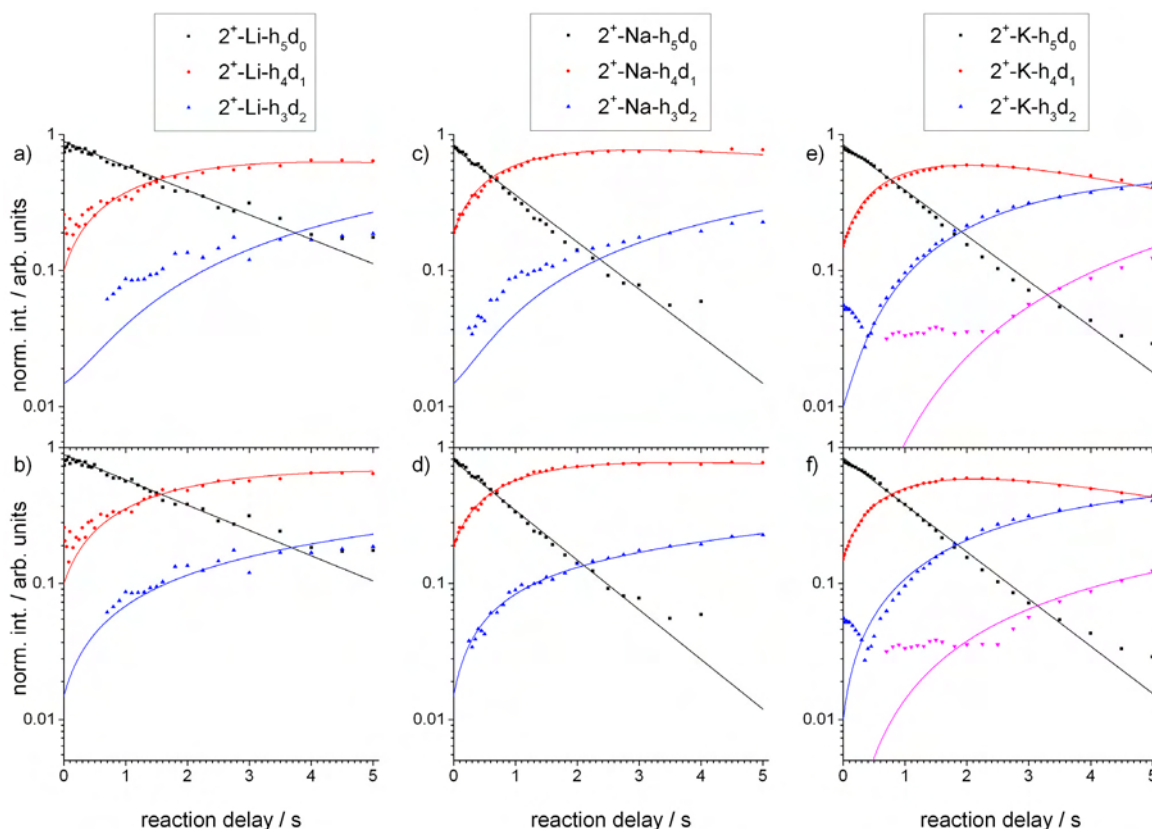


**Figure 33:** Normalized reactant and product intensities in the H/D exchange reactions of cationic  $2^+ \text{-M}$  ( $M = \text{Li, Na, K}$ ) with  $\text{ND}_3$ . The temporal evolution of the experimental data points (symbols) is fitted to pseudo first order kinetics (solid lines) which provides for relative partial rate constants. Fits arise through application of generic algorithm code. Fits in (a, c, e) assume single H/D exchange reactions per single  $\text{ND}_3$  collisions. Fits in (b, d, f) assume single and possible double H/D exchange reactions per single  $\text{ND}_3$  collisions. Quality of fits is comparable, clear evidence of H/D double exchange is thus missing. (cf. Table 11 for numerical data)

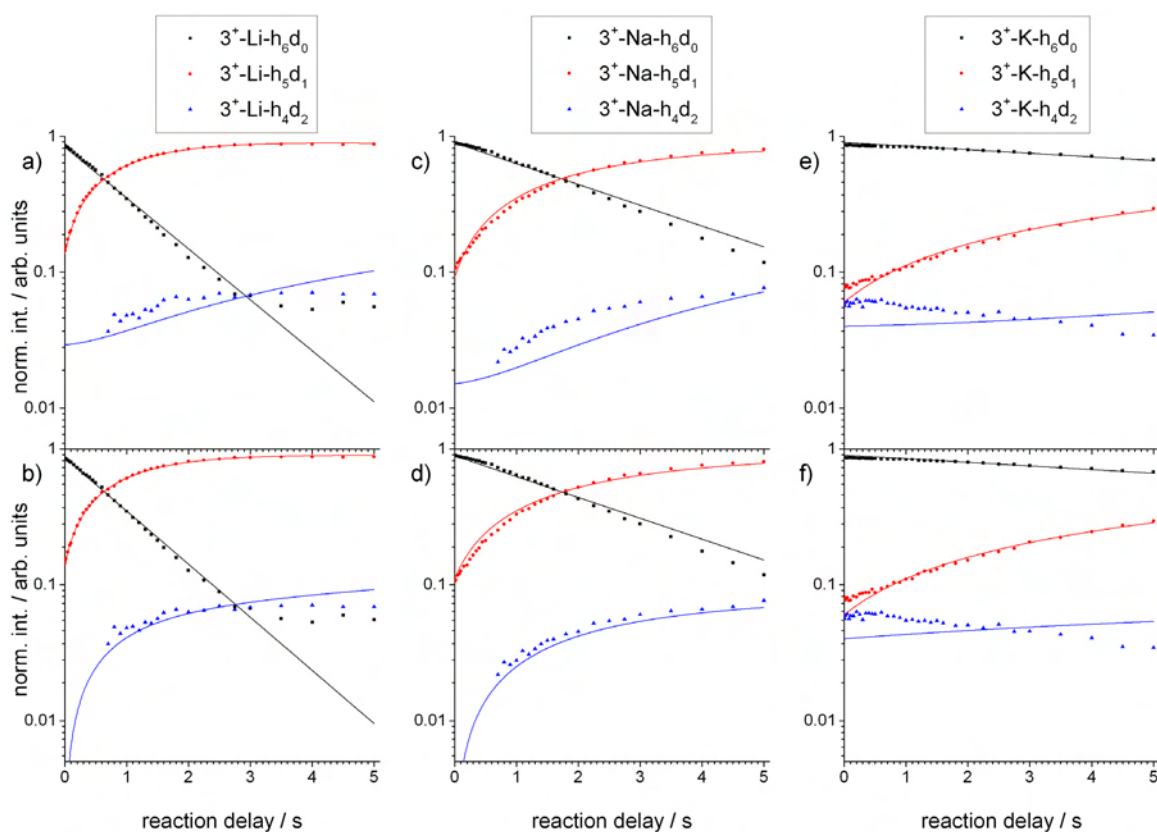


**Figure 34:** Normalized reactant and product intensities in the H/D exchange reactions of cationic  $3^+-M$  ( $M=Li, Na, K$ ) with  $ND_3$ . The temporal evolution of the experimental data points (symbols) is fitted to pseudo first order kinetics (solid lines) which provides for relative partial rate constants. Fits arise through application of generic algorithm code. Fits in (a, c, e) assume single H/D exchange reactions per single  $ND_3$  collisions. Fits in (b, d, f) assume single and possible double H/D exchange reactions per single  $ND_3$  collisions. Quality of fits is comparable, clear evidence of H/D double exchange is thus missing. (cf. Table 12 for numerical data)

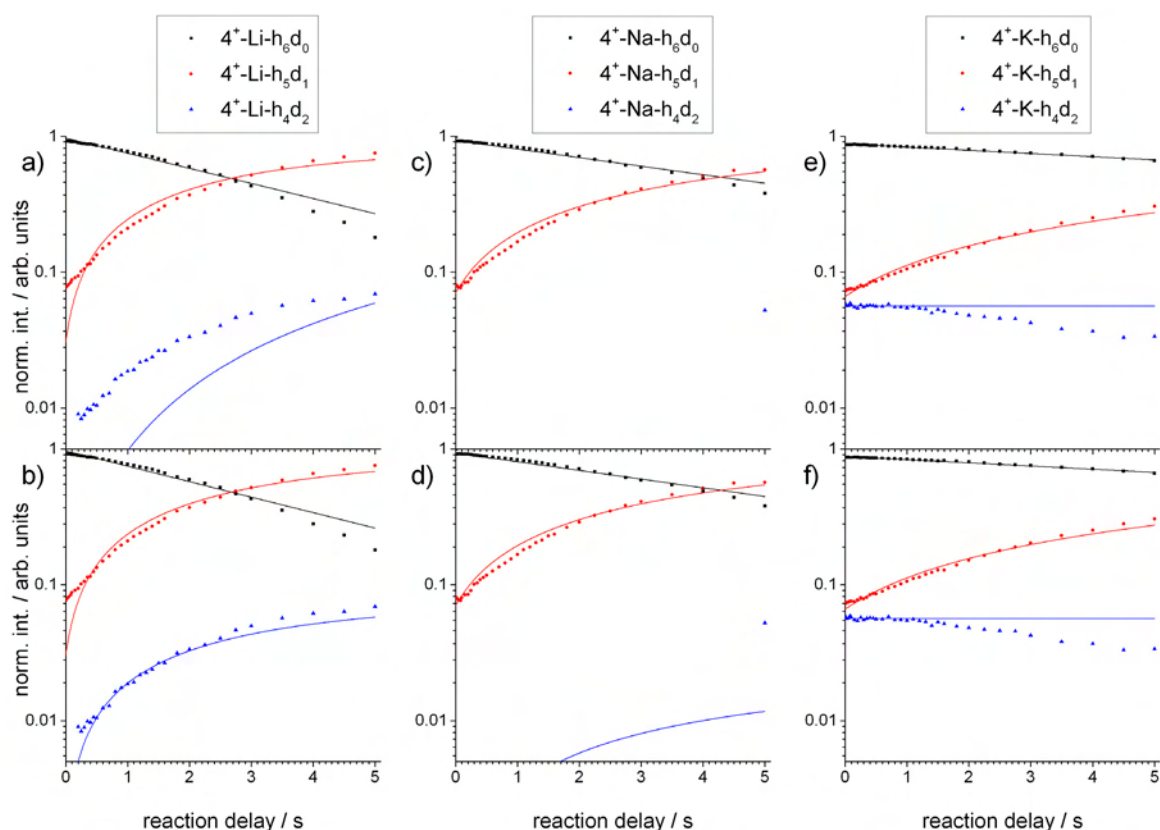


**Figure 35:** Normalized reactant and product intensities in the H/D exchange reactions of cationic  $4^+M$  ( $M=Li, Na, K$ ) with  $ND_3$ . The temporal evolution of the experimental data points (symbols) is fitted to pseudo first order kinetics (solid lines) which provides for relative partial rate constants. Fits arise through application of generic algorithm code. Fits in (a, c, e) assume single H/D exchange reactions per single  $ND_3$  collisions. Fits in (b, d, f) assume single and possible double H/D exchange reactions per single  $ND_3$  collisions. Quality of fits is comparable, clear evidence of H/D double exchange is thus missing. (cf. Table 13 for numerical data)





## Chapter V: Enhancement of vibrational bands derived by 2-color IR-MPD – a mechanistic study on [Carnosine-H,Zinc<sup>II</sup>]<sup>+</sup>

### V: Preamble

This chapter is formatted as to become a manuscript for publication. It is not submitted yet. All of the measurements, data evaluations, calculations and all of the text was done by myself. I received experimental support by Yevgeniy Nosenko, Maximilian Gaffga and Lars Barzen. Christoph Riehn and Gereon Niedner-Schatteburg helped with discussions.

### V-1: Abstract

The gas-phase structure of the zinc(II) cationized dipeptide carnosine is investigated using infrared multiple photon dissociation (IR-MPD) in the regions from 1300 to 2000  $\text{cm}^{-1}$  and from 2600 to 3800  $\text{cm}^{-1}$ . Fair agreement of experimental and theoretical spectra arises after optimization of correlation treatment and basis sets. A novel 2-color pump/probe scheme is applied in order to enhance the fragmentation efficiency of the IR-MPD process. We characterized this pump/probe scheme in terms of mode specific fragmentation pathways and the timing sequence and we obtained mode specific enhancement factors.

### V-2: Introduction

Structural conformation and the interaction with metal ions play a crucial role for the behavior of amino acids, peptides and proteins under physiological conditions. Therefore, it is important to understand the effect of ion size and polarizability of the metal ion on the structure. The carnosine-zinc(II)-complex [Carn-H,Zn<sup>II</sup>]<sup>+</sup> ( $1^+\text{-Zn}$ ) sells by the trade name polaprezinc as a drug on peptic ulcer [1]. Carnosine consists is a dipeptide of histidine (C-terminus) and  $\beta$ -alanine (N-terminus) and was first detected by W. Gulewitsch in meat extracts [2]. It is the major  $\beta$ -alanine source in the human body [3]. Carnosine itself and several related peptides have been studied for their physiological properties, metal binding behavior and crystal structure [1, 3-19]. The most stable conformer of protonated carnosine in the gas phase was identified by a combination of IR-MPD experiments and DFT calculations [20]. Interpretation of FTIR and Raman spectra of crystalline [Carn-H,Zn<sup>II</sup>]<sup>+</sup> complex suggest a four-fold coordination of the  $\text{Zn}^{2+}$  ion by the His-N atom, a

carboxylic oxygen atom, the amidic and aminic nitrogen atoms [15]. In contrast, the His- $\overline{\text{N}}$  tautomer seems to be more stable in solution [3]. DFT calculations of isolated **[Carn-H,Zn<sup>II</sup>]<sup>+</sup>** complexes suggest a four-fold coordination of the Zn<sup>2+</sup> ion by two oxygen and two nitrogen atoms [21].

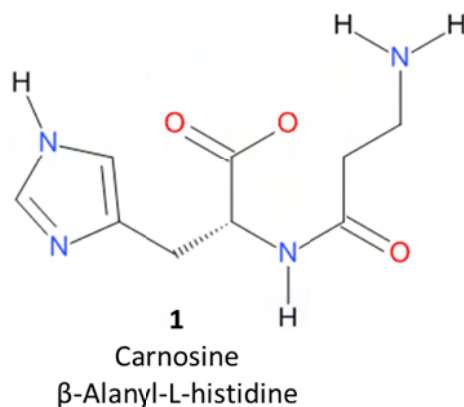


**Figure 1:** Structure and systematic name of the dipeptide carnosine (**1**). Histidine forms the C-terminus,  $\beta$ -alanyl the N-terminus.

Calculated dissociation enthalpies of **[Carn-H,Zn<sup>II</sup>]<sup>+</sup>** range around 260 kJ/mol. Such a high value causes challenges to the IR-MPD technique. It provides for an opportunity to test our resonant 2-color IR-MPD spectroscopy technique [22]. The **[Carn-H,Zn<sup>II</sup>]<sup>+</sup>** complex possesses several IR-active groups and allows for a number of combinations of pump and probe bands in order to estimate mode specific fragmentation enhancement factors.

We developed a generalized scheme of the four dipeptides carnosine, anserine, GlyHis and HisGly and their alkali metal adducts (cf. Chapter VI of this thesis) in order to classify the different structure motives of the isomers derived by DFT calculations. Now, we apply this scheme to the **[Carn-H,Zn<sup>II</sup>]<sup>+</sup>** complex.



We assign bands in IR-MPD spectra in a first approach with an incremental appraisal of the position of bands of archetypical peptide compounds (cf. Table 2) [23].

**Table 2:** Assignment of energy ranges to vibrational modes of various groups (marked with underlines) [23].

<b>group</b>	<b>mode</b>	<b>energy range / cm<sup>-1</sup></b>
free <u>COOH</u>	v <sub>s</sub>	3500 - 3650
free <u>NH</u>	v <sub>s</sub>	3400 - 3500
free <u>NH<sub>2</sub></u>	v <sub>as+ss</sub>	3300 - 3500
bridged <u>N-H-O</u>	v <sub>s</sub>	3100 - 3500
aromatic <u>CH</u>	v <sub>s</sub>	3000 - 3100
aliphatic <u>CH</u>	v <sub>s</sub>	2850 - 3000
<u>CO</u>	v <sub>s</sub>	1600 - 1800

### V-3: Methods

#### V-3.1: ESI-MS and CID

Electrospray ionization mass spectrometry (ESI-MS) was performed with an ion trap instrument (Bruker amaZonSL). The ion source provides cations in positive electrospray ionization mode. Scan speed was 32500 m/z / s in normal resolution scan mode (0.3 FWHM / m/z), scan range was at least 70 to 400 m/z. We mix solutions of ZnSO<sub>4</sub> and Carnosin in H<sub>2</sub>O at approx. 10<sup>-2</sup> mol/L in a 1:1 ratio. We dilute this solution with acetonitrile (1:10) and continuously infuse it into the ESI chamber at a flow rate of 2 μL/min using a syringe pump. Nitrogen was used as drying gas at a flow rate of 3.0 L/min at 220 °C and spray the solutions at a nebulizer pressure of 4 psi with the electrospray needle held at 4.5 kV. We held transfer parameters to the Paul trap of the mass spectrometer constant and used Helium as a buffer gas with a partial pressure of about 3 x 10<sup>-3</sup> mbar inside the ion trap. BrukerTrapControl 7.0 software controlled the instrument and we performed data analysis using Bruker Data Analysis 4.0 software.

#### V-3.2: IR-MPD

IR-MPD measurements were performed with the Bruker amaZonSL mass spectrometer (cf. ESI-MS part) after its modification. Two KTP/KTA optical parametric oscillator/amplifier (OPO/OPA,

LaserVision) systems, each pumped with a Q-switched 10 Hz injection seeded Nd<sup>3+</sup>:YAG laser (PL8000, Continuum) provided for tunable IR radiation ( $\delta\nu = 0.9 \text{ cm}^{-1}$  resp.  $\delta\nu = 0.3 \text{ cm}^{-1}$ ,  $\delta t = 7 \text{ ns}$ ) in order to record vibrational spectra via the multi-photon dissociation scheme. We used the OPA idler wave ( $\leq 10 \text{ mJ/pulse}$ ) of the one system to scan spectra (pump laser) within  $2800 - 3600 \text{ cm}^{-1}$ . On choice the second IR OPO/A served as probe laser, set to a selected and fixed vibrational resonance frequency. The probe laser beam was aligned counter-propagating with respect to the scanning pump laser beam. Each trapped and  $m/z$  isolated ion package was irradiated by 2 - 4 laser pulses (or pulse pairs in case of two-laser experiments) in order to produce sufficient fragment ions. IR spectra were recorded using Bruker chromatogram software for extracting the intensity of parent and fragment ions (three point averaging directly by BrukerTrapControl software). IR-MPD signal was evaluated corresponding to formula 1. Origin Plot Software served to apply a five point adjacent averaging for smoothing. IR frequency was calibrated by a wave meter (821B-NIR, Bristol instruments). Laser power curve was recorded in parallel to the IR-MPD spectra through digitizing the analog output of the laser power meter by an ample ADC input of the amaZonSL mass spectrometer electronics.

### V-3.3: Theoretical methods

DFT [24-27] calculations were performed at the B3LYP [28-31] level of theory using cc-pVDZ (C, H, N, O) [32] and Stuttgart RSC 1997 ECP (Zn) [33] basis sets and the Gaussian 03 and 09 packages [34, 35]. Standard convergence criteria were applied. We chose starting conformations of **[Carn-H,Zn<sup>II</sup>]<sup>+</sup>** in accordance to those derived by B. Reinhard [21]. Full geometry optimization of all nuclear coordinates yields multiple locally stable minimum structures. The lowest structure is assumed to represent the most stable isomer. We verified the three lowest energy structures on different levels of theory (B3P86 [28, 30, 31] and B97D [36]) in combination with different basis sets (Ahlichs VTZ [37] + Stuttgart RSC 1997 ECP (Zn)) (cf. Table 6). DFT predicted vibrational spectra at the B3LYP/cc-pVTZ level of theory were scaled by 0.965 [38].

### V-3.4: Estimation of photon number

In the IR-MPD processes, the fragmentation arises from the absorption of multiple photons. Their total number is a priori not known. The IR-MPD efficiency scales exponentially with the number  $n$  of absorbed photons. A corresponding formula was developed for the multiphoton ionization of molecules [39].

$$I_{fr}(\nu) \propto I(pf)^n \quad (1) \mid pf = \text{photon flux}$$

$$I(pf)^n \propto \frac{E}{N_{pulse}} \quad (2) \mid \text{pulse length} = \text{const.}$$

$$\log(I_{fr}(\nu)) \propto n \times \log\left(\frac{E}{N_{pulse}}\right) \quad (3)$$

Therefore we measured the fragmentation efficiency using different laser pulse energies. Double-logarithmic plots of fragmentation efficiency versus laser energy most often allow for linear fitting. The slope of the fit function is assumed to correspond to the number of photons that are necessary to induce fragmentation.

## V-4: Results

### V-4.1: ESI-MS and Collision Induced Dissociation

The resulting mass spectrum (MS) of a solution of carnosine and ZnSO<sub>4</sub> in water/acetonitrile (1:10) exhibits a signal at 288.8 m/z (most abundant mass) amongst a large variety of compounds. This signal can be assigned to the [Carn-H,Zn<sup>II</sup>]<sup>+</sup> complex by verification of its isotopic pattern (cf. Fig. 5). The experimental mass spectrum exhibits a constant shift of 0.2 m/z to lower masses with respect to the simulated isotopic distribution which is due to a deficient calibration of the mass spectrometer at times of recording the spectrum.

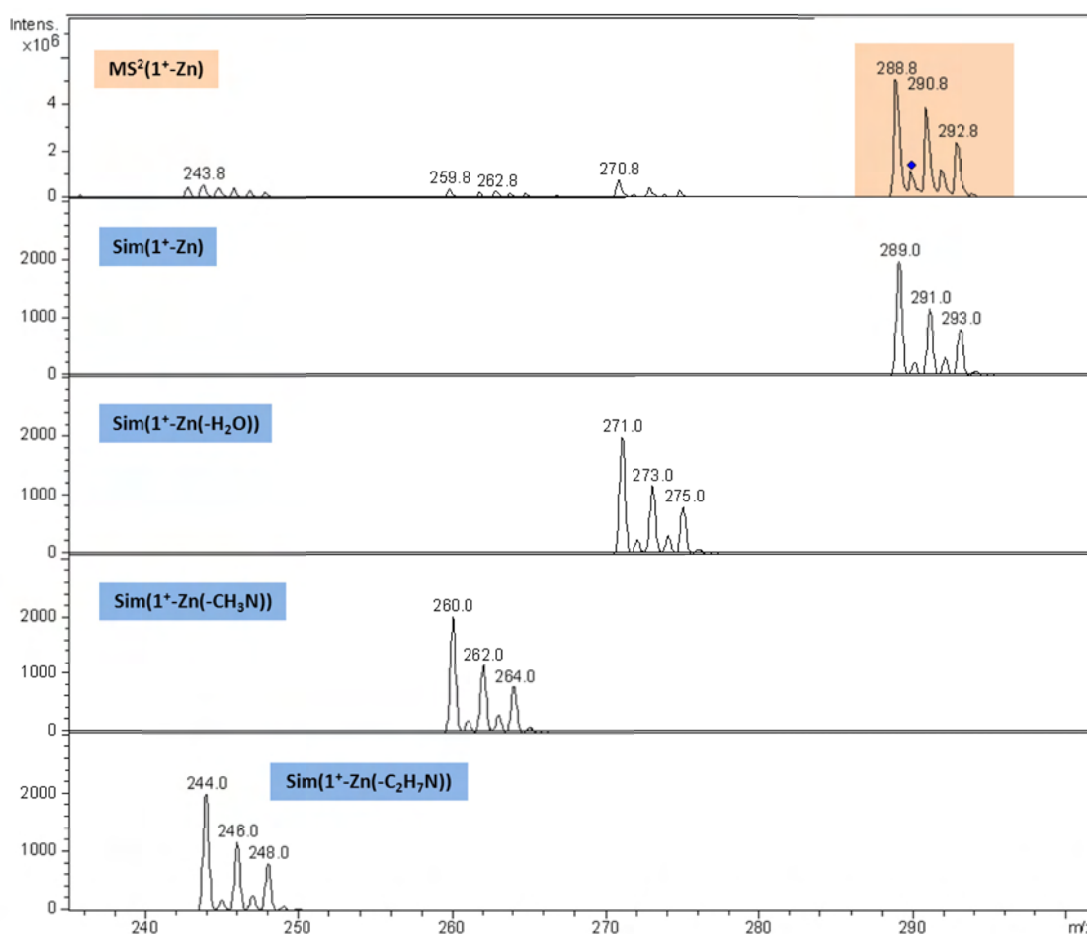


**Figure 5:** Mass spectrum ( $MS^2$ ) of  $[Carn-H,Zn^{II}]^+$  (top) and simulated isotope patterns of  $[Carn-H,Zn^{II}]^+$  and its fragments (cf. Table 3). Neutral losses are given in parenthesis within the row labels.

CID experiments yield a broad variety of fragment ions. We assigned several of them (cf. Fig. 5, 6 and Table 3) and estimated relative ratios of the fragmentation channels (cf. Table 4).  $Zn^{2+}$  preferentially remains bonded to the larger fragments. The  $[Carn-H,Zn^{II}]^+$  complex does not undergo a loss of  $NH_3$  in contrast to the protonated carnosine molecule (cf. Chapter IV, Table 3). There are only a few fragmentation pathways that are common to the  $[Carn-H,Zn^{II}]^+$  complex and protonated carnosine and its alkali ion complexes, e.g. the neutral loss of 18 m/z (loss of  $H_2O$ ).

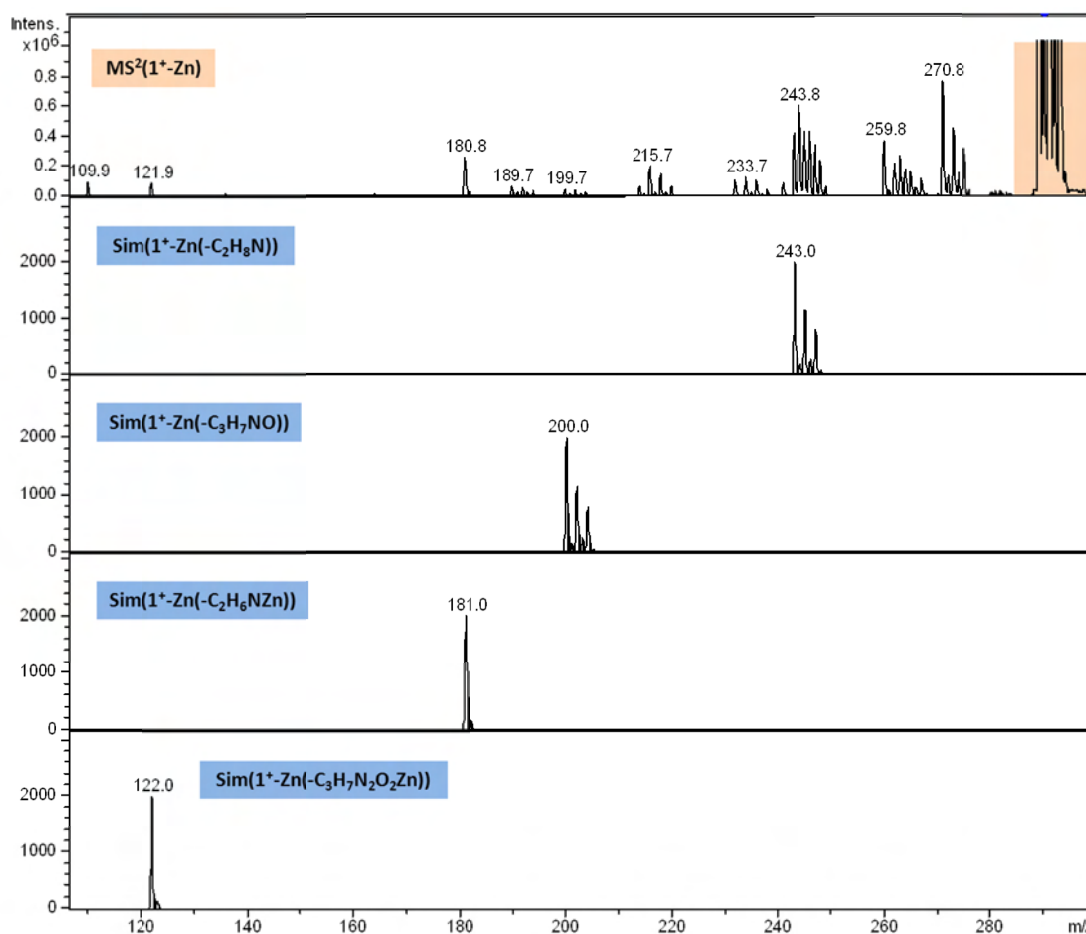


**Figure 6:** Mass spectrum ( $MS^2$ ) of  $[Carn-H,Zn^{II}]^+$  (top) and simulated isotope patterns of  $[Carn-H,Zn^{II}]^+$  and of its fragment (cf. Table 1).

**Table 3:** Characteristics of observed fragmentation channels (cf. Fig. 5 and 6). Mass losses are calculated due to the most abundant mass peaks of the parent and fragment ions.

mass of ionic fragment / m/z	ionic fragment	mass loss / m/z	neutral fragment
271	$[C_9H_{11}N_4O_2Zn]^+$	18	$H_2O$
260	$[C_8H_{10}N_3O_3Zn]^+$	29	$[CH_3N]$
244	$[C_7H_6N_3O_3Zn]^+$	45	$[C_2H_7N]$
243	$[C_7H_5N_3O_3Zn]^+$	46	$[C_2H_8N]$
216	$[C_6H_6N_3O_2Zn]^+$	73	$[C_3H_7NO]$
181	$[C_7H_7N_3O_3]^+$	108	$[C_2H_6NZn]$
122	$[C_6H_6N_2O_1]^+$	167	$[C_3H_7N_2O_2Zn]$
110	$[C_5H_8N_3]^+$	179	$[C_4H_5N_1O_3Zn]$



**V-4.2: 1- and 2-color IR-MPD spectra of  $[\text{Carn-H,Zn}^{\text{II}}]^+$** 

The 1-color IR-MPD spectrum of isolated  $[\text{Carn-H,Zn}^{\text{II}}]^+$  (cf. Fig. 7, top) exhibits two strong (3545 and 3485  $\text{cm}^{-1}$ ) and two minor bands (3359 and 3306  $\text{cm}^{-1}$ ) in the OH and NH stretch region and some very weak signals between 2800 and 3000  $\text{cm}^{-1}$ .

Using the difference frequency mixing (DFM) stage of the OPO/OPA system for the fingerprint region reveals a strong band at 1667  $\text{cm}^{-1}$  and two minor bands at 1900 and 1620  $\text{cm}^{-1}$ . (cf. Table 4). The application of a 2-color IR-MPD scheme (cf. Fig. 7, bottom, probe laser fixed at 3359  $\text{cm}^{-1}$  (black arrow)) exhibits a slight increase of the fragmentation efficiency for most bands.

We assigned the measured signals of  $[\text{Carn-H,Zn}^{\text{II}}]^+$  by references to known IR frequencies of OH, NH, CH and CO stretch motions (cf. Table 2). IR-MPD bands in the region of 3300 to 3500  $\text{cm}^{-1}$  correspond to stretch motions of the amine and amide groups. No hydrogen-bonded N-H stretching motions are observed in the region of 3070 to 3350  $\text{cm}^{-1}$ . Bands at 1690 and 1900  $\text{cm}^{-1}$  may indicate conjugated and non conjugated CO stretching vibrations, as characteristic for carboxylic and carbonylic groups, respectively.

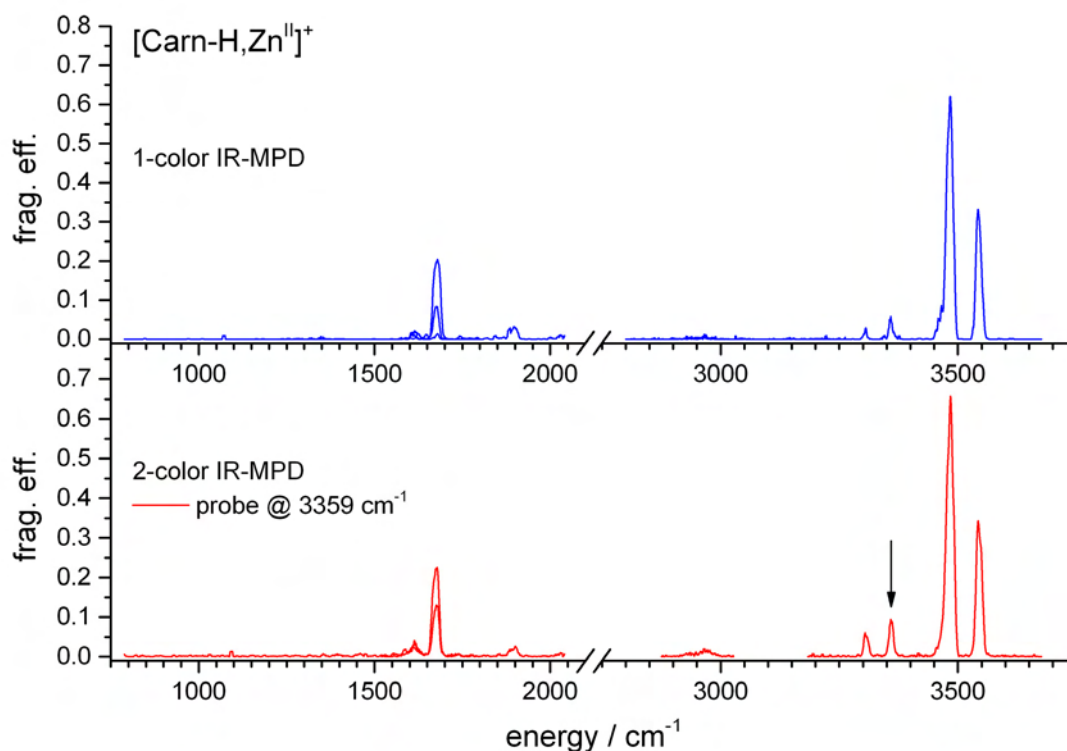


**Figure 7:** 1- (top) and 2-color (bottom, probe at 3359  $\text{cm}^{-1}$ ) IR-MPD spectrum of  $[\text{Carn-H,Zn}^{\text{II}}]^+$ .

### V-4.3: Calculations of structures, normal modes and IR spectra

We optimized possible structures (in part taken from [21]) at the B3LYP/cc-pVDZ (C, H, N, O) and Stuttgart 1997 ECP (Zn) level of theory (cf. Fig. 8).

In structure **a**), the deprotonated carnosine anion coordinates fourfold with the  $\text{Zn}^{2+}$  cation through a carboxylic and a carbonylic oxygen atom and through an imidazolic nitrogen atom and the terminal aminic nitrogen atom (cf. Fig. 8). The coordination with a single oxygen and three nitrogen atoms (structure **b**) is less stable (+10 kJ/mol), possibly due to a weaker interaction of the amidic nitrogen atom with the  $\text{Zn}^{2+}$  ion as compared to the amidic oxygen atom (in structure **a**)). Rotation of the N-terminus yields structure **c**). It allows for a hydrogen bridge between the  $\text{N}_a$  and  $\text{N}_{at}$  nitrogen atoms. This hydrogen bond can not compensate the enthalpic penalty of loosing the  $\text{Zn-NH}_2$  bond of **a**) and **b**) in favor of a (weaker)  $\text{Zn}^{\text{II}}\text{-O}$  bond. The protonation tautomer **d**) of structure **a**) is less stable by 82 kJ/mol and seems unlikely.

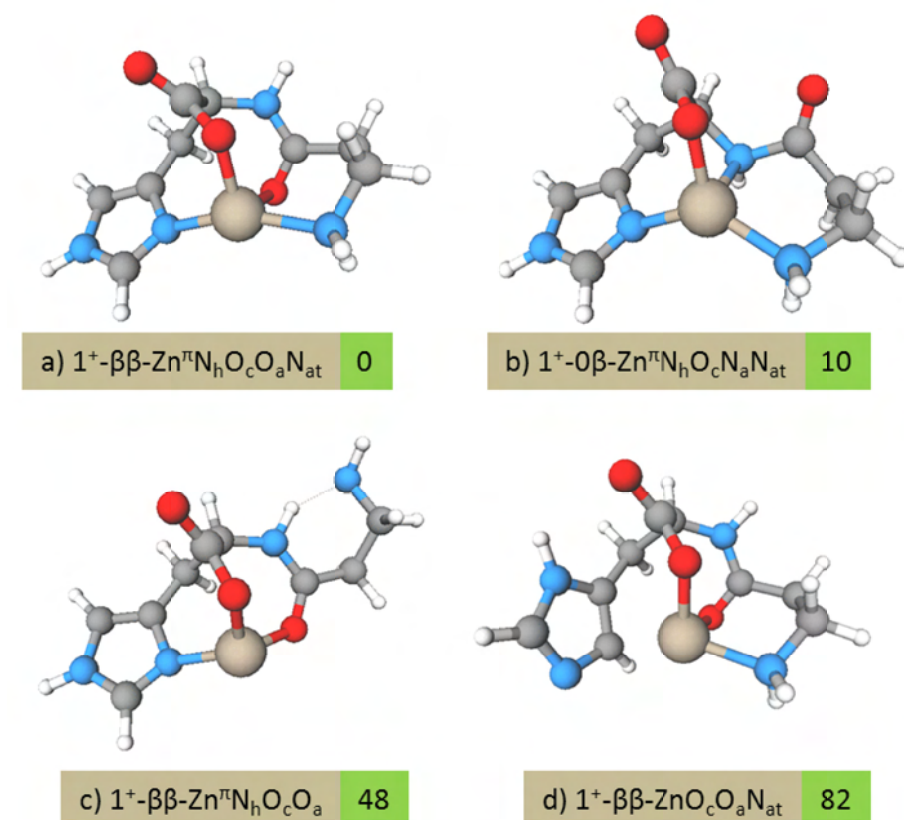


**Figure 8:** Most stable conformers of  $[\text{Carn-H}, \text{Zn}^{\text{II}}]^+$  and relative energies (in kJ/mol) as calculated at the B3LYP/cc-pVDZ (C, H, N, O) and Stuttgart 1997 ECP (Zn) level of theory (for definition of nomenclature, refer to page 123).

We checked the obtained structures against variation of DFT functional and basis set (cf. Table 6). The energetic order persists in all cases with variations by  $\pm 1$  kJ/mol (struct. **b**) and  $\pm 9$  kJ/mol (struct. **c**). Therefore, we used the well established B3LYP functional for calculations of IR absorption spectra of the three most stable isomers.

#### V-4.4: Comparison of IR-MPD spectra to DFT derived IR absorption spectra

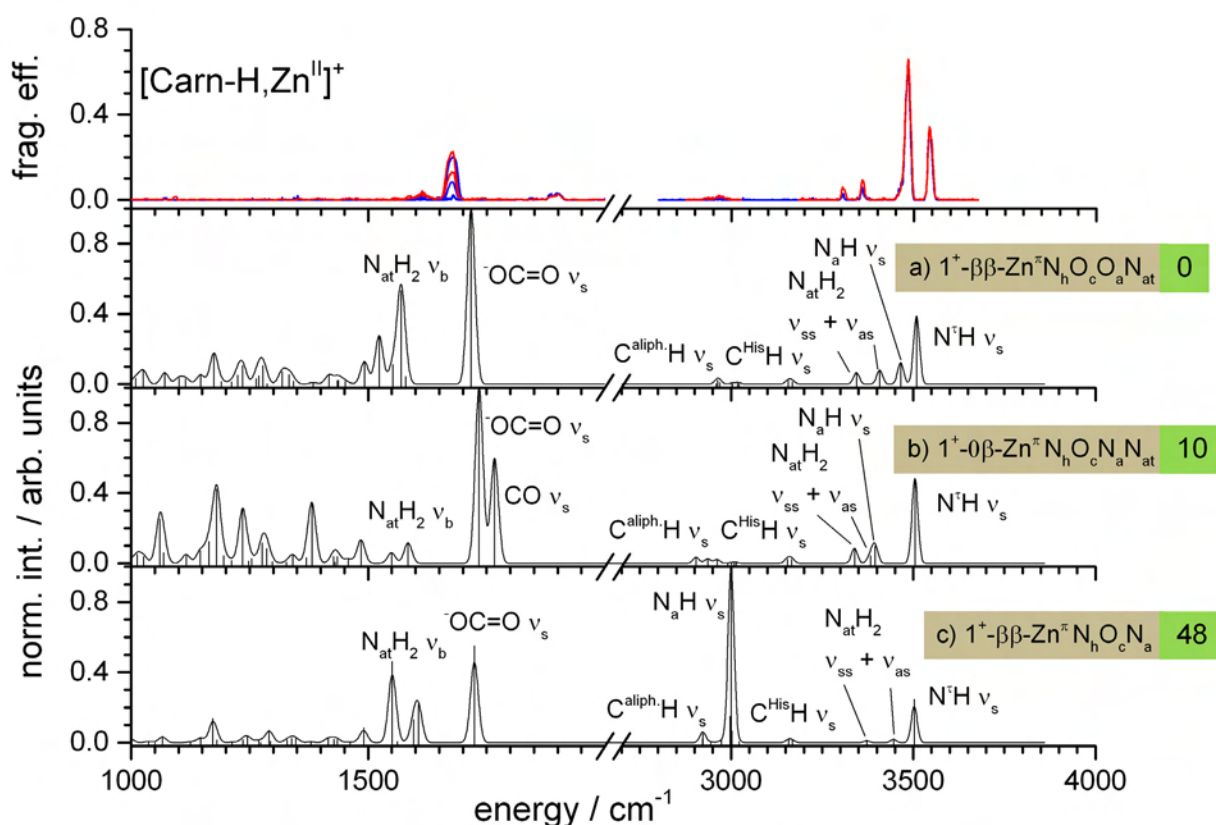


**Figure 9:** 1-color (blue) and 2-color (red) IR-MPD spectrum (top) and DFT derived absorption spectra of three energetic minimum structures of  $[\text{Carn-H, Zn}^{\text{II}}]^+$  (cf. Fig. 8, structures **a**-**c**) at the B3LYP/cc-pVTZ (C, H, N, O), Stuttgart 1997 ECP (Zn) level of theory (scaled by 0.965).

All four major peaks in the region from 3300 to 3600  $\text{cm}^{-1}$  can be found in the DFT derived IR absorption spectrum of **a**), calculated at the B3LYP/cc-pVTZ (C, H, N, O), Stuttgart 1997 ECP (Zn) level of theory. Even after scaling with a factor of 0.965 [38], the calculated position (3510  $\text{cm}^{-1}$ ) of the band at 3545  $\text{cm}^{-1}$  exhibits a shift of about 35  $\text{cm}^{-1}$  to lower frequency. A relative good accordance between the theoretical spectrum of **a**) and the experimental spectra can be seen for the band at 3485  $\text{cm}^{-1}$ . The IR-MPD band at 3545  $\text{cm}^{-1}$  corresponds to a stretching motion of the N'H group and the band at 3485  $\text{cm}^{-1}$  to the one of the amidic  $\text{N}_a\text{H}$  group. The IR-MPD bands at 3306 and 3360  $\text{cm}^{-1}$  exhibit a shift to the blue with respect to the calculated spectrum of **a**) by

approximately  $50\text{ cm}^{-1}$ . Relative intensities correlate to the experiment. These bands can be assigned to asymmetric and symmetric stretch motions of the terminal  $\text{NH}_2$  group ( $\text{N}^{\text{at}}\text{H}_2\text{ } \nu_{\text{as}} + \nu_{\text{ss}}$ ). The CH stretching motions of the imidazole ring ( $\text{C}^{\text{His}}\text{H } \nu_{\text{s}}$ ) can not be observed in the experimental spectrum. Aliphatic CH stretching motions ( $\text{C}^{\text{aliph}}\text{H } \nu_{\text{s}}$ ) can be observed in a minor band at  $2950\text{ cm}^{-1}$  in both (experimental and theoretical) spectra. In the *fingerprint* region ( $< 2000\text{ cm}^{-1}$ ) of the spectrum, only three bands at  $1900$ ,  $1667$  and  $1620\text{ cm}^{-1}$  could be obtained from the measurement. The theoretical spectrum exhibits a dominant peak for the C=O stretching motion of the  $\text{Zn}^{2+}$  bound  $\text{OC=O}$  ( $\text{OC=O } \nu_{\text{s}}$ ) which is redshifted by about  $170\text{ cm}^{-1}$  with respect to the measurement. The experimental peak at  $1900\text{ cm}^{-1}$  is very weak. The band at  $1667\text{ cm}^{-1}$  consists of an overlap two  $\text{NH}_2$  bending motions ( $\text{N}^{\text{at}}\text{H}_2\text{ } \nu_{\text{b}}$ ), combined with an amidic CO stretch motion and a NH & CH bending motion. These bending motions couple to the imidazole ring and the adjacent  $\text{CH}_2$  group. DFT derived IR absorptions shift approximately  $100\text{ cm}^{-1}$  to the red with respect to the peak at  $1667\text{ cm}^{-1}$ . The band at  $1620\text{ cm}^{-1}$  originates from a NH bending motion that is coupled to bending motions of the adjacent tertiary CH and the C=O group of the molecule.

We verified the influence of the DFT method on the IR absorption spectrum. All three depicted theoretical spectra of structure **a**) (cf. Fig. 17) exhibit in principle the same shape and relative intensities in the region above  $2500\text{ cm}^{-1}$ . Spectrum C4 was calculated with the B3P86 functional. It exhibits the largest differences in the *fingerprint* region as compared to all other spectra. The B97D functional (C5) leads to a strong shift of the total spectrum towards lower frequencies. Swapping the double zeta quality active electron basis sets of the Stuttgart 1997 ECP (C2 + C3) for a Ahlrichs VTZ base (C3) at the  $\text{Zn}^{2+}$  ion shows no significant influence to the DFT derived spectrum.

#### V-4.5: IR-MPD spectrum of $[\text{Carn-H-H}_2\text{O,Zn}^{\text{II}}]^+$ and DFT calculations of fragments

We measured an IR-MPD spectrum of the  $[\text{Carn-H-H}_2\text{O,Zn}^{\text{II}}]^+$  fragment ion (cf. Fig. 10) in order to compare these data to DFT predicted structures of fragments (cf. Fig. 11). Therefore we had to produce large amounts of the  $[\text{Carn-H-H}_2\text{O,Zn}^{\text{II}}]^+$  in the first place. We used the CapExit voltage to accelerate the ions in the CapExit region (cf. experimental scheme of the mass spectrometer in Chapter I) and to induce fragmentation prior to isolation and fragmentation in the ion trap. Eventually  $271$  to  $277\text{ m/z}$  ions add water. Those ions exhibit the same isotope pattern as the  $[\text{Carn-H,Zn}^{\text{II}}]^+$  parent ion. An increase of the storage time (without laser irradiation) leads to a slight decrease of intensity of the ions in the range of  $271$  to  $277\text{ m/z}$  and to a slight increase of ions in the range of  $289$  to  $295\text{ m/z}$ . This gives hint to gas phase reactions of the fragment ions with water molecules which are always present in the ion trap. Therefore, it was not possible to measure an IR-

MPD spectrum of the isolated  $[\text{Carn-H}(-\text{H}_2\text{O}),\text{Zn}^{\text{II}}]^+$  complex without a contribution of other complexes to the spectrum.

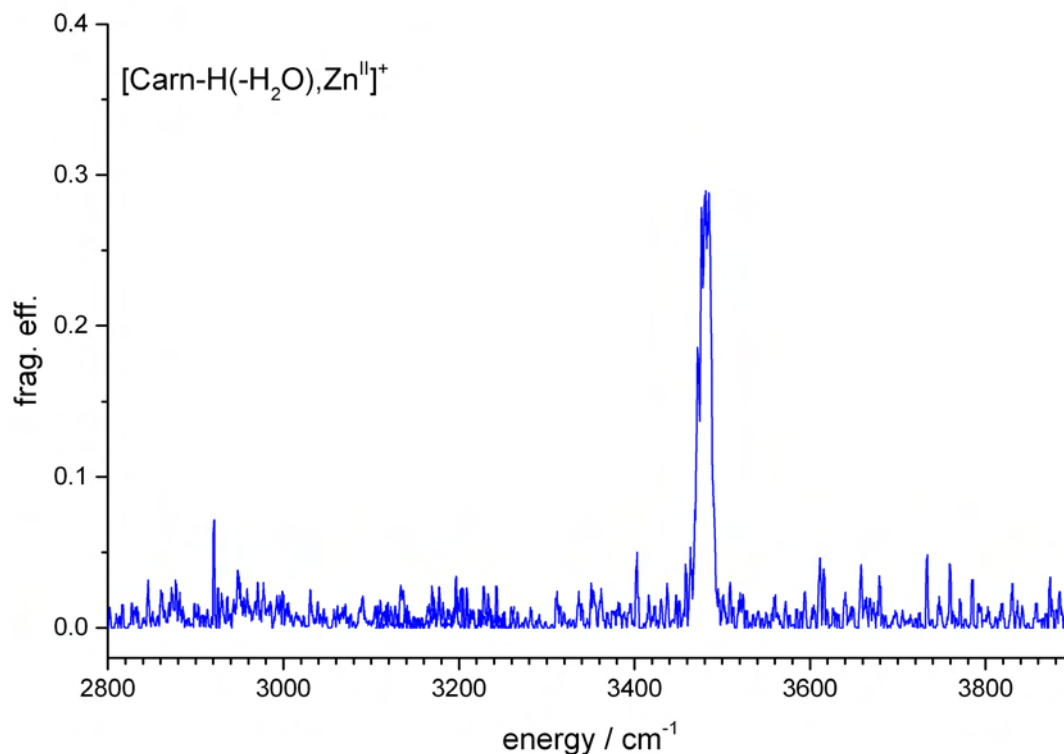


**Figure 10:** 1-color IR-MPD spectrum of  $[\text{Carn-H-H}_2\text{O},\text{Zn}^{\text{II}}]^+$  after CapExit fragmentation of  $[\text{Carn-H},\text{Zn}^{\text{II}}]^+$ .

We calculated DFT geometry optimized structures of complex  $[\text{Carn-H-H}_2\text{O},\text{Zn}^{\text{II}}]^+$  (cf. Fig. 11). The oxygen and hydrogen atoms of the water molecule can originate from various sites within the ionic complex. Therefore, we calculated minimum structures and relative energies of several conceivable products. We calculated relative dissociation energies (without BSSE corrections) according to Equation 4.

$$\Delta E = E(\text{H}_2\text{O}) + E(\text{Fragment}) - E(\text{Parent}) \quad (4)$$

Assuming isomer  $\mathbf{1}^+(-\text{H}_2\text{O})-\alpha\alpha-\text{Zn}^{\text{II}}\text{N}_h\text{O}_a\text{N}_{at}$  (cf. Fig. 11) as the most abundant isomer, at least three NH stretch bands can be expected in the IR spectrum. Only a single intense band at  $3485\text{ cm}^{-1}$  was observed. Due to increment appraisal, it can be assumed that this band corresponds to amidic  $\text{N}_a\text{H}$  stretch motions.

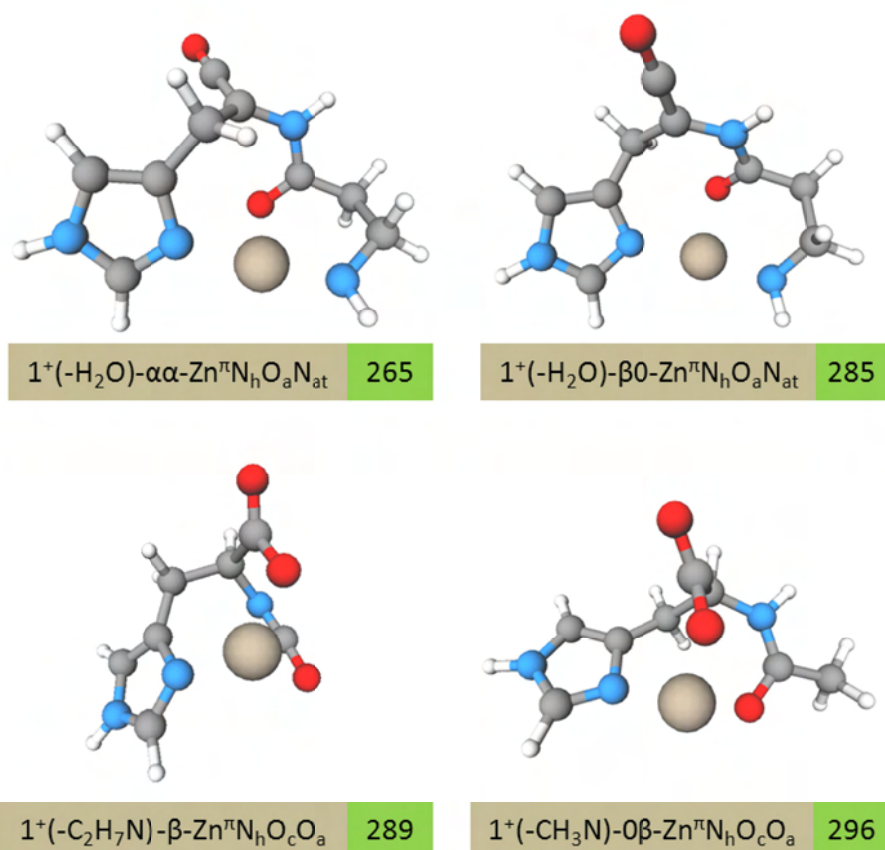


**Figure 11:** Possible structures of  $[\text{Carn-H}, \text{Zn}^{\text{II}}]^+$  after loss of various neutral fragments (given in parenthesis within the nomenclature) and corresponding relative energies calculated at the B3LYP/cc-pVDZ (C, H, N, O) and Stuttgart 1997 ECP (Zn) level of theory (in kJ/mol).

We cannot draw any definite conclusion on the structure of the  $[\text{Carn-H}(-\text{H}_2\text{O}), \text{Zn}^{\text{II}}]^+$  complex from the evaluation of experimental IR-MPD and calculated spectra.

#### V-4.6: Comparison of CID and IR-MPD channels with rel. abundance of different channels

We applied a resonant 2-color pump/probe scheme in order to enhance the fragmentation efficiency and to characterize the IR-MPD process in more detail. For that purpose, we scanned one IR laser (pump) while we set the other IR laser (probe) to a fixed frequency at the center of an absorption band of the  $[\text{Carn-H}, \text{Zn}^{\text{II}}]^+$  complex with a timing delay  $\Delta t$  of 100 ns.

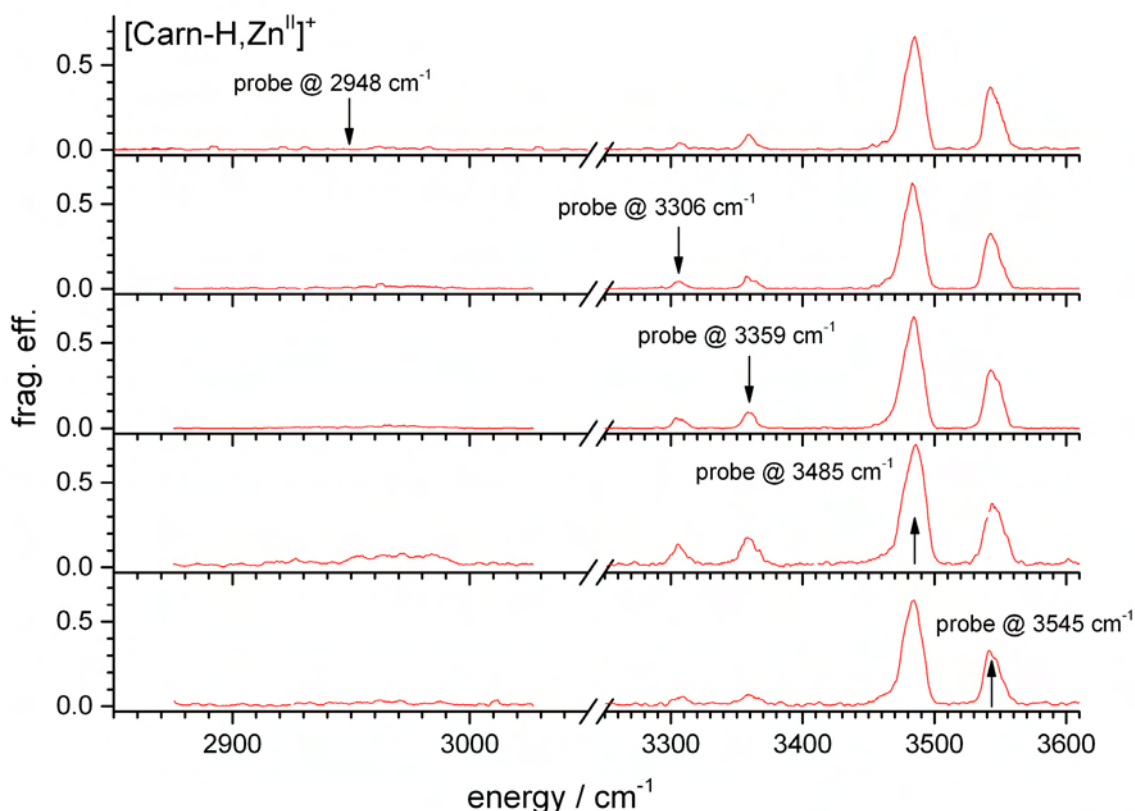


**Figure 12:** 2-color IR-MPD spectra of  $[\text{Carn-H,Zn}^{\text{II}}]^+$ , scan with pump laser system, probe laser held fixed at given frequencies (indicated by arrows), pump/probe delay  $\Delta t_{nb-bb} = 100$  ns.

Our current experimental protocol is the use of the broadband (*bb*) OPO/A laser system as pump laser and the use of the narrowband (*nb*) OPO/A laser system as probe laser. The photons of the pump laser irradiate the molecules in the ion trap approximately 100 ns before those of the probe laser. A systematic variation of timing delay is shown in section V-4.8. The IR-MPD spectra of the  $[\text{Carn-H,Zn}^{\text{II}}]^+$  complex shown in Fig. 12 correspond to this standard setup. Scans with the pump system and additional 5 point adjacent averaging of the derived data leads to smooth band profiles with FWHM between 10 and 20  $\text{cm}^{-1}$ . Changing the laser beams normally used for pump and probe and also the timing sequence leads to the spectra shown in Fig. 13. The probe laser has a smaller bandwidth and a lower scan velocity. This leads to a higher amount of available data and the spectra become more structured, even with the same post processing. The enhancement of IR-MPD efficiency does not depend on the choice of pump or probe lasers as scanning laser or photon source on a fixed frequency.

No enhancement of the IR-MPD signal can be observed while the probe laser is set to the CH bands at 2948  $\text{cm}^{-1}$ . Irradiation of the band at 3485  $\text{cm}^{-1}$  with the probe laser leads to a strong increase of



the intensity of the bands at 3306 and 3359  $\text{cm}^{-1}$  during a pump laser scan. Irradiation at 3305 or 3359  $\text{cm}^{-1}$  especially while scanning with the pump laser yields in a strong rise of the band at 3545  $\text{cm}^{-1}$ .

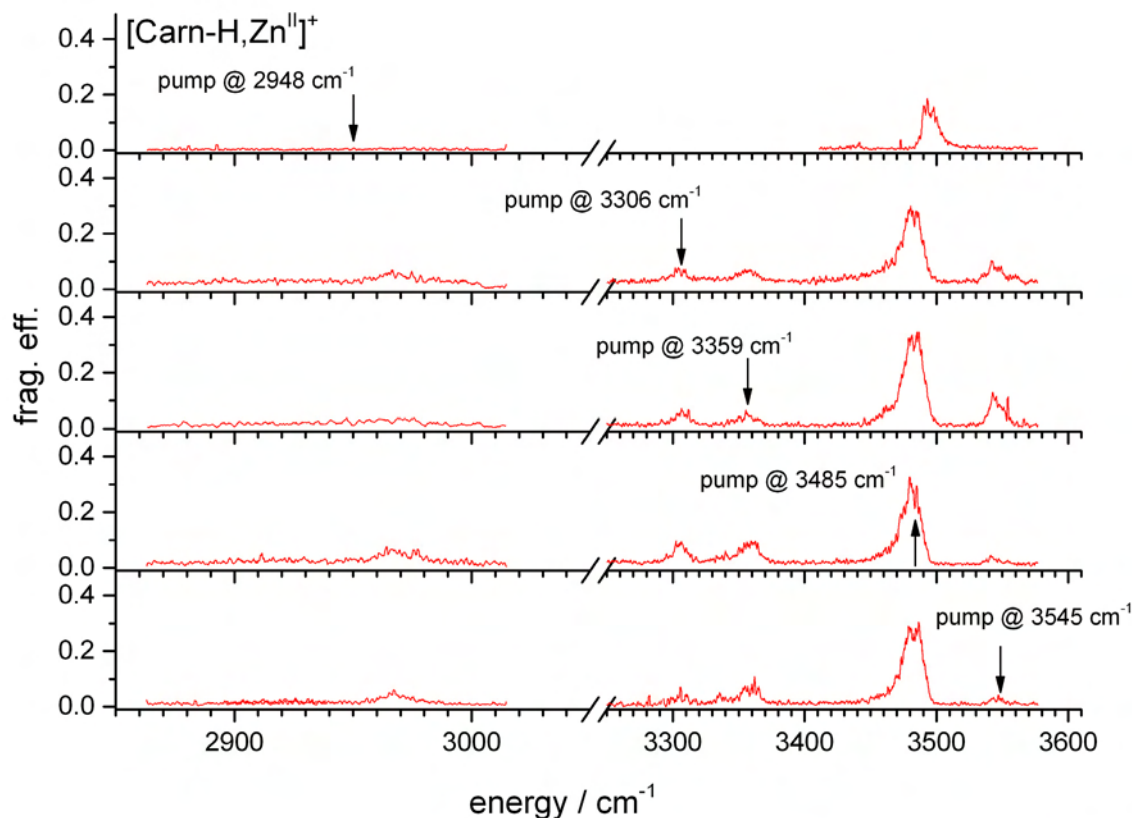


**Figure 13:** 2-color IR-MPD spectra of  $[\text{Carn-H, Zn}^{\text{II}}]^+$ , scan with probe laser system, pump laser held fixed at given frequencies,  $\Delta t_{\text{bb-nb}} = 100 \text{ ns}$ .

We determined the relative abundance of fragmentation channels by their contribution to the total ion intensity of the CID and IR-MPD spectra, respectively (cf. Table 4). CID leads to three main fragmentation channels with 23, 31 and 41% relative abundance and several minor (< 5%) channels (cf. Table 3 for assignments). All main fragmentation channels contain the  $\text{Zn}^{2+}$  ion in the ionic fragment. IR-MPD induced fragmentation exhibits minor differences in one or two color scan modes. IR-MPD fragmentation channels are strongly mode dependent for the  $[\text{Carn-H, Zn}^{\text{II}}]^+$  complex, however. The loss of  $\text{H}_2\text{O}$  becomes more favorable for the bands at 3545 and 3485  $\text{cm}^{-1}$  than within CID. The loss of  $[\text{CH}_3\text{N}]$  molecules (mass range 260-269  $m/z$ ) is strongly reduced and also the loss of  $[\text{C}_2\text{H}_{7/8}\text{N}]$  molecules (mass range 243-250  $m/z$ ) is less prevalent. This effect is even more distinct while pumping the bands at 3359 and 3306  $\text{cm}^{-1}$ . Those two weak bands exhibit the loss of  $\text{H}_2\text{O}$  as an almost exclusive channel. The fragmentation pattern in the absorption at 1900  $\text{cm}^{-1}$  corresponds to the patterns of the bands at 3545 and 3485  $\text{cm}^{-1}$ . IR-MPD at 1667  $\text{cm}^{-1}$  changes the



relative abundancies of fragments, the loss of H<sub>2</sub>O is suppressed and the loss of [CH<sub>3</sub>N] and [C<sub>2</sub>H<sub>7/8</sub>N] molecules is enhanced.

**Table 4:** Relative abundance<sup>a</sup> of fragment ions due to CID and IR-MPD induced fragmentation of [Carn-H,Zn<sup>II</sup>]<sup>+</sup> (289-293 m/z, cf. Table 3 for assignments). Relative abundances of similar magnitude are highlighted with the same color.

Method	Total frag. eff.	Mass ranges / m/z										
		270 - 278	260 - 269	243 - 250	232 - 236	227 - 229	214 - 218	201 - 204	190 - 193	181 - 182	122	110
CID	24	23	31	41	0	2	1	0	0	2	0	0
IR-MPD												
3545 cm <sup>-1</sup>	15	43	12	35	1	0	1	1	2	4	0	1
3545 cm <sup>-1</sup> & 3545 cm <sup>-1</sup>	14	50	10	32	1	0	1	0	2	4	0	0
3485 cm <sup>-1</sup>	15	54	11	29	1	0	1	0	1	3	0	0
3485 cm <sup>-1</sup> & 3545 cm <sup>-1</sup>	22	49	11	33	1	0	1	0	1	4	0	0
3359 cm <sup>-1</sup>	0.7	91	3	6	0	0	0	0	0	0	0	0
3359 cm <sup>-1</sup> & 3545 cm <sup>-1</sup>	0.9	91	2	7	0	0	0	0	0	0	0	0
3306 cm <sup>-1</sup>	0.2	95	0	5	0	0	0	0	0	0	0	0
3306 cm <sup>-1</sup> & 3545 cm <sup>-1</sup>	0.5	91	1	8	0	0	0	0	0	0	0	0
1900 cm <sup>-1</sup>	1	49	16	22	0	0	6	0	7	0	0	0
1900 cm <sup>-1</sup> & 3545 cm <sup>-1</sup>	2	59	14	26	1	0	0	0	0	0	0	0
1667 cm <sup>-1</sup>	24	11	28	42	2	0	2	1	4	5	1	1
1667 cm <sup>-1</sup> & 3545 cm <sup>-1</sup>	21	12	27	43	3	0	2	0	4	8	1	1

<sup>a</sup> Only fragments with a relative abundance > 1% were taken into account. Rel. abund. were normalized to the sum of parent and fragment intensities per single spectrum. Data is taken from energy dependence measurements (cf. Fig. 14 and 15).

#### V-4.7: Quantification of 2-color induced enhancement of fragmentation

A frequency dependent measurement of the fragmentation efficiency versus the energy of the laser pulse (and therefore the photon flux at a fixed frequency) can be used to estimate the required number of photons for a (multi-)photon induced dissociation process. Using an empirical formula

[39], the slope of a linear fit to a  $\log(\text{IR-MPD})/\log(\text{energy})$  plot (cf. Fig. 14 and 15) yields the average number of absorbed photons (cf. Table 5).

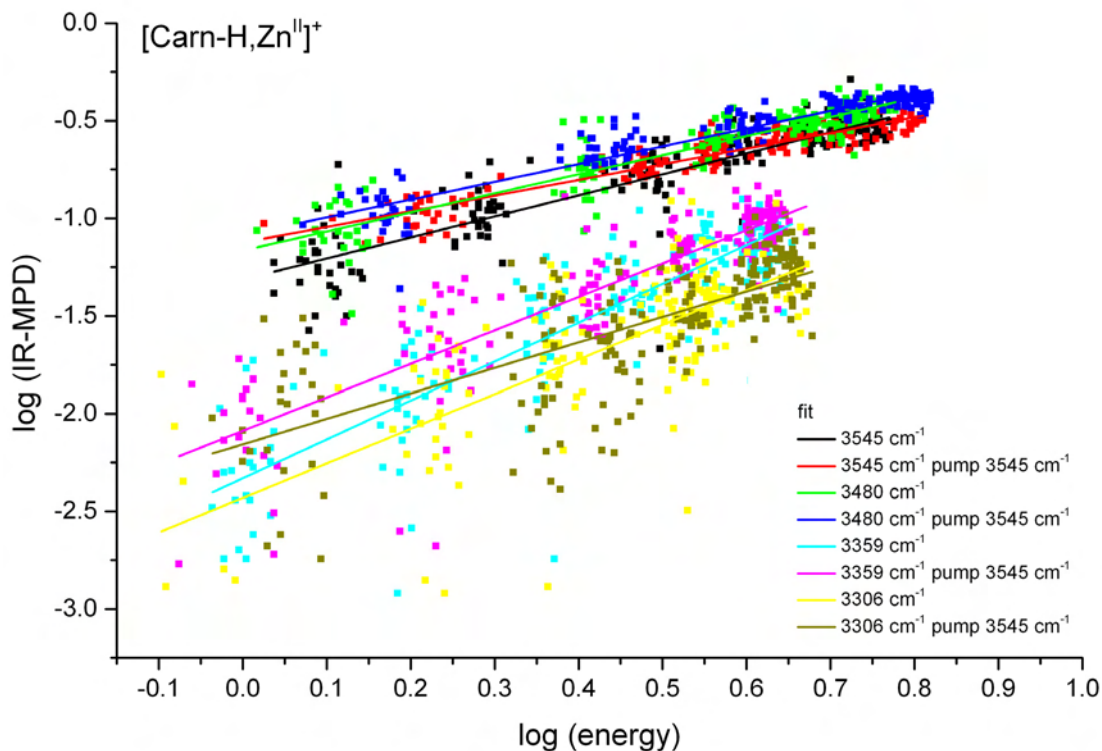


**Figure 14:**  $\log(\text{IR-MPD})/\log(\text{energy})$  plots and linear regression curves. These data allow for the determination of average number of photons in the fragmentation of  $[\text{Carn-H, Zn}^{\text{II}}]^+$ .

The bands at  $3545 \text{ cm}^{-1}$  and  $3485 \text{ cm}^{-1}$  exhibit a linear dependence of the fragmentation efficiency on the photon flux with a log-log slope of approximately one. The use of a second color (pump of the  $3485 \text{ cm}^{-1}$  band with probe at  $3545 \text{ cm}^{-1}$ ) does not change the slope considerably. Absorptions at  $3359 \text{ cm}^{-1}$  and  $3306 \text{ cm}^{-1}$  exhibit a slope of 2.0 (respectively 1.8 for the latter) for the one color process. The application of a second color (probe at  $3545 \text{ cm}^{-1}$ ) leads to a slight decrease (cf. Table 5) of the slope (to 1.7 resp. 1.3) of the linear fits (cf. Fig. 14).

We investigated the bands at  $1900 \text{ cm}^{-1}$  and  $1667 \text{ cm}^{-1}$  in more detail (cf. Fig. 15). Therefore we tested the dependence of the fragmentation efficiency of these bands towards all four bands above  $3000 \text{ cm}^{-1}$ . One color absorption at  $1900 \text{ cm}^{-1}$  leads to a slope of 1.6. The application of photons with  $3545$  or  $3485 \text{ cm}^{-1}$  leads to a slope of 0.5. The average number of photons is decreased by a factor of 3. Probing the bands at  $3359$  or  $3306 \text{ cm}^{-1}$  yields a lower decrease to at least a factor of 2 (slope 0.8).

Probing an additional band while pumping at  $1667\text{ cm}^{-1}$  flattens the slope of the fit function from 2.5 to 2.1 (probe @  $3545\text{ cm}^{-1}$ ), 1.6 (probe @  $3485\text{ cm}^{-1}$ ), 1.8 (probe @  $3359\text{ cm}^{-1}$ ) and 1.7 (probe @  $3306\text{ cm}^{-1}$ ). 2-color IR-MPD needs less photons to cause a fragmentation at  $1667\text{ cm}^{-1}$  than 1-color IR-MPD, but the effect is less than at  $1900\text{ cm}^{-1}$ .

**Table 5:** Pump and probe band frequency dependence on the slope of  $\log(\text{IR-MPD})/\log(\text{energy})$  plots estimated by linear fitting of experimental data (cf. Fig. 14 and 15). Product of slope and photon energy corresponds to a normalized energy absorption regarding the pump photon.

pump (& probe) band / $\text{cm}^{-1}$	slope	slope x pump photon energy / $\text{kJ/mole}$
3545	$1.1 \pm 0.1$	$46.7 \pm 4.2$
3485	$1.0 \pm 0.1$	$41.7 \pm 4.2$
3485 (probe @ 3545)	$0.9 \pm 0.1$	$37.5 \pm 4.2$
3359	$2.0 \pm 0.1$	$80.4 \pm 4.0$
3359 (probe @ 3545)	$1.7 \pm 0.1$	$68.3 \pm 4.0$
3306	$1.8 \pm 0.1$	$71.2 \pm 4.0$
3306 (probe @ 3545)	$1.3 \pm 0.1$	$51.4 \pm 4.0$
1900	$1.6 \pm 0.3$	$36.4 \pm 6.8$
1900 (probe @ 3545)	$0.5 \pm 0.1$	$11.4 \pm 2.3$
1900 (probe @ 3485)	$0.5 \pm 0.1$	$11.4 \pm 2.3$
1900 (probe @ 3359)	$0.8 \pm 0.2$	$18.2 \pm 4.5$
1900 (probe @ 3306)	$0.8 \pm 0.1$	$18.2 \pm 4.5$
1667	$2.5 \pm 0.1$	$49.9 \pm 2.0$
1667 (probe @ 3545)	$2.1 \pm 0.1$	$41.9 \pm 2.0$
1667 (probe @ 3485)	$1.6 \pm 0.1$	$31.9 \pm 2.0$
1667 (probe @ 3359)	$1.8 \pm 0.1$	$35.9 \pm 2.0$
1667 (probe @ 3306)	$1.7 \pm 0.1$	$33.9 \pm 2.0$

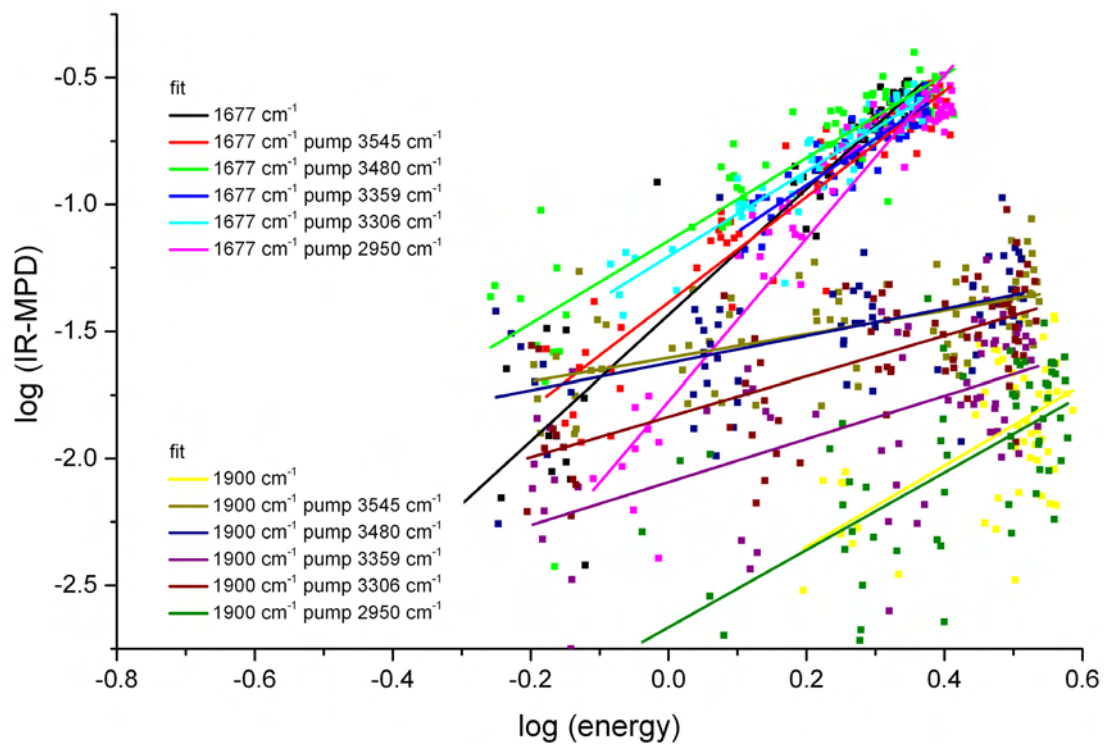


**Figure 15:**  $\log(\text{IR-MPD})/\log(\text{energy})$  plots and linear regression curves. These data allow for the determination of average number of photons in the fragmentation of  $[\text{Carn-H, Zn}^{\text{II}}]^+$ .

## V-4.8: Influence of the pump/probe delay

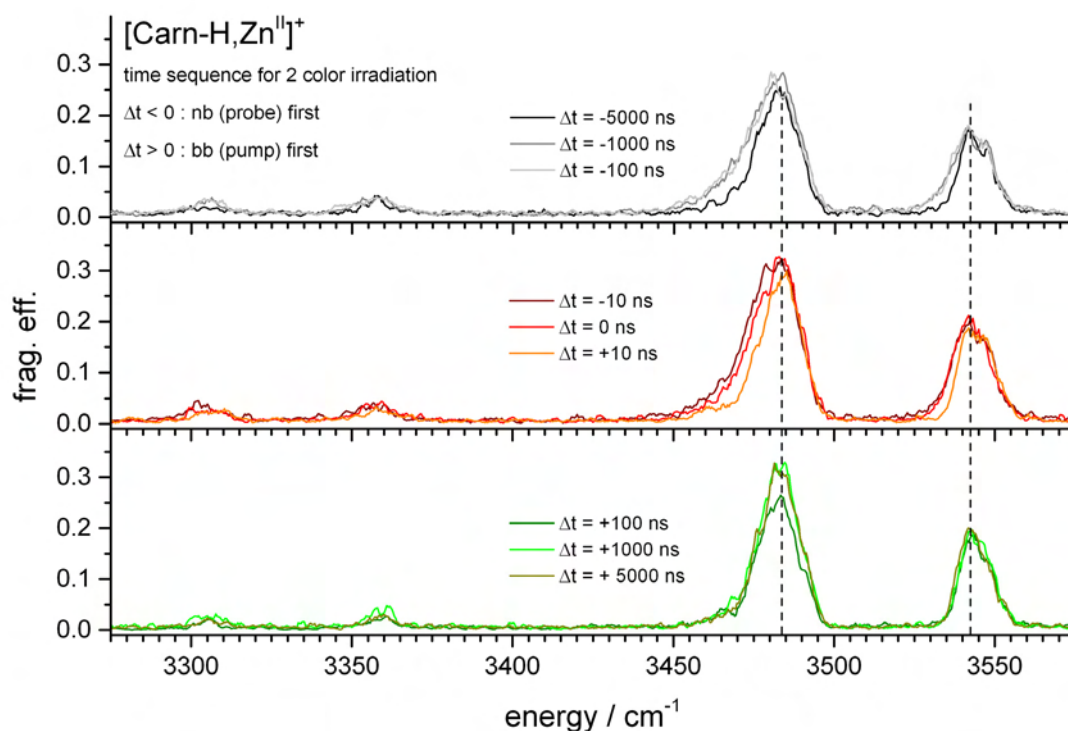


**Figure 16:** 2-color IR-MPD spectra of  $[\text{Carn-H, Zn}^{\text{II}}]^+$  due to the variation of  $\Delta t$  between pump (broadband OPO/A laser system (bb)) and probe (narrowband (nb) system) pulses.

We carried out a limited study of the temporal delay of pump and probe laser beams in order to study the effect on the band profile (cf. Fig. 16). We used the *bb* laser as scanning pump pulse and the *nb* laser as fixed probe pulse at  $3485 \text{ cm}^{-1}$ . We irradiated the  $[\text{Carn-H, Zn}^{\text{II}}]^+$  ions first with the probe laser beam and applied the pump laser after various delays (cf. Fig. 16, top). A spectral broadening on the „red side“ of the bands at  $3545$  and  $3485 \text{ cm}^{-1}$  appears for a delay of  $-1000 \text{ ns}$  and  $-100 \text{ ns}$  (probe before pump), whereas the black curve with a temporal delay of  $-5000 \text{ ns}$  is significantly smaller. The changeover of the temporal order of pump and probe beam leads to the spectra in the mid row of Fig. 16. The dark red curve with  $\Delta t = -10 \text{ ns}$  is just as broad as the two grey curves in the upper spectra, the red curve ( $\Delta t = 0 \text{ ns}$ ) gets a little smaller and the orange curve ( $\Delta t = 10 \text{ ns}$ ) is even smaller than the black one (top row). The spectra with  $\Delta t = 100, 1000$  and  $5000 \text{ ns}$  (bottom row) exhibit almost the same band shape, except for the  $\Delta t = 100 \text{ ns}$  measurement. Here, we observe a somewhat lower fragmentation efficiency within the  $3485 \text{ cm}^{-1}$  band.

## V-5: Discussion

**[Carn-H,Zn<sup>II</sup>]<sup>+</sup>** exhibits a fragmentation pattern, that differs from those of protonated carnosine and from its alkali metal complexes (cf. Chapter III and IV). The fragmentation of **[CarnH]<sup>+</sup>** leads to the preferential loss of NH<sub>3</sub>. This does not take place in the **[Carn-H,Zn<sup>II</sup>]<sup>+</sup>** complex. The difference may arise from the binding of the terminal NH<sub>2</sub> group to the Zn<sup>2+</sup> ion in the **[Carn-H,Zn<sup>II</sup>]<sup>+</sup>** complex. **[CarnLi]<sup>+</sup>** undergoes a loss of H<sub>2</sub>O as a minor channel which seems to be the only fragmentation channel which is common to **[Carn-H,Zn<sup>II</sup>]<sup>+</sup>**.

Adducts of large alkali metal ions (Rb<sup>+</sup> and Cs<sup>+</sup>) exhibit preferentially a splitting of these ions. Sole Zn<sup>2+</sup> fragment ions do not occur – they would not be trapped either. This m/z ratio lies beyond the stability region of the quadrupolar rf-field and a stable ion trajectory after excitation is not possible for this small fragment of low m/z. Anyway, formation of a double charged fragment ion from a singly-charged ion is unlikely under CID conditions in the gas phase.

The Zn<sup>2+</sup> ion is fourfold coordinated by electron donating parts of the carnosine molecule in the gas phase [21] as well as in the liquid phase [15]. Binding motives are different, nevertheless the higher charge of the Zn<sup>2+</sup> ion with respect to singly positive charged alkali ions favors the coordination of the terminal amine group to the Zinc ion in the gas phase (cf. Fig. 8). This coordination seems to compensate the loss of a hydrogen bond between the terminal amine and the amidic NH group in the **1<sup>+</sup>-0β-Li<sup>n</sup>N<sub>h</sub>O<sub>c</sub>O<sub>a</sub>** isomer of **[CarnLi]<sup>+</sup>** (cf. Chapter IV). The deprotonation of the carboxylic group prohibits the formation of a hydrogen bond between the carboxy group and the <sup>n</sup>N atom of the histidine ring which stabilizes the **1<sup>+</sup>-αα-M<sup>n</sup>N<sub>h</sub>O<sub>c</sub>O<sub>a</sub>** (M=Li, Na, K, Rb, Cs) isomers of carnosine-alkali complexes. This binding motive does not occur for the **[Carn-H,Zn<sup>II</sup>]<sup>+</sup>** complex.

The deprotonation of the carboxylic group of the carnosine molecule to form a singly-charged **[Carn-H,Zn<sup>II</sup>]<sup>+</sup>** complex makes it hard to clearly assign a charge solvated (CS) or salt bridge (SB) binding motive. Both motives can occur for doubly-charged alkali ions [40] and are also dependent on the chain length of the dipeptide [41]. The fourfold coordination of the Zn<sup>2+</sup> ion in the energetic minimum conformation **1<sup>+</sup>-ββ-Zn<sup>n</sup>N<sub>h</sub>O<sub>c</sub>O<sub>a</sub>N<sub>at</sub>** tends towards a CS motive while the deprotonation of the carboxylic group with an ion bound to the terminal amine can be interpreted in terms of a SB motive.

Structures of CID fragments are sometimes hard to assign due to proton shifts and reorganization processes within the energized parent molecular ion. The most challenging pathway is the mass loss of 18 m/z which can only be assigned under the assumption that a water molecule is formed. We calculated several possible ionic fragments and determined possible pathways and their relative energies. This method does not provide data on activation barriers. Therefore it does not provide for probabilities and branching ratios on competing fragment channels. However, this comparison is a useful starting point for further assignments of neutral losses. The  $1^+(-\text{H}_2\text{O})-\alpha\alpha\text{-Zn}^{\text{II}}\text{N}_h\text{O}_a\text{N}_{\text{at}}$  isomer is the most stable fragment structure (after the loss of  $\text{H}_2\text{O}$ , cf. Fig. 11) found in this study. The loss of a water molecule e.g. requires proton shifts from the backbone of the dipeptide to an oxygen atom of the carboxy group.

Our calculation of the loss of water from the  $[\text{Carn-H,Zn}^{\text{II}}]^+$  complex reveals a relatively high value for the dissociation enthalpy of at least  $\Delta_{\text{diss}}H$  265 kJ/mol. This value implies a multiple-photon absorption process. Taking the heat capacity of the molecule as a stored amount of energy useable for fragmentation into account, thus IR-MPD requires an absorption of at least 5 photons of  $3485\text{ cm}^{-1}$  (in the NH stretch region) in this case.

At least 8 vibrational bands can be seen in the 1- and 2-color IR-MPD spectra (cf. Fig. 7). Their comparison with calculated spectra exhibits a fair agreement with structure **a**) (cf. Fig. 8 and 9). All DFT predicted IR absorption bands may correlate to some experimental IR-MPD peak in the region above  $2500\text{ cm}^{-1}$ ,  $\text{C}^{\text{His}}\text{H}$  stretch motions exempt because of a gap in the experimental 2-color IR-MPD spectrum. The less strongly absorbing  $\text{N}_a\text{H}$  mode ( $3485\text{ cm}^{-1}$ ) exhibits a higher fragmentation efficiency in the experimental IR-MPD spectra than the stronger absorbing  $\text{N}^{\text{H}}$  mode ( $3545\text{ cm}^{-1}$ ). The energy deposited in  $\text{N}^{\text{H}}$  vibrations has to be redistributed through the molecule in order to energize some remote fragmentation channel. The  $\text{N}_a\text{H}$  group is often in direct neighborhood of the molecule's fragmentation sites. Nevertheless, these two bands exhibit similar fragment patterns (cf. Table 4). IR-MPD at  $3359$  and  $3306\text{ cm}^{-1}$  ( $\text{N}_{\text{at}}\text{H}_2$   $v_{\text{as}} + v_{\text{ss}}$ ) leads to a considerable increase of  $\text{H}_2\text{O}$  loss (fragment mass range 271-277 m/z) and fragment masses of 243 – 250 m/z drop significantly. Irradiation at  $1900\text{ cm}^{-1}$  ( $\text{OC=O}$   $v_s$ ) leads to a similar fragmentation pattern as at  $3545$  and  $3485\text{ cm}^{-1}$ . The band at  $1900\text{ cm}^{-1}$  yields a low fragmentation efficiency, although it should be the strongest absorber (due to calculations). Seemingly, the  $\text{C=O}$  stretch motion of the  $\text{Zn}^{2+}$  bound  $\text{CO}_2$  group does not energy effectively in other vibrational modes of the molecule. The band at  $1667\text{ cm}^{-1}$ , a superposition of several bending motions reveals a fragment pattern of its own. The loss of  $\text{H}_2\text{O}$  diminishes while there is a strong increase in the intensity of ions in the mass ranges of 260 – 269

and 243 – 250 m/z. Bending motions of groups within the backbone of the dipeptide seem to split the backbone preferentially and at the expense of otherwise likely proton shifts.

Non negligible discrepancies amongst measured and calculated spectra of **[Carn-H,Zn<sup>II</sup>]<sup>+</sup>** (cf. Fig. 9) may arise through the conceptual limitations in the harmonic normal mode approximation that is paramount to the vibrational analysis of the calculated force constants. The central position of the Zn<sup>2+</sup> within the carnosine complexes may have a strong influence on the bond strengths and the electronic environment of the N<sub>a</sub>H, N<sub>at</sub>H<sub>2</sub>, C<sub>a</sub>O and C<sub>c</sub>O<sub>2</sub><sup>-</sup> groups. Variation of the DFT functional has a small influence on the relative positions of the calculated normal modes.

We observed a small but reproducible enhancement of the fragmentation efficiency when applying a second resonant IR pulse for several combinations of bands (cf. Fig. 12, 13, 14 and 15). Probing the bands at 3545 and 3485 cm<sup>-1</sup> gives little rise of the signal strength for the N<sub>at</sub>H<sub>2</sub> stretching motions at 3359 and 3306 cm<sup>-1</sup> and vice versa. The higher amount of stored energy, compared to a one color irradiation, allows for a reduction of the number of photons provided from one laser. Therefore, pre-excited molecules can also be brought to fragmentation with the second laser. This cooperative effect leads to a lower number of photons of the pump color needed for fragmentation (cf. Table 5). Application of a second pulse reduces the average number of photons, estimated as the slope of the log/log plots. This effect is strongest when pumping vibrational modes in the fingerprint region.

Systematic uncertainties prevail in the determination of the photon number per IR-MPD event. If a part of the ions is not irradiated, a two state reactivity would have to be assumed for evaluation of the fragmentation kinetics. One part of the ions would need to be treated as unreactive isomers, which do not undergo an activation process (which would lead to a fragmentation), the other part as reactive isomers, which can undergo a fragmentation after the absorption of one or multiple photons. Therefore, the fragmentation efficiencies for irradiated ions may be systematically underestimated. In order to estimate the percentage of irradiated ions, an increase of photon flux would be needed until the slope within the log(IR-MPD)/log(energy) correlation would vanish. We anticipate, however, that the evaluated photon numbers are qualitatively correct.

Nevertheless, a distinct change in the slopes within the log(IR-MPD)/log(energy) correlation can be seen. Asymmetric and symmetric stretch motions of the terminal N<sub>at</sub>H<sub>2</sub> group as well as absorptions in the *fingerprint* region need to absorb less photons of the pump laser within the 2-color scheme. This effect is quite distinct for the *fingerprint* region.



Using a pump/probe laser scheme, in which the pump laser irradiates the ions ahead of the probe laser, corresponding IR-MPD bands do not broaden (cf. Fig. 16, bottom). Reverse temporal order does lead to a broadening of bands. Then, the probe laser causes a pre-heating of the ionic molecules. Therefore, the “blue side” of a band remains in position and slope while the “red side” is broadened and flattened (cf. Fig. 16, top).

## V-6: Conclusions

The binding motive of the **[Carn-H,Zn<sup>II</sup>]<sup>+</sup>** complex is related to a charge solvated binding motive of the carnosine alkali metal adducts with a fourfold complexation of the Zn<sup>2+</sup> ion. The **[Carn-H,Zn<sup>II</sup>]<sup>+</sup>** complex exhibits different fragmentation pathways under CID and IR-MPD than protonated carnosine and alkalinized carnosine complexes. Fair comparison of 1- and 2-color IR-MPD spectra to DFT predicted IR absorption bands provides evidence for a single isomer within the gas phase. An appropriate timing sequence of pump and probe lasers leads to an enhancement of fragmentation efficiency without thermal broadening. The complexation of the doubly charged cationic transition metal Zn<sup>2+</sup> by deprotonated carnosine leads to crucial conformational changes as compared to the alkali metal complexes studied in chapter III & IV. Former DFT calculations on the gas phase structure of **[Carn-H,Zn<sup>II</sup>]<sup>+</sup>** are compared to IR-MPD spectra. IR-MPD spectra exhibit several of the DFT predicted IR absorptions while the overall agreement in the position of bands is fair and satisfactory in part. The **[Carn-H,Zn<sup>II</sup>]<sup>+</sup>** complex is furthermore utilized in order to study the mode dependent enhancement of fragmentation efficiency by application of a resonant 2-color IR-MPD pump/probe scheme. Appropriately evaluated photon flux dependencies suffice to determine the number of photons that it takes to fragment the complex. It shows that the number of photons of the pump laser needed for fragmentation is reduced by the use of a second IR color. A reverse delay between pump and probe laser pulses broadens and shifts the IR-MPD bands by a probe laser pre-heating of the complex. This seizes when the probe laser is applied simultaneously or after the pump laser. CID and IR-MPD fragmentation channels differ in their relative abundance. Relative abundances of fragments are specific to the excited vibrational motions. This study provides essential first approaches on the mechanism of resonant 2-color IR-MPD spectroscopy.

**V-7: References**

1. Kohen, R., et al., *Antioxidant Activity Of Carnosine, Homocarnosine, And Anserine Present In Muscle And Brain*. Proceedings of the National Academy of Sciences of the United States of America, 1988. **85**(9): p. 3175-3179.
2. Gulewitsch, W. and S. Amiradzibi, *Carnosine, a new organic base of meat extracts*. Berichte Der Deutschen Chemischen Gesellschaft, 1900. **33**: p. 1902-1903.
3. Baran, E.J., *Metal complexes of carnosine*. Biochemistry-Moscow, 2000. **65**(7): p. 789-797.
4. Rinderknecht, H., V. Ma, and T. Rebane, *Synthesis Of Carnosine, Anserine and Isoanserine*. Journal of Organic Chemistry, 1964. **29**(7): p. 1968-&.
5. Lenz, G.R. and A.E. Martell, *Metal Complexes Of Carnosine*. Biochemistry, 1964. **3**(6): p. 750-&.
6. Crush, K.G., *Carnosine and Related Substances in Animal Tissues*. Comparative Biochemistry and Physiology, 1970. **34**(1): p. 3-&.
7. Yoshikawa, T., et al., *The Antioxidant Properties Of A Novel Zinc-Carnosine Chelate Compound, N-(3-Aminopropionyl)-L-Histidinato Zinc*. Biochimica Et Biophysica Acta, 1991. **1115**(1): p. 15-22.
8. Cho, C.H., *Protective Effects Of Zinc L-Carnosine (Z-103) On Reserpine-Induced Gastric-Ulceration In Rats*. Drug Development Research, 1992. **27**(1): p. 61-65.
9. Furuta, S., et al., *Residence Time Of Polaprezinc (Zinc L-Carnosine Complex) In The Rat Stomach And Adhesiveness To Ulcerous Sites*. Japanese Journal of Pharmacology, 1995. **67**(4): p. 271-278.
10. Hipkiss, A.R., *Carnosine, a protective, anti-ageing peptide?* International Journal of Biochemistry & Cell Biology, 1998. **30**(8): p. 863-868.
11. Torreggiani, A., G. Fini, and G. Bottura, *Effect of transition metal binding on the tautomeric equilibrium of the carnosine imidazolic ring*. Journal of Molecular Structure, 2001. **565**: p. 341-346.
12. Mineo, P., et al., *Electrospray mass spectrometric studies of L-carnosine (beta-alanyl-L-histidine) complexes with copper(H) or zinc ions in aqueous solution*. Rapid Communications in Mass Spectrometry, 2002. **16**(7): p. 722-729.
13. Diez, R.P. and E.J. Baran, *A density functional study of some physical properties of carnosine (N-beta-alanyl-L-histidine)*. Journal of Molecular Structure-Theochem, 2003. **621**(3): p. 245-251.
14. Klyuev, S.A., *Carnosine conformers*. Biophysics, 2006. **51**(4): p. 599-602602.
15. Wagner, C.C. and E.J. Baran, *Vibrational spectra of polaprezinc, a polymeric Zn(II) complex of carnosine*. Journal of Raman Spectroscopy, 2008. **39**(4): p. 474-477.
16. Demukhamedova, S.D., I.N. Alieva, and N.M. Godjayevev, *Spatial and electronic structure of monomeric and dimeric complexes of carnosine with zinc*. Journal of Structural Chemistry, 2010. **51**(5): p. 824-832.
17. Menges, F., C. Riehn, and G. Niedner-Schatteburg, *The Interaction of the Dipeptide Carnosine with Alkali Metal Ions Studied by Ion Trap Mass Spectrometry*. Zeitschrift Fur Physikalische Chemie-International Journal of Research in Physical Chemistry & Chemical Physics, 2011. **225**(5): p. 595-609.

18. Branham, M.L., et al., *Preparation, Spectrochemical, and Computational Analysis of L-Carnosine (2- (3-Aminopropanoyl)amino -3-(1H-imidazol-5-yl)propanoic Acid) and Its Ruthenium (II) Coordination Complexes in Aqueous Solution*. *Molecules*, 2011. **16**(12): p. 10269-10291.
19. Lucas, B., et al., *Infrared multiphoton dissociation spectroscopy of protonated N-acetyl-alanine and alanyl-histidine*. *International Journal of Mass Spectrometry*, 2005. **243**(2): p. 105-113.
20. Gregoire, G., et al., *Resonant infrared multiphoton dissociation spectroscopy of gas-phase protonated peptides. Experiments and Car-Parrinello dynamics at 300 K*. *Physical Chemistry Chemical Physics*, 2007. **9**(24): p. 3082-3097.
21. Reinhard, B.M., -, *Chemistry of microsolvated metal ions*. 2003, Kaiserslautern.
22. Nosenko, Y., et al., *Metalated Hoogsteen binding in a nucleobase pair mimic by two-color IR dissociation spectroscopy*. *Physical Chemistry Chemical Physics*, submitted.
23. Pretsch, E., P. Bühlmann, and M. Badertscher, *Structure determination of organic compounds : tables of spectral data*. 4th, rev. and enl. ed. 2009, Berlin: Springer. xv, 433 p.
24. Hohenberg, P. and W. Kohn, *Inhomogeneous Electron Gas*. *Physical Review B*, 1964. **136**(3B): p. B864-&.
25. Kohn, W. and L.J. Sham, *Self-Consistent Equations Including Exchange and Correlation Effects*. *Physical Review*, 1965. **140**(4A): p. 1133-&.
26. Parr, R.G. and W. Yang, *Density-functional theory of atoms and molecules*. International series of monographs on chemistry. 1989, New York: Clarendon Press. x, 333 p.
27. Salahub, D.R., et al., *The Challenge of d and f electrons : theory and computation*. ACS symposium series,. 1989, Washington, DC: American Chemical Society. x, 405 p.
28. Becke, A.D., *Density-Functional Exchange-Energy Approximation with Correct Asymptotic-Behavior*. *Physical Review A*, 1988. **38**(6): p. 3098-3100.
29. Lee, C.T., W.T. Yang, and R.G. Parr, *Development of the Colle-Salvetti Correlation-Energy Formula into a Functional of the Electron-Density*. *Physical Review B*, 1988. **37**(2): p. 785-789.
30. Miehlich, B., et al., *Results Obtained with the Correlation-Energy Density Functionals of Becke and Lee, Yang and Parr*. *Chemical Physics Letters*, 1989. **157**(3): p. 200-206.
31. Becke, A.D., *Density-Functional Thermochemistry .3. The Role of Exact Exchange*. *Journal of Chemical Physics*, 1993. **98**(7): p. 5648-5652.
32. Dunning, T.H., *Gaussian-Basis Sets for Use in Correlated Molecular Calculations .1. The Atoms Boron through Neon and Hydrogen*. *Journal of Chemical Physics*, 1989. **90**(2): p. 1007-1023.
33. Dolg, M., et al., *Relativistic and correlation effects for element 105 (hahnium, Ha): a comparative study of M and MO (M = Nb, Ta, Ha) using energy-adjusted ab initio pseudopotentials*. *The Journal of Physical Chemistry*, 1993. **97**(22): p. 5852-5859.
34. Frisch, M.J., et al., *Gaussian 03, Revision C.02*. 2003.
35. Frisch, M.J., et al., *Gaussian 09, Revision B.01*. 2009: Wallingford CT.
36. Hamprecht, F.A., et al., *Development and assessment of new exchange-correlation functionals*. *Journal of Chemical Physics*, 1998. **109**(15): p. 6264-6271.

37. Eichkorn, K., et al., *Auxiliary basis sets for main row atoms and transition metals and their use to approximate Coulomb potentials*. Theoretical Chemistry Accounts, 1997. **97**(1-4): p. 119-124.
38. Editor: Johnson III, R.D., *NIST Computational Chemistry Comparison and Benchmark Database* August 2011.
39. Chin, S.L., *Multiphoton Ionization of Molecules*. Physical Review A, 1971. **4**(3): p. 992.
40. Dunbar, R.C., et al., *Conformation Switching in Gas-Phase Complexes of Histidine with Alkaline Earth Ions*. Journal of Physical Chemistry B, 2009. **113**(30): p. 10403-10408.
41. Dunbar, R.C., et al., *Peptide Length, Steric Effects, and Ion Solvation Govern Zwitterion Stabilization in Barium-Chelated Di- and Tripeptides*. The Journal of Physical Chemistry B, 2009. **113**(31): p. 10552-10554.

## V-8: Supplementary material

**Table 6:** Gaussian version, DFT functional and basis sets used for calculation of the three lowest energy structures. Relative energies (in kJ/mol) of isomers **a)**, **b)** and **c)** of complex **[Carn-H,Zn<sup>II</sup>]<sup>+</sup>** (cf. Fig. 8), calculated at different levels of theory and basis sets.

Calculation number	Gaussian version	Theory level	Basis set (C,H,N,O)	Basis set (Zn)	Struct. a)	Struct. b)	Struct. c)
C1	g03	B3LYP	cc-pVDZ	Stuttgart RSC 1997 ECP	0	10	48
C2	g03	B3LYP	cc-pVTZ	Stuttgart RSC 1997 ECP	0	10	43
C3	g03	B3LYP	cc-pVTZ	Ahlrichs VTZ + Stuttgart RSC 1997 ECP	0	10	52
C4	g03	B3P86	cc-pVTZ	Stuttgart RSC 1997 ECP	0	11	48
C5	g09	B97D	cc-pVTZ	Stuttgart RSC 1997 ECP	0	11	57

**Table 7:** Selected IR-MPD vibrational frequencies (in cm<sup>-1</sup>) and corresponding values calculated for structure **1<sup>+</sup>-Zn<sup>n</sup>N<sub>h</sub>O<sub>c</sub>O<sub>a</sub>N<sub>at</sub>** of complex **[Carn-H,Zn<sup>II</sup>]<sup>+</sup>** at different levels of theory and basis sets (calculation numbers correspond to Table 6).

IR-MPD	C1	C2	C3	C4	C5	Assignment
3545	3623	3636	3637	3658	3575	N <sup>+</sup> H v <sub>s</sub>
3485	3575	3591	3592	3613	3531	N <sub>a</sub> H v <sub>s</sub>
3359	3507	3532	3532	3558	3484	N <sub>at</sub> H <sub>2</sub> v <sub>as</sub>
3306	3443	3465	3467	3488	3404	N <sub>at</sub> H <sub>2</sub> v <sub>ss</sub>
2948	3072	3071	3073	3082	2998	C <sup>aliph.</sup> H v <sub>s</sub>
1900	1805	1780	1784	1804	1726	OC=O v <sub>s</sub>
1667	1613	1626	1631	1626	1585	N <sub>at</sub> H <sub>2</sub> v <sub>b</sub>
1620	1579	1578	1580	1588	1534	N <sub>a</sub> H v <sub>b</sub>

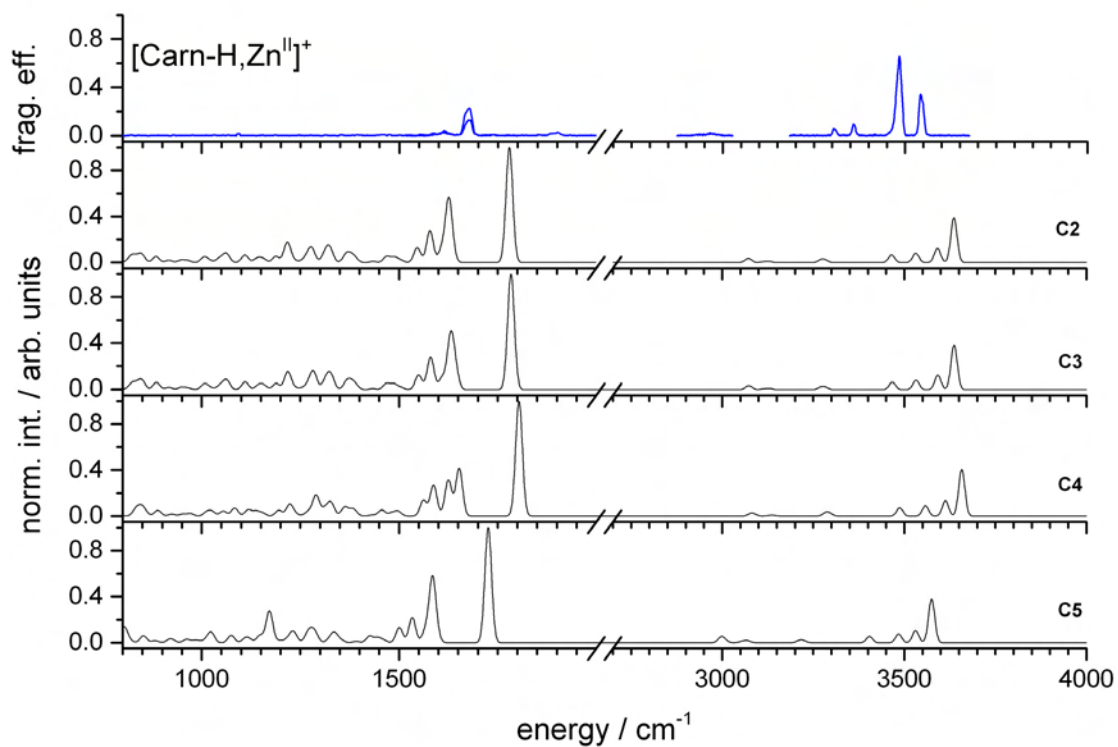


**Figure 17:** IR-MPD spectrum (top) and spectra of structure a) calculated with different combinations of theory and basis sets, cf. Table 6 for theory levels.

---

## Chapter VI: ESI-MS studies on reaction intermediates of a ruthenium-catalyzed hydroamidation of terminal alkynes

### VI: Preamble

This chapter reports on ESI-MS studies on reaction intermediates of a ruthenium-catalyzed hydroamidation of terminal alkynes within a collaborative research project with the research group of L.J. Goossen, TU Kaiserslautern. The results were published in two peer reviewed papers:

*A Practical and Effective Ruthenium Trichloride-Based Protocol for the Regio- and Stereoselective Catalytic Hydroamidation of Terminal Alkynes*

L.J. Goossen, M. Arndt, M. Blanchot, F. Rudolphi, F. Menges and G. Niedner-Schatteburg  
*Advanced Synthesis & Catalysis* (2008), 350(17), 2701

<http://dx.doi.org/10.1002/adsc.200800508>

*Mechanistic Investigation of the Ru-Catalyzed Hydroamidation of Terminal Alkynes*

M. Arndt, Kifah S. M. Salih, A. Fromm, L. J. Goossen, F. Menges and G. Niedner-Schatteburg  
*J. Am. Chem. Soc.* (2011), 133(19), 7428-7449

<http://dx.doi.org/10.1021/ja111389r>

The preparation of reaction mixtures was done by Matthias Arndt. ESI-MS measurements and the assignment of most ionic species were done by me. M. Arndt and I developed an experimental ESI-MS procedure to clarify the assignment of ionic species by isotopic labeling and the use of different alkenes. Lukas J. Goossen and Matthias Arndt mainly prepared the manuscripts. The other coworkers contributed with results from several experiments and revisions of the manuscripts.





## Chapter VII: Dysprosium-based mono-, di- and tri-metallic complexes – assignment of vibrational bands utilizing IR-MPD and H/D exchange reactions

### Keywords:

Single Molecule Magnets, Lanthanide, Dysprosium, Manganese, Nickel, ESI-MS, CID, IR-MPD, DFT, Gas Phase Reactions, H/D exchange

### VII: Preamble

We carried out an extensive ESI-MS investigation as preparatory work for this infrared multiple photon dissociation (IR-MPD) spectroscopy study in order to determine gas phase structures of isolated ionic metal organic complexes. The exploration of different fragmentation channels and the reaction behavior in gas phase hydrogen/deuterium exchange reactions enables structural assignments of the fragments and provides important spectroscopic data for further computational studies. These results were published in two joint publications within the collaborative research center “3MET” [1, 2]:

*From a Dy(III) Single Molecule Magnet (SMM) to a Ferromagnetic (Mn(II)Dy(III)Mn(II)) Trinuclear Complex*

A. Bhunia, M. Gamer, L. Ungur, L. Chibotaru, A. K. Powell, Y. Lan, P. W. Roesky, F. Menges, C. Riehn and G. Niedner-Schatteburg

Inorganic Chemistry (2012), 51(18), 9589-9597

<http://dx.doi.org/10.1021/ic300065x>

*Trinuclear nickel–lanthanide compounds*

A. Bhunia, M. Yadav, Y. Lan, A. K. Powell, F. Menges, C. Riehn, G. Niedner-Schatteburg, P. P. Jana, R. Riedel, K. Harms, S. Dehnen and P. W. Roesky

Dalton Transactions (2013), 42(7), 2445-2450

<http://dx.doi.org/10.1039/c2dt31023f>

The synthesis of the complexes was done by A. Bhunia. ESI-MS measurements and the assignment of all ionic species were done by me. A. Bhunia and P. W. Roesky mainly prepared the manuscripts. The other coworkers contributed with results from several experiments, *ab initio* calculations and revisions of the manuscripts.

This chapter is formatted as to become a manuscript for publication. It is not submitted yet. The experimental section of this chapter reports on own IR-MPD studies and hydrogen/deuterium exchange experiments in solution based on and compared with former experimental results. The manuscript was written by me.

### VII-1: Abstract

We report here on a structural study of four dysprosium based organometallic complexes. We examined three major variations of the spatial position of the incorporated transition metals. The basic complex contains one Dy<sup>3+</sup> cation and is able to incorporate up to two Mn<sup>2+</sup> cations or to attach one or two complexes of Ni<sup>2+</sup> with tris(2-aminoethyl)amine.

Attempts of utilizing DFT theory for assignment of vibrational bands failed within the geometry optimization at various theory levels. However, a combination of mass spectrometric and IR-MPD spectroscopic techniques with H/D exchange reactions in solution and in the gas phase gives insight into gas phase structures of the molecules. We assigned the most probable protonation sites within the cationic complexes.

### VII-2: Introduction

The synthesis of a [Mn<sub>12</sub>O<sub>12</sub>(OAc)<sub>16</sub>(H<sub>2</sub>O)<sub>4</sub>] complex was reported by Lis in 1980 [3] and this molecule has become the “Drosophila” in the study of Single Molecule Magnet behavior (SMM) [4]. Huge efforts have been put into the synthesis of SMMs and their characterization in order to understand their magnetic behavior and to achieve enhanced magnetic properties of new SMM molecules [5, 6].

The combination of high spin state transition metals (3d ions) with highly anisotropic lanthanide atoms (4f ions) can lead to single molecular magnetic behavior [7]. Especially the use of the Dy<sup>3+</sup> ion has attracted great interest, besides other lanthanide ions [8-11]. However, the overall symmetry imposed by the molecular binding motives can, in fact, play a key role in governing this effect. The cooperativity of the metal centers depends crucially on their spatial arrangement. The four

dysprosium based organometallic complexes within this study were synthesized in order to form Single Molecule Magnets. The SMM behavior relates strongly to the chemical environment of the incorporated metal ions.

For all studied molecules two deprotonated 2,2'-{[(2-aminoethyl)imino]bis[2,1-ethanediylnitriloethylidyne]}bis-2-hydroxybenzoic acids (furtheron named *salen*, or *salen-type*) are used as ligands for a central Dy<sup>3+</sup> ion. Each ligand incorporates two carboxy, two hydroxy, two imine and one terminal amine group. The presence of many electron donating groups allows for different binding motives of additional electrophilic species, such as e.g. 3d elements like Mn<sup>2+</sup> and Ni<sup>2+</sup>. Deprotonation of the hydroxy groups of the [Dy(C<sub>22</sub>H<sub>24</sub>N<sub>4</sub>O<sub>6</sub>)<sub>2</sub>H] complex (**1**, cf. Fig. 1) allows for the incorporation of two Mn<sup>2+</sup> ions adjacent to the Dy<sup>3+</sup> ion in order to form the [Dy(MnC<sub>22</sub>H<sub>22</sub>N<sub>4</sub>O<sub>6</sub>)<sub>2</sub>H] complex (**2**, cf. Fig. 1). Complexes **1** and **2** can undergo a deprotonation or a protonation under ESI-MS conditions in order to form anionic complexes **1**<sup>-</sup> and **2**<sup>-</sup> (cf. Fig. 1 for schematic drawings) or cationic complexes **1**<sup>+</sup> and **2**<sup>+</sup>. The addition of [Ni(NO<sub>3</sub>)<sub>2</sub>(H<sub>2</sub>O)<sub>6</sub>] and *tren* (*tren* = tris(2-aminoethyl) amine) to a solution of *salen* and [Dy(NO<sub>3</sub>)<sub>3</sub>(H<sub>2</sub>O)<sub>m</sub>] leads to complex **4** [2]. This complex can be observed as a doubly-charged positive ion with one nitrate counterion under ESI-MS conditions forming complex **4**<sup>2+</sup> (cf. Fig. 2 for schematic drawings). Mass spectra of solutions of **4** also exhibited protonated, doubly-charged complexes with a single [Ni(*tren*)]<sup>2+</sup> group (**3**<sup>2+</sup>).

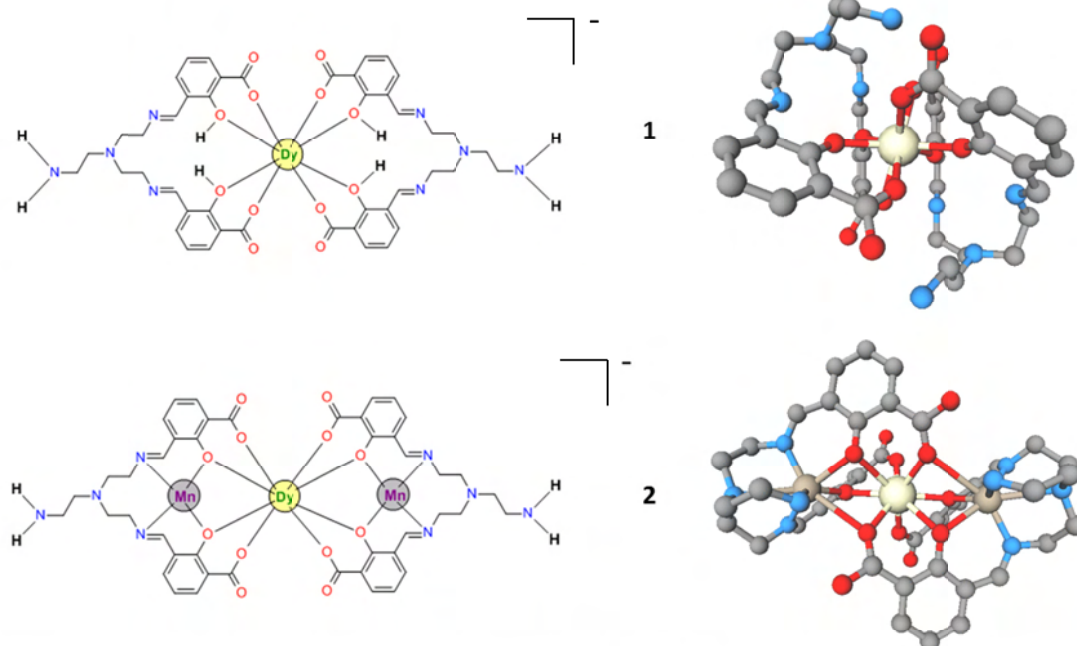


**Figure 1:** Schematic drawings (left) and crystal structures derived by X-ray diffraction measurements (right, counterions and hydrogen atoms omitted for clarity, taken from [1]) of complexes **1** and **2**. Charge states of the molecules within the drawings due to the shown composition.

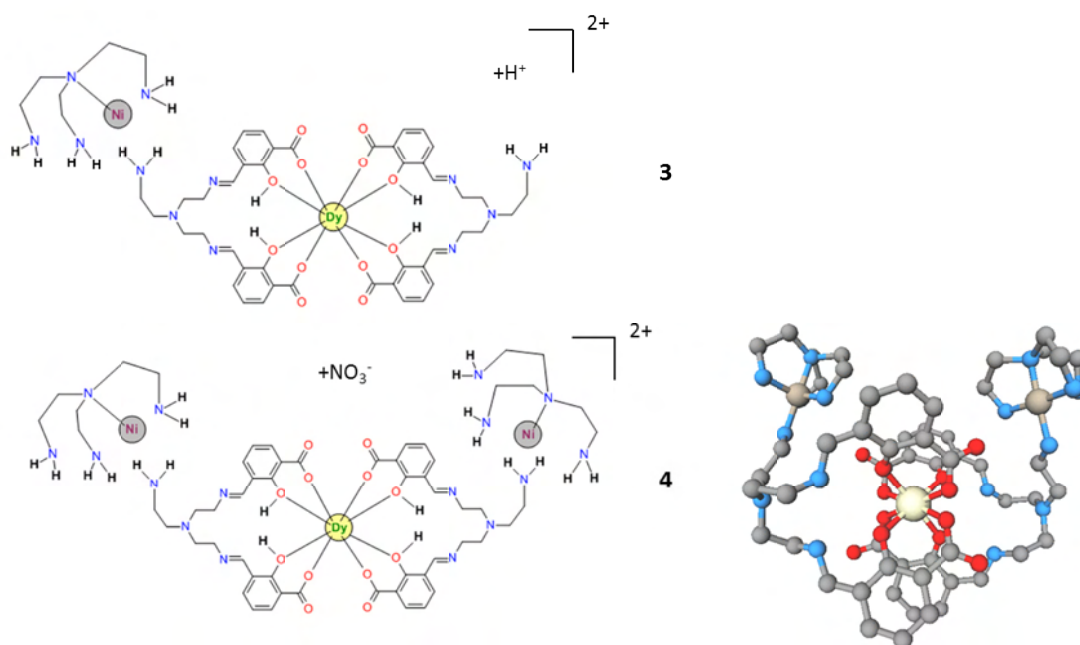


**Figure 2:** Schematic drawings (left) of **3** and **4** and crystal structures derived by X-ray diffraction measurements (right, counterions and hydrogen atoms are omitted for clarity, taken from [2]) of complex **4**. Charge states of the molecules within the drawings due to the shown composition.

We utilized IR-MPD spectroscopy on the deprotonated and protonated dysprosium based organometallic molecules **1-4**, and hydrogen/deuterium exchange in solution, in order to assign vibrational bands and the protonation sites of the four complexes (cf. Fig. 1 and 2, cf. [1, 2] for synthesis and mass spectrometric characterization of the molecules). This study provides useful spectroscopic data for further *ab initio* calculations of the molecules properties.

## VII-3: Methods

### VII-3.1: ESI-MS and CID

Electrospray ionization mass spectrometry (ESI MS) was performed on a Bruker Esquire 3000plus ion trap instrument in positive and negative ionization mode. Scan speed was 13000 m/z / s in standard resolution scan mode (0.3 FWHM / m/z) with a scan range of 15 to 2800 m/z. All spectra were accumulated for at least two minutes. Sample solutions in acetonitrile at concentrations of  $1 \times 10^{-4}$  mol/L were continuously infused into the ESI chamber at a flow rate of 2  $\mu$ L/min using a syringe pump. Nitrogen was used as drying gas at a flow rate of 3.0 L/min at 300 °C. The solutions were sprayed at a nebulizer pressure of 4 psi and the electrospray needle was typically held at 4.5 kV. The instrument was controlled by the Bruker Esquire Control 5.3 software and data analysis was performed using the Bruker Data Analysis 3.4 software.

### VII-3.2: Gas Phase reactions

H/D exchange with ND<sub>3</sub> as reaction gas was performed under single collision conditions in an Fourier-transform ion cyclotron resonance mass spectrometer (FT-ICR-MS, Bruker Apex III, equipped with a 7.0-T magnet and an APOLLO I electrospray ion source). The background pressure was held at approx.  $1.0 \times 10^{-8}$  mbar. Sample solutions in acetonitrile at concentrations of about  $1 \times 10^{-4}$  M were continuously infused into the ESI chamber at a flow rate of 2  $\mu$ L/min using a syringe pump. Nitrogen was used as drying gas with flow rate of 10.0 L/min at approx. 300 °C. The solutions were sprayed at a nebulizer pressure of 25 psi and the electrospray needle was typically held at 4.0 kV. Transfer parameters to the Penning trap of the mass spectrometer were held constant.

### VII-3.3: IR-MPD

IR-MPD measurements were performed with a modified Bruker amaZonSL ion trap mass spectrometer. Two KTP/KTA optical parametric oscillator/amplifier (OPO/A, LaserVision) systems, each pumped by a Q-switched 10 Hz injection seeded Nd<sup>3+</sup>:YAG laser (PL8000, Continuum),

provided tunable IR radiation ( $\delta\nu = 0.9 \text{ cm}^{-1}$  resp.  $\delta\nu = 0.3 \text{ cm}^{-1}$ ,  $\delta t = 7 \text{ ns}$ ) in order to record vibrational spectra via the multi-photon dissociation scheme. We used the OPA idler wave ( $\leq 10 \text{ mJ/pulse}$ ) of one system to record spectra by scanning from  $2800 - 3600 \text{ cm}^{-1}$  (pump laser). By choice, the second IR OPO/A served as probe laser, set to a selected and fixed vibrational resonance frequency. The probe laser beam was aligned counter-propagating with respect to the scanning pump laser beam. Probe pulses were delayed by  $100 \text{ ns}$  with respect to the scanning pump pulses (delay generator DG645, SRS). Each trapped and  $m/z$  isolated ion package was irradiated by 2-4 laser pulses (or pulse pairs in case of 2-color experiments) to produce sufficient fragment ions. IR spectra were recorded using the Bruker chromatogram software for extracting the intensity of parent and fragment ions (three point averaging directly by BrukerTrapControl software). The Origin software package was used to apply a five point adjacent averaging for smoothing. IR frequencies were calibrated by a wave meter (821B-NIR, Bristol instruments). A laser power curve was recorded in parallel to the IR-MPD spectra through digitizing the analog output of the laser power meter by an auxiliary ADC input of the amaZonSL mass spectrometer electronics.

## VII-4: Results and Discussion

### VII-4.1: H/D isotope exchange in solution

We used hydrogen/deuterium exchange (HDX) reactions in solution in order to estimate the number of exchangeable protons and to compare those numbers to HDX reactions in the gas phase. We analyzed solutions of **1**, **2**, **3** and **4** in acetonitrile/D<sub>2</sub>O (9:1) mixtures using ESI-MS and estimated the number of exchanged protons by the  $m/z$  shift of the isotopic pattern of protonated and deuterated species (cf. Table 2).

The cationic complex **1**<sup>+</sup> undergoes ten hydrogen/proton exchange reactions in solution, while the mass spectrum of the anionic complex **1**<sup>-</sup> exhibits an overlay of four, five and six times H/D exchanged complexes. The number of H/D exchanges of the cationic complex is consistent with the number of labile protons of the amine and hydroxy groups of the salen-type ligand. The incorporation of two Mn<sup>2+</sup> ions into complex **1** reduces as expected the number of exchangeable protons by a number of four. This results in six exchangeable protons for the cationic complex **2**<sup>+</sup> and four for the anionic complex **2**<sup>-</sup>. The trimetallic complex **2**<sup>-</sup> undergoes a complete exchange of all four protons in contrast to the monometallic species **1**. This indicates different HDX rates of the four aminic protons and the four hydroxylic protons while the negatively charged ions. Deprotonated hydroxy groups chelate the two Mn<sup>2+</sup> ions as can be seen within the crystal structure

of complex **2** (cf. Fig. 4). Therefore all four remaining labile protons in complex **2<sup>-</sup>** originate from amine groups. We assume a preference for the exchange of aminic protons in complex **1<sup>-</sup>**, in parallel to the complete exchange of all four aminic protons of the anionic complex **2<sup>-</sup>**.

**Table 2:** Composition of positive and negative species **1-4** before and after H/D exchange with D<sub>2</sub>O in an acetonitrile solution. Protons and deuterons are emphasized within the sum formular. Number of exchangeable protons is given in parenthesis (in column “nr. of exch.”)

reactant cations	product cations	number of H/D exchanges
<b>1<sup>+</sup></b> [Dy(C <sub>22</sub> H <sub>25</sub> N <sub>4</sub> O <sub>6</sub> ) <sub>2</sub> ] <sup>+</sup>	<b>1<sup>+</sup>-d<sub>x</sub></b> [Dy(C <sub>22</sub> H <sub>20</sub> D <sub>5</sub> N <sub>4</sub> O <sub>6</sub> ) <sub>2</sub> ] <sup>+</sup>	10 (10)
<b>2<sup>+</sup></b> [Dy(MnC <sub>22</sub> H <sub>23</sub> N <sub>4</sub> O <sub>6</sub> ) <sub>2</sub> ] <sup>+</sup>	<b>2<sup>+</sup>-d<sub>x</sub></b> [Dy(MnC <sub>22</sub> H <sub>20</sub> D <sub>3</sub> N <sub>4</sub> O <sub>6</sub> ) <sub>2</sub> ] <sup>+</sup>	6 (6)
<b>3<sup>+</sup></b> [Dy(C <sub>22</sub> H <sub>24</sub> N <sub>4</sub> O <sub>6</sub> ) <sub>2</sub> (Ni(C <sub>6</sub> H <sub>18</sub> N <sub>4</sub> )) <sub>1</sub> H] <sup>2+</sup>	<b>3<sup>+</sup>-d<sub>x</sub></b> [Dy(C <sub>22</sub> H <sub>20</sub> D <sub>4</sub> N <sub>4</sub> O <sub>6</sub> ) <sub>2</sub> (Ni(C <sub>6</sub> H <sub>12</sub> D <sub>6</sub> N <sub>4</sub> )) <sub>1</sub> D] <sup>2+</sup>	15 (15)
<b>4<sup>+</sup></b> [Dy(C <sub>22</sub> H <sub>24</sub> N <sub>4</sub> O <sub>6</sub> ) <sub>2</sub> (Ni(C <sub>6</sub> H <sub>18</sub> N <sub>4</sub> )) <sub>2</sub> (NO <sub>3</sub> ) <sub>2</sub> ] <sup>2+</sup>		decomp.
reactant anions	product anions	number of H/D exchanges
<b>1<sup>-</sup></b> [Dy(C <sub>22</sub> H <sub>24</sub> N <sub>4</sub> O <sub>6</sub> ) <sub>2</sub> ] <sup>-</sup>	<b>1<sup>-</sup>-d<sub>x</sub></b> [Dy(C <sub>22</sub> H <sub>21-22</sub> D <sub>2-3</sub> N <sub>4</sub> O <sub>6</sub> ) <sub>2</sub> ] <sup>-</sup>	4 – 6 (8)
<b>2<sup>-</sup></b> [Dy(MnC <sub>22</sub> H <sub>22</sub> N <sub>4</sub> O <sub>6</sub> ) <sub>2</sub> ] <sup>-</sup>	<b>2<sup>-</sup>-d<sub>x</sub></b> [Dy(MnC <sub>22</sub> H <sub>20</sub> D <sub>2</sub> N <sub>4</sub> O <sub>6</sub> ) <sub>2</sub> ] <sup>-</sup>	4 (4)
<b>3<sup>-</sup></b> not observed	<b>3<sup>-</sup>-d<sub>x</sub></b> not observed	
<b>4<sup>-</sup></b> not observed		

The cationic complex **3<sup>+</sup>** exhibits a replacement of 15 labile protons which is consistent with eight protons of the salen-type ligand plus six amino protons of the *tren* ligand and one extra proton out of solution. We did not observe the deprotonated species of complexes **3** and **4** under ESI-MS conditions. The addition of D<sub>2</sub>O leads furthermore to a decomposition of complex **4** resulting in the loss of the two [Ni(*tren*)]<sup>2+</sup> complexes to form **1<sup>-</sup>** or **1<sup>+</sup>**.

These HDX results show the ability of the cationic complexes **1<sup>+</sup>**, **2<sup>+</sup>** and **3<sup>+</sup>** to exchange all labile protons in solution. Furthermore a preferred replacement of aminic protons can be assumed. The cationic complex **2<sup>+</sup>** undergoes only two H/D exchange reactions with ND<sub>3</sub> in the gas phase while it

exchanges all six protons in solution. Under the assumption, that all aminic protons are equivalent and exhibit the same exchange rate constants, the two additional protons attached to  $2^-$  to form  $2^+$  can not be located at the amine groups of the complex. The most probable positions are either the hydroxylic or carboxylic groups of the complex. The exchange of the four aminic protons of  $2^+$  in the gas phase seems to be inhibited by the chelation of the  $Mn^{2+}$  ions by the aminic nitrogen atoms (cf. Fig. 1 and [1]).

## VII-4.2: IR-MPD spectra

### VII-4.2.1: Results for $1^+$

We measured IR-MPD spectra in order to elucidate the structure of the cationic complex in the gas phase. The 1-color IR-MPD spectrum of  $1^+$  reveals two intense bands at 2970 and 2874  $cm^{-1}$  in the OH, NH and CH stretch region and one at 1650  $cm^{-1}$  in the CO stretch region (cf. Fig. 3). The band at 2874  $cm^{-1}$  may correspond to CH stretching modes. The photon energy absorbed by these vibrational modes may therefore be more or less equally distributed within the whole complex. Using a 2-color scheme with a probe laser at 2874  $cm^{-1}$  increases all bands of the 1-color spectrum. Two additional new bands arise at 2600 to 2700  $cm^{-1}$  and at 1400 to 1500  $cm^{-1}$ .

No clear assignment of the bands in the OH, NH and CH stretch region is possible due to their broadness and overlap. We used H/D exchange in solution to facilitate a discrimination between OH/NH bands and those of CH. OH and NH bands bear labile, exchangeable protons which vibrational frequencies will shift to lower frequencies after exchange due to their higher reduced masses. This may result in additional gaps in the spectrum and a rise of new bands.

Comparing IR-MPD spectra of the protonated and H/D exchanged cationic and anionic complexes of **1** exhibits a clear reduction of bands in several regions of the spectrum (cf. Fig. 4). The cationic complex  $1^+$  exhibits an exchange of ten protons with deuterium. This results in only two remaining bands at 2850 – 2900  $cm^{-1}$  and at 3000  $cm^{-1}$  within the 1-color IR-MPD spectrum. These remaining bands correspond to aromatic and aliphatic CH stretching modes. Therefore, the bands in the IR-MPD spectrum of  $1^+$  in the region between 3000 and 3300  $cm^{-1}$  and around 2950  $cm^{-1}$  correspond to hydrogen bridged OH and to NH stretching modes.



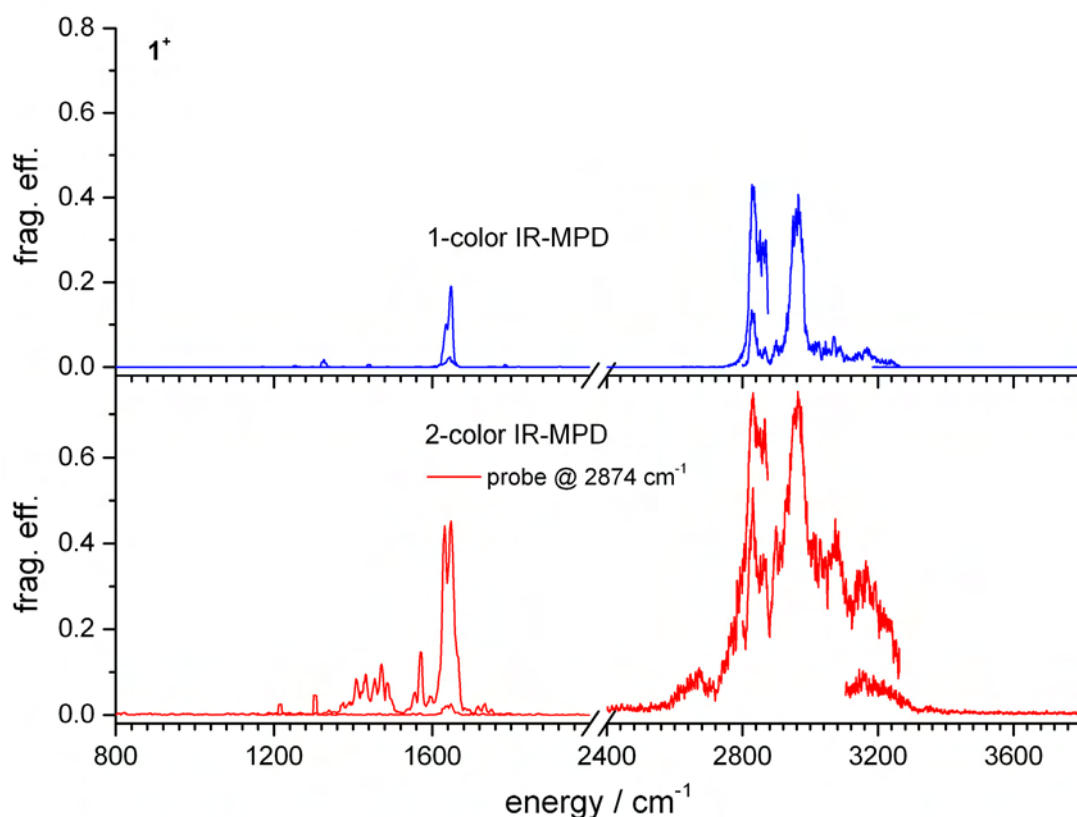


**Figure 3:** 1- and 2-color IR-MPD spectra of  $\mathbf{1}^+$ . Superimposed regions were measured with various photon fluxes.

The anionic complex  $\mathbf{1}^-$  undergoes only an exchange of four from up to eight labile protons. Only one band centered at  $2900\text{ cm}^{-1}$  disappears widely while there are small changes in the shape of the remaining bands.

We assume that the exchanged protons in complex  $\mathbf{1}^-$  originate from its amine groups. Due to the decrease of intensity for the band at  $2900\text{ cm}^{-1}$ , we assign this bands to hydrogen bound  $\text{NH}_2$  stretching modes. Those bands are strongly redshifted with respect to free  $\text{NH}_2$  stretching modes, which would occur around  $3300\text{ cm}^{-1}$ . No clear distinction between the symmetric and asymmetric  $\text{NH}_2$  stretching modes can be drawn from spectral data. The band at  $3080\text{ cm}^{-1}$  of  $\mathbf{1}^-$  and  $\mathbf{1}^- \mathbf{-d}_4$  can not be seen in the spectrum of cationic  $\mathbf{1}^+ \mathbf{-d}_{10}$ . We assume that this band corresponds to the OH stretching mode of the hydroxylic groups of the anionic complex  $\mathbf{1}^- \mathbf{-d}_4$ , which did not undergo a H/D exchange as discussed before. The IR-MPD spectrum of  $\mathbf{1}^+$  exhibits two bands at  $3080$  and  $3180\text{ cm}^{-1}$ . We identify the band at  $3080\text{ cm}^{-1}$  as the OH stretching mode of the hydroxylic groups, due to the (slightly shifted) frequency of these groups within the anionic complex  $\mathbf{1}^-$ . Two possible binding sites remain for the two additional protons (to form complex  $\mathbf{1}^+$  out of complex  $\mathbf{1}^-$ ), either

the amine or the carboxylic groups of the two ligands. No clear assignment of the positions of the additional protons can be concluded so far.

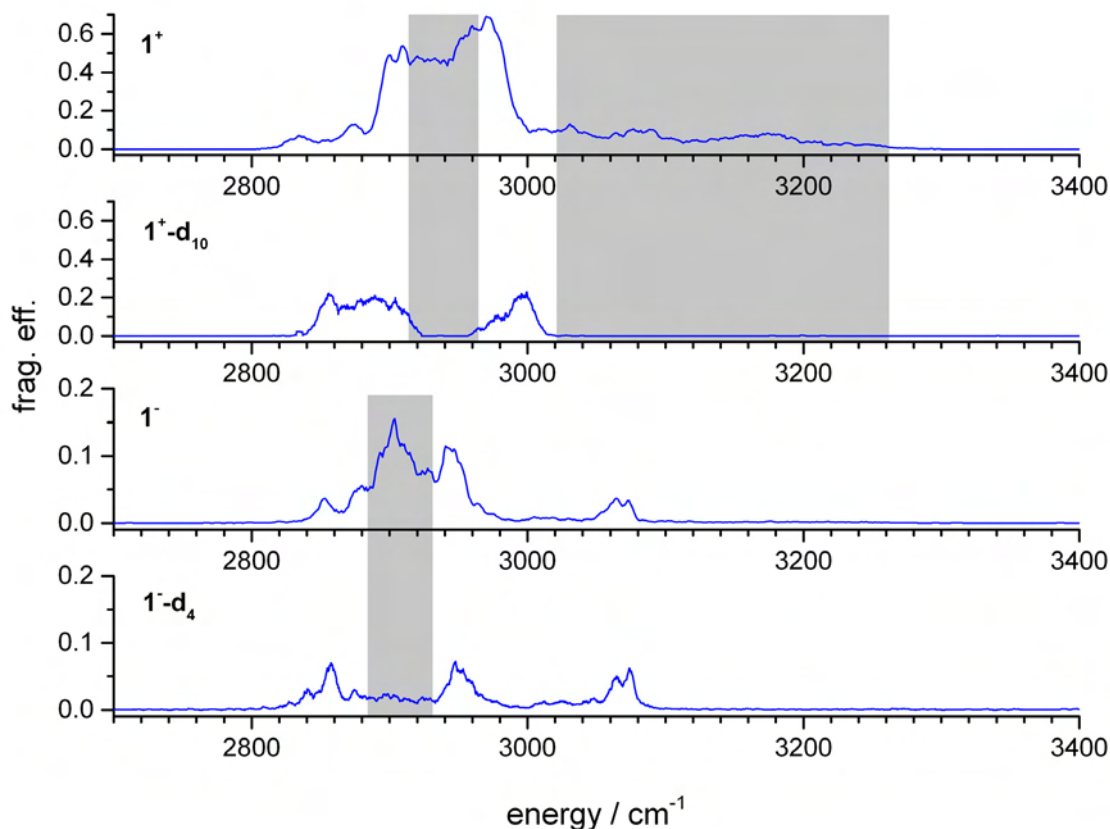
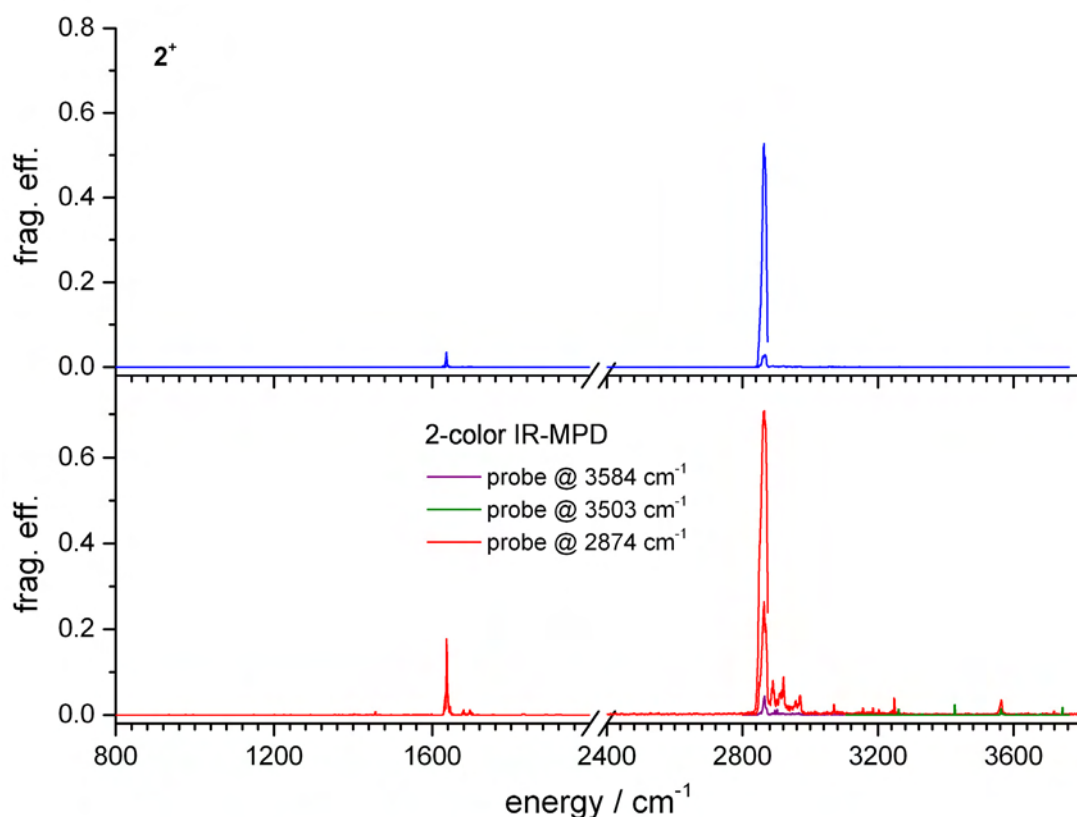


**Figure 4:** 1-color IR-MPD spectra of  $1^+$  a),  $1^+-d_{10}$  b),  $1^-$  c) and  $1^--d_4$  d). Grey regions highlight the decrease of fragmentation efficiency due to spectral shifts of deuterated groups.

#### VII-4.2.2: Results for $2^+$

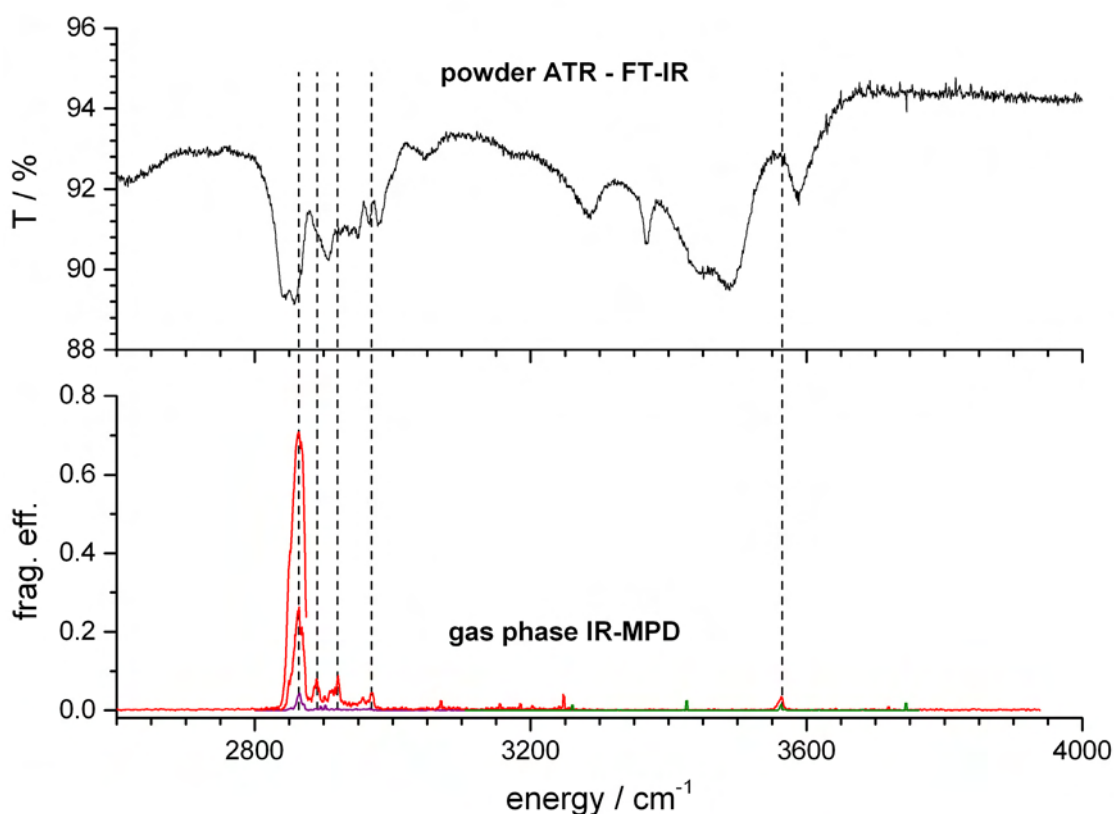
The 1-color IR-MPD spectrum of  $2^+$  exhibits one intense bands at  $2860\text{ cm}^{-1}$  in the CH stretch region and one minor at  $1650\text{ cm}^{-1}$  in the CO stretch region (cf. Fig. 5) due to increment assessment. Using a 2-color scheme with a probe laser at  $2874\text{ cm}^{-1}$  increases the band itself and all bands of the 1-color spectrum.

Additional sharp minor bands can be seen at 2890, 2920, 2970 and at  $3584\text{ cm}^{-1}$ . Irradiation with the probe laser fixed at  $3584\text{ cm}^{-1}$  results in no further enhancement of these bands (data not shown). The band at  $2860\text{ cm}^{-1}$  corresponds to absorptions of the aliphatic CH groups, which occurs at the same position in the IR-MPD spectrum of complex  $1^+$ . The minor bands in the 2-color IR-MPD spectrum of  $2^+$  may correspond to the stretching modes of aromatic CH groups.



**Figure 5:** 1- and 2-color IR-MPD spectra of  $2^+$ . Superimposed regions were measured with various photon fluxes.

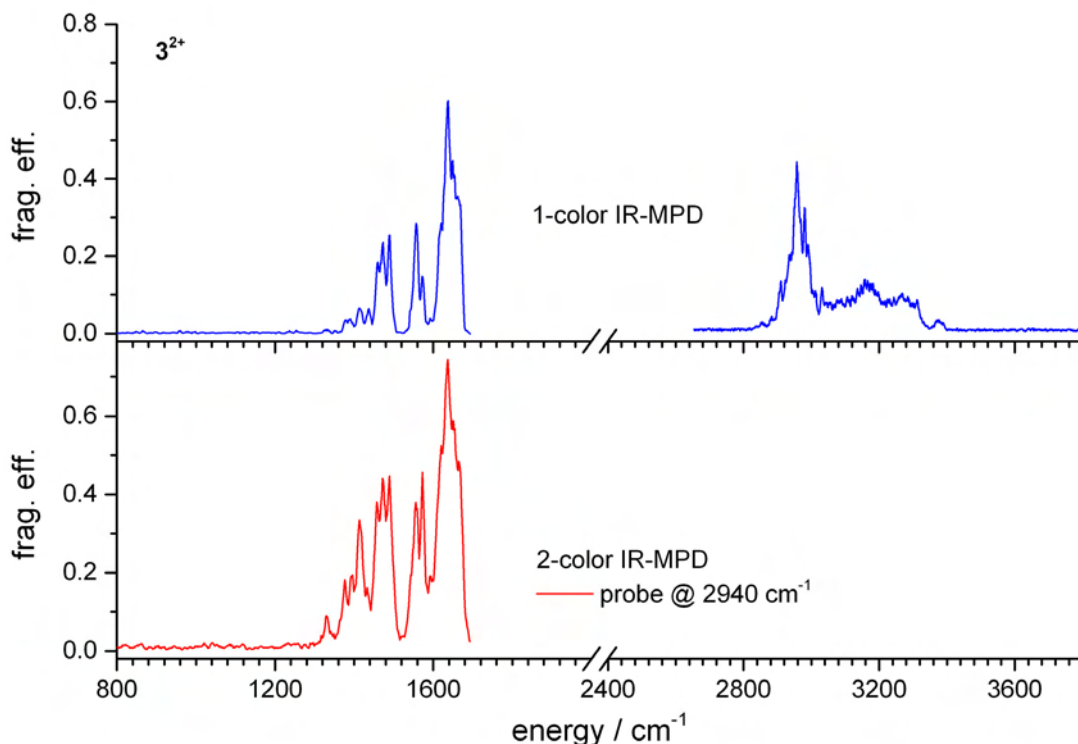
The crystal structure of complex **2** (cf. Fig. 4) reveals a close proximity of the terminal amine groups with the two  $\text{Mn}^{2+}$  ions [1]. Therefore, the aminic nitrogen atom can therefore not bind additional protons. An ineffective IVR process may cause dark bands for those groups due to the complexation of the  $\text{Mn}^{2+}$  ions. This effect may be explained by a heavy atom effect, which means that the energy transport from  $\text{NH}_2$  stretching modes to low lying vibrational motions of the  $\text{Mn}^{2+}$  ions and their ligands is hindered. We assign the minor band at  $3584\text{ cm}^{-1}$  in the 2-color IR-MPD spectrum of  $2^+$  (cf. Fig. 5) to a free OH stretch motion of the carboxylic groups by the following reasoning: There are two pairs of equivalent carboxylic groups within the molecule. They orient to coordinate in a Dy- $\mu$ -oxo-Mn motive. This inevitably forces the carboxylic OH groups to stick out of the complex and to dangle. Such dangling bonds are easily accessible to gas phase H/D exchange with  $\text{ND}_3$  as compared to the aminic protons, which are buried inside the complex.



**Figure 6:** IR-ATR spectrum of crystals of **2** and 2-color IR-MPD spectrum of **2**<sup>+</sup>.

The x-ray structure of **2** reveals a hydrated structure with the composition  $[\text{Dy}(\text{MnC}_{22}\text{H}_{23}\text{N}_4\text{O}_6)_2(\text{NO}_3) \cdot (\text{EtOH}) \cdot 8(\text{H}_2\text{O})]$  [1]. The IR-ATR spectrum of **2** (cf. Fig. 6 (top)) shows five partially overlapping intense bands in the region from 3200 to 3700  $\text{cm}^{-1}$  which correspond to NH and OH stretching modes due to known IR group frequencies. A huge number of bands can be seen in the region of aliphatic and aromatic CH stretching modes from 2800 to 3100  $\text{cm}^{-1}$ .

2-color IR-MPD spectra of **2**<sup>+</sup> (cf. Fig. 6 (bottom)) are in quite good agreement (dashed lines) with the CH stretch region of the IR-ATR spectrum. However, only one minor band can be seen in the OH and NH stretch region of the IR-MPD spectrum, which does not clearly correlate to a band in the IR-ATR spectrum. Several bands in the range of 3400 to 3700  $\text{cm}^{-1}$  in the IR-ATR spectrum of **2** may belong to hydrogen bonded OH stretching modes of incorporated water molecules. These bands vanish in the IR-MPD spectrum of the ionic species in the gas phase, of course.

**VII-4.2.3: Results for  $3^{2+}$** 

**Figure 7:** 1- and 2- color IR-MPD spectra of  $3^{2+}$ .

The 1-color IR-MPD spectrum of  $3^+$  exhibits an intense band at  $2950\text{ cm}^{-1}$  and two broad bands at  $3150$  and  $3270\text{ cm}^{-1}$  in the CH, NH and OH stretching regions, respectively. Several intense bands between  $1400$  and  $1700\text{ cm}^{-1}$  in the CO stretch region (cf. Fig. 7). Using a 2-color scheme with a probe laser fixed at  $2940\text{ cm}^{-1}$  increases all bands in the CO stretch region of the 1-color spectrum and some new bands emerge.

Several of the bands in the CH, NH and OH stretch region can be assigned as discussed before for complex  $1^+$ . The new band between  $3220$  to  $3340\text{ cm}^{-1}$  does not occur in the spectrum of  $1^+$  and can therefore be assigned to the  $\text{NH}_2$  stretching modes of the *tren* ligand. We utilized H/D exchange reactions in solution in order to facilitate a discrimination between bands corresponding to OH/NH stretching modes and those of CH groups. OH and NH bands bear labile, exchangeable protons which will shift to lower frequencies after H/D exchange. This may result in additional gaps in the spectrum and a rise of new bands at lower frequencies.

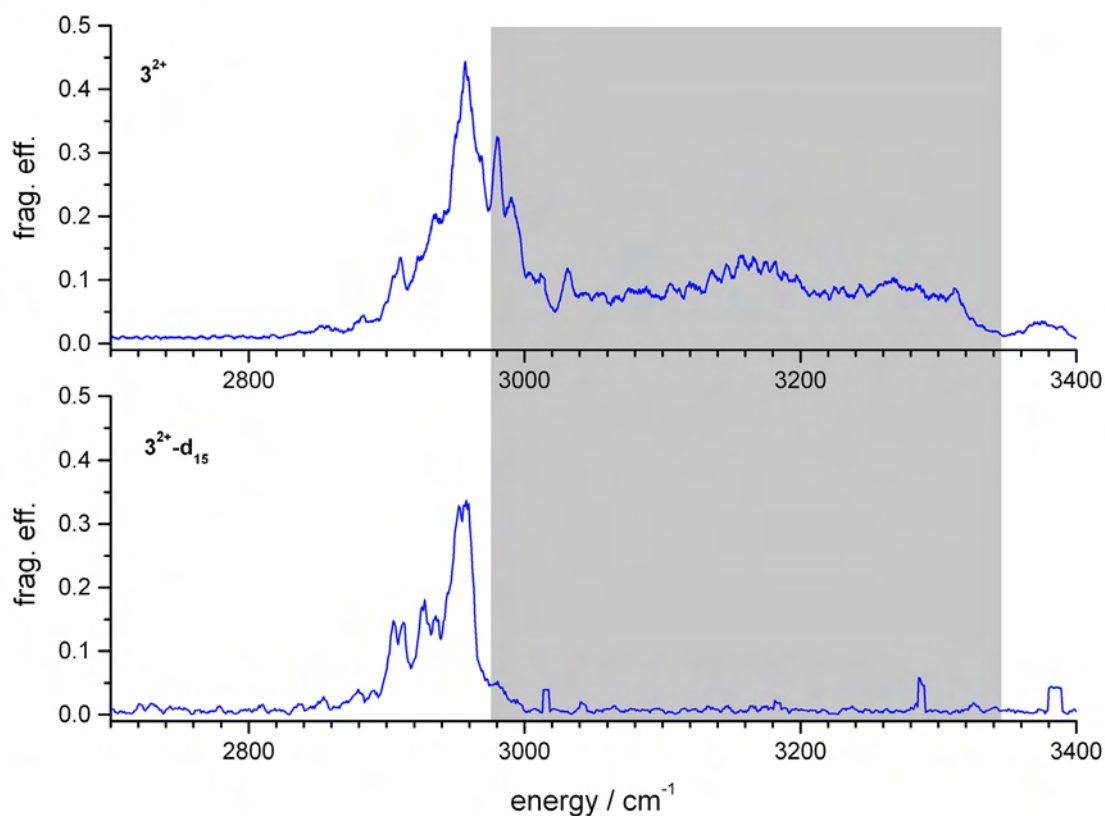


**Figure 8:** 1- color IR-MPD spectra of  $3^{2+}$  (top) and  $3^{2+}-d_{15}$ . The light grey region highlights the decrease of fragmentation efficiency due to spectral shifts of deuterated groups.

The dicationic species  $3^{2+}$  undergoes an exchange of all 15 acidic protons with deuterium in solution. Comparison of protonated and H/D exchanged species reveals a clear reduction of bands in the region between 2985 and 3350 cm<sup>-1</sup> (cf. Fig. 8). The remaining bands at 2850 – 2985 cm<sup>-1</sup> appear more structured due to a reduction of overlapping bands corresponding to NH stretching modes. The remaining bands correspond to aromatic and aliphatic CH stretching modes.

The IR-MPD spectrum of  $3^{2+}-d_{15}$  exhibits no gap between 2920 and 2960 cm<sup>-1</sup>, unlike the spectrum of  $1^+-d_{10}$  (cf. Fig. 4). The amine groups of complex  $3^{2+}$  may have a nonuniform binding behavior. One amine group is probably bound to the adjacent Ni<sup>2+</sup>(*tren*) complex  $3^{2+}$  (cf. Fig. 2) and the other amine group may interact with the carboxy group of the salen-type ligand like in complex **1** (cf. Fig. 1). We assume that the vibrational frequencies of the stretching modes of the Nickel bound amine group are shifted to the blue (3100 to 3220 cm<sup>-1</sup>). The second terminal amine group may form hydrogen bonds as discussed for complex **1**<sup>+</sup>. This binding behavior can explain the slight reduction

of fragmentation efficiency and the appearance of more structural features in the region from 2860 to 2970  $\text{cm}^{-1}$  (cf. Fig. 8).

#### VII-4.2.4: Results for $4^{2+}$

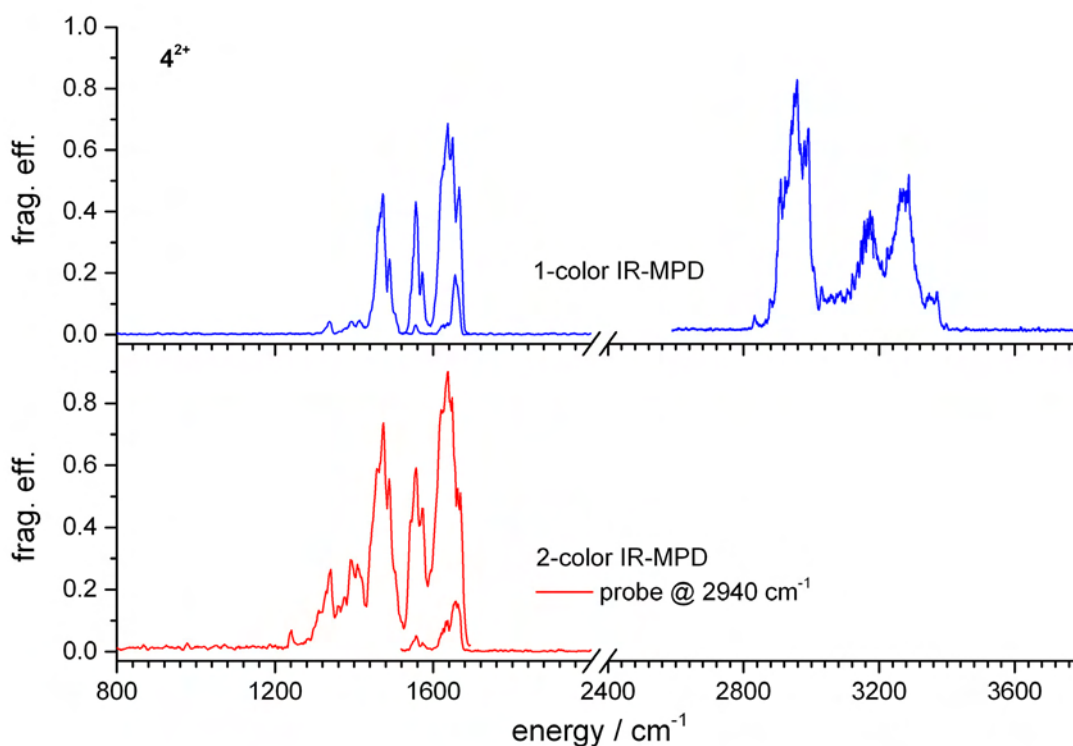


**Figure 9:** 1- and 2-color IR-MPD spectra of  $4^{2+}$ . Superimposed regions were measured with various photon fluxes.

The 1-color IR-MPD spectrum of  $4^{2+}$  reveals three intense bands at 2940, 3180 and 3270  $\text{cm}^{-1}$  in the CH and NH stretching region and several intense bands between 1400 and 1700  $\text{cm}^{-1}$  in the CO stretching region (cf. Fig. 9). A 2-color scheme with a probe laser at 2940  $\text{cm}^{-1}$  gives rise to new bands emerging. The *fingerprint* range of complex  $4^{2+}$  looks very similar to that of  $3^{2+}$ . The OH stretching band pattern looks different, more intense bands can be seen in the IR-MPD spectrum of  $4^{2+}$ .

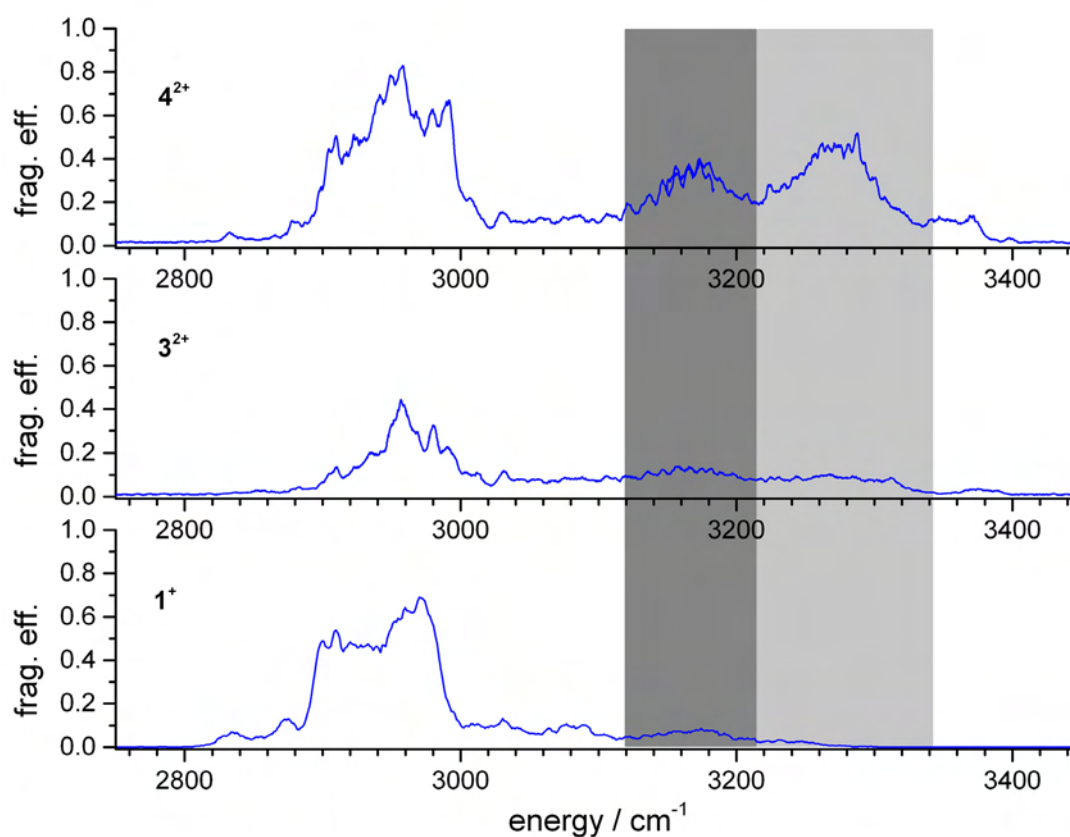


**Figure 10:** 1-color IR-MPD spectra of  $4^{2+}$ ,  $3^{2+}$  and  $1^+$ . The light grey field indicates the region of  $\text{NH}_2$  stretching modes of the tren ligand, the dark grey field the region of  $\text{NH}_2$  stretching modes of the salen-type ligand.

Comparison of the IR-MPD spectra of complexes  $3^{2+}$  and  $4^{2+}$  reveals similar positions of bands. Complex  $3^{2+}$  has a reduced fragmentation efficiency compared to complex  $4^{2+}$  (cf. Fig. 10). Complex  $4^{2+}$  incorporates two  $\text{Ni}^{2+}(\text{tren})$  ligands and both terminal amine groups of the salen-type ligand are equivalent (cf. Fig. 2). A larger number of similar  $\text{NH}_2$  groups leads to a higher absorption coefficient. This induces a higher fragmentation efficiency of complex  $4^{2+}$  for the bands at 3220 to 3340  $\text{cm}^{-1}$  and at 3120 to 3220  $\text{cm}^{-1}$  as compared to complex  $3^{2+}$ . The band at 3220 to 3340  $\text{cm}^{-1}$  (cf. Fig. 10, light grey), assigned to the  $\text{NH}_2$  stretching modes of the  $\text{Ni}^{2+}(\text{tren})$  complex, does not occur in the spectrum of complex  $1^+$ . The band at 3120 to 3220  $\text{cm}^{-1}$  (cf. Fig. 10, dark grey) is assigned to the  $\text{NH}$  stretching modes of the nickel bound terminal amine groups (one group in complex  $3^{2+}$  and two in  $4^{2+}$ ) of the salen-type ligand. The IR-MPD spectrum of  $1^+$  exhibits a band at the same position without any nitrogen-nickel interaction. In complex  $1^+$  there are two protons of the terminal amine groups that are hydrogen bound to oxygen atoms of the salicylic subunit of the ligand. We conclude that each of the two protons within complex  $1^+$  is located at one of those amine groups pointing outwards of the complex. Thus, the additional protons in complex  $1^+$  exhibit each



vibrational frequencies of the “free” (non hydrogen bound) NH stretching modes as present in complexes  $3^{2+}$  and  $4^{2+}$  as well.

## VII-5: Conclusions

H/D exchange reactions with  $D_2O$  in solution yielded an exchange of all labile (acidic) protons in case of the cationic complexes. Anionic complexes underwent a partial or a complete exchange of labile protons. We assigned the bands occurring in IR-MPD spectra of the protonated cationic complexes **1-4** with the help of IR-MPD spectroscopy on the deprotonated complex  $1^-$  and the H/D exchanged species  $1^+ - d_{10}$ ,  $1^- - d_4$  and  $3^{2+} - d_{15}$ . Complex  $1^+$  incorporates two protons bound to the terminal amine groups of the salen-type ligand (cf. Fig. 11, yellow circles).

In complex  $2^+$  the carboxy groups are the most likely protonation sites (dark blue circles). However, complex  $2^+$  exchanges only two protons in gas phase H/D exchange experiments with  $ND_3$  [1]. This corresponds likely to isomer  $2^+ - b$ ) where the carboxylic protons are not in direct neighborhood of the amine groups of the salen-type ligand (orange circles).

The evaluation of IR-MPD spectra of protonated and H/D exchanged species in comparison is a useful tool to assign the positions of additional protons and the binding motives of the terminal amine groups of the cationic species of complexes **1-4** in the gas phase. This is of special interest for studies on the magnetic properties of these complexes conducted in the gas phase, which are under way in the framework of our 3MET collaborative research center.

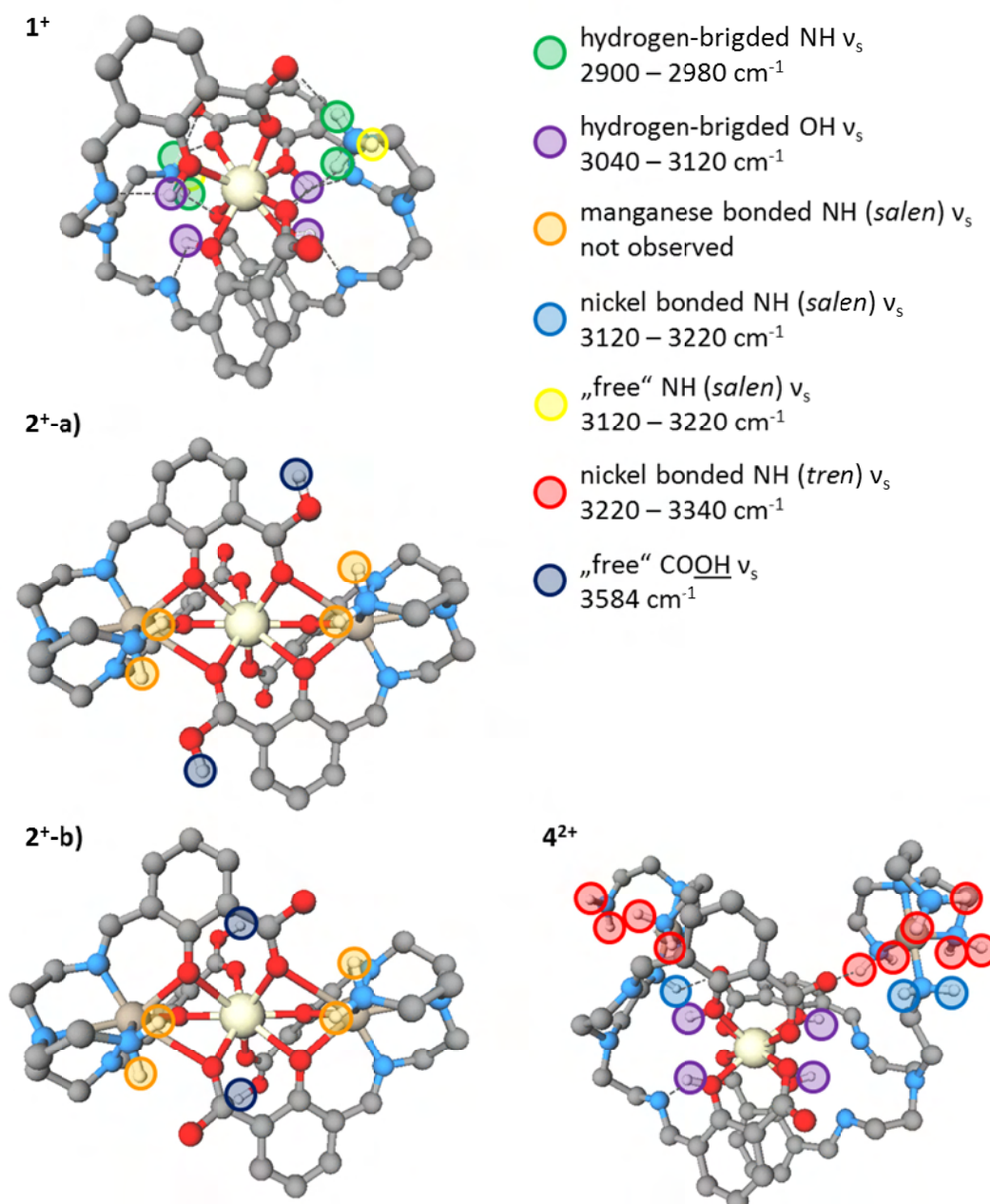


**Figure 11:** Cationic species of complexes **1**, **2** and **4** based on crystal structures derived by X-ray diffraction measurements [1, 2]. Complex **2** can exhibit at least two isomers **2<sup>+</sup>-a)** and **b)**. Positions of exchangeable protons (colored circles) are due to assignments derived by IR-MPD spectroscopy on protonated and deuterated complexes. Frequencies of XH ( $X = O, N$ ) stretching modes are according to experimental data. The colors of the circles indicate different binding motives of the incorporated protons. Dashed lines indicate hydrogen bonds. Note, that hydrogen atom positions are indicated in part (as opposed to structures in Fig. 1 and 2). Hydrogen atoms of CH groups are not shown.

**VII-6: References**

1. Bhunia, A., et al., *From a Dy(III) Single Molecule Magnet (SMM) to a Ferromagnetic Mn(II)Dy(III)Mn(II) Trinuclear Complex*. Inorganic Chemistry, 2012. **51**(18): p. 9589-9597.
2. Bhunia, A., et al., *Trinuclear nickel-lanthanide compounds*. Dalton Transactions, 2013. **42**(7): p. 2445-2450.
3. Lis, T., *Preparation, Structure, and Magnetic-Properties of a Dodecanuclear Mixed-Valence Manganese Carboxylate*. Acta Crystallographica Section B-Structural Science, 1980. **36**(Sep): p. 2042-2046.
4. Bagai, R. and G. Christou, *The Drosophila of single-molecule magnetism:  $Mn_{12}O_{12}(O_2CR)_{16}(H_2O)_4$* . Chemical Society Reviews, 2009. **38**(4): p. 1011-1026.
5. Christou, G., et al., *Single-molecule magnets*. Mrs Bulletin, 2000. **25**(11): p. 66-71.
6. Gatteschi, D., et al., *Large Clusters of Metal-Ions - the Transition from Molecular to Bulk Magnets*. Science, 1994. **265**(5175): p. 1054-1058.
7. Sessoli, R. and A.K. Powell, *Strategies towards single molecule magnets based on lanthanide ions*. Coordination Chemistry Reviews, 2009. **253**(19-20): p. 2328-2341.
8. Hewitt, I.J., et al., *Coupling  $Dy_3$  Triangles Enhances Their Slow Magnetic Relaxation*. Angewandte Chemie-International Edition, 2010. **49**(36): p. 6352-6356.
9. Hewitt, I.J., et al., *Opening up a dysprosium triangle by ligand oximation*. Chemical Communications, 2009(44): p. 6765-6767.
10. Ishikawa, N., et al., *Mononuclear lanthanide complexes with a long magnetization relaxation time at high temperatures: A new category of magnets at the single-molecular level*. Journal of Physical Chemistry B, 2004. **108**(31): p. 11265-11271.
11. Ishikawa, N., *Single molecule magnet with single lanthanide ion*. Polyhedron, 2007. **26**(9-11): p. 2147-2153.



## Chapter VIII: Ru-catalysts for transfer hydrogenation: a combined study of collision and light induced activation processes and experimental and DFT derived gas phase reactivities

### Keywords:

Transfer Hydrogenation, Ruthenium, Pyridine, Pyrimidine, Base free Activation, Alcohol, Ketone, Mass Spectrometry, IR-MPD, DFT, Gas Phase Reactions, Isotope Labeling, CID, RRKM

### VIII: Preamble

This chapter gives an extensive introduction to a joint publication with the research group of Prof. W. Thiel, TU Kaiserslautern [1] on the reaction mechanism of a novel ruthenium (Ru(II)) based catalyst for transfer hydrogenation. The synthesis of the complexes was done by L. Ghoochany and C. Kerner. ESI-MS measurements and the assignment of all ionic species were done by me. L. Ghoochany and W. Thiel mainly prepared the manuscript of [1]. The other coworkers contributed with results from several experiments, *ab initio* calculations and revisions of the manuscripts.

The experimental section of this chapter reports on own CID and IR-MPD studies, gas phase reaction experiments and *ab initio* calculations partially based on former results. This chapter is written by me and formatted as to become a manuscript for publication. It is not submitted yet.

### VIII-1: Abstract

The activation process of three differently substituted ruthenium  $[(\eta^6\text{-cymene})\text{Ru}^{\text{II}}\text{Cl}(\text{apypm})]\text{BPh}_4$  complexes for transfer hydrogenation is studied by collision induced dissociation (CID). It leads to the same activation process as observed in solution, which is the loss of HCl from the precursor molecule. During this process the Ru-N bound pyrimidine ring of the ligand rotates about  $160^\circ$  to form a Ru-C bond after proton abstraction from the carbon atom. Isotopic labeling of two precursor molecules gives clear evidence for the proposed activation mechanism.

The three complexes need different CID voltages for fragmentation. So called “thermometer ions” allow for a conversion of the voltage scale of a mass spectrometer to activation energies. Fragmentation energies of the cationic  $[(\eta^6\text{-cymene})\text{RuCl}(\text{apypm})]^+$  complexes in the gas phase

derived by CID correlate quite well to DFT predicted activation barriers. CID and DFT estimated activation energies again correlate to reaction efficiencies found in solution.

The exchange of the chlorido anion with anions of different basicity gave CID derived activation energies in good agreement with the HSAB concept. Besides CID, also infrared multiple-photon excitation is capable to induce an activation of the  $[(\eta^6\text{-cymene})\text{RuCl}(\text{apypm})]^+$  catalyst. We used 1- and resonant 2-color IR-MPD in order to elucidate the gas phase structure of the ruthenium catalyst precursor. 2-color IR-MPD is capable to detect several dark bands, however only a few vibrational absorption bands could be recorded.

Gas phase reactions of the three  $[(\eta^6\text{-cymene})\text{Ru}(\text{apypm})]^+$  catalysts with  $\text{D}_2$  lead to a mass shift of +4 m/z, which is interpreted in terms of a disproportionation of  $\text{D}_2$  and a nucleophilic addition of D to the ruthenium atom. The addition of  $\text{D}_2$  can be seen as an alternative process to the abstraction of dihydrogen from an alcohol. DFT based modeling of the reaction coordinate at the B3LYP/cc-pVTZ level of theory exhibits up to three transition states and different activation barriers according to the substituents. Gas phase reactions of the catalytical active complexes with  $\text{D}_2\text{O}$  lead to an addition of OD to the complex and a consecutive loss of HD.

## VIII-2: Introduction

Ruthenium and rhodium based catalysts are widely used for transfer hydrogenation reactions [2-9]. They can yield a high enantioselectivity with prochiral starting materials [10]. Transfer hydrogenation reactions with ruthenium catalysts were widely performed with  $\text{H}_2$  as a hydrogen source. This is dangerous due to the use of gaseous hydrogen and the search for effective catalysts in solution is a great field of research. Homogeneous reactions are nowadays often carried out in isopropanol which serves as both, solvent and source of hydrogen, while it is oxidized to acetone. The formation of ruthenium dihydrogen species in solution is known as well as the formation of hydride species. [4, 5] The reaction with dihydrogen can even take place in water [11]. The underlying activation and reaction processes are a great field of research studied at a huge variety of ruthenium bearing catalysts.

Common catalysts have to be activated with the help of a base [12-15]. This leads to additional waste and the search for alternative activation processes is of special interest in terms of sustainable chemistry. A base free protocol was developed from Ghoochany et al. for a new type of Ru-catalyst.

Those  $[(\eta^6\text{-cymene})\text{RX}(\text{apypm})]\text{BPh}_4$  catalysts contain p-cymene, a chlorido anion (alternatively X = I, Br,  $\text{CF}_3\text{SO}_3$ ,  $\text{CH}_3\text{COO}$ ) bound to the ruthenium, a substituted 2-R-4-(2-pyridinyl)pyrimidine (*apypm*) ligand (cf. Fig. 1) and a  $\text{B}(\text{Ph})_4^-$  counterion. The variation of substituents leads to the following complexes: **1** ( $\text{R}=\text{NH}_2$ ), **2** ( $\text{R}=\text{N}(\text{CH}_3)_2$ ) and **3** ( $\text{R}=\text{N}(\text{CH}_2)_4$ ), which gave different conversion efficiencies for the transfer hydrogenation from isopropanol to acetophenone (cf. Table 1, taken from [1]).

**Table 1:** Reaction conditions: acetophenone (2.5 mmol), catalyst ( $1.25 \times 10^{-2}$  mmol), KOH ( $1.25 \times 10^{-1}$  mmol), isopropanol (25 mL),  $82^\circ\text{C}$ ; the reactions were monitored by GC [1].

catalyst	R	conversion (%)	time (min)
1	$\text{NH}_2$	35	360
2	$\text{NMe}_2$	100	90
3	$\text{N}(\text{CH}_2)_4$	97	20

It was shown that IR-MPD is capable to elucidate the gas phase structure of metal complexes and their reaction products [16-19]. A comparison of CID and IR-MPD experiments were compared with respect to the fragmentation pathways of  $[\text{MX}_2(\text{CO})_2(\text{dcbpy})]$  ( $\text{M} = \text{Ru}, \text{Os}$ ;  $\text{X} = \text{Cl}, \text{Br}, \text{I}$ ;  $\text{dcbpy} = 2,2'$ -bipyridine-4,4'-dicarboxylic acid) complexes [20].

Several density functional theory (DFT) studies were carried out in order to elucidate the activation processes of alcohols and other dihydrogen sources at metal-centered catalysts [21-24]. Also Ru-catalysts with secondary amino-oxazolines were studied, suggesting an activation of the  $\text{NH}_2$  group by proton abstraction [25]. Therefore the underlying activation mechanism and relative activation barriers are strongly dependent on the chelating ligands.

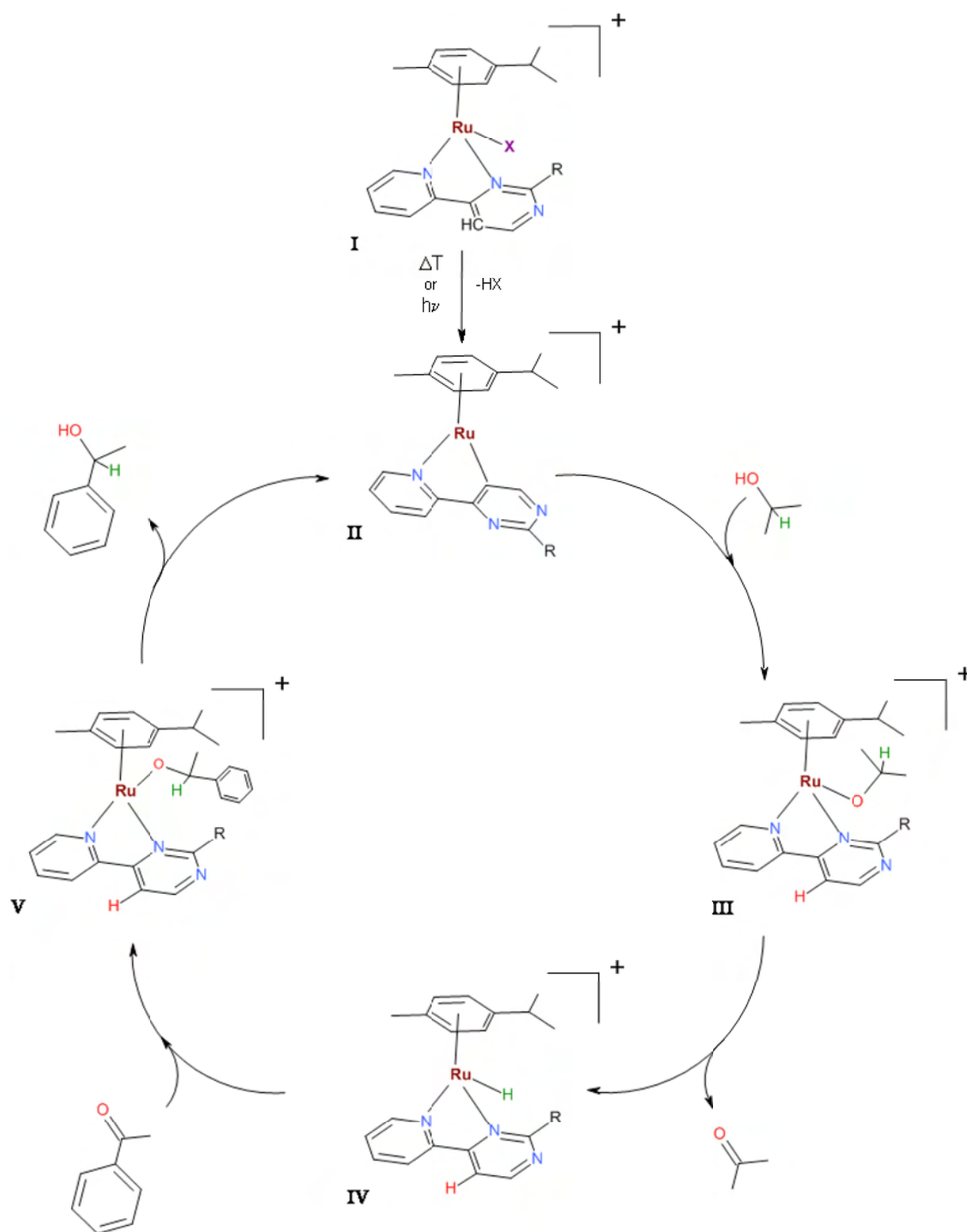


**Figure 1:** Proposed activation mechanism for catalysts  $1^+$ ,  $2^+$  and  $3^+$  ( $[(\eta^6\text{-cymene})\text{RuX}(\text{apypm})]^+$ ;  $\text{R} = \text{NH}_2$  ( $1$ ),  $\text{N}(\text{CH}_3)_2$  ( $2$ ),  $\text{NC}_4\text{H}_8$  ( $3$ );  $\text{X} = \text{I}, \text{Br}, \text{Cl}, \text{CF}_3\text{SO}_3, \text{CH}_3\text{COO}$ ) ( $\text{I} \rightarrow \text{II}$ ) and reaction mechanism for a transfer hydrogenation from isopropanol to acetophenone catalyzed by the activated catalyst species  $\text{II}$  ( $1^+(-\text{HX})$ ,  $2^+(-\text{HX})$ ,  $3^+(-\text{HX})$ ).



**VIII-2.1: Activation process of the  $[(\eta^6\text{-cymene})\text{RuCl}(\text{apypm})]^+$  catalyst precursors**

We used electrospray ionization at solutions of **1**, **2** and **3** in acetonitrile, isolated singly charged cations in a Paul trap of a mass spectrometer (cf. Table 2) and fragmented them by CID. All three complexes showed the loss of HCl as the major fragmentation pathway (see Fig. 2). Only complex **1**<sup>+</sup> showed an additional loss of H<sub>2</sub> (ca. 60%) which may arise from the isopropyl group of the cymene ligand of the molecule forming an isopropylene group. Hence Ghoochany et al. synthesized a benzene containing complex **4** ( $[(\eta^6\text{-benzene})\text{RuCl}(\text{apypm})]\text{BPh}_4$ ). Its cation **4**<sup>+</sup> exhibited only the loss of HCl (cf. Fig. 2 b)). The H<sub>2</sub> loss detected for **1**<sup>+</sup> originates from the p-cymene ligand.

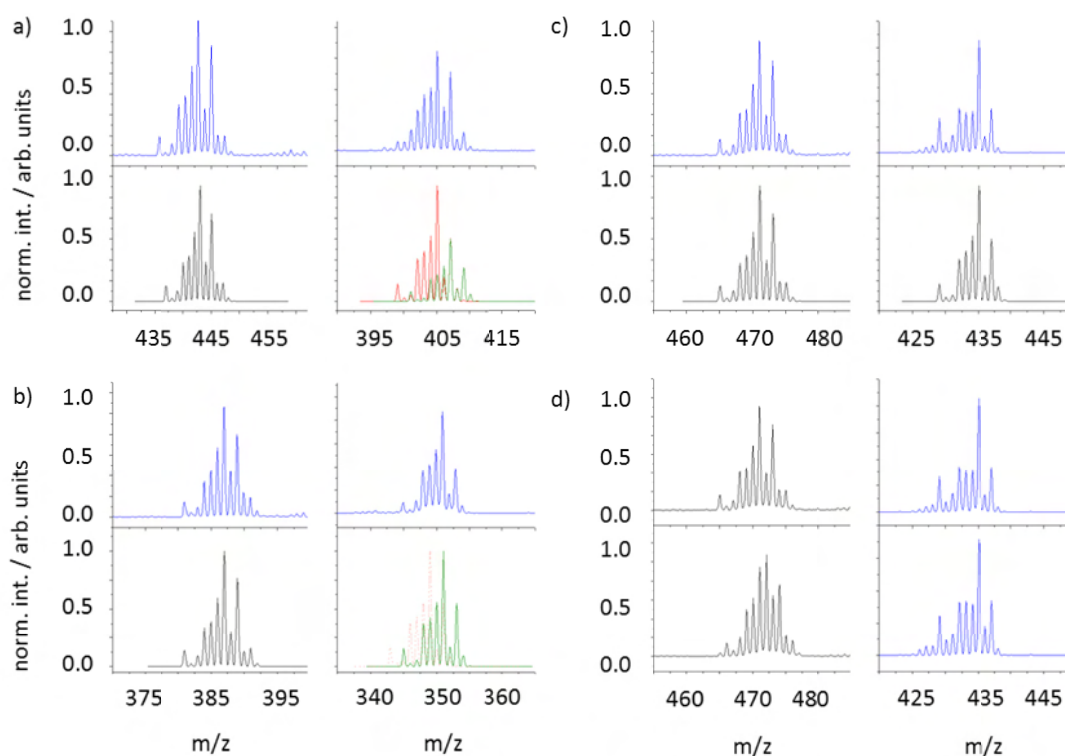


**Figure 2:** Isotope patterns (normalized intensity) of **1**<sup>+</sup> and **1**<sup>+</sup>(-HCl) (a)), **4**<sup>+</sup> and **4**<sup>+</sup>(-HCl) (b)), **2-h**<sup>+</sup> and **2**<sup>+</sup>(-HCl) (c)), **2-d**<sup>+</sup> and **2**<sup>+</sup>(-DCI) (d)). Each segment (a, b, c, d) shows the experimental data of the non-activated (top left), the activated (top right) and the corresponding simulations of the isotopic patterns (bottom left and right). For **1**<sup>+</sup> (a) the combined loss of HCl and H<sub>2</sub> is shown in red in the simulation (a) bottom right).

**Table 2:** Composition and observed masses of the precursors  $1^+$ - $4^+$  and CID ionic fragment masses. Only fragment masses of HCl losses are listed. Masses are due to the most abundant isotopomers. (for mass spectra of isotope patterns cf. Fig. 2)

catalyst	sum formular	parent mass / m/z	fragment mass / m/z
$1^+$	$[\text{Ru}(\text{C}_{10}\text{H}_{14})(\text{C}_9\text{H}_6\text{N}_3(\text{NH}_2))\text{Cl}]^+$	443.06	407.08
$2^+$	$[\text{Ru}(\text{C}_{10}\text{H}_{14})(\text{C}_9\text{H}_6\text{N}_3(\text{N}(\text{CH}_3)_2)\text{Cl})]^+$	471.09	435.11
$3^+$	$[\text{Ru}(\text{C}_{10}\text{H}_{14})(\text{C}_9\text{H}_6\text{N}_3(\text{N}(\text{CH}_2)_4)\text{Cl})]^+$	497.10	461.13
$4^+$	$[\text{Ru}(\text{C}_6\text{H}_6)(\text{C}_9\text{H}_6\text{N}_3(\text{NH}_2))\text{Cl}]^+$	386.99	351.02

We assumed the direct cleavage of a proton from one of the substituents  $\text{NH}_2$ ,  $\text{N}(\text{CH}_3)_2$  or  $\text{N}(\text{CH}_2)_4$  together with the chlorido anion attached to the ruthenium atom as a first model for the activation process. This would lead tentatively to the formation of a Ru-N bond for  $1^+$  and to a Ru-C bond for  $2^+$  and  $3^+$ , respectively (cf. Fig. 3, process I).

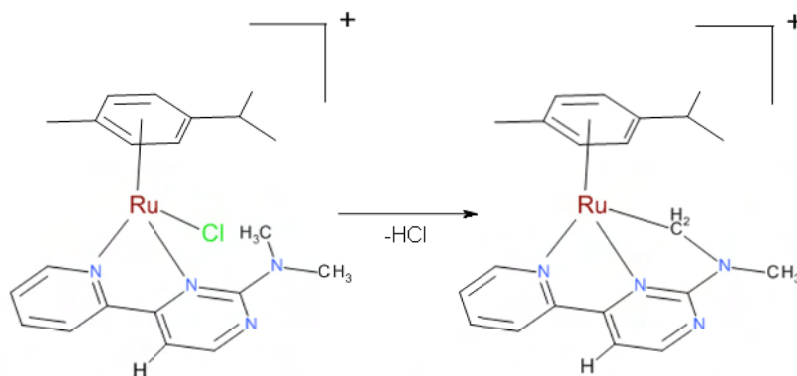


**Figure 3:** Possible dissociation process I of  $2^+$  (left) by a direct cleavage of a proton from the substituent  $\text{N}(\text{CH}_3)_2$  (right).

As an alternative explanation of the activation process, we discussed a mechanism taking the rotation of the pyrimidine ring into account (process II). The rotational barrier might be related to the size of the substituents. For this process to occur, a weakening of the pyrimidine N-Ru bond has to take place. In a second step the pyrimidine ring has to rotate and the proton in the 6 position has to be activated to form a HCl neutral fragment while a Ru-C bond is formed. The remaining complex has a +16 VE ruthenium center (cf. Fig. 4).

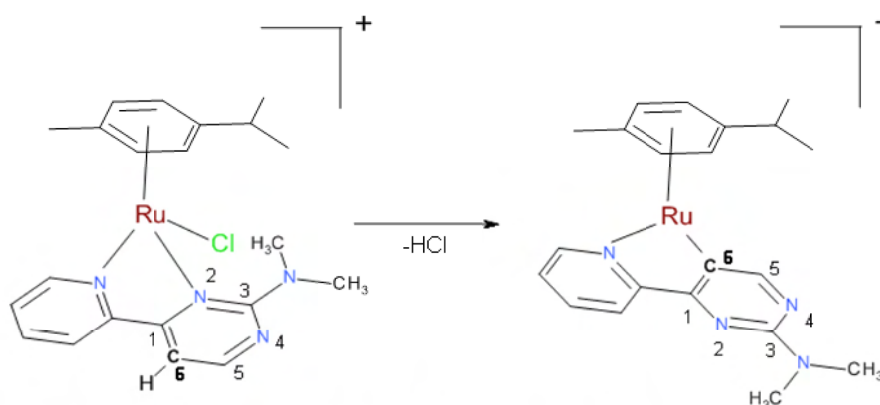


**Figure 4:** Possible dissociation process II of  $2^+$  (left) by rotation of the pyrimidine ring (labeled with numbers) and cleavage of a proton from the C6 position (bold) (right).

In order to distinguish between the two activation models Ghoochany et al. synthesized two C6 deuterated complexes  $1^+ \text{-d}$  and  $2^+ \text{-d}$  (cf. Fig. 5). ESI-MS spectra of the isotope labeled cations of  $1^+ \text{-d}$  and  $2^+ \text{-d}$  exhibit a mass shift of +1 m/z, proving the deuterium insertion (cf. Fig. 2 d)). NMR spectra gives evidence to the C6 position of the deuterium atom. Activation of the complexes  $1^+ \text{-d}$  and  $2^+ \text{-d}$  with CID leads to a loss of DCl which proves model process II.

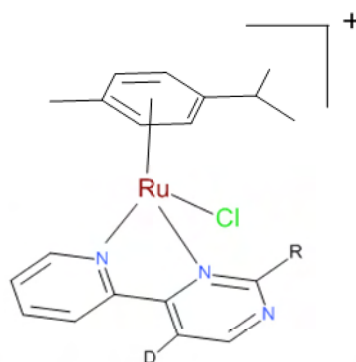


**Figure 5:** C6 deuterated cationic complex. R =  $\text{NH}_2$  for  $1^+ \text{-d}$  and R =  $\text{N}(\text{CH}_3)_2$  for  $2^+ \text{-d}$ .

### VIII-2.2: How to correlate CID fragmentation amplitudes with DFT calculated dissociation enthalpies

The three catalyst **1**, **2** and **3** exhibited strongly different reactivities (cf. Table 1) in solution which may arise from the rotation taking place several times in the cycle. We estimated relative activation barriers by a systematic variation of the fragmentation amplitude during the CID process. The CID process can be understood as a heating of the molecule via collisions with He atoms if an additional

electric field induces an acceleration of the ionic species. Inelastic collisions of the ion with He atoms transfer a part of the collision energy to inner degrees of freedom of the molecule. As soon as enough energy is stored in the molecule, it dissociates via the energetic most favorable paths.

It recently was shown that with substituted benzyropyridinium ions, so-called “thermometer ions”, it is possible to calibrate the internal scales of the mass spectrometers fragmentation amplitudes towards appearance energies ( $E_{\text{LAB}}^{50\%}$ ) of the fragment ions [26-30]. The precision of such an approach is compromised if additional fragmentation channels are taken into account [29]. For several “thermometer ions” a late transition state can be assumed, while the activation process of  $[(\eta^6\text{-cymene})\text{RuCl}(\text{apypm})]^+$  comprises an early transition state [1]. Nevertheless, we want to check if the calibration of the MS fragmentation amplitudes by “thermometer ions” yields reasonable activation energies for the HCl loss of the complexes  $1^+$ - $3^+$ .

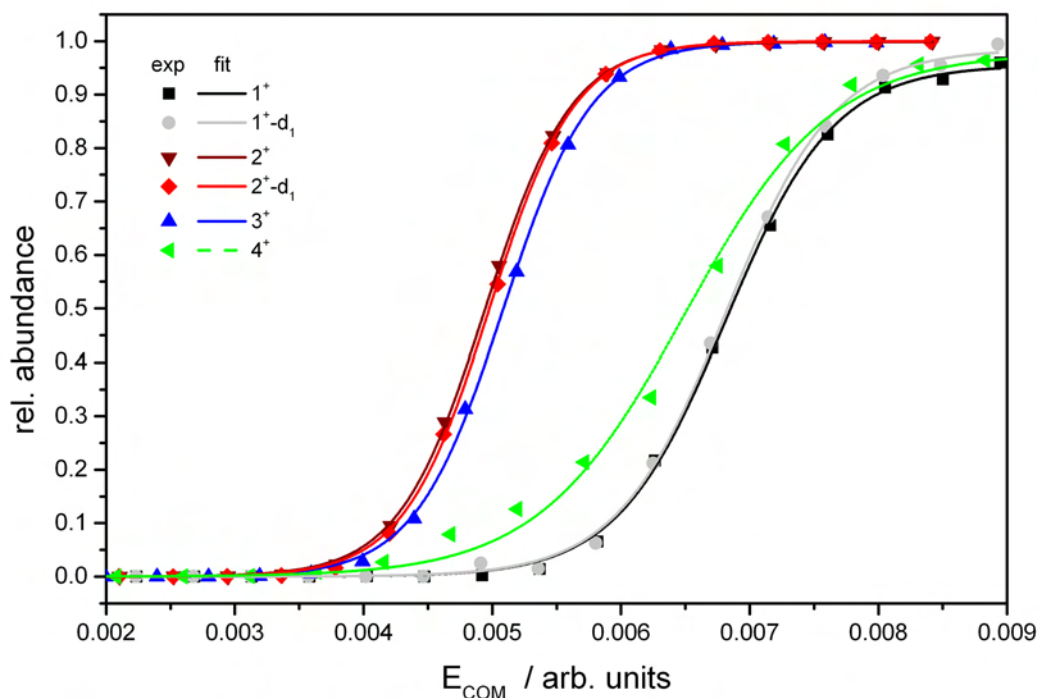


**Figure 6:** CID appearance curves for activated species of  $1^+$  (■),  $1^+\text{-d}$  (●),  $2^+$  (▼),  $2^+\text{-d}$  (◆),  $3^+$  (▲) and  $4^+$  (◄). Lines were derived from sigmoidal fits of the measured values.

The internal fragmentation amplitude of the mass spectrometer has to be transformed into a center-of-mass (COM) system in order to derive relative activation energies from CID experiments. This COM correction takes the different masses of the complexes into account and therefore the different efficiencies of the energy transfer during collisions.

Comparison of the COM corrected appearance curves of the fragments exhibits the highest activation barriers (corresponding to  $E_{\text{COM}}^{50\%}$ , for definition cf. Fig. 9 and formular 3) for  $\mathbf{1}^+$  and  $\mathbf{1}^+\text{-d}$  (cf. Fig. 6).  $\mathbf{1}^+$ ,  $\mathbf{1}^+\text{-d}$ ,  $\mathbf{2}^+$  and  $\mathbf{2}^+\text{-d}$  show a comparable behavior for the protonated and deuterated ligand. The small differences of calculated fragmentation ratios ( $\blacksquare$ ,  $\bullet$  and  $\blacktriangledown$ ,  $\blacklozenge$ ) between the two species may on the one hand arise due to fluctuations during the measurements and on the other hand from different vibrational energies of CH and CD, respectively. As there is no clear trend to higher or lower fragmentation amplitudes for the deuterated species in respect of the protonated species it can be ruled out that the shift arises from different energies of the vibrational ground-states.

For  $\mathbf{2}^+$ ,  $\mathbf{2}^+\text{-d}$  and  $\mathbf{3}^+$  the activation energy is much lower than the ones of  $\mathbf{1}^+$  and  $\mathbf{1}^+\text{-d}$ . The difference in the slope and the  $E_{\text{CID}}^{50\%}$  values of  $\mathbf{1}^+$  and  $\mathbf{4}^+$  may arise from the lower heat capacity of  $\mathbf{4}^+$  due to the absence of the isopropyl and methyl group of the cymene ligand. The same amount of energy transferred to the molecule by collisions with He can be distributed to less degrees of rotational and vibrational freedom and promotes the rotation of the pyrimidine ring. Steric hindrance of the benzene ligand to the rotation of the pyrimidine ring may be lower within  $\mathbf{4}^+$  than the hindrance of cymene to the same rotation within  $\mathbf{1}^+$ .

### VIII-2.3: Correspondence of CID derived fragmentation amplitudes of $[(\eta^6\text{-cymene})\text{RuX}(\text{apypm})]^+$ catalysts to DFT derived activation enthalpies of “thermometer ions”

“Thermometer ions” can be used to calibrate the internal fragmentation amplitude of the mass spectrometer towards calculated activation energies. We used a COM transformed fragmentation amplitude where 50% ( $E_{\text{CID}}^{50\%}$ ) of a molecular parent species is fragmented as a degree of energy needed for fragmentation.

Different activation processes are discussed for the “thermometer ions” [28-30]. We took those “thermometer ions” into account which exhibit a direct cleavage of the cationic substituted benzylium ion. This is the case for the following substituents: p-Cl, p-CN, p-H, p-OCH<sub>3</sub>. Other substituents lead to a mixture of products: p-F, p-CH<sub>3</sub>, o-CH<sub>3</sub>. We assumed a 1:1 ratio of the competing reaction pathways for the latter three as a rough estimation. We used DFT calculations in order to derive temperature (298.15 K) corrected binding energies at the B3LYP/G6-31\* level of theory for all seven molecules. We compared experimental data with ab initio calculations of the activation process of catalysts  $\mathbf{1}^+\text{-}\mathbf{3}^+$  [1].

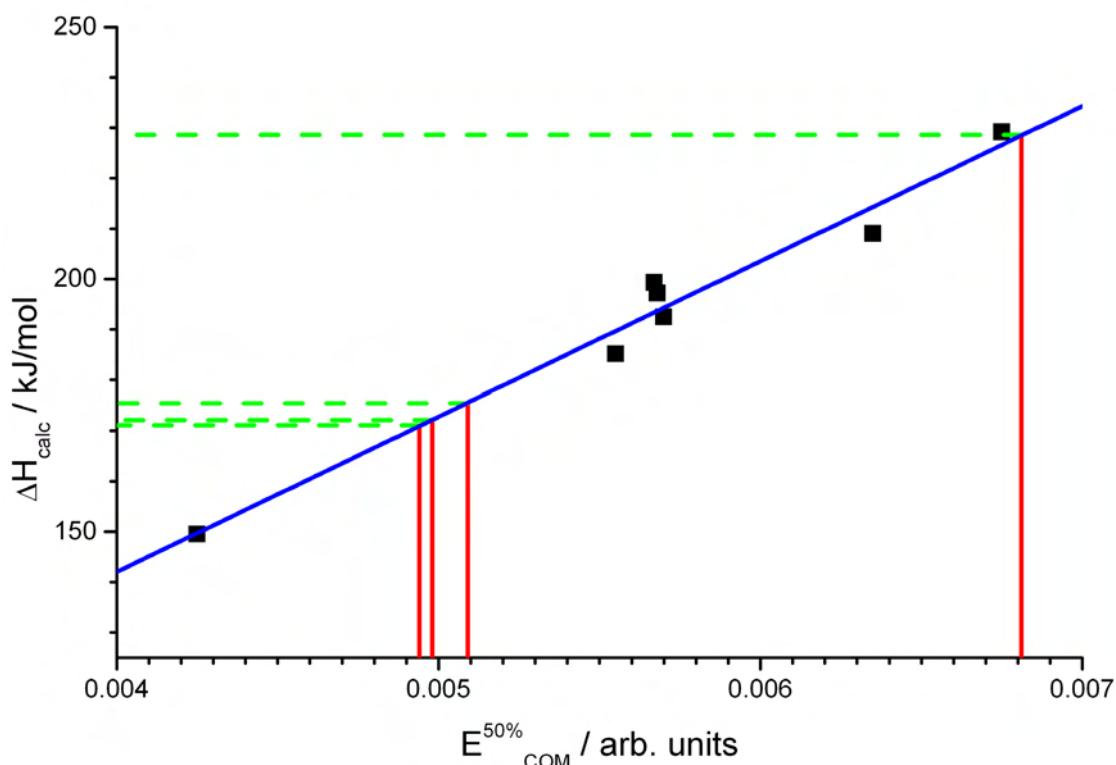


**Figure 7:** DFT derived dissociation enthalpies of “thermometer ions” at the B3LYP/G6-31\* level of theory vs. their experimental  $E^{50\%}_{CID}$  values derived from sigmoidal fits of the center of mass transferred appearance curves (■) (cf. Fig. 9). The blue line results from a linear fit function. Measured appearance amplitudes ( $E^{50\%}_{CID}$ ) of  $1^+-(d)$ ,  $2^+-(d)$  and  $3^+$  are shown in red ( $2^+$  and  $2^+-(d)$  overlap). Green lines are the projection of the  $E^{50\%}_{CID}$  values to the dissociation enthalpy scale.

We related DFT derived dissociation enthalpies of seven “thermometer ions” to their experimental  $E^{50\%}_{CID}$  values derived from sigmoidal fits of the center of mass transferred appearance curves (cf. Fig. 7, black squares). We applied a linear fit function to those data pairs (blue line). We used the linear fit function in order to estimate  $\Delta H_{fit}$  values (green lines) from  $E^{50\%}_{CID}$  values (red lines) of the HCl, DCl loss respectively, from  $1^+-(d)$ ,  $2^+-(d)$  and  $3^+$ .

The suggested use of the  $E^{AE}_{COM}$  value [30] led to a larger deviation of the linear fit of the  $\Delta H_{calc}$  values of “thermometer ions” vs. their CID appearance amplitude with respect to the fit of the  $E^{AE}_{COM}$  values (cf. Fig. 8).

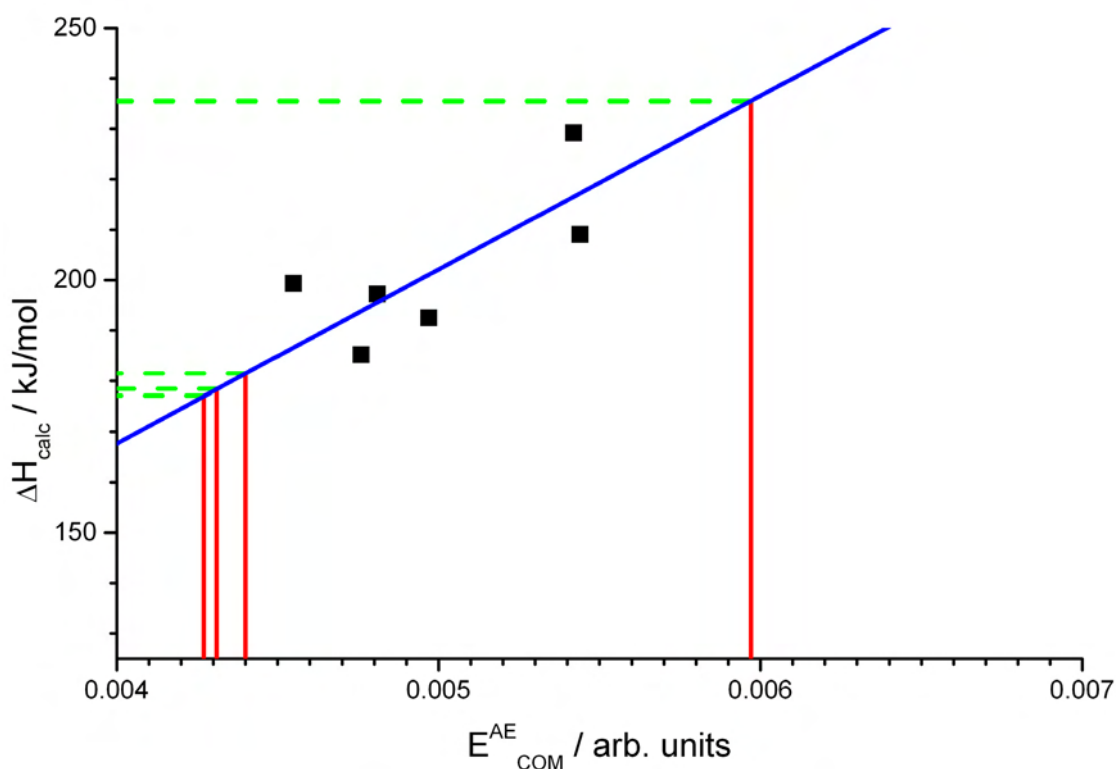


**Figure 8:** DFT derived dissociation enthalpies of “thermometer ions” at the B3LYP/G6-31\* level of theory vs. their experimental  $E_{COM}^{AE}$  values derived from sigmoidal fits of the center of mass transferred appearance curves (■) (cf. Fig. 9). The blue line results from a linear fit function. Measured appearance amplitudes ( $E_{COM}^{AE}$ ) of  $1^{+(-d)}$ ,  $2^{+(-d)}$  and  $3^{+}$  are shown in red ( $2^{+}$  and  $2^{+(-d)}$  overlap). Green lines are the projection of the  $E_{COM}^{AE}$  values to the dissociation enthalpy scale.

The cations  $1^{+(-d)}$ ,  $2^{+(-d)}$  and  $3^{+}$  exhibit a loss of HCl (respectively DCl) and  $1^{+}$  a loss of  $H_2$  in addition (cf. Fig. 2). The underlying mechanism of the C-H activation of  $1^{+}$ - $3^{+}$  implies a tight (late) transition state [1], which might lead to a kinetic shift in the appearance energies obtained by CID. Due to the kinetic shift the dissociation energies might be overestimated.

No quantitative conclusions could be drawn due to different mechanisms for bond cleavage. However, the semi-quantitative analysis results in a qualitative trend of activation energies (loss of HCl or DCl) of the Ru-catalysts  $1^{+(-d)}$ ,  $2^{+(-d)}$  and  $3^{+}$  with respect to the “thermometer ions” (cf. Table 3).

**Table 3:** Estimated enthalpies ( $\Delta H_{\text{fit}}$ ) of catalysts **1<sup>+</sup>(-d)**, **2<sup>+</sup>(-d)** and **3<sup>+</sup>** (cf. Fig. 7) and calculated ZPE corrected enthalpies ( $\Delta\Delta H$ ) for the transition state of HCl loss, DCl respectively (data according to [1]).

complex	$\Delta H_{\text{fit}} /$ kJ/mol	$\Delta\Delta H /$ kJ/mol
<b>1<sup>+</sup>-h</b>	229	195
<b>1<sup>+</sup>-d</b>	229	195
<b>2<sup>+</sup>-h</b>	171	151
<b>2<sup>+</sup>-d</b>	172	151
<b>3<sup>+</sup></b>	175	153

### VIII-3: Methods

#### VIII-3.1: ESI-MS and CID

Electrospray ionization mass spectrometry (ESI-MS) was performed with two ion trap instrument (Bruker Esquire 6000 for CID and amaZonSL for IR-MPD). The ion source yields anions/cations in negative/positive electrospray ionization mode. Scan speed was 13000 m/z / s in normal resolution scan mode (0.3 FWHM / m/z), scan range was at least 70 to 400 m/z. Sample solutions of **1-4** and alkali-halids in water/acetonitrile 9:1 at concentrations of approximately  $1 \times 10^{-4}$  M were continuously infused into the ESI chamber at a flow rate of 2  $\mu\text{L}/\text{min}$  using a syringe pump. We use nitrogen as drying gas at a flow rate of 3.0 to 4.0 L/min at 220 °C up to 300 °C and spray the solutions at a nebulizer pressure of 3 to 4 psi with the electrospray needle held at 4.5 kV. We held transfer parameters to the Paul trap of the mass spectrometer constant and used Helium as a buffer gas with a partial pressure of about  $3 \times 10^{-3}$  mbar inside the ion trap. BrukerEsquireControl 5.3 (Esquire) and BrukerTrapControl 7.0 (amaZonSL) software controlled the instrument and we performed data analysis using Bruker Data Analysis 4.0 software.



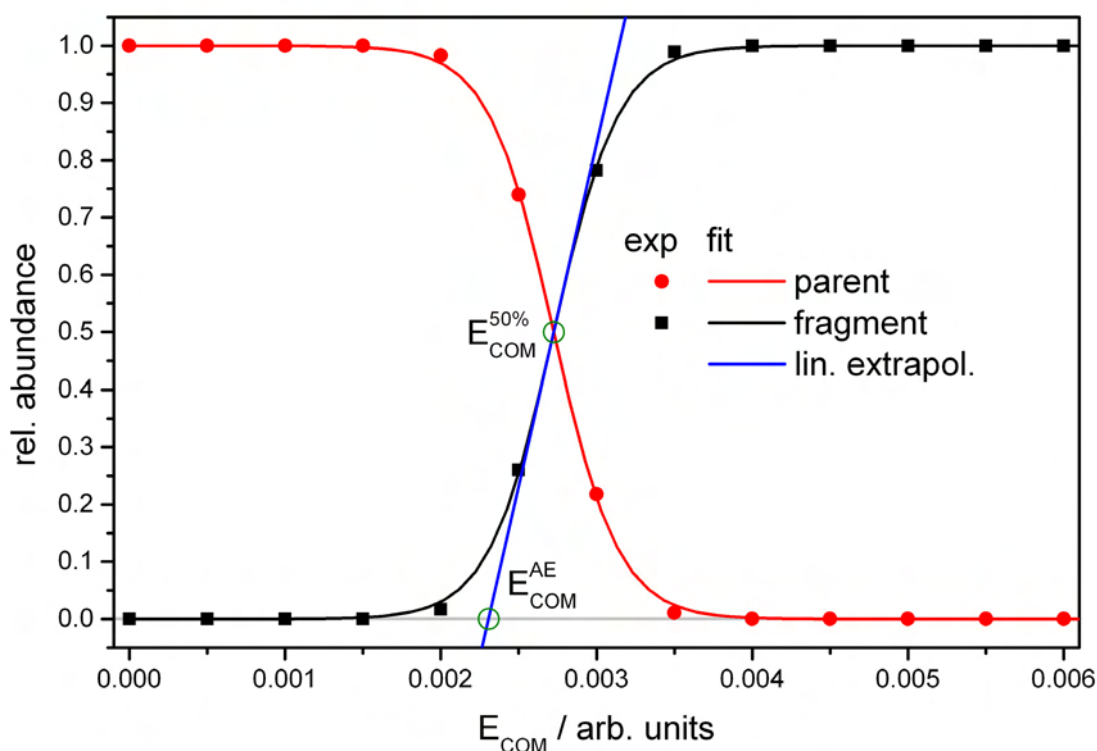


**Figure 9:** Relative abundances  $I_{tot}^p(E_{COM})$  (●) and  $I_{tot}^{fr}(E_{COM})$  (■) for the para-fluoro-benzylpyridinium parent cation and its ionic fragment. Sigmoid functions  $I_{fit}^p(E_{COM})$  (—) and  $I_{fit}^{fr}(E_{COM})$  (—) were derived from fits of the measured values. The blue line (—) was derived from the slope of the sigmoid fit function at  $E_{COM}^{50\%}$ . Positions of the  $E_{COM}^{50\%}$  and the  $E_{COM}^{AE}$  values are marked with green circles.

Relative abundances of fragments were calculated according to:

$$I_{tot}^{fr}(E_{LAB}) = \frac{\sum_i I_i^{fr}(E_{LAB})}{\sum_i I_i^{fr}(E_{LAB}) + \sum_i I_i^p(E_{LAB})} \quad (1a)$$

and breakdown curves of parent intensities accordingly:

$$I_{tot}^p(E_{LAB}) = \frac{\sum_i I_i^p(E_{LAB})}{\sum_i I_i^{fr}(E_{LAB}) + \sum_i I_i^p(E_{LAB})} \quad (1b)$$

The amount of energy transferred by a single collision is dependent on the velocity and mass of the collision gas and the ion. The center-of-mass energy is the theoretical amount of energy that can be absorbed in such a reaction. Center of mass transferred fragmentation magnitudes  $E_{COM}$  were calculated from internal amplitudes  $E_{LAB}$  according to formular 2.  $m_{ion}$  was chosen according to the

isotopically averaged mass of the molecule.

$$E_{COM} = \frac{m_{He}}{(m_{He} + m_{ion})} E_{LAB} \quad (2)$$

Thereby  $I_{tot}^{fr,p}(E_{LAB})$  converts to  $I_{tot}^{fr,p}(E_{COM})$ . Those entities may fit to analytical functions:

$$I_{fit}^{fr}(E_{COM}) = \frac{1}{(1 + e^{(E_{COM}^{50\%} - E_{COM})B})} \quad (3a)$$

$$I_{fit}^p(E_{COM}) = \frac{1}{(1 + e^{-(E_{COM}^{50\%} - E_{COM})B})} \quad (3b)$$

A phenomenological  $E_{COM}^{50\%}$  value can be derived by the center of these sigmoid fit functions

$I_{fit}^{fr,p}(E_{COM})$  (cf. Equation 3a and 3b) applied to experimental data  $I_{tot}^{fr,p}(E_{COM})$  using a least-squares criterion.  $E_{COM}^{50\%}$  is the amplitude at which the sigmoid function has reached half of its maximum,  $E_{COM}$  is the fragmentation amplitude and B describes the rise of the sigmoid curve. Alternatively,  $E_{COM}^{AE}$  values can be used to determine activation energies (AE) under consideration of the slope of the sigmoid function [11].  $E_{COM}^{AE}$  values were derived by linear extrapolation of the slope at the  $E_{COM}^{50\%}$  value to the baseline (cf. Fig. 9, lower green circle).

Resulting  $E_{COM}^{50\%}$  values can be compared qualitatively or quantitatively within one group of molecules. Activation energies derived from *ab initio* calculations on the dissociation pathway of an ion can be correlated to experimental  $E_{COM}^{50\%}$  values. Substituted benzyropyridinium ions, so-called “thermometer ions”, can be used to calibrate the internal scales of the mass spectrometers fragmentation amplitudes towards appearance energies of the fragment ions [27-31].

We used a nomenclature for the observed species according to Table 4.

**Table 4:** Nomenclature of the observed species for listed molecules in mass spectra.

species	abbreviation	molecules
cationic complex with chlorido ligand	$M^+$	$M = 1, 2, 3, 4$
activated cationic complex	$M^+(-HX)$	$M = 1, 2, 3, 4;$ $X = I, Br, OSO_2CF_3, O_2CCH_3$
deuterated cationic complex	$M^+-d$	$M = 1, 2$
protonated and deuterated cationic complex	$M^+(-d)$	$M = 1, 2$
cationic complex after ligand exchange	$2^+-X$	$X = I, Br, OSO_2CF_3, O_2CCH_3$

### VIII-3.2: IR-MPD

IR-MPD measurements were performed with the ion trap mass spectrometer (cf. ESI-MS part) after its modification. Two KTP/KTA optical parametric oscillator/amplifier (OPO/A, LaserVision) systems pumped with two Q-switched 10 Hz injection seeded Nd<sup>3+</sup>:YAG lasers (PL8000, Continuum) provided for tunable IR radiation ( $\delta\nu = 0.9 \text{ cm}^{-1}$  resp.  $\delta\nu = 0.3 \text{ cm}^{-1}$ ,  $\delta t = 7 \text{ ns}$ ) in order to record vibrational spectra via the multi-photon dissociation scheme. We used the OPA idler wave ( $\leq 10 \text{ mJ/pulse}$ ) of the one system to scan spectra (pump laser) within  $2800 - 3600 \text{ cm}^{-1}$ . On choice the second IR OPO/A served as probe laser, set to a selected and fixed vibrational resonance frequency. The probe laser beam was aligned counter-propagating with respect to the scanning pump laser beam. Probe pulses were delayed by 100 ns with respect to the scanning pump pulses (delay generator DG645, SRS). Each trapped and  $m/z$  isolated ion package was irradiated by 2-4 laser pulses (or pulse pairs in case of two-laser experiments) in order to produce sufficient fragment ions. IR spectra were recorded using Bruker chromatogram software for extracting the intensity of parent and fragment ions (three point averaging directly by BrukerTrapControl software). IR-MPD signal was evaluated corresponding to formula 1. Origin Plot Software served to apply a five point adjacent averaging for smoothing. IR frequency was calibrated by a wave meter (821B-NIR, Bristol instruments). Laser power curve was recorded in parallel to the IR-MPD spectra through digitizing the analog output of the laser power meter by an ample ADC input of the amaZonSL mass spectrometer electronics.

### VIII-3.3: Theoretical methods

DFT calculations on the D<sub>2</sub> addition to  $1^+(-HCl)$ ,  $2^+(-HCl)$  and  $3^+(-HCl)$  were performed at the B3LYP [32-35] level of theory using cc-pVDZ (C, H, D, N, O) [36], cc-pVTZ (C, H, D, N, O) and

Stuttgart RSC 1997 ECP (Ru) [37] basis sets and the Gaussian 03 and 09 packages [38, 39]. DFT calculations on the “thermometer ions” were performed at the B3LYP/6-31G\* [40, 41] level of theory using standard convergence criteria. Thermal energies, enthalpies and free enthalpies were calculated at 298.15 K (RT conditions).

#### VIII-3.4: Gas phase reactions

Gas phase reactions with D<sub>2</sub>, D<sub>2</sub>O, CH<sub>4</sub> and CH<sub>3</sub>OH were performed under single collision conditions at a background pressure in the range of 1 and 5 x 10<sup>-9</sup> mbar (dependent on gas) in a Bruker Apex III FT-ICR-MS equipped with a 7.0-T magnet and an APOLLO I electrospray ion source. The partial pressure of the reaction gas was set to a constant value and we waited for passivation of the instruments surfaces (high vacuum part) for at least one hour. Sample solutions in acetonitrile at concentrations of approximately 1 x 10<sup>-4</sup> M were continuously infused into the ESI chamber at a flow rate of 3 μL/min using a syringe pump. Nitrogen was used as drying gas with flow rate of 10.0 L/min at approximately 300 °C. The solutions were sprayed at a nebulizer pressure of 25 psi and the electrospray needle was typically held at 4.0 kV. Transfer parameters to the Penning trap of the mass spectrometer were held constant.

#### VIII-3.5: Determination of rate constants

We used transition state theory (4) as a model in order to derive relative rate constants [42]. We used free enthalpies for the highest transition state derived from DFT calculations (at RT conditions) as free enthalpies of activation.

$$k = k_B T / h \exp(-\Delta^\ddagger G^0 / RT) \quad (4)$$

## VIII-4: Results and Discussion

### VIII-4.1: Influence of the coordinating anion

#### VIII-4.1.1: Experimental results

The chloride anion of  $2^+$  was exchanged with iodide, bromide, triflate ( $\text{CF}_3\text{SO}_3^-$ ) or acetate ( $\text{CH}_3\text{COO}^-$ ) in order to compare the dissociation barriers of the neutral fragment  $\text{HX}$  ( $\text{X} = \text{I}, \text{Br}, \text{Cl}, \text{OSO}_2\text{CF}_3, \text{O}_2\text{CCH}_3$ ) by CID. We measured CID appearance curves and applied a center-of-mass correction to the derived  $E_{\text{LAB}}^{50\%}$  values (cf. Fig. 10). Experimental CID appearance curves of  $2^+\text{-Cl}$  and  $2^+\text{-OSO}_2\text{CF}_3$  exhibit the same slope, while  $2^+\text{-Br}$  and  $2^+\text{-I}$  show smaller slopes. Acetate anions are so weakly bound that only the activated complex of  $2^+$  occurs under ESI-MS conditions. This leads to a relative order of the phenomenological activation energy of the four substances:

$$E_{\text{COM}}^{50\%}(2^+\text{-OSO}_2\text{CF}_3) < E_{\text{COM}}^{50\%}(2^+\text{-Cl}) < E_{\text{COM}}^{50\%}(2^+\text{-Br}) < E_{\text{COM}}^{50\%}(2^+\text{-I})$$

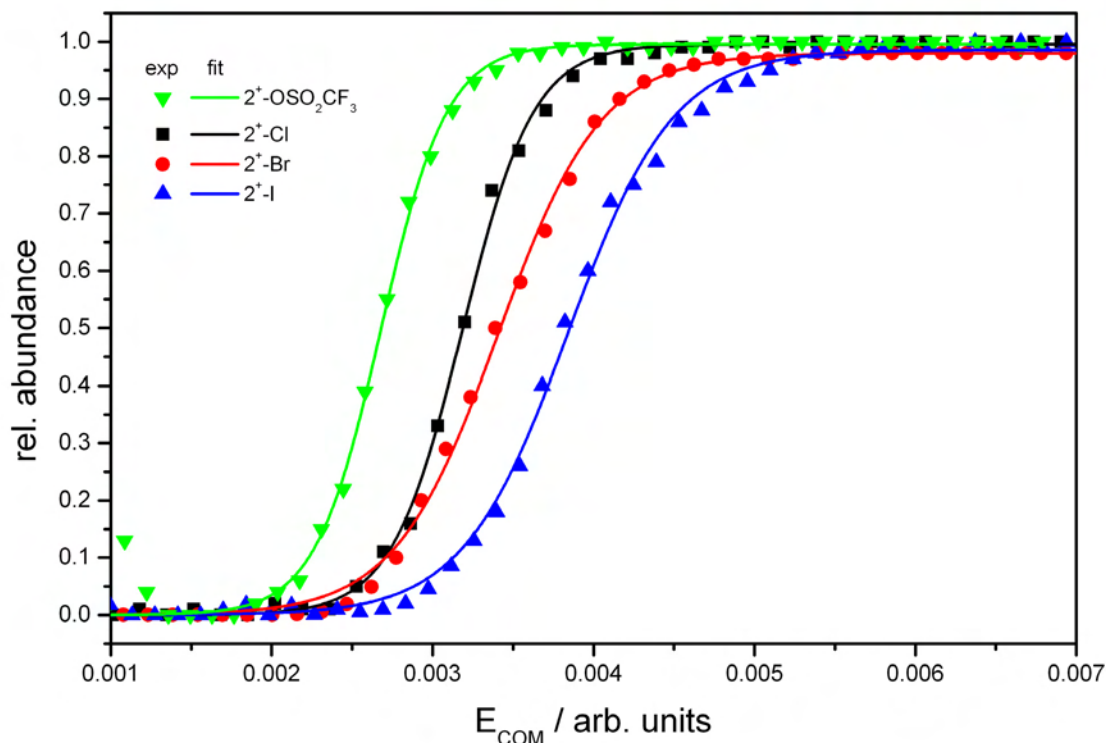


**Figure 10:** CID appearance curves for the loss of  $\text{HX}$  ( $\text{X} = \text{OSO}_2\text{CF}_3, \text{Cl}, \text{Br}, \text{I}$ ) from  $2^+\text{-OSO}_2\text{CF}_3$  ( $\blacktriangledown$ ),  $2^+\text{-Cl}$  ( $\blacksquare$ ),  $2^+\text{-Br}$  ( $\bullet$ ) and  $2^+\text{-I}$  ( $\blacktriangle$ ). Lines derived from sigmoidal fits of the measured values.

The  $E_{\text{COM}}^{50\%}$  value of  $2^+ \text{-Cl}$  (cf. Fig. 10) differs from the one derived from former measurements (cf. Fig. 6) because two different mass spectrometers were used for the two measurements.

#### VIII-4.1.2: Discussion and Conclusion

Due to the HSAB concept iodide is the most soft base, followed by bromide, while chloride,  $\text{CF}_3\text{SO}_3^-$  and  $\text{CH}_3\text{COO}^-$  are relatively hard bases. Although the ruthenium (II) cation can be seen as a compromise between “softness and acidity” [31]. In the present study ruthenium behaves as a soft base due to its size, its low oxidation state of +II in the complex and its ability to attach a p-cymene ligand, which is also a soft base. In addition, the  $\text{CF}_3\text{SO}_3^-$  anion has the largest size and is therefore the weakest bound substituent besides acetate anions. These experimental findings are in line with the HSAB concept.

### VIII-4.2: IR-MPD spectra of $[(\eta^6\text{-cymene})\text{RuCl}(\text{apypm})]^+$ catalysts

#### VIII-4.2.1: Experimental results

We measured IR-MPD spectra of cationic complexes  $1^+$  and  $2^+$  in order to elucidate their structures. The 1-color IR-MPD spectrum of complex  $1^+$  exhibits only a small peak at  $3476 \text{ cm}^{-1}$  (cf. Fig. 11, top). Using a 2-color scheme with a probe laser fixed at  $3476 \text{ cm}^{-1}$  gives an increase of this band and an additional band at  $2983 \text{ cm}^{-1}$  appears (cf. Fig. 11, mid, green line).

Probing this new band at  $2983 \text{ cm}^{-1}$  with a second laser (probe) delivers a third band at  $3345 \text{ cm}^{-1}$  (cf. Fig. 11, mid, red line). Those bands can be related to different CH and  $\text{NH}_2$  stretching modes. The band at  $3476 \text{ cm}^{-1}$  can be assigned to the asymmetric  $\text{NH}_2$ , the one at  $3345 \text{ cm}^{-1}$  to the symmetric  $\text{NH}_2$  and the one at  $2983 \text{ cm}^{-1}$  to an aromatic or aliphatic CH stretching mode.

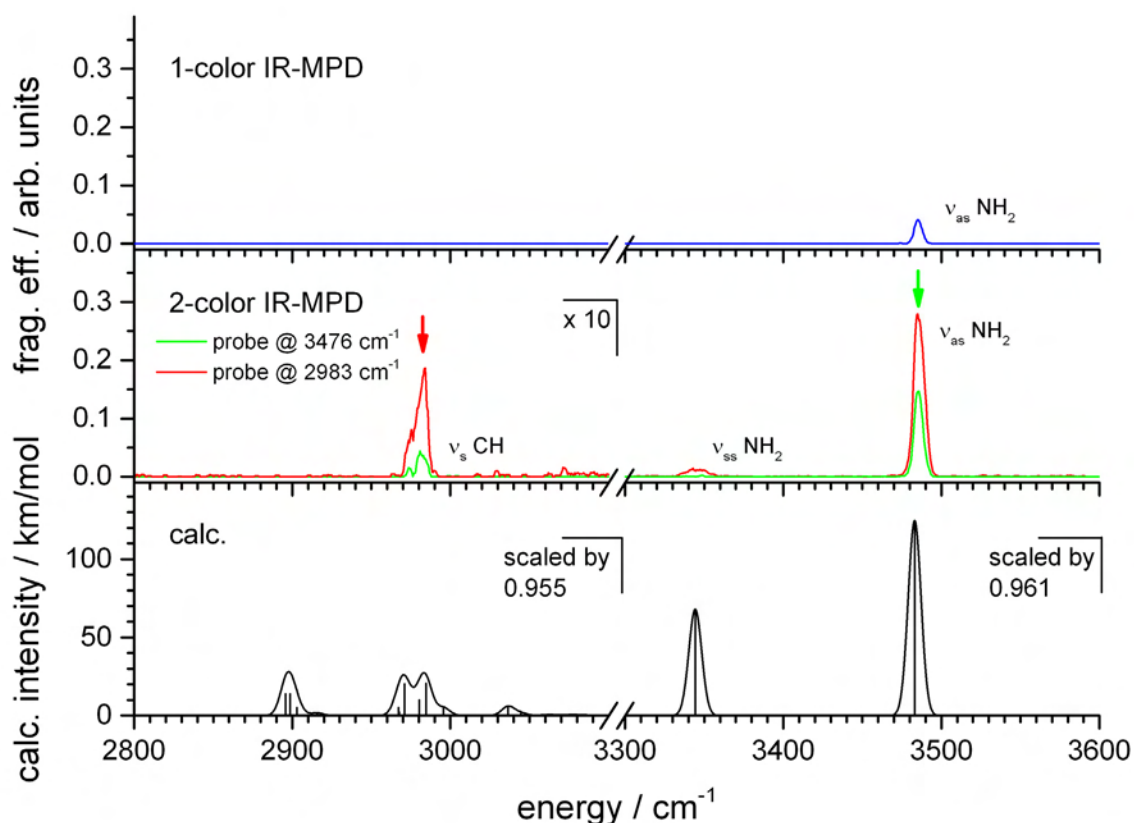


**Figure 11:** 1 (top) and 2-color (mid) IR-MPD spectra of  $\mathbf{1}^+$ . The green line arises from the pump laser while the probe laser is fixed at 3476  $\text{cm}^{-1}$  (green arrow), 2983  $\text{cm}^{-1}$  (red arrow) for the red line respectively. DFT predicted IR absorption spectrum of  $\mathbf{1}^+$  (bottom) at the B3LYP/cc-pVDZ (C, H, N, Cl) and Stuttgart 1997 ECP (Ru) level of theory, scaled by 0.961 (above 3200  $\text{cm}^{-1}$ ), 0.955 (under 3200  $\text{cm}^{-1}$ ) respectively. See Table 4 for numerical values of band peak positions and assignment of bands.

We used DFT calculations at the B3LYP/cc-pVDZ (C, H, N, Cl) and Stuttgart 1997 ECP (Ru) level of theory in order to predict linear IR absorption spectra. We obtained a scaling factor of 0.961 from the DFT predicted IR absorption spectrum of complex  $\mathbf{1}^+$  due to the position of the asymmetric and symmetric  $\text{NH}_2$  stretching mode within the experimental spectrum (cf. Fig. 11, bottom).

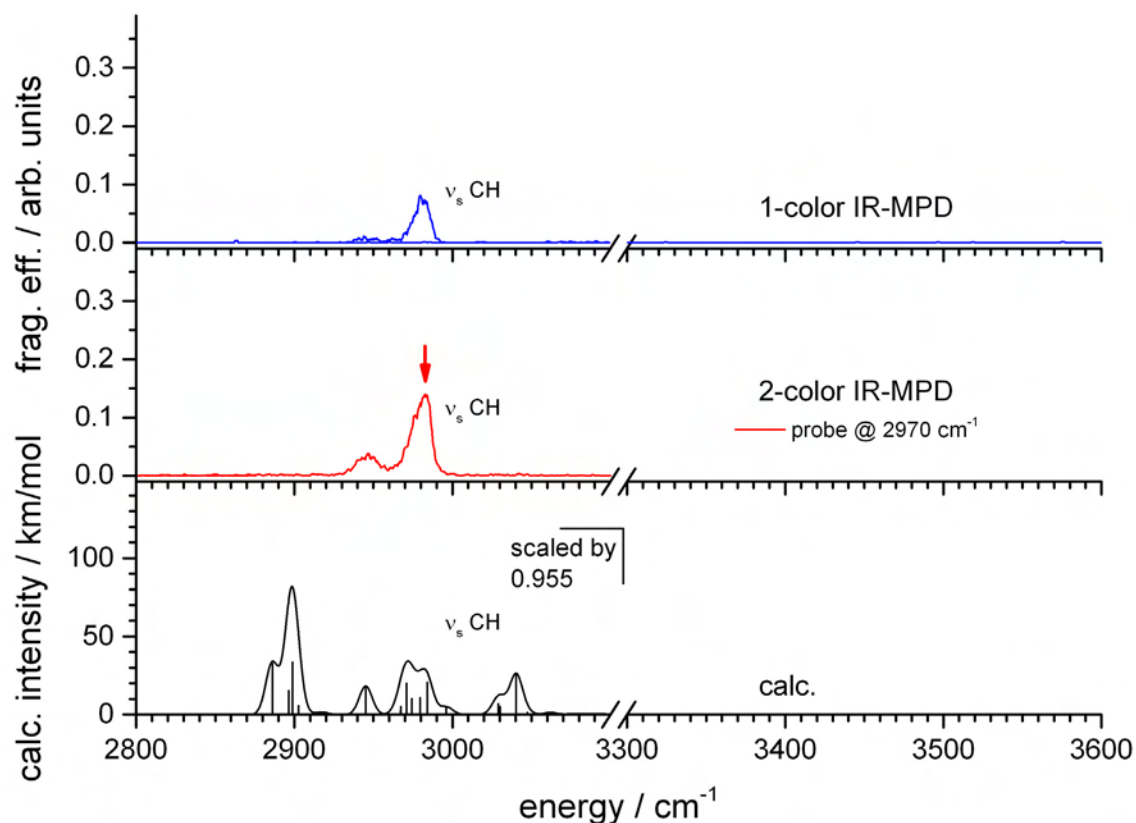


**Figure 12:** 1 (top) and 2-color (mid) IR-MPD spectra of  $2^+$ . The red line arises from the pump laser while the probe laser is fixed at  $2970\text{ cm}^{-1}$  (red arrow). DFT predicted IR absorption spectrum of  $2^+$  (bottom) at the B3LYP/cc-pVDZ (C, H, N, Cl) and Stuttgart 1997 ECP (Ru) level of theory, scaled by 0.955. See Table 4 for numerical values of band peak positions and assignment of bands.

The 1-color IR-MPD spectrum of  $2^+$  exhibits in contrast to the one of  $1^+$  two bands at  $2945$  and  $2980\text{ cm}^{-1}$  (cf. Fig. 12, top). Using a 2-color scheme with a probe laser fixed at  $2970\text{ cm}^{-1}$  increases both bands (cf. Fig. 12, mid, red line). We applied the determined scaling factor for the CH stretch region (0.955) to the DFT predicted IR absorption spectrum of cation  $2^+$  (cf. Fig. 12, bottom). This leads to a good agreement between the experimental and DFT predicted spectrum.



**Table 5:** Assignment of experimental derived bands to DFT predicted IR absorption bands (after scaling with 0.955 ( $< 3200 \text{ cm}^{-1}$ ), 0.961 ( $> 3200 \text{ cm}^{-1}$ ) respectively) of  $1^+$  and  $2^+$ . Values according to depicted data in Fig. 11 and 12. Some minor intense absorptions are not listed. Underlines indicate the atoms involved in the vibrational motions. (Abbreviations: calc. = calculated; cy = cymene; pyr = pyrimidine; ss = symmetric stretch; as = asymmetric stretch)

$1^+$			$2^+$		
IR-MPD / $\text{cm}^{-1}$	calc. / $\text{cm}^{-1}$	assignment	IR-MPD / $\text{cm}^{-1}$	calc. / $\text{cm}^{-1}$	assignment
				2887	$\nu_{\text{ss}}(\text{N}(\underline{\text{C}}\text{H}_3)_2)$
	2896	$\nu_{\text{ss}}(\text{cy}-\text{CH}(\underline{\text{C}}\text{H}_3)_2)$		2897	$\nu_{\text{ss}}(\text{N}(\underline{\text{C}}\text{H}_3)_2$ + $\text{cy}-\text{CH}(\underline{\text{C}}\text{H}_3)_2)$
	2899	$\nu_{\text{ss}}(\text{cy}-\text{CH}(\underline{\text{C}}\text{H}_3)_2)$		2901	$\nu_{\text{ss}}(\text{cy}-\underline{\text{C}}\text{H}_3)$
			2946	2945	$\nu_{\text{as}}(\text{N}(\underline{\text{C}}\text{H}_3)_2)$
	2967	$\nu_{\text{ss}}(\text{cy}-\underline{\text{C}}\text{H}_3)$		2967	$\nu_{\text{as}}(\text{cy}-\underline{\text{C}}\text{H}_3)$
2975	2971	$\nu_{\text{as}}(\text{cy}-\text{CH}(\underline{\text{C}}\text{H}_3)_2)$		2970	$\nu_{\text{as}}(\text{cy}-\text{CH}(\underline{\text{C}}\text{H}_3)_2)$
	2980	$\nu_{\text{as}}(\text{cy}-\text{CH}(\underline{\text{C}}\text{H}_3)_2)$	2976	2974	$\nu_{\text{as}}(\text{N}(\underline{\text{C}}\text{H}_3)_2)$
2984	2985	$\nu_{\text{as}}(\text{cy}-\text{CH}(\underline{\text{C}}\text{H}_3)_2)$		2978	$\nu_{\text{as}}(\text{cy}-\text{CH}(\underline{\text{C}}\text{H}_3)_2)$
	2996	$\nu_{\text{ss}}(\text{cy}-\underline{\text{C}}\text{H}_3)$		2983	$\nu_{\text{as}}(\text{cy}-\underline{\text{C}}\text{H}_3)$
	3037	$\nu_{\text{s}}(\text{pyr}-5\underline{\text{C}}\text{H})$		3029	$\nu_{\text{s}}(\text{N}(\underline{\text{C}}\text{H}_3)_2$ + $\nu_{\text{s}}(\text{pyr}-5\underline{\text{C}}\text{H})$
				3040	$\nu_{\text{as}}(\text{N}(\underline{\text{C}}\text{H}_3)_2) \rightarrow \text{Cl}$
3346	3343	$\nu_{\text{ss}}(\underline{\text{N}}\text{H}_2)$			
3485	3483	$\nu_{\text{as}}(\underline{\text{N}}\text{H}_2)$			

#### VIII-4.2.2: Discussion

Only a few of the bands predicted by DFT calculations could be detected from IR-MPD spectroscopy (cf. Fig. 11, 12). Therefore it is difficult to find a reliable assignment of bands. We used the intensity distribution and the shape of the derived bands in order to estimate appropriate scaling factors. The application of different scaling factors for the assignment of different vibrational modes within the IR-MPD spectra of  $1^+$  and  $2^+$  leads to a good agreement of measured and DFT predicted IR absorption bands, especially in case of the spectra of  $2^+$ . This scaling factor does not provide an exact position of the bands corresponding to CH stretching modes. Correlation of the most intense IR absorptions in the CH region ( $2950 - 3010 \text{ cm}^{-1}$  after scaling) to the experimental band at  $2983 \text{ cm}^{-1}$  yields a scaling factor of 0.955. A scaling factor of 0.97 was published for the B3LYP/cc-pVDZ level of theory [43]. This scaling factor would shift the DFT

predicted bands more to the blue and is therefore not applicable. The scaling factor of 0.955 correlates quite well to the factor 0.957 derived from the comparison of DFT predicted IR absorption spectra and experimental IR-MPD spectra in Chapter VI of this thesis.

The band at  $2984\text{ cm}^{-1}$  within the 2-color IR-MPD spectrum of  $1^+$  corresponds to an overlap of several asymmetric CH stretching modes of the methyl groups of the p-cymene ring (cf. Fig. 11 and Table 5). The band itself exhibits a small shoulder on the red side at  $2975\text{ cm}^{-1}$  which also corresponds to a combination of aliphatic CH stretching modes.

The band centered at  $2976\text{ cm}^{-1}$  within the 1- and 2-color IR-MPD spectrum of  $2^+$  also corresponds to an overlap of several asymmetric CH stretching modes of the methyl groups of the p-cymene ring at which also asymmetric CH stretching modes of the methyl groups of the dimethyl-amine group contribute (cf. Fig. 12 and Table 5). The band at  $2945\text{ cm}^{-1}$  corresponds also to an asymmetric CH stretching mode of the methyl groups of the dimethyl-amine group and can therefore not be detected in the spectrum of  $1^+$ . No fragmentation is caused by vibrational excitation of the stretch of the N-CH<sub>2</sub>-H proton in the direction to the Cl anion bound to the ruthenium atom. Neither a direct proton transfer to the Cl<sup>-</sup> anion takes place after vibrational excitation nor it induces a rotation of the pyrimidine ring unlike other asymmetric CH stretching modes. It is obvious within this assignment of bands that only asymmetric CH stretching modes on either ligand can be detected by IR-MPD.

Higher fragmentation efficiency in the CH stretch region of  $2^+$  compared to  $1^+$  may arise from the lower activation barrier for the loss of HCl from  $2^+$  which was also predicted by DFT calculations (cf. Table 3). Furthermore an additional photon absorption takes place at the dimethyl-amine group giving rise to bands according to its CH stretching modes.

While  $1^+$  needs 195 kJ/mol to reach the transition state,  $2^+$  needs only 151 kJ/mol (due to calculations in ). The photon energy at  $2980\text{ cm}^{-1}$  is by conversion 35.6 kJ/mol. Collisions with He thermalize the ions in the trap to approximately 300 K which corresponds to an enthalpy of approximately 65 kJ/mol stored in the degrees of freedom. As a rough estimation the ions have to absorb at least 3 photons in case of  $2^+$  and 4 photons in case of  $1^+$  in order to reach the transition state for the HCl loss. The photon energy at  $3476\text{ cm}^{-1}$  is by conversion 41.6 kJ/mol. This leads to a 3 photon absorption within the assumed approximation.

CID and IR-MPD experiments exhibit the same main fragmentation channel, the loss of HCl. CID results in an additional loss of H<sub>2</sub> for **1**<sup>+</sup> which cannot be observed within IR-MPD although asymmetric CH stretching modes could forward H<sub>2</sub> losses. IVR processes are fast compared to the subsequent absorption of multiple photons and energy cannot be stored locally which would be needed for an IR-MPD elimination of H<sub>2</sub> from **1**<sup>+</sup>.

### VIII-4.2.3: Conclusions

We achieved an enhancement of the most intense band by 2-color IR-MPD. Furthermore, the 2-color pump/probe scheme gave rise to an additional band which could not be detected in a one color scan of **1**<sup>+</sup>. The increase of a third band is of special interest because of two points. First, the irradiation with the probe laser at a frequency, which does not lead to a fragmentation, is capable to support the appearance of a new band. Second, the excitation of the symmetric NH<sub>2</sub> stretch does not support the appearance of the symmetric NH<sub>2</sub>. This either results from too low laser power at the frequency of the symmetric NH<sub>2</sub> stretch as a weak absorbing mode or from an ineffective coupling of energy into the torsional mode of the pyrimidine ring which corresponds to the dark bands of symmetric CH stretching modes.

## VIII-4.3: Gas phase reactions of [(η<sup>6</sup>-cymene)RuCl(apypm)]<sup>+</sup> catalysts

### VIII-4.3.1: Experimental results

ESI-MS provided cations of **M**<sup>+</sup> (M=**1-3**). We used a collision cell (integrated in the ion transfer path to the ICR cell) in order to fragment a fraction of the precursor molecules **M**<sup>+</sup> leading to activated **M**<sup>+</sup>(-HCl) complexes (loss of H<sup>35</sup>Cl, Δm=36; loss of H<sup>37</sup>Cl, Δm=38 m/z) in the corresponding mass spectra (cf. Fig. 13, 21 and 24, top). We performed gas phase reactions of the cationic complexes **M**<sup>+</sup> and their catalytical active complexes **M**<sup>+</sup>(-HCl) with collision gases D<sub>2</sub> (cf. Fig. 13, 21 and 24), D<sub>2</sub>O (cf. Fig. 14, 22 and 25) and CH<sub>3</sub>OH (no reaction observed) under single collision conditions (pressure in the range of 1 to 5 x 10<sup>-9</sup> mbar) in order to study their gas phase reaction behavior. We varied reaction delays from 0 to at least 240 s in varying steps in order to derive relative partial rate constants from a pseudo first order kinetic fit of relative intensities of the parent ions and their reaction products (cf. Fig. 15, 23, 26 and Table 5).

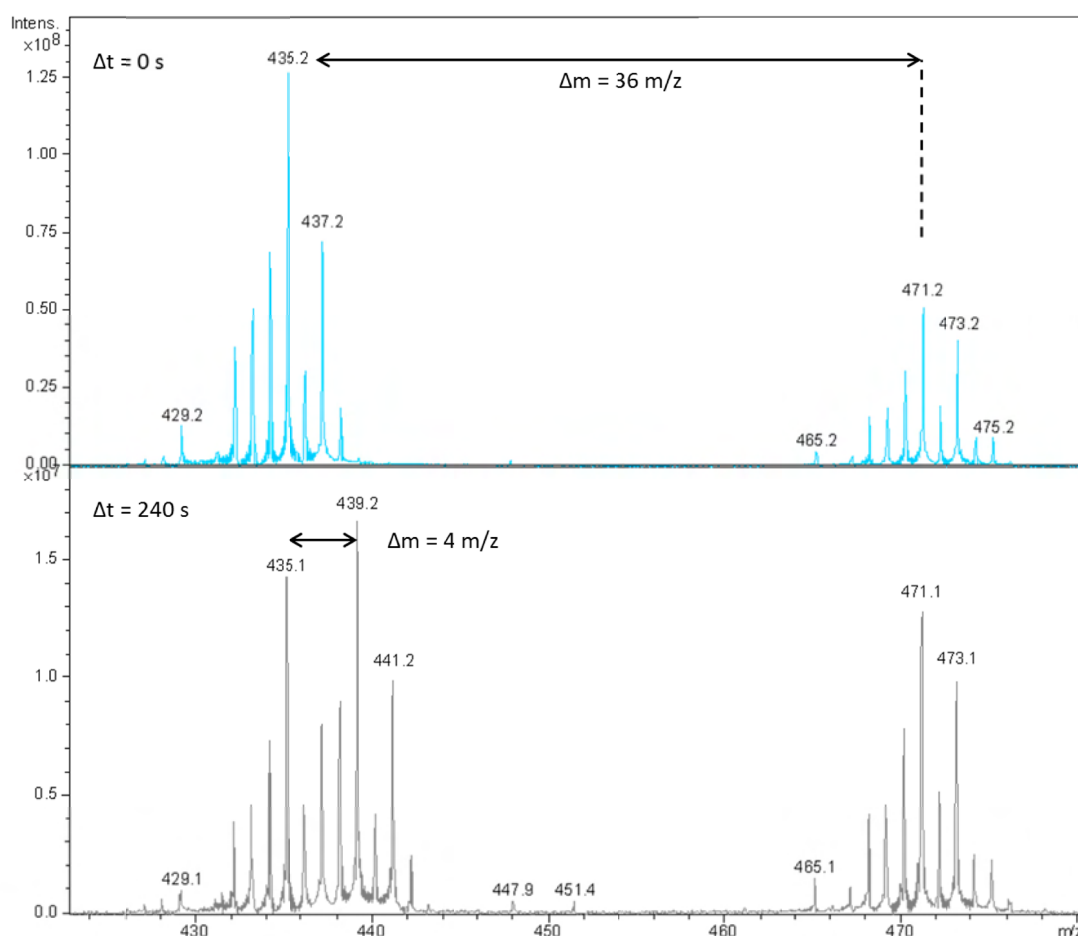


**Figure 13:** Section of the FT-ICR mass spectra of complexes  $2^+$  and  $2^+(-\text{HCl})$  at  $\Delta t = 0$  s (top) and after 240 s reaction time (bottom) with  $\text{D}_2$ . The isotope pattern at 471.2 m/z (most abundant mass) correlates to complex  $2^+$  and the one at 435.2 m/z (most abundant mass) to the activated complex  $2^+(-\text{HCl})$ . 439.2 m/z corresponds to the reaction product of complex  $2^+(-\text{HCl})$  with  $\text{D}_2$  ( $p = 5 \times 10^{-9}$  mbar,  $T = 298$  K).

The mass spectrum detected after 240 s delay for the reaction of  $\text{D}_2$  ( $p = 5 \times 10^{-9}$  mbar) with the activated species  $2^+(-\text{HCl})$  exhibits an overlay of an additional isotopic pattern (shift of +4 m/z) which corresponds to the addition of a  $\text{D}_2$  molecule (cf. Fig 13, bottom). The non activated complex  $2^+$  undergoes no reaction during the same reaction delay. We used  $\text{D}_2$  instead of  $\text{H}_2$  because a mass shift of +4 m/z (caused by addition of one  $\text{D}_2$  molecule) is easier to distinguish from the parent species than a shift of +2 m/z ( $\text{H}_2$ ) within the broad isotopic pattern of the parent species.

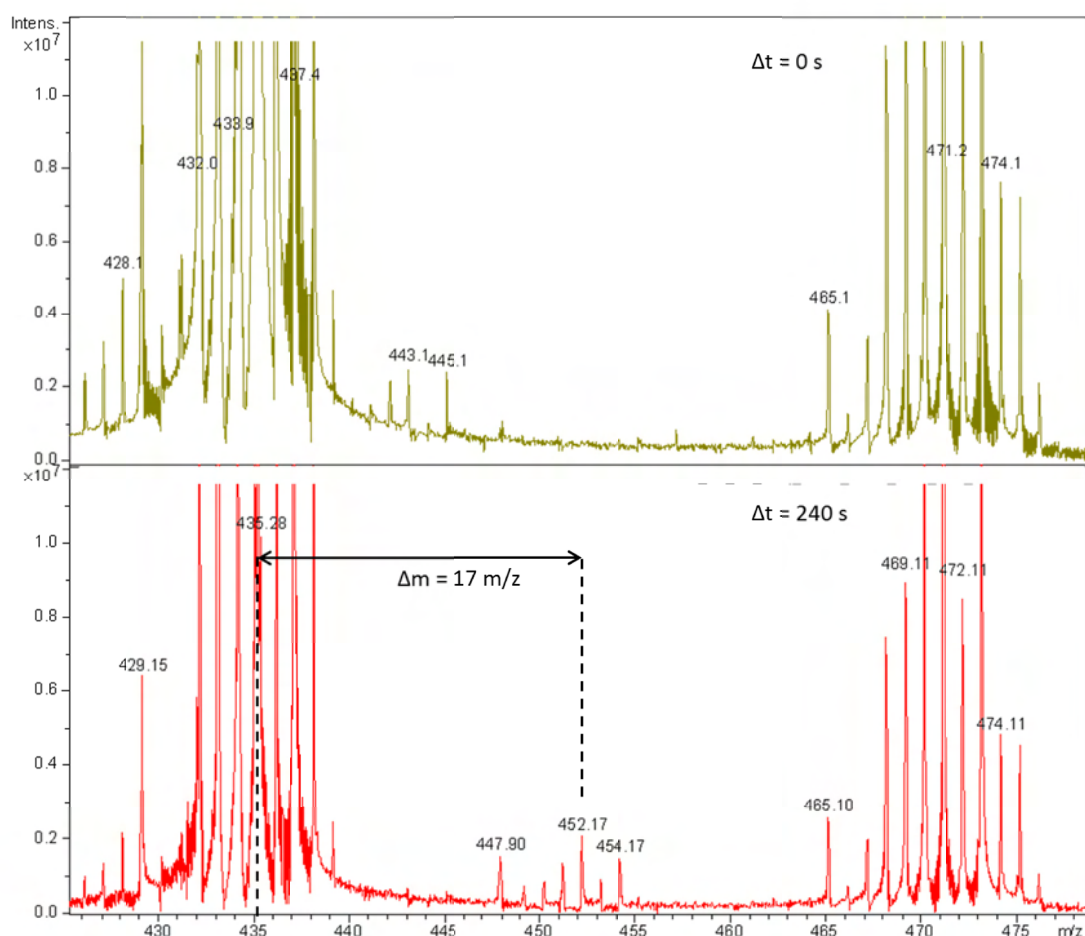


**Figure 14:** Section of the FT-ICR mass spectra of complexes  $2^+$  and  $2^+(-\text{HCl})$  at  $\Delta t = 0$  s (top) and after 240 s reaction time (bottom) with  $\text{D}_2\text{O}$  ( $p = 1 \times 10^{-9}$  mbar,  $T = 298$  K). The isotope pattern at 471.2 m/z (most abundant mass) correlates to complex  $2^+$  and the one at 435.2 m/z (most abundant mass) to the activated complex  $2^+(-\text{HCl})$ . Spectra are enlarged to highlight the isotopic pattern at 452.2 m/z (most abundant mass) corresponding to an addition of OD to complex  $2^+(-\text{HCl})$ . (cf. Fig. 13 for the full intensity distribution of the isotope pattern of  $2^+(-\text{HCl})$ )

We carried out gas phase reactions with  $\text{D}_2\text{O}$  in order to check if water can be bound to the cationic catalysts  $\text{M}^+$  and/or their activated species  $\text{M}^+(-\text{HCl})$ . Furthermore, it is known that  $\text{D}_2\text{O}$  is capable to exchange acidic protons like those of the amino-group of  $1^+$ . Gas phase reactions with  $\text{D}_2\text{O}$  ( $1 \times 10^{-9}$  mbar) led to the appearance of a mass of shift of  $\Delta m = +17$  m/z with respect to the activated precursor ions  $\text{M}^+(-\text{HCl})$  while  $\text{M}^+$  undergoes no reaction with  $\text{D}_2\text{O}$  (cf. Fig. 14, 22 and 25). A H/D exchange reaction with  $\text{D}_2\text{O}$  can neither be observed for catalyst  $1^+$  nor for the activated species  $1^+(-\text{HCl})$ .

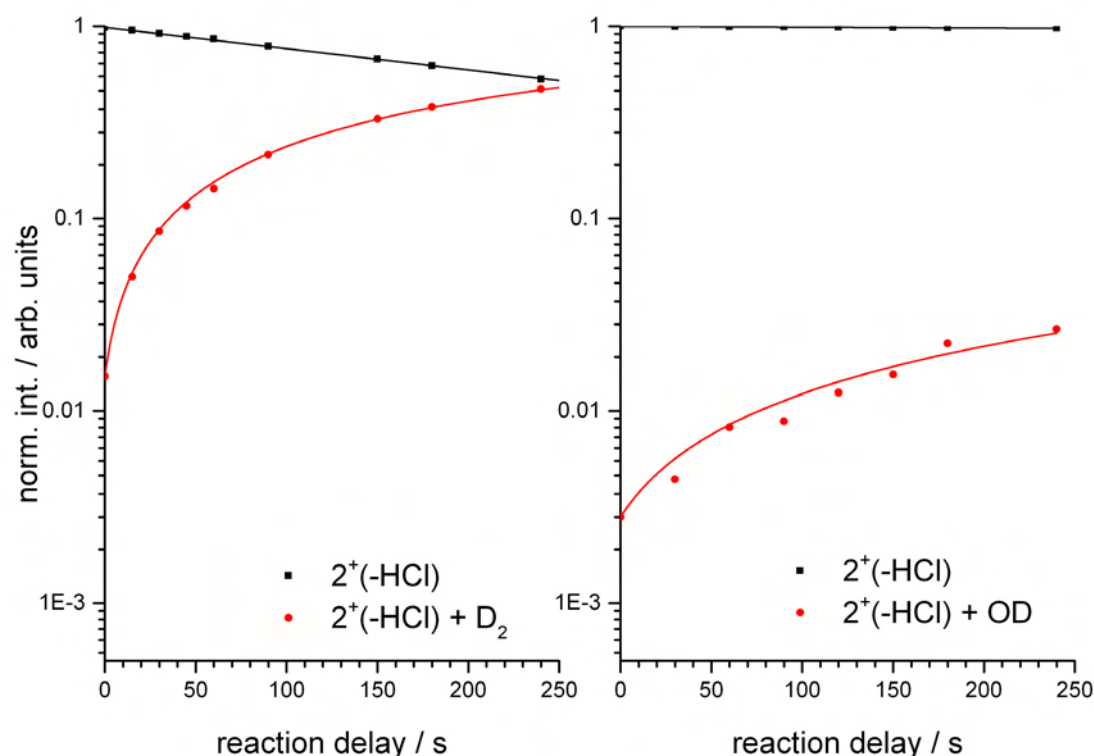


**Figure 15:** Normalized reactant (437  $m/z$  isotope (●)) and product (441  $m/z$  isotope (●)) intensities in the reactions of catalyst  $2^+(-\text{HCl})$  with  $\text{D}_2$  ( $p = 5 \times 10^{-9}$  mbar,  $T = 298$  K) (a). Normalized reactant (437  $m/z$  isotope (●)) and product (454  $m/z$  isotope (●)) intensities in the reactions of catalyst  $2^+(-\text{HCl})$  with  $\text{D}_2\text{O}$  ( $p = 1 \times 10^{-9}$  mbar) (b). The temporal evolution of the experimental data points (symbols) is fitted to pseudo first order kinetics (solid lines) which provides for relative partial rate constants. Fits correlate to single  $\text{D}_2$  addition reactions (a) and to reactions leading to an addition of  $\text{D}_2\text{O}$  under subsequent loss of HD (b) per single collision. Fits arise through application of generic algorithm code. (cf. Table 5 for numerical data)

**Table 6:** Relative partial rate constants  $k$  and standard deviations ( $\times 10^{-3}$ , arb. units) by single  $\text{D}_2$  addition per collision of  $\text{M}^+(-\text{HCl})$  ( $X=1-3$ ) with  $\text{D}_2$  ( $p= 5 \times 10^{-9}$  mbar) in the gas phase as obtained from fitting experimental data ( $k(\text{D}_2)$ ) and by addition of  $\text{D}_2\text{O}$  under subsequent loss of HD per collision of  $1^+-3^+$  with  $\text{D}_2\text{O}$  ( $p= 1 \times 10^{-9}$  mbar) ( $k(\text{D}_2\text{O})$ ) (cf. Fig. 15, 23 and 26).

catalytical active complex	$k(\text{D}_2)$	$k(\text{D}_2\text{O})$
$1^+(-\text{HCl})$	$2.2 \pm 0.3$	$0.30 \pm 0.01$
$2^+(-\text{HCl})$	$1.2 \pm 0.2$	$0.11 \pm 0.01$
$3^+(-\text{HCl})$	$2.5 \pm 0.2$	$0.10 \pm 0.01$

Relative partial rate constants for the reaction of  $1^+(-\text{HCl})$  and  $3^+(-\text{HCl})$  with  $\text{D}_2$  are comparable while those for  $2^+(-\text{HCl})$  are approximately two times lower (cf. Table 6).  $1^+(-\text{HCl})$  undergoes the

fastest reaction with D<sub>2</sub>O. Relative partial rate constants for the reactions of **2<sup>+</sup>(-HCl)** and **3<sup>+</sup>(-HCl)** with D<sub>2</sub>O approximately three times lower.

#### VIII-4.3.2: Discussion and conclusions

We used the peak intensities of correlating educt and product isotopes which can clearly be separated within the shift of the overall isotopic pattern (cf. Fig. 13, bottom) for the pseudo first order fit. Especially the peak at 437 m/z (for **2<sup>+</sup>(-HCl)**) is neither influenced by minor isotopes masses +4 m/z (due to D<sub>2</sub> addition) nor does it overlap with higher isotopes. Nevertheless we calculated rate constants with different isotope pairs to estimate standard deviations (cf. Table 5). The linear behavior (in a logarithmic plot) of the decrease of the catalytical active complex (cf. Fig. 15) confirms the assumption of a pseudo first order reaction process.

The temperature of the apparatus was approximately 300 K. Collisions of the ions with remaining gas molecules during the transfer to the ICR cell lead to a thermal equilibrium. We assume the same temperature for the reaction gas due to a long equilibration time with the surrounding walls of the vacuum chamber. Due to the weak binding energy of D<sub>2</sub> we do not assume a physisorption under this reaction conditions. The addition of D<sub>2</sub> to the catalytical active complex can be assigned to a disproportional split of the dihydrogen bond leading to a cationic D<sup>+</sup> and an anionic D<sup>-</sup>. We assume here the protonation of the 6C position of the pyrimidine ring and an nucleophilic addition of a deuterium anion to the ruthenium atom. This can be considered as the reverse reaction of the HCl loss, where D<sub>2</sub> takes the place of the former H and Cl atoms. The proof of the conformation of the proposed products of the D<sub>2</sub> addition would be carried out by IR-MPD spectroscopy.

In a simple addition of D<sub>2</sub>O a mass shift of +20 m/z would be expected. A shift of +17 m/z can be explained by the addition of OD and the simultaneous loss of HD. Interestingly D<sub>2</sub>O showed neither with the non activated nor the activated cation of **1<sup>+</sup>(-HCl)** a H/D exchange with the two amino protons (cf. Fig. 22). We can rule out the possibility of an OD insertion and a simultaneous loss of DCl in the sense of a collisional activation. This mechanism would lead to a mass loss of -19 m/z (most abundant masses) starting from the non-activated species which is +2 m/z higher in mass than the observed species.

### VIII-5: DFT based modeling of the reaction of $[(\eta^6\text{-cymene})\text{RuCl}(\text{apypm})]^+$ catalysts with $\text{D}_2$ and $\text{D}_2\text{O}$

We used a DFT based modeling of the reaction of activated  $[(\eta^6\text{-cymene})\text{RuCl}(\text{apypm})]^+$  catalysts  $\text{M}^+(\text{-HCl})$  ( $\text{M}=\mathbf{1-3}$ ) with  $\text{D}_2$  in order to relate partial rate constants derived from experiments to rate constants according to the Arrhenius equation and to transition state theory. A DFT based modeling of the HCl loss from  $[(\eta^6\text{-cymene})\text{RuCl}(\text{apypm})]^+$  served as a starting point for exploration of local minima and transition states within the reaction coordinate of the  $\text{D}_2$  addition to  $\text{M}^+(\text{-HCl})$  [1].

#### VIII-5.1: Results from DFT calculations for the reaction of $\text{M}^+(\text{-HCl})$ with $\text{D}_2$

We derived local minimum and transition state structures and corresponding relative energies and (free) enthalpies of the  $\text{D}_2$  addition to the catalytical active complexes  $\text{M}^+(\text{-HCl})$  ( $\text{M}=\mathbf{1-3}$ ) from DFT calculations at the B3LYP/cc-pVTZ (H, D, C, N) and Stuttgart 1997 ECP (Ru) level of theory (cf. Fig. 16, 27 and 28).

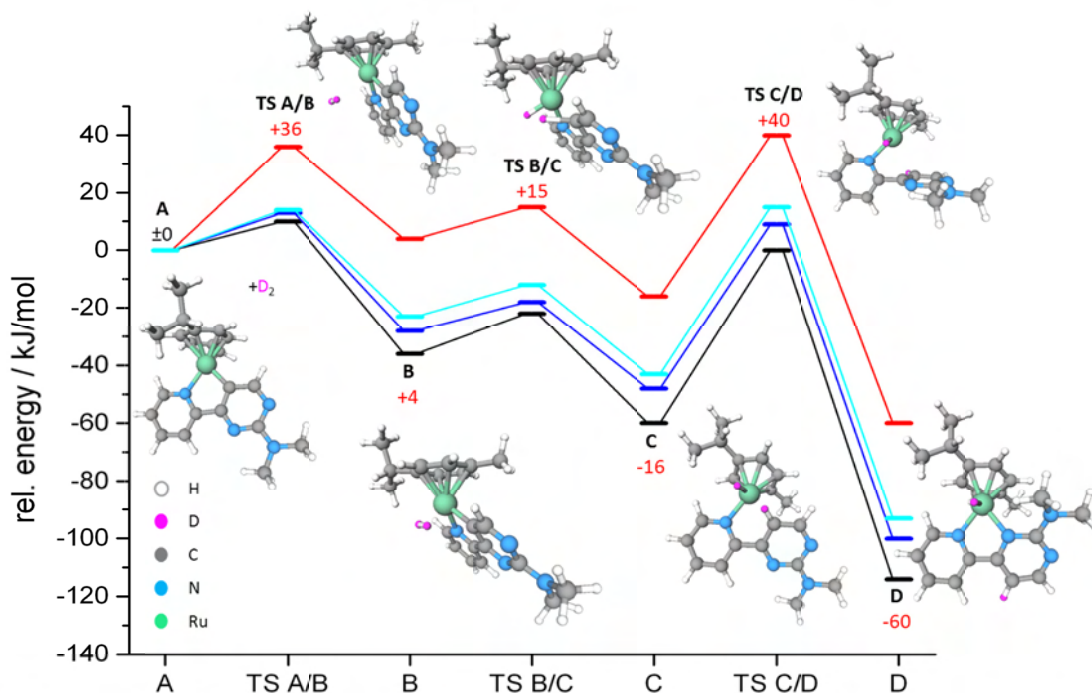


**Figure 16:** Reaction coordinate of  $\text{D}_2$  insertion at the catalytical active complex  $\mathbf{2}^+(\text{-HCl})$ . Structures derived from DFT calculations at the B3LYP/cc-pVTZ (H, D, C, N) and Stuttgart 1997 ECP (Ru) level of theory. (—) exhibits the uncorrected DFT energies, (---) zero-point energies, (····) thermal corrected (RT) energies and (---) free enthalpies (corresponding values labeled in red). The energy scale (in kJ/mol) is relative to the separated molecules  $\mathbf{2}^+(\text{-HCl})$  and  $\text{D}_2$  set to zero. **A**, **B**, **C** and **D** indicate local DFT energy minimum structures, **TS** indicates a transition state between adjacent minima. (cf. Table 6 for numerical data)

$\text{D}_2$  approaches the conformation **A** of  $\mathbf{2}^+(\text{-HCl})$  which corresponds to the energetic minimum



structure of the catalytical active complex. The molecules have to pass a barrier of +36 kJ/mol (transition state **TS A/B**) which arises from the change in the angle between the ring planes. Structure **B** is +4 kJ/mol less stable in free enthalpy than the separated molecules and exhibits an increase of the D(1)-D(2) bond length (cf. Fig. 17) and also a slight increase of the Ru-C distance.

DFT energies give a local minimum **B** and a corresponding transition state **TS B/C**. The split of D<sub>2</sub> takes place at **TS B/C** where the distances of D(1)-D(2), D(1)-Ru and D(2)-C reach the same value. This transition state is +11 kJ/mol higher in free enthalpy than **B** (cf. Table 6). The shortening of the C-D bond and a change of the dihedral angle in the *apypm* ligand (cf. Fig. 17, step **C**) lead to structure **C** which is -16 kJ/mol more stable in free enthalpy than structure **B**. The rotation of the pyrimidine ring is hindered by a high transition state **TS C/D** of +40 kJ/mol in respect to **C**. **TS C/D** is +4 kJ/mol higher in free enthalpy than the **TS A/B**, while it is -4 kJ/mol lower in thermal energy. The product **D** is -60 kJ/mol more stable in free enthalpy than the separated molecules. DFT derived free enthalpies of the reaction of complexes **M<sup>+</sup>(-HCl)** (M = 1, 2, 3) with D<sub>2</sub> are summarized in Table 7.

**Table 6:** DFT derived relative energies and free enthalpies for reaction steps during the D<sub>2</sub> insertion at **2<sup>+</sup>(-HCl)** at the B3LYP/cc-pVTZ (H, D, C, N) and Stuttgart 1997 ECP (Ru) level of theory (cf. Fig. 16).

reaction step	DFT energy / kJ/mol	Zero-point energy / kJ/mol	Thermal energy / kJ/mol	Free enthalpy / kJ/mol
A	0	0	0	0
TS A/B	10	14	13	36
B	-36	-23	-28	4
TS B/C	-22	-12	-18	15
C	-60	-43	-48	-16
TS C/D	0	15	9	40
D	-114	-93	-100	-60

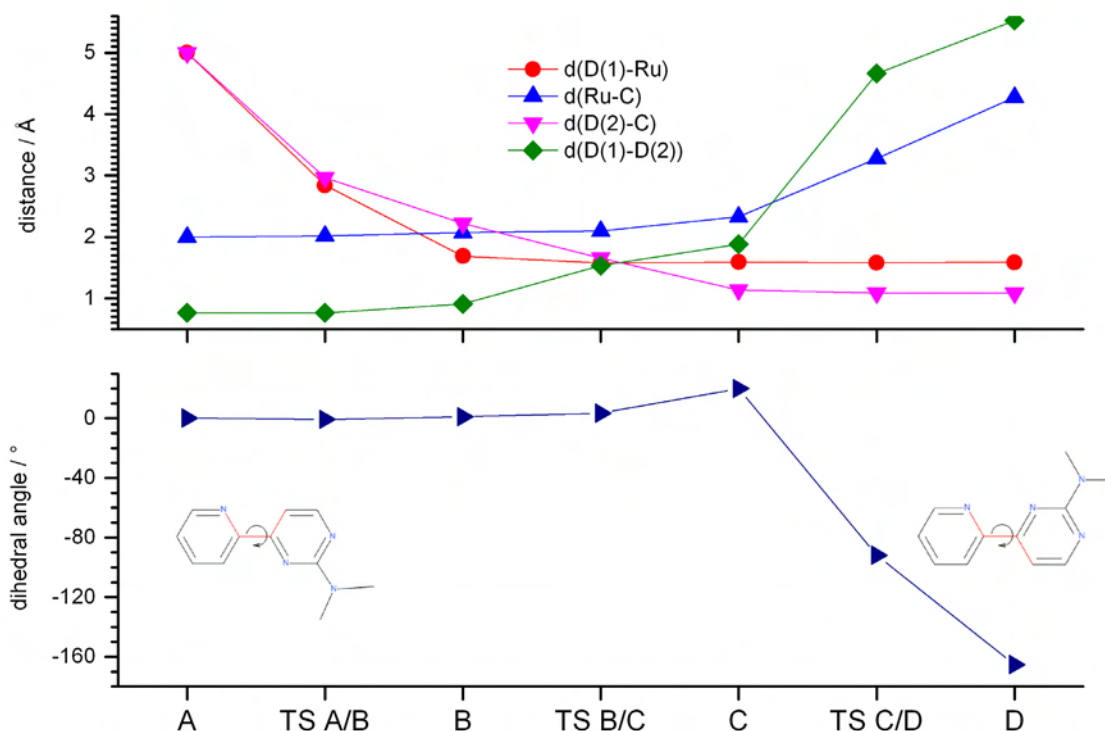


**Figure 17:** Selection of DFT (B3LYP/cc-pVDZ (H, D, C, N) and Stuttgart 1997 ECP (Ru) level of theory) derived atom distances (top) and dihedral angle (bottom) defined by N-C-C-C (red lines within the insets) during  $D_2$  insertion at the catalytical active complex of  $2^+(-HCl)$ . D(1) corresponds to the deuterium anion which is added to the Ru atom, D(2) to the deuterium cation added to the pyrimidine ring C6 atom (bound to Ru in step A).

**Table 7:** DFT derived free enthalpies (kJ/mol; 298.15 K) for reaction steps during the  $D_2$  insertion at  $M^+(-HCl)$  ( $M=1-3$ ) at the B3LYP/cc-pVTZ level of theory (cf. Fig. 16, 27 and 28).

reaction step	$1^+(-HCl)$	$2^+(-HCl)$	$3^+(-HCl)$
A	0	0	0
TS A/B	18	36	27
B	-18	4	-7
TS B/C	-13	15	6
C	-30	-16	-28
TS C/D	22	40	32
D	-118	-60	-71

We estimated relative rate constants for the reaction of complexes  $\mathbf{M}^+(\text{-HCl})$  with  $\text{D}_2$  in order to compare the DFT derived free enthalpies to experimental data (cf. Table 6, 7 and 8 and page 188 for formular). We assume constant pre-exponential coefficients and RT conditions for the calculations. We used free enthalpies of the highest transition state in the reaction coordinate of the  $\text{D}_2$  insertion as free enthalpies of activation.

**Table 8:** Rate constants due to transition state theory (TST) estimated by DFT derived free enthalpies (kJ/mol; 298.15 K) for the highest transition states *TS C/D* during the  $\text{D}_2$  insertion at  $\mathbf{M}^+(\text{-HCl})$  ( $\text{M}=\mathbf{1-3}$ ) (cf. Table 7). Cf. Table 6 for relative partial rate constants derived from pseudo first order kinetic fits of experimental data.

rate constant	$\mathbf{1}^+(\text{-HCl})$	$\mathbf{2}^+(\text{-HCl})$	$\mathbf{3}^+(\text{-HCl})$
$k_{\text{A-TS C/D}}$	$6 \times 10^{-4}$	$5 \times 10^{-7}$	$2 \times 10^{-5}$

$\mathbf{2}^+(\text{-HCl})$  exhibits the highest transition state for the reaction with  $\text{D}_2$  in DFT derived free enthalpy within the reactions of  $\mathbf{M}^+(\text{-HCl})$  with  $\text{D}_2$  and therefore the lowest rate constant within the transition state theory model (cf. Table 8).  $\mathbf{1}^+(\text{-HCl})$  yields the highest rate constant, followed by  $\mathbf{3}^+(\text{-HCl})$ .

#### VIII-5.2: Results from DFT calculations for the reaction of $\mathbf{2}^+(\text{-HCl})$ with $\text{D}_2\text{O}$

We derived several possible structures from DFT calculations, taking the OD insertion and subsequent loss of HD to  $\mathbf{2}^+(\text{-HCl})$  into account (cf. Fig. 18). None of the calculated structures is lower in energy than the separated molecules. Therefore we can not propose a suitable explanation of the observed reaction behavior.

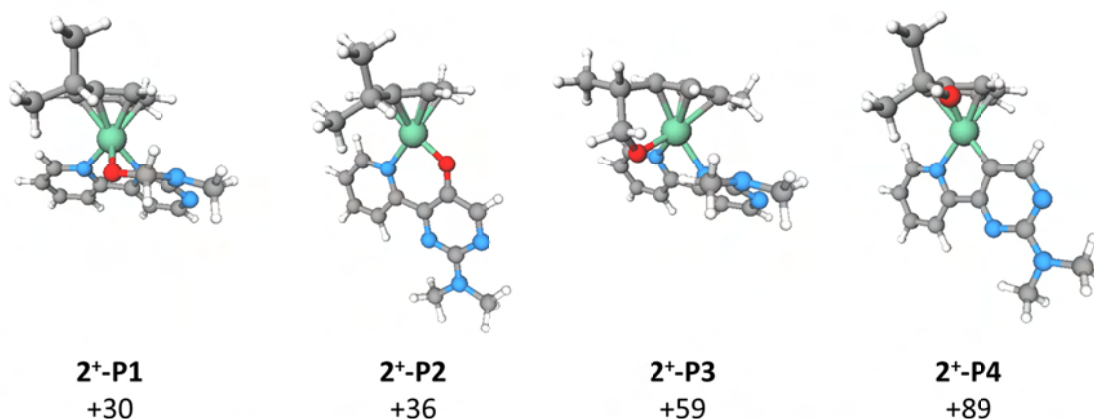


**Figure 18:** Selection of possible reaction products of activated  $\mathbf{2}^+(\text{-HCl})$  with  $\text{D}_2\text{O}$  during loss of OD and DFT energies in kJ/mol relative to the separate molecules.

### VIII-5.3: Relation of experimental results from gas phase reactions with data derived from DFT modeling

DFT based modeling of the reaction of  $[(\eta^6\text{-cymene})\text{RuCl}(\text{apypm})]^+$  catalysts with  $\text{D}_2$  exhibits three transition states for the nucleophilic addition of anionic  $\text{D}^-$  to the ruthenium atom and the electrophilic addition of  $\text{D}^+$  to the C6 atom of the pyrimidine ring (cf. Fig. 16, 27 and 28 and Table 7 for numerical values). The transition state *TS B/C* for the split of the di-deuterium molecule is lower in free enthalpy than the transition state *TS A/B* for the approach of  $\text{D}_2$  to the ruthenium atom and also lower than the transition state *TS B/C* for the rotation of the pyrimidine ring to yield the reaction product **D**. The latter both can therefore be considered as the rate determining steps of the reaction.

Relative rate constants derived from pseudo first order kinetic fits of experimental data for the addition of  $\text{D}_2$  at complexes **1<sup>+</sup>(-HCl)** and **3<sup>+</sup>(-HCl)** are similar while the one of **2<sup>+</sup>(-HCl)** is two times lower (cf. Table 6). Rate constants calculated due to transition state theory (TST) differ in several orders of magnitude under the assumption of constant pre-exponential factors (cf. Table 8). Nevertheless, the TST derived rate constant of the  $\text{D}_2$  addition to **2<sup>+</sup>(-HCl)** is significantly lower than the ones of **1<sup>+</sup>(-HCl)** and **3<sup>+</sup>(-HCl)** and can be compared qualitative to the experimental data. Assuming the insertion of  $\text{D}_2$  to the ruthenium complexes as a reversed HCl elimination process, it is striking that **1<sup>+</sup>(-HCl)** and **3<sup>+</sup>(-HCl)** show comparable reaction rates for the addition of  $\text{D}_2$  while the DFT derived free enthalpies of activation for the elimination of HCl differ about 42 kJ/mol (cf. Table 3). Within the  $\text{D}_2$  addition reaction two enthalpic comparable transition states have to be passed, an early one (*TS A/B*) slightly lower in energy and a late one (*TS C/D*) slightly higher in energy. Within the HCl elimination reaction (cf. Fig. 19, taken from [1]) the enthalpic barrier to reach the first transition state is comparable to the yield of enthalpy during the last step of the  $\text{D}_2$  insertion (*TS C/D*  $\rightarrow$  **D**) (cf. Fig. 16, 27 and 28 and Table 7), the rotation of the pyrimidine ring. The second and third transition states are the rate determining steps of the HCl elimination and clearly higher in enthalpy than **TS1** (cf. Fig. 19). It can be assumed that the attraction of the ruthenium atom to the dipolar HCl is stronger than the attraction to the nonpolar  $\text{D}_2$  molecule.

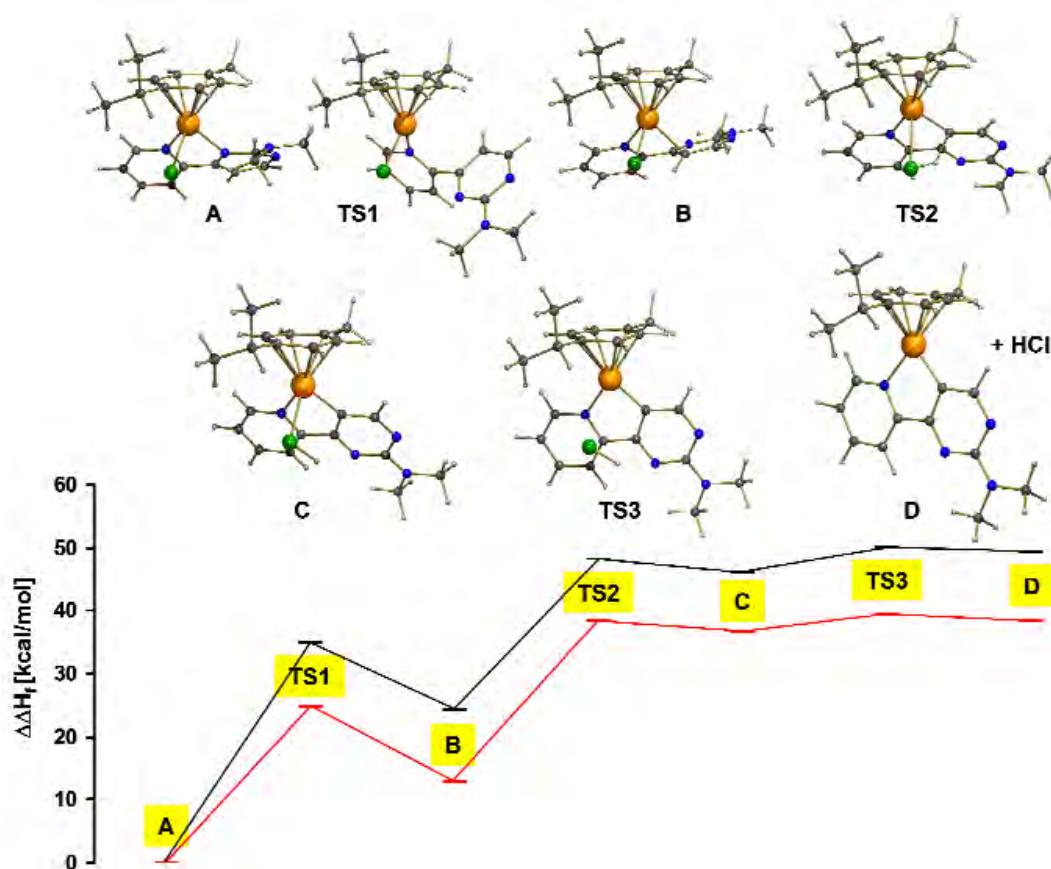


**Figure 19:** “Calculated geometries leading to the elimination of HCl from the cation  $2h^+$ ; calculated enthalpies  $\Delta\Delta H_f$  (kcal/mol) for the cations  $2h^+$  (red line) and  $2a^+$  (black line)” (Fig. and caption taken from [1]). “ $2a^+$ ” equates to  $1^+$  and “ $2h^+$ ” to  $2^+$  within the used nomenclature (cf. Table 4). Conversion factor from kcal/mol to kJ/mol: 4.12

In the reaction with  $D_2O$ ,  $2^+(-HCl)$  and  $3^+(-HCl)$  exhibit the same reaction rate while  $1^+(-HCl)$  reacts three times faster. Due to varying pressures and gases with different ionization potentials (significant for pressure measurement) we cannot carry out a quantitative comparison between the rate constants for the reactions with  $D_2$  and  $D_2O$ . We can not propose a mechanism for the simultaneous OD addition and HD loss only from gas phase reactions. Useful information could be achieved by IR-MPD spectroscopy of the reaction products which are yet not available.

We added the observed gas phase reactions to the proposed reaction scheme (cf. Fig. 1) in order to combine reaction models derived from reactions in solution and in the gas phase (cf. Fig. 20).

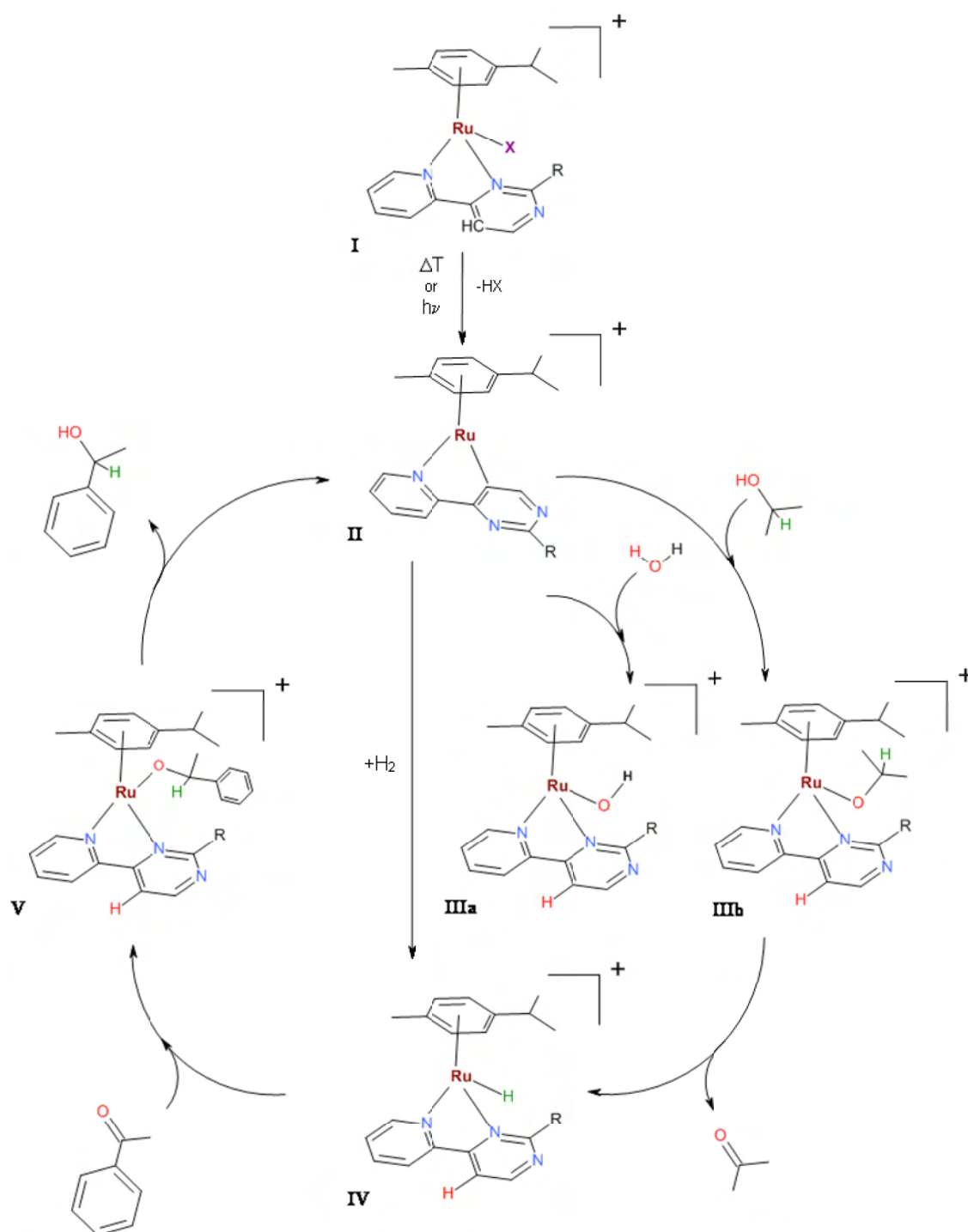


**Figure 20:** Proposed activation mechanism for catalysts **1**<sup>+</sup>, **2**<sup>+</sup> and **3**<sup>+</sup> ( $[(\eta^6\text{-cymene})\text{RuX}(\text{apypm})]^+$ ; R = NH<sub>2</sub> (**1**), N(CH<sub>3</sub>)<sub>2</sub> (**2**), NC<sub>4</sub>H<sub>8</sub> (**3**); X = I, Br, Cl, CF<sub>3</sub>SO<sub>3</sub>, CH<sub>3</sub>COO) (**I** → **II**) and reaction mechanism for a transfer hydrogenation from isopropanol to acetophenone catalyzed by the activated catalyst species **II** (**1**<sup>+</sup>(-HX), **2**<sup>+</sup>(HX), **3**<sup>+</sup>(-HX)). Pathway from **II** to **IIIa** shows the addition of water. Reaction of H<sub>2</sub> with **II** leads directly to **IV**.

## VIII-7: Conclusions

We studied several ruthenium catalysts for transfer hydrogenation reactions with a multitude of methods in order to elucidate the activation process, its gas-phase structure and its reaction behavior. CID measurements on isotopic labeled species led to the following conclusion about the activation process of the catalyst: a nitrogen-ruthenium bond is broken, the pyrimidine ring of the substituted 2-R-4-(2-pyridinyl)pyrimidine ligand rotates about  $160^\circ$  and a carbon-ruthenium bond is formed under subsequent loss of a HCl (or DCl) molecule.

A systematic variation of CID fragmentation amplitudes led to a phenomenological order of activation energies for catalysts with three differently substituted *apypm* ligands[1]. The mass spectrometers CID amplitude was calibrated with a set of “thermometer ions”. CID breakdown curves were used for determination of  $E_{\text{com}}^{50\%}$  values of the three catalysts under study. Finally, activation energies were estimated by means of the calibration. The resulting activation energies showed a qualitative correlation to DFT derived activation energies. These results are part of a manuscript which was submitted to *Chemistry – A European Journal* and is currently in the review process [1].

Further studies on this series of transition metal complexes included CID on ligand exchanged species, 1- and 2-color IR-MPD spectroscopy, gas phase reactions with  $D_2$  and DFT based modeling of the reaction coordinate of the  $D_2$  insertion. The exchange of the anionic chlorido ligand in solution led to three complexes with different fragmentation thresholds. CID derived activation amplitudes correspond well to the order predicted by the hard/soft acids/bases (HSAB) concept.

1-color IR-MPD experiments on two complexes showed only a few bands. Resonant 2-color IR-MPD increased the overall fragmentation efficiency and uncovered several dark bands. DFT derived IR absorption spectra correlate well to IR-MPD spectra while some bands are still not observable.

Gas phase reactions with  $D_2$  showed an increase of the mass of the activated complex of +4 m/z. This was interpreted in terms of an incorporation of a  $D_2$  molecule under heterolytic cleavage of the  $D_2$  molecule and can be compared to a back reaction of the activation. The reaction coordinate of the  $D_2$  incorporation was modeled with DFT at the B3LYP/cc-pVTZ level of theory and different activation energies were derived dependent on the substituent. Reactions of three differently

substituted complexes with  $D_2$  resulted in different relative partial rate constants. The comparison to rate constants derived from transition state theory showed a qualitative but not quantitative correlation to the experimental results. This study contributes to our ongoing work on the assignment and isolation of reaction intermediates in the gas phase. Studies on the dynamics of the activation process are on the way as well as an estimation of rate constants for the  $D_2$  insertion using RRKM theory.



**VIII-8: References**

1. Ghoochany, L.T., et al., *C-H Activation at a ruthenium(II) complex: The key step for a base free catalytic transfer hydrogenation*. European Journal of Inorganic Chemistry, accepted.
2. Ikariya, T., K. Murata, and R. Noyori, *Bifunctional transition metal-based molecular catalysts for asymmetric syntheses*. Organic & Biomolecular Chemistry, 2006. **4**(3): p. 393-406.
3. Zassinovich, G., G. Mestroni, and S. Gladiali, *Asymmetric Hydrogen Transfer Reactions Promoted by Homogeneous Transition Metal Catalysts*. Chemical Reviews, 1992. **92**(5): p. 1051-1069.
4. Noyori, R. and S. Hashiguchi, *Asymmetric transfer hydrogenation catalyzed by chiral ruthenium complexes*. Accounts of Chemical Research, 1997. **30**(2): p. 97-102.
5. Naota, T., H. Takaya, and S.I. Murahashi, *Ruthenium-catalyzed reactions for organic synthesis*. Chemical Reviews, 1998. **98**(7): p. 2599-2660.
6. Yamakawa, M., H. Ito, and R. Noyori, *The metal-ligand bifunctional catalysis: A theoretical study on the ruthenium(II)-catalyzed hydrogen transfer between alcohols and carbonyl compounds*. Journal of the American Chemical Society, 2000. **122**(7): p. 1466-1478.
7. Clapham, S.E., A. Hadzovic, and R.H. Morris, *Mechanisms of the H<sub>2</sub>-hydrogenation and transfer hydrogenation of polar bonds catalyzed by ruthenium hydride complexes*. Coordination Chemistry Reviews, 2004. **248**(21-24): p. 2201-2237.
8. Gladiali, S. and E. Alberico, *Asymmetric transfer hydrogenation: chiral ligands and applications*. Chemical Society Reviews, 2006. **35**(3): p. 226-236.
9. Azua, A., et al., *Alternative Energy Input for Transfer Hydrogenation using Iridium NHC Based Catalysts in Glycerol as Hydrogen Donor and Solvent*. Organometallics, 2012. **31**(10): p. 3911-3919.
10. Shimizu, H., et al., *Developments in Asymmetric Hydrogenation from an Industrial Perspective*. Accounts of Chemical Research, 2007. **40**(12): p. 1385-1393.
11. Grundler, P.V., et al., *Kinetic studies on the first dihydrogen aquacomplex, [Ru(H<sub>2</sub>)(H<sub>2</sub>O)<sub>5</sub>]<sup>2+</sup>: Formation under H<sub>2</sub> pressure and catalytic H/D isotope exchange in water*. Inorganica Chimica Acta, 2006. **359**(6): p. 1795-1806.
12. Ohkuma, T., et al., *Practical Enantioselective Hydrogenation of Aromatic Ketones*. Journal of the American Chemical Society, 1995. **117**(9): p. 2675-2676.
13. Fujii, A., et al., *Asymmetric transfer hydrogenation of ketones with a formic acid-triethylamine mixture catalyzed by chiral ruthenium(II) complexes*. Abstracts of Papers of the American Chemical Society, 1996. **211**: p. 158-ORGN.
14. Fujii, A., et al., *Ruthenium(II)-catalyzed asymmetric transfer hydrogenation of ketones using a formic acid-triethylamine mixture*. Journal of the American Chemical Society, 1996. **118**(10): p. 2521-2522.
15. Sandoval, C.A., et al., *Mechanism of asymmetric hydrogenation of acetophenone catalyzed by chiral eta(6)-arene-N-tosylethylenediamine-ruthenium(II) complexes*. Chemistry-an Asian Journal, 2006. **1**(1-2): p. 102-110.

16. MacAleese, L. and P. Maitre, *Infrared spectroscopy of organometallic ions in the gas phase: From model to real world complexes*. Mass Spectrometry Reviews, 2007. **26**(4): p. 583-605.
17. Wu, G.H., D. Chapman, and A.J. Stace, *Trapping and recording the collision- and photo-induced fragmentation patterns of multiply charged metal complexes in the gas phase*. International Journal of Mass Spectrometry, 2007. **262**(3): p. 211-219.
18. Jasikova, L., et al., *Aromatic C-H bond activation revealed by infrared multiphoton dissociation spectroscopy*. Journal of Mass Spectrometry, 2012. **47**(4): p. 460-465.
19. Roithova, J., *Characterization of reaction intermediates by ion spectroscopy*. Chemical Society Reviews, 2012. **41**(2): p. 547-559.
20. Janis, J., et al., *Fragmentation Pathways of  $[MX_2(CO)_2(dcbpy)]$  ( $M = Ru, Os$ ;  $X = Cl, Br, I$ ;  $dcbpy=2,2'$ -bipyridine-4,4'-dicarboxylic acid) Complexes*. Organometallics, 2010. **29**(5): p. 1070-1078.
21. Di Tommaso, D., S.A. French, and C.R.A. Catlow, *The  $H_2$ -hydrogenation of ketones catalysed by ruthenium(II) complexes: A density functional theory study*. Journal of Molecular Structure-Theochem, 2007. **812**(1-3): p. 39-49.
22. Prokopchuk, D.E. and R.H. Morris, *Inner-Sphere Activation, Outer-Sphere Catalysis: Theoretical Study on the Mechanism of Transfer Hydrogenation of Ketones Using Iron(II) PNNP Eneamido Complexes*. Organometallics, 2012. **31**(21): p. 7375-7385.
23. Prokopchuk, D.E., et al., *Spectroscopic and DFT Study of Ferraaziridine Complexes Formed in the Transfer Hydrogenation of Acetophenone Catalyzed Using  $trans$ - $[Fe(CO)(NCMe)(PPh_2C_6H_4CH=NCH_2)_2-\kappa^4 P,N,N,P](BF_4)_2$* . Organometallics, 2012. **31**(8): p. 3056-3064.
24. Nakajima, Y., et al., *Theoretical Study of Dihydrogen Activation by a Trinuclear Ruthenium  $\mu_3$ -Imido Complex*. Organometallics, 2012. **31**(15): p. 5342-5348.
25. Gomez, M., et al., *Ruthenium complexes containing chiral N-donor ligands as catalysts in acetophenone hydrogen transfer - New amino effect on enantioselectivity*. European Journal of Inorganic Chemistry, 2005(21): p. 4341-4351.
26. Gabelica, V. and E. De Pauw, *Internal energy and fragmentation of ions produced in electrospray sources*. Mass Spectrometry Reviews, 2005. **24**(4): p. 566-587.
27. Zins, E.L., et al., *Theoretical and experimental study of tropylium formation from substituted benzylpyridinium species*. Journal of Mass Spectrometry, 2009. **44**(1): p. 12-17.
28. Zins, E.L., et al., *Investigations of the fragmentation pathways of benzylpyridinium ions under ESI/MS conditions*. Journal of Mass Spectrometry, 2009. **44**(12): p. 1668-1675.
29. Barylyuk, K.V., et al., *Fragmentation of Benzylpyridinium "Thermometer" Ions and Its Effect on the Accuracy of Internal Energy Calibration*. Journal of the American Society for Mass Spectrometry, 2010. **21**(1): p. 172-177.
30. Zins, E.L., C. Pepe, and D. Schroder, *Energy-dependent dissociation of benzylpyridinium ions in an ion-trap mass spectrometer*. Journal of Mass Spectrometry, 2010. **45**(11): p. 1253-1260.
31. Shen, J., R.C. Dunbar, and G.A. Olah, *Gas-Phase Benzyl Cations from Toluene Precursors*. Journal of the American Chemical Society, 1974. **96**(19): p. 6227-6229.
32. Becke, A.D., *Density-Functional Exchange-Energy Approximation with Correct Asymptotic-*

- Behavior*. Physical Review A, 1988. **38**(6): p. 3098-3100.
33. Lee, C.T., W.T. Yang, and R.G. Parr, *Development of the Colle-Salvetti Correlation-Energy Formula into a Functional of the Electron-Density*. Physical Review B, 1988. **37**(2): p. 785-789.
  34. Miehlich, B., et al., *Results Obtained with the Correlation-Energy Density Functionals of Becke and Lee, Yang and Parr*. Chemical Physics Letters, 1989. **157**(3): p. 200-206.
  35. Becke, A.D., *Density-Functional Thermochemistry .3. The Role of Exact Exchange*. Journal of Chemical Physics, 1993. **98**(7): p. 5648-5652.
  36. Dunning, T.H., *Gaussian-Basis Sets for Use in Correlated Molecular Calculations .1. The Atoms Boron through Neon and Hydrogen*. Journal of Chemical Physics, 1989. **90**(2): p. 1007-1023.
  37. Dolg, M., et al., *Relativistic and correlation effects for element 105 (hahnium, Ha): a comparative study of M and MO (M = Nb, Ta, Ha) using energy-adjusted ab initio pseudopotentials*. The Journal of Physical Chemistry, 1993. **97**(22): p. 5852-5859.
  38. Frisch, M.J., et al., *Gaussian 03, Revision C.02*. 2003.
  39. Frisch, M.J., et al., *Gaussian 09, Revision B.01*. 2009: Wallingford CT.
  40. Ditchfie.R, W.J. Hehre, and J.A. Pople, *Self-Consistent Molecular-Orbital Methods .9. Extended Gaussian-Type Basis for Molecular-Orbital Studies of Organic Molecules*. Journal of Chemical Physics, 1971. **54**(2): p. 724-&.
  41. Rassolov, V.A., et al., *6-31G\*basis set for third-row atoms*. Journal of Computational Chemistry, 2001. **22**(9): p. 976-984.
  42. IUPAC. *Compendium of Chemical Terminology, 2nd ed. (the "Gold Book")*, in IUPAC. *Compendium of Chemical Terminology, 2nd ed. (the "Gold Book")*, A.D. McNaught and A. Wilkinson, Editors. 1997, Blackwell Scientific Publications: Oxford.
  43. Byrd, E.F.C., C.D. Sherrill, and M. Head-Gordon, *The theoretical prediction of molecular radical species: a systematic study of equilibrium geometries and harmonic vibrational frequencies*. Journal of Physical Chemistry A, 2001. **105**(42): p. 9736-9747.

## VIII-9: Supplementary material

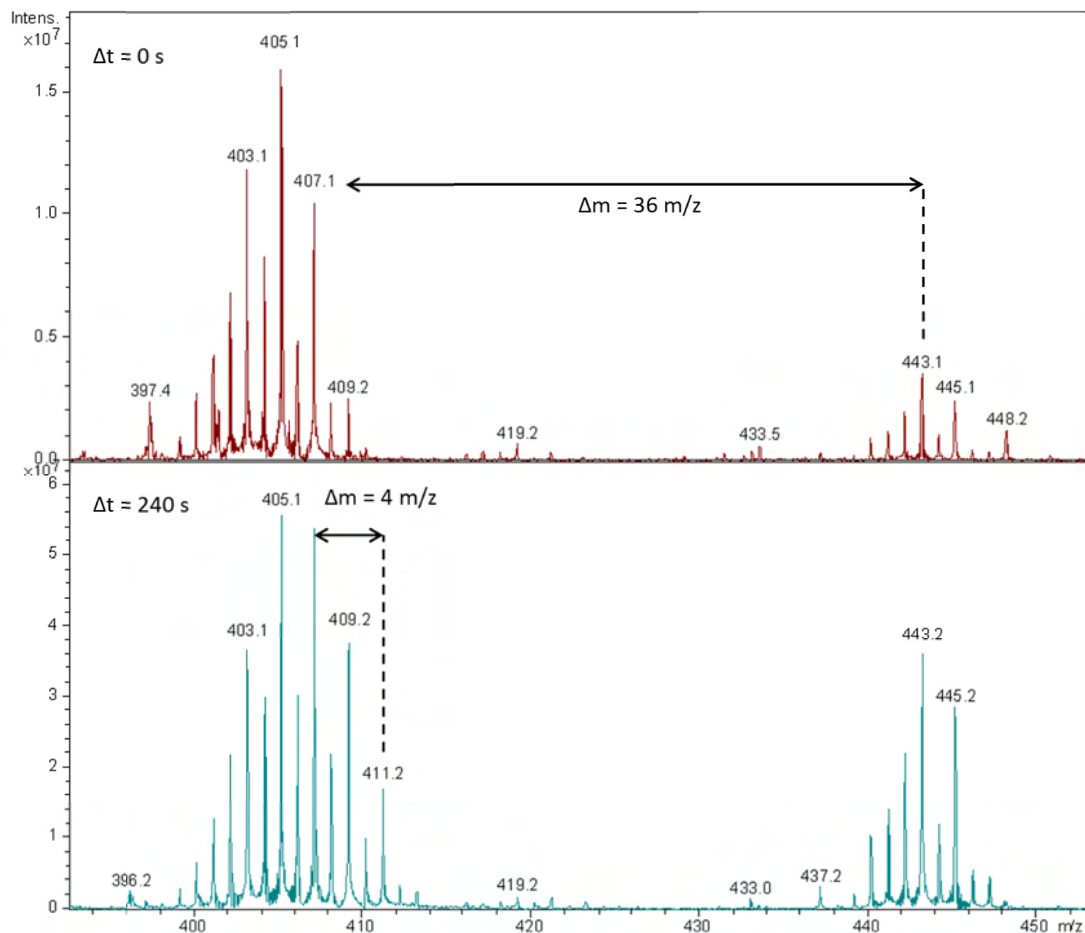


**Figure 21:** Section of the FT-ICR mass spectra of complexes  $1^+$  and  $1^+(-\text{HCl})$  at  $\Delta t = 0$  s (top) and after 240 s reaction time (bottom) with  $\text{D}_2$ . The isotope pattern at 443.1 m/z (most abundant mass) correlates to complex  $1^+$  and the one at 405.2 m/z (most abundant mass) to the activated complex  $1^+(-\text{H}^{37}\text{Cl})$ . 411.2 m/z corresponds to the reaction product of complex  $1^+(-\text{HCl})$  with  $\text{D}_2$  ( $p = 5 \times 10^{-9}$  mbar,  $T = 298$  K).

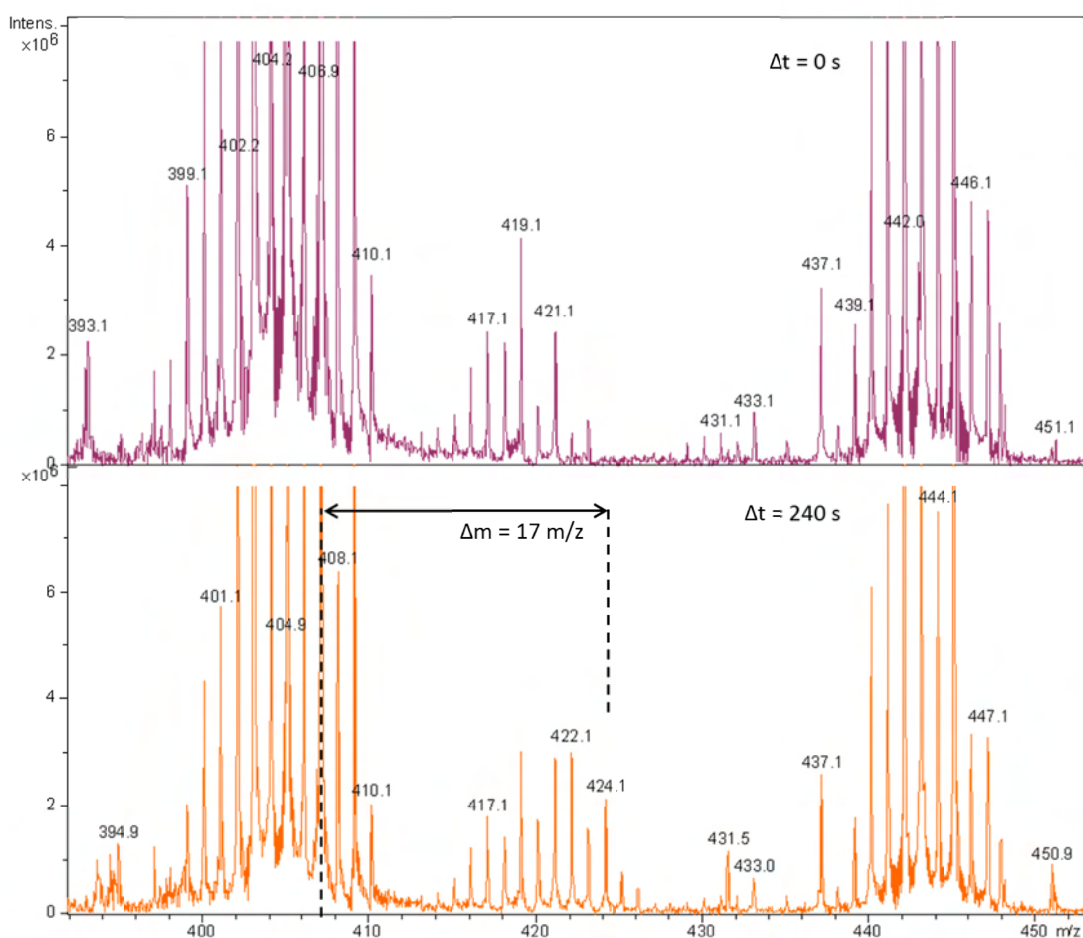


**Figure 22:** Section of the FT-ICR mass spectra of complexes  $1^+$  and  $1^+(-\text{HCl})$  at  $\Delta t = 0$  s (top) and after 240 s reaction time (bottom) with  $\text{D}_2\text{O}$  ( $p = 1 \times 10^{-9}$  mbar,  $T = 298$  K). The isotope pattern at 443.0 m/z (most abundant mass) correlates to complex  $1^+$  and the one at 406.9 m/z (most abundant mass) to the activated complex  $1^+(-\text{HCl})$ . Spectra are enlarged to highlight the isotopic pattern at 424.1 m/z (most abundant mass) corresponding to an addition of OD to complex  $1^+(-\text{HCl})$ . (cf. Fig. 21 for the full intensity distribution of the isotope pattern of  $1^+(-\text{HCl})$ )

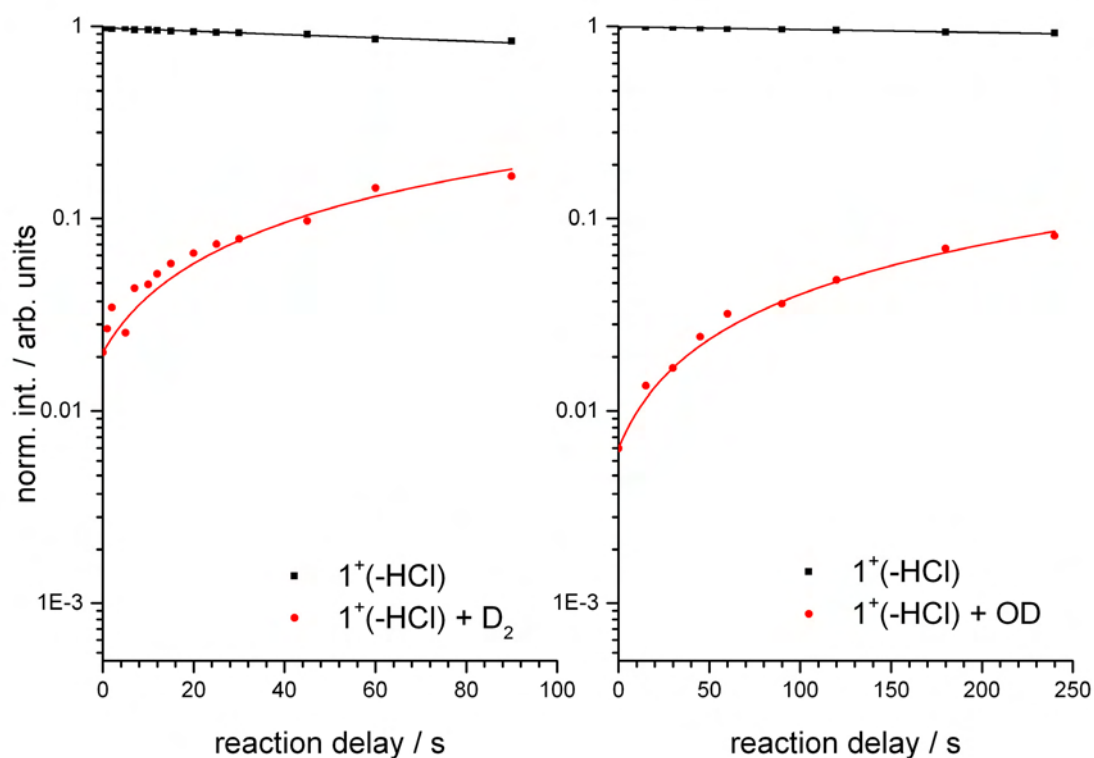


**Figure 23:** Normalized reactant (407  $m/z$  isotope (●)) and product (411  $m/z$  isotope (●)) intensities in the reactions of catalyst  $1^+(-\text{HCl})$  with  $\text{D}_2$  ( $p = 5 \times 10^{-9}$  mbar,  $T = 298$  K) (a). Normalized reactant (405  $m/z$  isotope (●)) and product (422  $m/z$  isotope (●)) intensities in the reactions of catalyst  $1^+(-\text{HCl})$  with  $\text{D}_2\text{O}$  ( $p = 1 \times 10^{-9}$  mbar) (b). The temporal evolution of the experimental data points (symbols) is fitted to pseudo first order kinetics (solid lines) which provides for relative partial rate constants. Fits correlate to single  $\text{D}_2$  addition reactions (a) and to reactions leading to an addition of  $\text{D}_2\text{O}$  under subsequent loss of HD (b) per single collision. Fits arise through application of generic algorithm code. (cf. Table 5 for numerical data)

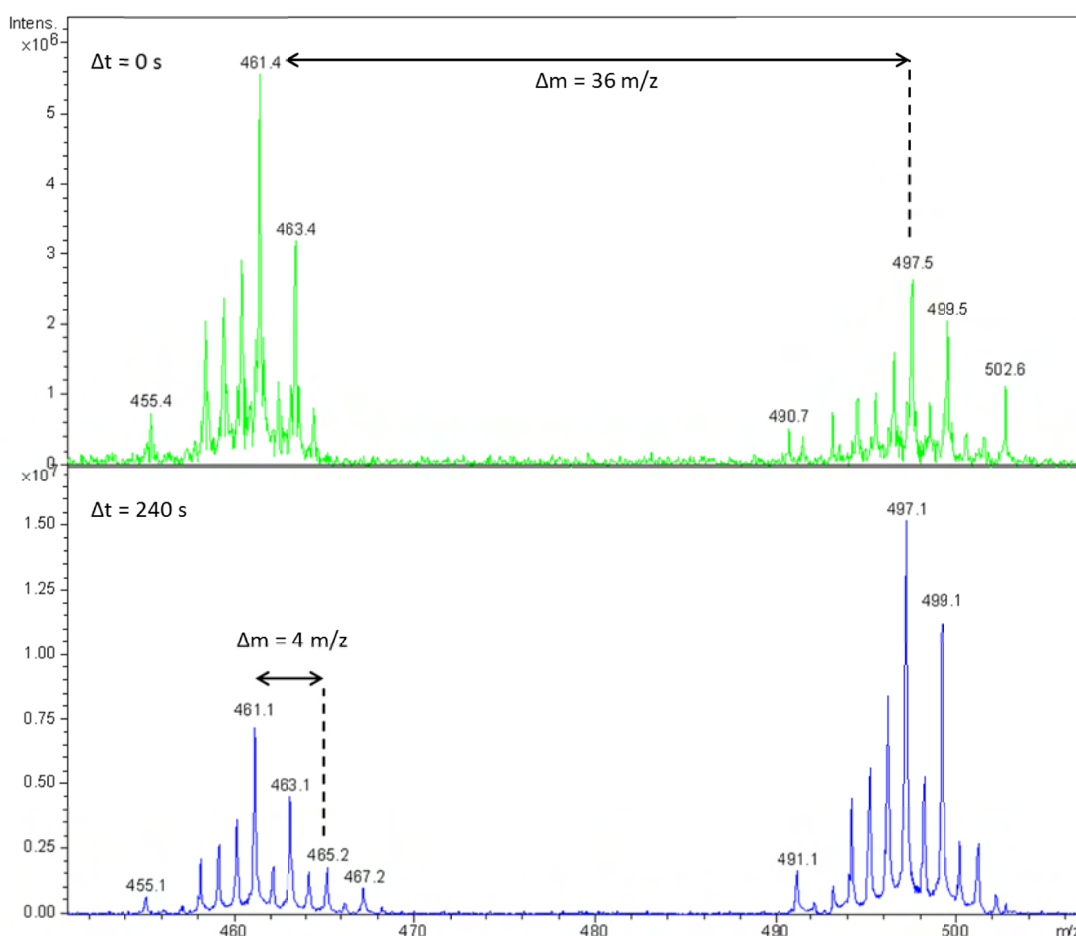


**Figure 24:** Section of the FT-ICR mass spectra of complexes  $3^+$  and  $3^+(-\text{HCl})$  at  $\Delta t = 0$  s (top) and after 240 s reaction time (bottom) with  $\text{D}_2$ . The isotope pattern at 497.5 m/z (most abundant mass) correlates to complex  $3^+$  and the one at 461.4 m/z (most abundant mass) to the activated complex  $3^+(-\text{HCl})$ . 465.2 m/z corresponds to the reaction product of complex  $3^+(-\text{HCl})$  with  $\text{D}_2$  ( $p = 5 \times 10^{-9}$  mbar,  $T = 298$  K).

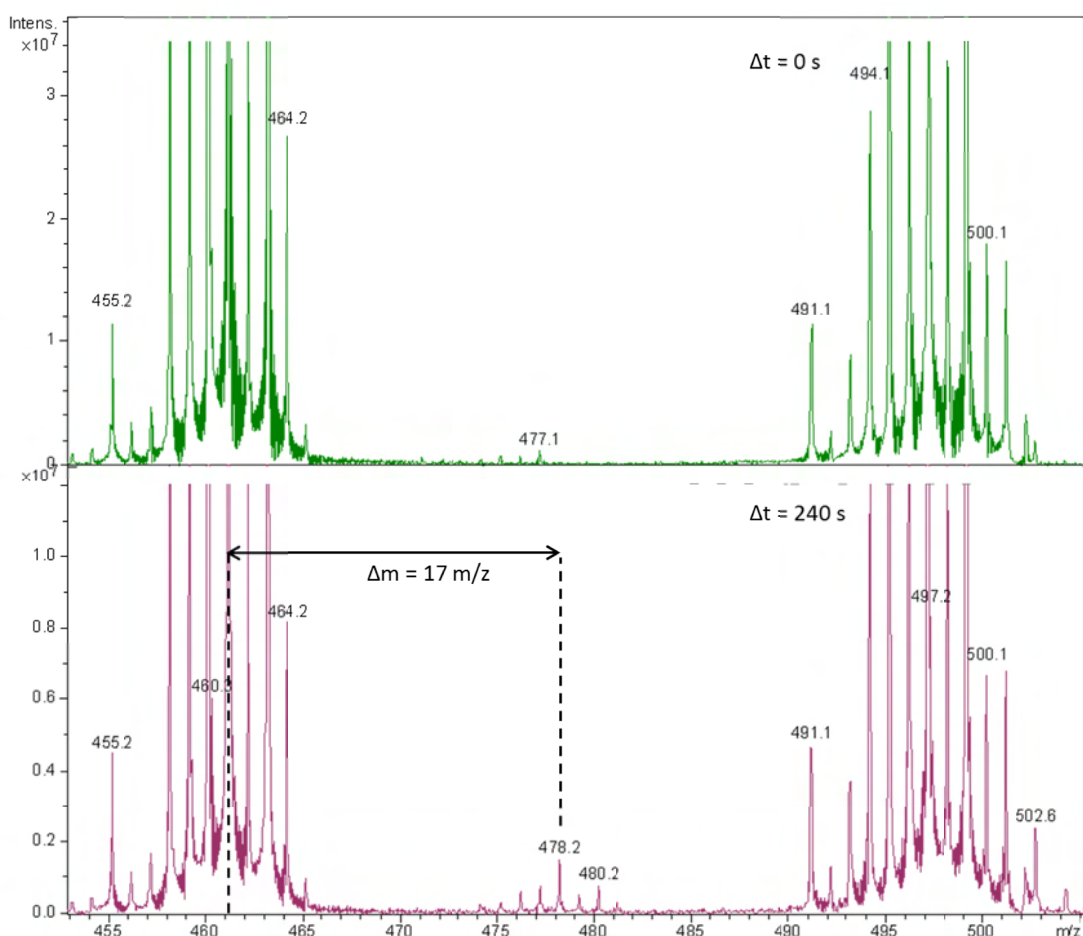


**Figure 25:** Section of the FT-ICR mass spectra of complexes  $3^+$  and  $3^+(-\text{HCl})$  at  $\Delta t = 0$  s (top) and after 240 s reaction time (bottom) with  $\text{D}_2\text{O}$  ( $p = 1 \times 10^{-9}$  mbar,  $T = 298$  K). The isotope pattern at 497.3 m/z (most abundant mass) correlates to complex  $3^+$  and the one at 461.1 m/z (most abundant mass) to the activated complex  $3^+(-\text{HCl})$ . Spectra are enlarged to highlight the isotopic pattern at 478.1 m/z (most abundant mass) corresponding to an addition of OD to complex  $3^+(-\text{HCl})$ . (cf. Fig. 24 for the full intensity distribution of the isotope pattern of  $3^+(-\text{HCl})$ )



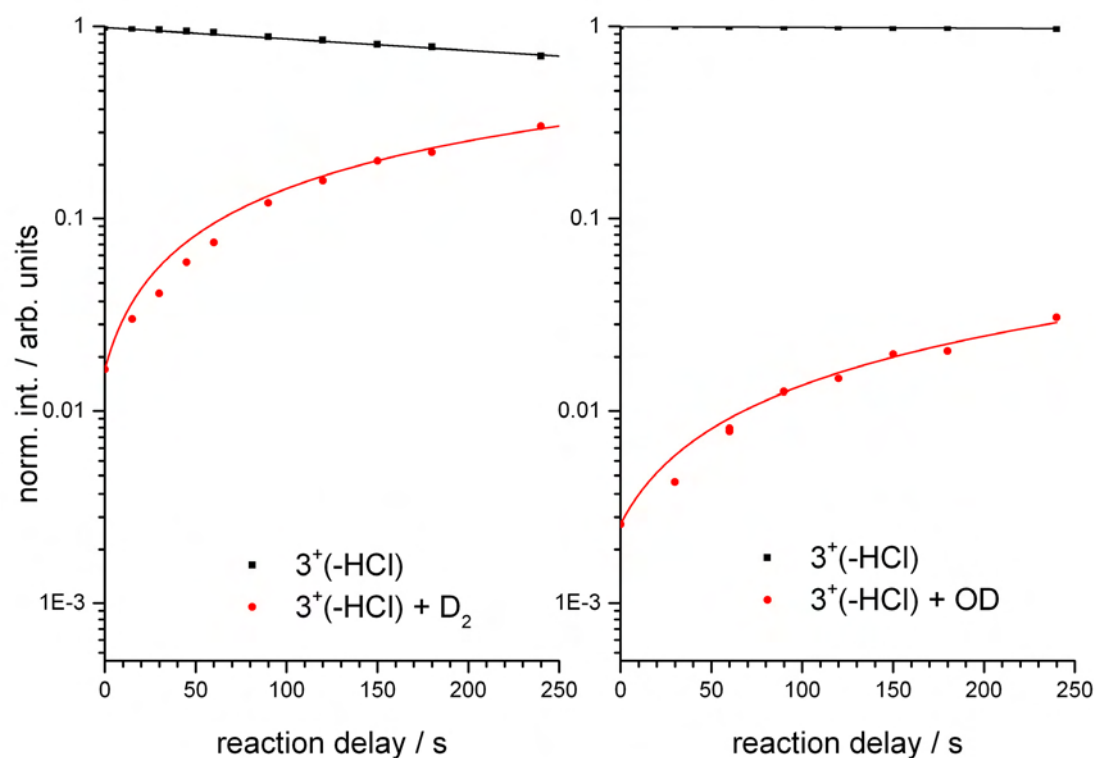


**Figure 26:** Normalized reactant (461 m/z isotope (●)) and product (465 m/z isotope (●)) intensities in the reactions of catalyst 3<sup>+</sup>(-HCl) with D<sub>2</sub> ( $p = 5 \times 10^{-9}$  mbar,  $T = 298$  K) (a). Normalized reactant (437 m/z isotope (●)) and product (454 m/z isotope (●)) intensities in the reactions of catalyst 3<sup>+</sup>(-HCl) with D<sub>2</sub>O ( $p = 1 \times 10^{-9}$  mbar) (b). The temporal evolution of the experimental data points (symbols) is fitted to pseudo first order kinetics (solid lines) which provides for relative partial rate constants. Fits correlate to single D<sub>2</sub> addition reactions (a) and to reactions leading to an addition of D<sub>2</sub>O under subsequent loss of HD (b) per single collision. Fits arise through application of generic algorithm code. (cf. Table 5 for numerical data)

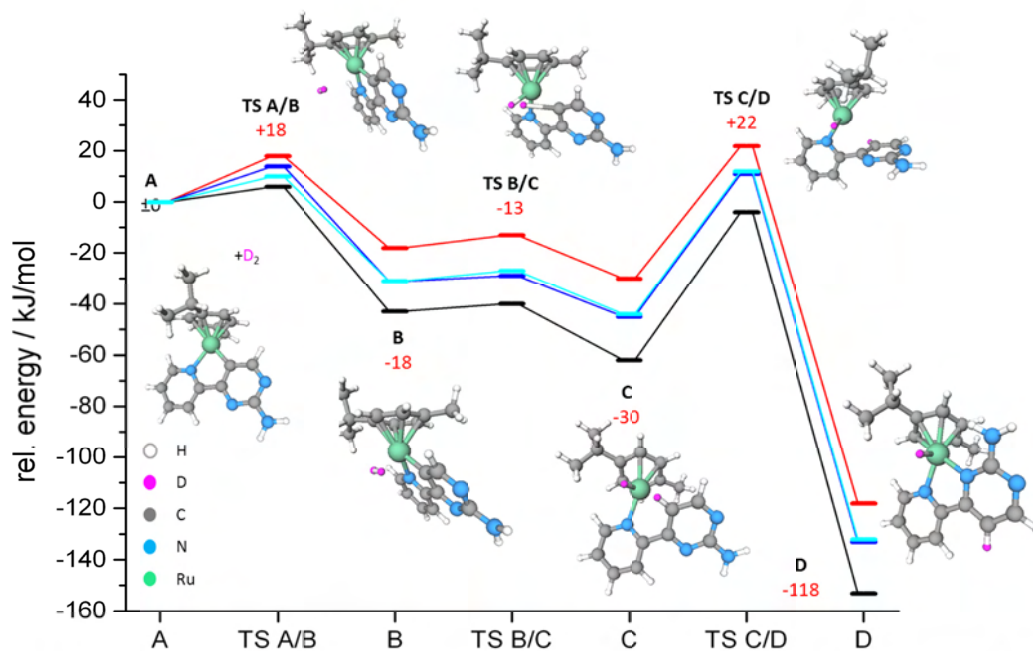


**Figure 27:** Reaction coordinate of  $D_2$  insertion at the catalytical active complex  $1^*(-HCl)$ . Structures derived from DFT calculations at the B3LYP/cc-pVTZ (H, D, C, N) and Stuttgart 1997 ECP (Ru) level of theory. (–) exhibits the uncorrected DFT energies, (–) zero-point energies, (–) thermal corrected (RT) energies and (–) free enthalpies (corresponding values labeled in red). The energy scale (in kJ/mol) is relative to the separated molecules  $1^*(-HCl)$  and  $D_2$  set to zero. A, B, C and D indicate local DFT energy minimum structures, TS indicates a transition state between adjacent minima.

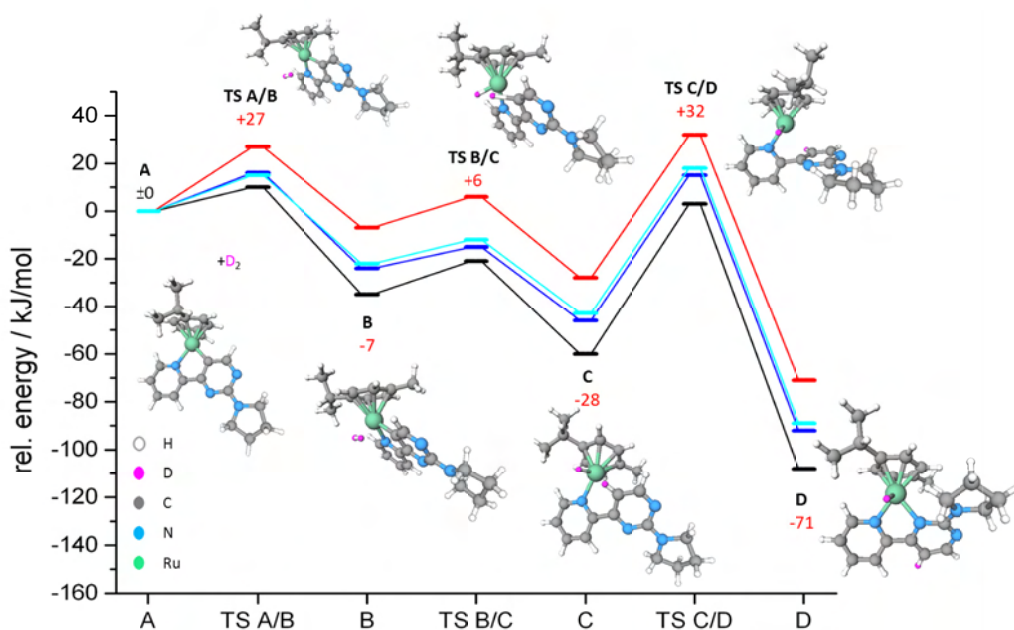


**Figure 28:** Reaction coordinate of  $D_2$  insertion at the catalytic active complex  $3^+(-HCl)$ . Structures derived from DFT calculations at the B3LYP/cc-pVTZ (H, D, C, N) and Stuttgart 1997 ECP (Ru) level of theory. (–) exhibits the uncorrected DFT energies, (–) zero-point energies, (–) thermal corrected (RT) energies and (–) free enthalpies (corresponding values labeled in red). The energy scale (in kJ/mol) is relative to the separated molecules  $3^+(-HCl)$  and  $D_2$  set to zero. A, B, C and D indicate local DFT energy minimum structures, TS indicates a transition state between adjacent minima.



## Chapter IX: The [ ${}^4\text{CpCo}$ ] ${}_2(\mu\text{-C}_2\text{Ph}_2)$ ] complex and its oxidation behavior studied with ESI-MS, IR-MPD and TD-DFT – vibrational excitation of electronic excited states

### Keywords:

Cobalt, Diphenylethine,  ${}^4\text{Cp}$ ,  ${}^{18}\text{O}$  isotope labeling, Oxidation, Mass Spectrometry, CID, IR-MPD, DFT & TD-DFT

### IX Preamble

The synthesis of the [ ${}^4\text{CpCo}$ ] ${}_2(\mu\text{-C}_2\text{Ph}_2)$ ] complex was done by Julia Becker. All ESI-MS measurements on this complex and the assignment of most ionic species were done by me. A part of the results from ESI-MS experiments is published in the diploma thesis of J. Becker. J. Schommer studied (additional) reactions of the complex in solution and did further ESI-MS experiments under my supervision. These results are published as a student research project thesis.

This chapter reports on own ESI-MS and IR-MPD experiments and on *ab initio* calculations. This chapter is written by me and formatted as to become a manuscript for publication. It is not submitted yet.

### IX-1: Abstract

The complex [ ${}^4\text{CpCo}$ ] ${}_2(\mu\text{-C}_2\text{Ph}_2)$ ] forms various cations [ ${}^4\text{CpCo}$ ] ${}_2(\mu\text{-C}_2\text{Ph}_2)\text{X}^+$  ( $\text{X}=\text{H}$ ,  $\text{CH}_3\text{CN}$ ,  $\text{O}$ ,  $\text{Cl}$ ) by electrospray ionization (ESI-MS).  ${}^{18}\text{O}$  isotope labeling experiments verify the capability of the complex to bind  $\text{O}^{2-}$  out of solvent water. Infrared multiple-photon dissociation (IR-MPD) spectroscopy in the near IR exhibits either metal-to-ligand charge-transfer (MLCT) bands or vibrational excited states, depending on the oxidation state. A systematic screening of functionals and basis sets suggests the use of B3LYP and B97D functionals in conjunction with cc-pVDZ and Stuttgart 1997 ECP basis sets for further calculations, which identify high and low spin ground states in four reaction adducts. IR-MPD spectra in the mid- and near-IR region of [ ${}^4\text{CpCo}$ ] ${}_2(\mu\text{-C}_2\text{Ph}_2)]^+$  and its reaction products are compared with calculated IR absorption spectra and electronic transition spectra by TD-DFT.

## IX-2: Introduction

Cobalt complexes are of great scientific and technological interest, e.g. because of their ability to split water in H<sub>2</sub> and O<sub>2</sub> [1]. Cobalt is more abundant and cheaper than commonly used metals as e.g. platinum. Several complexes are yet developed which are capable to act as photocatalytic H<sub>2</sub>-evolving systems by using sunlight as an energy source. Those cobalt based H<sub>2</sub>-evolving catalysts have the need for an effective electronic coupling to a photosensitizer [2].

Properties of metal clusters usually depend on their size, on their geometry and on their oxidation state. Redox reaction involves valence electrons and it can be expected that electronic near-IR spectra depend sensitively on the oxidation state changes. Charged cobalt clusters and their reaction adducts with alcohols in the gas phase have been intensively studied by (multiple-)photon dissociation spectroscopy in the mid and near-IR region (IR-(M)PD) [3-5]. Results from time-dependent density functional theory (TD-DFT) were compared to IR-PD spectra of Co<sub>n</sub><sup>+</sup>(CH<sub>3</sub>OH)<sub>3</sub> (n = 1-3) in the region of 2800 to 6800 cm<sup>-1</sup> [5]. The HOMO-LUMO gap was found to change with cluster size and with the binding sites of the methanol. Also for small cationic cobalt and vanadium clusters electronic transitions in the near-IR region have been found [6, 7]. Those broad absorptions have been assigned by TD-DFT to 3d electronic transitions [6, 8].

Cobaltocene [Cp<sub>2</sub>Co] was synthesized by Fischer et al. in 1953 [9] which was followed by the synthesis of a huge variety of cobaltocene derivatives. Koelle et al. showed in the early 80ies that halogen bridged Co-dimers of the type [Cp\*CoX]<sub>2</sub> are accessible in good yields by salt metathesis [10]. [(CO)<sub>6</sub>Co<sub>2</sub>(μ-C<sub>2</sub>Ph<sub>2</sub>)] was the first complex with only one organic molecule as a bridge between two metal ions [11]. The sp<sup>3</sup> carbon atoms of the μ<sub>2</sub> acetylide bridge coordinate in a tetrahedric environment. Eaton et al. synthesized such a cobalt-dimer complex **1** with two anionic Cp<sup>-</sup> ligands and silyl substituents at the C<sub>2</sub> ligand [12] (cf. Fig. 1). X-ray diffraction studies found this complex to reveal the shortest metal-metal bond at that time.

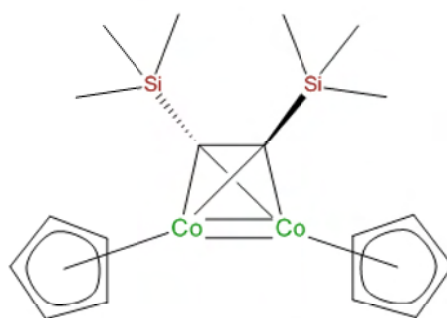


**Figure 1:** Structure of the neutral complex **1** [12].

The use of DFT is nowadays the state of the art for a huge variety of applications. Several publications report on the advantages and disadvantages of DFT functionals for the appropriate calculation of e.g. bond lengths and relative energies [13-15].

In the course of her diploma thesis work J. Becker, member in the research team of Prof. H. Sitzmann, synthesized complexes [ ${}^4\text{CpCo}$ ] ${}_2(\mu\text{-C}_2\text{Ph}_2)$  (**2**) (cf. Fig. 2,  ${}^4\text{Cp}$  = tetraisopropylcyclopentadiene) - dark red, almost black, crystals. This complex exhibits a formal double  $\text{Co}^{\text{I}}\text{-Co}^{\text{I}}$  bond, stabilized by two terminal  ${}^4\text{Cp}^-$  and a bridging  $\text{C}_2\text{Ph}_2$  ligand. Our ESI-MS studies confirmed redox activity of **2**. It yields adducts by simple addition of ions and chelating molecules from solution, and it is capable to electrolyze water. This manifests in a color change in solution. We utilized a combination of ESI-MS, mid- and near-IR spectroscopy and TD-DFT calculations to characterize **2**, its reaction products, and its electronic properties.

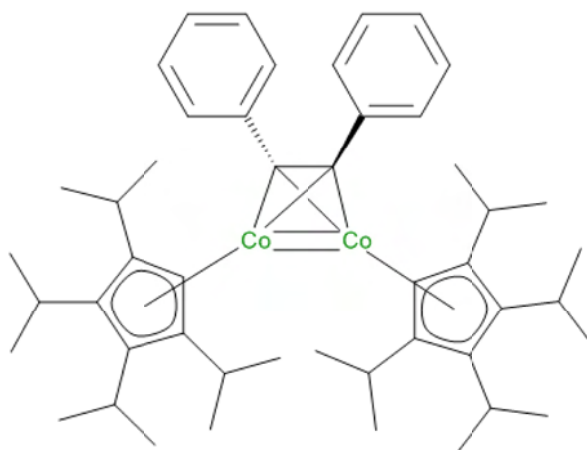


**Figure 2:** Structure of the neutral complex **2**.

## IX-3: Methods

### IX-3.1: ESI-MS and CID

Electrospray ionization mass spectrometry (ESI-MS) was performed with an ion trap instrument (Bruker amaZonSL). The ion source yields cations in positive electrospray ionization mode. Scan speed was 32500 m/z / s in normal resolution scan mode (0.3 FWHM / m/z), scan range was at least 70 to 1000 m/z. Sample solutions in tetrahydrofuran (THF) at concentrations of appr.  $1 \times 10^{-4}$  M were continuously infused into the ESI chamber at a flow rate of 2  $\mu$ L/min using a syringe pump. We use nitrogen as drying gas at a flow rate of 3.0 L/min at 220 °C and spray the solutions at a nebulizer pressure of 4 psi with the electrospray needle held at 4.5 kV. We held transfer parameters to the Paul trap of the mass spectrometer constant and used Helium as a buffer gas with a partial pressure of about  $3 \times 10^{-3}$  mbar inside the ion trap. BrukerTrapControl 7.0 software controlled the instrument and we performed data analysis using Bruker Data Analysis 4.0 software.

### IX-3.2: IR-MPD

IR-MPD measurements were performed with the ion trap mass spectrometer (cf. ESI-MS part) after its modification. A KTP/KTA optical parametric oscillator/amplifier (OPO/A, LaserVision) system pumped with a Q-switched 10 Hz injection seeded Nd<sup>3+</sup>:YAG lasers (PL8000, Continuum) provided for tunable IR radiation ( $\delta\nu = 0.9 \text{ cm}^{-1}$ ,  $\delta t = 7 \text{ ns}$ ) in order to record vibrational spectra via the multi-photon dissociation scheme. We used alternatively the OPA idler or signal wave ( $\leq 10 \text{ mJ/pulse}$ ) of the system to scan spectra within 2800 - 3600  $\text{cm}^{-1}$ , 3700 – 7400  $\text{cm}^{-1}$  respectively. Each trapped and m/z isolated ion package was irradiated by 2 laser pulses in order to produce sufficient fragment ions. IR spectra were recorded using Bruker chromatogram software for extracting the intensity of parent and fragment ions (three point averaging directly by BrukerTrapControl software). IR-MPD signal was evaluated corresponding to formula 1 (fr = fragment, p = parent)

$$I_{tot}^{fr} = \frac{\sum_i I_i^{fr}}{\sum_i I_i^{fr} + \sum_i I_i^p} \quad (1)$$

Origin Plot Software served to apply a five point adjacent averaging for smoothing. IR frequency was calibrated by a wave meter (821B-NIR, Bristol instruments). Laser power curve was recorded in parallel to the IR-MPD spectra through digitizing the analog output of the laser power meter by an ample ADC input of the amaZonSL mass spectrometer electronics.



Relative photon fluxes (rpf) were estimated by normalization of recorded laser power at various amplification levels to the lowest amplification level and adjacent averaging of the derived values.

### ***IX-3.3: Theoretical methods***

DFT [16-19] calculations were performed at various levels of theory (BLYP, B3LYP, B3PB86, BPW91 [20-23], PBE1PBE [24, 25] and B97D [26]) with cc-pVDZ (C, H, N, O, Si, Cl), cc-pVTZ [27, 28] respectively, Stuttgart RSC 1997 ECP [29] and cc-pVTZ-NR (Co) [30] basis sets using the Gaussian 03 and 09 packages [31, 32]. Additional MP2 calculations were performed employing the same basis. Standard convergence criteria for energy optimization were applied. The crystal structure of **1** was chosen as starting conformation [12]. The optimized structure of complex **1** was used as initial geometry for geometry optimization of complex **2** with various multiplicities and adducts with some alternations: Si(CH<sub>3</sub>) groups were substituted by phenyl rings, four protons of the cyclopentadienyl-ligands were exchanged with isopropyl groups. The optimized structures were checked for minima by 2<sup>nd</sup> derivative (frequency) calculations. Most of the depicted and discussed structures exhibited no imaginary eigenvalues, some of them, especially for high multiplicities exhibit some of those.

Electronic excitation energies and oscillator strengths were determined by TD-DFT [33-39] methods using the B3LYP/cc-pVDZ and Stuttgart RSC 1997 ECP level of theory, B97D respectively, as implemented in the Gaussian 03 and 09 packages. Excitation energies were checked for negative values indicating an electronic transition from an electronic excited state to an energetically lower state. TD-DFT calculations exhibiting such negative transitions are not used for comparison with IR-MPD derived spectra.

We used the *extensible computational chemistry environment* (Pacific Northwest National Laboratory, Richland, Washington (ECCE) [40]) in order to build structures, to execute calculations and to parse them for DFT energies, vibrational frequencies and IR intensities. The use of the Gaussian 09 package and of TD-DFT calculations is not implemented in ECCE yet, results from those calculations were parsed with homemade scripts.

## IX-4: Results of ESI-MS and IR-MPD on complex 2 and its reaction products

### IX-4.1: ESI-MS

The positive ESI mass spectrum of a solution of **2** exhibits an intense peak at 525.6 m/z and at 762.6 m/z the monomeric cation of  $2^+$  (cf. Fig. 3).  $2^+$  corresponds to an oxidation product of **2** under ESI-MS conditions with a formal triple charge  $[\text{Co}_2]^{3+}$  unit. Subsequent collision induced dissociation (CID) of  $2^+$  via a  $\text{MS}^2$  experiment reveals the loss of  $\text{C}_2\text{Ph}_2$  and of  $\text{H}_2$ . Isolation of 580.4 m/z and CID in an  $\text{MS}^3$  experiment reveals various fragment ions which can partly be assigned by the combination of losses of various likely molecules, such as  $\text{CH}_4$ ,  $\text{C}_2\text{H}_4$ ,  $\text{C}_2\text{H}_6$  and  $\text{C}_3\text{H}_6$ , supported by isotopic simulations of assumed fragment ion compositions.

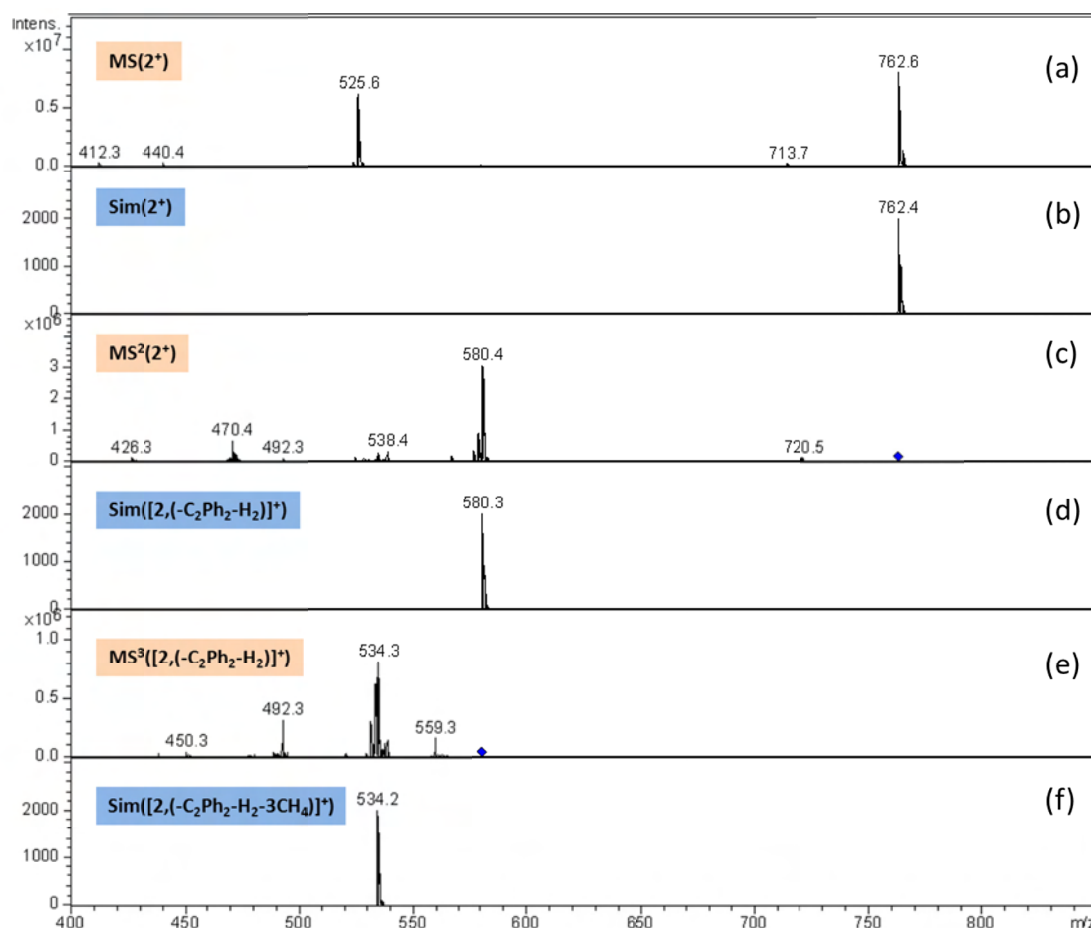


**Figure 3:** Mass spectrum (MS) of a solution of **2** in THF (a). Simulation of the isotopic distribution according to  $2^+$  (b).  $\text{MS}^2$  of  $2^+$  (768.3 m/z) exhibits multiple fragments (c), which can be assigned to the combination of losses of  $\text{C}_2\text{Ph}_2$ ,  $\text{H}_2$ ,  $\text{C}_2\text{H}_4$ ,  $\text{C}_2\text{H}_6$  and  $\text{C}_3\text{H}_6$ . Simulation of the isotopic distribution according to  $[2,(-\text{C}_2\text{Ph}_2-\text{H}_2)]^+$  (d).  $\text{MS}^3$  of  $[2,(-\text{C}_2\text{Ph}_2-\text{H}_2)]^+$  (580.4 m/z) (e) and simulation of the isotopic distribution according to  $[2,(-\text{C}_2\text{Ph}_2-\text{H}_2)]^+$  (f) (cf. Table 1 for abbreviations and sum formulas).

The mass spectrum of complex **2** after addition of 0.5 Vol.%  $\text{H}_2^{16}\text{O}$  or  $\text{H}_2^{18}\text{O}$  to a solution of complex **2** in THF exhibits an intense peak of cationic  $\mathbf{2}^+$  as a main species (cf. Fig. 4). Additionally a peak at 778.3 m/z or 780.3 m/z occurs in the mass spectrum which is assigned to the addition of either  $^{16}\text{O}^{2-}$  or  $^{18}\text{O}^{2-}$  to the  $\text{Co}_2$  unit in order to form  $[\mathbf{2},^{16}\text{O}]^+$  or  $[\mathbf{2},^{18}\text{O}]^+$ . Cationic  $[\mathbf{2},^{18}\text{O}]^+$  corresponds to an oxidation product of complex **2** by elimination of  $\text{H}_2$  under ESI-MS conditions and reveals a formal oxidation state of the  $[\text{Co}_2]$  unit of +5. Under otherwise identical reaction conditions the admixture of  $\text{H}_2^{16}\text{O}$  leads to a shifted peak at 778.3 m/z,  $\Delta m = -2$  m/z compared to the  $\text{H}_2^{16}\text{O}$  experiment.

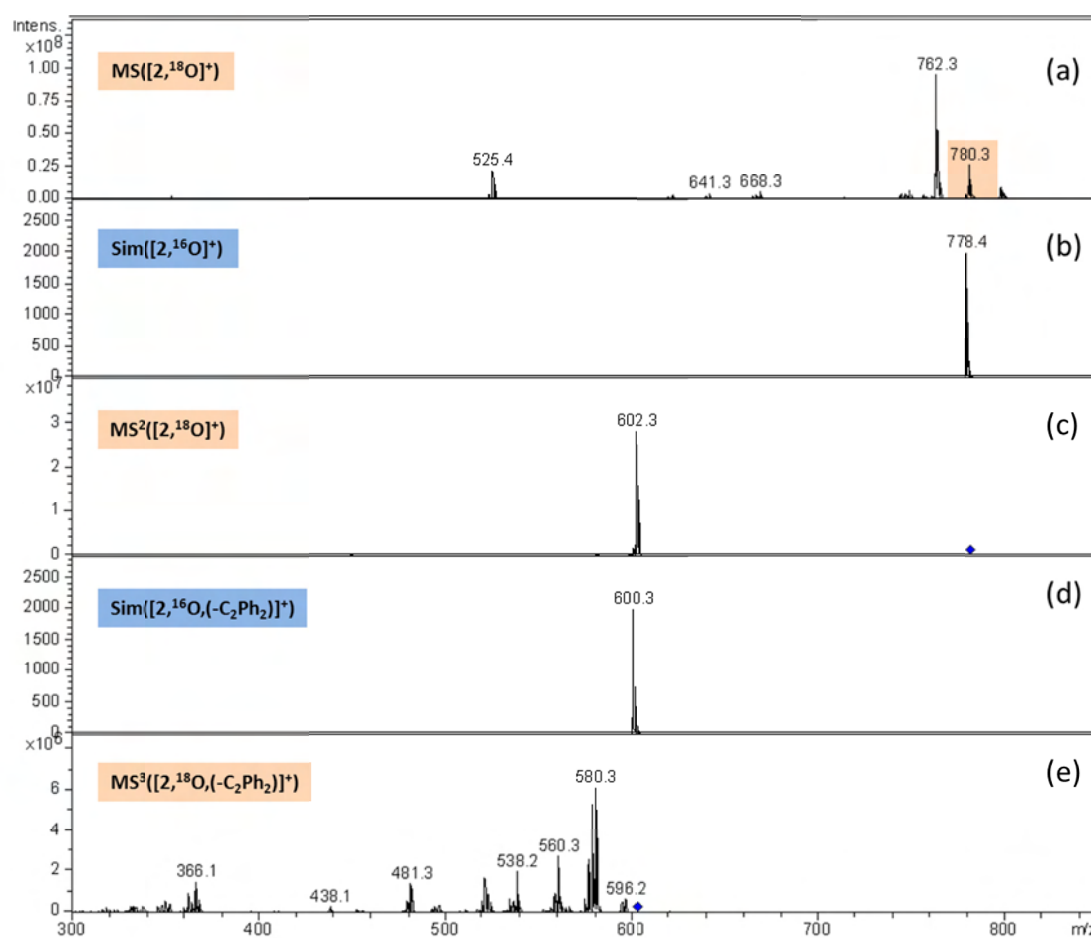


**Figure 4:** Mass spectrum of complex **2** after addition of 0.5 Vol.%  $^{18}\text{OH}_2$  to a solution of complex **2** in THF (a). Simulation of the isotopic distribution according to  $[\mathbf{2},^{16}\text{O}]^+$  (b).  $\text{MS}^2$  of cationic  $[\mathbf{2},^{18}\text{O}]^+$  (780.3 m/z) exhibits the loss of  $\text{C}_2\text{Ph}_2$  (602.3 m/z) (c). Simulation of the isotopic distribution according to  $[\mathbf{2},^{16}\text{O},(-\text{C}_2\text{Ph}_2)]^+$  (d).  $\text{MS}^3$  of  $[\mathbf{2},^{18}\text{O},(-\text{C}_2\text{Ph}_2)]^+$  exhibits multiple fragments, which correlate to the combination of losses of  $\text{H}_2$ ,  $\text{C}_2\text{H}_4$ ,  $\text{C}_2\text{H}_6$  and  $\text{C}_3\text{H}_6$  molecules (e) (cf. Table 1 for abbreviations and sum formulas).

CID of  $[2,^{18}\text{O}]^+$  leads to dominant loss of  $\text{C}_2\text{Ph}_2$  to form  $[2,^{18}\text{O},(-\text{C}_2\text{Ph}_2)]^+$ . Subsequent CID of fragment  $[2,^{18}\text{O},(-\text{C}_2\text{Ph}_2)]^+$  ( $\text{MS}^3$ ) exhibits several neutral losses which are assigned to combinational losses of molecules like  $\text{CH}_4$ ,  $\text{C}_2\text{H}_4$ ,  $\text{C}_2\text{H}_6$  and  $\text{C}_3\text{H}_6$ .

ESI-MS of a solution of complex **2** in dry THF (cf. Fig. 19) yields 797.4 m/z, assigned to a  $[2,\text{Cl}]^+$  complex. This corresponds to an oxidation product of complex **2** with a formal +4 charge of the  $[\text{Co}_2]$  unit. The addition of acetonitrile to a solution of complex **2** in dry THF leads to ESI spectra with a bundle of isotopic peaks centered at 804.3 m/z (cf. Fig. 20 and 21). We assign these to  $[2,\text{CH}_3\text{CN}]^+$  and  $[2,\text{H},\text{CH}_3\text{CN}]^+$ . Cationic  $[2,\text{CH}_3\text{CN}]^+$  corresponds to an oxidation product of complex **2** with a formal +3 charge of the  $[\text{Co}_2]$  unit. In  $[2,\text{H},\text{CH}_3\text{CN}]^+$  the formal +2 charge of the  $[\text{Co}_2]$  unit is the same as in  $2^+$ .

Sum formulas of observed cations of **2** and its reaction products observed under ESI-MS conditions, formal charge states of the  $[\text{Co}_2]$  unit, parent and main fragment masses and a selection of assigned neutral losses are summarized in Table 1.

**Table 1:** Masses<sup>a)</sup> of cationic species of **2** observed in ESI-MS spectra, abbreviations used in text<sup>b)</sup>, corresponding sum formulas, formal charge states of the  $[\text{Co}_2]$  unit, selected main  $\text{MS}^2$  fragment masses<sup>a)</sup> and corresponding neutral fragments.

mass / m/z	assignment	formula	formal $[\text{Co}_2]$ charge	main ionic fragments / m/z	corresponding neutral fragments
762.3	$2^+$	$\text{Co}_2\text{C}_{48}\text{H}_{68}^+$	+3	580.4	$\text{C}_2\text{Ph}_2$ , n $\text{H}_2$
763.3	$[2,\text{H}]^+$	$\text{Co}_2\text{C}_{48}\text{H}_{69}^+$	+2	582.4	$\text{C}_2\text{Ph}_2$ , n $\text{H}_2$
778.3	$[2,^{16}\text{O}]^+$	$\text{Co}_2\text{C}_{48}\text{H}_{68}^{16}\text{O}^+$	+5	600.3	$\text{C}_2\text{Ph}_2$
780.3	$[2,^{18}\text{O}]^+$	$\text{Co}_2\text{C}_{48}\text{H}_{68}^{18}\text{O}^+$	+5	602.3	$\text{C}_2\text{Ph}_2$
797.3	$[2,\text{Cl}]^+$	$\text{Co}_2\text{C}_{48}\text{H}_{68}\text{Cl}^+$	+4	619.2 470.2	$\text{C}_2\text{Ph}_2$ $\text{C}_2\text{Ph}_2$ , $\text{C}_2\text{H}_4$ , $\text{C}_3\text{H}_6$ , n $\text{H}_2$ , $\text{HCl}$
803.3	$[2,\text{CH}_3\text{CN}]^+$	$\text{Co}_2\text{C}_{48}\text{H}_{68}(\text{CH}_3\text{CN})^+$	+3	762.2 568.2	$\text{CH}_3\text{CN}$ $^4\text{Cp}$ , $\text{H}_2$
804.3	$[2,\text{H},\text{CH}_3\text{CN}]^+$	$\text{Co}_2\text{C}_{48}\text{H}_{69}(\text{CH}_3\text{CN})^+$	+2	762.2 568.2	$\text{CH}_3\text{CN}$ $^4\text{Cp}$ , $\text{H}_2$

<sup>a)</sup> All masses are due to the most abundant mass peak and confirmed by isotopic composition.

## IX-4.2: IR-MPD spectra

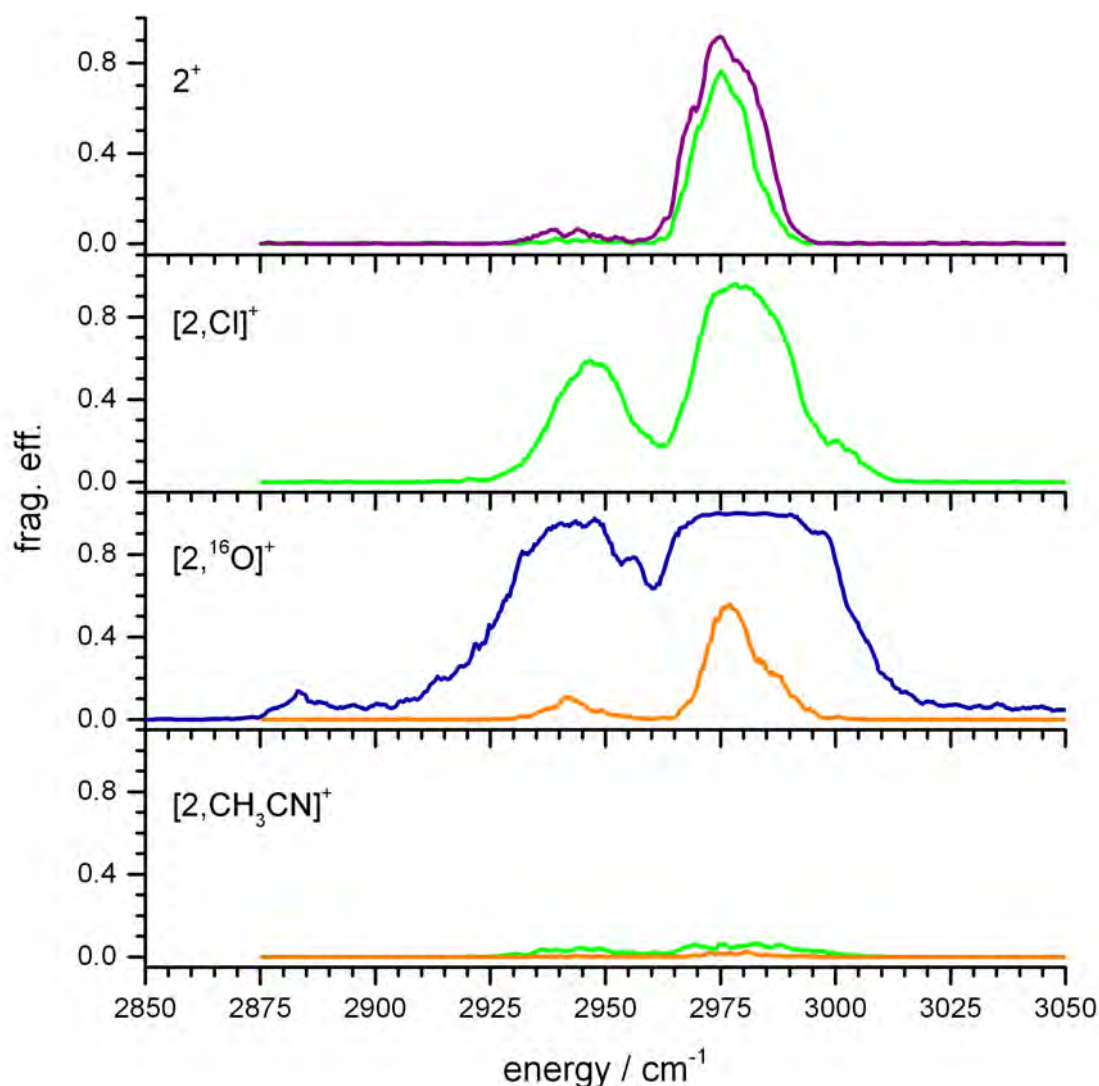


**Figure 5:** IR-MPD spectra of  $2^+$ ,  $[2,\text{Cl}]^+$ ,  $[2,{}^{16}\text{O}]^+$  and  $[2,\text{CH}_3\text{CN}]^+$ , recorded by variation of photon fluxes. Same colors represent equal relative photon fluxes (rpf): orange – rpf = 0.8, green – rpf = 1, violett – rpf = 1.26, blue – rpf = 2

There are up to three bands in the IR-MPD spectra of 2850 to 3050  $\text{cm}^{-1}$  of cationic  $2^+$  and of its reaction products (cf. Fig. 5). The spectra of all four species exhibit two main bands at 2980  $\text{cm}^{-1}$  and 2945  $\text{cm}^{-1}$ , the intensity of the latter band varies. Cations  $[2,\text{Cl}]^+$  and  $[2,{}^{16}\text{O}]^+$  fragment easier than  $2^+$  and  $[2,\text{H},\text{CH}_3\text{CN}]^+$ . The latter one exhibits a very low fragmentation efficiency for both bands. High photon flux, which leads to a saturation of the 2980  $\text{cm}^{-1}$  band (blue line) gives rise to a weak third band at 2880  $\text{cm}^{-1}$  in  $[2,{}^{16}\text{O}]^+$ .

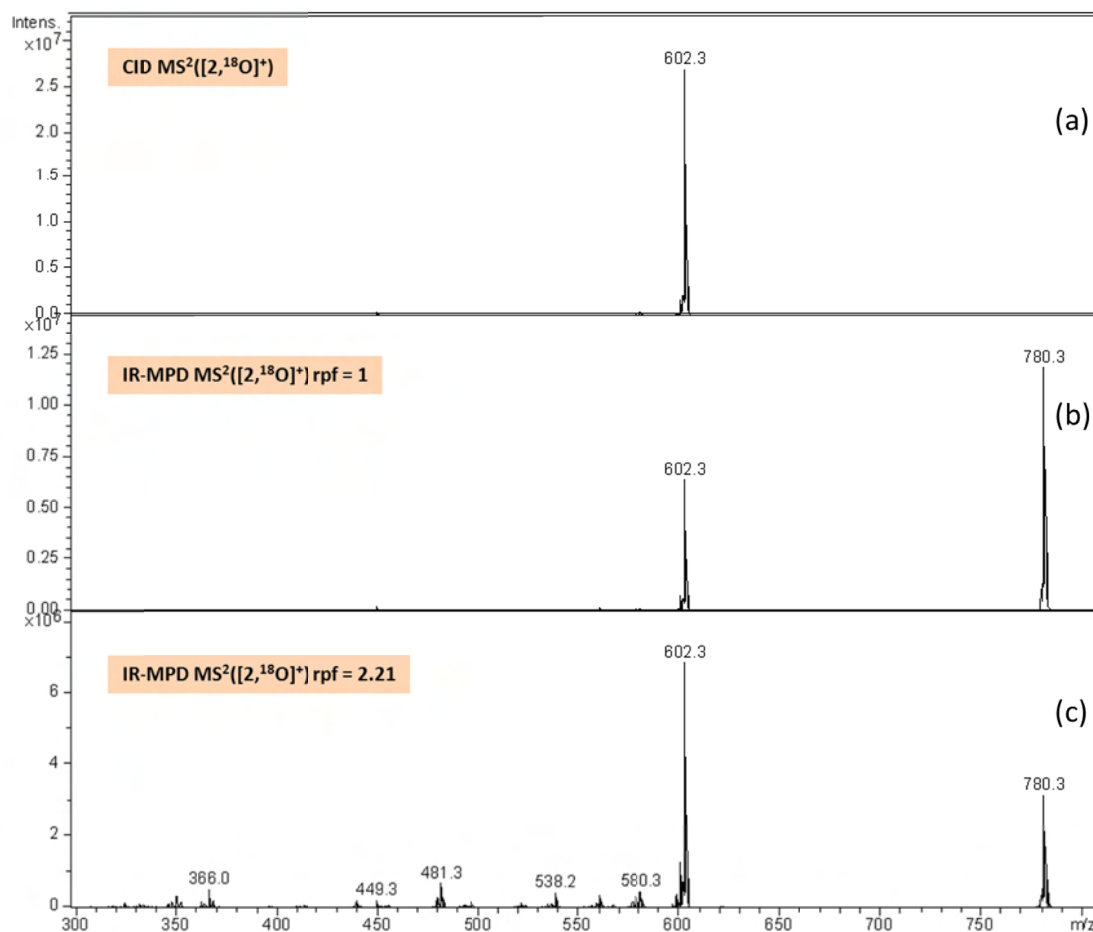


**Figure 6:**  $MS^2$  spectrum of isolated  $[2,^{18}O]^+$  ( $778.3\ m/z$ ) during CID (a).  $MS^2$  spectrum of isolated  $[2,^{18}O]^+$  ( $778.3\ m/z$ ) during IR-MPD with low relative photon flux ( $rpf = 1$ ) (b) and high relative photon flux ( $rpf = 2.21$ ) (c). Both IR-MPD spectra are summarized over single mass spectra within the band at  $2978\ cm^{-1}$ .

Fragmentation via IR-MPD not only yields in the most abundant CID fragmentation channels (loss of  $C_2Ph_2$ ). It also leads to a couple of fragments are assigned to the loss of isopropyl groups from the  $^4Cp$  rings (cf. Fig. 6 and Table 1). The contribution of multiple neutral loss channels to the overall fragment ion intensity varies with the photon flux and the IR strength of the vibrational modes of the  $[2,^{18}O]^+$  ions. Note, that CID causes complete parent depletion while IR-MPD does not. This points to incomplete/partial illumination by the IR laser of the trapped ion cloud.

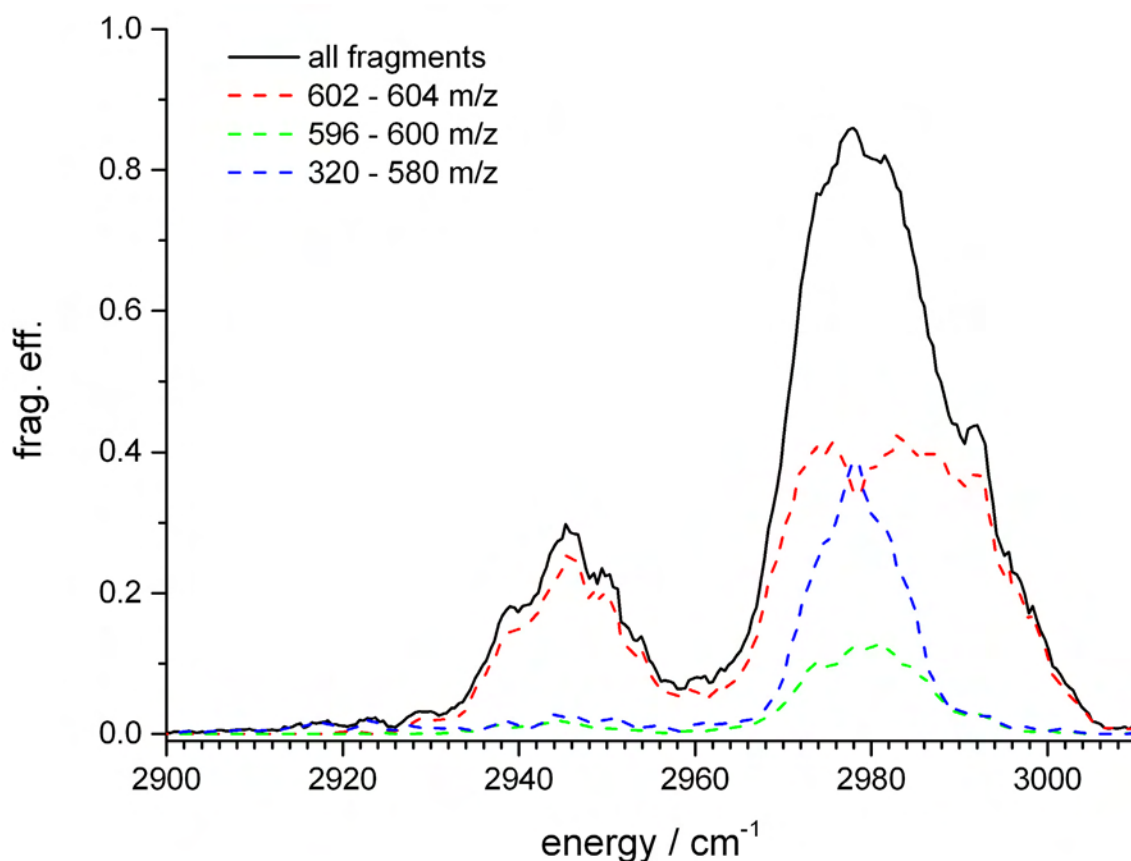


**Figure 7:** IR-MPD spectra of  $[2,^{18}\text{O}]^{+}$ . Dashed lines exhibit the contribution of  $\text{C}_{2}\text{Ph}_{2}$  ( $602 - 604 \text{ m/z}$ ) and  $n \text{ H}_{2}$  ( $596 - 600 \text{ m/z}$ ,  $n=1-3$ ) losses and of multiple fragments from  $^{4}\text{Cp}$  ( $320 - 580 \text{ m/z}$ ) to the overall fragmentation efficiency.

We studied the relative contribution of partial fragments to the overall fragmentation efficiency in the case of the most fragile complex  $[2,^{18}\text{O}]^{+}$ . This is meant to investigate the energy dissipation within the complex towards the fragmentation channels (cf. Fig. 7). The loss of  $\text{C}_{2}\text{Ph}_{2}$  is the dominant channel for the band at  $2945 \text{ cm}^{-1}$ . As soon as the overall fragmentation efficiency exceeds 40% within the  $2978 \text{ cm}^{-1}$  band the contribution of additional losses of  $\text{H}_{2}$  molecules and higher fragments from the  $^{4}\text{Cp}$  ligands rises. 50% of the overall fragmentation efficiency in the center of the  $2978 \text{ cm}^{-1}$  band arises from the contribution of masses between 320 and 600  $\text{m/z}$ . The relative contribution of the loss of  $\text{C}_{2}\text{Ph}_{2}$  stays at approximately 40% in the center region of the  $2978 \text{ cm}^{-1}$  band. The band at  $2945 \text{ cm}^{-1}$  arises almost only from  $\text{C}_{2}\text{Ph}_{2}$  loss.

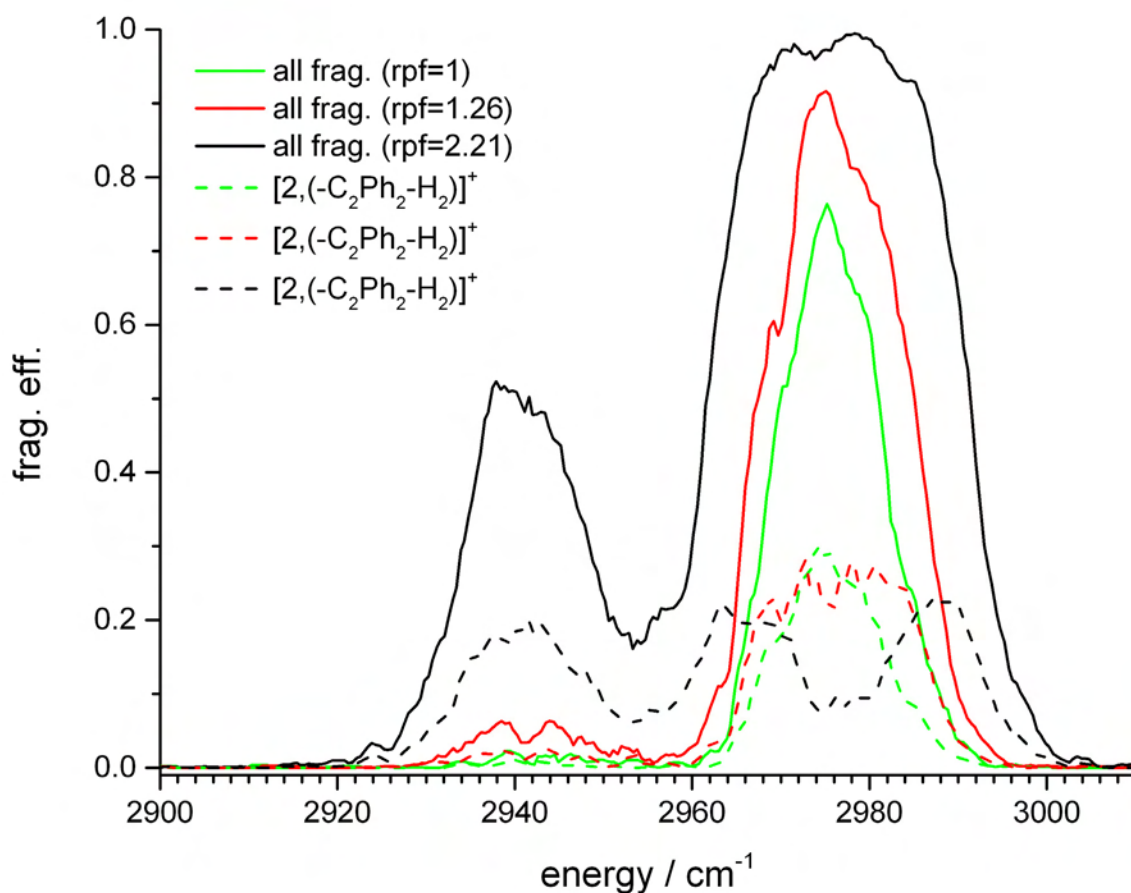


**Figure 8:** IR-MPD spectra of  $2^+$  (solid lines, all ionic fragments) and likely contributions of  $[2,(-C_2Ph_2-H_2)]^+$  fragments (dashed lines) recorded by variation of relative photon fluxes (rpf). At high photon flux, the fragment seems to decay further by additional photon absorption (cf. dip in black dashed curve).

Variation of photon flux during the IR-MPD of  $2^+$  in the region from 2900 to 3100  $cm^{-1}$  exhibits an increase of the fragmentation efficiency until the band at 2980  $cm^{-1}$  is saturated (cf. Fig. 8). The combined loss of  $C_2Ph_2$  and  $H_2$  (dashed lines) is not directly proportional to the photon flux while it exhibits the same trend for low fluxes. High photon flux reduces the contribution of  $C_2Ph_2$  and  $H_2$  losses to the overall frag. eff. (black dashed line).



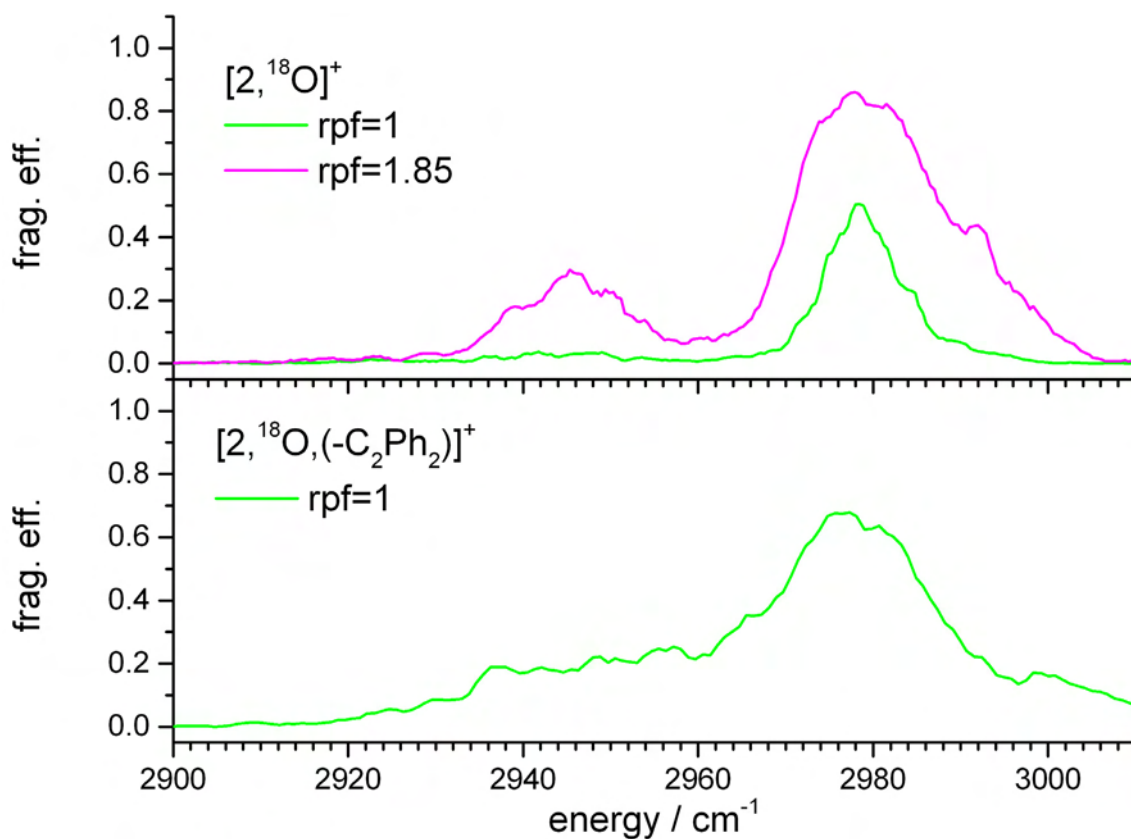


**Figure 9:** IR-MPD spectra of  $[2, ^{18}\text{O}]^+$  and its main fragment  $[2, ^{18}\text{O}, (-\text{C}_2\text{Ph}_2)]^+$ , recorded with different photon fluxes.

We measured IR-MPD spectra of complex  $[2, ^{18}\text{O}]^+$  and of its fragment  $[2, ^{18}\text{O}, (-\text{C}_2\text{Ph}_2)]^+$  in order to compare the contribution of both species to the overall bands within the spectra of  $[2, ^{18}\text{O}]^+$  (cf. Fig. 9). The spectrum of the main fragment of  $[2, ^{18}\text{O}, (-\text{C}_2\text{Ph}_2)]^+$  after the loss of  $\text{C}_2\text{Ph}_2$  exhibits a similar shape of the band in the region from 2960 to 3000  $\text{cm}^{-1}$ . In the region above 3000  $\text{cm}^{-1}$  an additional broad band appears while the band at 2945  $\text{cm}^{-1}$  in the parent spectrum is flattened and broadened. Comparable photon fluxes enhance the overall fragmentation efficiency of the  $[2, ^{18}\text{O}, (-\text{C}_2\text{Ph}_2)]^+$  cation with respect to the one of  $[2, ^{18}\text{O}]^+$ .

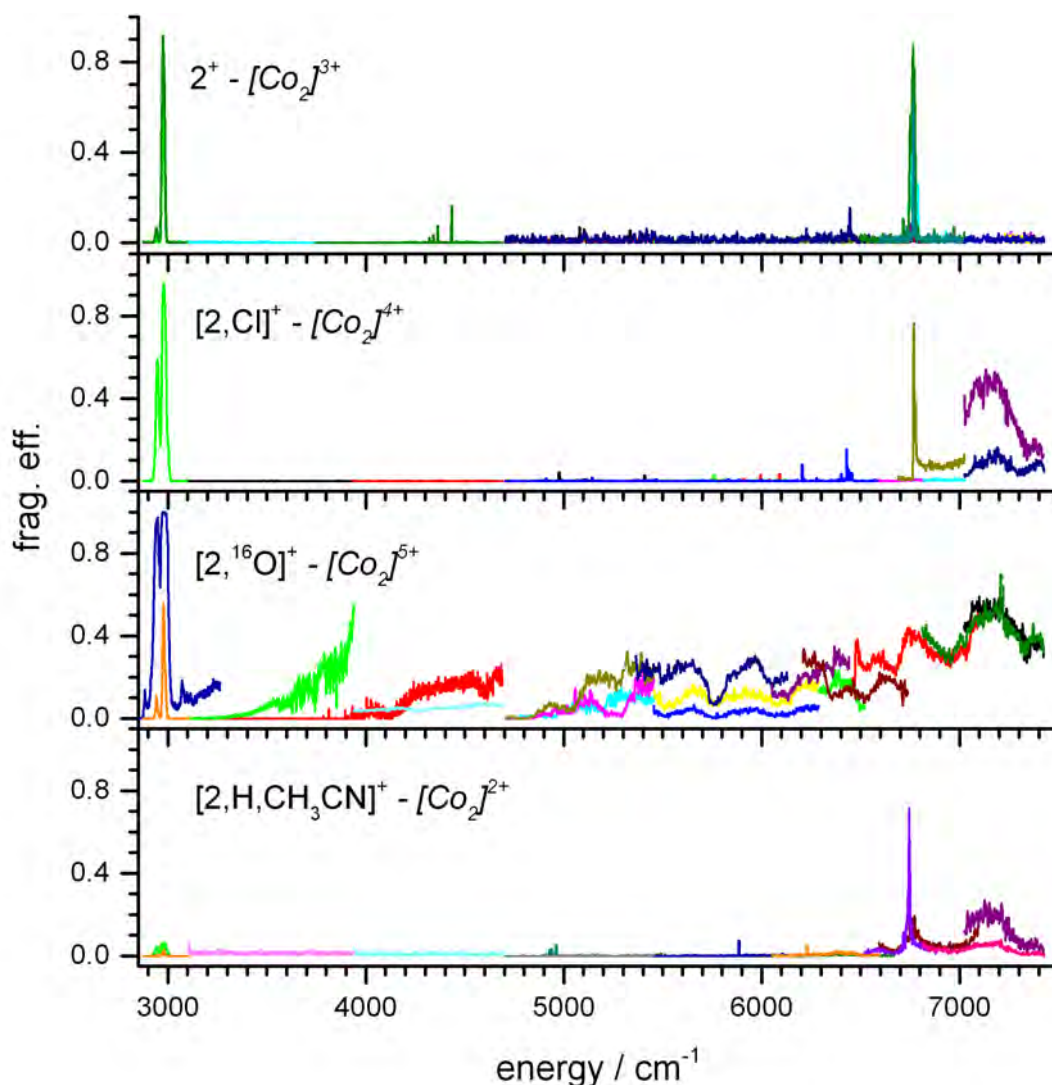


**Figure 10:** IR-MPD spectra of  $2^+$ ,  $[2,\text{Cl}]^+$ ,  $[2,^{16}\text{O}]^+$  and  $[2,\text{H},\text{CH}_3\text{CN}]^+$  recorded with various photon fluxes. Formal charge state of the  $[\text{Co}_2]$  unit is emphasized. Color of lines is arbitrarily chosen, multiple assigned regions are measured with various photon fluxes.

Spectra in the mid- to near-IR region ( $2800$  to  $7500\text{ cm}^{-1}$ ) of  $2^+$  and of its adducts exhibit several bands (cf. Fig. 10).  $2^+$  and  $[2,\text{H},\text{CH}_3\text{CN}]^+$  exhibit a sharp band at  $6750\text{ cm}^{-1}$  the latter one an additional inhomogeneously broad band at  $7000$  to  $7300\text{ cm}^{-1}$ . Furthermore  $[2,\text{H},\text{CH}_3\text{CN}]^+$  exhibits a quite high fragmentation efficiency for the near-IR bands, while the mid-ID bands at  $2800$  to  $3000\text{ cm}^{-1}$  are relatively weak.  $[2,\text{Cl}]^+$  exhibits broad bands at  $7000$  to  $7300\text{ cm}^{-1}$ , much like  $[2,\text{H},\text{CH}_3\text{CN}]^+$ .  $[2,^{16}\text{O}]^+$  exhibits several broad bands in the range of  $3000$  to  $7400\text{ cm}^{-1}$ .

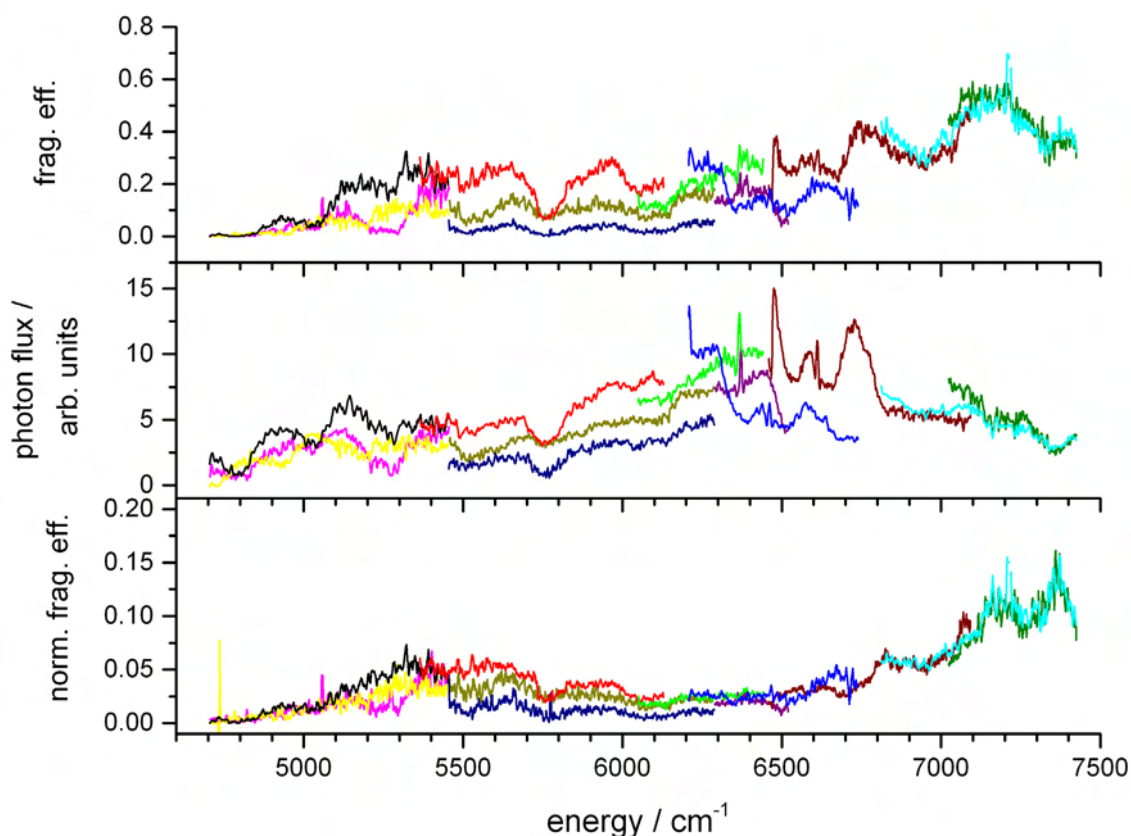


**Figure 11:** Near IR-MPD spectra of  $[2,^{16}\text{O}]^+$  (top), laser intensities (middle) and power normalized spectra (bottom). Variations in photon flux arise in part from experimental complications, see text.

Intensities of these bands strongly depend on photon flux, which varies significantly (cf. Fig. 11, mid). We normalized the fragmentation efficiency linearly by the photon flux. The normalized fragmentation efficiency reveals more clear structured and largely reproducible spectra (cf. Fig. 11, bottom). Two main bands emerge at 5000 to 6000  $\text{cm}^{-1}$  with a center at 5500  $\text{cm}^{-1}$  and at 6500 to 7400  $\text{cm}^{-1}$  with a maximum at 7390  $\text{cm}^{-1}$ . Especially in the region from 5000 to 6000  $\text{cm}^{-1}$  linear power scaling seems to fail.

Scan by scan variation are non negligible and have to find attention in the future. Further complications arise from trace gas absorption lines because of unappropriately lacking purging opportunities. These deficiencies need to be helped in the next future.

#### IX-4.3: Discussion

Some of the  $[2,^{18}\text{O}]^+$  ions (cf. Fig. 6 bottom) do not fragment at high photon fluxes. This can be interpreted by the assumption that the ion cloud does not completely overlap with the focused laser beam. The beam of gaussian shape does not irradiate all ions equally. They absorb different

amounts of photons. 40% of all fragmented  $[2,^{18}\text{O}]^+$  molecules absorb by two laser pulses (200 ms storage time in the Paul trap, 100 ms between two laser pulses) an amount of photons that suffices to loose  $\text{C}_2\text{Ph}_2$  (cf. Fig. 7).

Effective IR-MPD implies fast internal vibrational redistribution (IVR) that enables the subsequent absorption of multiple photons. The loss of  $\text{C}_2\text{Ph}_2$  from complex  $[2,^{16/18}\text{O}]^+$  seems to be favored. It occurs more efficient and may be faster than the desintegration of the  $^4\text{Cp}$  ligands (cf. Fig. 6, band at  $2945\text{ cm}^{-1}$ ). It can be assumed that the loss of  $\text{C}_2\text{Ph}_2$  leads to a change in the distances and angles of the  $[\text{Co}_2\text{O}]$  unit of the  $[2,^{18}\text{O},(-\text{C}_2\text{Ph}_2)]^+$  ion. Therefore the IR-MPD derived bands with contributions of fragment channels other than the loss of  $\text{C}_2\text{Ph}_2$  may not reflect bands only derived from  $[2,^{18}\text{O}]^+$ . Furthermore they also exhibit contributions of the  $[2,^{18}\text{O},(-\text{C}_2\text{Ph}_2)]^+$  fragment and of other fragment ions (cf. Fig. 9).

In contrast to  $[2,^{18}\text{O}]^+$ , in  $2^+$  the loss of  $\text{C}_2\text{Ph}_2$  is not the preferred fragmentation channel (cf. Fig. 8). This also shows in CID experiments where the loss of  $\text{C}_2\text{Ph}_2$  comes along with fragmentations of the isopropyl groups of the  $^4\text{Cp}^-$  ligands (cf. Fig. 3). These two fragmentation channels seem to be energetically more or less equivalent.

The IR-MPD spectrum of the  $602.3\text{ m/z}$  fragment helps vibrational assignment of  $[2,^{18}\text{O}]^+$  (cf. Fig. 9). The first fragmentation process (loss of  $\text{C}_2\text{Ph}_2$ ) heats up the molecule while the internal rotation of the  $^4\text{Cp}$  rings is no longer sterically hindered. Further energy input enables to split of  $\text{H}_2$ ,  $\text{C}_2\text{H}_2$  and  $\text{C}_2\text{H}_4$ . The recorded IR-MPD spectrum thus consists of a superposition of the spectral contributions from the  $[2,^{18}\text{O},(-\text{C}_2\text{Ph}_2)]^+$  and further fragment ions. The loss of the  $\text{C}_2\text{Ph}_2$  moiety results in a lower heat capacity of the molecule. Lower heat capacity and the energy stored in rotational degrees of freedom enable a rise in fragmentation efficiency even within same photon flux as in the spectra of  $[2,^{18}\text{O}]^+$  ( $\text{rpf} = 1$ ). The bands at  $2980\text{ cm}^{-1}$  and  $2945\text{ cm}^{-1}$  remain even after the loss of the  $\text{C}_2\text{Ph}_2$  molecule. Therefore, it can be stated, that those two bands correspond to aliphatic CH vibrational stretching modes of the  $^4\text{Cp}$  ligands.

The sharp bands at  $6750\text{ cm}^{-1}$  for  $2^+$  and  $[2,\text{H},\text{CH}_3\text{CN}]^+$  may correspond to metal-to-ligand charge-transfer (MLCT) bands, while the broad bands for  $2^+$ ,  $[2,^{16}\text{O}]^+$  and  $[2,\text{H},\text{CH}_3\text{CN}]^+$  may correspond to vibrations of excited electronic states (cf. Fig. 10). Note the correlation with the formal charges at the  $[\text{Co}_2]$  unit.

The observed reaction products confirm that the  $[\text{Co}_2]$  unit in complex **2** may obtain four charge states (cf. Table 1). **High charge states** of the  $[\text{Co}_2]$  unit lead to a **favoured loss of  $\text{C}_2\text{Ph}_2$** . **Low charge states** enable contributions of **fragments out of the  $^4\text{Cp}$  ligands**. The addition of  $\text{X}$  ( $\text{X}=\text{H}^+$ ,  $\text{CH}_3\text{CN}$ ,  $\text{Cl}^-$ ,  $^{16/18}\text{O}^{2-}$ ) to complex **2** changes IR-MPD fragmentation patterns. Variation of  $\text{X}$  binding sites seem likely. The surprising stability of  $[\mathbf{2},\text{H},\text{CH}_3\text{CN}]^+$  withstands a definite interpretation. At least two structures are conceivable (cf. Fig. 12). The reaction of  $\text{CH}_3\text{CN}$  with cobalt-acetylene is known to yield heteroaromatic species in solution [41].

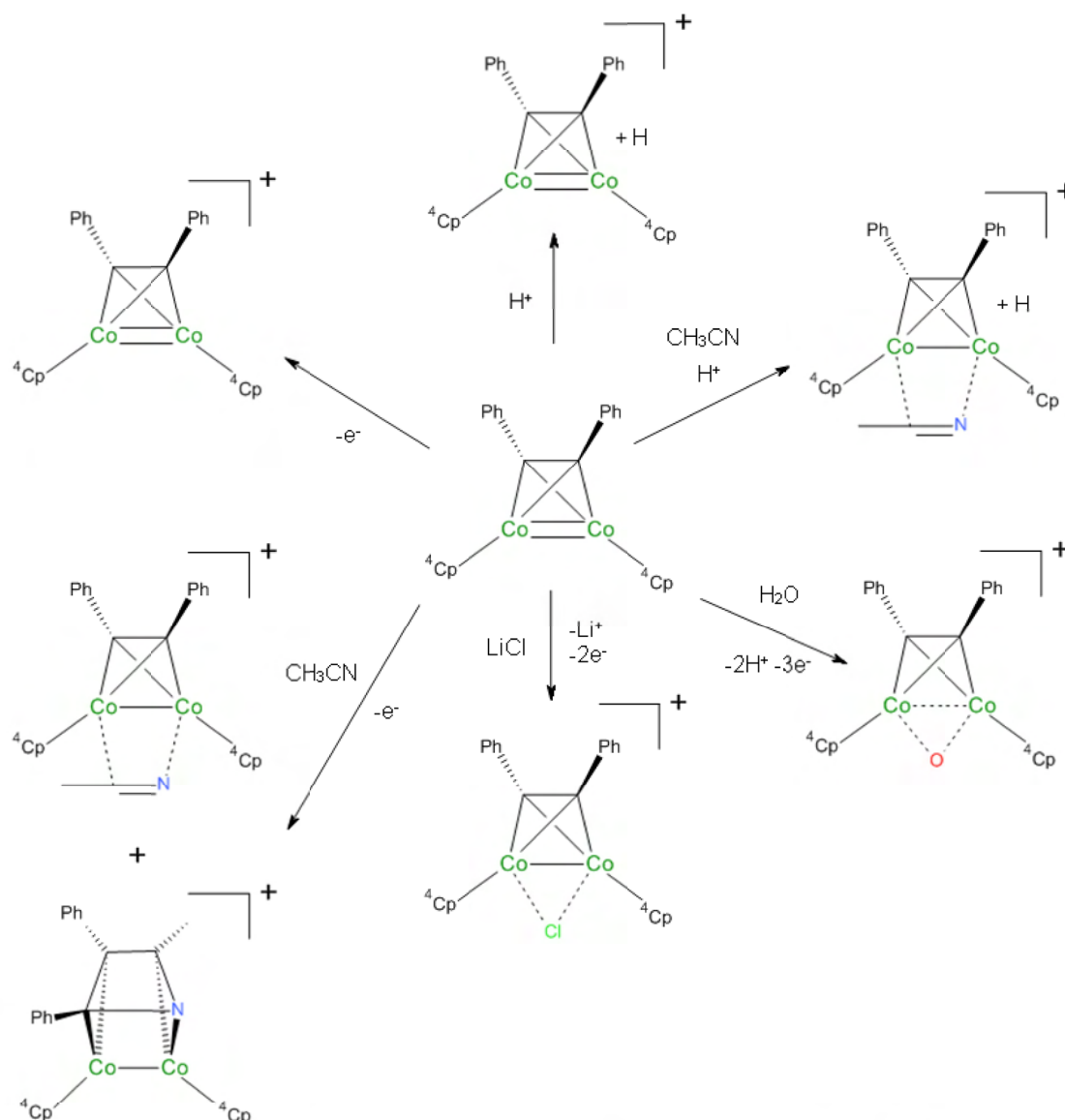


**Figure 12:** Possible structures of reaction products of **2** (center) after addition of acetonitrile,  $\text{H}_2^{16/18}\text{O}$  or  $\text{LiCl}$  to solutions of **2** in THF monitored by ESI-MS as cationic complexes.

### IX-5: Gauging the level of DFT theory by the help of model complex **1**

We performed DFT calculations of complex **1** to gauge the level of theory. The crystal structure of complex **1** was determined by X-ray analysis [12]. Complex **1** has less free/hindered rotors (such as isopropyl groups at  $^4\text{Cp}$ ) than complex **2**. Less steric hinderance and less dispersion interaction has to be regarded (cf. Fig. 13), while the main binding motive at the  $[\text{Co}_2]$  unit is the same. We applied a variation of functionals and basis sets on complex **1**, and we examined the influence of the multiplicity on geometry and energetics.

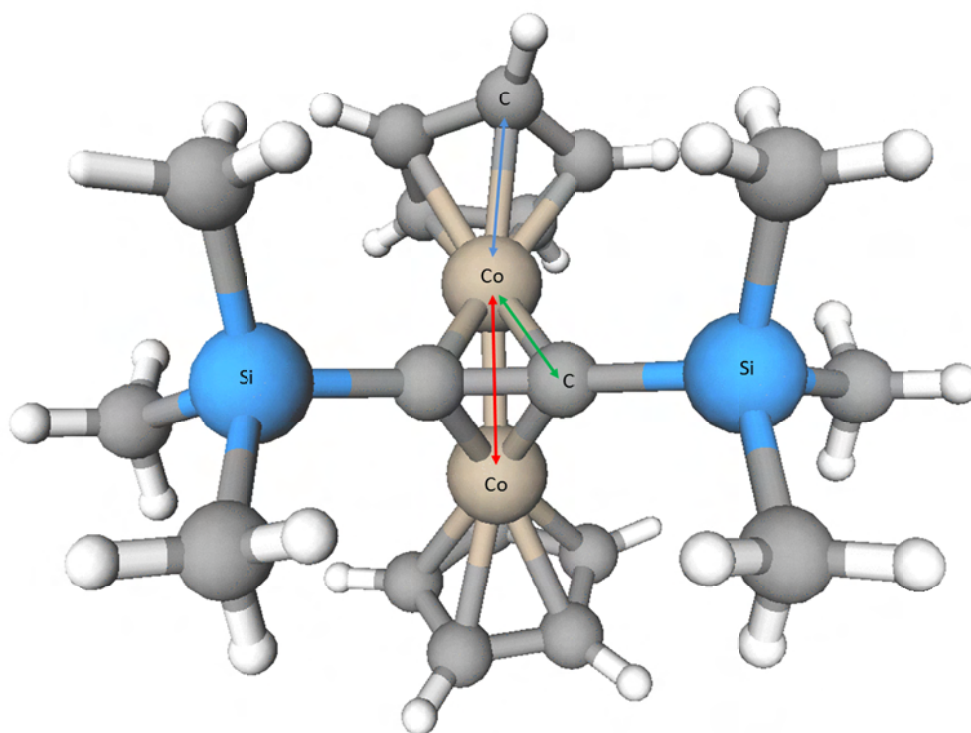


**Figure 13:** Crystal structure of **1** [12]. Arrows represent the distances between Co-Co (-), Co-Cp (-) and Co-C<sub>2-bridge</sub> (-) to be discussed in the text and in Fig. 14.

#### IX-5.1: Results of calculations on complex **1**

We choose three representative distances,  $d(\text{Co-Co})$ ,  $d(\text{Co-Cp})$  and  $d(\text{Co-C}_{2\text{-bridge}})$ , for evaluation. Those distances correlate directly to the electronic environment of the  $[\text{Co}_2]$  unit, and they represent the resulting structural changes.

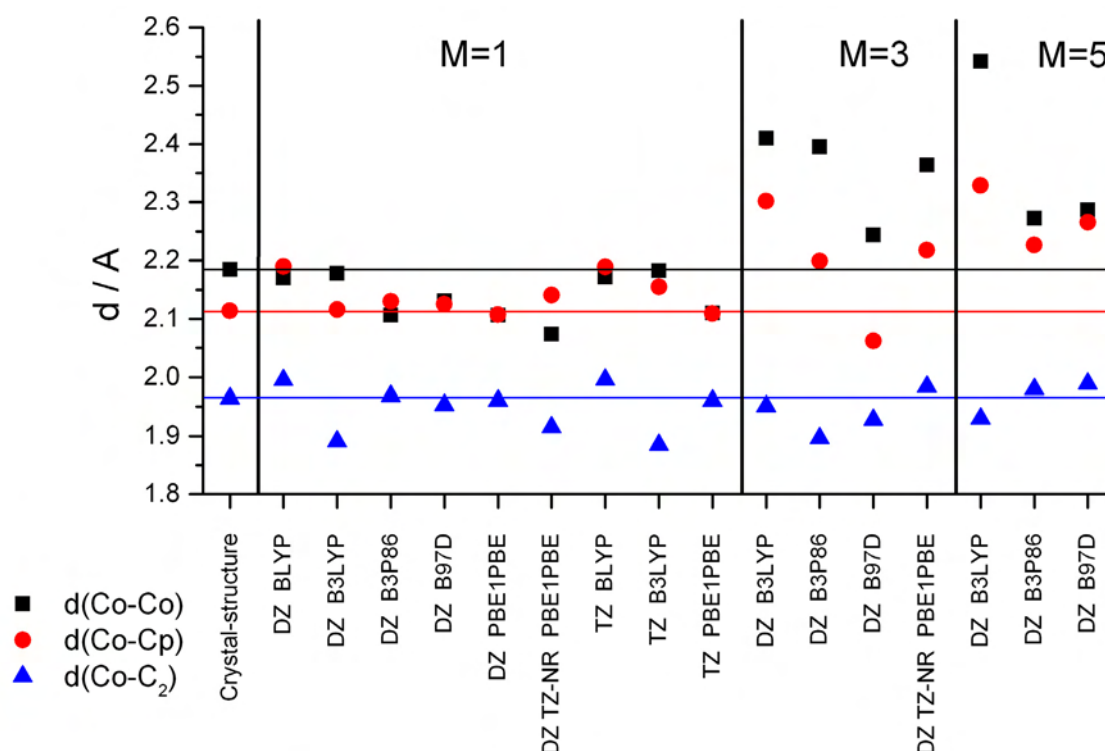


**Figure 14:** Selected atom distances in **1** (as of Fig. 13) as calculated by various combinations of basis set (DZ = cc-pVDZ, TZ = cc-pVTZ (H, C, Si) and Stuttgart 1997 ECP (Co, not labelled) or TZ-NR = Stuttgart 1997 ECP and cc-pVTZ-NR (Co)) and DFT functional (labeled), and multiplicity (M). For energetics refer to Table 2. Solid lines indicate the distances within the bulk.

The results of the model calculations are depicted in Fig. 14. No combination of basis set and functional predicts all three chosen distances as observed in the X-ray crystal structure. The B3LYP functional with cc-pVDZ or cc-pVTZ (C, H, Si) and Stuttgart 1997 ECP (Co) basis sets matches the  $d(\text{Co-Co})$  and  $d(\text{Co-}^4\text{Cp})$  X-ray distances well, while it underestimates the  $d(\text{Co-C}_2)$  X-ray distance in low spin state ( $M=1$ ). B3P86, B97D and PBE1PBE functionals combined with cc-pVDZ and Stuttgart 1997 ECP basis sets exhibit a good agreement to the  $\text{Co-}^4\text{Cp}$  and  $\text{Co-C}_2$  X-ray bond distances, while the calculated  $\text{Co-Co}$  distance is in all cases predicted shorter than in the crystal structure. Applying an additional non-relativistic cc-pVTZ-NR basis to the Stuttgart 1997 ECP for the Cobalt atoms at the PBE1PBE level leads to a deviation in all distances. The use of triple zeta basis sets does not increase the quality of the derived results significantly and is therefore not used further. DFT calculations with  $M=3$  and  $M=5$  exhibit in all cases an elongation of the  $\text{Co-Co}$  bond distance and show no clear trend for the other both distances.



Comparison of relative energies of the lowest three multiplicities exhibits two trends for the three selected functionals (cf. Table 2). B3LYP and B3P86 estimate M=3 as the ground state while B97D exhibits comparable values for M=1 and M=3. B3LYP and B3P86 exhibit the same trend in relative energies.

**Table 2:** Relative energies in kJ/mol for **1** in different multiplicities and by various theory levels, all calculated with cc-pVDZ (C, H, N, O, Cl) and Stuttgart 1997 ECP (Co) basis sets. Some low lying imaginary frequencies prevail in most cases. They are attributed to conceptional numerical limitations.

<b>multiplicity</b>	<b>B3LYP</b>	<b>B3P86</b>	<b>B97D</b>
1	71	64	0
3	0	0	5
5	28	23	67

### IX-5.2: DFT calculations of complex 2

We used B3LYP and B97D functionals for the calculation of different reaction products of **2** under ESI-MS conditions as described before. We selected up to seven characteristic bond distances (cf. Fig. 15).

Change in multiplicity has a strong influence to the length of the Co-Co bond, as well as to the Co-C<sub>2</sub> distances within all molecules while the Co-<sup>4</sup>Cp(CH) and Co-X distances are only slightly affected (cf. Fig. 15). The reaction of an oxygen atom with **2**<sup>+</sup> leads to an asymmetric distortion of the molecule which has a crucial influence to the Co-C<sub>2</sub> interaction in M=6\* (cf. structures depicted in Fig. 15). The reaction of a Cl<sup>-</sup> anion with complex **2**<sup>+</sup> has a smaller influence on the Co-C<sub>2</sub> (n=1,2) bond lengths while it is less strongly bound to the two Cobalt atoms than anionic O<sup>2-</sup>. B97D and B3LYP calculations exhibit same trends in all characteristic bond lengths.



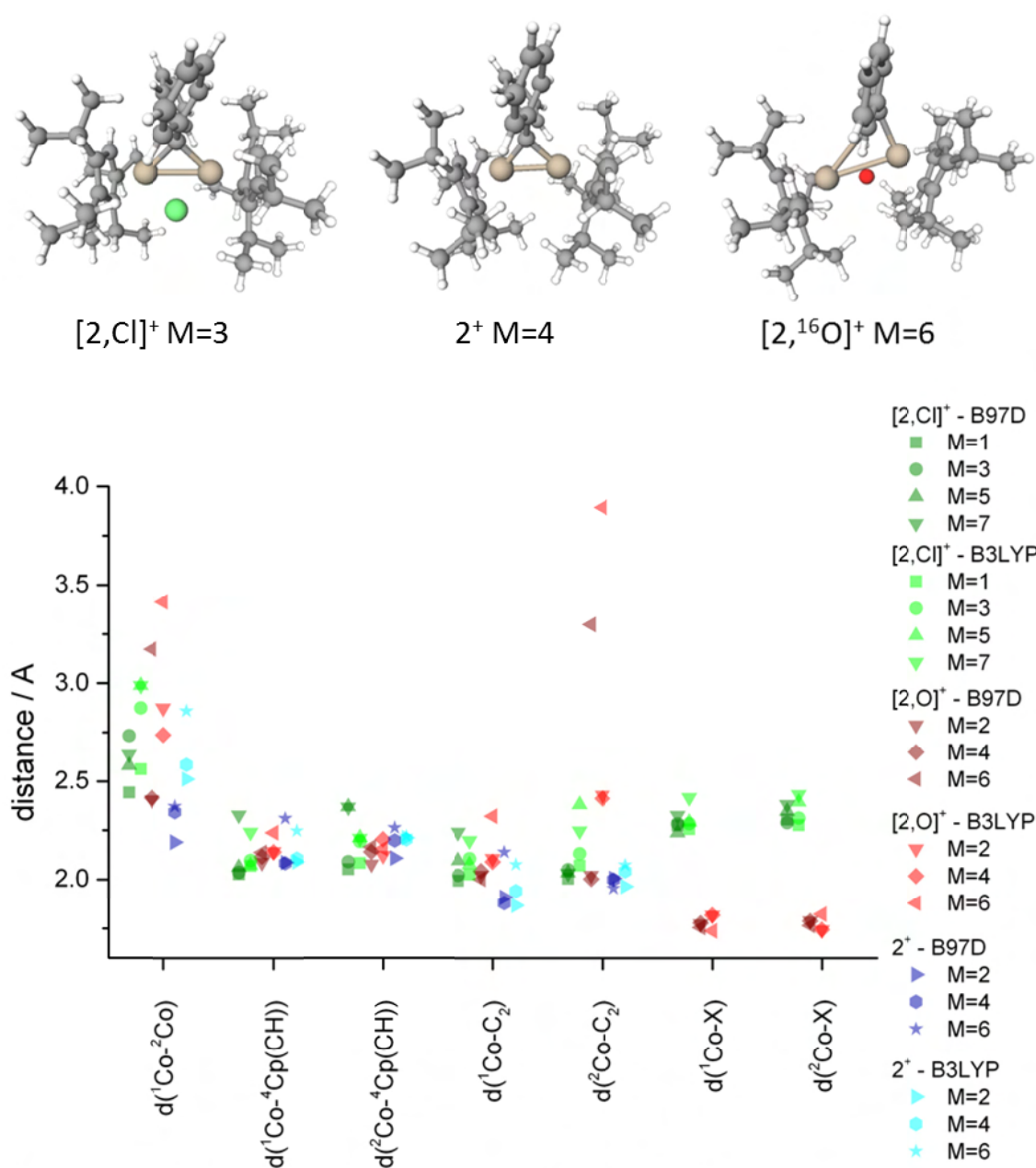


**Figure 15:** Distances of selected atoms within  $2^+$ ,  $[2,\text{Cl}]^+$  and  $[2,^{16}\text{O}]^+$  for different multiplicities at the B3LYP/cc-pVDZ (C, H, O, Cl) and Stuttgart 1997 ECP (Co) level of theory, B97D respectively. Insets are calculated with B3LYP.  $d^n(\text{Co}-\text{C}_2)$  ( $n=1,2$ ) corresponds to the distance between one cobalt atom to the left carbon atom of the  $\text{C}_2\text{Ph}_2$  bridge, seen above the main axes along Co-Co. ( $X=\text{Cl}, \text{O}$ )

All structures derived with B3LYP do not exhibit the lowest multiplicity as the ground state (cf. Table 3), whereas DFT calculations with B97D exhibit mostly the lowest multiplicity as the ground state, except for  $[2,^{16}\text{O}]^+$ .

**Table 3:** Relative energies in kJ/mol for  $2^+$ ,  $[2,^{16}\text{O}]^+$ ,  $[2,\text{Cl}]^+$  and  $[2,\text{H},\text{CH}_3\text{CN}]^+$  in different multiplicities, as calculated at the B3LYP/cc-pVDZ (C, H, N, O, Cl) and Stuttgart 1997 ECP (Co) level of theory, B97D respectively.

multiplicity	$2^+$		$[2,^{16}\text{O}]^+$		multiplicity	$[2,\text{Cl}]^+$		$[2,\text{H},\text{CH}_3\text{CN}]^+$	
	B3LYP	B97D	B3LYP	B97D		B3LYP	B97D	B3LYP	B97D
2	27	0	61	6	1	49	0	0	
4	0	42	33	0	3	0	38	26	
6	1	117	0	103	5	12	73		
					7	28	136		

### IX-5.3: Discussion

Packing effects in the crystal could lead to differences between the experimental atom distances derived from X-ray analysis and DFT derived bond lengths. The appropriate description of the third row transition metals varies strongly by the DFT functional [42].

DFT calculations at higher multiplicities exhibit in all cases an elongation of the d(Co-Co) atom distance and most often also an elongation of the d(Co-Cp) bond length (cf. Fig. 14). It can be assumed that highspin multiplicities  $M > 1$  would increase the overall volume of the molecule and would not reflect the binding behavior within the unit cell of the crystal. We assume that the structure derived by X-ray analysis of the crystal is in its electronic ground state.

The DFT functionals B3LYP and B3P86 exhibit the same trend in relative energies (cf. Table 2) for various multiplicities and predict  $M=3$  as the most stable spin state, whereas B97D predicts  $M=1$  as the most stable state. The use of the B97D functional leads to results that seem to agree better with X-ray data in terms of the proposed  $M=1$  ground state. Nevertheless, we use the DFT functionals B97D as well as B3LYP combined with cc-pVDZ and Stuttgart 1997 ECP basis sets for further DFT calculations in order to compare their influence to the prediction of bond lengths in minimum structures of singly and multiply oxidized reaction products of  $2^+$  at various multiplicities (cf. Fig. 15).

There are large variations in the predicted  $[\text{Co}_2]$  bond length of  $2^+$ ,  $[2,\text{Cl}]^+$  and  $[2,^{16}\text{O}]^+$  (cf. Fig. 15). Cobalt-Cobalt distances derived from DFT at the B97D level of theory are in all cases shorter than those derived at the B3LYP level, while there is no clear correlation between the chosen functional and other bond lengths. Interestingly, both functionals predict more or less constant  $d(^1\text{Co-X})$  and

$d({}^2\text{Co-X})$  ( $X = \text{Cl}, \text{O}$ ) atom distances for several multiplicities of  $[\mathbf{2},\text{Cl}]^+$  and  $[\mathbf{2},{}^{16}\text{O}]^+$  while the  $d({}^4\text{Co}-{}^2\text{Co})$  distance strongly depends on the chosen conditions. We can not identify an appropriate level of theory to describe the electronic structure of the  $[\text{Co}_2]$  unit in complexes **1** and **2**. Therefore, we compare IR-MPD derived absorption bands to those predicted by DFT and TD-DFT at the B97D and B3LYP level of theory.

## **IX-6: Comparison of IR-MPD spectra of $2^+$ and of its reaction products with DFT predictions**

### **IX-6.1: IR-MPD spectra and DFT predicted IR absorption bands of complex $2^+$ and of its reaction products**

We used DFT calculations at the B3LYP/cc-pVDZ (C, H, N, Cl) and Stuttgart 1997 ECP (Co) level of theory, B97D respectively, in order to predict IR absorption spectra of  $2^+$  and of its reaction products  $[\mathbf{2},\text{Cl}]^+$ ,  $[\mathbf{2},{}^{16}\text{O}]^+$  and  $[\mathbf{2},\text{H},\text{CH}_3\text{CN}]^+$  (cf. Table 3). We estimated a scaling factor of 0.957 from the DFT predicted IR absorption spectrum of complex  $2^+$  at the B3LYP level of theory by scaling the position of the asymmetric CH stretching modes to the experimental spectrum, and a scaling factor of 0.9723 for spectra derived at the B97D level of theory, respectively (cf. Fig. 16 and 17 and Table 4 for numerical values).

DFT derived IR absorption bands at  $2975\text{ cm}^{-1}$  correspond to asymmetric stretching modes of aliphatic CH groups of the  ${}^4\text{Cp}^-$  ligands while these bands below  $2850\text{ cm}^{-1}$  correspond to the symmetric stretching modes of the same groups. Stretching modes of aromatic CH groups occur as a small band just above  $3000\text{ cm}^{-1}$  (cf. Table 4).

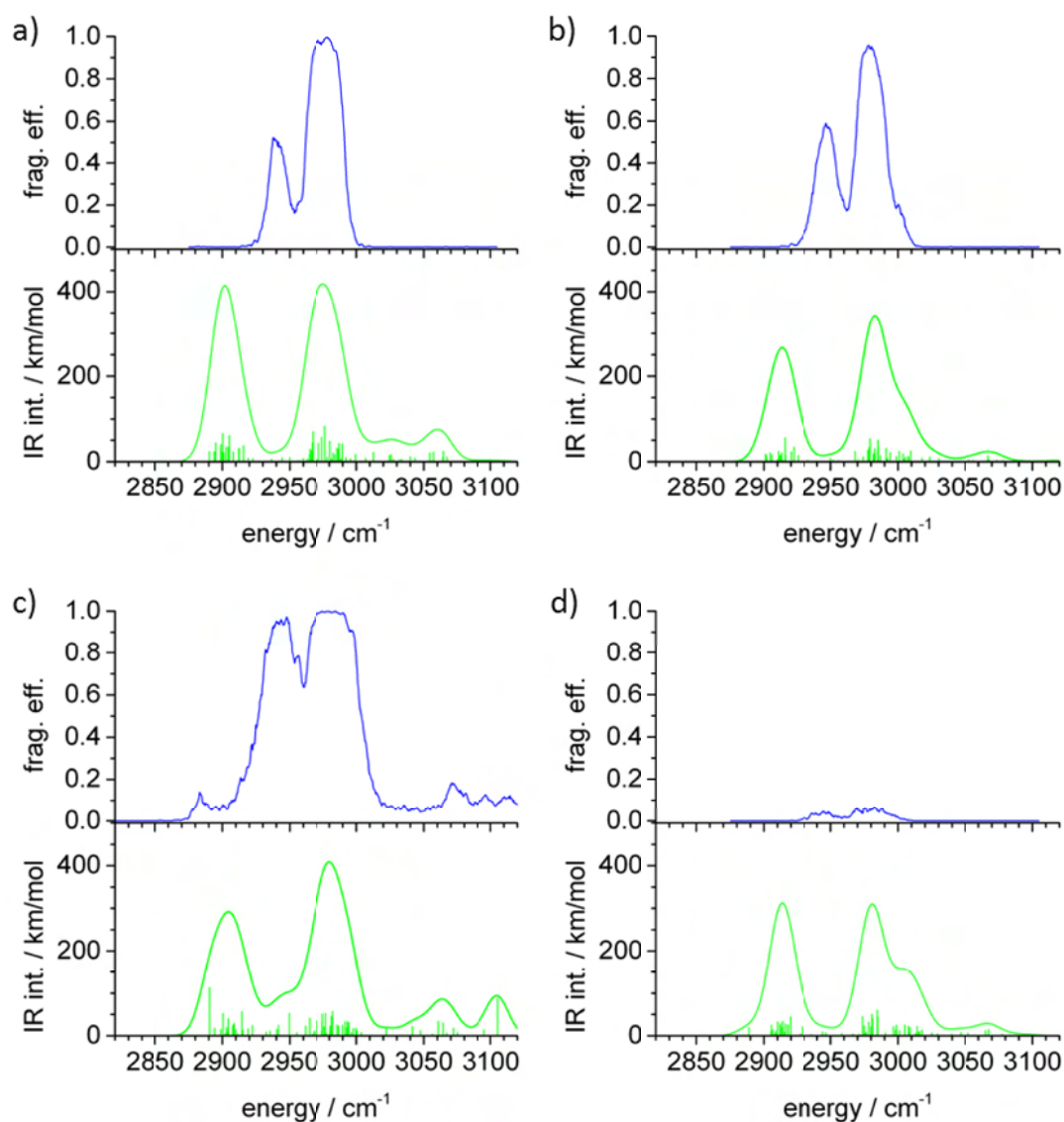


**Figure 16:** Experimental IR-MPD spectra (blue) and calculated DFT IR absorption spectra (green) of the minimum energy structures of  $2^+$  (a) ( $M=4$ ),  $[2,\text{Cl}]^+$  (b) ( $M=3$ ),  $[2,^{16}\text{O}]^+$  (c) ( $M=6$ ) and  $[2,\text{H},\text{CH}_3\text{CN}]^+$  (d) ( $M=3$ ) at the B3LYP/cc-pVDZ level of theory. Frequencies are scaled by 0.957. Calculated spectra are obtained by superposition of their gaussian profiles with FWHM of  $10\text{ cm}^{-1}$ .

Calculated IR spectra of  $2^+$ ,  $[2,\text{Cl}]^+$ ,  $[2,^{16}\text{O}]^+$  and  $[2,\text{H},\text{CH}_3\text{CN}]^+$  at the B3LYP level of theory exhibit an almost constant position of the most intense band at  $2975\text{ cm}^{-1}$  (cf. Fig. 16), whereas, the most intense band within the IR spectra of  $[2,\text{Cl}]^+$  and  $[2,^{16}\text{O}]^+$  derived at the B97D level of theory exhibit a shift to the red (cf. Fig. 17).

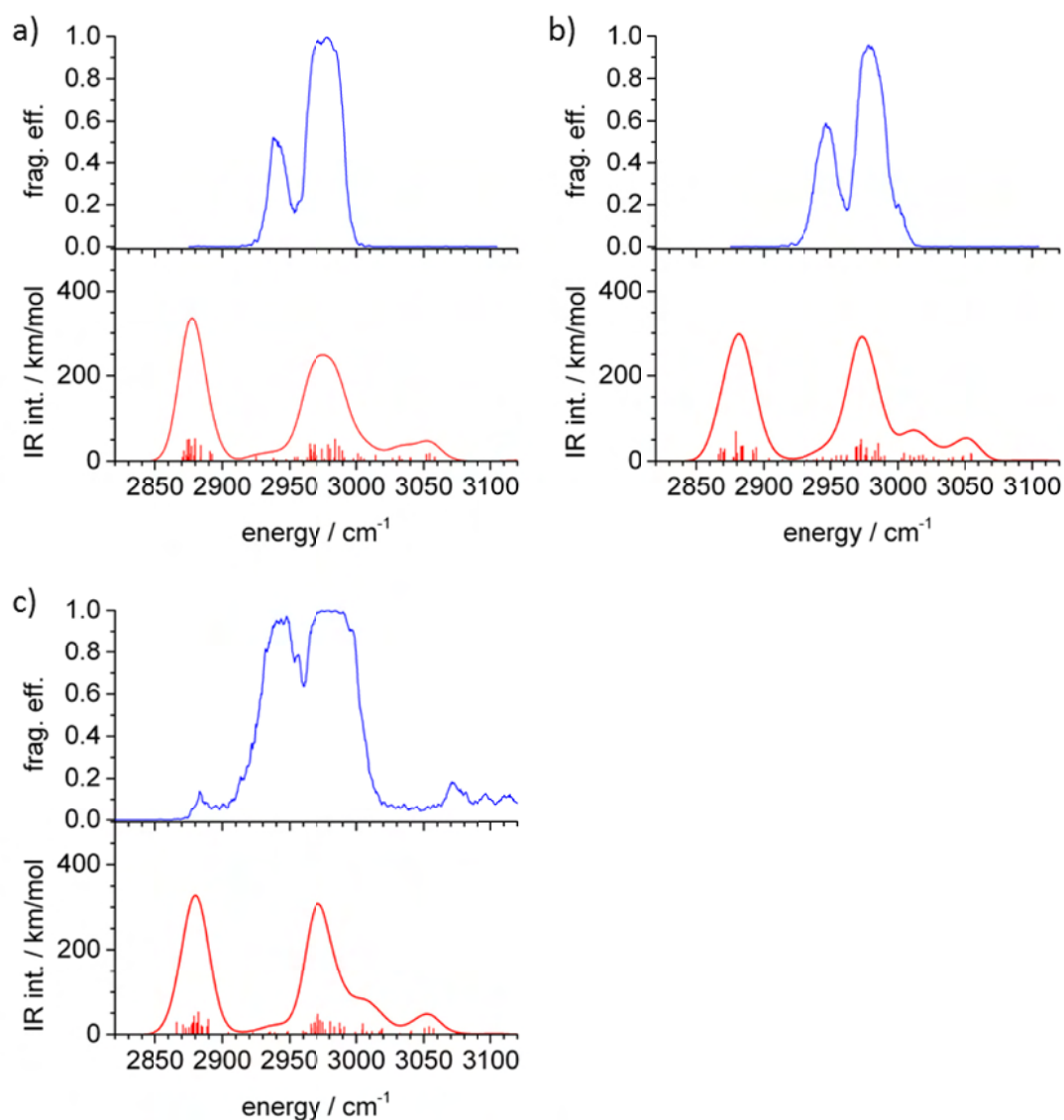


**Figure 17:** Experimental IR-MPD spectra (blue) and DFT derived IR absorption spectra (red) of the minimum energy structures of  $2^+$  (a) ( $M=4$ ),  $[2,\text{Cl}]^+$  (b) ( $M=1$ ) and  $[2,^{16}\text{O}]^+$  (c) ( $M=6$ ) at the B97D/cc-pVDZ level of theory. Frequencies are scaled by 0.9723. Calculated spectra are obtained by superposition of their gaussian profiles with FWHM of  $10\text{ cm}^{-1}$ .

It is evident, that the DFT predicted symmetric CH stretching modes do not agree with the measured frequencies in the IR-MPD spectra. Only the IR-MPD spectrum of  $[2,^{16}\text{O}]^+$  exhibits a band at  $2985\text{ cm}^{-1}$  at the theoretical predicted position (cf. Fig. 16 c) and 17 c), blue lines). None of the weak absorbing aromatic CH stretching modes of the  $\text{C}_2\text{Ph}_2$  ligand can clearly be assigned, a weak band at  $3072\text{ cm}^{-1}$  can only be observed for complex  $[2,^{16}\text{O}]^+$ .

**Table 4:** Assignment of experimental IR-MPD bands to calculated vibrational modes at the B3LYP/cc-pVDZ level of theory (after scaling with 0.9570), B97D/cc-pVDZ (after scaling with 0.9723) respectively, of  $2^+$ ,  $[2,Cl]^+$ ,  $[2,^{16}O]^+$  and  $[2,H,CH_3CN]^+$ . Values are according to depicted data in Fig. 16 and 17. Underlines indicate the atoms involved in the vibrational motions. (Abbreviations: calc. = calculated; arom. CH = CH stretching modes within the  $C_2Ph_2$  ligand; aliph. CH = CH stretching modes within the  $^4Cp$  ligand; ss = symmetric stretch; as = asymmetric stretch)

$2^+$			$[2,Cl]^+$			assignment
IR-MPD / $cm^{-1}$	B3YLP calc. / $cm^{-1}$	B97D calc. / $cm^{-1}$	IR-MPD / $cm^{-1}$	B3YLP calc. / $cm^{-1}$	B97D calc. / $cm^{-1}$	
	2902	2878		2913	2882	$v_{ss}$ (aliph. ( <u>CH</u> <sub>3</sub> ))
2940			2947			
2975	2975	2975	2979	2983	2974	$v_{as}$ (aliph. ( <u>CH</u> <sub>3</sub> ))
	3026	3033		3067	3011	$v_s$ (arom. <u>CH</u> )
	3060	3052		3120	3051	
$[2,^{16}O]^+$			$[2,H,CH_3CN]^+$			assignment
IR-MPD / $cm^{-1}$	B3YLP calc. / $cm^{-1}$	B97D calc. / $cm^{-1}$	IR-MPD / $cm^{-1}$	B3YLP calc. / $cm^{-1}$	B97D calc. / $cm^{-1}$	
	2905	2880		2914		$v_{ss}$ (aliph. ( <u>CH</u> <sub>3</sub> ))
		2941				
2884			2945			
2942						
2977	2980	2971	2981	2981		$v_{as}$ (aliph. ( <u>CH</u> <sub>3</sub> ))
	3063	3005				
3072				3066		$v_s$ (arom. <u>CH</u> )
	3105	3053				

### IX-6.2: IR-MPD spectra and TD-DFT predicted IR absorption bands of complex $2^+$ and its reaction products

Beyond vibrational analysis we aimed to model NIR electronic spectra of  $2^+$ ,  $[2,Cl]^+$ ,  $[2,^{16}O]^+$  and  $[2,H,CH_3CN]^+$  (cf. Fig. 10). We applied time-dependent density functional theory (TD-DFT) for several multiplicities. We aimed to correlate the experimental transitions to HOMO/LUMO gaps in the cases of  $2^+$ ,  $[2,Cl]^+$ ,  $[2,^{16}O]^+$  and  $[2,H,CH_3CN]^+$  (cf. Fig. 18). TD-DFT calculation of some multiplicities at the B3LYP/cc-pVDZ level of theory led to negative transition energies, e.g. for  $2^+$  (M=6),  $[2,Cl]^+$  (M=5) and  $[2,^{16}O]^+$  (M=2 and 4). This correlates mostly to the trend in relative energies which also exhibits that those multiplicities do not correspond to minimum structures. We

calculated additionally the TD-DFT transitions of minimum structures at the B97D/cc-pVDZ level of theory (red lines).

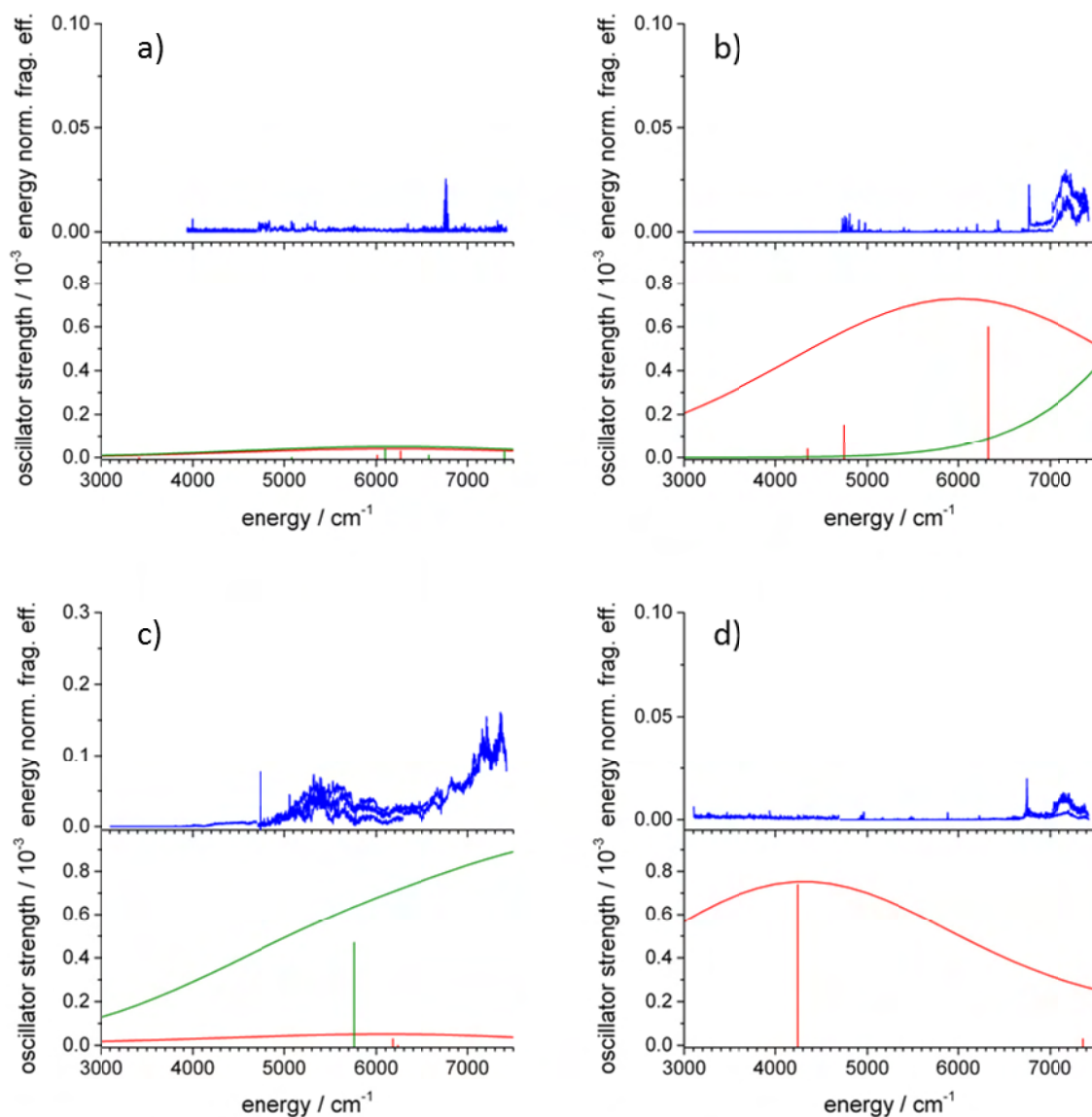


**Figure 18:** 1-color IR-MPD spectra and calculated electronic transitions of the minimum structures of  $2^+$  ( $M=4$ ) (a),  $[2,\text{Cl}]^+$  ( $M=3$ ) (b),  $[2,^{16}\text{O}]^+$  ( $M=6$ ) (c) and  $[2,\text{H},\text{CH}_3\text{CN}]^+$  ( $M=3$ ) (d) by TD-DFT at B3LYP/cc-pVDZ (red lines). Green lines exhibit electronic transitions of the minimum structures of  $2^+$  ( $M=2$ ) (a),  $[2,\text{Cl}]^+$  ( $M=1$ ) (b) and  $[2,^{16}\text{O}]^+$  ( $M=2$ ) (c) TD-DFT at the B97D/cc-pVDZ level. Fragmentation efficiencies are normalized linearly to photon flux. Calculated spectra are obtained by superposition of their gaussian profiles with FWHM of  $2000\text{ cm}^{-1}$ .

Ions in the trap are at approximately 300K and the spectra should be affected by thermal broadening. We converted each line to a Gaussian function of full width at half maximum (FWHM) of  $2000\text{ cm}^{-1}$  in order to simulate a thermal absorption spectrum. This value was taken from the

work of Hirabayashi et al [5]. Found transitions visualized in Fig. 18, numerical values documented in Table 5. No correlation of calculation and experiment was found.

**Table 5:** TD-DFT predicted transitions at the B3LYP/cc-pVDZ level of theory of  $2^+$ ,  $[2,Cl]^+$ ,  $[2,^{16}O]^+$  and  $[2,H,CH_3CN]^+$ , B97D/cc-pVDZ respectively. Values according to depicted data in Fig. 18. (Abbreviations: calc. = calculated; OS = oscillator strength)

$2^+$		$[2,Cl]^+$					
B3LYP calc. / $cm^{-1}$	OS / $10^{-4}$	B97D calc. / $cm^{-1}$	OS / $10^{-4}$	B3LYP calc. / $cm^{-1}$	OS / $10^{-4}$	B97D calc. / $cm^{-1}$	OS / $10^{-4}$
3418	0	5082	0	4351	4	10578	175
6010	1	6095	4	4747	15	11052	53
6262	3	6579	1	6326	60	12115	46
		7403	3			12294	132
$[2,^{16}O]^+$		$[2,H,CH_3CN]^+$					
B3LYP calc. / $cm^{-1}$	OS / $10^{-4}$	B97D calc. / $cm^{-1}$	OS / $10^{-4}$	B3LYP calc. / $cm^{-1}$	OS / $10^{-4}$		
2856	0	5760	47	4245	74		
6179	3	8568	1	7364	3		
6232	0	8800	81	8299	12		
		11256	4				

### IX-6.3: Discussion of vibrational and electronic spectra

A scaling factor of 0.97 was published for the B3LYP/cc-pVDZ level of theory [43]. In the spectral database [44] no scaling factor is given for the B97D functional. A scaling factor of 0.97 would shift the DFT predicted bands at the B3LYP level more to the blue and is therefore not applicable. The scaling factor of 0.957 derived from comparison of experimental IR-MPD spectra to DFT predicted IR absorptions bands correlates quite well to the factor 0.955 derived from the comparison of DFT predicted IR absorption spectra at the B3LYP/cc-pVDZ and Stuttgart 1997 ECP level of theory and experimental IR-MPD spectra in Chapter IV of this thesis.

There is poor overall agreement of experimental IR-MPD spectra and calculated DFT spectra. The calculated minimum structures of  $2^+$  and of its reaction products  $[2,Cl]^+$ ,  $[2,^{16}O]^+$  and  $[2,H,CH_3CN]^+$  do not necessarily represent the actual structure of the isolated ions in the gas phase. It can be assumed that rotations of the isopropyl-groups of the  $^4Cp^-$  ligands and of the ligand itself are multiply excited at an approximated temperature of 300 K. Those rotational excitations could lead to a weakening of metal-ligand interactions and therefore to an overall change of the gas phase structure.



Multiple excited rotations lead to a broadening of IR-MPD derived bands and could exhibit an additional shift of bands due to the change in the other all structure of the excited molecules. Molecular structures derived from DFT calculations represent “frozen” molecules at a local minimum of the potential energy surface. IR-MPD is applied to “warm” molecules at ca. 300 K and the absorption of multiple photons transfers additional energy in the molecules. Those two contrary worlds, “cold” DFT structures and “warm” IR-MPD bands do not agree within our study.

The IR-MPD spectrum of  $2^+$  (cf. Fig. 18, black line) can be assigned to an overlap of the DFT spectra of the anionic  ${}^4\text{Cp}^-$  ligand and of the cationic complex  $2^+$  under the assumption that neither symmetric CH stretching modes of the isopropyl groups in both molecules nor the aromatic CH stretching modes of the  $\text{C}_2\text{Ph}_2$  ligand contribute to the overall spectrum. It can be assumed that a weakening of the  $\text{Co-}{}^4\text{Cp}$  interaction within the molecule  $2^+$  takes place.

TD-DFT calculations at the chosen levels of theory are not able to predict the electronic transitions found in the experimental spectra. This may be due to the deficient description of the binding behavior within the complex found in the vibrational analysis. It can be assumed that the position of electronic transitions by TD-DFT crucially depends on an appropriate description of the metal-ligand interaction.

## IX-7: Conclusions

The cationic reaction products and the complex itself were subject of IR spectroscopic characterization. IR-MPD efficiency changed crucially with modification of the complex, yielding [ ${}^4\text{CpCo}$ ] ${}_2(\mu\text{-C}_2\text{Ph}_2)\text{X}^+$  ( $\text{X}=\text{H}$ , ( $\text{H}+\text{CH}_3\text{CN}$ ),  $\text{Cl}$ ,  $\text{O}$ ). The contribution of various fragmentation channels to the overall fragmentation efficiency was studied in detail. An increase of photon flux resulted in a saturation of preferred  $\text{C}_2\text{Ph}_2$  loss, additional alkyl fragments out of the  ${}^4\text{Cp}$  rings arising. Several absorption bands were found in the mid- and near-IR region. A model system from literature was used to identify seemingly levels of DFT theory by reference to X-ray crystal structure data. The B3LYP and the B97D functional with cc-pVDZ and Stuttgart 1997 ECP basis sets were identified for calculations of the complex [ ${}^4\text{CpCo}$ ] ${}_2(\mu\text{-C}_2\text{Ph}_2)^+$  and of its reaction products. An elongation of the Co-Co bond distance was observed for the cationic reaction products with  $\text{Cl}^-$  and  $\text{O}^{2-}$ . Calculations with B3LYP and B97D resulted in different electronic ground states. We did not obtain a good agreement of calculated vibrational modes and recorded IR-MPD spectra.

DFT predicted more absorption bands than observed, especially those corresponding to aliphatic symmetric  $\text{CH}_n$  ( $n=2, 3$ ) and aromatic CH stretching modes. Future 2-color IR-MPD experiments might resolve currently prevailing discrepancies.

TD-DFT calculations yielded several electronic transitions that do not correspond to the IR-MPD spectra. The chosen levels of theory for DFT and TD-DFT calculations does not seem to be appropriate. IR-MPD spectra have to be remeasured in order to normalize the spectra to photon flux. Furthermore, a different strategy has to be developed for *ab initio* calculations on the complexes under study.

**IX-8: References**

1. Artero, V., M. Chavarot-Kerlidou, and M. Fontecave, *Splitting Water with Cobalt*. *Angewandte Chemie-International Edition*, 2011. **50**(32): p. 7238-7266.
2. Wang, M., et al., *Light-driven hydrogen production catalysed by transition metal complexes in homogeneous systems*. *Dalton Transactions*, 2009(33): p. 6458-6467.
3. Bialach, P.M., et al., *Structures of isolated  $\text{Co}^{-2}(\text{alcohol})_1$  cluster anions*. *Physical Chemistry Chemical Physics*, 2009. **11**(44): p. 10403-10408.
4. Bialach, P.M., et al., *IR spectroscopy on isolated  $\text{Co}^{-n}(\text{alcohol})_m$  cluster anions ( $n=1-4$ ,  $m=1-3$ ): Structures and spin states*. *Journal of Chemical Physics*, 2010. **133**(19).
5. Hirabayashi, S., et al., *Vibrational and electronic spectra of  $\text{Co}_n^+(\text{CH}_3\text{OH})_3$  ( $n=1-3$ ) measured by infrared photodissociation spectroscopy*. *Chemical Physics Letters*, 2010. **490**(1-3): p. 19-23.
6. Minemoto, S., A. Terasaki, and T. Kondow, *Electronic structures of cobalt cluster cations: Photodissociation spectroscopy of  $\text{Co}_n^+\text{Ar}$  ( $n=3-5$ ) in the visible to near-infrared range*. *Journal of Chemical Physics*, 1996. **104**(15): p. 5770-5775.
7. Minemoto, S., A. Terasaki, and T. Kondow, *Electronic and geometric structures of vanadium cluster ions;  $\text{V}_n^+$  ( $n=3-5$ ), studied by optical absorption spectroscopy*. *Journal of Electron Spectroscopy and Related Phenomena*, 2000. **106**(2-3): p. 171-178.
8. Minemoto, S., et al., *Analysis of optical absorption spectra of transition metal cluster ions by the spin-polarized DV-X alpha method*. *Zeitschrift Fur Physik D-Atoms Molecules and Clusters*, 1997. **40**(1-4): p. 13-16.
9. Fischer, E.O. and R. Jira, *Di-Cyclopentadienyl-Kobalt(Ii)*. *Zeitschrift Fur Naturforschung Section B-a Journal of Chemical Sciences*, 1953. **8**(6): p. 327-328.
10. Koelle, U., F. Sistig, and J. Gersdorf, *CoCpBr Intermediates in the Cyclopentadienylation of  $\text{CoBr}_2$  with NaCp*. *Journal of Organometallic Chemistry*, 1982. **233**(2): p. 253-258.
11. Sly, W.G., *The Molecular Configuration Of Dicobalt Hexacarbonyl Diphenylacetylene*. *Journal of the American Chemical Society*, 1959. **81**(1): p. 18-20.
12. Eaton, B., J.M. Oconnor, and K.P.C. Vollhardt, *Stepwise Assembly of a Trinuclear Bis(carbyne) Complex from Cyclopentadienylcobalt Units and Bis(Trimethylsilyl)Acetylene - Isolation and Conversion of  $\text{Cp}_2\text{M}_2(\text{RC}=\text{CR})$  and  $(\text{CpM})_3(\text{RC}=\text{CR})$   $\text{M} = \text{Co}$  and  $\text{R} = (\text{CH}_3)_3\text{Si}$* . *Organometallics*, 1986. **5**(2): p. 394-397.
13. Bauschlicher Jr, C.W., *A comparison of the accuracy of different functionals*. *Chemical Physics Letters*, 1995. **246**(1-2): p. 40-44.
14. Wodrich, M.D., C. Corminboeuf, and P.v.R. Schleyer, *Systematic Errors in Computed Alkane Energies Using B3LYP and Other Popular DFT Functionals*. *Organic Letters*, 2006. **8**(17): p. 3631-3634.
15. Zhang, G. and C.B. Musgrave, *Comparison of DFT Methods for Molecular Orbital Eigenvalue Calculations*. *The Journal of Physical Chemistry A*, 2007. **111**(8): p. 1554-1561.

16. Hohenberg, P. and W. Kohn, *Inhomogeneous Electron Gas*. Physical Review B, 1964. **136**(3B): p. B864-&.
17. Kohn, W. and L.J. Sham, *Self-Consistent Equations Including Exchange and Correlation Effects*. Physical Review, 1965. **140**(4A): p. 1133-&.
18. Parr, R.G. and W. Yang, *Density-functional theory of atoms and molecules*. International series of monographs on chemistry. 1989, New York: Clarendon Press. x, 333 p.
19. Salahub, D.R., et al., *The Challenge of d and f electrons : theory and computation*. ACS symposium series,. 1989, Washington, DC: American Chemical Society. x, 405 p.
20. Becke, A.D., *Density-Functional Exchange-Energy Approximation with Correct Asymptotic-Behavior*. Physical Review A, 1988. **38**(6): p. 3098-3100.
21. Miehlich, B., et al., *Results Obtained with the Correlation-Energy Density Functionals of Becke and Lee, Yang and Parr*. Chemical Physics Letters, 1989. **157**(3): p. 200-206.
22. Becke, A.D., *Density-Functional Thermochemistry .3. The Role of Exact Exchange*. Journal of Chemical Physics, 1993. **98**(7): p. 5648-5652.
23. Perdew, J.P., *Density-Functional Approximation for the Correlation-Energy of the Inhomogeneous Electron-Gas*. Physical Review B, 1986. **33**(12): p. 8822-8824.
24. Perdew, J.P., K. Burke, and M. Ernzerhof, *Generalized gradient approximation made simple*. Physical Review Letters, 1996. **77**(18): p. 3865-3868.
25. Adamo, C. and V. Barone, *Toward reliable density functional methods without adjustable parameters: The PBE0 model*. Journal of Chemical Physics, 1999. **110**(13): p. 6158-6170.
26. Hamprecht, F.A., et al., *Development and assessment of new exchange-correlation functionals*. Journal of Chemical Physics, 1998. **109**(15): p. 6264-6271.
27. Dunning, T.H., *Gaussian-Basis Sets for Use in Correlated Molecular Calculations .1. The Atoms Boron through Neon and Hydrogen*. Journal of Chemical Physics, 1989. **90**(2): p. 1007-1023.
28. Woon, D.E. and T.H. Dunning, *Calculation of the Electron-Affinities of the 2nd Row Atoms - Al-Cl*. Journal of Chemical Physics, 1993. **99**(5): p. 3730-3737.
29. Dolg, M., et al., *Relativistic and correlation effects for element 105 (hahnium, Ha): a comparative study of M and MO (M = Nb, Ta, Ha) using energy-adjusted ab initio pseudopotentials*. The Journal of Physical Chemistry, 1993. **97**(22): p. 5852-5859.
30. Balabanov, N.B. and K.A. Peterson, *Systematically convergent basis sets for transition metals. I. All-electron correlation consistent basis sets for the 3d elements Sc-Zn*. Journal of Chemical Physics, 2005. **123**(6).
31. Frisch, M.J., et al., *Gaussian 03, Revision C.02*. 2003.
32. Frisch, M.J., et al., *Gaussian 09, Revision B.01*. 2009: Wallingford CT.
33. Bauernschmitt, R. and R. Ahlrichs, *Treatment of electronic excitations within the adiabatic approximation of time dependent density functional theory*. Chemical Physics Letters, 1996. **256**(4-5): p. 454-464.
34. Casida, M.E., et al., *Molecular excitation energies to high-lying bound states from time-dependent density-functional response theory: Characterization and correction of the time-dependent local density approximation ionization threshold*. Journal of Chemical Physics, 1998. **108**(11): p. 4439-4449.

35. Stratmann, R.E., G.E. Scuseria, and M.J. Frisch, *An efficient implementation of time-dependent density-functional theory for the calculation of excitation energies of large molecules*. Journal of Chemical Physics, 1998. **109**(19): p. 8218-8224.
36. Van Caillie, C. and R.D. Amos, *Geometric derivatives of excitation energies using SCF and DFT*. Chemical Physics Letters, 1999. **308**(3-4): p. 249-255.
37. Van Caillie, C. and R.D. Amos, *Geometric derivatives of density functional theory excitation energies using gradient-corrected functionals*. Chemical Physics Letters, 2000. **317**(1-2): p. 159-164.
38. Furche, F. and R. Ahlrichs, *Adiabatic time-dependent density functional methods for excited state properties*. Journal of Chemical Physics, 2002. **117**(16): p. 7433-7447.
39. Scalmani, G., et al., *Geometries and properties of excited states in the gas phase and in solution: Theory and application of a time-dependent density functional theory polarizable continuum model*. Journal of Chemical Physics, 2006. **124**(9).
40. Black, G., et al., *The extensible computational chemistry environment: A problem solving environment for high performance theoretical chemistry*. Computational Science - Iccs 2003, Pt Iv, Proceedings, 2003. **2660**: p. 122-131.
41. Sakurai, H. and J. Hayashi, *Reaction of " $\pi$ -Cyclopentadienyldicarbonylcobalt with Silyl-substituted Acetylenes*. Journal of Organometallic Chemistry, 1972. **39**(2): p. 365-&.
42. Koch, W. and M.C. Holthausen, eds. *A Chemist's Guide to Density Functional Theory*. 2. ed. 2001, Wiley-VCH: Weinheim. 300.
43. Byrd, E.F.C., C.D. Sherrill, and M. Head-Gordon, *The theoretical prediction of molecular radical species: a systematic study of equilibrium geometries and harmonic vibrational frequencies*. Journal of Physical Chemistry A, 2001. **105**(42): p. 9736-9747.
44. Editor: Johnson III, R.D., *NIST Computational Chemistry Comparison and Benchmark Database* August 2011.

## IX-9: Supplementary material

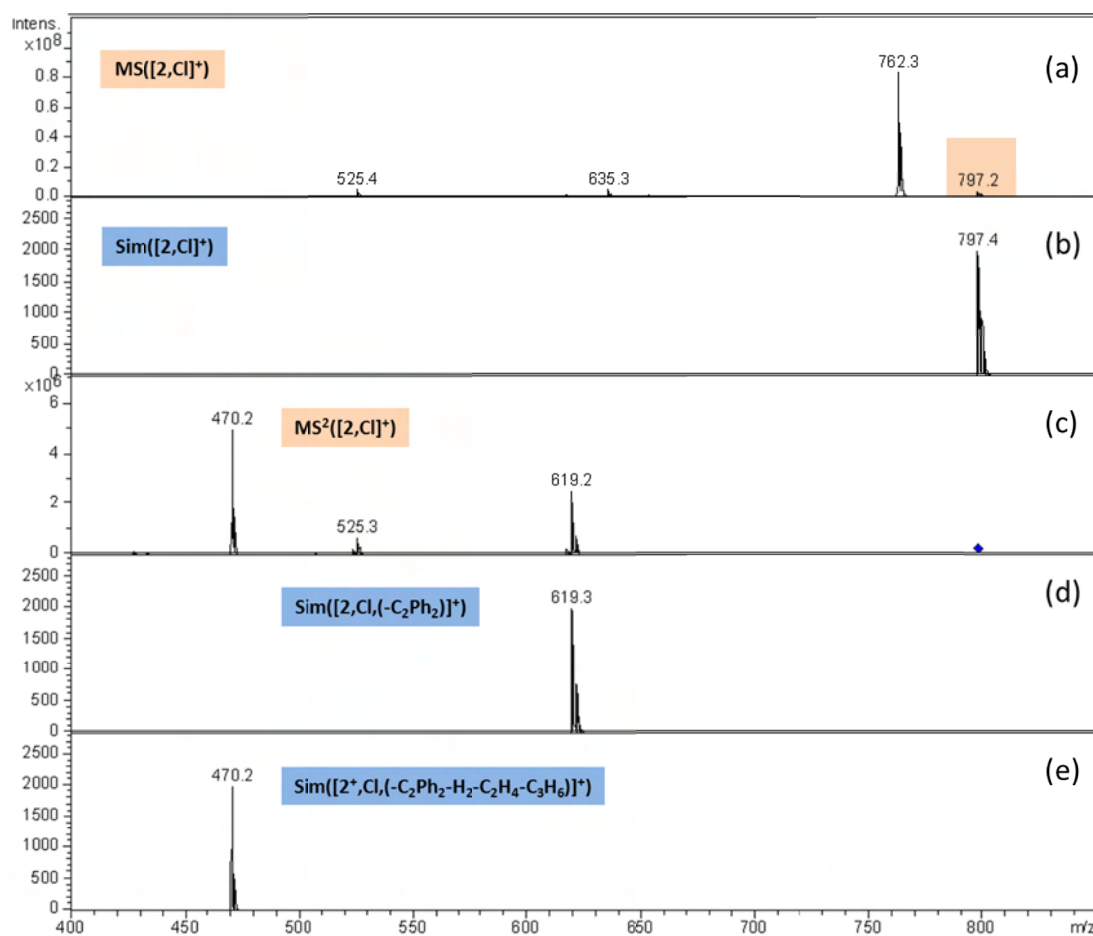


**Figure 19:** Mass spectrum of a solution of 2 in dry THF after addition of crystalline LiCl. Simulation of the isotopic distribution according to  $[2,Cl]^+$ . MS<sup>2</sup> of  $[2,Cl]^+$  (797.2  $m/z$ ) exhibits few fragments, which can be assigned to the combination of losses of  $C_2Ph_2$ ,  $H_2$ ,  $C_2H_4$ ,  $C_2H_6$  and  $C_3H_6$ . Simulations of the isotopic distribution according to  $[2,Cl,(-C_2Ph_2)]^+$  and  $[2^+,Cl,(-C_2Ph_2-H_2-C_2H_4-C_3H_6)]^+$ . (cf. Table 1 for abbreviations and sum formulas)

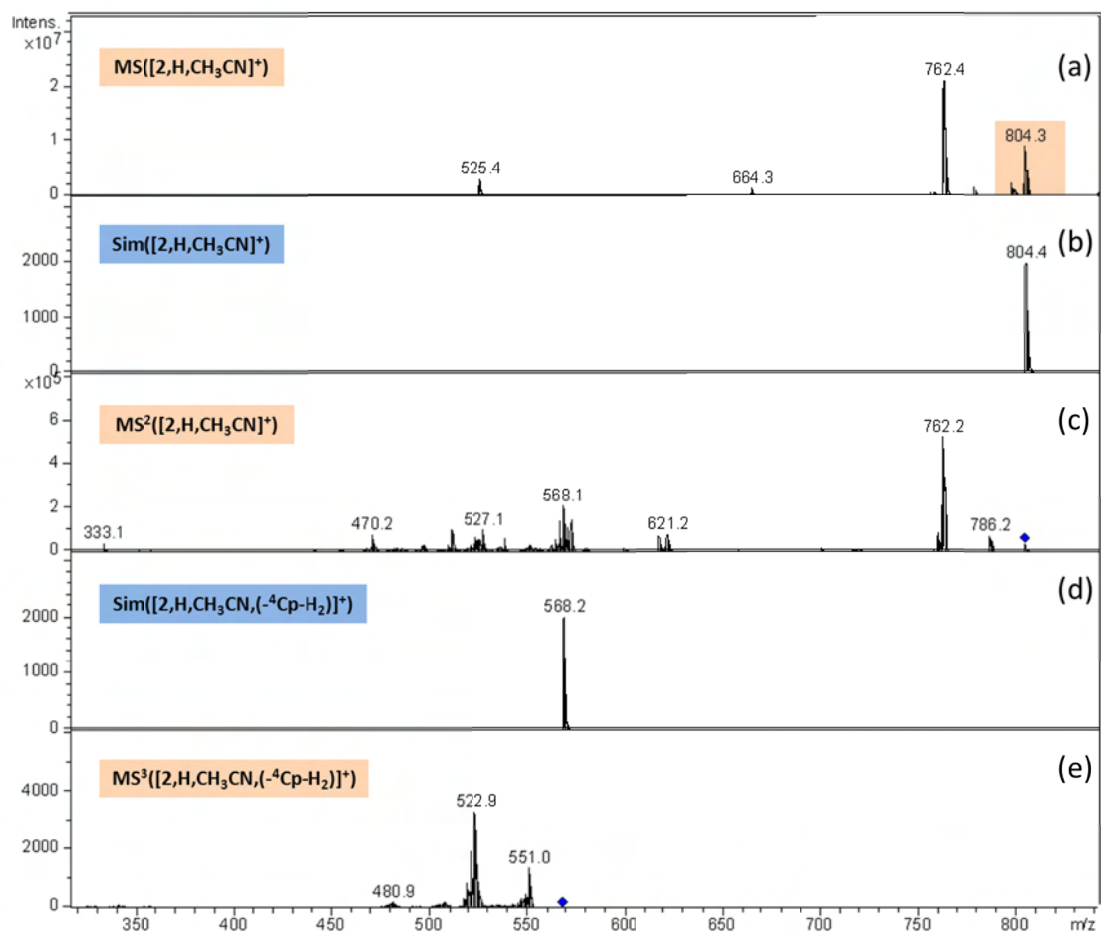


**Figure 20:** Mass spectrum of a solution of **2** in dry THF after addition of acetonitrile. Simulation of the isotopic distribution according to  $[2, \text{H}, \text{CH}_3\text{CN}]^+$ .  $\text{MS}^2$  of  $[2, \text{H}, \text{CH}_3\text{CN}]^+$  (804.3 m/z) exhibits few fragments, which can be assigned to the combination of losses of  $\text{CH}_3\text{CN}$ ,  $^4\text{Cp}$ ,  $\text{H}_2$ ,  $\text{C}_2\text{H}_4$ ,  $\text{C}_2\text{H}_6$  and  $\text{C}_3\text{H}_6$ . Simulations of the isotopic distribution according to  $[2, \text{H}, \text{CH}_3\text{CN}, (^4\text{Cp-H}_2)]^+$ .  $\text{MS}^3$  of  $[2, \text{H}, \text{CH}_3\text{CN}, (^4\text{Cp-H}_2)]^+$  (cf. Table 1 for abbreviations and sum formulas)

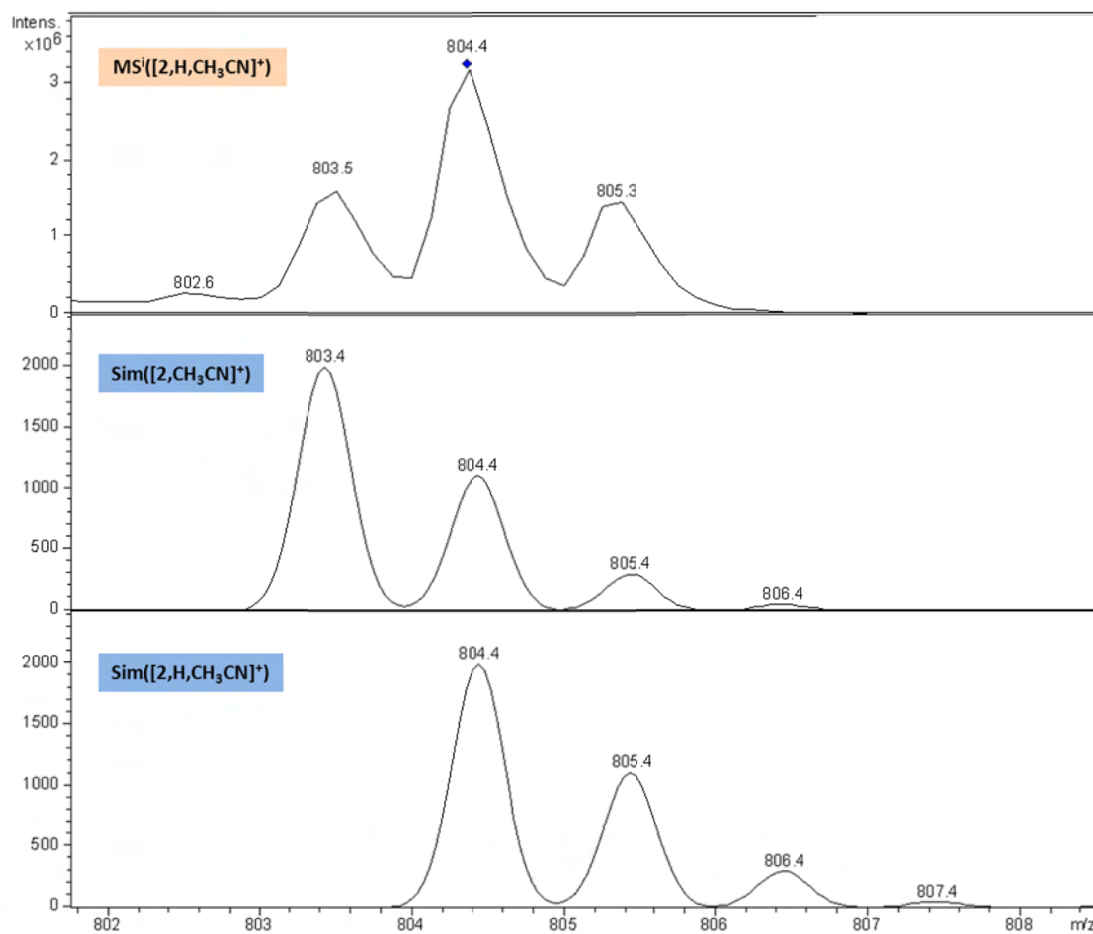


**Figure 21:** Section of a mass spectrum ( $MS^i$ ) of a solution of **2** in dry THF after addition of acetonitrile. Simulation of the isotopic distribution of the isolated reaction species is assigned to an overlap of complexes  $[2,CH_3CN]^+$  and  $[2,H,CH_3CN]^+$ . (cf. Table 1 for abbreviations and sum formulas)



## Chapter X: Appendix

### X-1: Documentation of data processing

VisualBasic script used for data processing inside the DataAnalysis software (comments marked with '):

```
'global variables
dim NP           'number of parent ions
dim MP()         'mass table of parent ions
dim NF           'number of fragments
dim MF()         'mass table of fragment ions
dim dmLeftMP    'lower limit of parent masses
dim dmRightMP   'upper limit of parent masses
dim dmLeftMF    'lower limit of fragment masses
dim dmRightMF   'upper limit of fragment masses
dim filenamezent 'name of the output file
dim inputfile   'path and name of the input file
```

```
inputfile = Analysis.Path
```

```
Sub Form_OnLoad
```

```
    NP=1           'number of parents
    redim MP(NP-1)
    MP(0)=359
```

```
    NF=2           'number of fragments
    redim MF(NF-1)
    MF(0)=132.9
    MF(1)=151
```

```
inputfile = Left(inputfile, Len(inputfile) - 2)
inputfile = inputfile & "_" & NP & "P" & NF & "F.txt"
filenamezent = inputfile
```

```
dmLeftMP=0.5
dmRightMP=0.5
dmLeftMF=0.5
dmRightMF=0.5
```

```
ShowDm
ShowListParent
ShowListFragment
```

```
End Sub
```

```
Sub ShowDm
```

```
    edDmLeftMP=dmLeftMP
    edDmRightMP=dmRightMP
    edDmLeftMF=dmLeftMF
    edDmRightMF=dmRightMF
```

```
End Sub
```

```
Sub ReadDm
```

```
    dmLeftMP=edDmLeftMP
    dmRightMP=edDmRightMP
    dmLeftMF=edDmLeftMF
```

```
    dmRightMF=edDmRightMF
End Sub
```

```
Sub ShowListParent
    dim i
    ListParent.clear
    for i=0 to NP-1
        ListParent.AddItem(MP(i))
    next
End Sub
```

```
Sub ShowListFragment
    dim i
    ListFragment.clear
    for i=0 to NF-1
        ListFragment.AddItem(MF(i))
    next
End Sub
```

```
Sub btAddMP_Click
    NP=NP+1
    redim preserve MP(NP-1)
    MP(NP-1)=edMP
    ShowListParent
End Sub
```

```
Sub btAddMF_Click
    NF=NF+1
    redim preserve MF(NF-1)
    MF(NF-1)=edMF
    ShowListFragment
End Sub
```

```
Sub btClearMP_Click
    NP=0
    redim preserve MP(0)
    ShowListParent
End Sub
```

```
Sub btClearMF_Click
    NF=0
    redim preserve MF(0)
    ShowListFragment
End Sub
```

```
Sub btClearLastMP_Click
    if NP=0 then exit sub
    NP=NP-1
    redim preserve MP(NP-1)
    ShowListParent
End Sub
```

```
Sub btClearLastMF_Click
    if NF=0 then exit sub
    NF=NF-1
    redim preserve MF(NF-1)
    ShowListFragment
End Sub
```

```
Sub btExit_Click
```

```
form.close
End Sub

Sub btRun1_Click
    dim i,n
    dim chrom

    Analysis.Chromatograms.clear
    ReadDm

    dim TIC      'creation of the total ion chromatogram (TIC)
    ' type "TIC, +All MS FullScan"
    Set TIC = CreateObject("DataAnalysis.TICChromatogramDefinition")
    TIC.MSFilter.Type = daMSFilterAll
    TIC.ScanMode      = daScanModeFullScan
    TIC.Polarity      = daBoth
    ' load and display the TIC
    Analysis.Chromatograms.AddChromatogram TIC

    dim CP      'creation of parent chromatograms
    redim CP(NP-1)
    for i=0 to NP-1
        set CP(i)= CreateObject("DataAnalysis.EICChromatogramDefinition")
        CP(i).Range = MP(i)
        CP(i).WidthLeft = dmLeftMP
        CP(i).WidthRight = dmRightMP
        CP(i).MSFilter.Type = daMSFilterAll
        Analysis.Chromatograms.AddChromatogram CP(i)
    next

    dim CF      'creation of fragment chromatograms
    redim CF(NF-1)
    for i=0 to NF-1
        set CF(i)= CreateObject("DataAnalysis.EICChromatogramDefinition")
        CF(i).Range = MF(i)
        CF(i).WidthLeft = dmLeftMF
        CF(i).WidthRight = dmRightMF
        CF(i).MSFilter.Type = daMSFilterAll
        Analysis.Chromatograms.AddChromatogram CF(i)
    next

    dim PW1      'external input 1, laser power measurement
    Set PW1 = CreateObject("DataAnalysis.VARChromatogramDefinition")
    dim PW2      'external input 2, laser power measurement
    Set PW2 = CreateObject("DataAnalysis.VARChromatogramDefinition")
    'PW1.Color = daRed
    'PW1.VariableName = "UV Signal 1"
    'PW2.Color = daBlack
    'PW2.VariableName = "UV Signal 2"
    'PW.VariableName = "Vacuum High"
    'Analysis.Chromatograms.AddChromatogram PW1
    Analysis.Chromatograms.AddChromatogram PW2

    dim NS

    set Chrom=Analysis.Chromatograms(1)
    NS=Chrom.size      'number of chromatograms

    dim Parent, Fragment, IRMPD, Tps, PWs
    dim rt, intense
```

```

redim Parent(NS)      'table of all parent ions
redim Fragment(NS)    'table of all fragment ions
redim IRMPD(NS)       'table of IRMPD spectra
redim Tps(NS)         'table of time data
redim PWs1(NS)        'table of external input 1 data
redim PWs2(NS)        'table of external input 2 data

for n=2 to NP+1        'processing of parent chromatograms
  set chrom = Analysis.Chromatograms(n)
  chrom.ChromatogramData rt, intensite
  for i=0 to NS-1      'sum of parent intensities
    parent(i)=parent(i)+intensite(i)
  next
next

for n=NP+2 to NP+NF+1 'processing of fragment chromatograms
  set chrom = Analysis.Chromatograms(n)
  chrom.ChromatogramData rt, intensite
  for i=0 to NS-1      'sum of fragment intensities
    fragment(i)=fragment(i)+intensite(i)
  next
next

'processing of external input data
set chrom = Analysis.Chromatograms(n)
chrom.ChromatogramData rt, intensite
for i=0 to NS-1      'sum of intensities
  'pws1(i)=intensite(i)
  pws2(i)=intensite(i)
next

'calculation of IRMPD signal
for i=0 to NS-1
  if (Parent(i)<>0) and ((parent(i)+fragment(i))<>0) then
    IRMPD(i)=(fragment(i)/(Parent(i)+fragment(i)))
  end if
next

'write output file
Dim Filepath,Filename
Filepath=Analysis.path
Filename=filenamezent

Dim fso,filehandle, file, f
dim s
Set fso = CreateObject("Scripting.FileSystemObject")
Set fTS = fso.CreateTextFile(filename)
s="num" & " " & "time" & " " & "power" & " " & "parent" & " " & "fragment" & " " & "IRMPD"
fts.WriteLine s
for i=0 to NS-1
  s=i & " " & rt(i) & " " & pws2(i) & " " & parent(i) & " " & fragment(i) & " " & IRMPD(i)
  fts.WriteLine s
next

fts.close
form.close

End Sub

Sub btRun2_Click

```

```
dim i,n,j
dim chrom

Analysis.Chromatograms.clear
ReadDm

dim TIC      'creation of the total ion chromatogram (TIC)
'type "TIC, +All MS FullScan"
Set TIC = CreateObject("DataAnalysis.TICChromatogramDefinition")
TIC.MSFilter.Type = daMSFilterAll
TIC.ScanMode      = daScanModeFullScan
TIC.Polarity      = daBoth
' load and display the TIC
Analysis.Chromatograms.AddChromatogram TIC

dim CP      'creation of parent chromatograms
redim CP(NP-1)
for i=0 to NP-1
  set CP(i)= CreateObject("DataAnalysis.EICChromatogramDefinition")
  CP(i).Range      = MP(i)
  CP(i).WidthLeft  = dmLeftMP
  CP(i).WidthRight = dmRightMP
  CP(i).MSFilter.Type = daMSFilterAll
  Analysis.Chromatograms.AddChromatogram CP(i)
next

dim CF      'creation of fragment chromatograms
redim CF(NF-1)
for i=0 to NF-1
  set CF(i)= CreateObject("DataAnalysis.EICChromatogramDefinition")
  CF(i).Range      = MF(i)
  CF(i).WidthLeft  = dmLeftMF
  CF(i).WidthRight = dmRightMF
  CF(i).MSFilter.Type = daMSFilterAll
  Analysis.Chromatograms.AddChromatogram CF(i)
next

dim PW1     'external input 1, laser power measurement
Set PW1 = CreateObject("DataAnalysis.VARChromatogramDefinition")
dim PW2     'external input 2, laser power measurement
Set PW2 = CreateObject("DataAnalysis.VARChromatogramDefinition")
'PW1.Color      = daRed
'PW1.VariableName = "UV Signal 1"
'PW2.Color      = daBlack
'PW2.VariableName = "UV Signal 2"
'PW.VariableName = "Vacuum High"
'Analysis.Chromatograms.AddChromatogram PW1
'Analysis.Chromatograms.AddChromatogram PW2

dim NS

set Chrom=Analysis.Chromatograms(1)
NS=Chrom.size      'number of chromatograms

dim Parent, Fragment, IRMPD, Tps, PWs
dim rt, intensite
redim Parent(NS)    'table of all parent ions
redim Fragment(NS)  'table of all fragment ions
redim IRMPD(NS)     'table of IRMPD spectra
redim Tps(NS)       'table of time data
```

```

redim PWS1(NS)      'table of external input 1 data
redim PWS2(NS)      'table of external input 2 data

for n=2 to NP+1      'processing of parent chromatograms
  set chrom = Analysis.Chromatograms(n)
  chrom.ChromatogramData rt, intensite
  for i=0 to NS-1    'sum of parent intensities
    parent(i)=parent(i)+intensite(i)
  next
next

for n=NP+2 to NP+NF+1 'processing of fragment chromatograms
  set chrom = Analysis.Chromatograms(n)
  chrom.ChromatogramData rt, intensite
  for i=0 to NS-1    'sum of fragment intensities
    fragment(i)=fragment(i)+intensite(i)
  next
next

'processing of external input data
set chrom = Analysis.Chromatograms(n)
chrom.ChromatogramData rt, intensite
for i=0 to NS-1    'sum of intensities
  'pws1(i)=intensite(i)
  pws2(i)=intensite(i)
next

'calculation of IRMPD signal
for i = 0 to NS-1
for j = 0 to NP-1
  IRMPDP(i) = IRMPDP(i) + parent(i,j)
next
next

for i = 0 to NS-1
for j = 0 to NF-1
  IRMPDF(i) = IRMPDF(i) + fragment(i,j)
next
next

for i=0 to NS-1
  if (IRMPDP(i)<>0) and ((IRMPDP(i)+IRMPDF(i))<>0) then
    IRMPD(i)=(IRMPDF(i)/(IRMPDP(i)+IRMPDF(i)))
  end if
next

'write output file
Dim Filepath,Filename
Filepath=Analysis.path
Filename=filenamezent

Dim fso,filehandle, file, f
dim s
Set fso = CreateObject("Scripting.FileSystemObject")
Set fTS = fso.CreateTextFile(filename)
masses = MP(0) & " "
s="num" & " " & "time" & " " & "power" & " "
for k = 0 to NP - 1
s = s & MP(k) & " "
next

```

```
for k = 0 to NF - 1
s = s & MF(k) & " "
next
s = s & "IRMPD"
fts.WriteLine s

for i = 0 to NS-1
  fts.Write(i)
  fts.Write(" ")
  fts.Write(rt(i))
  fts.Write(" ")
  fts.Write(pws2(i))
  fts.Write(" ")
for j = 0 to NP-1
  fts.Write(Parent(i,j))
  fts.Write(" ")
next
for k = 0 to NF-1
  fts.Write(Fragment(i,k))
  fts.Write(" ")
next
  fts.Write(IRMPD(i))
  fts.WriteBlankLines(1)
next

fts.close
form.close
```

End Sub

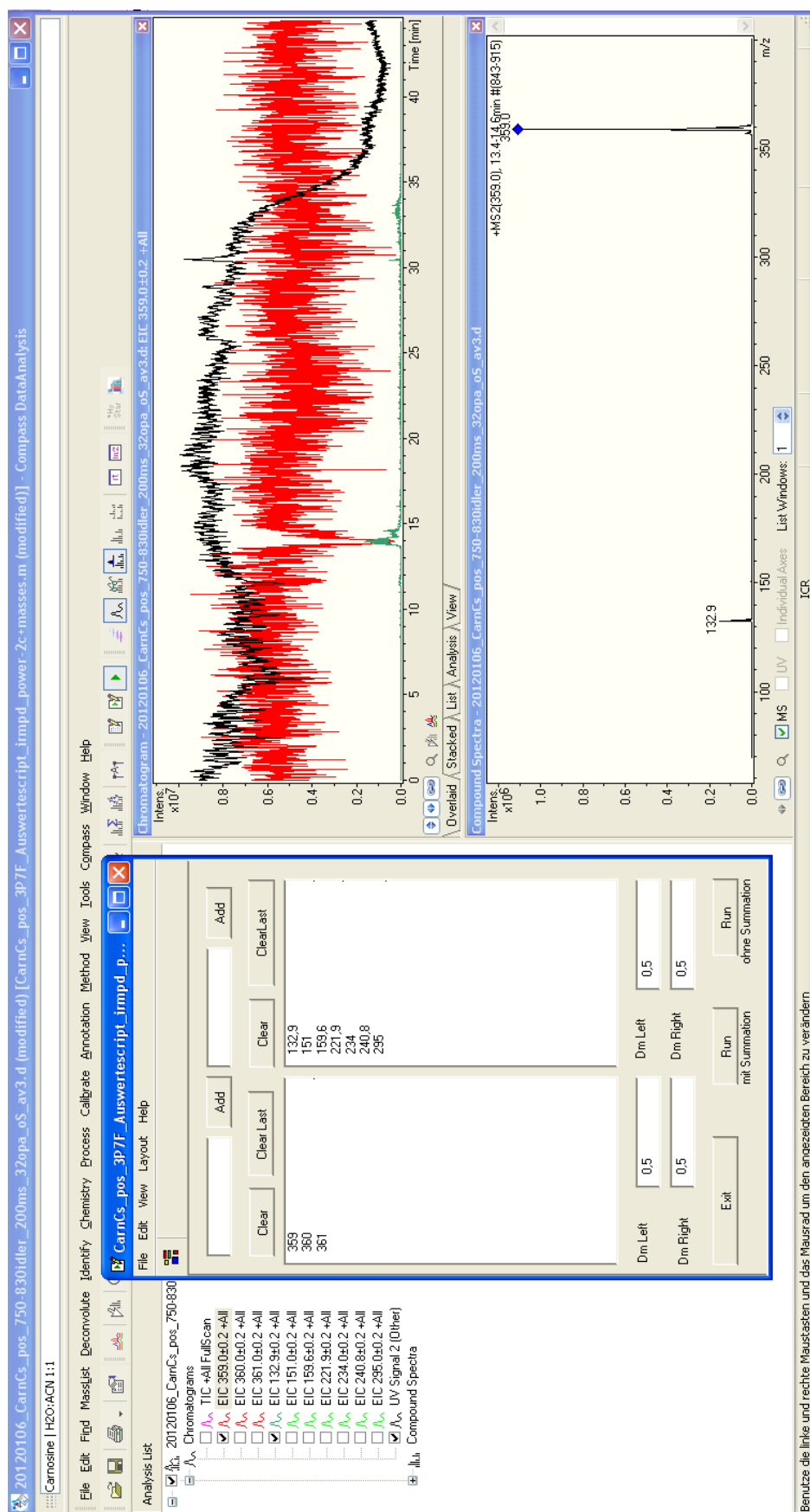


**Figure 1:** Screenshot of the DataAnalysis program (background) and the front-end for data processing (blue highlighted window).



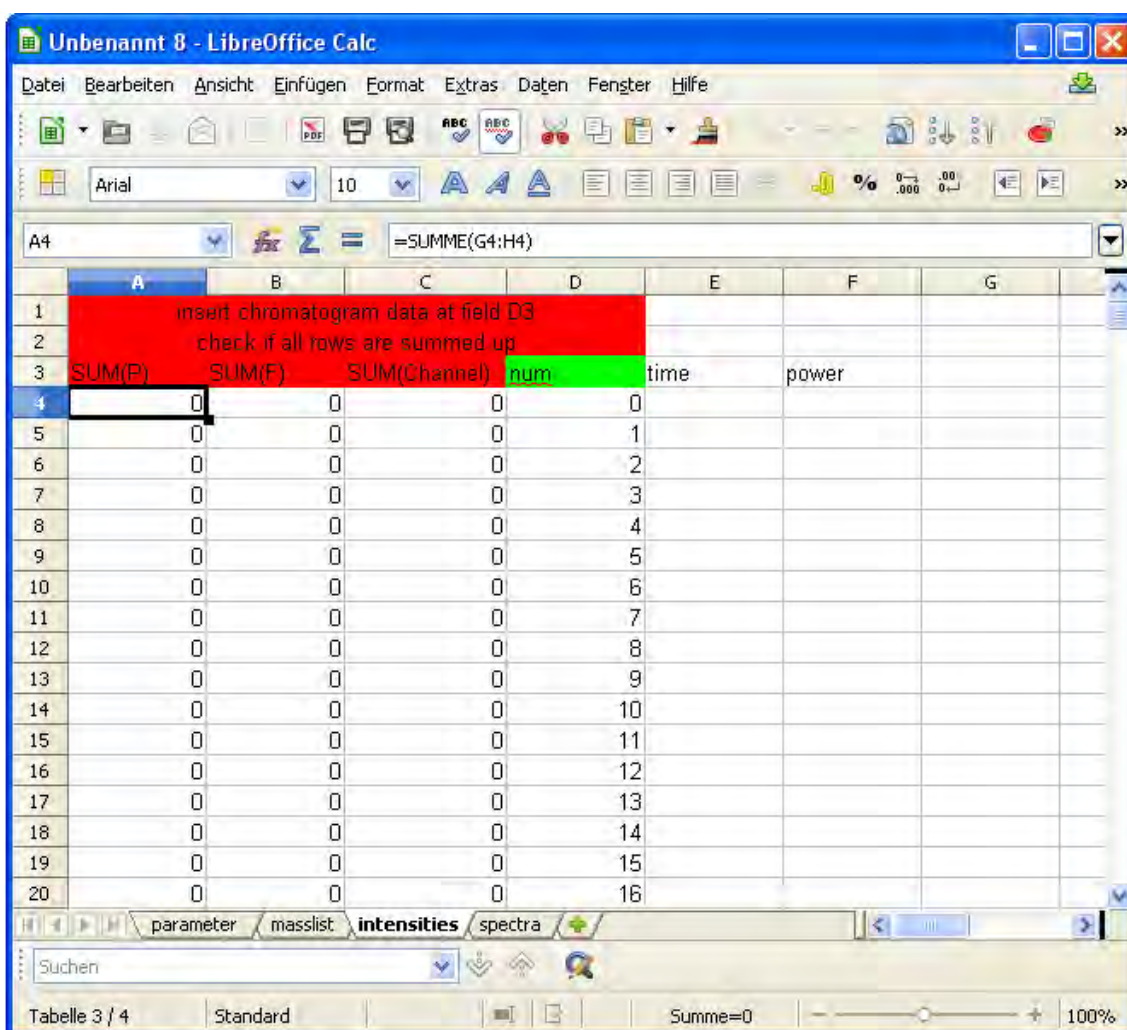


**Figure 2:** Screenshot of the LibreOffice Calc template sheet for data import.

Mass to charge ratios of the parent and fragment ions serve as input data for the VisualBasic script. Intensities of each given  $m/z$  ratio are automatically exported from all single mass spectra by chromatogram functions (cf. Fig. 1, e.g. EIC  $359 \pm 0.2$  (red line, EIC = extracted ion chromatogram)) supported by the DataAnalysis software. Number, time, digitized powermeter output and intensity of each  $m/z$  ratio from single mass spectra is imported into a LibreOffice Calc template sheet. Parent channels are summed up, fragment channels respectively. Furthermore, single fragment channels can be extracted (cf. Fig. 2). Fragmentation efficiency is calculated in the “spectra” sheet of the template file (cf. Fig. 3, column “IRMPD”). Wavenumbers are calculated using the starting wavelength, the scan velocity and the time delay of each mass spectrum. Calculated spectra are directly displayed in a graph window.

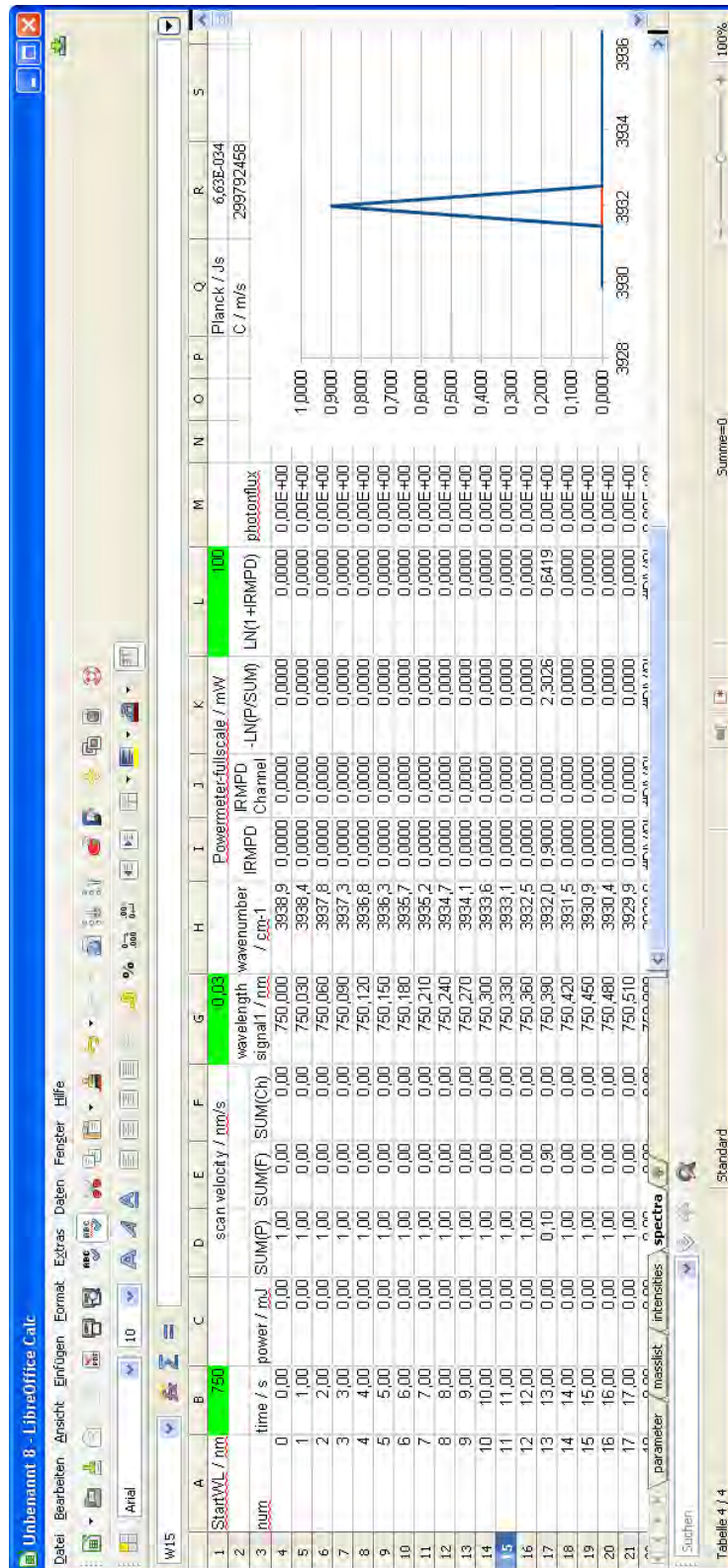


Figure 3: Screenshot of the LibreOffice Calc template sheet for calculation of spectra. Some artificial data is inserted for exemplification.

## Chapter XI: Summary and Outlook

This thesis reports on investigations on the structure and reactivity of dipeptide-alkali metal complexes, a series of ruthenium bearing catalysts, dysprosium based single molecule magnets and organometallic di-cobalt complexes. A variety of experimental and theoretical methods was used dependent on the problem: collision induced dissociation, hydrogen/deuterium exchange reactions, gas phase reactions with  $D_2$ , infrared multiple-photon dissociation and the determination of minimum energy structures, IR absorption spectra, transition states and electronic transitions based on density functional theory.

A case study was carried out to explore the **influence of alkali metal ions** on the gas phase structure of the dipeptide **Carnosine**. CID experiments on protonated Carnosine and its alkali metal complexes in an ion trap resulted in different fragment pathways dependent on the size of the alkali metal. The complexation of small ions ( $Li^+$  and  $Na^+$ ) promoted the cleavage of bonds in the molecules backbone under CID, while  $Rb^+$ - and  $Cs^+$ -Carnosine complexes underwent the exclusive loss of the alkali metal. **CID breakdown curves** reflected the different binding behavior of the alkali ions to Carnosine. Gas phase **H/D exchange** reactions with  $D_2O$  resulted in the exchange of several protons of the protonated dipeptide, while its alkali metal complexes underwent no exchange reactions. DFT derived energetical **minimum isomers** exhibited only **charge solvated tridentate structures**, whereas salt bridge as well as charge solvated binding motives are reported in literature on complexes of alkali metal ions and oligopeptides. This study was published in a similar version as a paper in *Zeitschrift für Physikalische Chemie*.

A combination of the four dipeptides **Carnosine**, **Anserine**, **GlyHis** and **HisGly** with **alkali metal ions** was investigated with the help of CID, IR-MPD spectroscopy and H/D exchange reactions with  $ND_3$ . The aim of the survey was to elucidate the influence of the methyl-group at the histidine ring, of the peptide sequence and chain length on the binding motives of the alkali ions. The experimental results were compared to DFT derived minimum energetical isomers. A moderate accordance was found for DFT predicted IR absorptions to IR-MPD spectra. A **systematic nomenclature** was developed reflecting all binding motives of the four dipeptides to alkali ions. Carnosine complexes all alkali metal ions in an uniform motive. DFT derived **energetical minimum isomers** of the three other dipeptides showed strong **conformational changes** with increasing size of the alkali ion. The most favored binding motive of all peptides was the **tridentate**

**complexation** of the alkali ion by a carboxylic and an amidic oxygen atom, while the electron donating nitrogen atom either belongs to the Histidine ring or the amine group. The ability to form **hydrogen bonds** in a certain binding motive is essential for the preference of the Histidine or amine nitrogen atom as an electron donor. The **charge solvated binding motive** is the most common within all found isomers. Several structures exhibited hydrogen bonded protons. Those can be interpreted as intermediates between the charge solvated and the salt bridge binding motive. **CID breakdown curves** of the cationic complexes of the dipeptides with  $K^+$ ,  $Rb^+$  and  $Cs^+$  resulted in a fair agreement of  $E_{com}^{50\%}$  values with DFT derived Gibbs free binding energies. CID led to multiple fragments of the  $Li^+$  and  $Na^+$  dipeptide complexes and to an insufficient correlation between the  $E_{com}^{50\%}$  values and metal-dipeptide free binding enthalpies. Gas phase **H/D exchange** reactions of the protonated dipeptides with  $ND_3$  resulted in the exchange of all labile protons with comparable relative partial rate constants. The assumption of coexisting single and double exchange reactions per single collision led to an enhancement in quality of the pseudo first order kinetic fits of the experimental derived data. The  $Li^+$ ,  $Na^+$  and  $K^+$  complexes of the dipeptides exhibited a reduction in the number of exchanged protons, significantly lower rate constants for H/D exchange and only single exchange reactions.

The complexation of the doubly charged cationic transition metal  $Zn^{2+}$  by deprotonated Carnosine led to crucial conformational changes with respect to the alkali metal complexes. Former DFT calculations on the gas phase structure of  $[Carn-H, Zn^{II}]^+$  were now compared to IR-MPD spectra. IR-MPD spectra exhibited several of the DFT predicted IR absorptions while the overall agreement in the position of bands is only partially satisfactory. The complex  $[Carn-H, Zn^{II}]^+$  was furthermore used in order to study the **band dependent enhancement** of fragmentation efficiency by application of a resonant **2-color IR-MPD** pump/probe scheme. In literature, it is assumed that the slopes of linear fits to the log-log scale of experimental data (fragmentation efficiency vs. laser pulse energy) correlate to the number of photons needed for fragmentation. No reasonable number of photons for the fragmentation of the molecule was derived with this approach. However, it could be shown that the number of photons of the pump laser needed for fragmentation is reduced by the use of a second IR color. The change of the delay between the pump and probe laser pulse had an influence on the shape of the absorption bands. Irradiation with the probe laser pulse before the pump laser caused a **heating of the molecule** which resulted in a broadening of bands. No broadening was observed when the probe laser was applied simultaneously or after the pump laser. CID and IR-MPD fragmentation channels differed in their relative abundance. Furthermore, **relative abundancies of fragments** were specific to the excited vibrational motions. This study

provides essential approaches for the further study of the mechanism of resonant 2-color IR-MPD spectroscopy.

Several **ruthenium catalysts for transfer hydrogenation reactions** were synthesized by L. Ghoochany (research group W. Thiel, TU Kaiserslautern). CID measurements on isotopic labeled species led to the following conclusion about the **activation process** of the catalyst: a nitrogen-ruthenium bond is broken, the **pyrimidine ring** of the substituted 2-R-4-(2-pyridinyl)pyrimidine ligand **rotates about 160°** and a **carbon-ruthenium bond** is formed under subsequent loss of a HCl (or DCl) molecule. The mass spectrometers CID amplitude was calibrated with a set of “thermometer ions”. **CID breakdown curves** were used for determination of  $E_{\text{com}}^{50\%}$  values of three differently substituted catalysts. Finally, activation energies were estimated by means of the calibration. The resulting activation energies showed a qualitative correlation to DFT derived activation energies. These results are part of a manuscript which was submitted to *Chemistry – A European Journal* and is currently in the review process. Further studies on this series of transition metal complexes included CID on ligand exchanged species, **1- and 2-color IR-MPD spectroscopy, gas phase reactions with D<sub>2</sub> and DFT based modeling** of the reaction coordinate of the D<sub>2</sub> insertion. The exchange of the anionic chlorido ligand in solution led to three complexes with different fragmentation thresholds. CID derived activation amplitudes correspond well to the order predicted by the hard/soft acids/bases (HSAB) concept. 1-color IR-MPD experiments on two complexes showed only a few bands. Resonant 2-color IR-MPD increased the overall fragmentation efficiency and uncovered several dark bands. DFT derived IR absorption spectra correlate well to IR-MPD spectra while some bands are still not observable. Gas phase reactions with D<sub>2</sub> showed an increase of the mass of the activated complex of +4 m/z. This was interpreted in terms of an **incorporation of a D<sub>2</sub> molecule** under heterolytical cleavage of the D<sub>2</sub> molecule and can be compared to a back reaction of the activation. The **reaction coordinate** of the D<sub>2</sub> incorporation was modeled with **DFT at the B3LYP/cc-pVTZ level of theory** and different activation energies were derived dependent on the substituent. Reactions of three differently substituted complexes with D<sub>2</sub> resulted in different relative partial rate constants. The comparison to rate constants derived from transition state theory showed a qualitative but not quantitative correlation to the experimental results. This study contributes to our ongoing work on the assignment and isolation of reaction intermediates in the gas phase. Studies on the dynamics of the activation process are on the way as well as an estimation of rate constants for the D<sub>2</sub> insertion using RRKM theory.

A series of **dysprosium based complexes** was synthesized by A. Bhunia (research group P. W. Roesky, KIT) and studied within the collaborative research center SFB/TRR 88 “3MET”. We contributed to this work with **ESI-MS, CID** and experiments on **H/D exchange reactions** with  $\text{ND}_3$  in the gas phase. Those complexes consist of a central triple-charged dysprosium cation and two identical *salen*-type ligands which allow for a complexation of up to two transition metals. The monometallic dysprosium complex shows **single molecule magnet (SMM)** behavior in SQUID measurements, while the incorporation of two **double-charged manganese cations** leads to ferromagnetic behavior. The interaction of terminal amine groups with the manganese ions caused a hinderance of the exchange H/D exchange reaction with  $\text{ND}_3$  in the gas phase. Alternatively, the terminal amine groups of the monometallic dysprosium complex allow for the bond of **two  $\text{Ni}^{2+}$  (*tren*) complexes**. ESI-MS studies showed anionic as well as cationic complexes due to deprotonation or protonation in solution. **CID studies** led to fragmentation schemes which correlate quite well to the predicted structures of the complexes. These results are part of two publications in *Inorganic Chemistry* and *Dalton Transactions*. Further studies on this series of mono-, di- and trimetallic complexes are reported in this thesis. **H/D exchange** reactions with  $\text{D}_2\text{O}$  in solution yielded in an exchange of all labile protons for the cationic complexes. Anionic complexes underwent a partial or a complete exchange of labile protons. A comparison of **1- and 2-color IR-MPD** spectra of anionic and cationic complexes as well as H/D exchanged species allowed for the assignment of vibrational bands. Furthermore, preferred **protonation sites** were derived by comparing the results of IR-MPD experiments and H/D exchange reactions in solution and in the gas phase. This study contributes to our ongoing work on the determination of magnetic properties of isolated ions in the gas phase at the Helmholtz-Zentrum Berlin.

The complex  $[(^4\text{CpCo})_2(\mu\text{-C}_2\text{Ph}_2)]$  ( $^4\text{Cp}$  = tetraisopropyl-cyclopentadiene) was synthesized by J. Becker (research group H. Sitzmann, TU Kaiserslautern). The cationic complex and several reaction products were characterized by ESI-MS. Some of the experimental data contributed to the diploma thesis of J. Becker. The cationic reaction products and the complex itself were subject of **IR spectroscopic characterization**. IR-MPD efficiency changed crucially with modification of the complex, yielding  $[(^4\text{CpCo})_2(\mu\text{-C}_2\text{Ph}_2)\text{X}]^+$  ( $\text{X}=\text{H}, (\text{H}+\text{CH}_3\text{CN}), \text{Cl}, \text{O}$ ). The contribution of various fragmentation channels to the overall fragmentation efficiency was studied in detail. An increase of photon flux resulted in a saturation of preferred  $\text{C}_2\text{Ph}_2$  loss, additional alkyl fragments out of the  $^4\text{Cp}$  rings arising. Several **absorption bands** were found in the **mid- and near-IR region**. A model system from literature was used to identify seemingly levels of **DFT theory** by reference to X-ray crystal structure data. The **B3LYP** and the **B97D** functional with cc-pVDZ and Stuttgart 1997 ECP

basis sets were identified for calculations of the complex  $[(^4\text{CpCo})_2(\mu\text{-C}_2\text{Ph}_2)]^+$  and of its reaction products. An elongation of the Co-Co bond distance was observed for the cationic reaction products with  $\text{Cl}^-$  and  $\text{O}^{2-}$ . Calculations with B3LYP and B97D resulted in different electronic ground states. We did not obtain a good agreement of calculated vibrational modes and recorded IR-MPD spectra. DFT predicted more absorption bands than observed, especially those corresponding to aliphatic symmetric  $\text{CH}_n$  ( $n=2, 3$ ) and aromatic CH stretch motions. Future 2-color IR-MPD experiments might resolve currently prevailing discrepancies. **TD-DFT calculations** yielded several electronic transitions that do not correspond to the IR-MPD spectra. The chosen levels of theory for DFT and TD-DFT calculations does not seem to be appropriate. IR-MPD spectra have to be remeasured in order to normalize the spectra to photon flux. Furthermore, a different strategy has to be developed for *ab initio* calculations on the complexes under study.

A combination of various methods applied to isolated ions in the gas phase and in solution allowed for the study of their structure, binding energies and reactivity. 1- and 2-color IR-MPD spectroscopy combined with DFT predicted absorption spectra of different isomers enabled an assignment of vibrational bands and binding motives of the molecules. The derived results are important for further studies on the binding behavior of peptides and the reaction behavior of metal complexes.

## Kapitel XI: Zusammenfassung und Ausblick

Diese Arbeit beschäftigt sich mit der Struktur und Reaktivität von Dipeptid-Alkalimetall Komplexen, einer Reihe rutheniumhaltiger Katalysatoren, dysprosiumbasierter Einzelmolekülmagnete und organometallischer Di-Kobalt Komplexe. Eine Vielzahl an experimentellen und theoretischen Methoden wurde in Abhängigkeit zur Fragestellung auf die Moleküle angewandt: stoßinduzierte Fragmentation (CID), Wasserstoff/Deuterium Austauschreaktionen, Gasphasenreaktionen mit  $D_2$ , Infrarot-Multiphotonendissoziations-Spektroskopie (IR-MPD) und die Bestimmung von energetisch günstigen Isomeren, IR Absorptionsspektren, Übergangszuständen und elektronischen Übergängen mittels Dichtefunktionaltheorie.

Es wurde eine Voruntersuchung über den **Einfluss von Alkalimetallionen** auf die Struktur des Dipeptides **Carnosin** in der Gasphase durchgeführt. CID Experimente an protoniertem Carnosin und seinen Alkalimetall Komplexen wiesen unterschiedliche Fragmentationskanäle in Abhängigkeit zur Größe des Alkaliions auf. Die Komplexierung kleiner Ionen ( $Li^+$  und  $Na^+$ ) begünstigte Bindungsbrüche im Rückgrat des Peptids innerhalb des CID Prozesses, während die  $Rb^+$ - und  $Cs^+$ -Carnosin Komplexe den Verlust des Alkaliions als exklusiven Fragmentationskanal aufwiesen. **CID breakdown curves** spiegeln die unterschiedlichen Bindungsverhältnisse der Alkaliionen an Carnosin wieder. **Gasphasenreaktionen mit  $D_2O$**  ergaben den Austausch mehrerer Protonen des protonierten Dipeptids, während dessen Alkalimetallkomplexe keine Austauschreaktionen eingingen. DFT ermittelte Isomere niedrigster Energie wiesen nur **dreizählige charge solvated Strukturen** auf, während in der Literatur *salt bridge* als auch *charge solvated* Bindungsmuster für Komplexe der Alkalimetalle mit Oligopeptiden berichtet werden. Diese Studie wurde in ähnlicher Form in der Zeitschrift für Physikalische Chemie als Artikel veröffentlicht.

Eine Kombination der vier Dipeptide **Carnosin, Anserin, GlyHis und HisGly** mit **Alkalimetallionen** wurde mit Hilfe von CID, IR-MPD Spektroskopie und H/D Austauschreaktionen mit  $ND_3$  untersucht. Ziel war die Aufklärung des Einflusses der Methylgruppe am Histidinring und der Peptidsequenz und -länge auf die Bindungsmotive der Alkaliionen. Die experimentellen Ergebnisse wurden mit den durch DFT ermittelten Isomeren niedrigster Energie verglichen. Es zeigte sich eine moderate Übereinstimmung der mit DFT berechneten IR Absorptionsspektren mit den IR-MPD Spektren. Es wurde eine **systematische Benennung**



entwickelt, die alle Bindungsmotive der vier Dipeptide zu den Alkaliionen berücksichtigt. Carnosin komplexiert alle Alkaliionen mit einem einheitlichen Bindungsmuster. DFT ermittelte Strukturen **niedrigster Energie** der drei anderen Dipeptide wiesen starke **konformationelle Änderungen** mit steigender Größe des Alkaliions auf. Das vorherrschende Bindungsmuster aller Dipeptide war die **dreizählige Komplexierung** der Alkaliions durch ein carboxylisches und ein amidisches Sauerstoffatom, während das elektronenliefernde Stickstoffatom entweder zum Histidinring oder zur Aminogruppe des Dipeptids gehört. Die Möglichkeit zur Ausbildung von **Wasserstoffbrückenbindungen** innerhalb eines bestimmten Bindungsmotivs ist essentiell für die Bevorzugung des Histidin-Stickstoffatoms oder desamins als Elektronendonator. Das **charge solvated Bindungsmotiv** ist das verbreitetste innerhalb aller gefundenen Isomere. Mehrere Strukturen wiesen wasserstoffbrückengebundene Protonen auf. Diese können als Übergänge zwischen den *charge solvated* und den *salt bridge* Bindungsmotiven gesehen werden. **CID breakdown curves** der kationischen Komplexe der Dipeptide mit  $K^+$ ,  $Rb^+$  und  $Cs^+$  ergaben eine angemessene Übereinstimmung der  $E_{com}^{50\%}$  Werte mit DFT ermittelten freien Bindungsenthalpien. CID führte zu einer Vielzahl an Fragmentationskanälen der  $Li^+$  und  $Na^+$  Dipeptid-Komplexe und zu einer unbefriedigenden Übereinstimmung zwischen den  $E_{com}^{50\%}$  Werten und den freien Metall-Dipeptid Bindungsenthalpien. **Gasphasen H/D-Austauschreaktionen** der protonierten Dipeptide mit  $ND_3$  ergaben einen Austausch aller labilen Protonen mit vergleichbaren relativen partiellen Geschwindigkeitskonstanten. Die Annahme einer parallelen Einfach- und Doppelaustauschreaktion innerhalb eines Einzelstoßes führte zu einer Erhöhung der Qualität der kinetischen fits pseudo erster Ordnung an die experimentellen Daten. Die  $Li^+$ ,  $Na^+$  und  $K^+$  Dipeptid-Komplexe wiesen eine Verringerung der Gesamtzahl ausgetauschter Protonen, signifikant niedrigere Geschwindigkeitskonstanten für den H/D Austausch und nur Einfachaustauschreaktionen auf.

Die Komplexierung des doppelt geladenen Übergangsmetallkations  $Zn^{2+}$  durch ein deprotoniertes Carnosinmolekül führt zu einer grundlegenden Veränderung der Konformation gegenüber den Alkalimetallionenkomplexen. Frühere DFT Rechnungen der Gasphasenstruktur von **[Carn-H, $Zn^{II}$ ] $^+$**  wurden jetzt mit IR-MPD Spektren verglichen. Die IR-MPD Spektren wiesen mehrere der von DFT vorhergesagten IR-Absorptionen auf, wobei die Gesamtübereinstimmung der Bandenpositionen nicht befriedigend war. Der Komplex **[Carn-H, $Zn^{II}$ ] $^+$**  wurde weitergehend dafür benutzt, um die **bandenspezifische Verstärkung** der Fragmentationseffizienz durch die Anwendung eines resonanten **2-Farben IR-MPD pump/probe** Schemas zu untersuchen. Die Steigungen der linearen fits der doppellogarithmisch aufgetragenen experimentellen Daten (Fragmentationseffizienz gegen Pulsenergie des Lasers) sollen zu der Zahl der zur Fragmentation benötigten Photonen korrelieren.

Mit diesem Ansatz konnte keine nachvollziehbare Photonenzahl für eine Fragmentation des Moleküls ermittelt werden. Dennoch konnte gezeigt werden, dass sich die Zahl der zur Fragmentation benötigten Photonen des *pump* Lasers durch die Verwendung einer zweiten Laserfarbe verringert. Die Änderung des zeitlichen Abstands zwischen dem *pump* und *probe* Laserpuls hat einen Einfluss auf die Form der Absorptionsbanden. Das Einstrahlen des *probe* Lasers vor dem *pump* Laser führte zu einem **Aufheizen der Moleküle**, das sich in einer Verbreiterung von Banden äußerte. Keine Verbreiterung wurde beobachtet, wenn der *probe* Laser gleichzeitig oder nach dem *pump* Laser eingestrahlt wurde. CID und IR-MPD **Fragmentationskanäle** unterschieden sich in ihrer **relativen Häufigkeit**. Zudem war die relative Häufigkeit der Fragmente spezifisch für die angeregte Schwingung. Diese Studie zeigt grundlegende Ansätze für weitergehende Untersuchungen des Mechanismus der resonanten 2-Farben IR-MPD Spektroskopie auf.

Mehrere **rutheniumhaltige Katalysatoren für Transferhydrogenierungsreaktionen** wurden von L. Ghoochany (Arbeitsgruppe W. Thiel, TU Kaiserslautern) synthetisiert. CID Messungen von isotopenmarkierten Komplexen führten zu folgenden Schlussfolgerungen über den **Aktivierungsprozess des Katalysators**: eine Ruthenium-Stickstoff Bindung wird gespalten, der **Pyrimidinring** des substituierten 2-R-4-(2-pyridinyl)pyrimidin Liganden **rotiert um ca. 160°** und eine **Ruthenium-Kohlenstoff Bindung** wird unter gleichzeitiger Abspaltung eines HCl (oder DCl) Moleküls gebildet. Die CID Amplitude des Massenspektrometers wurde mit Hilfe einer Reihe von "Thermometerionen" kalibriert. **CID breakdown curves** wurden zur Ermittlung der  $E_{\text{COM}}^{50\%}$  Werte dreier unterschiedlich substituierter Katalysatoren genutzt. Mit Hilfe der Kalibrierung wurden schließlich Aktivierungsenergien abgeschätzt. Die erhaltenen Aktivierungsenergien zeigen eine qualitative Korrelation zu den mit DFT ermittelten Aktivierungsenergien. Diese Ergebnisse sind Teil eines Manuskriptes, das bei *Chemistry – A European Journal* eingereicht wurde und sich gegenwärtig im Überarbeitungsprozess befindet. Weitere Studien an dieser Reihe von Rutheniumkomplexen umfassten CID Experimente an ligandenausgetauschten Komplexen, **1- und 2-Farben IR-MPD Spektroskopie, Gasphasenreaktionen mit D<sub>2</sub>** und die **DFT basierte Modellierung** der Reaktionskoordinate der D<sub>2</sub> Aufnahme. Der Austausch des anionischen Chlorido Liganden in Lösung führte zu drei Komplexen mit unterschiedlichen Fragmentationsschwellen. Die mittels CID ermittelten Fragmentationsamplituden entsprechen der durch das HSAB Konzept vorhergesagten Reihenfolge. 1-Farben IR-MPD Messungen an zwei der Komplexe zeigten nur wenige Banden. Resonante 2-Farben IR-MPD Spektroskopie erhöhte die Gesamtfragmentationseffizienz und machte mehrere dunkle Banden sichtbar. DFT berechnete IR Absorptionsspektren stimmen gut mit den IR-MPD Spektren überein, wobei immer noch mehrere

Banden nicht sichtbar sind. Gasphasenreaktionen mit  $D_2$  zeigten eine Massenzunahme der aktivierten Komplexe um +4 m/z. Dies wurde als eine Aufnahme eines  $D_2$  Moleküls unter heterolytischer Spaltung des  $D_2$  interpretiert und kann mit der Rückreaktion der Aktivierung verglichen werden. Die **Reaktionskoordinate** der  **$D_2$  Aufnahme** wurde mit Hilfe von **DFT auf dem B3LYP/cc-pVDZ Theorielevel** modelliert und es wurden unterschiedliche Aktivierungsenergien in Abhängigkeit des Substituenten ermittelt. Die Reaktionen dreier unterschiedlich substituierter Komplexe mit  $D_2$  ergaben unterschiedliche relative partielle Geschwindigkeitskonstanten. Der Vergleich zu nach der Theorie des Übergangszustandes ermittelten Geschwindigkeitskonstanten zeigt eine qualitative aber keine quantitative Korrelation zu den experimentellen Ergebnissen. Diese Studie trägt zu unserer anhaltenden Arbeit an der Zuordnung und Isolation von Reaktionsintermediaten in der Gasphase bei. Derzeit laufen Arbeiten an der Untersuchung der Dynamik des Aktivierungsprozesses sowie auch an der Abschätzung von Geschwindigkeitskonstanten für die  $D_2$  Aufnahme anhand der RRKM Theorie.

Eine Reihe **dysprosiumbasierter Komplexe** wurde von A. Bhunia (Arbeitsgruppe P.W. Roesky, KIT) synthetisiert und innerhalb des Transregio-Sonderforschungsbereichs SFB/TRR 88 "3MET" untersucht. Wir trugen mit **ESI-MS, CID**, sowie mit Experimenten zu **H/D Austauschreaktionen** in der Gasphase zu diesen Untersuchungen bei. Diese Komplexe bestehen aus einem zentralen dreifach-geladenen Dysprosium Kation und zwei identischen *salen* Liganden, die die Komplexierung von bis zu zwei weiteren Übergangsmetallen erlauben. Der einmetallige Dysprosium Komplex zeigt in SQUID Messungen das Verhalten eines **Einzelmolekülmagneten**, während die Aufnahme **zweier zweifach geladener Mangan Kationen** zu **ferromagnetischem Verhalten** führte. Die Wechselwirkung der terminalen Amingruppen mit den Manganionen führte zu einer Hinderung der H/D Austauschreaktion mit  $ND_3$  in der Gasphase. Alternativ ermöglichen die terminalen Amingruppen des monometallischen Dysprosium Komplexes die **Bindung** von bis zu **zwei  $Ni^{2+}(tren)$  Komplexen**. ESI-MS Untersuchungen zeigten durch Deprotonierung oder Protonierung in Lösung sowohl anionische als auch kationische Komplexe. CID Untersuchungen führten zu Fragmentationsschemata, die gut mit der angenommenen Struktur der Komplexe korrelieren. Diese Ergebnisse sind Teil zweier Publikationen in *Inorganic Chemistry* und *Dalton Transactions*. In dieser Arbeit werden weitere Untersuchungen an dieser Reihe von ein-, zwei- und dreimetalligen Komplexen vorgestellt. **H/D Austauschreaktionen** mit  $D_2O$  in Lösung führten zu einem Austausch aller austauschbaren Protonen der kationischen Komplexe. Anionische Komplexe zeigten einen teilweisen oder vollständigen Austausch. Der Vergleich von **1- und 2-Farben-IR-MPD** Spektren anionischer, kationischer und H/D ausgetauschter Komplexe ermöglichte die

Zuordnung von Schwingungsbanden. Des Weiteren wurden die **bevorzugten Protonierungsstellen** durch einen Vergleich von IR-MPD Experimenten mit den Ergebnissen der H/D Austauschreaktionen in Lösung und in der Gasphase ermittelt. Diese Studie trägt zu unserer anhaltenden Arbeit an der Bestimmung magnetischer Eigenschaften isolierter Ionen in der Gasphase am Helmholtz-Zentrum Berlin bei.

Der Komplex  $[(^4\text{CpCo})_2(\mu\text{-C}_2\text{Ph}_2)]$  ( $^4\text{Cp}$  = tetraisopropyl-cyclopentadiene) wurde von J. Becker (Arbeitsgruppe H. Sitzmann, TU Kaiserslautern) synthetisiert. Der kationische Komplex und mehrere seiner Reaktionsprodukte wurden mittels ESI-MS charakterisiert. Ein Teil der experimentellen Daten trägt auch zu der Diplomarbeit von J. Becker bei. Kationische Reaktionsprodukte und der Komplex selbst wurden weitergehend mittels **IR-MPD** untersucht. Die IR-MPD Fragmentationseffizienz änderte sich deutlich mit dem an den Komplex  $[(^4\text{CpCo})_2(\mu\text{-C}_2\text{Ph}_2)\text{X}]^+$  gebundenen Atom/Molekül ( $\text{X}=\text{H}$ ,  $(\text{H}+\text{CH}_3\text{CN})$ ,  $\text{Cl}$ ,  $\text{O}$ ). Der Beitrag verschiedener Fragmentationskanäle zur Gesamtfragmentationseffizienz wurde im Detail untersucht. Eine Erhöhung des Photonenflusses führte zu einer Sättigung des Beitrags des meistens bevorzugten Verlust von  $\text{C}_2\text{Ph}_2$  und zu einer Fragmentierung der Alkylketten der  $^4\text{Cp}$ -Ringe. Mehrere **Absorptionsbanden** wurden im **mittleren und nahen Infrarot** gefunden. Ein Modellsystem aus der Literatur wurde verwendet, um ein ausreichendes Theorielevel für die DFT Rechnungen zu ermitteln. Kriterium für das Theorielevel war die ausreichende Beschreibungen der Bindungsverhältnisse innerhalb der Kristallstruktur. Das **B3LYP** und das **B97D** Funktional in Zusammenhang mit cc-pVDZ und Stuttgart 1997 ECP Basissätzen wurde für weitere Rechnungen des Komplexes  $[(^4\text{CpCo})_2(\mu\text{-C}_2\text{Ph}_2)]^+$  und seiner Reaktionsprodukte verwendet. Eine Verlängerung des Co-Co Bindungsabstandes konnte für die kationischen Reaktionsprodukte mit  $\text{Cl}^-$  und  $\text{O}^{2-}$  beobachtet werden. DFT Rechnungen mit den B3LYP und B97D Funktionalen führten zu unterschiedlichen elektronischen Grundzuständen. Es konnte keine gute Übereinstimmung zwischen den mit DFT berechneten IR Absorptionsbanden und den IR-MPD Spektren erzielt werden. Mehrere durch DFT berechnete Absorptionsbanden konnten nicht gefunden werden, besonders diejenigen, die zu symmetrischen Streckenschwingungen aliphatischer  $\text{CH}_n$  ( $n=2,3$ ) oder aromatischer CH Gruppen gehören. Die energetisch günstigsten Strukturen aus den Rechnungen beider Funktionalen wurden für zeitabhängige DFT Rechnungen genutzt. Es wurden mehrere elektronische Übergänge im nahen Infrarot berechnet. Diese zeigten eine moderate Übereinstimmung mit den IR-MPD Spektren. Die Wahl des Theorielevels für die DFT und **TD-DFT Rechnungen** scheint nicht ausreichend zu sein, um die experimentellen Ergebnisse zu beschreiben. Die IR-MPD Spektren müssen nochmals gemessen werden, um eine Normalisierung

der Spektren anhand des Photonenflusses vornehmen zu können. Des Weiteren muss eine andere Strategie zur Ermittlung eines geeigneten Theorielevels die *ab initio* Berechnung der untersuchten Moleküle erarbeitet werden.

Eine Kombination verschiedener Methoden angewendet auf isolierte Ionen in der Gasphase und in Lösung ermöglichte die Untersuchung ihrer Struktur, Bindungsenergie und Reaktivität. 1- und 2-Farben IR-MPD Spektroskopie verbunden mit DFT berechneten Absorptionsspektren verschiedener Isomere ermöglichte die Zuordnung von Schwingungsbanden und Bindungsmotiven der Moleküle. Die erhaltenen Ergebnisse sind wichtig für weitere Studien über das Bindungsverhalten von Peptiden und dem Reaktionsverhalten von Metallkomplexen.



## List of Publications

*A Practical and Effective Ruthenium Trichloride-Based Protocol for the Regio- and Stereoselective Catalytic Hydroamidation of Terminal Alkynes*

L.J. Goossen, M. Arndt, M. Blanchot, F. Rudolphi, **F. Menges** and G. Niedner-Schatteburg

Advanced Synthesis & Catalysis (2008), 350(17), 2701

<http://dx.doi.org/10.1002/adsc.200800508>

*X-ray absorption spectroscopy of mass-selected transition metal clusters using a cyclotron ion trap: An experimental setup for measuring XMCD spectra of free clusters*

S. Peredkov, A. Savci, S. Peters, M. Neeb, W. Eberhardt, H. Kampschulte, J. Meyer, M. Tombers, B. Hofferberth, **F. Menges** and G. Niedner-Schatteburg

Journal of Electron Spectroscopy and Related Phenomena (2011), 184(3-6), 113-118

<http://dx.doi.org/10.1016/j.elspec.2010.12.031>

*The interaction of the dipeptide carnosine with alkali metal ions studied by ion trap mass spectrometry*

**F. Menges**, C. Riehn and G. Niedner-Schatteburg

Zeitschrift f. Phys. Chem. (2011), 225(5), 595-609

<http://dx.doi.org/10.1524/zpch.2011.0107>

*Mechanistic Investigation of the Ru-Catalyzed Hydroamidation of Terminal Alkynes*

M. Arndt, Kifah S. M. Salih, A. Fromm, L. J. Goossen, **F. Menges** and G. Niedner-Schatteburg

J. Am. Chem. Soc. (2011), 133(19), 7428-7449

<http://dx.doi.org/10.1021/ja111389r>

*From a Dy(III) Single Molecule Magnet (SMM) to a Ferromagnetic (Mn(II)Dy(III)Mn(II)] Trinuclear Complex*

A. Bhunia, M. Gamer, L. Ungur, L. Chibotaru, A. K. Powell, Y. Lan, P. W. Roesky, **F. Menges**, C. Riehn and G. Niedner-Schatteburg

Inorganic Chemistry (2012), 51(18), 9589-9597

<http://dx.doi.org/10.1021/ic300065x>

*Trinuclear nickel–lanthanide compounds*

A. Bhunia, M. Yadav, Y. Lan, A. K. Powell, **F. Menges**, C. Riehn, G. Niedner-Schatteburg, P. P. Jana, R. Riedel, K. Harms, S. Dehnen and P. W. Roesky

Dalton Transactions (2013), 42(7), 2445-2450

<http://dx.doi.org/10.1039/c2dt31023f>

*Structure-Reactivity Relationships for the Hydrogenation of Carbon Dioxide with Ruthenium Complexes Bearing Pyridinylazolato Ligands*

K. Muller, Y. Sun, A. Heimermann, **F. Menges**, G. Niedner-Schatteburg, C. van Wüllen and W. R. Thiel

Chemistry – A European Journal (published online)

<http://dx.doi.org/10.1002/chem.201204199>

*Investigation by two-color IR dissociation spectroscopy of Hoogsteen-type binding in a metalated nucleobase pair mimic*

Y. Nosenko, **F. Menges**, C. Riehn and G. Niedner-Schatteburg

Phys. Chem. Chem. Phys. (2013), Advance Article

<http://dx.doi.org/10.1039/C3CP44283G>

*Heterobimetallic Cuprates Consisting of a Redox-Switchable, Silicon-Based Metalloligand: Synthesis, Structures, Electronic Properties, and Catalytic Activities*

S. Styra, S. González-Gallardo, F. Armbruster, P. Oña-Burgos, E. Moos, M. Vonderach, P. Weis, O. Hampe, **F. Menges**, M. Gaffga, G. Niedner-Schatteburg and F. Breher

Chemistry - A European Journal (published online 06/2013)

<http://dx.doi.org/10.1002/chem.201300586>

*C-H Activation at a ruthenium(II) complex: The key step for a base free catalytic transfer hydrogenation*

L. Taghizadeh Ghoochany, S. Farsadpour, **F. Menges**, Y. Sun, G. Niedner-Schatteburg and W. R. Thiel

*European Journal of Inorganic Chemistry (accepted)*



---

## Danksagung

Herrn Prof. Dr. Gereon Niedner-Schatteburg möchte ich für die Betreuung, die gute Zusammenarbeit und den mir eingeräumten Freiraum während meiner Dissertation danken. Auch für die vielen tiefgreifenden Diskussionen und die Entwicklungsmöglichkeiten, die ich hier mit anstoßen und erleben konnte.

Herrn Prof. Dr. Markus Gerhards danke ich für die Übernahme des Zweitgutachtens und für die vielen spannenden Diskussionen auf dem PC Flur. Herrn Prof. Dr. Werner Thiel für die Übernahme des Kommissionsvorsitzes und für die Offenheit für Kooperationsprojekte.

Herrn PD Dr. Christoph Riehn möchte ich für die Betreuung und die stete Diskussionsbereitschaft, die gute Kooperation und Orientierung in meinen Forschungsfeldern danken.

Lars Barzen gilt mein besonderer Dank innerhalb der Doktorand\_innengruppe, für seine stete Bereitschaft mir zuzuhören und viele Projekte innerhalb des Arbeitskreis mit anzustoßen.

Der „alten Garde“ Anita Lagutschenkov, Britta Pfeffer, Stephanie Jaberg, Bernd Hofferberth und Heinrich Kampschulte möchte ich für die Hilfe beim Einstieg in den Arbeitskreis und die Unterstützung der Herausbildung meiner technischen Fähigkeiten danken.

Yevgeniy Nosenko danke ich für das Einbringen neuer Techniken und Fähigkeiten in unsere gemeinsamen Projekte, die stete Hilfsbereitschaft und das präzise Diskutieren.

Den langjährigen Kolleg\_innen Christine Merkert, Jennifer Meyer, Matthias Tombers und Thomas Kolling danke ich für die gemeinsame Zeit und die gegenseitige Hilfe.

Maximilian Gaffga danke ich für die Hilfe bei vielen Messungen, das Eintreten in meine Fußstapfen und das er mich als Betreuer akzeptiert hat.

Den „Neuen“, Jonathan Meyer, Jennifer Mohrbach, Joachim Hewer, Dimitri Imanbaew und Johannes Lang danke ich für die Fortführung unserer Projekte und das engagierte Einbringen in unseren Arbeitskreis.

Dr. Marc Proscenc danke ich für die wissenschaftlichen Anregungen und gute, unverkrampte Diskussionen. Prof. Dr. Christoph van Wüllen danke ich für die Bereitstellung der Recheninfrastruktur und seiner lebendigen Art des Diskutierens.

Ein besonderer Dank an Hilde Seelos, Sybille Heieck, Petra Wetzels, Hans-Peter Meyer und Frau Krull für die jahrelange Hilfe und dem Abarbeiten der Papierberge.

Den Kolleg\_innen aus dem Arbeitskreis Gerhards und van Wüllen ein Dank für die gemeinsame Zeit, aus persönlichen Gründen insbesondere an Tobias Martin.

Gedankt sei auch den vielen Arbeitskreisen der eigenen und anderer Universitäten für die gute Zusammenarbeit und die fruchtbaren Kooperationen:

AK Gooßen (TU Kaiserslautern), AK Thiel (TU Kaiserslautern), AK Sitzmann (TU Kaiserslautern), AK Roesky (KIT Karlsruhe), AK Breher (KIT Karlsruhe), AK Brutschy (Uni Frankfurt/Main)

Gedankt sei auch den studentischen Hilfskräften, die mir über die Jahre viel zugearbeitet haben, den Vertiefungsstudierenden und Studienarbeitern, die ich betreuen durfte, den Studierenden, Mitarbeiter\_innen und Wissenschaftler\_innen aus dem Fachbereich (insbesondere der Chemikalienausgabe und dem Dekanat) und aus der „großen Welt“, die mir persönliche Rückmeldungen gegeben haben und die mich unterstützt haben.

Den Pfadfindern der DPSG Stamm Fridtjof Nansen Kaiserslautern gilt mein besonderer Dank für dutzende Fahrten, schöne Abende, die gemeinsame Arbeit und für die gegenseitige Unterstützung in allen Lebenslagen. Mein Pfadfindersein hat dieses hier erst mit ermöglicht.

Den KoKroaches gilt mein Dank für die gemeinsame Kulturarbeit, den vielen Diskussionen und der schönen Atmosphäre in unserem RoachHouse. Die Heterogenität, das Eintauchen in andere Welten und die die gemeinsame Arbeit gibt Kraft.

Eingebettet ist diese Arbeit als Teil meines Lebens natürlich auch in meine Familie, die zwar in dieser Liste weit hinten steht, aber dies nichts über ihre Rolle dabei aussagt. Vielen Dank an Nicole, Olga und Jürgen für eure Unterstützung.

Der Hans-Böckler-Stiftung danke ich für ein 3-jähriges Promotionsstipendium danken, das mir den Austausch mit vielen spannenden Wissenschaftler\_innen aus unterschiedlichsten Themenbereichen ermöglicht hat.

Eine Dankesliste kann nie abschließend sein, daher bitte ich alle, die ich übersehen, oder nicht namentlich erwähnt habe, mir dieses nachzusehen. Fühlt euch trotzdem bedankt, wenn ihr es nicht mit Recht erwarten würdet, würdet ihr nicht in diese Danksagung hineingeschaut haben.

---

## Curriculum Vitae

Name: Fabian Menges

### Education

- Sep 2007 – June 2013      TU Kaiserslautern, Kaiserslautern (Germany)  
PhD student in Physical Chemistry in the group of Prof. Dr. Niedner-Schatteburg (overall grade “*summa cum laude*”)
- Nov 2001 – Sep 2007      TU Kaiserslautern, Kaiserslautern (Germany)  
Diploma in Chemistry in the group of Prof. Dr. Niedner-Schatteburg (overall grade 1.7)
- Oct 1999 – Nov 2001      TU Kaiserslautern, Kaiserslautern (Germany)  
Basic studies in Chemistry
- Aug 1989 – Jun 1998      Max-Planck-Gymnasium, Ludwigshafen (Germany)  
German Abitur (overall grade 2.8)
- Aug 1985 – Jun 1989      Luitpold-Schule, Ludwigshafen (Germany)



**Eidesstattliche Erklärung:**

Hiermit erkläre ich, Dipl. Chem. Fabian Menges, an Eides statt, dass ich die vorliegende Arbeit gemäß der Promotionsordnung des Fachbereichs Chemie der Technischen Universität Kaiserslautern selbstständig und ohne Benutzung anderer als der angegebenen Quellen und Hilfsmittel verfasst habe.

Alle Stellen der Arbeit, die wörtlich oder sinngemäß aus Veröffentlichungen oder aus anderen fremden Mitteilungen entnommen wurden, sind als solche einzeln kenntlich gemacht.

Kaiserslautern, 19.06.2013

---

